

BNWL-SA-3093
VOLUME II

MASTER

LECTURE SERIES
FAST REACTOR SAFETY TECHNOLOGY
AND PRACTICES

VOLUME II
ACCIDENT ANALYSIS

March 1970

BATTELLE



NORTHWEST

BATTELLE MEMORIAL INSTITUTE

PACIFIC NORTHWEST LABORATORIES

BATTELLE BOULEVARD P. O. BOX 999 RICHLAND WASHINGTON 99352

BNWL-SA-3093
VOLUME II

DISTRIBUTION OF THIS DOCUMENT IS ~~LIMITED~~

DISCLAIMER

This report was prepared as an account of work sponsored by an agency of the United States Government. Neither the United States Government nor any agency Thereof, nor any of their employees, makes any warranty, express or implied, or assumes any legal liability or responsibility for the accuracy, completeness, or usefulness of any information, apparatus, product, or process disclosed, or represents that its use would not infringe privately owned rights. Reference herein to any specific commercial product, process, or service by trade name, trademark, manufacturer, or otherwise does not necessarily constitute or imply its endorsement, recommendation, or favoring by the United States Government or any agency thereof. The views and opinions of authors expressed herein do not necessarily state or reflect those of the United States Government or any agency thereof.

DISCLAIMER

Portions of this document may be illegible in electronic image products. Images are produced from the best available original document.

LEGAL NOTICE

This report was prepared as an account of work sponsored by the United States Government. Neither the United States nor the United States Atomic Energy Commission, nor any of their employees, nor any of their contractors, subcontractors, or their employees, makes any warranty, express or implied, or assumes any legal liability or responsibility for the accuracy, completeness or usefulness of any information, apparatus, product or process disclosed, or represents that its use would not infringe privately owned rights.

PACIFIC NORTHWEST LABORATORY
operated by
BATTTELLE MEMORIAL INSTITUTE
for the
U. S. ATOMIC ENERGY COMMISSION
Under Contract # AT(45-1) 1830

LECTURE SERIES
FAST REACTOR SAFETY TECHNOLOGY AND PRACTICES

VOLUME II
ACCIDENT ANALYSES

LEGAL NOTICE
This report was prepared as an account of work sponsored by the United States Government. Neither the United States nor the United States Atomic Energy Commission, nor any of their employees, nor any of their contractors, subcontractors, or their employees, makes any warranty, express or implied, or assumes any legal liability or responsibility for the accuracy, completeness or usefulness of any information, apparatus, product or process disclosed, or represents that its use would not infringe privately owned rights.

Compiled by
P. L. Hofmann
Reactor & Plant Technology Department
FFTF

March 1970

BATTELLE MEMORIAL INSTITUTE
PACIFIC NORTHWEST LABORATORIES
RICHLAND, WASHINGTON 99352

LIST OF CONTRIBUTORS

W. L. Bunch

C. L. Fies

C. D. Flowers

G. L. Fox

A. L. Gunby

J. W. Hagan

J. P. Hale

J. E. Hanson

H. G. Johnson

J. E. Krajicek

W. W. Little, Jr.

R. N. Madsen

A. Padilla, Jr.

R. E. Peterson

P. R. Shire

D. E. Simpson

D. D. Stepnewski

A. E. Waltar

TABLE OF CONTENTS

<u>Number</u>	<u>Title</u>	<u>Author</u>
<u>Volume 1 - Safety Practices and Background Information</u>		
I.	Safety and Regulatory Requirements and Practices	D. E. Simpson
II.	Key Problems in Fast Reactor Safety	D. E. Simpson
III.	Classification of Fast Reactor Accidents and Accident Severity Levels	D. D. Stepnewski
IV.	Biological Effects of Radiation	W. L. Bunch
V.	Shielding Fundamentals	W. L. Bunch
VI.	Reactor Siting Problems	J. P. Hale
VII.	Fundamentals of Fast Reactor Kinetics	W. W. Little, Jr.
VIII.	Principal Reactivity Coefficients	W. W. Little, Jr.
IX.	Sodium Fluid Dynamics	A. Padilla, Jr.
<u>Volume 2 - Accident Analyses</u>		
X.	Fuel Failure Mechanics and Failure Propagation	J. E. Hanson
XI.	Reactivity Accidents	D. D. Stepnewski and C. L. Fies
XII.	Analysis of Loss of Cooling Accidents	H. G. Johnson et al.
XIII.	Reactor Protection Systems	C. L. Fies
XIV.	Protective Instrumentation	R. E. Peterson
XV.	Mathematical Models of Reactor Power Excursions	A. E. Waltar
XVI.	Mathematical Models of Reactor Disassembly	A. E. Waltar
XVII.	Energy Release Mechanisms	A. Padilla, Jr.
XVIII.	Effects of Reactor Accidents on Reactor Vessel and Head	G. L. Fox
XIX.	Sodium Fires	P. R. Shire
XX.	Survey of Fast Reactor Safety R&D Programs	J. W. Hagan

X. FUEL FAILURE MECHANICS AND FAILURE PROPAGATION

J. E. Hanson

A. Introduction

This lecture will address itself to those aspects of fuel pin performance which relate to the safety characteristics of the Fast Test Reactor. Postulated fuel failure mechanisms and thresholds for the principal classes of accidents in fast reactors will be defined and then related to the design safety criteria for the fast test reactor.

B. Background

To provide a foundation for this discussion, I would like to briefly review the current FFTF reference fuel pin design. As illustrated in Figure X.1, the cladding is 20% cold worked 316 stainless steel, 0.230 inch outside diameter with a 15 thousandth inch wall thickness. The fuel column is 36 inches long and is composed of mixed oxide fuel pellets of about 90% of theoretical density.

For the purpose of the analyses which I will be discussing later, the steady-state operating conditions of the fuel pin were determined to be as illustrated on the next figure (Fig. X.2). We also assumed, for purposes of fission gas inventory calculations, that the fuel has been burned to 80,000 MWd/MT peak. This results in the formation of 287 cc of fission gas at STP.

The end-of-life steady-state internal pressure in the fuel pin is a function of the fission gas released from the fuel. In determining the required fission gas plenum volume for a particular fuel pin design, it is usually customary to assume that all the fission gas generated in the fuel is released to the pin plenum. For the analysis of fuel pin behavior under

accident conditions, this is not satisfactory since, as illustrated by the next figure (Fig. X.3), not all the fission gas is released. The data presented in this graph represents most of the mixed oxide fuel fission gas release data available today. As can be seen, irrespective of fuel form and heat generation rate, there seems to be a saturation effect so that at burnups of about 50 to 60,000 MWd/MT, roughly 80% of the gas is being released from the fuel. The significance of the fact that fission gases are retained in the fuel lies in the potential for these gases, upon release and expansion, to become the driving force for fuel redistribution and a possible cause of fuel pin failure propagation. I shall further develop this point later on.

C. Radiation Effects - Fuel and Cladding

Just for a little additional background, I would like to briefly illustrate the effect of radiation on fuel and cladding. The next figure (Fig. X.4) illustrates the characteristic effect of fissioning in a ceramic fuel pellet. The center hole is formed by redistribution of the porosity initially present in the pellet and by the densification of fuel subjected to temperatures beyond about 1450°C. The white inclusions in the irradiated fuel pellet are metallic fission products, such as ruthenium, molybdenum, palladium, and technetium which agglomerate and form little ingots. In some cases, usually when the fuel has been molten late in life, these ingots can become relatively massive. Only recently have we seen any evidence that these metallic fission products may interact with the cladding. Since our observations, which have yet to be completed, are based on a fuel specimen which was subjected to rather extreme operating conditions, we cannot yet draw any

definite conclusions about the potential magnitude of this problem except to say that, in the past, the ingots have been relatively well behaved and rather inert as far as fuel and cladding compatibility were concerned.

Fuel pin cladding material in a liquid-metal-cooled, oxide-fueled reactor really takes a beating. On the outside surface, the sodium coolant can cause corrosion and erosion. Usually, as illustrated by the next figure (Fig. X.5) which shows cladding taken from a fuel pin exposed to 1060°F sodium in the CCTL MK-I test, the effect of the sodium environment is tolerable. It is known, however, that the impurity content of the sodium can have a substantial effect on the resistance of the metal to corrosion so coolant chemistry must be carefully controlled at all times.

Subjecting the stainless steel cladding material to neutron bombardment results in the formation of voids which manifest themselves as a volume increase of the metal. The next figure (Fig. X.6) is an electron microscope picture of stainless steel irradiated in EBR-II. This is a fairly recently discovered phenomenon, and the basic mechanisms involved are not yet understood. Understandably, a great deal of attention is being given to learning, first of all, how to live with metal swelling in the design of the FTR and, secondly, what can be done from a metallurgical basis to minimize or eliminate swelling in metals for fast-reactor applications. On the inner surface, the cladding is subjected to deformation caused by fuel swelling and growth induced by the accumulation of fission products and also to chemical attack by fission products. At the moment, iodine and cesium seem to be the nasty actors which attack the grain boundaries and cause degradation of the metal properties. The next figure (Fig. X.7) illustrates the extent of fuel-

cladding interaction observed in one irradiation test specimen. The metallic stringers are cladding material which is believed to have been deposited in the fuel by a transport process which involves iodine. Only recently with the aid of the electron microprobe has it been possible to identify some of the elements involved in these reactions and then only after very careful preparation of the samples.

An effect of time at elevated temperature is embrittlement of the cladding by the precipitation of carbide at the grain boundaries. This is illustrated in Figure X.8. Some recent test results indicate that radiation may enhance the carbide precipitation.

By now you will recognize that I have given myself a number of excuses for telling you I cannot really predict how a fuel pin will behave under long-term steady-state conditions much less accident conditions. So from here on in, it is mostly intuition backed up by a small number of relevant tests.

D. Steady-State Failure

Barring initial startup fuel pin failures, which would most likely be the result of manufacturing defects such as a faulty weld, undetected cladding defects or coolant flow blockage by a sleeping bag in the primary piping, it is fairly obvious that steady-state fuel pin failures would result from degradation of the cladding by chemical attack or overstressing. The location and nature of the failure are extremely difficult to predict under these conditions. In general, due to the higher cladding temperature at the upper end of the fuel pin, this is where one would expect failure to occur under steady-state conditions, since cladding strength is minimum and chemical

activity maximum here. Unfortunately, most of the mixed oxide fuel pins irradiated in a liquid metal environment which have failed have not failed where one would most expect. There have been a number of mixed oxide fuel pin failures in EBR-II, but these have all occurred with encapsulated fuel pins. In general, it was concluded that somehow a gas bubble was formed at the bottom of the pin and then, while floating to the top of the capsule along the very tight pitch spiral wire wrap, it caused melting of the cladding. How the pins would behave under this kind of steady-state failure in a flowing sodium environment is not known. There is some evidence from DFR irradiations of oxide pins that propagation is rather mild if it occurs at all. One trefoil rig showed some evidence of propagation, but it certainly could not have been called catastrophic. The recent failures of the 77-pin subassemblies, believed to be due to gas entrainment in the down-flowing coolant, are really very encouraging since:

- The pin failures did not propagate to adjacent subassemblies, and
- Not all the pins in the subassemblies failed.

It is interesting to note that DFR personnel could "hear" pins popping with their acoustic boiling detectors and that the reactor operation was continued even after failure was suspected.

Fission-gas-leaking pins have been experienced in Rapsodie, but post-irradiation examination of the suspected pins failed to disclose the defects leading one to at least consider the possibility of porous end plugs.

E. Transient Condition Failure Behavior

One of the first tasks we faced was to establish a failure criterion. That is, what cladding stress or strain defined failure. Actually, in our analyses we considered the five criteria shown on the next figure (Fig. X.9).

The non-elastic effective strain limit considers only permanent deformation due to creep and plasticity strain due to exceeding the yield strength of the material.

The total effective strain limit considers elastic (recoverable) strains in addition to the creep and plasticity strains.

The stress criterion based on the yield point means that when the effective stress at any point in the cladding reaches the yield strength of the material, failure occurs.

Criterion Number 4 states that failure occurs when the effective stress at all points in the cladding equals the yield strength. This is true ductile behavior of the cladding.

Criterion 5 represents an extremely brittle condition by defining failure as occurring as soon as the inner surface of the cladding reaches a tensile stress condition. This would cause a crack on the inner surface of the cladding to propagate outward.

Ordinarily, one would not seriously consider Criterion 5 for austenitic stainless steel. However, recent experimental data obtained from burst tests of fuel pin cladding lightly irradiated in EBR-II makes us wonder. Specifically, sections of fuel pins PNL-1-3 and PNL-1-6 which were irradiated in EBR-II to approximately 8500 MWd/MT burnup ($\sim 3 \times 10^{21}$ ϕ t total) were subjected to burst tests at 900°F. The next figure (Fig. X.10) summarizes the burst test results. Two points were significant:

- The brittle failure characteristic of the cladding is not entirely consistent, but
- It occurred more times than not.

The next figure (Fig. X.11) illustrates the microstructures of the cladding after burst testing. It is significant to note that the cracks propagate from the inner surface of the cladding, thus forcing one to conclude that Criterion Number 5 is closest to reality in this case. This cladding failure characteristic was also observed during the post-irradiation examination of mixed oxide fuel pins which were transient irradiated in TREAT.⁽¹⁾

F. Postulated Fuel Pin Behavior under Power Excursion Accidents

The accidents analyzed were reactivity additions of \$5/second and \$50/second from steady-state operating conditions. The calculations did not consider reactor scram. It is well to note that when calculations are made which include the scram circuitry working, fuel pin conditions do not even approach those about to be described.

Normalized power-time histories for the two power excursion cases are given in the next figure (Fig. X.12). The principal response of the fuel pin to these power pulses is illustrated in Figure X.13. As seen, the internal pressure increases very rapidly after a slight delay time. The delay time appears to be inversely proportional to the reactivity addition rate. That is, for the \$5/second ramp rate, the delay time is about 0.25 second and for the \$50/second ramp rate the delay time is about 0.025 second; a factor of ten increase in reactivity addition rate decreases the internal pressure response time by a factor of ten. The delay time, or the time required for

the start of the very fast pressure increase in the fuel pin, is related to the time for fuel melting to progress radially outward to regions of the fuel which still contain fission gases. The values given for the different curves are the steady-state fission gas release values assumed to calculate the initial steady-state gas pressure and the extent of fuel melting required to release fission gases. It is assumed that during transient melting of the fuel, fission gases retained in the fuel from steady-state operation are released as soon as the fuel attains the melting point. The extent and progression of fuel melting during the transients are illustrated in the next two figures (Fig's X.14A and X.14B). These curves were determined from TIGER V computer code analyses as were the cladding temperature histories as shown in Figure X.15.

With the internal pressure history and the cladding temperature history established, the stress-strain history of the cladding can be determined. The PECT-1 computer code was used for these calculations. The next figure (Fig. X.16) summarizes the calculations for the \$50/second transient and the five failure criteria. Of most interest are the hoop stress distributions for each failure criterion. It is seen that at the start-of-steady state (SSS) conditions, the hoop stress is negative (compressive) on the inner surface of the cladding. At time zero, which corresponds to the end of fuel pin life and the initiation of the accident, the hoop stress is still negative at the inner surface. The remaining curves depict the stress distribution at the time, internal pressure, and temperature conditions that satisfy the failure criteria.

Figure X.17 summarizes the time, internal pressure, and cladding temperatures at which failure is expected to occur for each of the criteria. It is seen that in each case Criterion 5 predicts the earliest failure. It is significant to note, however, the very small difference in time for predicted failure for the various criteria. Failure is expected to occur at 27 to 29 inches above the bottom of the fuel column which is the upper terminus of the center void in the fuel. Because failure under these conditions could appear to be initiated by high fission gas pressures, one must anticipate the rapid explosion of gases and probably molten fuel during such an accident. It should be pointed out that for this analysis we purposely did not pick the "hottest" pin in the reactor but a pin which we felt would, when we said it failed, guarantee that fuel pin failures had indeed occurred and the reactor was well on the way to a DBA.

G. Postulated Fuel Pin Behavior under Loss of Coolant Accidents

A similar analysis was performed for the two loss-of-coolant accidents: flow coastdown and pipe rupture.

The fundamental differences in fuel pin behavior between loss-of-coolant accidents and power excursion accidents are:

- In a loss-of-coolant accident, fuel temperatures remain relatively constant during the initial phase of the accident, whereas in the power excursion accident, fuel temperatures rise very rapidly (if they did not, we of course would not get a Doppler effect).
- Cladding temperatures in power excursion accidents remain relatively constant during the initial phases

of the accident, whereas in the loss-of-coolant accidents, cladding temperatures follow the coolant temperature history rather closely.

The next two figures (Fig's X.18A and X.18B) illustrate the coolant flow during the flow coastdown and pipe rupture accidents used in this analysis. Figure X.19 illustrates the cladding temperature histories and Figure X.20 shows the internal pressure histories. The temperature and pressure histories are input, along with steady-state history of the fuel pin, for the PECT code which provides the detailed analysis of the stress-strain history of the cladding. The results of this analysis for the flow coastdown accident are shown in Figure X.21. As in the discussion on pin behavior during the power excursion accident, the conditions to satisfy the various failure criteria are shown. Figure X.22 illustrates these conditions for the pipe rupture accident. A better summary is given in Figure X.23 which tabulates the time and cladding temperature at which failure is expected to occur for the various criteria. It is seen that Criterion 5 would predict fuel pin failure during steady-state and prior to end-of-life burnup. From these results, we would conclude that failure would occur at the top of the fuel column at a cladding surface temperature in the neighborhood of 1600°F.

Finally, comparison of the conditions at failure just described to those previously selected for the fuel damage criteria for the FFTF accident severity levels (Fig. X.24) shows good agreement. Further confirmation of these values through refined calculational procedures and experimental data are required. Of particular importance is the continued assessment of the impact of the intergranular fracture behavior of the fuel pin cladding on steady-state and accident performance limits.

References

- (1) J. E. Hanson and J. H. Field, "Experimental Studies of Transient Effects in Fast Reactor Fuels, Series III, Pre-Irradiated Mixed Oxide ($\text{PuO}_2\text{-UO}_2$) Irradiations Final Report, Transient Irradiations," GEAP-4469, July 1967.

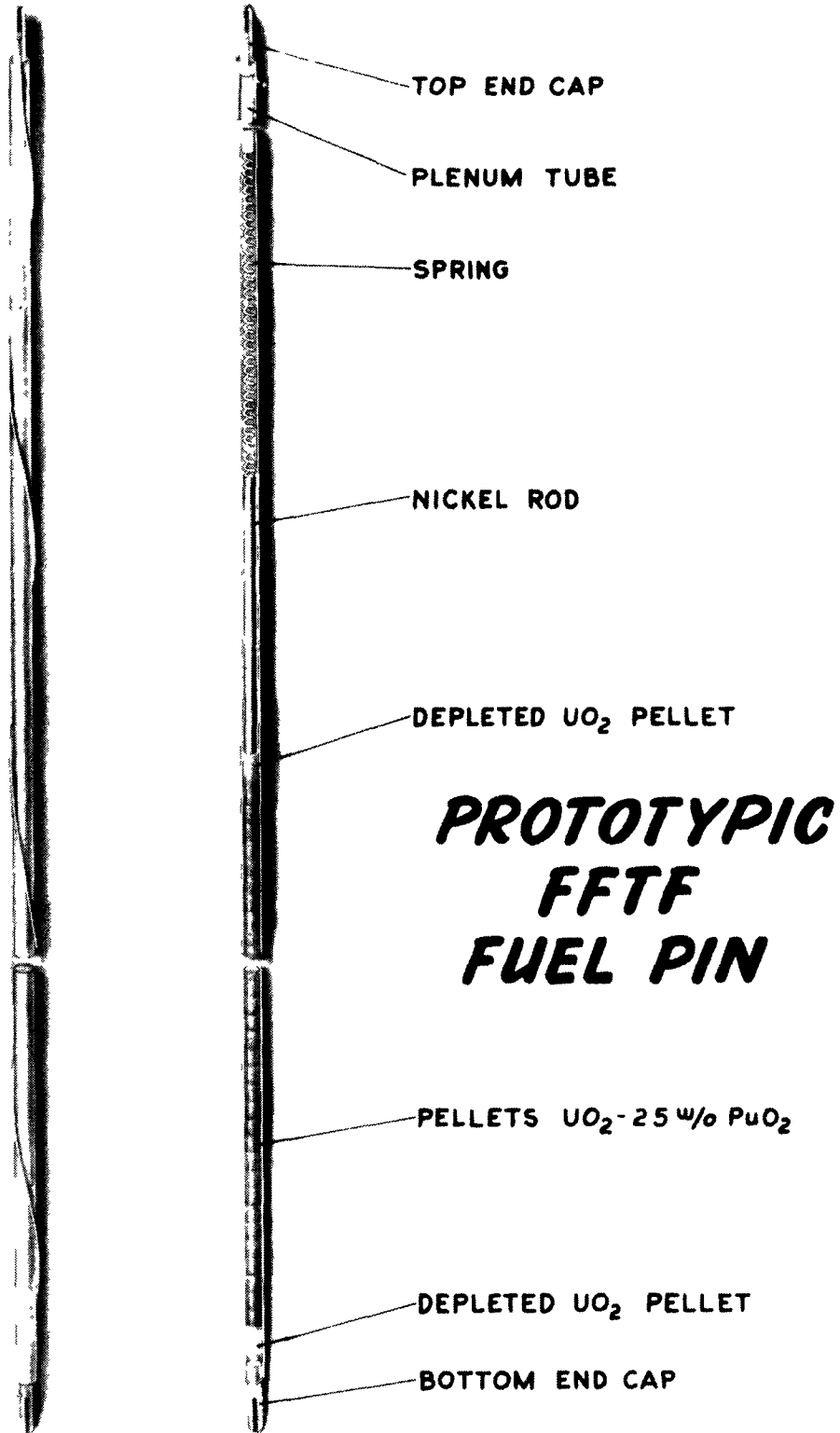


Figure X.1

STEADY STATE OPERATING CONDITIONS

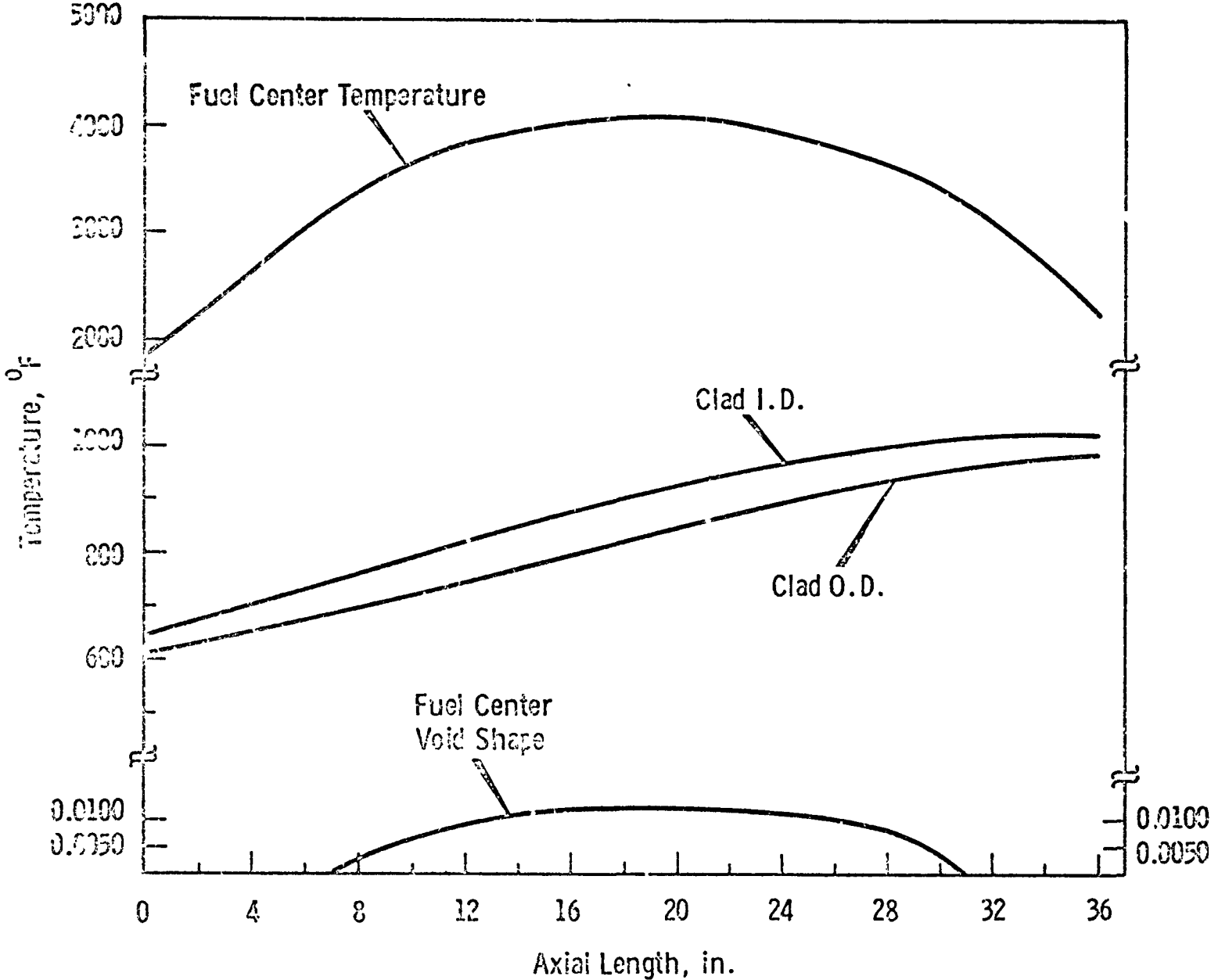


Figure X.2

FISSION GAS RELEASE FROM MIXED OXIDE PRF AND APO FUEL PINS

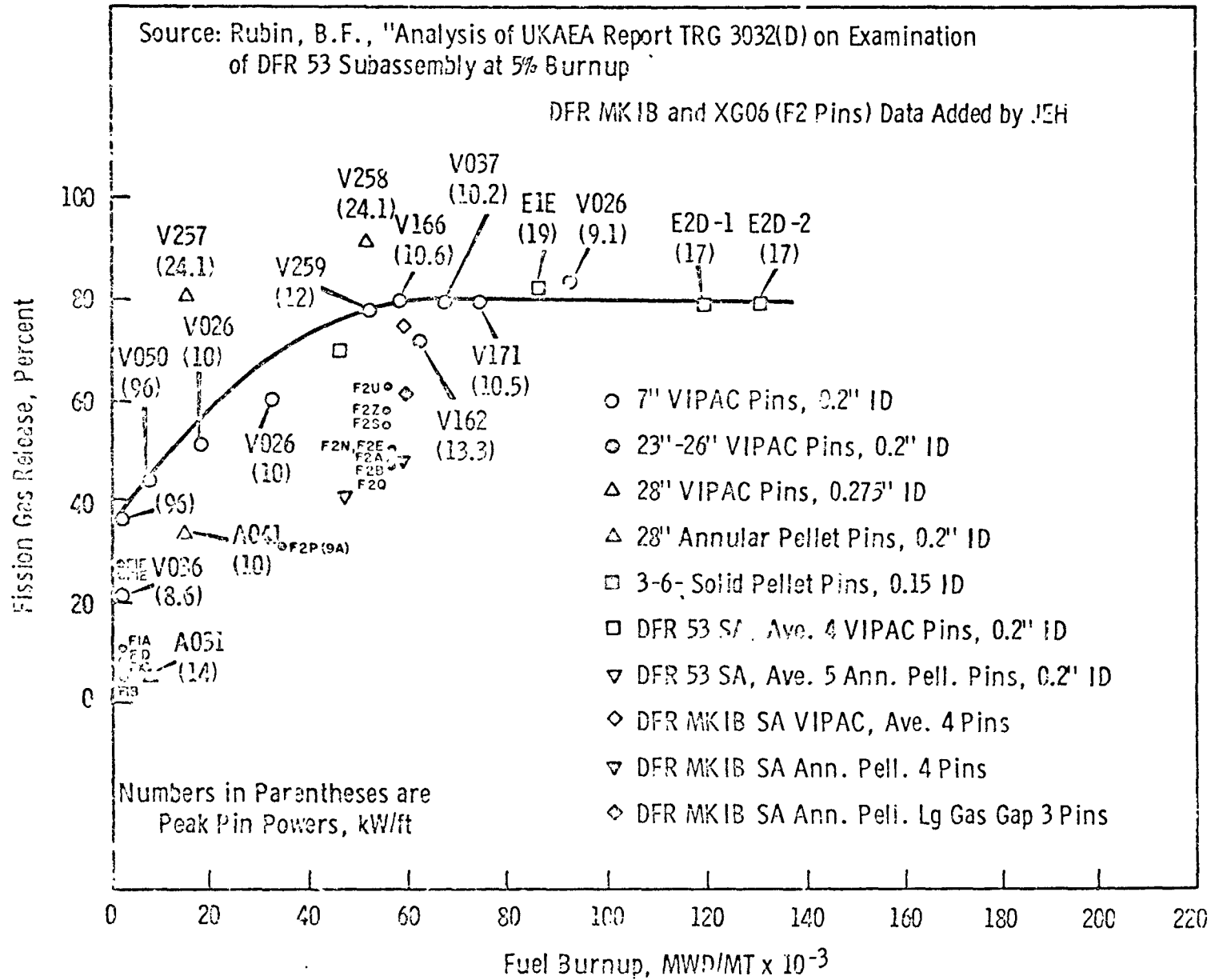
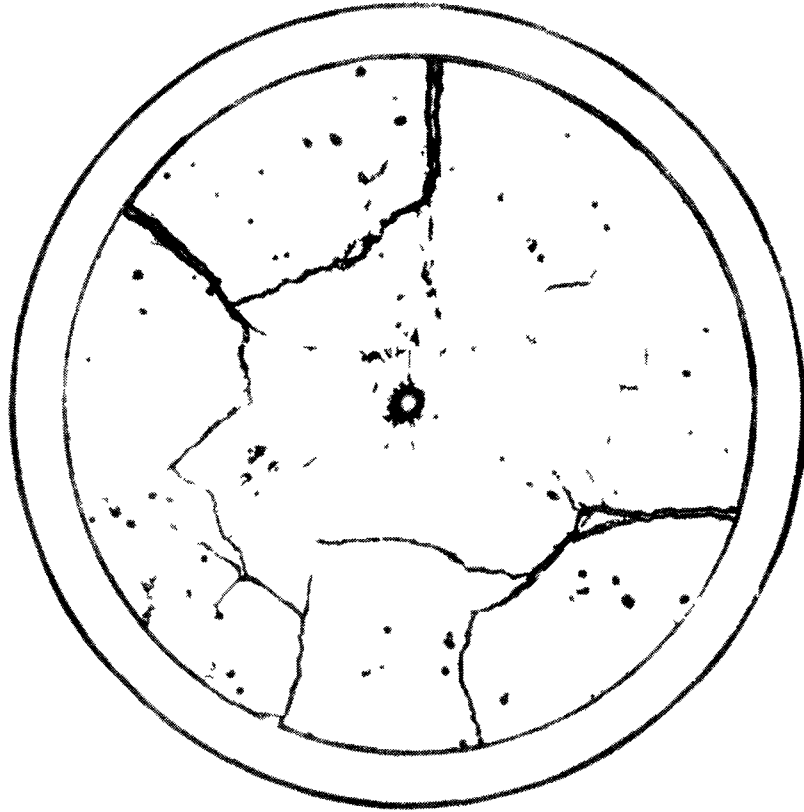


Figure X.3



111 2 1 1

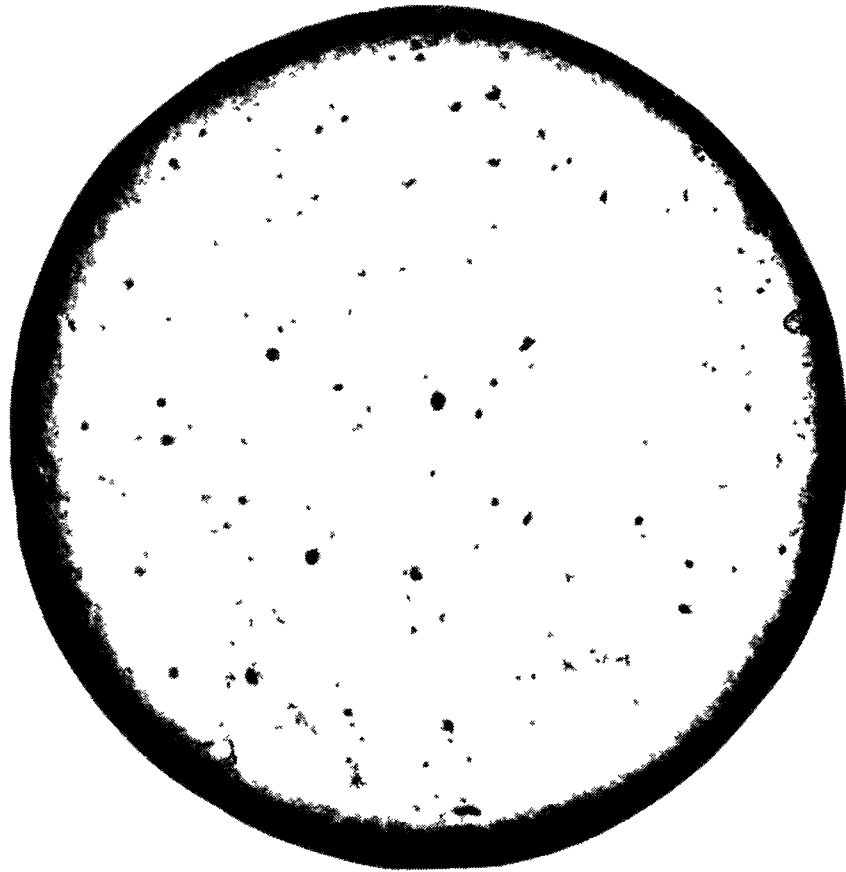
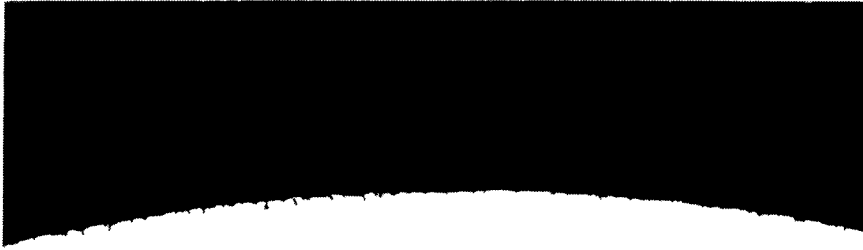


Figure X.4

CLADDING SURFACE AT FIRST RANDOM POSITION ON
FUEL ROD IN 9000 HR, 1060 F SODIUM FLOW TEST



UNETCHED
100X



ETCHED
100X

Figure X.5

VOID FORMATION IN STAINLESS STEEL IRRADIATED
IN A FAST FLUX

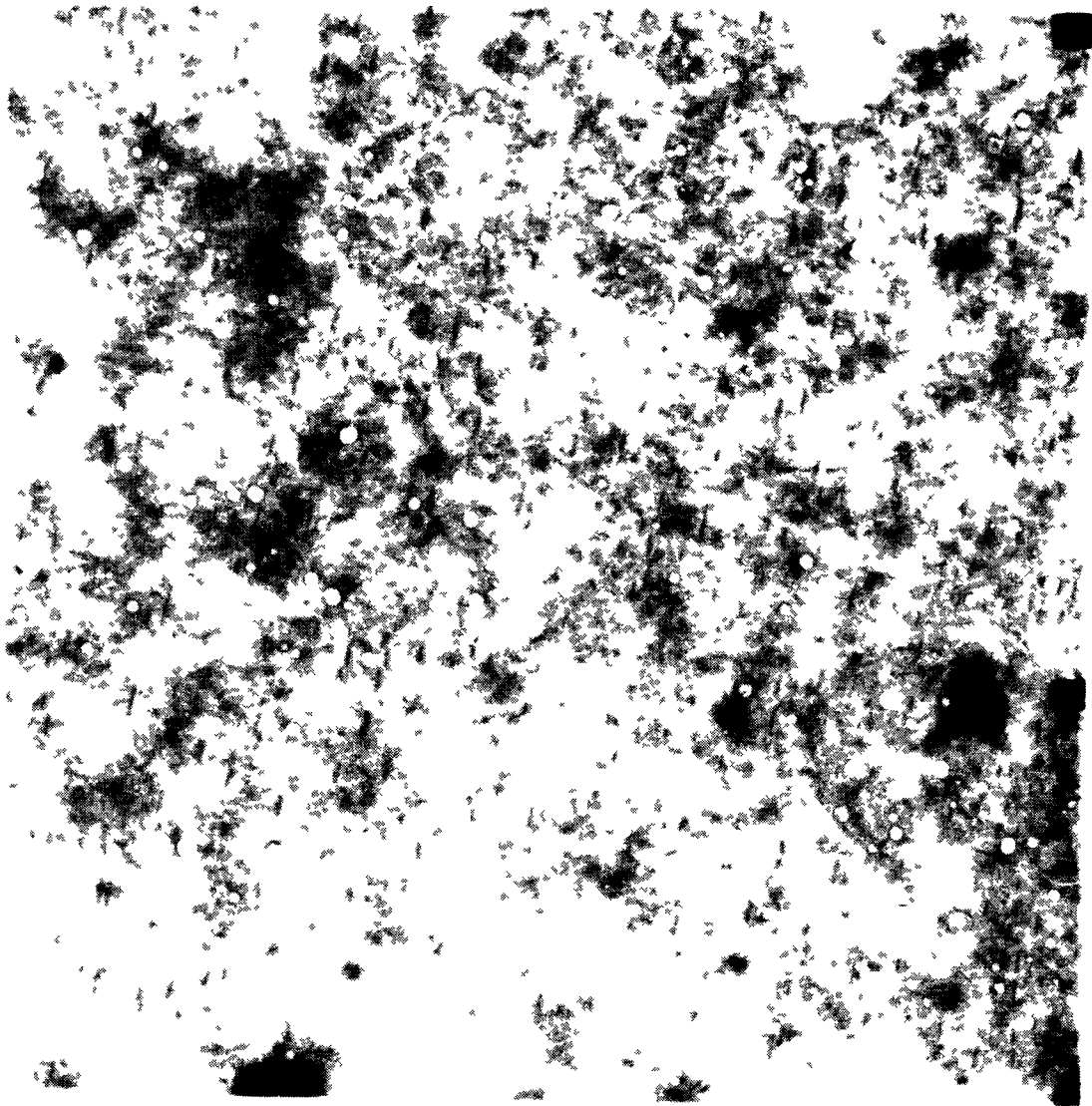
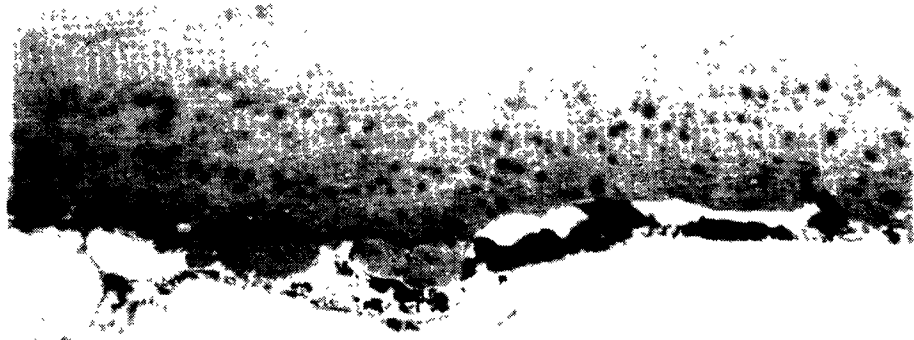


Figure X.6



250X



750X

Fuel Cladding Interaction in BNW-1-6-G

Figure X.7

CARBIDE PRECIPITATION AT THE GRAIN BOUNDARIES. 304 STAINLESS STEEL



Figure X.8

FAILURE CRITERIA

1. NON-ELASTIC EFFECTIVE STRAIN

$$\epsilon_{eff}^N = 0.2\%$$

2. TOTAL EFFECTIVE STRAIN

$$\epsilon_{eff}^T = 0.2\%$$

3. YIELD POINT

$$\sigma_{eff} = \sigma_y \text{ AT ONE POINT}$$

4. DUCTILE FAILURE

$$\sigma_{eff} = \sigma_y \text{ AT EVERY POINT}$$

5. BRITTLE FAILURE - STRESS AT INNER SURFACE OF CLADDING BECOMES TENSILE.

Figure X.9

SUMMARY OF BIAXIAL TEST DATA
LOAD RATE ~20 psi/SEC

<u>SPECIMEN</u>	<u>PRE-TEST HEAT TIME</u>	<u>TEST TEMP.</u>	<u>BURST PRESS.</u>	$\sigma = 7.34 \text{ Pi}$ <u>@ I. D. HOOP STRESS</u>	<u>LIFETIME</u>	<u>$\Delta D/D$ %</u>
"E" LOT-COLD	4 HR.	901 °F	7760 psi	56,960 psi	BURST	19.2%
H ₁ PLENUM (PNLI-6)	5-1/2 HR.	932 °F	8050 psi	59,090 psi	BURST	18.4%
C ₂ FUELED (PNLI-6)	7 HR.	900 °F	@ 3300 psi	22,020 psi	BURST	0.25% 1.0%
C ₃ FUELED (PNLI-6)	5-1/2 HR.	897 °F	9830 psi	72,150 psi	BURST	9.6%
C ₂ FUELED (PNLI-6)	3 HR.	900 °F	3700 psi	27,160 psi	BURST	0.3%
C ₂ FUELED (PNLI-3)	3 HR.	1000 °F	9100 psi	66,790 psi	BURST	6.7%
G ₄ FUELED (PNLI-3)	2 HR.	900 °F	5300 psi	38,900 psi	BURST	

X.21

Figure X.10

CLADDING MICROSTR OF



TRANSGRANULAR FAILURE

21-000013

POWER-TIME HISTORIES

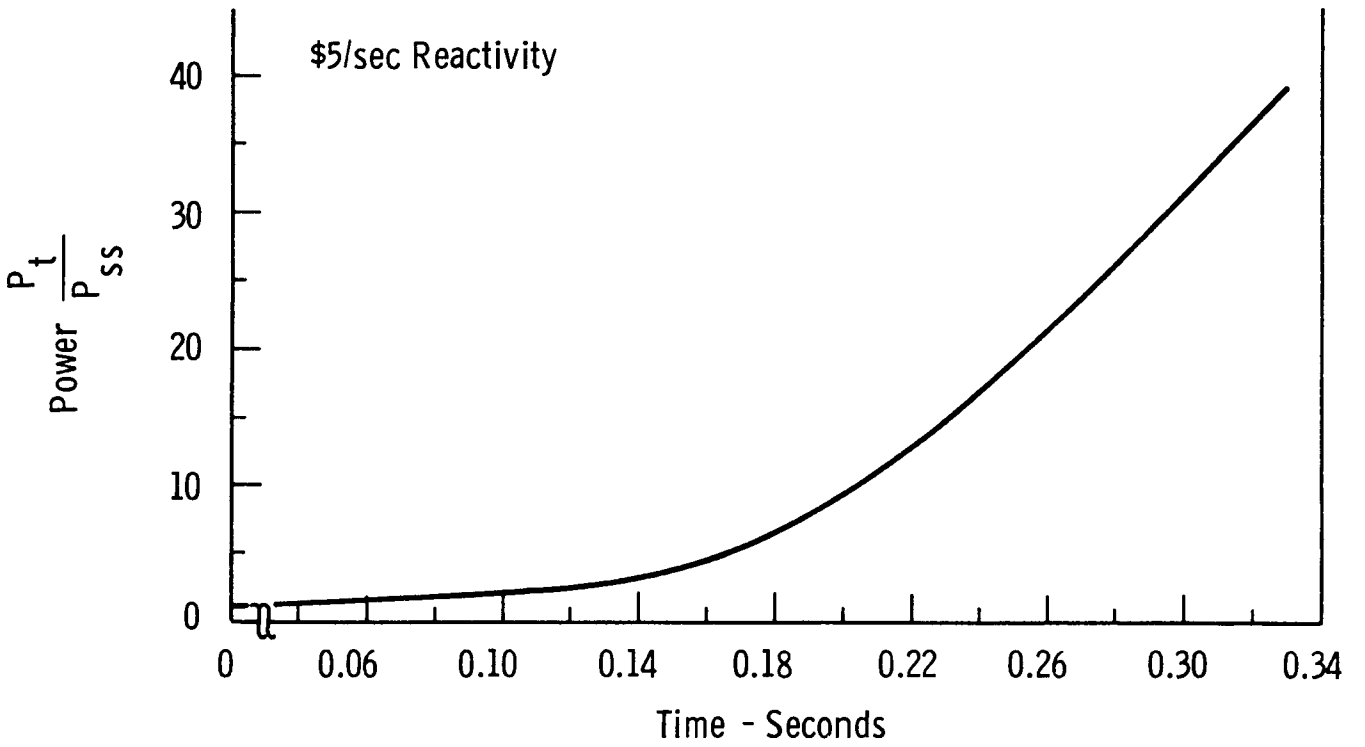
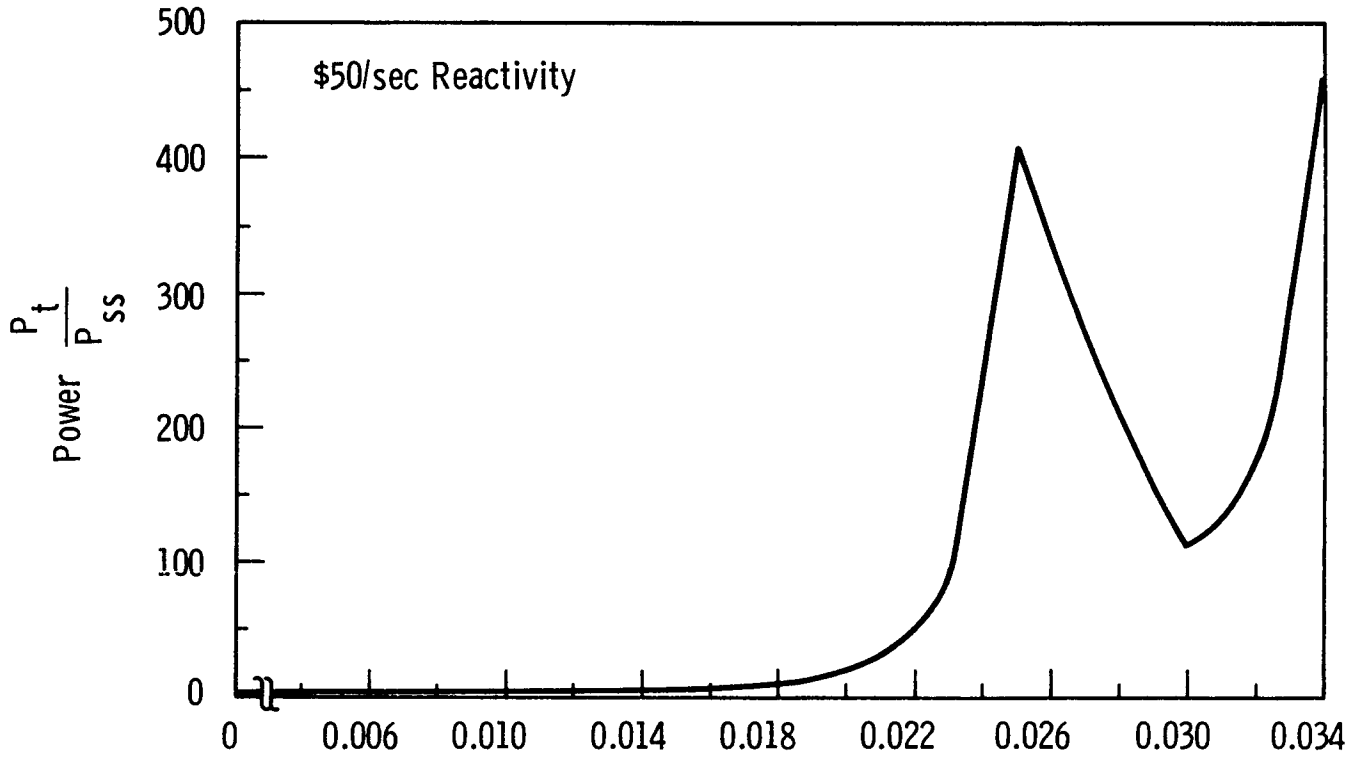


Figure X.12

PRESSURE HISTORY
FOR \$50/SEC TRANSIENT

PRESSURE HISTORY
FOR \$5/SEC TRANSIENT

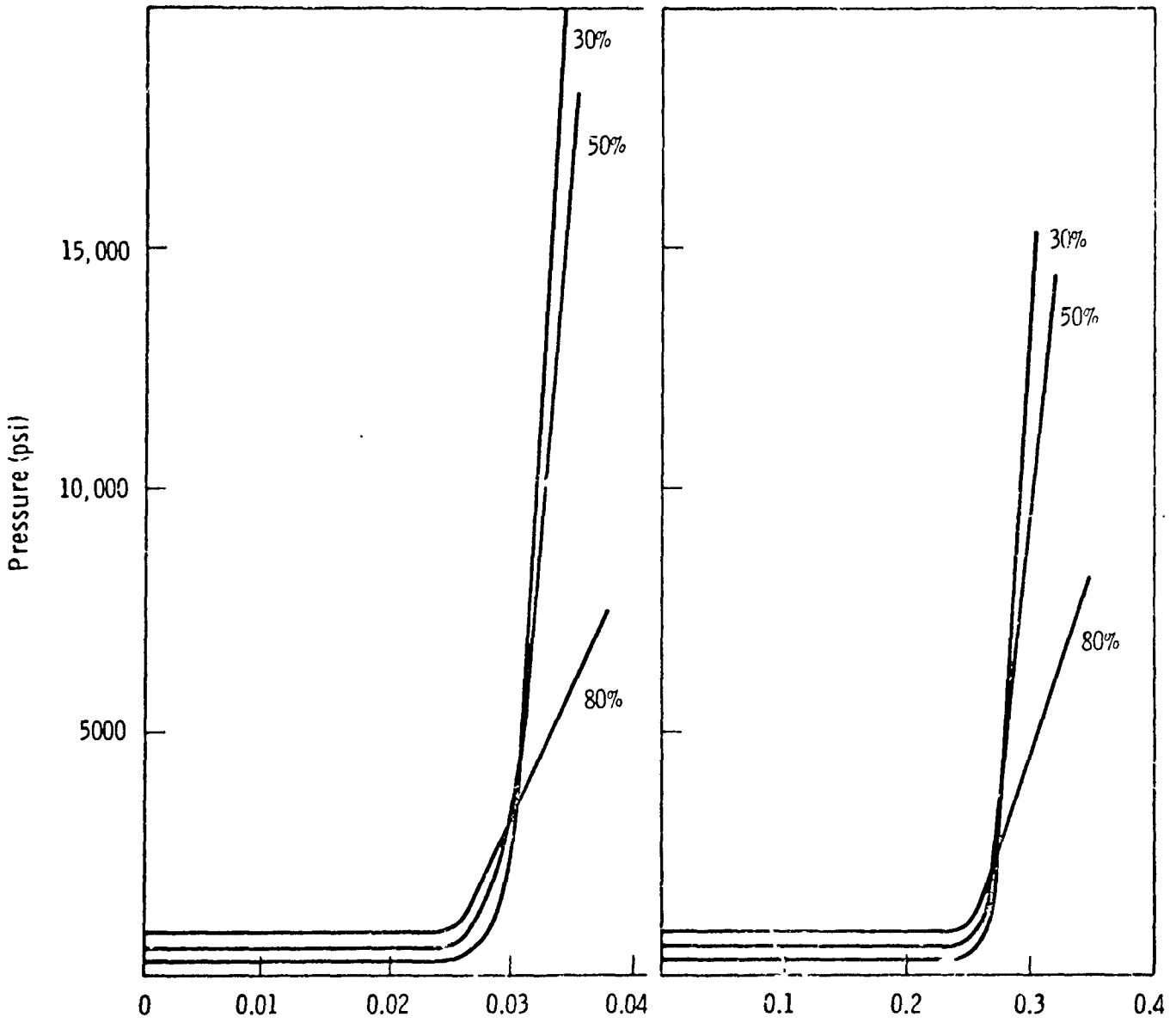


Figure X.13

AREA FRACTION OF FUEL MELTED, RELEASING GAS AND CENTRAL VOID VOLUME VS FUEL LENGTH AND TIME FOR \$50/SEC POWER TRANSIENT

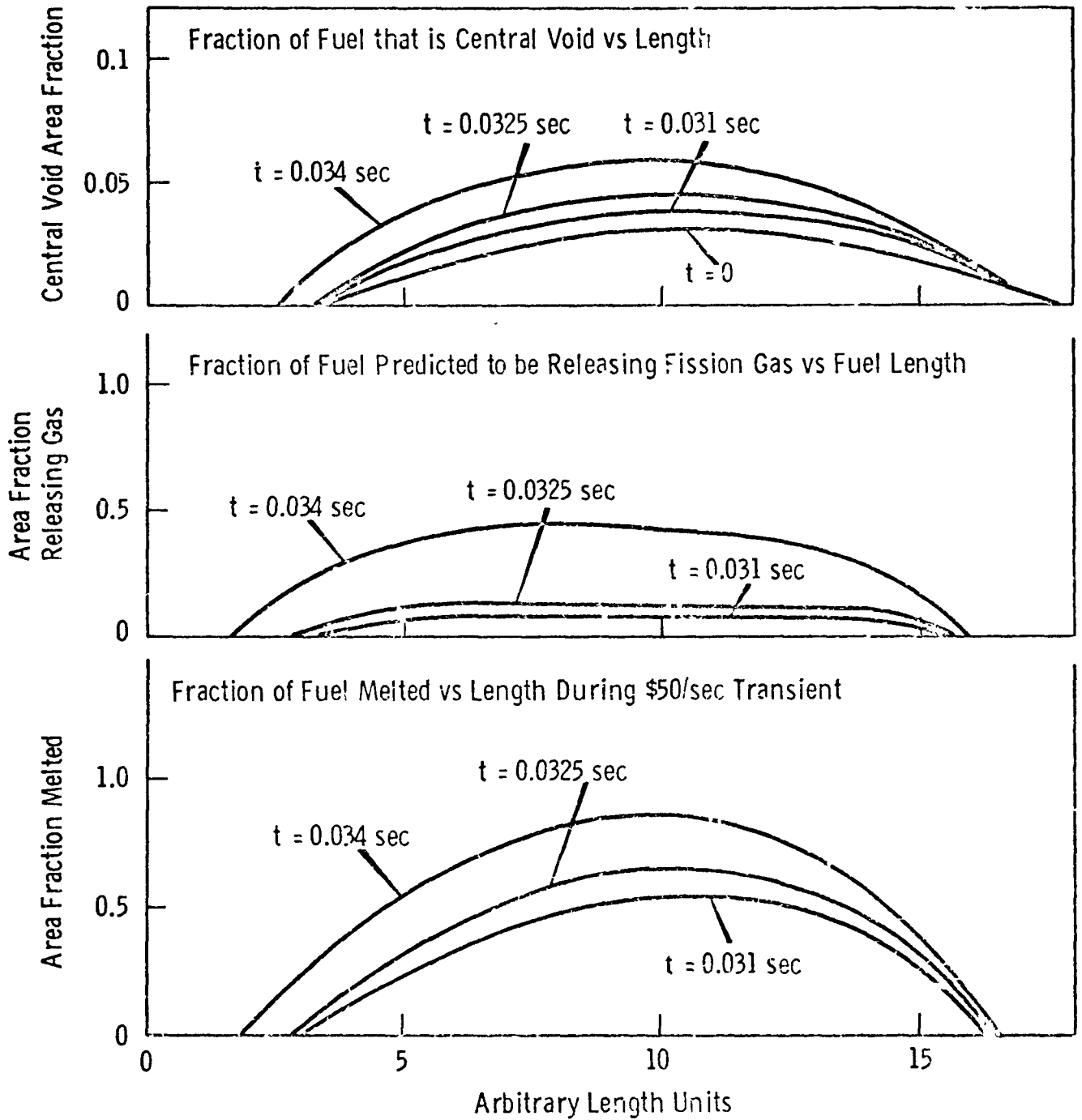


Figure X.14A

AREA FRACTION OF FUEL MELTED, RELEASING GAS AND CENTRAL VOID VOLUME VS FUEL LENGTH AND TIME AFTER \$5/SEC POWER TRANSIENT

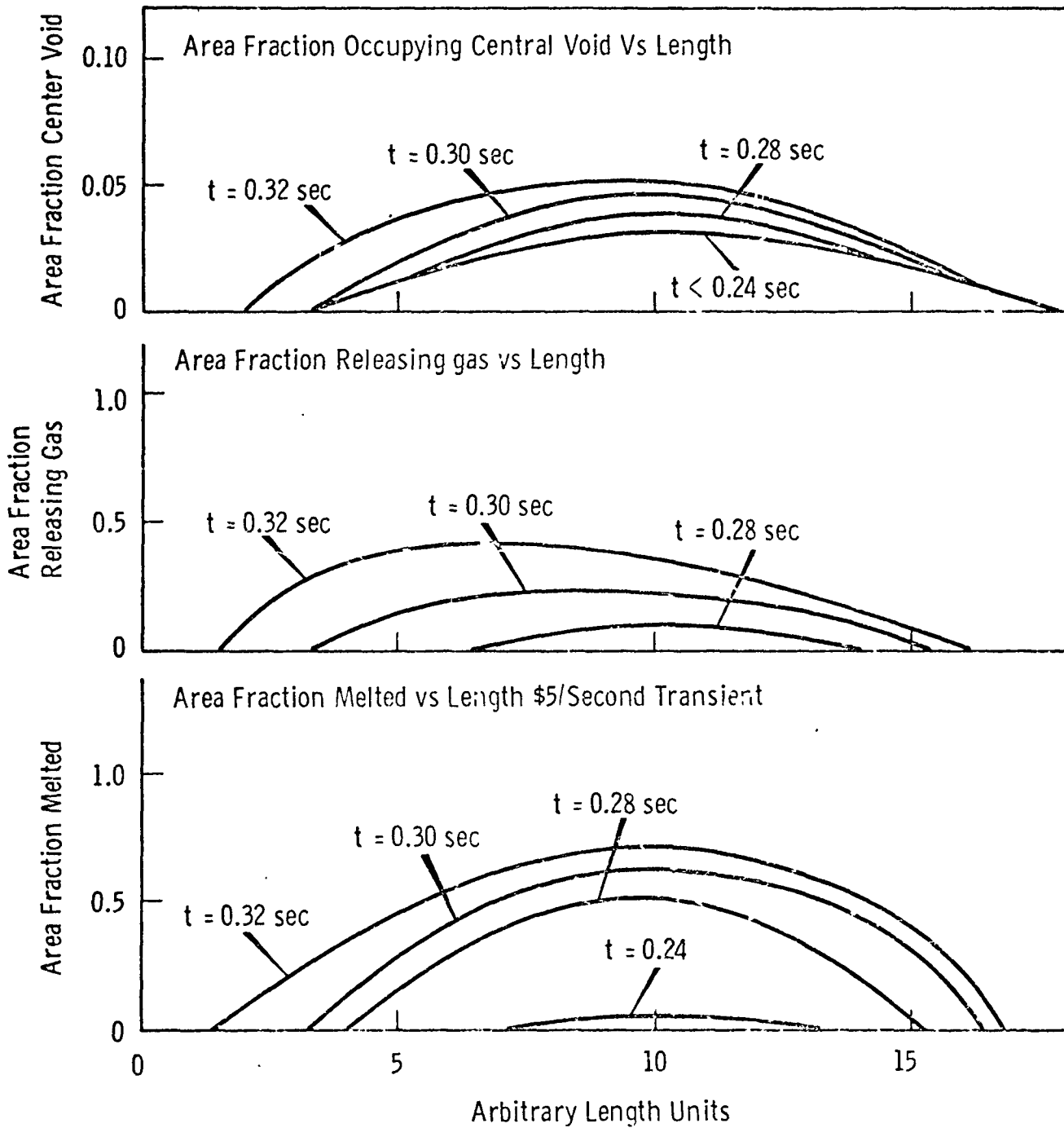
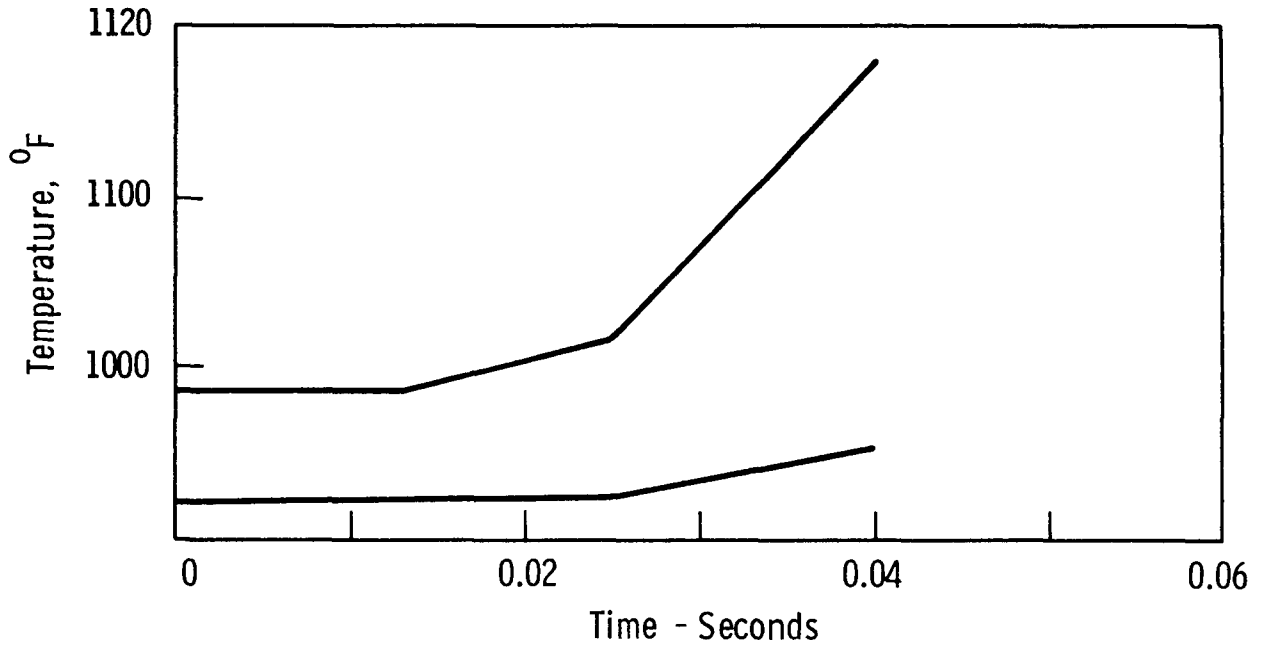


Figure X.14B

INNER AND OUTER SURFACE TEMPERATURE HISTORIES DURING A \$50/SEC REACTIVITY TRANSIENT



INNER AND OUTER SURFACE TEMPERATURE HISTORIES DURING A \$5/SEC REACTIVITY TRANSIENT

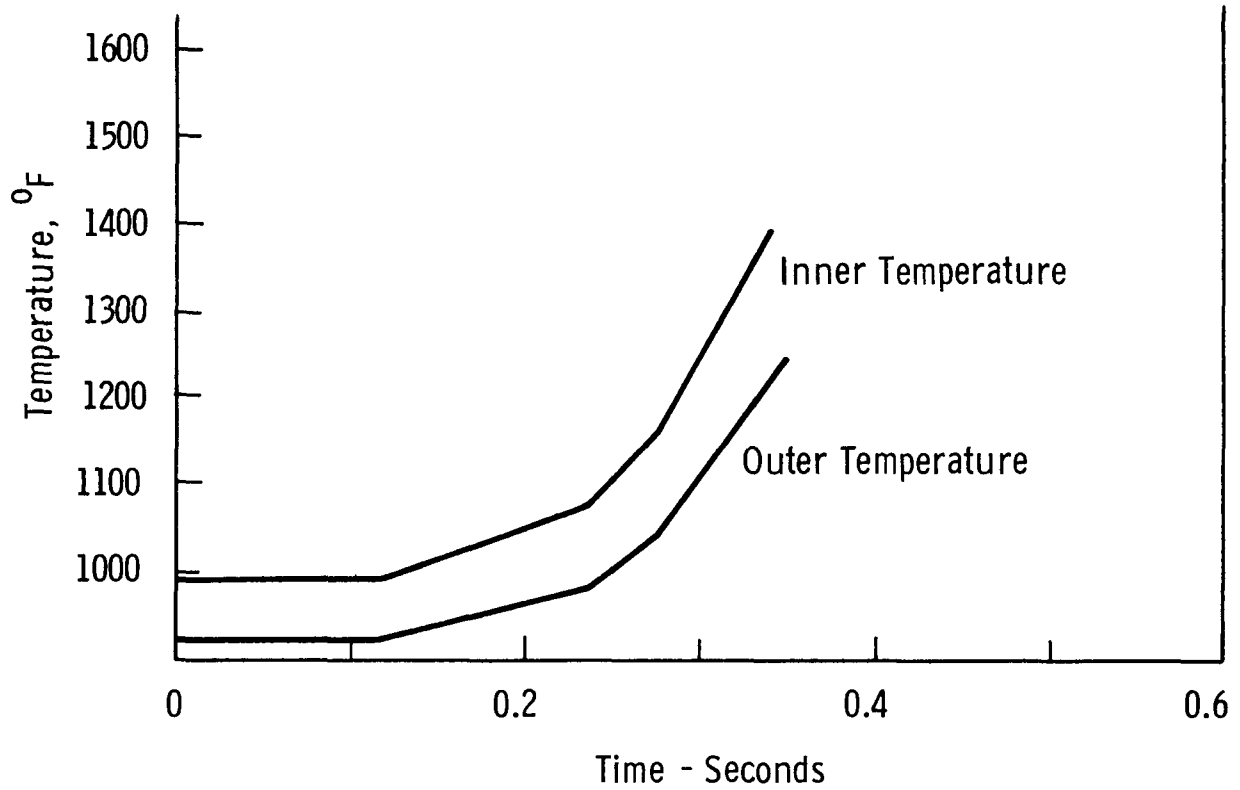


Figure X.15

STRESS DISTRIBUTION DURING A \$50/SEC REACTIVITY TRANSIENT
 AT NODE 14 FOR 80% FISSION GAS RELEASE AND UNIRRADIATED
 MATERIAL

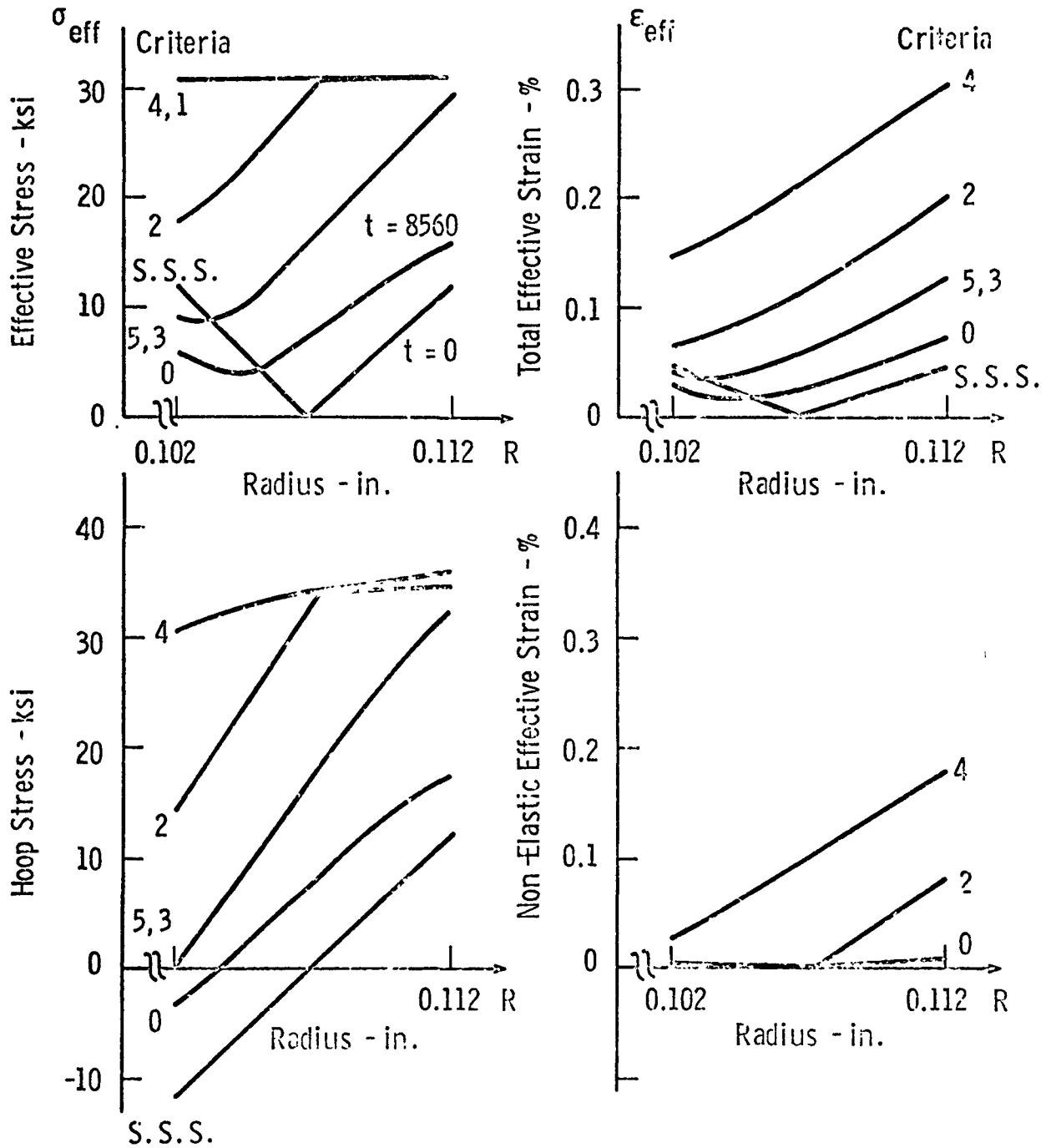


Figure X.16

TIME FOR FAILURE
 \$50/SECOND ACCIDENT - 80% SS GAS RELEASE

<u>TIME SECONDS</u>	<u>PRESSURE PSIG</u>	<u>T_{ID}_{OF}</u>	<u>T_{OD}</u>	<u>CRITERION</u>
0	800	987	924	-
0.027	2242	1035	928	5
0.029	3742	1055	932	2
0.031	3992	1080	936	3
0.034	5242	1105	943	4 & 1

X.29

Figure X.17

PIPE RUPTURE ACCIDENT - NORMALIZED FLOWRATE VS TIME

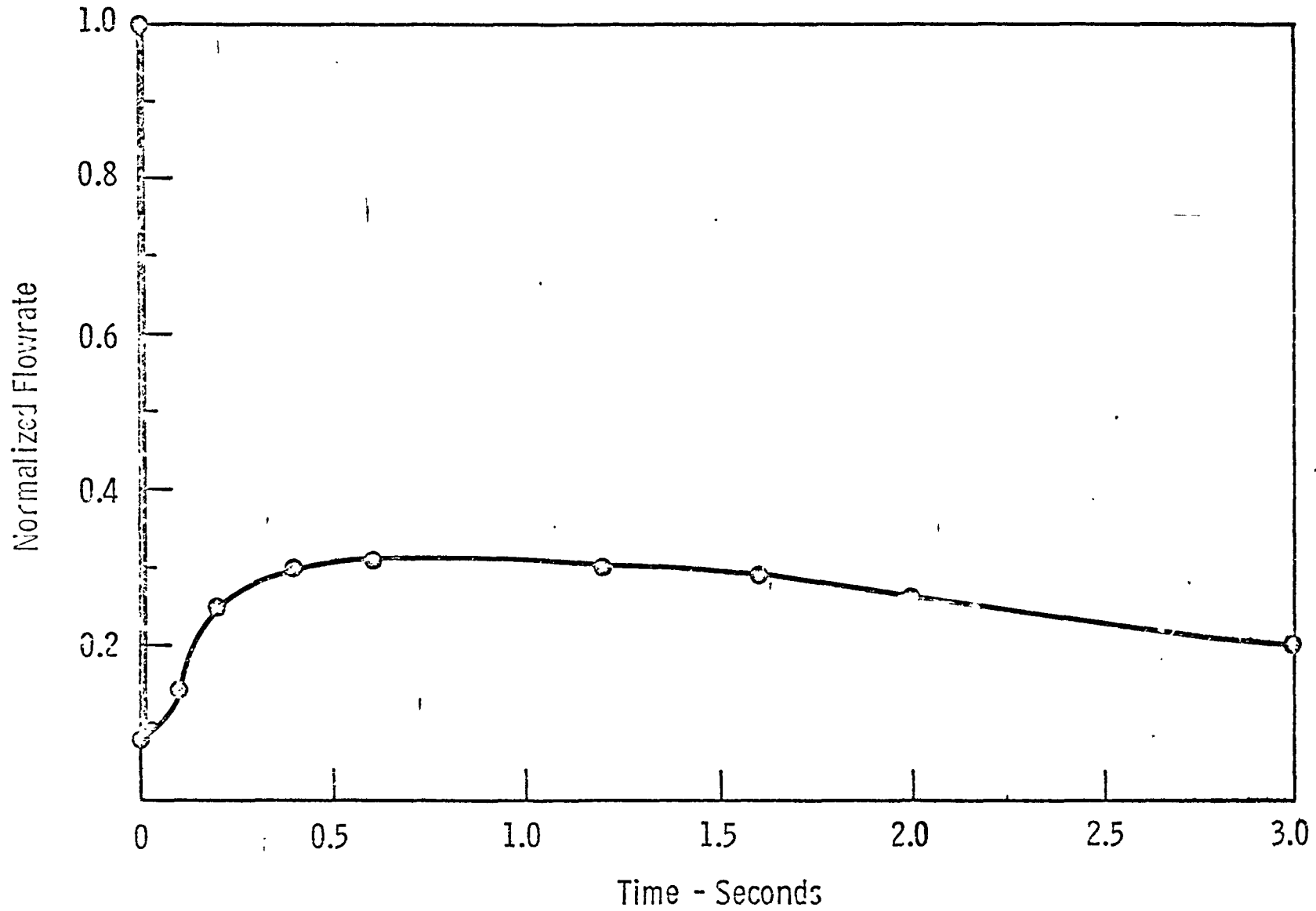


Figure X.18A

FLOW COASTDOWN - NORMALIZED FLOWRATE VS TIME

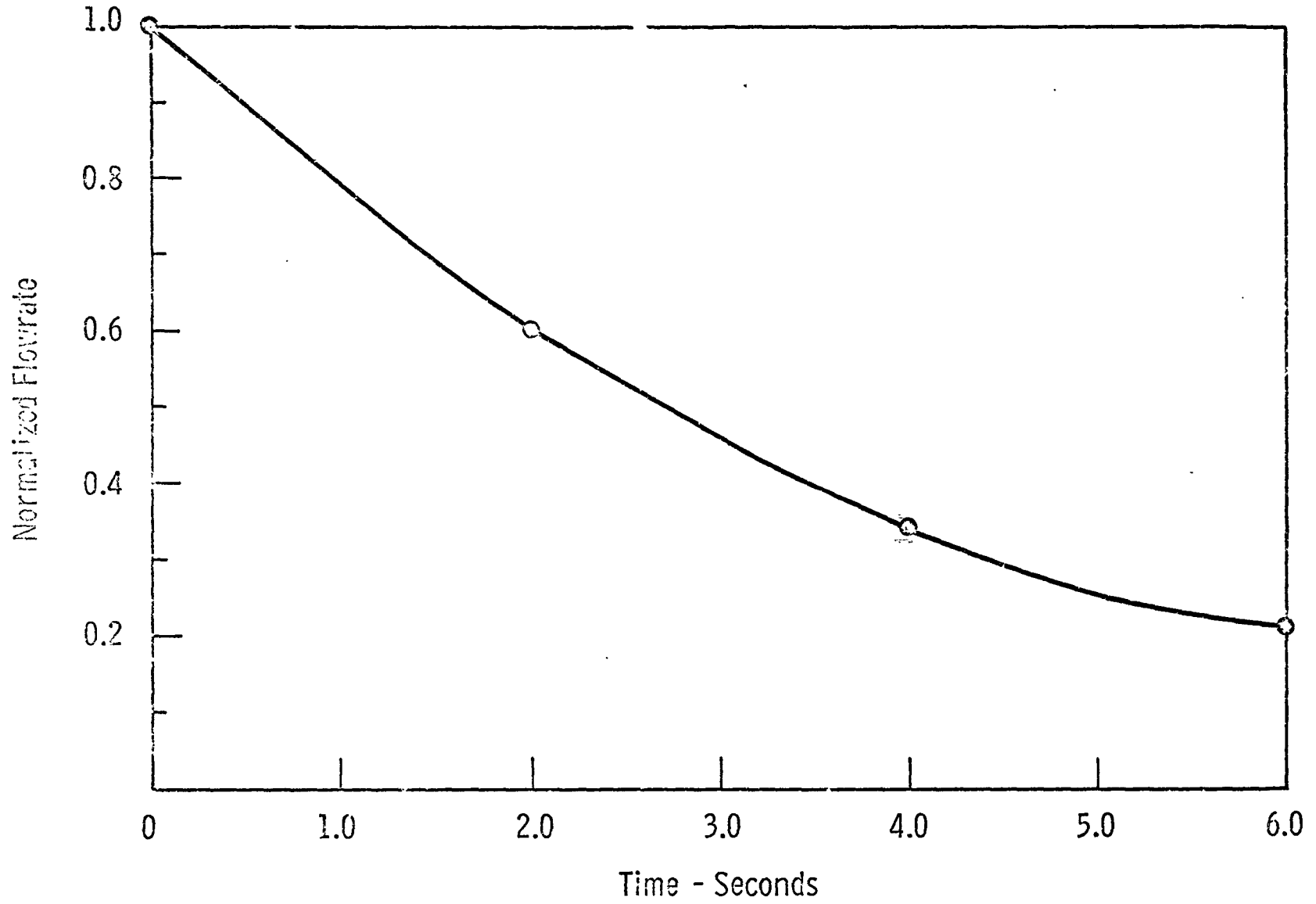


Figure X.18B

CLADDING TEMPERATURE HISTORY - FLOW COASTDOWN AND PIPE RUPTURE

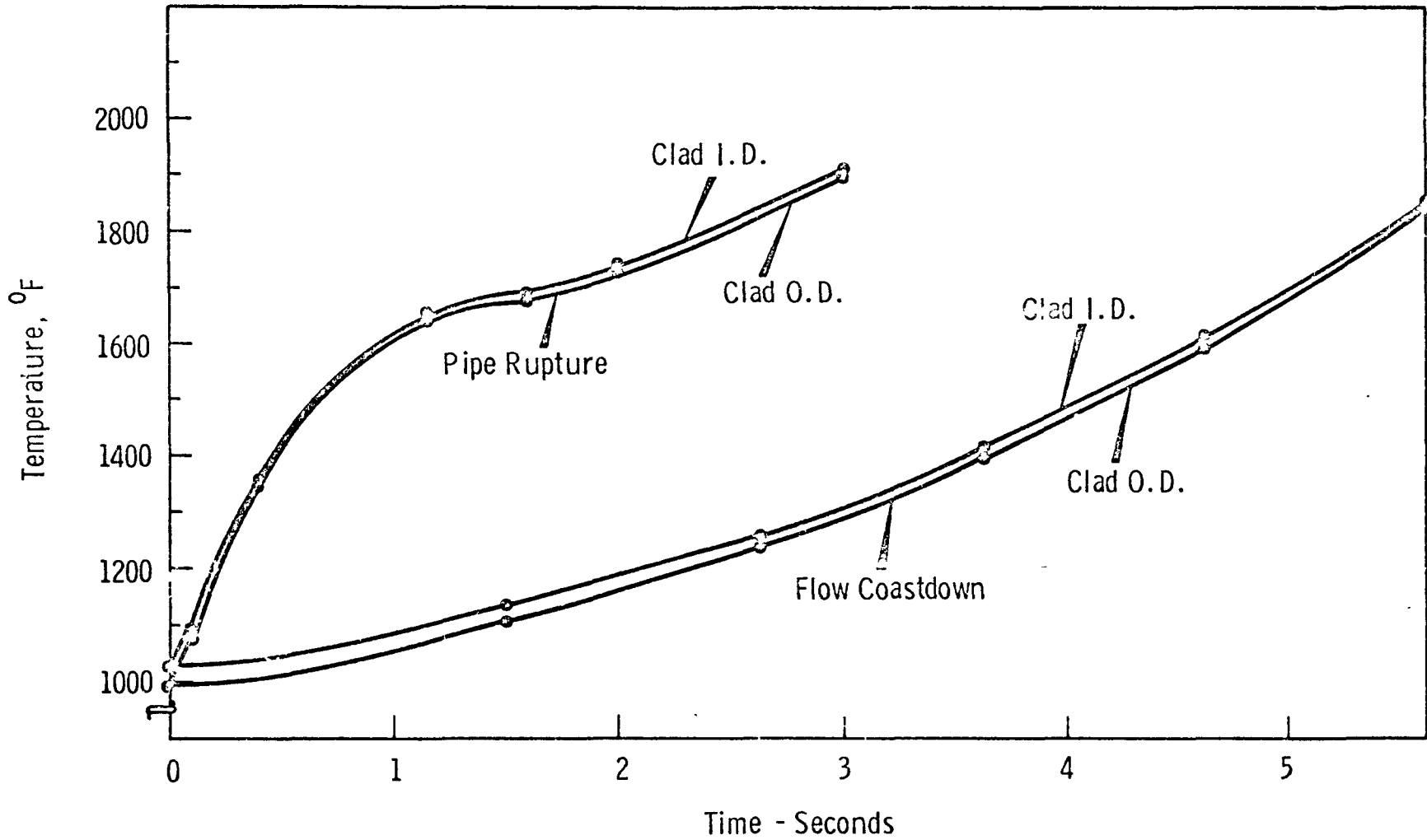


Figure X.19

INTERNAL PRESSURE HISTORY WITH 80% GAS RELEASE

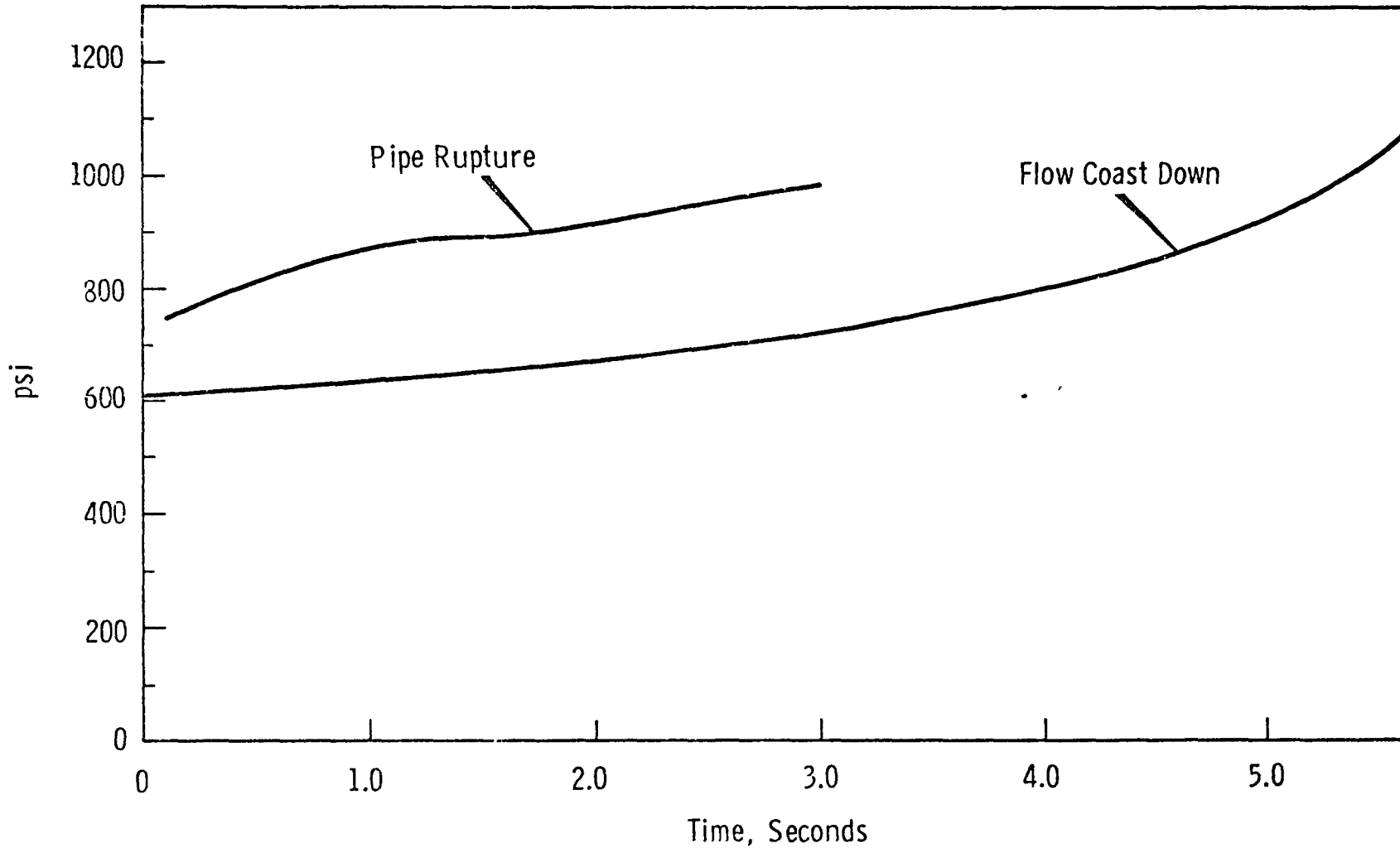


Figure X.20

DISTRIBUTIONS DURING FLOW COASTDOWN AT NODE 18

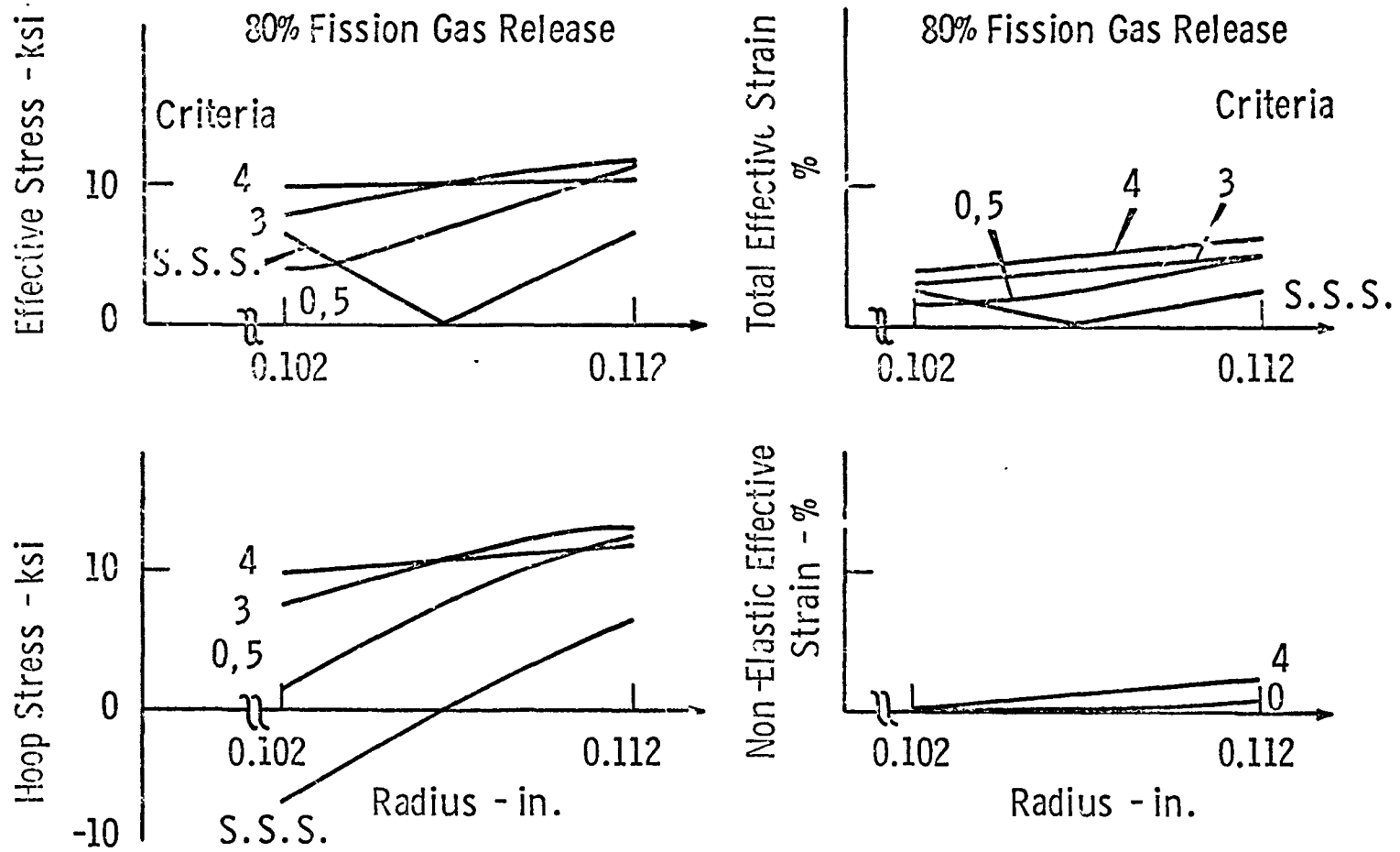


Figure X.21

DISTRIBUTIONS DURING PIPE RUPTURE AT NODE 18

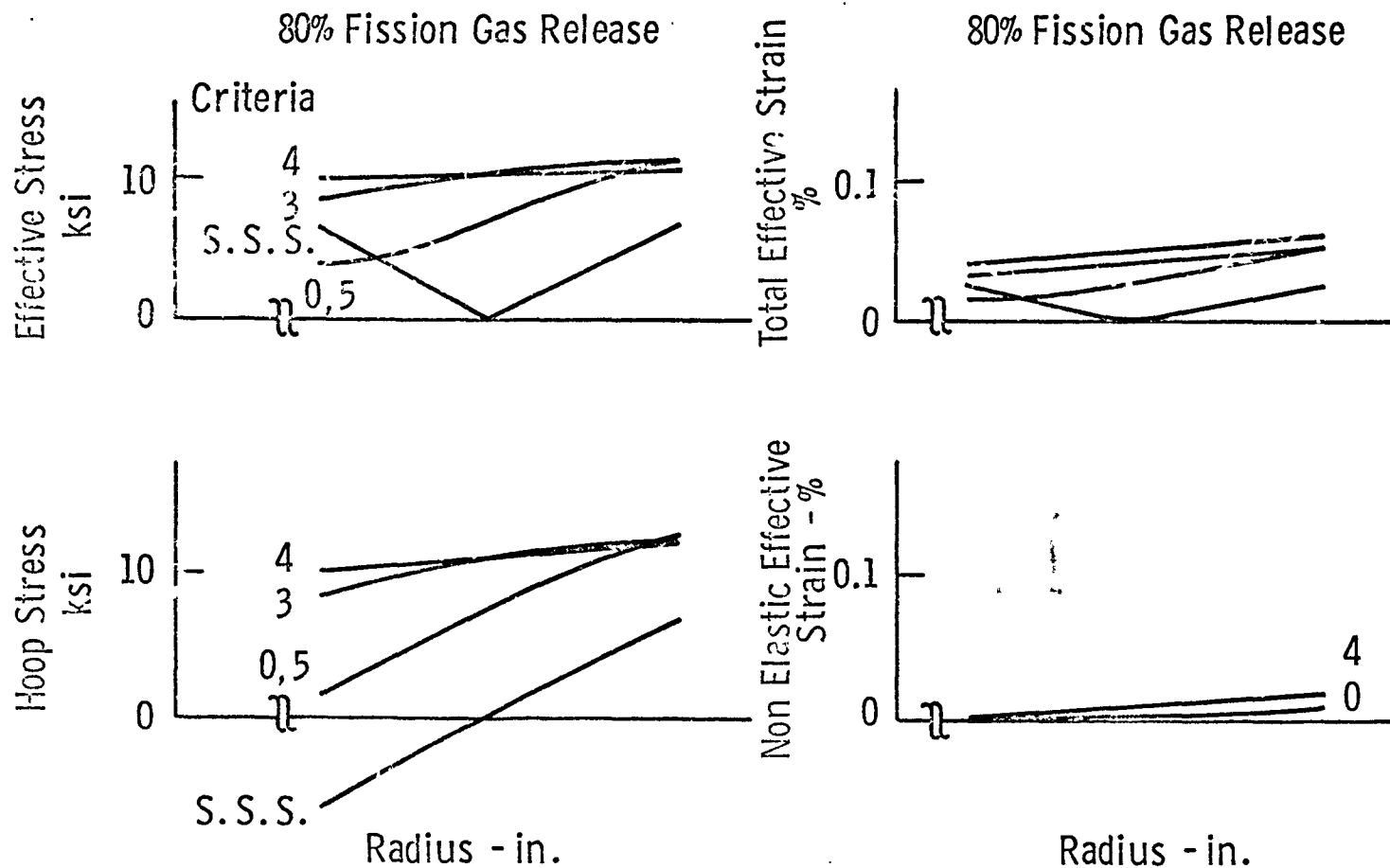


Figure X.22

FAILURE CONDITIONS

FLOW COASTDOWN

NODE #18

<u>TIME</u> ~SEC	<u>INNER PRESSURE</u> ~PSI	<u>INNER TEMPERATURE</u> ~°F	<u>OUTER TEMPERATURE</u> ~°F	<u>CRITERION</u>
0	800	1025	990	5 (80%)
4.39	1124	1626	1607	3
4.52	1141	1658	1640	4
4.55	1144	1663	1646	$\epsilon_{eff}^T \approx 0.1\%$

PIPE RUPTURE

NODE #18

0	800	1025	990	5 (80%)
1.16	1129	1636	1621	3
1.22	1141	1657	1642	4
1.24	1145	1665	1649	1 & 2

Figure X.23

**OXIDE FUEL DAMAGE CRITERIA
FOR THE FFTF ACCIDENT SEVERITY LEVELS**

TENTATIVE DATA

ACCIDENT SEVERITY LEVELS	FUEL MATRIX DAMAGE CRITERIA				CLADDING DAMAGE CRITERIA
	CROSS-SECTIONAL AREA \geq TMELT		PEAK FUEL TEMPERATURE		PEAK TEMP.
	NEW FUEL	IRRADIATED	NEW FUEL	IRRADIATED	IRRADIATED
DESIGN BASIS ACCIDENT					
DISRUPTIVE ACCIDENT					
MAJOR ACCIDENT	70%	50%			1600 °F
MINOR ACCIDENT	20%	20%			1300 °F
OPERATIONAL INCIDENT	0	0	5100 °F	4950 °F	1200 °F
NORMAL OPERATING ZONE			4350 °F	4200 °F	1100 °F

X.37

Figure X.24

XI. REACTIVITY ACCIDENTS

D. D. Stepnewski and C. L. Fies

A. Introduction

In the course of designing the reactivity control system of a nuclear reactor, it is necessary to analyze in detail certain potential reactivity perturbations. These perturbations vary in intensity and speed of occurrence from slow changes, such as fuel burnup, to accidents which may be hypothesized to introduce positive reactivity into the core at the rate of a 100 \$/sec or more. The latter type of reactivity insertion will be discussed in Chapter XVI, Mathematical Models for Reactor Disassembly. This discussion will be limited to upsets which constitute an off-normal condition, and which may require plant protective action to arrest or correct. The organization which will be used in this chapter is to first briefly discuss computational methods commonly used in reactivity accident analysis, and then illustrate the application of these methods to a number of reactivity accidents of the type traditionally analyzed for inclusion in safety analysis reports.

B. Computational Methods

1. Summary Description of Codes

The analysis of reactivity transients requires the use of heat transfer-neutronic coupled digital computer codes which provide a model of the reactor core. Two codes which are suitable for this purpose are FORE II and MELT II. FORE II is described in detail elsewhere. A summary description of the code is as follows: "FORE II is a coupled thermal hydraulics - point kinetics digital computer code designed to calculate significant reactor

XI.2

parameters under steady-state conditions, or as functions of time during transients. The transients may result from a programmed reactivity insertion or a power change. Variable inlet coolant flow rate and temperature are considered. The code calculates the reactor power, the individual reactivity feedbacks, and the temperature of coolant, cladding, fuel, structure, and additional material for up to seven axial positions in three channel types which represent radial zones of the reactor. The heat of fusion accompanying fuel melting, the liquid metal voiding reactivity, and the spatial and the time variation of the fuel cladding gap coefficient due to changes in gap size are considered. FORE II is valid only while the core retains its initial geometry.

The significant material properties are specified in the input as functions of temperature or pressure, and the external effects as a function of time by tables. The feedback reactivity includes contributions due to the Doppler effect, density changes, dimensional changes (includes bowing and deformation), coolant voiding, and control rods. Any single-phase coolant may be used. Although the code is biased toward fast reactors, it can be used for a thermal spectrum reactor as a steady-state heat transfer code and as a transient point kinetics code."⁽¹⁾

MELT-II is a coupled neutronics-heat transfer code which was designed primarily for investigating fast reactor core behavior under major accident conditions. However, this code can also be used to investigate less severe transients. A detailed description of the formulation of the MELT-II code is the subject of Chapter XV, Mathematical Models for Reactor Power Excursions. The capabilities of the MELT-II code are summarized as follows: MELT-II is

capable of calculating temperatures in up to 10 radial channels (fuel pin at 10 radial locations), each consisting of up to 20 axial segments and 15 radial nodes (12 fuel nodes plus the bond, clad, and coolant nodes). Thermal conductivity and specific heat can be specified as a function of temperature, and all pin materials are allowed to undergo one phase change. Coolant plenum inlet temperature can be specified as a function of time and the flow rate within each channel can be time dependent. Initial steady-state power due to fission product heating can be specified in addition to the neutronic power.

An implicit scheme is used to obtain fuel pin temperatures and a variable time step algorithm is used to govern the neutronics computations. Feedback due to Doppler, axial fuel expansion, axial clad expansion, sodium density change, fuel collapse and sodium voiding can be accommodated. Spatial weighting factors can be used for the Doppler and sodium feedback effects. Scram conditions can be initiated by a power, period, or sodium outlet temperature trip and, in all cases, the actual scram reactivity change can be delayed beyond the trip setting by a specified time.

For accident conditions which do not lead to a prompt critical situation, a zero lifetime approximation can be employed to minimize computer time. A mixed mode option has also been developed to combine the calculational advantages of the "exact" point kinetics formulation with the zero lifetime approach.⁽²⁾

MELT-II is similar to FORE II with some differences in treatment of gap coefficient between fuel matrix and clad and spatial Doppler effect treatment. It also uses a different variable time step procedure. Extensive

comparisons between MELT-II and FORE II have been made. (See Chapter XV, Mathematical Models for Power Reactor Excursions.) Good agreement was obtained between MELT-II, FORE II, and the exact solution in steady-state problems. For transients, comparisons were made with finite difference solutions, and again the agreement was good, with the discrepancy in the neighborhood of 1 or 2%.⁽³⁾

2. Input to Reactivity Analysis Codes

a. Basic Properties

In applying these codes to reactivity accident analysis, it is first necessary to establish steady-state condition in the core. The input to the code for this purpose consists of the basic core neutronics characteristics. These include power, axial and radial power distribution, fraction of power generated in the clad and coolant, the delayed neutron fraction and decay constants, and the various reactivity coefficients. Physical properties of the system are also inputted. These properties include thermal conductivity, coefficient of expansion, viscosity, specific heat for sodium all as a function of temperature. Similar properties are required for the fuel matrix and cladding.

In general, interest is centered on the condition (temperature) of the hottest pin in the core, since damage criteria are based on the hot pin in the hot channel. The hot pin is characterized in terms of average properties through the use of hot channel factors as shown in Table XI.1. It can be noted that all elements of the direct hot channel factors result in temperature increases relative to average conditions. Interchannel coolant mixing compensates for intra-subassembly flow maldistribution, but the effect is very

Table XI.1
ENGINEERING HOT CHANNEL FACTORS

FACTOR	COOLANT	FILM	CLAD	GAP	FUEL
A. Direct		-			
1. Inlet Flow Maldistribution	1.05	1.02	-	-	-
2. Intra-Subassembly Flow Maldistribution	1.15	1.06	-	-	-
3. Inter-Channel Coolant Mixing	0.99	-	-	-	-
4. Power Control Band	1.02	1.02	1.02	1.02	1.02
5. Wire Wrap Temperature Peaking	-	2.00 ¹	-	-	-
Product	1.219	2.206	1.02	1.02	1.02
B. Statistical					
6. Fissile Fuel Maldistribution	<u>+2.3%</u>	<u>+3.3%</u>	<u>+3.3%</u>	<u>+3.3%</u>	<u>+3.3%</u>
7. Power Level Measurement	9.0	9.0	9.0	9.0	9.0
8. Burned Rod Reload	1.2	1.2	1.2	1.2	1.2
9. Rod Diameter, Pitch and Bow	2.0 ¹	0.9	-	-	-
10. Film and Gap Coefficient	-	33.	-	40.	-
11. Fuel and Clad Conductivity and Thickness	-	-	12.	-	10.
Statistical Combination	9.58%	34.4%	15.41%	41.15%	13.90%
	COOLANT	FILM	CLAD	GAP	FUEL
Combined Factor	1.336	2.965	1.177	1.440	1.162

1. For Clad Temperature Only;
Less for Fuel Temperature

slight. The statistical factors do not always occur with the same sign so that when combined, the total is less than the sum, but larger than the biggest single component.

The results of the application of the hot channel factors are shown in Figure XI.1. The radial temperature distribution within the hot fuel pin is shown at the point of maximum temperature for steady-state conditions. The input to the code must be suitably adjusted to obtain the steady-state temperature profile to use as the starting point for the temperature changes to follow from the reactivity transient. The steady-state temperatures in the hot pin establish the margin to the point of failure. As shown on Figure XI.1, steady-state fuel temperature in the hot pin is approximately 4400°F; thus, the margin is about 450°F before the fuel begins to melt. Similarly, the inner clad temperature of the hottest point in the hottest pin is approximately 1100°F, which allows a 100°F margin before reaching 1200°F, a tentative lower limit for no damage to the clad.

b. Power Coefficients

The next component of code input which will be considered is reactivity temperature coefficients. The main temperature dependent reactivity effects are:

- (1) The Doppler effect
- (2) Coolant density effects
- (3) Core structural dimensional effects, including:
 - (a) Movement of the core relative to control elements
 - (b) Axial expansion of fuel pins
 - (c) Radial movement of fuel pins
 - (d) Thermal bowing of fuel.

XI.7

The equations defining the foregoing effects and uncertainties in their calculation have been treated in Chapter VIII, Reactor Kinetics Parameters. The discussion given here will only touch upon the application of these coefficients to particular analyses and the values used.

For most analyses of reactivity transients, the axial expansion coefficient is assumed to be zero. Ignoring the axial expansion coefficients results in conservative analysis for most positive reactivity accidents. However, for accidents such as cold sodium insertion, this is not conservative. Coefficients of axial expansion have been calculated to be $-4.5 \times 10^{-6} \Delta k/^\circ\text{C}$, and $-2.8 \times 10^{-6} \Delta k/^\circ\text{C}$ based on cladding and fuel expansion, respectively. These coefficients were calculated by increasing the height of the core by a small percentage while maintaining the total mass of the core constant. A radial expansion coefficient calculated for FFTF is $-3 \times 10^{-6} \Delta k/^\circ\text{C}$ based on the change in coolant outlet temperature. This coefficient is based on a reactivity change of .9¢ per mil change in radius with positive reactivity associated with decreasing radius. The radial expansion coefficient is not normally taken into account in the analysis of reactivity excursions. It is dependent on the temperature change of the structure and coolant in the core, hence it is a rather slow acting effect. Again, however, for an accident such as cold sodium insertion, it is applied to be conservative.

The coolant temperature effect will also be present during reactivity transients. Since the coolant temperature coefficient is computed by the same methods used to calculate void coefficient, the reactivity effect may be positive or negative, depending upon location of the disturbance in the core,

and the prospects for neutron leakage. For a large sodium cooled fast reactor such as the 1000 Mw electrical designs, a slightly positive sodium temperature coefficient is obtained. For a very small reactor, 500 liters or less, a small negative coefficient is obtained. For FFTF, with a size of approximately 1000 liters, it appears that the coefficient will be quite small and may be either positive or negative. To be conservative, a zero coolant temperature coefficient has been used for positive temperature changes, and a value of $-1.5 \times 10^{-6} \Delta k/^\circ\text{C}$ for accidents such as cold sodium insertion where a negative coefficient gives a conservative result.

The Doppler coefficient is, of course, the predominant prompt acting feedback effect. In most reactivity transient analyses, the Doppler coefficient is considered the only reliable prompt power coefficient. This is because the Doppler is based strictly on the change of fuel temperature which occurs regardless of the speed with which the transient takes place. All of the foregoing coefficients would have very little effect in the case of a high reactivity ramp rate. As a conservative value, a Doppler coefficient $\beta \frac{dk}{dT} = -.004$ has been used in the analysis which will be subsequently discussed. It should be noted that the coefficients stated here are preliminary values, subject to revision, and indeed have been changed since these calculations were made.

c. Protection System Dynamics

The last major element of code input to be discussed here is the protection system dynamics. Protection system characteristics are usually entered as a negative reactivity ramp which is delayed for a given amount of time after a certain trip point such as high power or high coolant outlet

temperature has been reached. The variables which must be considered to determine the control system dynamics are: the initial position of the rods, safety rod acceleration, rod worth, and response time.

1) Initial Safety Rod Position

The starting position of the scram rods relative to the core center line will influence the rate of poison insertion for a given control or safety system. Figure XI.2 shows the fraction of rod worth inserted versus distance from initial rod position. It can be seen that the rate of insertion is highest for the initial position of 20 cm below the top of the active zone or core interface. This occurs since rod movement is started on the steep portion of the characteristic integral rod worth "S" curve. However, for the same displacement from the core top face, total rod worth inserted increases as the initial rod position is raised away from the core centerline. In the analysis to be discussed here, the initial rod position was taken at the top axial core interface.

2) Safety Rod Acceleration

Figure XI.3 shows the fraction of total rod worth inserted as a function of time for three different rod acceleration values, and for the rods at the core interface. These curves were obtained from the data on Figure XI.2, combined with a typical integral rod worth curve. It can be seen that the gain in response is substantial in increasing acceleration from 1 to 2 g's, whereas the gain in going from 2 to 3 g's is somewhat less. Figure XI.3 is based on the ideal relation for frictionless uniform acceleration, $d = 1/2 at^2$. Figure XI.4 reflects the more realistic situation where frictional and hydraulic forces are considered. The figure shows rod displacement

in inches versus time in seconds. The lower curve shows the time distance relationship for gravity fall of the 640 lb FFTF safety rods. The frictionless one g curve is also plotted on the figure for comparison. It can be seen that a 14" spring assist, with a spring constant of 640 lbs, results in a response curve essentially equal to the ideal one g curve for the first 200 milliseconds. The two curves then spread after the spring assist has been completed. Thus, gravity fall plus a one g spring is effectively only a one g system. The reactivity analyses to be discussed here are based on such a system, i.e., one g or two g's depending on the point of view. The fact that the real system departs from idealized performance after 0.2 secs is not very important since the significant period in suppressing effects of a reactivity ramp is the time range within the initial 200 msec.

3) Scrammable Rod Worth

Minimum scrammable worth requirements must provide sufficient poison to bring the reactor to subcritical conditions and maintain in that state under all conditions. Numerical values of rod worth will depend upon safety criteria adopted for any particular reactor core under consideration. Complete criteria have been formulated for the FFTF nuclear control system.⁽⁴⁾ A summary⁽⁵⁾ of reactivity control worth requirements are given in Table XI.2. The reactivity analyses in this chapter are based on a nuclear control system consisting of six in-core poison elements. B_4C enriched with B^{10} is the control material used. Out of the six in-core rod positions, three of these accommodate primary safety rods with a maximum worth of 6-8\$ each and a total worth for all three rods of approximately 4.8% $\Delta k/k$. There are three in-core positions for shim rods with a worth of approximately 4.0\$ each, and a total worth of 3.6% $\Delta k/k$. There are also 15 peripheral control rods worth approxi-

TABLE XI.2

Reactivity-Control Worth Requirements

	<u>Oper- tional Control</u>	<u>Primary Safety</u>	<u>Secondary Safety</u>	<u>Op. Control- Pri. Safety</u>	<u>Op. Control- Sec. Safety</u>
Temperature Defect					
(a) Hot Oper. to Hot Standby	0.5%	0.5%	0.5	0.5	0.5
(b) Hot Standby to 600 °F	0.3	0.3		0.3	0.3
(c) 600 °F to 400 °F		0.2		0.2	
Fuel Burnup Allowance (Equil. 3 Cycle)	2.6			2.6	2.6
Test Shim & Operating Flexibility	1.8			1.8	1.8
Reactivity-Control Burnup	0.3	0.2	0.2	0.3	0.3
Accident Reactivity Insertion		} 1.5	1.2	} 1.5	1.2
Minimum Shutdown Margin	<u>1.0</u>				
Subtotal	6.5	2.7	1.9	7.2	6.7
20% Uncertainties	1.3	0.5	0.4	1.4	1.3
Total Exclusive of Stuck Rod	7.8	3.2	2.3	8.6	8.0
Stuck Rod Provision (Max. Worth Element)		X		Y	
Total	7.8	3.2 + X	2.3	8.6 + Y	8.0
Design Options					
(a)	*	*	*		
(b) (Reference Design)		*			*
(c)			*	*	

mately 1\$ each. These rods are scrammable; however, they are not equipped with gravity assist springs and have a slower response than the in-core rods. All six in-core rods are designed to be accelerated into the core with a force of one g. The analysis given here is based on two primary safety rods worth 3.2% $\Delta k/k$, responding to a scram signal. Thus, allowance is made for one rod to remain stuck in its out-of-core position. All in-core rods will scram, and analyses also show the results for six rods entering the core.

4) Safety System Response Time

The response time depends on three components - sensor, logic circuit, and rod release delays. Conditions sensed by the nuclear flux instrumentation (ion chamber and its associated amplifier) are capable of achieving a response of 1 msec or less when operating in the power range. This implies that for accident conditions detected by the high level neutron monitors, the response time of the complete scram system will be governed by the response of the logic and actuators. Reed relays are planned for use in the logic and safety circuits. These devices are expected to introduce response delays of 25 to 50 msec. The rod release mechanism delay depends upon design. With the roller-nut type of rod drive, a magnetic field holds rollers against a lead screw. The magnetic field decays off in the msec range, and springs kick the rollers free, releasing the rod. An allowance of 75 msec was provided for rod release delay. This time, combined with a delay of 25 msec in the power range nuclear channels and protection logic, results in a total time delay of 100 msec. This is the time span from receipt of signal by the flux monitors to the point in time at which the safety rods commence travel.

Negative reactivity ramps representing performance of the reactor scram system as used in the reactivity transient analysis reported here are shown on Figure XI.5. These curves are based on rod worths, acceleration, and response time as discussed above. The bottom curve assumes two of the three safety rods scram, thus observing the stuck rod provision. This curve was used in the analyses. The top curve shows response of the system as designed, i.e., the in-core shim rods are accelerated into the core along with the primary safety rods.

C. Application to Reactivity Accidents

1. Slow Reactivity Insertion Accidents

This general category includes accidents which produce a reactivity ramp which is well below the design speed of the protection system or accidents where the total amount of positive reactivity insertion is small. A complete list of accidents of this type should be determined by fault tree analysis for any particular reactor. Examples of accidents in this category, which are discussed here, are uncontrolled rod withdrawal caused by operator error or instrumentation failure, and cold sodium insertion.

a. Uncontrolled Rod Withdrawal

Figure XI.6 shows the reactor power response to the continuous withdrawal of a safety rod and a peripheral control rod. The analysis of this fault assumed a cold shutdown initial condition with a prompt neutron power of 4 KW. Fault indication would be obtained from the control rod drive and from period meters in addition to the flux level trips shown. It is seen that the 40 MW power trip is reached in about 17 secs. The transients are based on a design limited maximum withdrawal rate of 15"/min. Figure XI.7

shows the thermal response of hot channel fuel. It is seen that peak hot channel temperature rises to only about 1000°F before reaching the intermediate level trip, and this accident is easily controlled by the reactor protection system.

b. Cold Sodium Insertion

The analysis of this potential accident required the use of the FFTF hybrid simulation of the primary coolant system to obtain the sodium temperature transient, and MELT-II to determine the core thermal and neutronic response. The incident was postulated to occur as follows. The reactor is at low power with one heat transport loop operating at low flow to maintain a full core delta T. The other two heat transport loops are isothermal at 350°F with primary pump motors running but EM clutches disengaged. At time zero, the EM clutches on the isothermal loops are engaged at about 60 percent excitation current (with a time constant of one second) and the two loops begin pouring cold sodium into the reactor inlet plenum. The transient continues with constant 350°F sodium temperature from the two loops limited only by the circuit time of the primary loop which is about 22 seconds. This accident might also be considered representative of one which might happen if control valves in the primary loop opened abruptly during pump testing with the reactor critical. Figure XI.8 shows the reactivity response with a Doppler coefficient of $T \frac{dk}{dT} = -.004$. Other feedback terms in this calculation were:

Sodium Temperature Coefficient $\Delta k/^\circ K$ -2.67×10^{-6}

Clad Expansion Coefficient $\Delta k/^\circ K$ -4.0×10^{-6}

Radial Expansion Coefficient $\Delta k/^\circ K$ -9.0×10^{-6}

It is seen that for the first three seconds, the reactivity insertion rate is about 30¢/sec. The Doppler feedback is initially positive since the cold sodium is cooling the fuel until neutron energy starts heating it at three seconds; the Doppler then starts turning the ramp around. The expansion and density feedbacks, however, continue to insert some positive reactivity because the temperature of the sodium coolant continues to fall during this time period. This analysis does not include reactor scram; however, protection against the 30¢/sec reactivity ramp is well within the capability of the FFTF scram system. Figure XI.9 shows the power rise as a result of this accident. Trip points which are available to stop this power rise are the low range, intermediate, and high range neutron flux monitors which would trip at 10^{-1} Mw, 40 Mw, and 440 Mw, respectively. The power rate-of-change channels would also trip.

2. Rapid Reactivity Insertion Accidents

This category represents accidents causing a reactivity ramp and a total amount of positive insertion that tests the capability of the protection system and establishes the speed at which it must operate. Examples in this category include single subassembly fuel compaction by gravity and structural failure of a partially inserted control rod.

a. Fuel Compaction Accidents

The meltdown of a single fuel subassembly is considered a serious accident and considerable design effort is applied to reduce the probability of such an accident to acceptable levels. Hence, fuel slumping is never expected to occur. However, it is useful and instructive to analyze this

accident, and the reactivity transients resulting from it have been used as the design basis for the protection system.

In analyzing this accident, a reactivity ramp is first estimated from the displacement of fuel from the lower worth region of the core to the maximum worth region at the center by gravitational force. In these calculations the top 40% of the fuel subassembly is assumed to move to the central 20% of the subassembly. This movement is physically possible since the fuel matrix occupies only 31.1 volume percent⁽⁶⁾ of a driver subassembly in the core inner region. Based on a 90 cm core, the centroid of the upper 40% of a subassembly is 27 cm from the center, and with gravity collapse, time required for this movement is about 235 msec. The reactivity insertion involved in the foregoing fuel movement is estimated from reactivity coefficient profiles such as those given on Figure XI.10. This plot shows relative worth of core constituents as a function of axial distance from the core midplane. Material worths in $\Delta k/kg$ are also shown. The reactivity change is obtained by computing the difference in reactivity of the upper 60% of the subassembly before and after slumping. The sodium is assumed to be voided, along with the stainless steel, although the latter effect is very small. For a driver subassembly containing 6 kg fissile material and 30 kg fertile material, the compacted condition provides a positive reactivity increase of approximately 60¢. The insertion rate ramp thus becomes $.60/.235$ or about 2.6 \$/sec.

Estimates of the total reactivity insertion and ramp rates have been made for a broad spectrum of fuel assemblies which might be used in driver, closed loop or open loop test positions in the core.⁽⁷⁾ The most severe potential accident of this type identified would introduce reactivity at a

rate of 4.4 $\$/\text{sec}$, bounded at 1 $\$$ total insertion. The fuel specimen in question would contain approximately 8.4 kg fissile material and 23.2 kg fertile material. This is currently considered an upper limit on fissile loading in the FFTF core and corresponds to the maximum cooling capability of the open loop position.

FFTF safety system response to a 5 $\$/\text{sec}$ reactivity ramp is shown on Figures XI.11 and XI.12. Reactor scram trip occurs at 440 Mw at about 10 msec on Figure XI.11, and with a 100 msec delay, the rods start into the core at 110 msec, turning the power ramp around at about 170 msec for the six rod case, and somewhat later for the two rod case. Figure XI.12 shows a maximum fuel temperature rise in the hot channel of about 200 and 400 $^{\circ}\text{F}$, respectively, for the two and six scram rod cases. Since peak steady-state fuel temperature is about 4400 $^{\circ}\text{F}$ (Figure XI.1), centerline fuel melting temperatures are not reached in either case.

b. Structural Failure of Control Rod

Another limiting case reactivity insertion accident involves the structural failure of a partially inserted control rod. This event could occur if cooling were lost to the rod causing melting of the rod cladding and subsequent collapse of the rod material. One would expect this process to occur rather slowly with the melting taking place over many seconds. It is difficult to predict the exact progression of the melting, however, and for this reason, a limiting case situation is postulated. It is assumed that an in-core control rod with the maximum allowable worth of 4 $\$$ is partially inserted in the core. The bottom section of the rod, x cm in length, is located about the core centerline as shown in Figure XI.13. It is pessimistically assumed

that the rod fails at the distance $1/2 x$ above core centerline and the section of the rod below the failure point drops through distance y to the position indicated as x_1 . Since the rod worth at x is larger than the worth at x_1 , a net position reactivity insertion occurs. This positive insertion is divided by the time calculated for the rod to fall by gravity through distance y to obtain the reactivity ramp.

Figure XI.14 shows total reactivity insertion and ramp rate for various initial rod positions. The distance from the bottom of the rod to the failure point, x , was varied from 20 cm to 70 cm. The difference in rod worth between positions x and x_1 increases to a maximum at x equal to approximately 38 cm and then decreases. The ramp rate varies as a function of both worth difference and drop time reaching a maximum at approximately 42 cm. It can be seen that this particular accident is bounded by a total insertion of 1.2\$ with a ramp rate of 4\$/sec.

References

- (1) J. N. Fox, B. E. Lawler, H. R. Butz, FORE II, A Computational Program for the Analysis of Steady-State and Transient Reactor Performance, GEAP-5273, September 1966.
- (2) E. R. Astley, FFTF Monthly Informal Technical Progress Report, October 1968, BNWL 915, pp 3.69-3.70.
- (3) E. R. Astley, FFTF Periodic Technical Report, October 1968 through February 1969, BNWL 941, May 1969, pp 3.17-3.24.
- (4) Battelle Northwest, Design Safety Criteria for the Fast Flux Test Facility, BNWL-823, June 17, 1968, Section 14.
- (5) *ibid*, p. 14-50.
- (6) W. W. Little, Jr., L. L. Maas, Nuclear Parameters and Parametric Studies for the Fast Test Reactor, BNWL-1067, June 1969.
- (7) C. L. Fies, FFTF Scram System Response Requirements and Parametric Analyses, BNWL-1226-FF1 (to be issued).

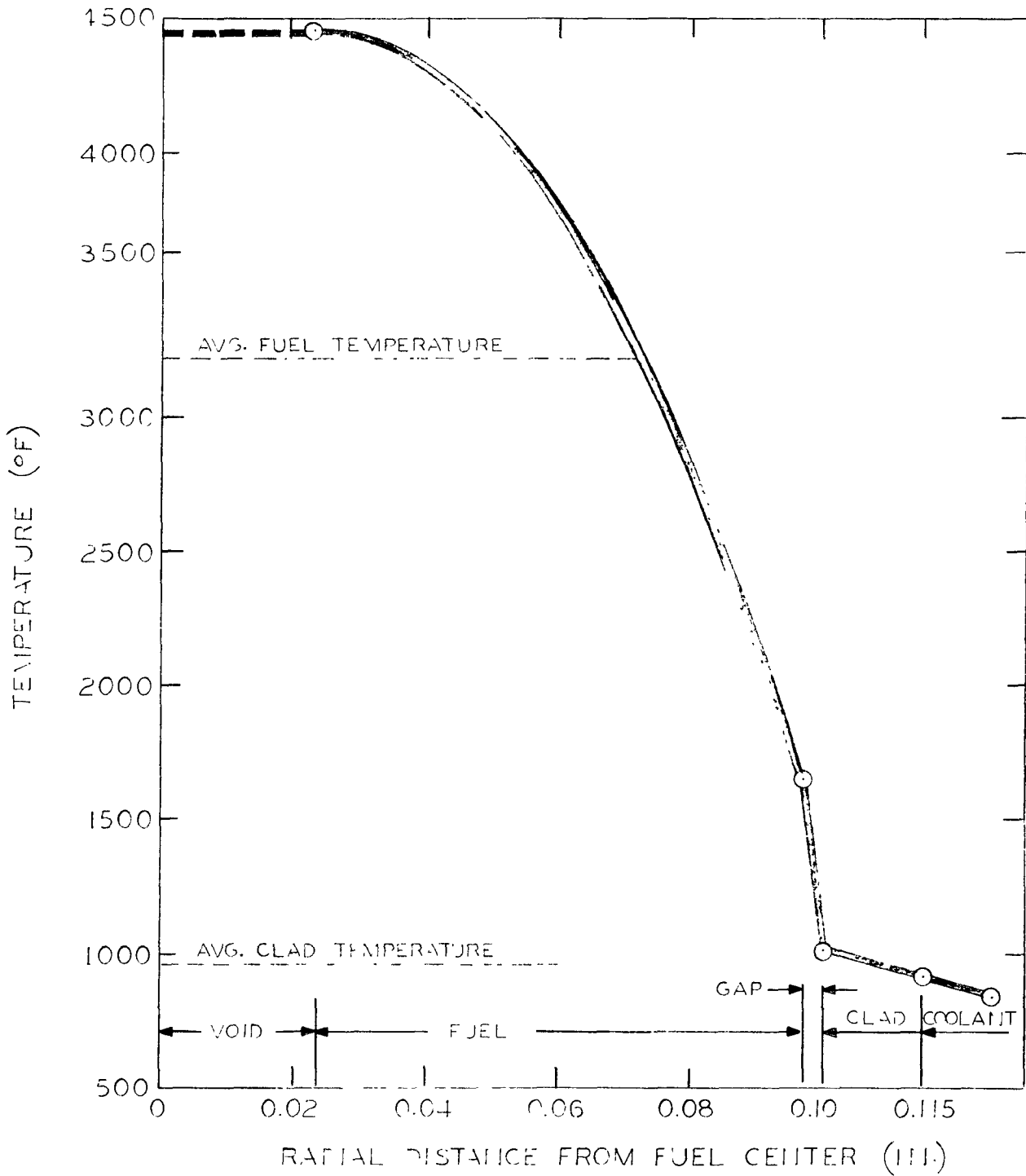


Figure XI.1 RADIAL TEMPERATURE DISTRIBUTION THROUGH HOT FUEL PIN AT POINT OF MAXIMUM TEMPERATURE

XI.21

Figure XI.2

FRACTION OF ROD INSERTED AS A FUNCTION OF DISTANCE INSERTED FROM INITIAL POSITION FOR VARIOUS INITIAL POSITIONS

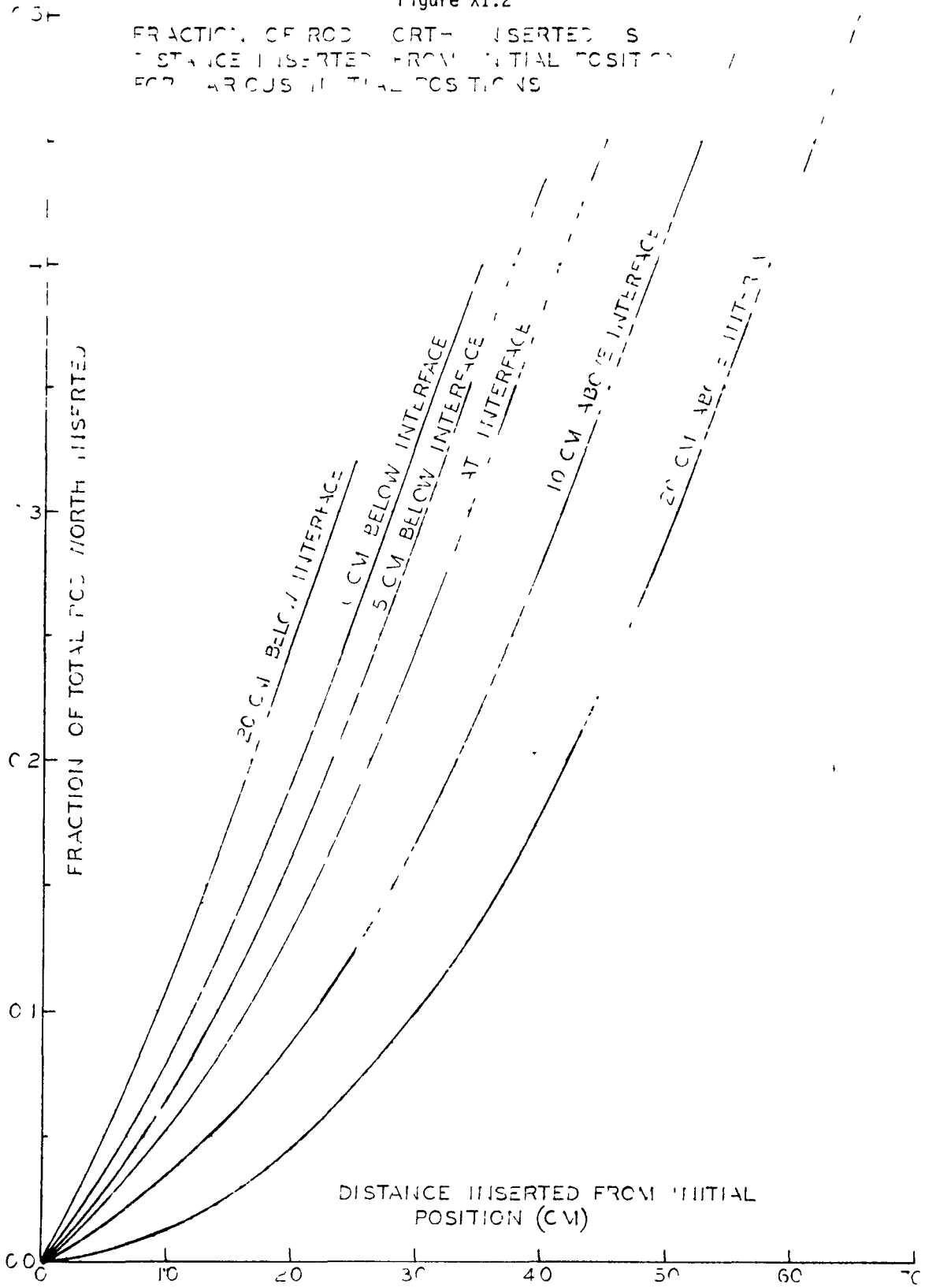
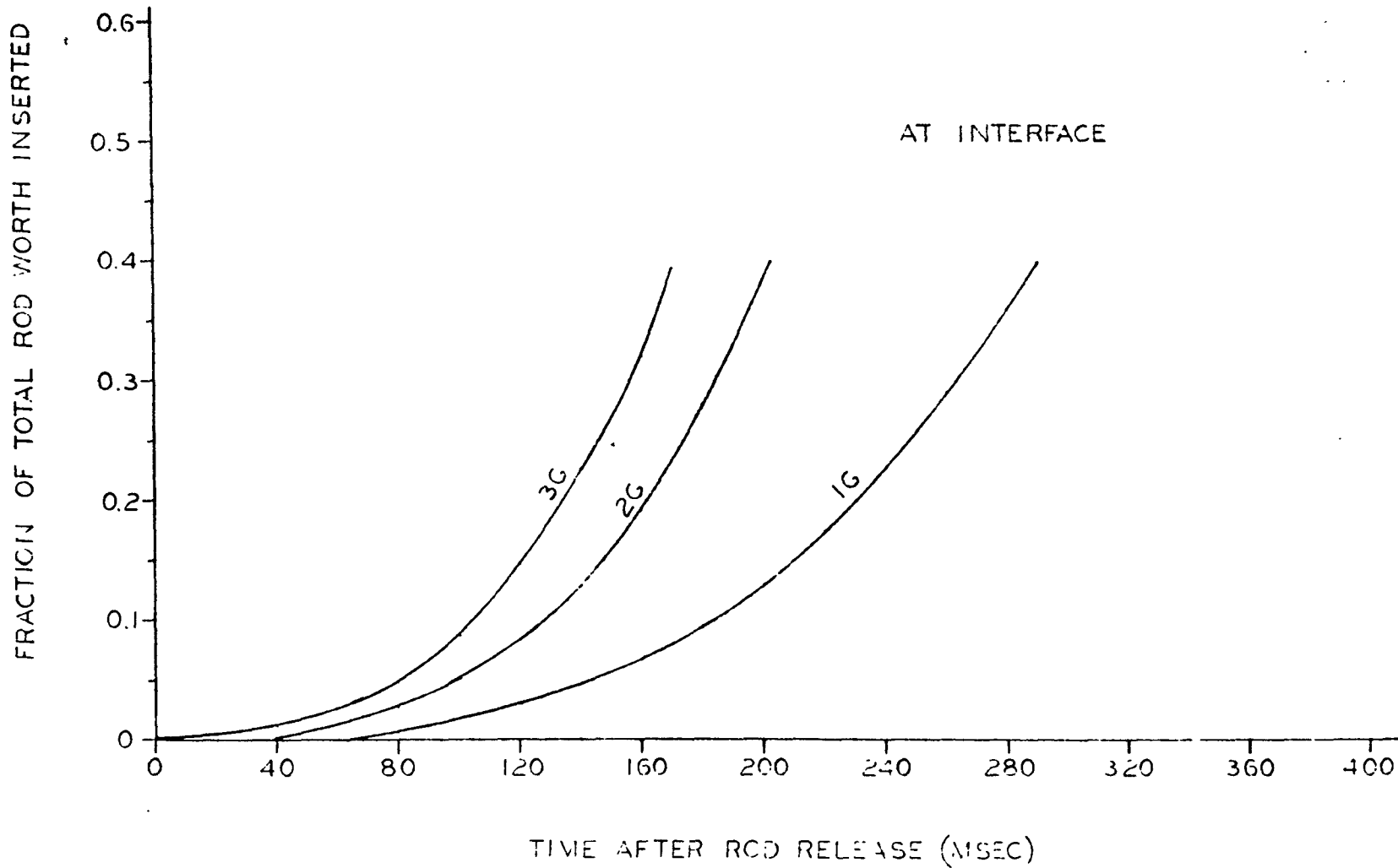


Figure XI.3

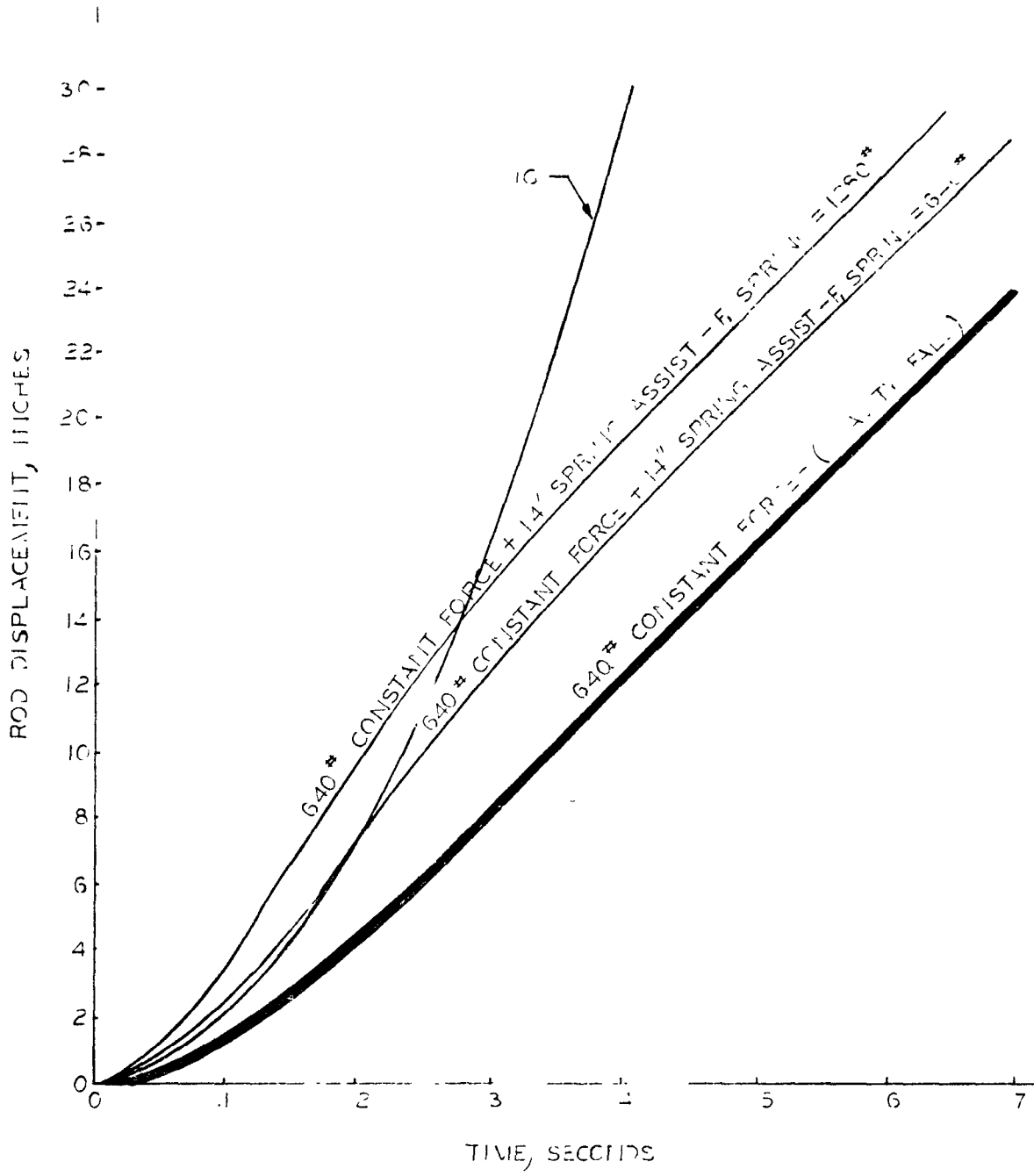
ROD WORTH INSERTED VS. TIME FOR ROD ACCELERATIONS OF 1, 2, AND 3G - INITIAL POSITION AT AXIAL INTERFACE.



XI.23

Figure XI.4

SORVAL INSERTION RATES - SPRING ASSIST
COMPARED TO 1G ACCELERATION



XI.24

Figure XI.5

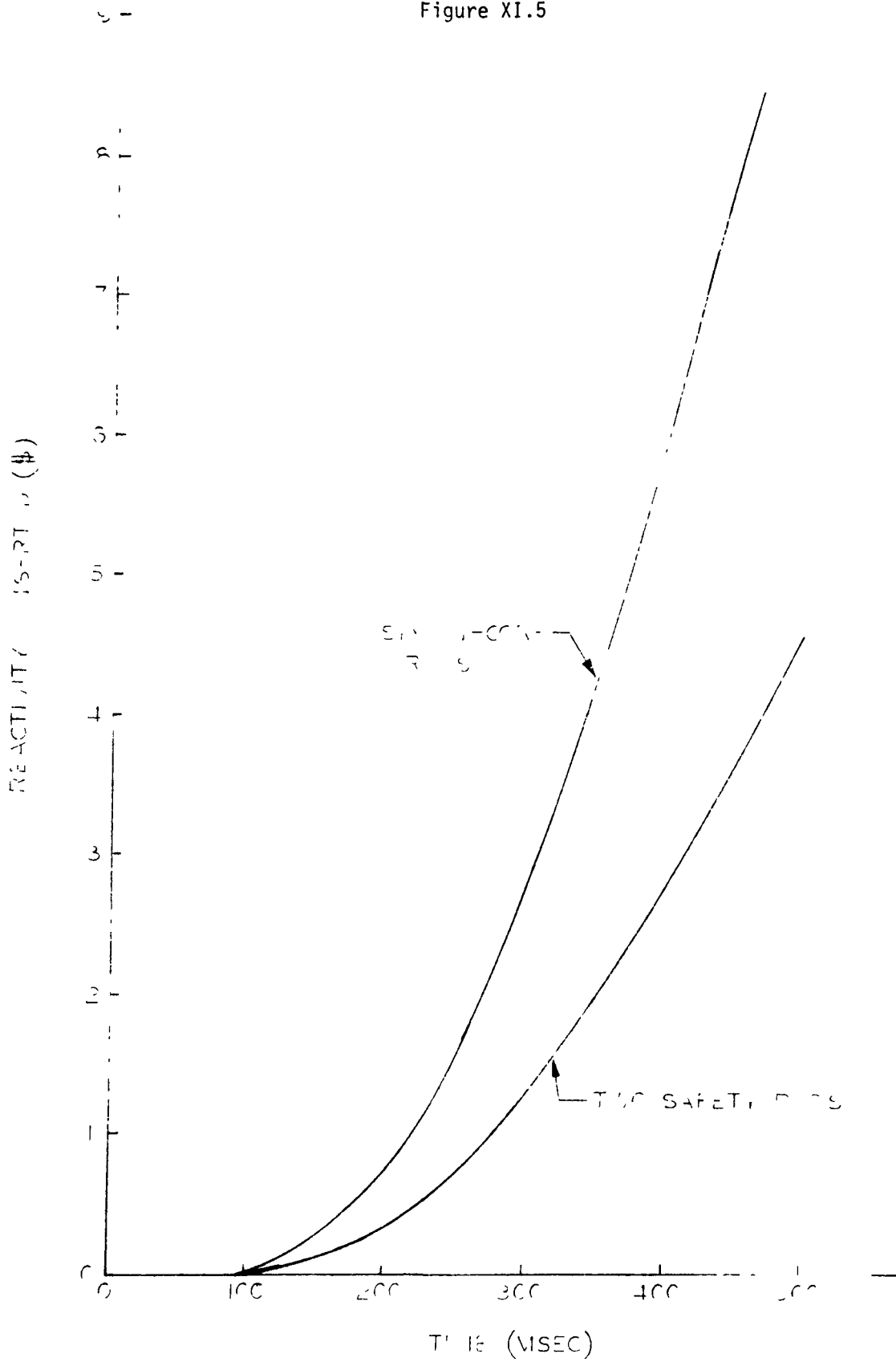
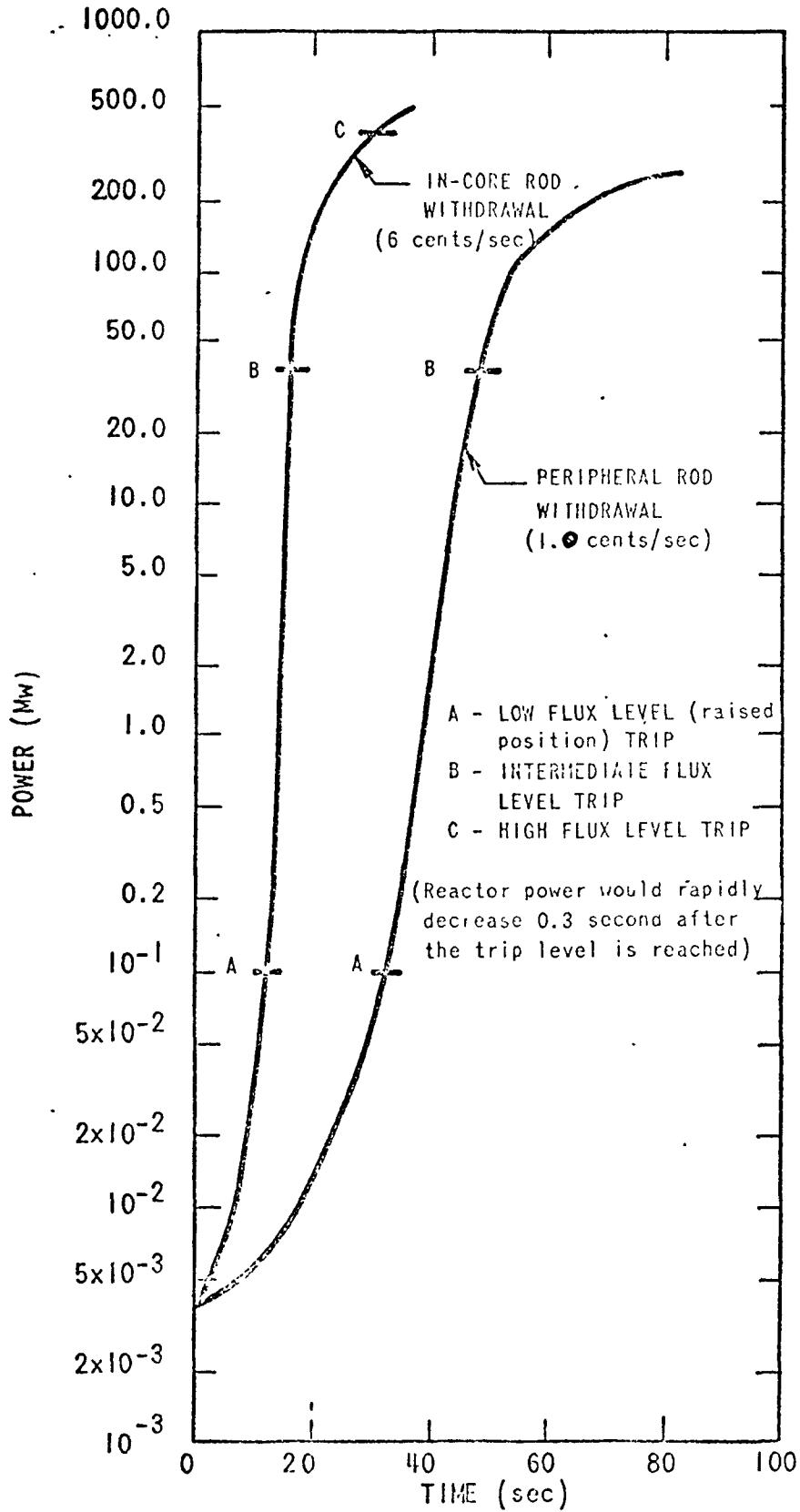
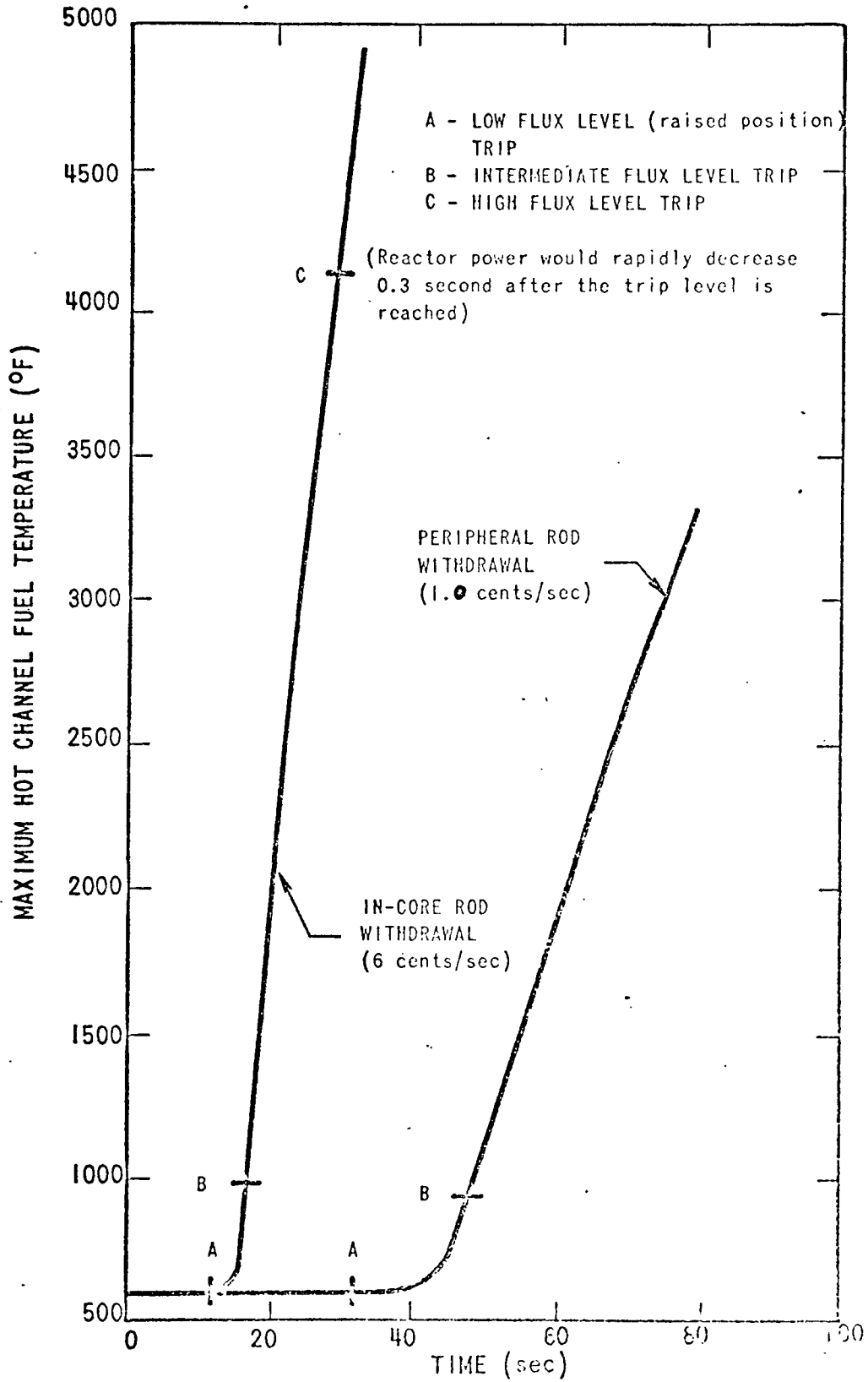


Figure XI.6



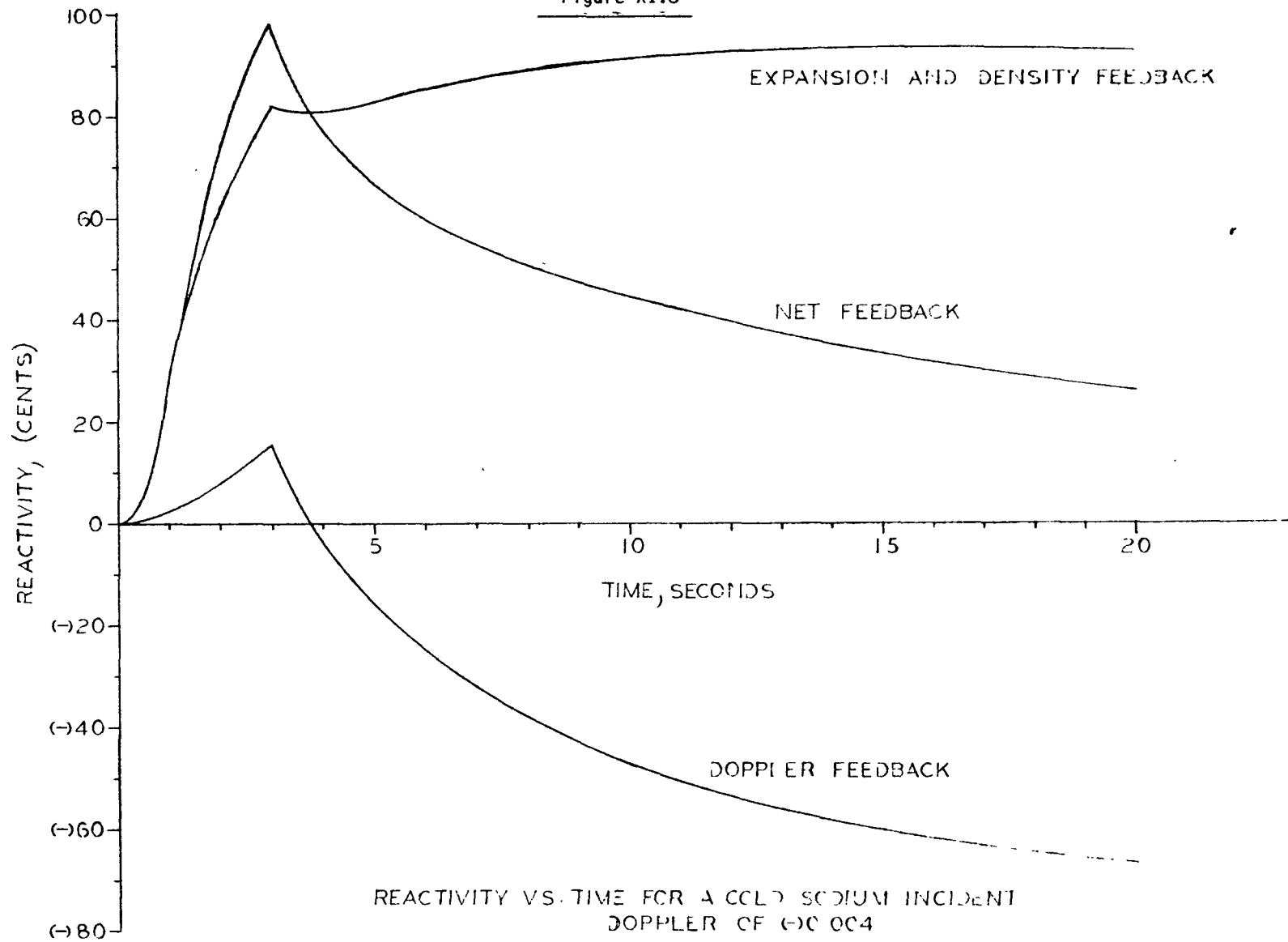
The Effect of a Continuous Rod Withdrawal Initiated at Reactor Power = 0.001%

Figure XI.7



The Effect of a Continuous Rod Withdrawal Initiated at Reactor Power = 0.001%

Figure XI.8



XI.28

Figure XI.9

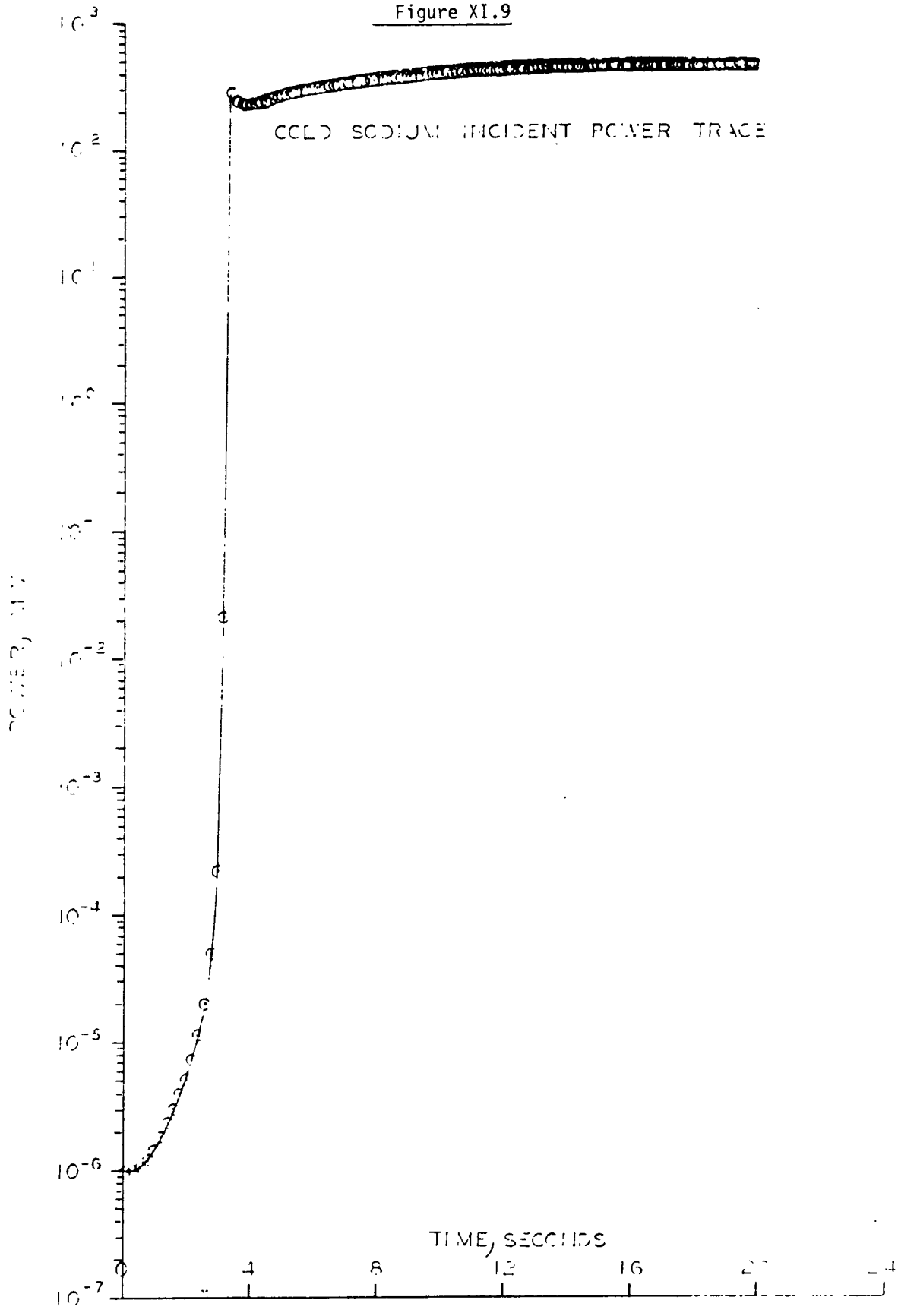
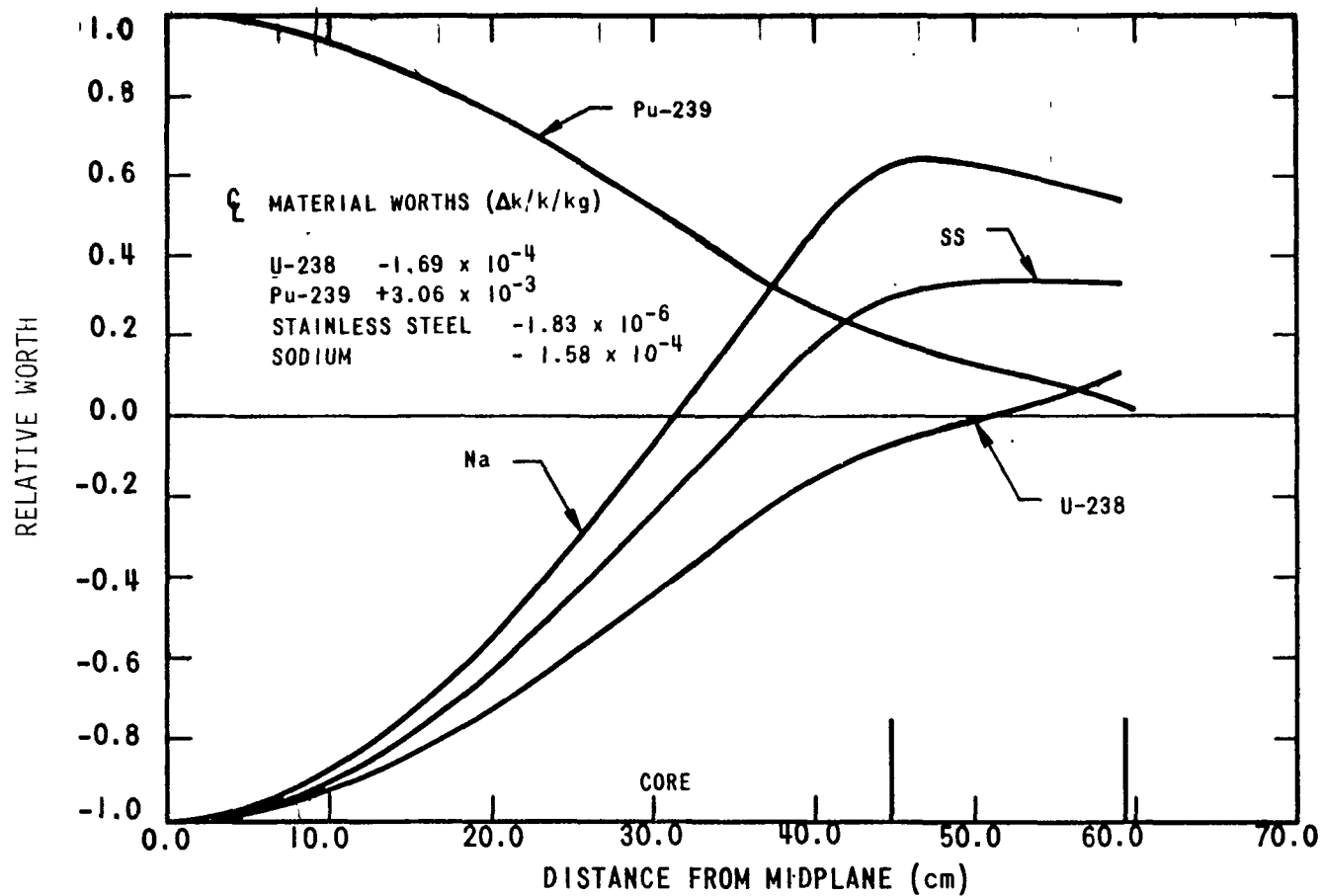


Figure XI.10



Normalized Axial Reactivity Coefficient Profiles at Radial Center

XI.30

Figure XI.11

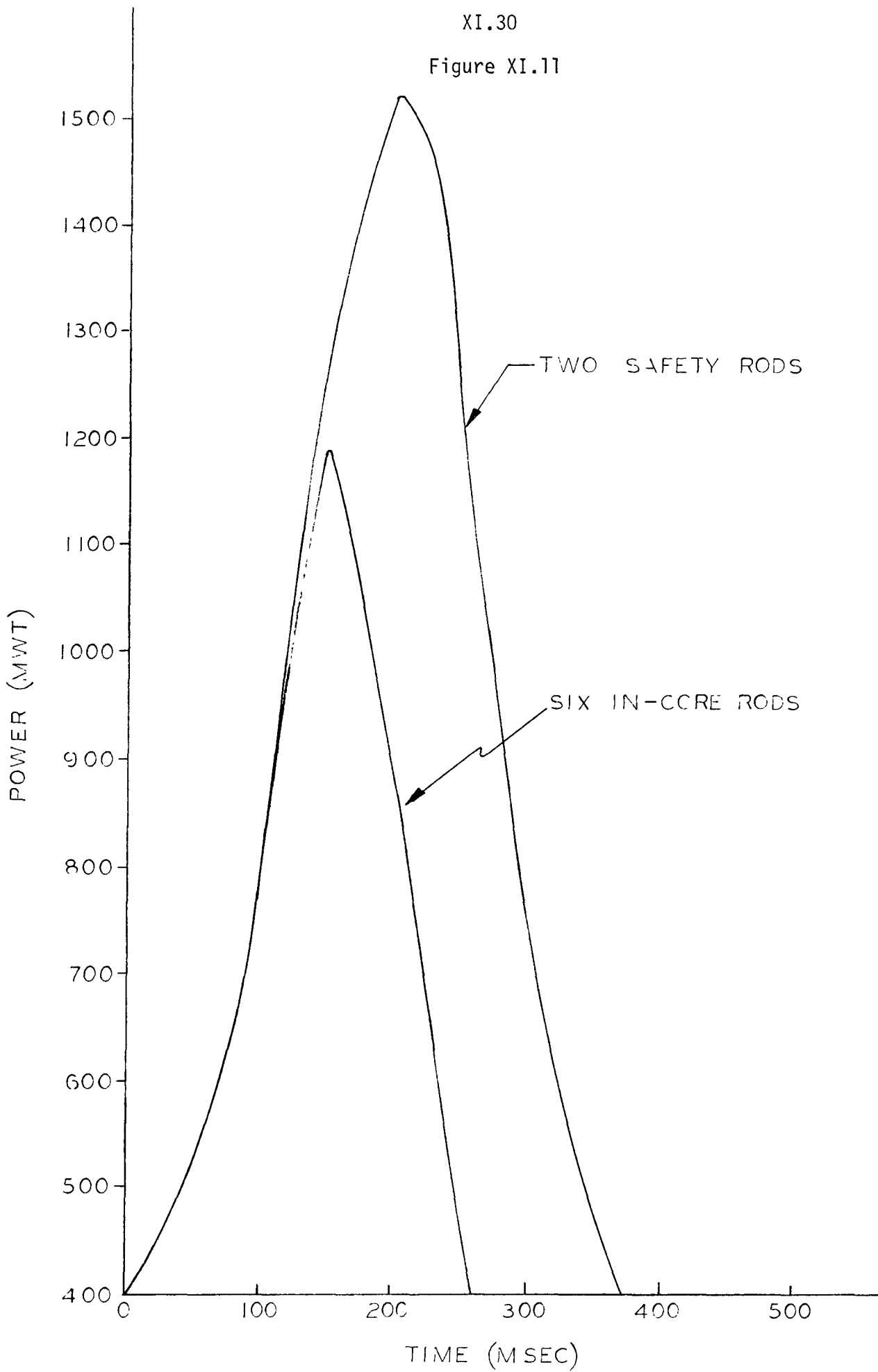
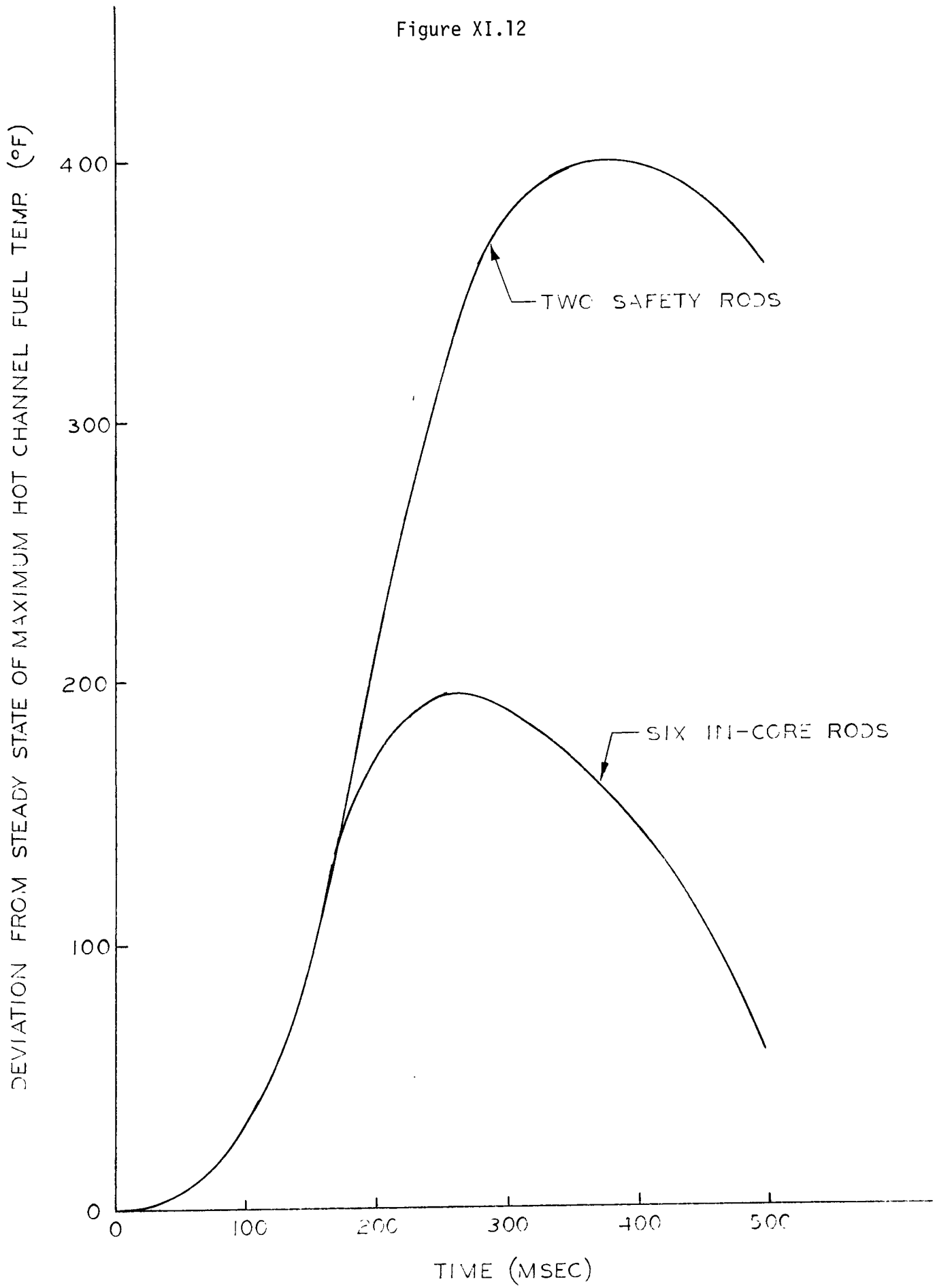


Figure XI.12



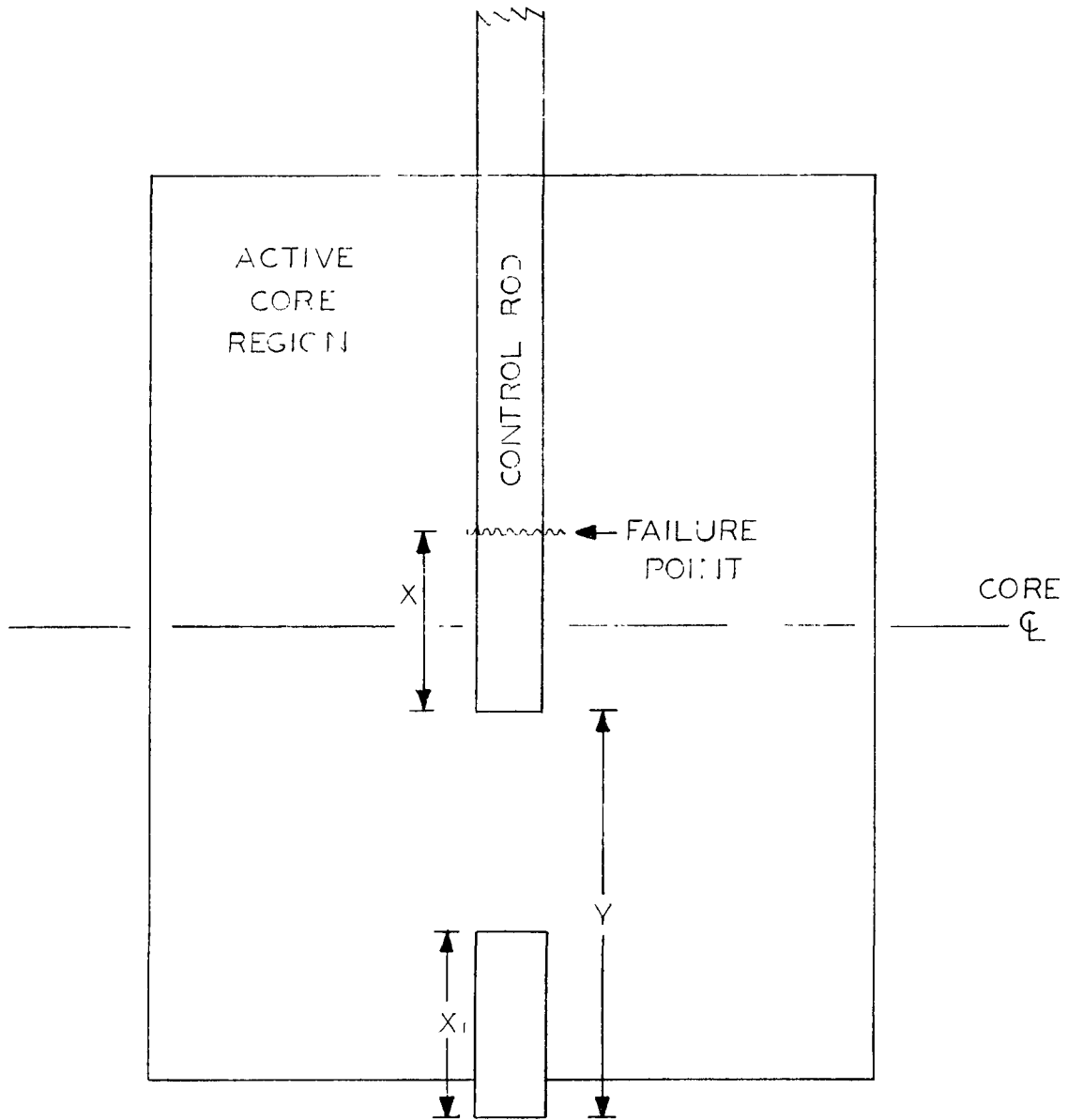
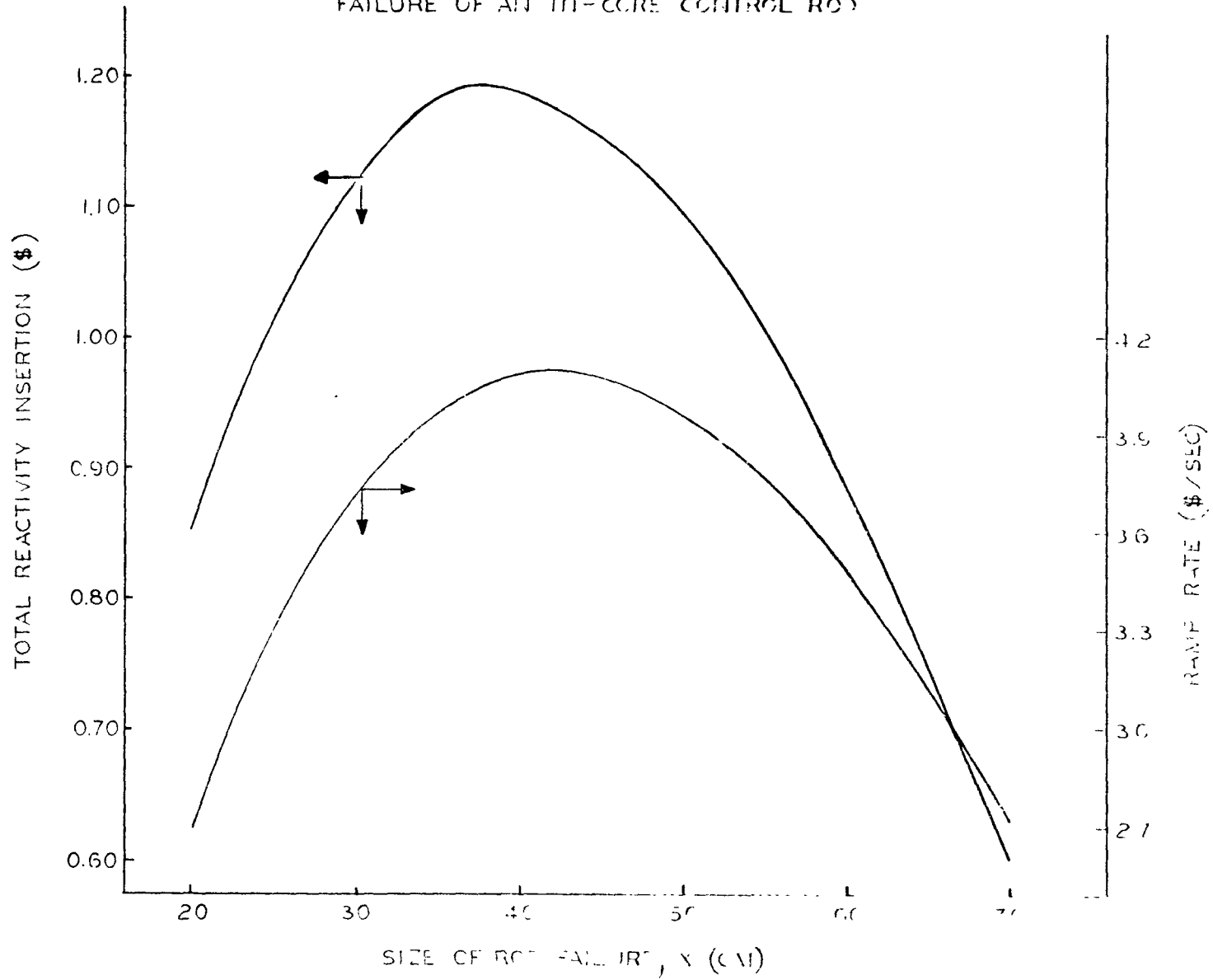


Figure XI.13 MODEL FOR STRUCTURAL FAILURE OF AN IN-CORE CONTROL ROD

Figure XI.14 TOTAL REACTIVITY INSERTION AND RAMP RATE FOR STRUCTURAL FAILURE OF AN III-CORE CONTROL ROD



XII. ANALYSIS OF LOSS OF COOLING ACCIDENTS

Compiled by H. G. Johnson

Contributions by:

C. D. Flowers
A. L. Gunby
H. G. Johnson
J. E. Krajicek
R. N. Madsen

A. Introduction

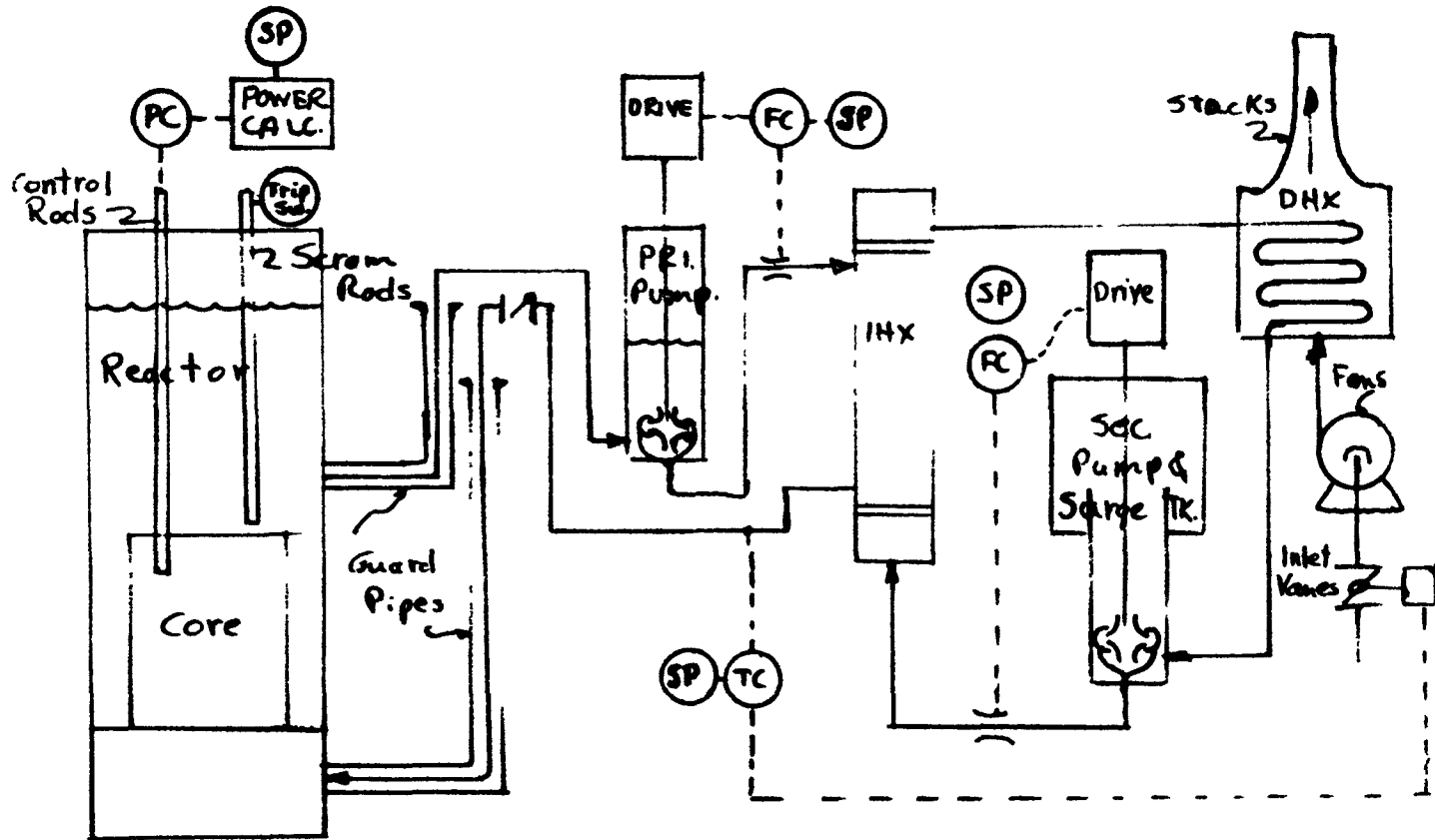
The subject of this lecture is limited to the description of the simulation methods used for analysis of failures of heat transport system components, including the failures of active components and passive components. Failures of pumps, fans, and process controls are examples of active component failures. A pipe break is an example of a passive component failure.

Attention is directed to single failures and situations involving sequential or concurrent faults. In the latter case, we usually combine the failure of an active or passive component with the concurrent (or sequential) failure of a primary protective action trip.

The worst case approach is often followed for conceptual design work. For example, the instantaneous loss of secondary coolant flow to an IHX can be used to represent the worst possible situation for any type of secondary or tertiary loop failure: the need for separate analysis for many real life type failures is then eliminated if the worst case analysis shows that the reactor can be shut down safely (while meeting established safety criteria) even for the worst case. The analysis of the real life failures is then done as a part of detailed design in order to optimize on such things as trip points, reactivity insertion rates, etc.

The reactor and heat transport system analyzed is depicted in Figure XII.1. Components included in the simulation models are:

FIGURE XII.1



XII.2

Reactor & HTS Schematic

(one of 3 identical HTS circuits shown)

E/12/69

XII.3

- Reactor and core
- Primary and secondary pumps and drives
- IHX and DHX (heat exchangers)
- Connecting piping
- Secondary surge tanks
- DHX fans
- Air flow dampers
- Process controllers and sensors
- Safety guard standpipes or tanks
- Safety system trip switches

For emergency cooling analysis, especially for pipe rupture and total loss of electrical power accidents, it is necessary that piping elevations and component arrangements be carefully simulated.

The modeling of components is discussed in paragraph C below.

B. Required System Performance

In order to make the transient analysis more than just an interesting exercise, it is necessary that some comparison criteria be available so that the calculated system performance can be compared against the required performance in order to establish the practicality of the then existing plant design. Safety criteria and limiting thermal shock criteria are the standards for comparison.

XII.4

1. Safety Criteria

The safety criteria for loss of cooling accidents are summarized in Tables XII.1 - XII.3. The damage limits are shown in Table XII.1; note that the criteria are based on cladding temperatures rather than fuel conditions for these loss of cooling accidents. The faults are defined and classified in Table XII.2, and finally the allowable core damage is shown in Table XII.3, where single and concurrent faults are considered.

2. Thermal Shock Criteria

Safety criteria simply establish maximum allowable temperature levels, but rates of temperature change and the amount of the temperature change are also vital to component design. The number of such cycles in the life of the plant is also important: the number of cycles is generally established by other design groups. Early in design the tentative system response to controlling accidents is determined and used as input to component design. The simulation models at this time are usually quite simple; consequently, a worst case approach is taken to give conservative rates and total temperature steps. Subsequently, it is necessary to adjust system performance to live within these component design transients.

C. Determination of System Performance

1. Computer Solutions to Problems

Analysis is performed using digital or analog-hybrid computers. The all digital approach is used where a great amount of detail is required, including such things as temperature dependent physical properties. For economic reasons,

TABLE XII.1

DAMAGE CLASSIFICATION FOR LOSS-OF-COOLING ACCIDENTS
INITIAL CORE IRRADIATED FUEL

<u>Accident Severity Level Classification</u>	<u>Fuel Cladding Damage Criteria For Loss-of-Flow Accident</u>	<u>Criteria Basis</u>
Disruptive Accident	Temperature > 1600 °F	Sodium Boiling
Major Accident	Temperature 1300 °F to 1600 °F	*
Minor Accident	Temperature 1200 °F to 1300 °F	
Operational Incident (no damage)	Temperature < 1200 °F	No damage stainless steel cladding limit

*The 1300 °F limit is based on reactivity accident criteria.

TABLE XII.2

DEFINITION OF FAULTS

- (1) Anticipated Fault -- May occur one or more times during lifetime of facility
- (2) Unlikely Fault -- Should not occur during reactor lifetime
- (3) Major Fault -- Should not occur in several reactor lifetimes. Results in damage associated with a major accident
- (4) Protective Action Failure -- Concurrent with any of above three faults.

Examples of the above types of faults are listed below:

<u>Anticipated Faults</u>	<u>Unlikely Faults</u>	<u>Major Faults</u>
Loss of flow with pump coastdown	Loss of flow without pump coastdown (pump seizure)	Pump casing rupture -- Loss of coolant from sump
IHX tube leak	IHX tube rupture	
BPA power failure	Circuit failure (to motor)	IHX containment shell rupture
Crack in primary pipe		
Check valve failure to close (Alternatively, the check valve failure to close could be considered as the failure of a primary protective action)	Pipe leak corrosion -- erosion primary pipe	Pipe rupture in primary loop
	Sodium hammer -- failure of valve dash pot	

TABLE XII.3

ALLOWABLE CORE DAMAGE FOR ACCIDENTS

<u>NUMBER OF SIMULTANEOUS INDEPENDENT OCCURRENCES</u>				<u>MAXIMUM ALLOWABLE CORE DAMAGE</u>				
<u>Anticipated Fault(s)</u>	<u>Unlikely Fault(s)</u>	<u>Major Fault(s)</u>	<u>Protective Action Failure</u>		<u>Operational Incident</u>	<u>Minor Accident</u>	<u>Major Accident</u>	<u>Disruptive Accident</u>
			<u>Primary</u>	<u>+ Backup</u>				
1					X			
	1					X		
		1					X	
	1		✓				X	
1			✓				X	
1	1						X	
2							X	
	2							X
		1	✓					X
	1		✓	✓				X
1		1						X
	1	1						X
1	1		✓					X
2	1							X
2			✓					X
3								X
1			✓	✓				X

the transient times are usually limited to one or two minutes, and preferably to less than 30 seconds. The hybrid is a good tool for parametric transient studies and is a must for process control work. There is no time limit for hybrid runs.

a. Dynasar Digital Simulation

The G. E. proprietary Dynasar code has been used for FFTF systems simulation work to date. Dynasar is a general purpose dynamic system analyzer code which is suitable for the evaluation of large, complex, linear and nonlinear systems describable by differential and algebraic equations. The code can handle up to 200 simultaneous integrations as set up by up to 1050 algebraic "boxes". A box is the name given each separate multiplier, summer, integrator, switch, etc. Integration is performed by a modified Adams Moulton 4 point history predictor-corrector technique in which the time steps are continually modified to maximize them while still meeting an error criterion. The integration process is started by a modified Euler method for the first 4 time points. A disadvantage of the Dynasar code is that the same time step is used for all integrations at a given time plane, with the time step, of course, determined by the time constant of the controlling integration.

To date we have been able to simulate only the reactor vessel and core and two primary loops (including the secondary side of the IHX's), because that amount of the system uses all available Univac 1108 storage

XII.9

capacity. Separate Dynasar codes are available for the secondary loops. These secondary loop codes then allow a determination of forcing data for the reactor plus primary loop programs.

Data decks only are required for Dynasar applications. REMOD and PRIM are the names given to the data decks for the reactor and primary loop codes, respectively.

b. Analog-Hybrid Simulation

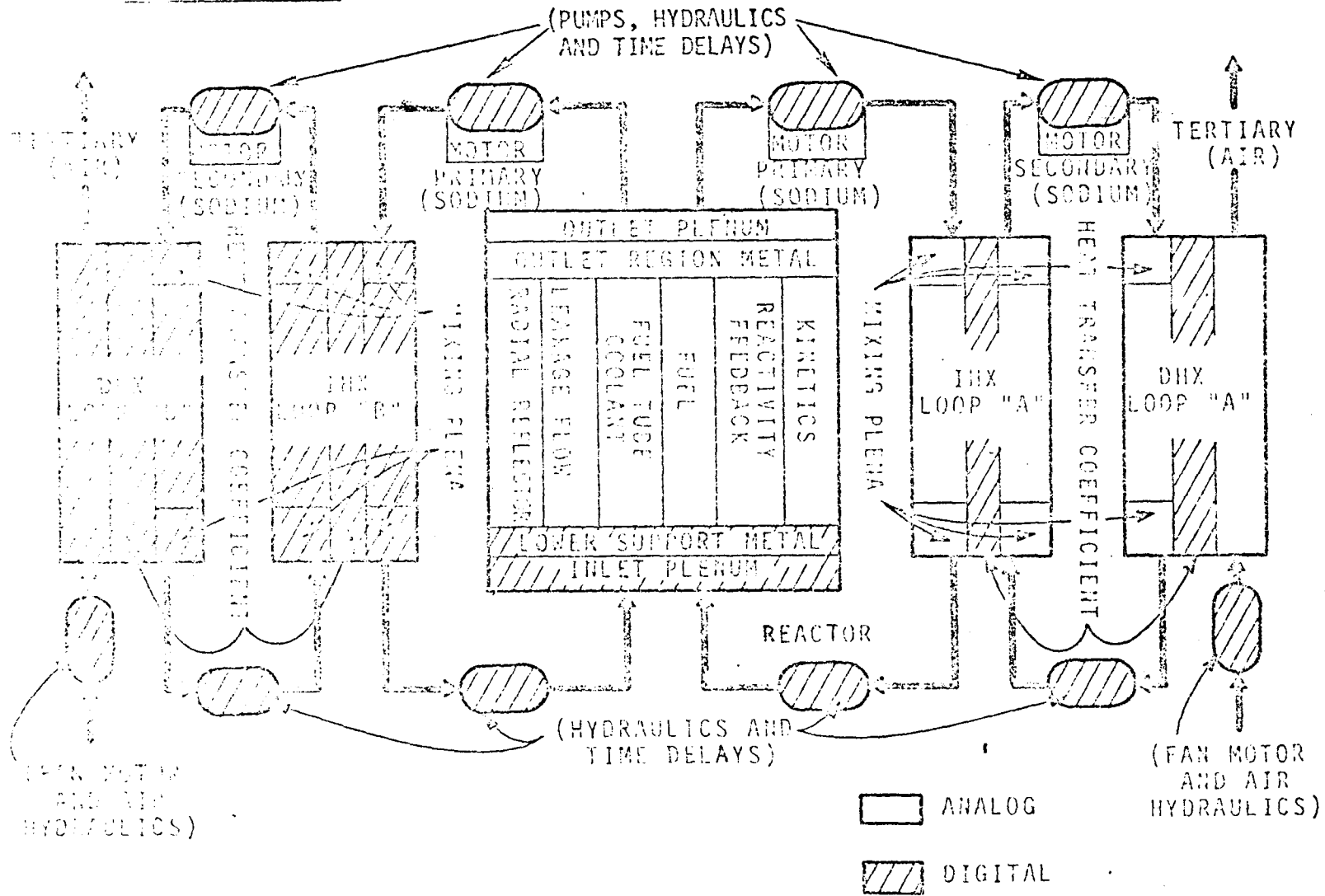
The FFTF hybrid consists of an AD-4 Applied Dynamics Analog computer with 200 amplifiers, including 48 integrators; a 16K, 18 bit word, PDP-9 Digital Equipment Corp. digital computer; interfacing equipment; and peripheral equipment such as recorders and an on-line printer.

All of the reactor and HTS are simulated with the hybrid models. Division of components between the digital and analog computers is shown in Figure XII.2.

Digital integrations are performed using an explicit method. Different time steps are used in the various parts of the system with integrations performed only as needed for accuracy. The digital programs are coded using the recently invented SIMPL-I language.⁽¹⁾

Refer to Appendix I for a brief summary of hybrid simulation used for conceptual design work.

Figure XII.2 FFTF SYSTEM HYBRID SIMULATION



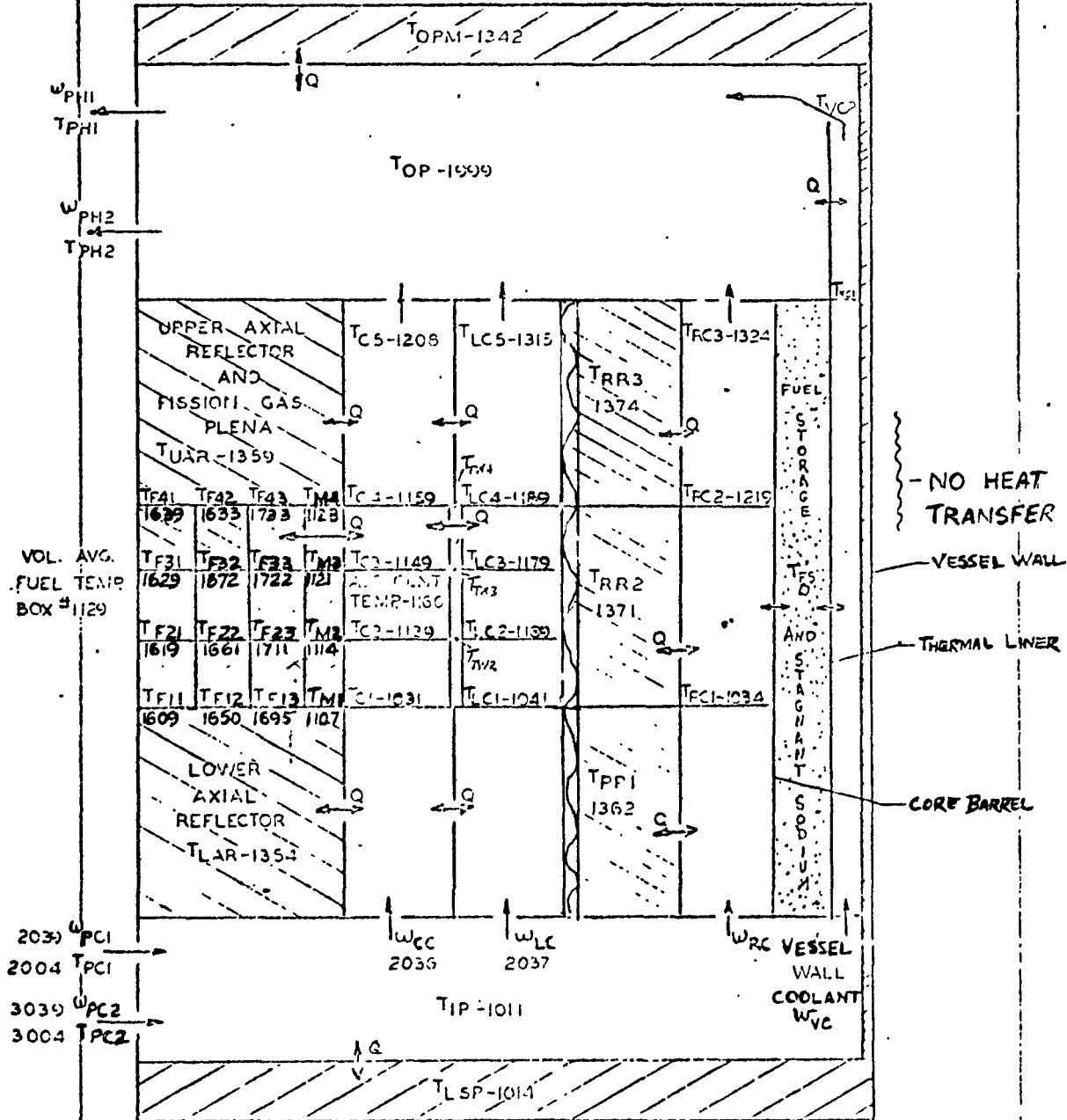
D. Mathematical Models of Reactor and HTS

1. Reactor Model Description

The reactor model is based on the FFTF vertical core reactor concept V-A depicted in drawing SK-3-14545. The model divides the reactor into 44 separate nodes where reactor temperatures are calculated. The nodal breakdown is shown in Figure XII.3. Inlet and outlet mixing plenums are simulated. There are four flow paths through the reactor: (1) average driver fuel tube coolant, (2) average leakage coolant outside of driver fuel tubes, (3) average radial reflector coolant, and (4) vessel wall coolant.

The following solid material regions have been simulated as separate nodes representing average conditions within the reactor vessel; fuel, fuel cladding, lower and upper axial reflectors, driver fuel duct wall (in core zone), inlet plenum metal, outlet plenum metal, radial reflectors (includes radial reflectors, shields, control rods, etc.), and a region that represents the fuel storage region outside of the reactor core barrel (simulated as stagnant sodium). Heat transfer between all adjacent regions is included (indicated by double pointed arrows in Figure XII.3).

Heat generation is included in the following regions; fuel, axial reflectors, and radial reflectors. The total reactor power includes power generated by fast (prompt) neutrons and power generation by beta and gamma decay of fission products. The neutron power is calculated by the simple point kinetics equations with the assumption that the neutron lifetime is small enough (neutron lifetime 10^{-7} for fast reactors) to make the neutron power calculation algebraic. (i.e., neglect $\lambda^* dP/dt$ term - restricts reactivity insertions to less than +1) Three reduced neutron decay groups



are assumed for input to the neutron power calculation. Three groups are also assumed to represent the fission product decay heat generation. As well, the following reactivity feedback terms are simulated: Doppler sodium temperature, and structural effects. A reactor power controller is also simulated.

Feedback coefficients are as follows:

Doppler Feedback

$$\delta k_{\text{Doppler}} = \alpha_D \ln \left(\frac{\bar{T}_{\text{Fuel}}}{\bar{T}_{\text{Fuel, Ref.}}} \right)$$

where

\bar{T}_{Fuel} = Volume average fuel temperature (absolute)

$\bar{T}_{\text{Fuel, Ref.}}$ = Reference steady-state volume average fuel temperature (absolute)

α_D = Doppler feedback coefficient = $T \frac{dk}{dT} = -0.004$ (assumed)

Sodium Temperature Feedback

$$\delta k_{\text{Coolant}} = \alpha_{\text{CLT}} \left(\bar{T}_C - \bar{T}_{C, \text{Ref.}} \right)$$

where

\bar{T}_C = Average driver channel coolant temperature in core region

$\bar{T}_{C, \text{Ref.}}$ = Reference average driver channel coolant temperature in core region

α_{CLT} = Sodium temperature feedback coefficient = $-1.39 \times 10^{-6} \text{ } ^\circ\text{F}^{-1}$

Structural Feedbacks

Two types of structural feedbacks have been included:

- (1) Core radial expansion feedback, δk_{ST1}

$$\delta k_{ST1} = \alpha_E \left(\bar{T}_C - \bar{T}_{C, \text{Ref.}} \right)$$

where

\bar{T}_C = Average driver channel coolant temperature in core region

$\bar{T}_{C, \text{Ref.}}$ = Reference average driver channel coolant temperature in core region

α_E = Core radial expansion feedback coefficient = $-4 \times 10^{-6} \text{ } ^\circ$
(assumed)

Note: -

The tube temperature has been assumed to be the same as the average tube coolant temperature.

- (2) Tube bowing feedback, δk_{ST2}

$$\delta k_{ST2} = \alpha_B \left(\Delta T_{\text{Core}} - \Delta T_{\text{Core, Ref.}} \right)$$

where

ΔT_{Core} = Tube coolant axial temperature difference across core

$\Delta T_{\text{Core, Ref.}}$ = Reference steady-state tube coolant axial temperature difference across core

α_B = Tube bowing feedback coefficient = $+6.25 \times 10^{-7} \text{ } ^\circ\text{F}^{-1}$
(assumed)

The structural feedback simulation is grossly simplified. However, the individual structural feedback coefficients are small and of opposite sign and the net structural feedback has very little effect on the total reactivity. Other reactivities that are included to make up the total reactivity include scram reactivity which is forced on the system by separate input, and control reactivity which is calculated by the reactor controller simulation.

Miscellaneous temperatures that are calculated include average fuel, average driver fuel channel coolant, hot channel core outlet, and hot channel maximum clad.

The total reactor simulation contains 52 differential equations of which 44 calculate reactor temperatures, six calculate total reactor power and two calculate power controller response. The remainder of the simulation consists of algebraic calculations and function generators.

All sodium, fuel, cladding and driver tube wall material properties are input as a function of temperature at each node point. Reflector and plenum metal properties have been assumed constant.

a. Power Calculations

Total power is neutron power plus fission product power.

1) Neutron Power

Single point kinetics (3 groups assumed) with prompt jump assumption, (i.e., $\ell^* \frac{dn}{dt} = 0$ assumed)

$$P_N = \frac{\sum_{i=1}^3 (\lambda_i \ell^* C_i)}{\beta - \delta k} \quad \text{from} \quad \frac{dP_N}{dt} = \frac{\delta K - \beta}{\ell^*} + \sum_{i=1}^3 \lambda_i C_i$$

where P_N is equivalent to n and

δk is equivalent to ρ

$$\frac{d(\lambda_i \ell^* C_i)}{dt} = \lambda_i \beta_i P_N - \lambda_i (\lambda_i \ell^* C_i) \quad i = 1, 2, 3$$

restrictions: $\delta k < +\beta$

2) Fission Product

Fission product data used with 3-group approximation as follows:

$$\frac{dP_{FPi}}{dt} = \lambda_{FPi} (\beta_{FPi} P_{Tot.} - P_{FPi}) \quad i = 1, 2, 3$$

$$P_{FP \text{ Total}} = \sum_{i=1}^3 P_{FPi}$$

b. Reactor Power Controller

A "bang-bang" type of controller is simulated. Controller reactivity is determined by control rod position and a control rod worth curve. Although the rod actually moves in finite steps, the rod insertion step inputs have been assumed linear with rate.

The rod position and movement is determined by the following equation:

$$X = X_i + r_1 \int_0^t N dt$$

where

X = rod position

X_i = initial rod position (steady state)

r_1 = insertion rate

$$N = \begin{cases} +1 & \text{if } P_{Tot.} \leq P_{Tot.} - 2.5\% P_{Tot.} \\ 0 & \text{if } P_{Tot.} \text{ within } \pm 2.5\% \text{ deadband} \\ -1 & \text{if } P_{Tot.} \geq P_{Tot.} + 2.5\% P_{Tot.} \end{cases}$$

i.e., If power increases $N = -1$ and rod position X decreases, thus providing less positive reactivity. Opposite when power decreases.

NOTE: Controller time constant of 0.1 sec. assumed, and initial rod position selected as that amount of δk required to offset the steady state sodium temperature feedback δk (arbitrary).

c. Thermal Calculations

Transient reactor temperatures are calculated by performing an energy balance on each node or node point in the system. Such an energy balance is

$$[\text{Rate of Change of Thermal Energy}] = [\text{Energy In}] - [\text{Energy Out}]$$

more specifically

$$\begin{aligned} \left[\begin{array}{c} \text{Rate of Change} \\ \text{of} \\ \text{Thermal Energy} \end{array} \right] &= \left[\begin{array}{c} \text{Energy In} \\ \text{With} \\ \text{Flowing Fluid} \end{array} \right] + \left[\begin{array}{c} \text{Energy In} \\ \text{by} \\ \text{Conduction or Convection} \end{array} \right] \\ &+ \left[\begin{array}{c} \text{Internal} \\ \text{Heat} \\ \text{Generation} \end{array} \right] - \left[\begin{array}{c} \text{Energy Out} \\ \text{With} \\ \text{Flowing Fluid} \end{array} \right] - \left[\begin{array}{c} \text{Energy Out} \\ \text{by} \\ \text{Conduction or Convection} \end{array} \right] \end{aligned}$$

The above equation applies to a three-dimensional problem.

However, for our simulation the following assumptions have been made: (cylindrical coordinates r, X, θ)

1. Flowing fluid energy in axial direction (X) only considered
2. Conduction and/or convection heat transfer only in radial direction considered (axial conduction neglected)
3. Uniform heat generation assumed
4. All changes in θ direction neglected
5. Surface work energy neglected.

The above assumptions are necessary to make the problem solution possible. The resulting solution is satisfactory for our total system simulation approach.

The energy balance terms in differential form are:
(Note balance on temperature T)

$$\left[\begin{array}{c} \text{Rate of Change} \\ \text{of} \\ \text{Thermal Energy} \end{array} \right] = \rho V C_p \frac{dT}{dt}$$

$$\left[\begin{array}{c} \text{Energy In} \\ \text{With} \\ \text{Flowing Fluid} \end{array} \right] = W C_p (T_{in} - T_{Ref.})$$

$$\left[\begin{array}{c} \text{Energy In} \\ \text{by} \\ \text{Conduction or Convection} \end{array} \right] = (UA)(T^* - T)$$

$$\left[\begin{array}{c} \text{Internal} \\ \text{Heat} \\ \text{Generation} \end{array} \right] = q$$

$$\begin{array}{l} \text{Energy Out} \\ \text{With} \\ \text{Flowing Fluid} \end{array} = WC_p (T_{\text{out}} - T_{\text{Ref.}})$$

$$\begin{array}{l} \text{Energy Out} \\ \text{by} \\ \text{Conduction or Convection} \end{array} = (UA) (T' - T)$$

T^* & T' = temperatures of adjacent regions

$T_{\text{Ref.}}$ = Ref. temperature (drops out in final equation)

Combining the above terms the final equation becomes:

$$\rho VC_p \frac{dT}{dt} = -WC_p (T_{\text{out}} - T_{\text{in}}) + q + (UA)(T^* - T) - (UA)(T' - T)$$

Starting with the basic equation and applying the same simplifying assumptions we get the same equation in the differential form.

$$\rho VC_p \frac{dT}{dt} = -WC_p \left(\frac{\partial T}{\partial X} \right) + q' + (UA)(T^* - T) - (UA)(T' - T)$$

More specific equations for the types of regions simulated within the reactor follow.

1) Mixing Plena

Perfect mixing assumed

$$(\rho bVC_p) \frac{dT_p}{dt} = W_1 C_1 (T_{1i} - T_p) + W_2 (T_{2i} - T_p) - (UA)(T_p - T_M)$$

where

T_p = plenum temperature (outlet temperature)

T_{1i} = inlet temperature for flow W_1

T_{2i} = inlet temperature for flow W_2

W_1 = flow into plenum

W_2 = flow into plenum

C_p = plenum specific heat

C_1 = inlet 1 specific heat

C_2 = inlet 2 specific heat

V = plenum volume

b = fraction of volume effective in mixing

ρ = plenum density

(UA) = heat transfer coefficient times heat transfer area

T_M = metal or other temperature that provides temperature gradient with plenum temperature for heat transfer

Common assumption: All specific heats are equal.

2) Single Axial Node Solid Regions With q

$$(\rho V \hat{C}) \frac{dT_s}{dt} = \frac{q}{L} - (UA) (T_s - \bar{T}_c)$$

$$\bar{T}_c = \frac{T_{ci} + T_{co}}{2}$$

where

T_s = solid temperature

\bar{T}_c = average coolant temperature

T_{ci} = coolant inlet temperature
 T_{co} = coolant outlet temperature
 V' = volume/unit length
 A' = heat transfer area/unit length
 U = overall heat transfer coefficient
 q = heat generation
 L = node length
 ρ = coolant density
 c = coolant specific heat

3) Single Axial Node Coolant Regions With Heat Transfer To/From Solid

$$(\rho V' C) \frac{dT_{co}}{dt} = - \frac{W_c C}{L} (T_{co} - T_{ci}) + (UA') (T_s - \bar{T}_c)$$

$$\bar{T}_c = \frac{T_{ci} + T_{co}}{2}$$

where

T_{co} = coolant outlet temperature

T_{ci} = coolant inlet temperature

T_s = solid temperature

W_c = coolant flow rate

All other nomenclature same as *above*.

If heat transfer with parallel coolant region exists, an additional $(UA')\Delta T$ term is included with ΔT simulated as the difference between the average coolant temperatures in each node.

NOTE: The following assumption is made in arriving at the above equation:

$$\frac{d\bar{T}_c}{dt} = \frac{dT_{co}}{dt}$$

rate of change
of average temperature = rate of change
of outlet temperature

4) Core Zone Fuel Temperatures

Fuel temperatures are calculated at four axial locations, and are interpreted as the temperature at that location and not as node volume temperatures. The heat generation is equally divided radially and a chopped cosine power distribution is assumed to obtain the heat generation at each specific axial location.

The thermal equations are written on a per-unit-length basis and are essentially the same as the equation for a solid with q .

The reason for writing the fuel temperatures at specific axial locations is that the core coolant temperatures are calculated at specific axial locations with finite difference techniques used to approximate the spatial temperature derivative term .

5) Core Zone Coolant Temperatures

$$(\rho V \dot{C}) \frac{dT_{cn}}{dt} = -W_c C_{cn} \left(\frac{\partial T_{cn}}{\partial x} \right) + \left(\begin{array}{c} \text{Heat Transfer} \\ \text{from} \\ \text{clad} \end{array} \right) - \left(\begin{array}{c} \text{Heat Transfer} \\ \text{to} \\ \text{Tube Wall} \end{array} \right)$$

$$n = 2,3,4$$

$$\text{for } n = 2 \quad \frac{\partial T_{c2}}{\partial x} = \frac{T_{c3} - T_{c1}}{2\Delta}$$

$$n = 3 \quad \frac{\partial T_{c3}}{\partial x} = \frac{T_{c4} - T_{c2}}{2\Delta}$$

$$n = 4 \quad \frac{\partial T_{c4}}{\partial x} = \frac{T_{c2} - 4T_{c3} + 3T_{c4}}{2\Delta}$$

$$\Delta = \frac{L_{\text{core}}}{3}$$

T_{c1} = core inlet temperature

W_c = coolant flow

6) Hot Channel Temperatures

Since the reactor model is calculated for reactor average conditions hot channel factors must be applied to calculate maximum temperatures in the reactor. Two hot channel temperatures are of interest; maximum core outlet coolant temperature, and maximum clad temperature.

Following BNWL-1064

To calculate core coolant hot channel temperature we should use:

$$\Delta T_{\text{HC clnt.}} = \alpha_{\Delta h} \cdot \alpha_{\text{orificing corrector}} \cdot \Delta T_{\text{clnt. average}}$$

$$\alpha_{\Delta h} = \text{Direct} \times \text{Statistical}$$

$$\alpha_{\Delta h} = 1.219 \times 1.0958$$

$$\alpha_{\Delta h} = 1.336$$

$$\alpha_{\text{orificing corrector}} = \frac{\text{center channel nominal } \Delta T \text{ with maximum clad orificing}}{\text{center channel nominal } \Delta T \text{ with equal } \Delta T \text{ orificing}}$$

$$\alpha_{\text{orificing corrector}} = \frac{361.5}{300} = 1.205$$

$$\alpha_{\Delta h} \cdot \alpha_{\text{orificing corrector}} = (1.336) (1.205) = \underline{\underline{1.610}}$$

The coolant hot channel temperature is then

$$T_{\text{HC clnt.}} = T_{\text{cl}} \uparrow 1.610 \left(T_{\text{c4}} - T_{\text{cl}} \right) \uparrow$$

core inlet temp.
avg. core ΔT

(T_{c4} = avg. core outlet)

To calculate maximum clad temperature we apply the film hot channel factor and radial power factor to the film ΔT and we apply the clad hot channel factor and radial power factor to the clad ΔT as follows:

$$\Delta T_{\text{film HC}} = \alpha_R \cdot \alpha_f \Delta T_{\text{film avg.}} \quad *(see\ note\ below)$$

$$\Delta T_{\text{clad HC}} = \alpha_R \cdot \alpha_{\text{clad}} \Delta T_{\text{clad avg.}} \quad *(see\ note\ below)$$

Then

$$T_{\text{clad max. HC}} = T_{\text{HC clnt}} + \alpha_R \cdot \alpha_f \Delta T_{\text{film avg.}} + \alpha_R \cdot \alpha_{\text{clad}} \Delta T_{\text{clad avg.}}$$

NOTE: $\Delta T_{\text{film avg.}}$ and $\Delta T_{\text{clad avg.}}$ are at top of core since this is location of

maximum clad temperature.

$$\alpha_f = \alpha_f^{\text{Direct}} \cdot \alpha_f^{\text{Statist.}} = (2.206)(1.344) = \underline{2.965}$$

$$\alpha_{\text{clad}} = \alpha_{\text{clad}}^{\text{Direct}} \cdot \alpha_{\text{clad}}^{\text{Statist.}} = (1.02)(1.1541) = \underline{1.177}$$

$$\alpha_R = \underline{1.40}$$

$$\frac{\alpha_R \cdot \alpha_f = 4.151}{\alpha_R \cdot \alpha_{\text{clad}} = 1.648}$$

*NOTE: The present model calculates mid-radius clad temperature only. Model will be modified to calculate average clad inside and outside temperatures at top of core so that $\Delta T_{\text{film avg.}}$ and $T_{\text{clad avg.}}$ will be available for hot channel calculations.

The heat transfer core model selection has been justified by comparisons with detailed TIGER models. Models studied are listed in Table XII.4. Results are shown in Figure XII.4 and XII.5 after scrams with and without flow coastdowns.

TABLE XII.4 CORE MODELS STUDIED

<u>Core Model 1:</u>	3 Radial Fuel Nodes
	1 Clad Node
	4 Axial Fuel Temps.
	3 Axial Coolant Temps. - Finite diff. sol.
<u>Core Model 2:</u>	3 Radial Fuel Nodes
	1 Clad Node
	1 Axial Node - Instant mixing assumed in coolant.
<u>Core Model 3:</u>	1 Radial Fuel Node $R_f = \frac{(r_o/.707r_o)}{2\pi k}$
(3A - same as 3 except has 2 Radial Fuel Nodes at each Axial Location)	1 Clad Node
	4 Axial Fuel Temps.
	3 Axial Coolant Temps. - Finite diff. sol.
<u>Core Model 4:</u>	1 Radial Fuel Node $R_f = \frac{(r_o/.707r_o)}{2\pi k}$
(4A - same as 4 except has 3 Axial Nodes)	1 Clad Node
	4 Axial Fuel Temps. (Avg.)
	4 Axial Coolant Temps. (Avg.) - 4 single nodes with instant mixing in each.
<u>TIGER Model B:</u>	7 Radial Fuel Nodes (All unsingered fuel 34" pin)
	1 Clad Node
	18 Axial Fuel Temps. (Avg.)
	18 Axial Coolant Temps. (Avg.) - single nodes with instant mixing in each.

Figure XII.4 BULK CORE COOLANT OUTLET TEMPERATURE FOR LOSS OF POWER TO ALL PUMP MOTORS WITH IMMEDIATE SCRAM
 XII.28 IMMEDIATE SCRAM

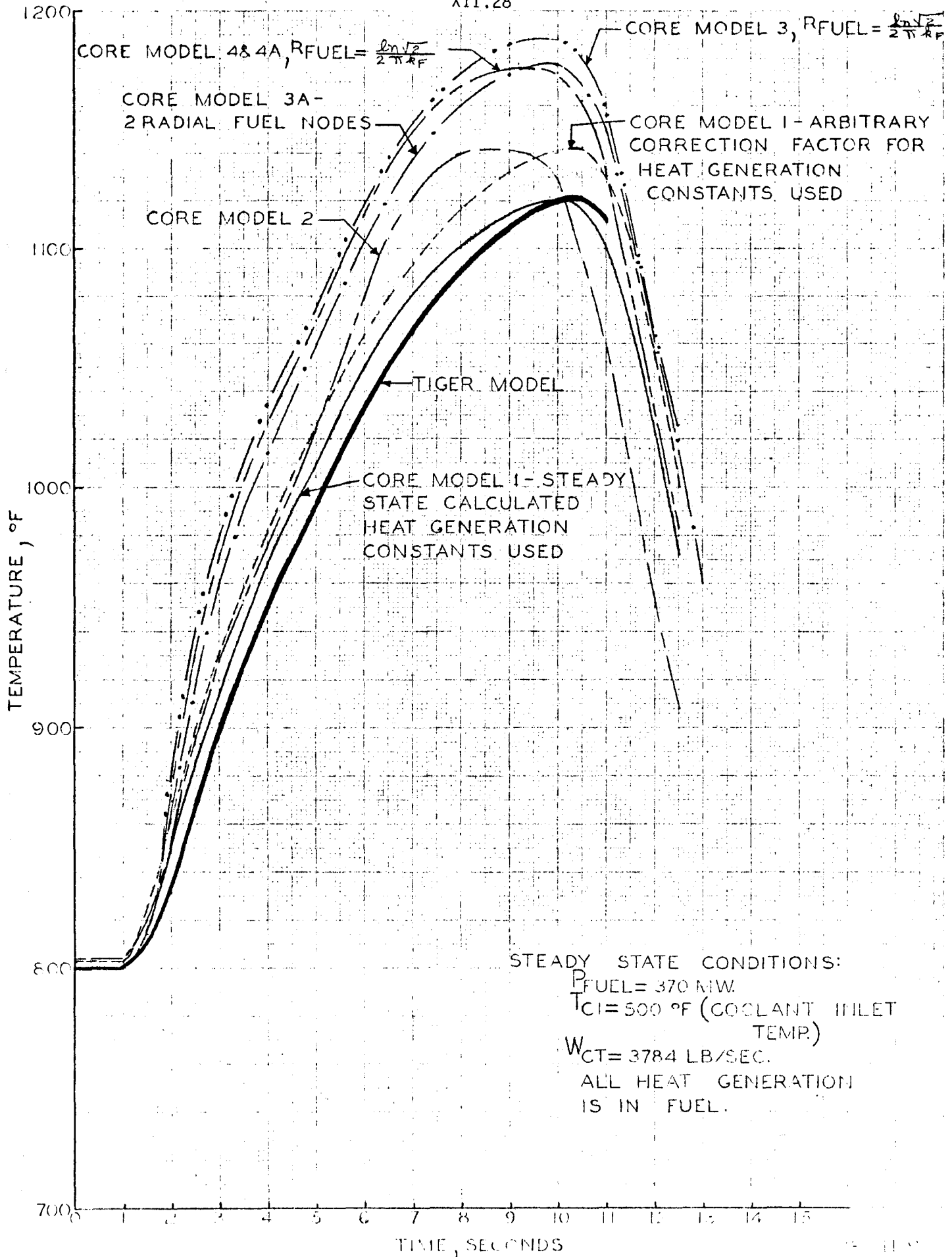
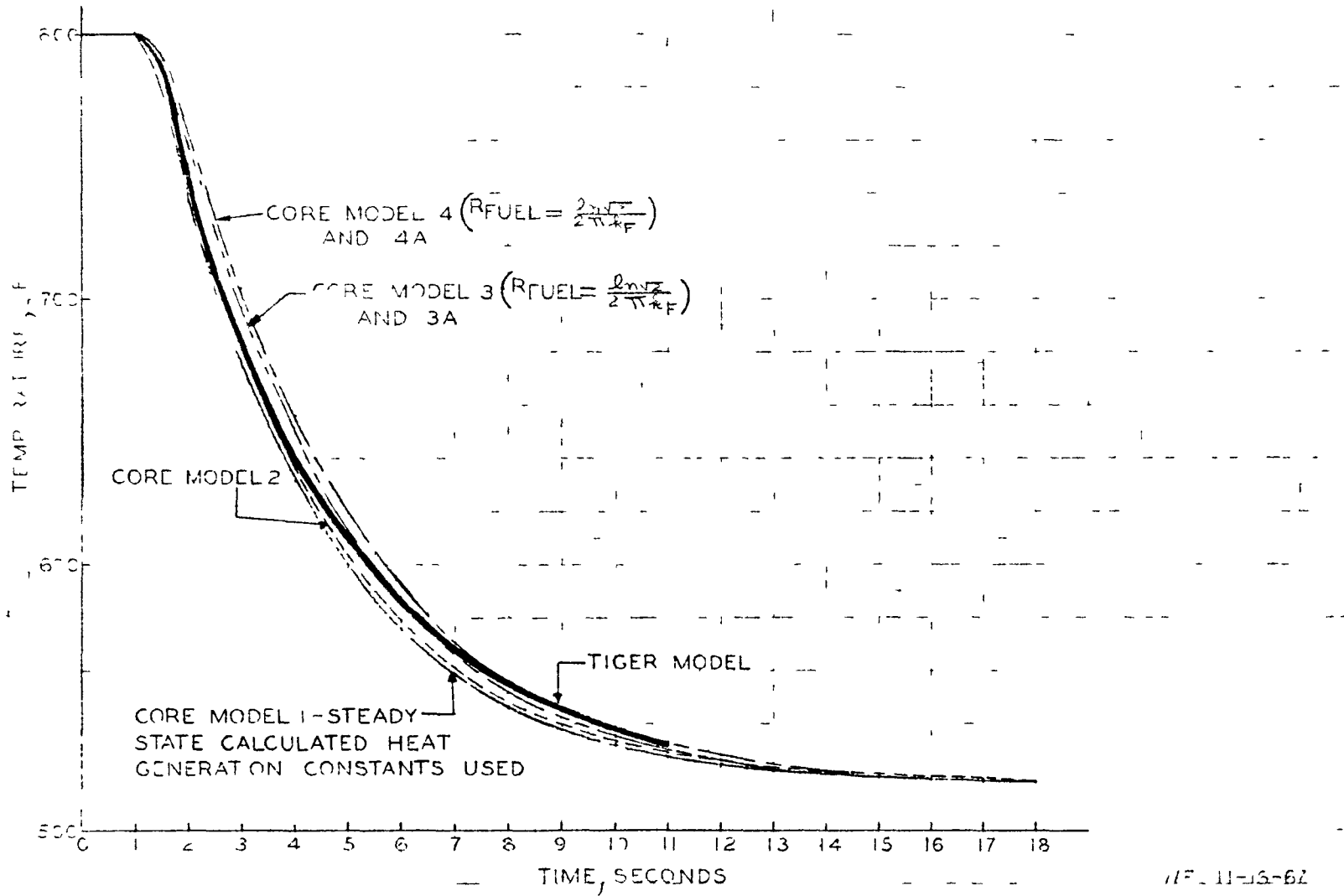


FIGURE XII.5

BULK CORE COOLANT OUTLET TEMPERATURE FOR 1G ROD ACCELERATION SCRAM
 (TOTAL REACTIVITY=15%) WITH FULL FLOW



2. System Hydraulics

a. Primary Loops Hydraulics

The primary loops hydraulics simulation will be discussed for a pipe rupture in one loop near the reactor vessel inlet. The hydraulics simulation for non-rupture conditions is similar.

The total pipe rupture simulation consists of the reactor and two independent primary heat transport system (HTS) loops. Each heat transport loop includes an intermediate heat exchanger (IHX), primary pump and pump drive, transport delays between components, and primary loop hydraulics.

The primary loops hydraulics are coupled with the reactor hydraulics to make a completely interdependent multiple loop hydraulics simulation. A schematic of the multiple loop primary system is shown in Figure XII.6 with a pipe rupture near the reactor vessel inlet in Loop 1. Loop 1 represents one HTS loop and Loop 2 represents two HTS loops for a total of three primary loops. Four parallel flow paths are simulated through the reactor:

W_{Ra} = total flow through driver subassemblies and open loops

W_{Rb} = total flow through bypass around driver subassemblies

W_{Rc} = total flow through radial reflector region

and W_{Rd} = total flow through vessel wall cooling annulus.

The basic equation of motion is used to derive the fluid flow transient equations with the following assumptions:

1. One-dimensional flow
2. Incompressible fluid, i.e., constant density

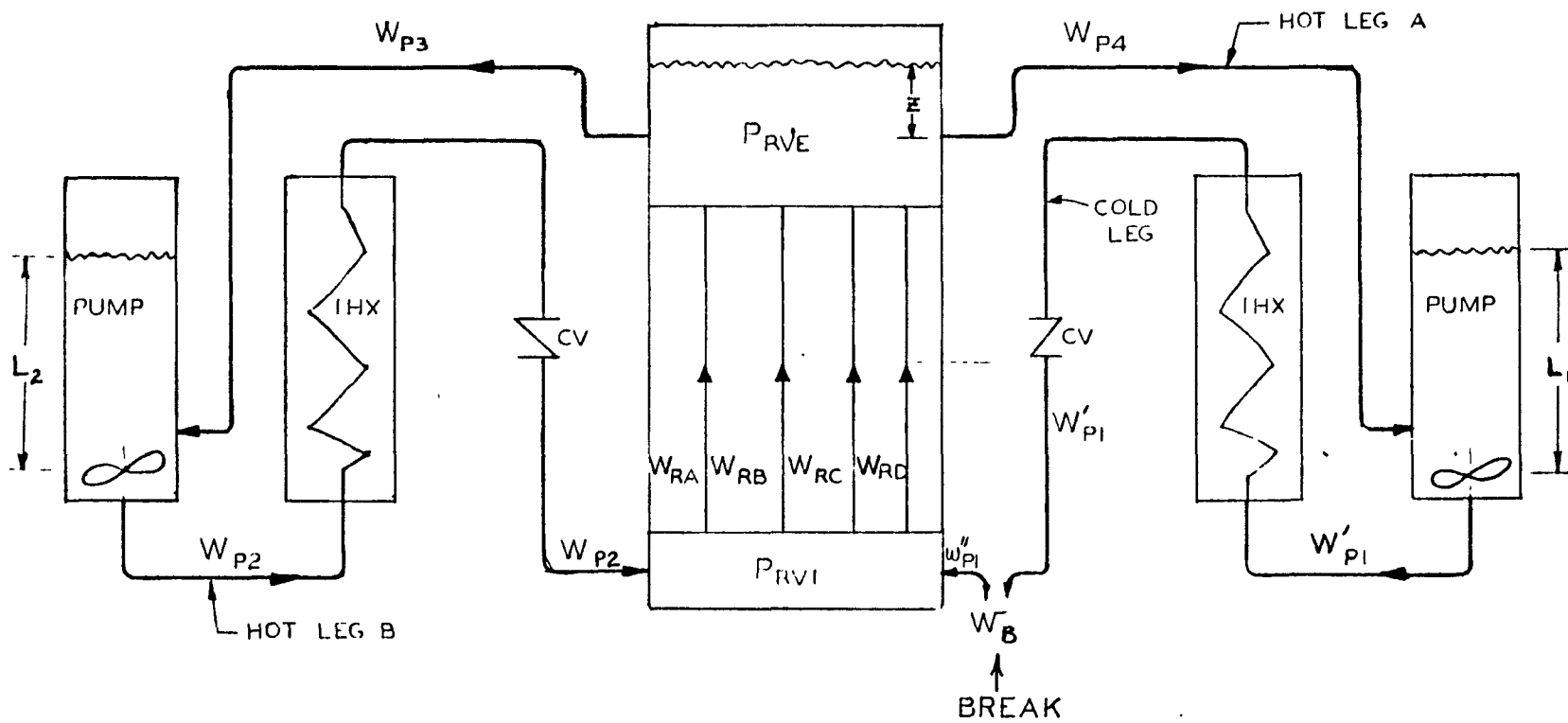


Figure XII.6 REACTOR AND PRIMARY LOOPS HYDRAULICS - SINGLE INLET LINE WITH RUPTURE

NOTE: BEFORE THE BREAK $W_{PI} = W'_{PI} = W''_{PI}$

3. Mean or bulk velocity assumed for entire tube cross-section
4. Equation is written for flow in pipe section, i.e., the macroscopic form of basic equation of motion is used.

With above assumptions we get the following equation:

$$\frac{\partial u}{\partial t} + u \frac{\partial u}{\partial x} + \frac{g_c}{\rho} \frac{\partial P}{\partial x} + g \frac{\partial Z}{\partial x} + F g_c = 0 \quad (1)$$

where

u = mean pipe velocity, ft/sec

P = pressure, lbf/ft²

g = local gravitational acceleration, ft/sec²

g_c = Newton's Law conversion factor = $32.2 \frac{\text{lbm} \cdot \text{ft}}{\text{lbf} \cdot \text{sec}^2}$

F = frictional loss ft(lbf.)/lbm-ft

Z = vertical elevation, ft.

x = dimension in direction of flow, ft.

ρ = density, lbm/ft³.

To obtain the simple mechanical energy balance at steady state we define the friction loss as follows:

$$F = \frac{(4f) u |u|}{2D g_c} \quad (2)$$

where

$(4f)$ is assumed to be the Moody friction factor

D = pipe inside diameter, ft.

Substitution of F into equation (1) results in the following equation

$$\frac{\partial u}{\partial t} + u \frac{\partial u}{\partial x} + \frac{g_c}{\rho} \frac{\partial P}{\partial x} + g \frac{\partial Z}{\partial x} + \frac{4fu |u|}{2D} = 0 \quad (3)$$

If we expand equation (3) and let

$$u = \frac{W}{A\rho} \quad (4)$$

where W = mass flow rate, lbm/sec

A = pipe cross section, ft²

and apply the continuity equation for incompressible flow

$$\frac{\partial \rho}{\partial t} = - \frac{1}{A} \frac{\partial W}{\partial x} = 0 \quad (5)$$

we get the following equation:

$$\frac{1}{gcA} \dot{W} = \frac{w^2}{9cA^2\rho^2} \frac{\partial \rho}{\partial x} + \frac{w^2}{9cA^3\rho} \frac{\partial A}{\partial x} - \frac{\partial P}{\partial x} - \frac{g}{9c} \frac{\partial Z}{\partial x} - \frac{4fw|w|}{29cDA\rho} \quad (6)$$

Relationship (6) can be integrated over a section of pipe length Δx :

$$\frac{1}{9c} \int_{x_1}^{x_1 + \Delta x_1} \frac{\dot{W}}{A} dx = \frac{1}{9c} \int_{x_1}^{x_1 + \Delta x_1} \frac{w^2}{\rho^2} \frac{d\rho}{A^2} + \frac{1}{9c} \int_{x_1}^{x_1 + \Delta x_1} \frac{w^2}{A^3} \frac{dA}{\rho} - \int_{P_1}^{P_2} \frac{dP}{\rho} - \frac{g}{9c} \int_{Z_1}^{Z_2} \rho dZ - \frac{1}{9c} \int_{x_1}^{x_1 + \Delta x_1} \frac{4fw|w|}{2DA^2\rho} dx \quad (7)$$

Weight-flow-rate is independent of position from equation (5). We assume a constant density of coolant in the section of pipe over which the integral is performed:

$$\frac{\dot{W}}{9c} \int_{x_1}^{x_1 + \Delta x_1} \frac{dx}{A} = \frac{w^2}{29c\rho} \left(\frac{1}{A_1^2} - \frac{1}{A_2^2} \right) - (P_2 - P_1) - \frac{g}{9c} \rho (Z_2 - Z_1) - \frac{w|w|}{29c\rho} \int_{x_1}^{x_1 + \Delta x_1} \frac{4fdx}{DA} \quad (8)$$

We define the inertial loss coefficient to be:

$$a \equiv \frac{1}{9c} \int_{x_1}^{x_1 + \Delta x_1} \frac{dx}{A} \quad (9)$$

We define the friction loss coefficient to be:

$$c \equiv \frac{1}{2gc} \int_{x_1}^{x_1 + \Delta x_1} \frac{4fdx}{DA^2} \quad (10)$$

Then

$$P_2 - P_1 = -a\bar{w} + \frac{w^2}{2gc\bar{\rho}} \left(\frac{1}{A_1^2} - \frac{1}{A_2^2} \right) - \frac{g}{gc} \bar{\rho} (Z_2 - Z_1) - \frac{c\bar{w}|w|}{\bar{\rho}} \quad (11)$$

Equation (11) is valid for any coolant section (forced or natural convection) where a constant density assumption is valid.

b. Coefficient Evaluation

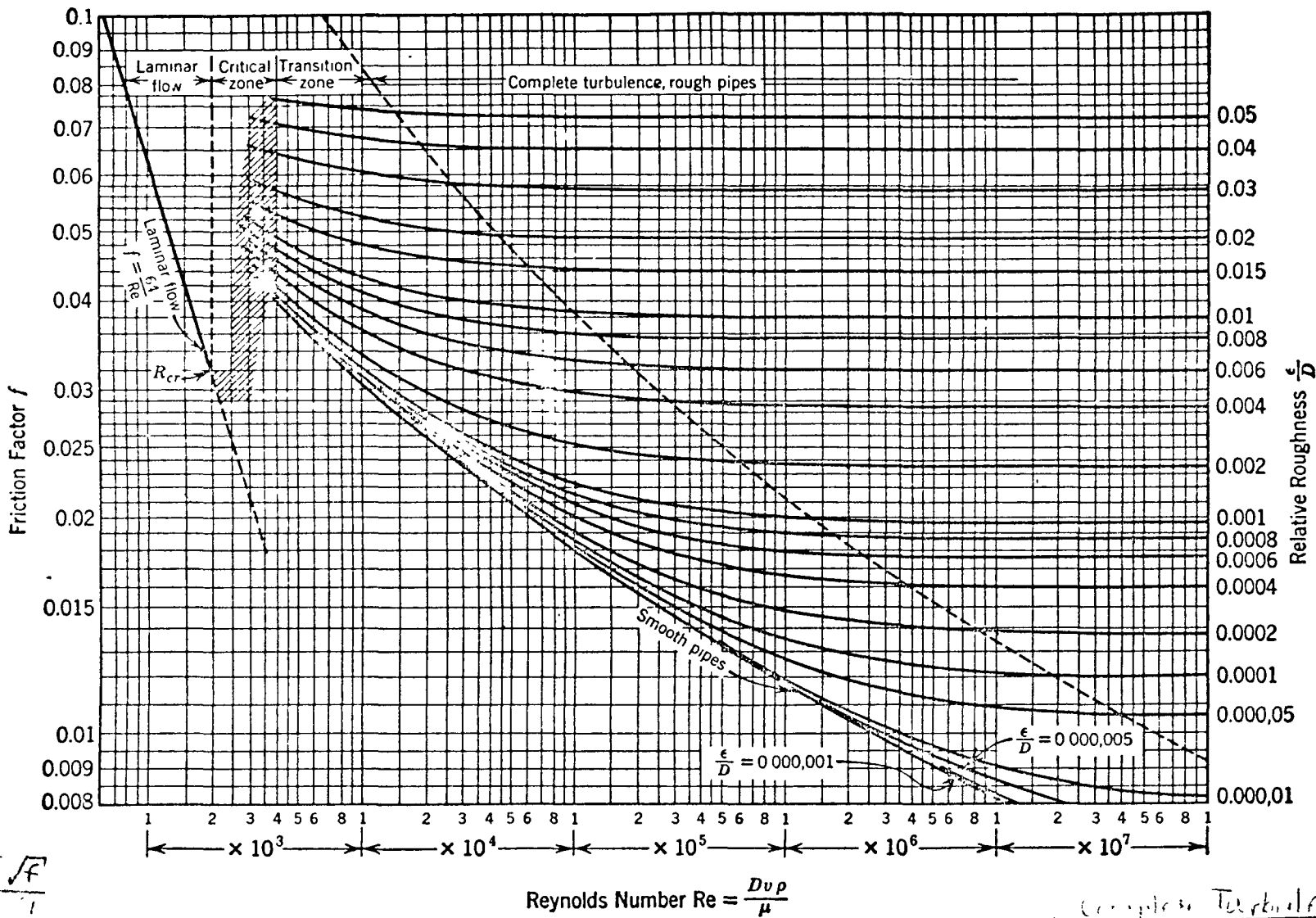
1) Inertial loss coefficient

The inertial loss coefficient is dependent only upon pipe geometry. The pipe run will be divided into sections of constant flow area (average areas and lengths will be used for non-uniform pipe and fittings) and the integral will be evaluated over each section:

$$a = \frac{1}{gc} \sum_{i=1}^N \frac{\Delta x_i}{A_i}$$

2) Friction coefficient

The Fanning friction factor is a function of flow regime as expressed by Reynold's Number, pipe material as described by absolute roughness, and pipe geometry in terms of diameter; Figure XII.7 depicts these relationships. A relative pipe roughness of .0001 is assumed in all pipe sections and the friction factor (4f) in each pipe section is obtained by determining the Reynolds Number for input to a friction factor table. The friction loss coefficient c is a function of pipe geometry and friction factor. The pipe run will be divided into sections of straight-runs of constant flow



Smooth pipe
 $\frac{1}{\sqrt{f}} = 2.0 \log_{10} \frac{Re \sqrt{f}}{2.5}$

Transition zone
 $\frac{1}{\sqrt{f}} = -1.8 \log_{10} \left(\frac{\epsilon/D}{3.7} + \frac{5.1}{Re \sqrt{f}} \right)$

Fig. XII.7 Friction factor as a function of Reynolds number with relative roughness as a parameter

From L. F. Moody "Friction Factors for Pipe Flow"
 Trans. ASME, 66 676 (1944)

Complete Turbulence Region
 $\frac{1}{\sqrt{f}} = 2.0 \log_{10} \left(\frac{3.7}{\epsilon/D} \right)$

area or sections of non-uniform pipe and fittings. For uniform pipe sections

$$\int_{x_1}^{x_1 + \Delta x_1} \frac{4f dx}{DA^2} = \sum_{i=1}^N \frac{4f_i \Delta x_i}{D_i A_i^2}$$

For sections of non-uniform pipe and fittings, conventional velocity head friction factors will be used:

$$\int_{x_1}^{x_1 + x_1} \frac{4f dx}{DA^2} = \sum_{i=1}^M \frac{K_i}{A_i^2}$$

Thus the friction loss coefficient is:

$$c \equiv \frac{1}{29c} \left[\sum_{i=1}^N \frac{4f_i \Delta x_i}{D_i A_i^2} + \sum_{i=1}^M \frac{K_i}{A_i^2} \right]$$

Table XII.5 sets forth the K values which will be used.

3) Natural Circulation Simulation

Natural circulation is accounted for in the hydraulics equation (11) by including a density times an elevation difference term for various sections through the primary system piping and components. In the driver fuel channel (W_{RA}), four $\rho \Delta Z$ terms are included; one from the vessel inlet to the core bottom using core inlet density, one from the core bottom to the top of the active fuel using the average density for the core, one from the top of the fuel to the tube outlet using tube outlet density, and one from the tube outlet to the vessel outlet using vessel outlet density. Flow channels W_{RB} , W_{RC} and W_{RD} each use two natural circulation terms.

Table XII.5

Fitting	Velocity Heat Factor K
Welding Tee Through Branch	1.36
90° Welding Elbow L.R.	.315
90° Welding Elbow S.R.	.455
45° Welding Elbow	.208
Gate Valve, Open	.208
Sudden Expansion	1.0
Sudden Contraction	.5

Moving on around the loop there is a $\rho\Delta Z$ term for the primary hot leg piping from the reactor vessel outlet nozzle to the pump inlet nozzle using hot leg density. There is also a $\rho\Delta Z$ term for the hot leg piping from the pump to the IHX using pump discharge density (based on pump barrel sodium temperature).

Through the IHX there are six natural circulation terms, one for each mixing plenum and one for each axial node through the IHX, with each term employing the average density in that region. This accounts for IHX thermal centerline shift during a transient. Completing the loop there is one $\rho\Delta Z$ term for the cold leg piping from the IHX to the reactor vessel inlet.

c. Method of Solution

Before a break there are eight (8) unknown flow rates; four through the reactor and two in each primary loop simulated. The loop flows before the break are: (see figure XII.6)

W_{p1} = flow from pump to reactor inlet, Loop 1

W_{p2} = flow from pump to reactor inlet, Loop 2

W_{p3} = flow from reactor outlet to pump, Loop 2

W_{p4} = flow from reactor outlet to pump, Loop 1

After the break there are nine (9) flow rates, four through the reactor and the following five loop flow rates:

W'_{p1} = flow from pump to break, Loop 1

W_{p1}'' = flow from break to reactor inlet, Loop 1

W_{p2} = flow from pump to reactor inlet, Loop 2

W_{p3} = flow from reactor outlet to pump, Loop 2

W_{p4} = flow from reactor outlet to pump, Loop 1

The above flow rates are determined by applying equation (11) from known pressure point to known pressure point in the system. The known pressures are: (1) reactor vessel outlet pressure determined by sodium pool depth, Z , and the reactor cover gas pressure, P_g (assumed to be zero at all times), (2) pump pressures above impellers determined by the pump barrel sodium levels, L_1 and L_2 , and pump cover gas pressure (assumed to be zero at all times), and (3) the pressure outside the break, P_a .

The reactor vessel pool depth Z , and the pump barrel levels L_1 and L_2 are calculated as a function of time by applying a simple mass balance in each sodium reservoir.

Before the break we apply equation (11) from the pressure in pump 1 to the pressure at the reactor vessel exit. We obtain four equations by applying the equation from the pump to the reactor inlet plenum and from the reactor inlet plenum through each of the four flow channels through the reactor. This results in four equations and five unknown flow rate derivatives, \dot{W}_{p1} (before break), \dot{W}_{RA} , \dot{W}_{RB} , \dot{W}_{RC} , and \dot{W}_{RD} . A fifth equation is obtained by applying equation (11) from the pressure in pump 2 to the pressure at the reactor vessel exit. Flow, \dot{W}_{p2} , is eliminated by performing a mass balance on the inlet plenum and by defining the total reactor flow, \dot{W}_p , as the sum of the four flows through the reactor. Finally, with five equations and five unknowns we can solve for the following flow rate derivatives (before break): \dot{W}_{p1} , \dot{W}_{RA} , \dot{W}_{RB} , \dot{W}_{RC} , and \dot{W}_{RD} .

Integration of the resulting flow rate derivatives yields the flow rates. The flow in loop 2, \dot{W}_{p2} can be solved by a simple mass balance on the reactor inlet plenum. The other two flow rates in the system W_{p3} and W_{p4} can be solved for directly by applying equation (11) between the known pressures at the reactor vessel exit and the pump barrels.

After the break the solution method is the same, but the simultaneous solution of the five equations yields the flow rate from the break (known pressure) to the reactor inlet (W_{p1}'') instead of W_{p1} . The flow rate from the pump to the break in loop 1 can be solved for directly after the break by applying equation (11).

The break pressure and flow out the break are a function of the type of break. Two types of breaks have been investigated: (1) a break that is simply a hole in the pipe that can have any specified break flow area, and (2) a complete double-ended pipe rupture. The orifice equation is used for flow out of the hole-type break. A coefficient of one is used for all hole sizes and flow rates. Unrestricted flow from both open ends of the pipe is assumed for the double-ended break, with each exit loss taken as one velocity head. Static pressure over the break due to the collection of sodium is accounted for in those cases where break outflow collects in a guard standpipe or guard sump. The pressure outside the break, P_a , for a break near the reactor inlet nozzle is determined by the sodium level in the sodium collecting standpipe. This pressure is strictly a static pressure due only to the sodium level above the break at any time. The dynamic effects of the standpipe filling are ignored; this gives a worst case solution. The level is calculated as a function of time and the standpipe is assumed to be empty before

the break. The surrounding gas pressure is assumed to be zero gauge. The standpipe height and flow area are input values. The standpipe is used only for breaks near the reactor inlet, downstream of the check valve.

The inlet line check valve has been simulated to begin closing once reverse flow in the line is detected. The valve disc is assumed to be damped to prevent damaging sodium hammer shocks and is programmed to close over three seconds. Check valve pressure loss data for a typical tilting disk check valve are included in the simulation for both the full open valve and the closing valve for flows in the normal direction. Check valve pressure loss for reverse flow is calculated using the drag force concept with the loss being a function of disk position. The drag coefficient is given a numerical value of one. For breaks upstream of the check valve, cases have been studied for the valve both closing and sticking open. More exact check valve dynamics is discussed later.

The hydraulics simulation for pipe breaks in other primary loop locations is essentially the same as for the break location just discussed. The loop flows are calculated from known pressure to known pressure around the loops. For multiple reactor inlet pipes the methods are the same but there are more equations and more unknown flows to calculate when performing a mass balance around the reactor inlet plenum. The non-rupture system hydraulics solution is identical to the rupture solution before the break. Therefore, non-rupture transients can be studied using the rupture model.

d. Check Valve Simulation

1) Introduction

A mathematical model which represents the transient characteristics of a tilting disk check valve has been programmed for use on the digital computer using Dynasyar⁽²⁾. The basic check valve model was developed by E. B. Pool, and it is discussed in ASME Papers 62-WA-219 and 62-WA-200. The model considers moments acting on the valve disk which are caused by pivot pin friction, valve disk weight, torsional springs, and fluid pressure. For FFTF analysis a damping moment has been added to Pool's model.

The check valve program has been added to another program which represents the FFTF primary heat transport system. The two combined programs couple the effects of heat transport system flow transients and check valve characteristics. This discussion presents the check valve model development of the dashpot term, and describes the method used to calculate check valve pressure loss.

2) Discussion

The differential equation which represents the check valve disk motion is*

$$I\ddot{\theta} = W_S L \sin \theta + S\theta - \mu W_S R_B - \frac{\bar{r}(A_p - A_o)}{29c_D} \left(\frac{\dot{W}}{C_D A_o} \right)^2 \sin \left[\frac{\pi}{2} - (\theta - \alpha) \right] \quad (12,$$

$$+ \left[\pm (B^2 + F^2) \left(\frac{U}{K_f} \right)^2 + 2BC \frac{U\dot{\theta}}{K_f K_d} \pm (C^2 + G^2) \left(\frac{\dot{\theta}}{K_d} \right)^2 \right]$$

This equation is of the form $I\ddot{\theta}$ equals the summation of moments acting on the valve disk. The terms on the right side of the equation are the valve disk weight moment, the torsional spring moment, the pivot pin friction moment, the dashpot moment, and the fluid moment, respectively. Figures XII.8A and XII.8B below show the moment directions both before and after the velocity reverses. It is assumed that the dashpot has already engaged in each case.

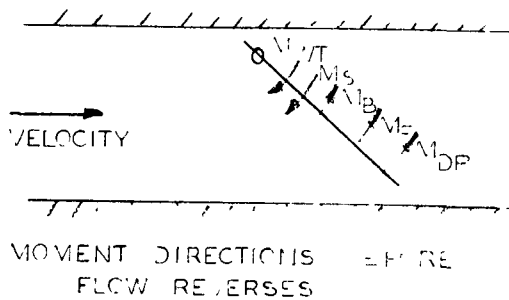


FIGURE XII.8A

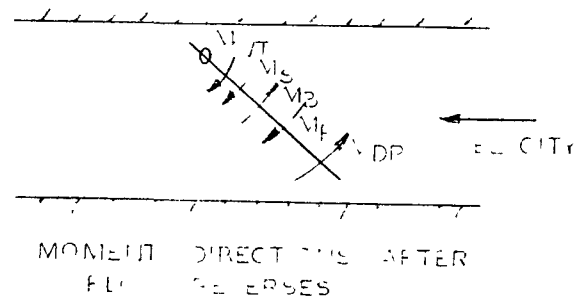


FIGURE XII.8B

M_B = BEARING MOMENT
 M_{DP} = DAMPING MOMENT
 M_F = FLUID MOMENT
 M_S = SPRING MOMENT
 M_T = TORSION MOMENT

CLOCKWISE MOMENTS ARE POSITIVE

* List of symbols is given in Section 3.

The fluid velocity at which valve disk motion is impending can be calculated from equation (12) with all of the time derivatives set equal to zero. The resulting expression is

$$U = K_f \frac{W_S L \sin \theta + S\theta - \mu W_S R}{B^2 + F^2} \quad (13)$$

The check valve portion of the program calculates check valve disk angle by solving the check valve equation, (12), at various mass flow rates. The check valve equation has a practical lower limit for the valve disk angle because a discontinuity occurs at the point where the valve angle is zero. Logic has been developed to stop the solution of equation (12) when an arbitrary minimum angle is reached. At the arbitrary minimum angle, the valve is assumed to be closed, and the mass flow rate is set equal to zero. The minimum valve disk angle is an input quantity, and it can be selected to be any desired value.

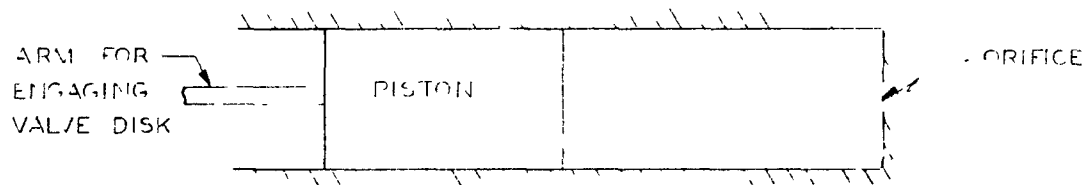
Steady state as well as transient conditions can exist where the valve disk has reached the full open position. At the instant the mass flow rate exceeds the mass flow rate required to hold the valve disk at the full open position, the solution of equation (12) is stopped. The upper limit for the valve disk angle is predetermined by the valve design, and it is a known quantity for any given value. The velocity or mass flow rate which corresponds to the maximum valve disk angle can be calculated from the steady state form of the check valve equation which is equation (13).

The dashpot can be set to engage at any desired valve disk angle, and once engaged the damping normally continues throughout the remainder of the closing transient. The angle at which the cashpot engaged is an input quantity and requires specification in the program input data.

The damping moment which was added to Pool's check valve equation is

$$M_{DP} = \frac{\bar{r}(A_p - A_o)}{29c_p} \left(\frac{\dot{W}}{C_D A_o} \right)^2 \sin \left[\frac{\pi}{2} - (\theta - \alpha) \right] \quad (14)$$

This term was developed with the aid of Figure XII.9, the concept of conservatism of mass, and the following assumptions: It is assumed that the fluid density is a function of temperature only. As the piston moves from left to right, a quantity



SIMPLE PISTON AND CYLINDER APPARATUS WHICH ACTS AS A DASHPOT

FIGURE XII.9

of mass ahead of the piston is displaced. At any instant the same amount of fluid that is displaced by the piston, passes through the orifice. With these concepts the dashpot term development follows from the system of equations below.

$$V_p = r\dot{\theta} \quad (15)$$

$$\dot{W}_{piston} = \dot{W}_{orifice} = \rho A_p r \dot{\theta} \quad (16)$$

$$\Delta P = \frac{1}{29c_p} \left(\frac{\dot{W}}{C_D A_o} \right)^2 \quad (17)$$

$$M_{DP} = \bar{r}(\Delta P)(A_p - A_o) \quad (18)$$

Equation (17) represents the pressure differential between the fluid inside the dashpot and fluid outside the dashpot which is at ambient pressure. It is apparent from this equation that the differential pressure is zero when the flow through the orifice is zero.

When equation (16) is substituted into equation (17), the differential pressure, ΔP , is not zero at the instant the dashpot is engaged because the valve disk angular velocity is not zero at this instant. To circumvent this problem, an average mass flow rate, \bar{W} , is used to represent the mass flow rate through the dashpot orifice until the condition is reached where $\bar{W} = \dot{W}$. \bar{W} is defined as $\frac{1}{t_e - t_c} \int_{t_c}^{t_e} \dot{W} dt$ where t_c is the time at which contact occurs between the valve disk and dashpot, and t_e is the time when $\dot{W} = \bar{W}$.

The net force on the fluid inside the cylinder is calculated by summing the fluid forces around the inside of the cylinder at any given time. It is assumed that a uniform pressure distribution always exists inside the cylinder. The result is $\int \vec{p} \cdot \vec{n} dA = \Delta P (A_p - A_o)$. When this equation is multiplied by the length r , the result is equation (7) which is the dashpot moment.

The contact angle between the valve disk and the arm attached to the dashpot piston is not always $\frac{\pi}{2}$, and the piston velocity must be corrected to account for the situation. The correct term is $\sin [\frac{\pi}{2} - (\theta - \alpha)]$. θ is the angle the valve disk makes with the plane normal to the flow direction. α is one half the valve disk angle at the time the valve disk engages the dashpot arm. This choice for α keeps the contact angle between the dashpot arm and the valve disk reasonably close to $\frac{\pi}{2}$ throughout the damped portion of the closing transient.

The three terms within the brackets that form the fluid moment expression can be positive or negative depending upon the sign of the fluid velocity. During a transient where the flow reverses, the fluid moment changes from a negative opening moment to a positive closing moment.

The fluid moment term contains two dimensionless quantities, K_f and K_d , which are determined by experiment. These coefficients are plotted in figure 1 in reference (4). The coefficients are in dimensionless form and apply to any size tilting disk check valve with a bulb type body. It is of interest to note that the coefficients K_f and K_d limit the check valve model application. The check valve model applies to both tilting disk and swing check valves, but each change in internal valve body geometry, valve disk shape, or valve disk weight distribution requires a different set of K_f and K_d values.

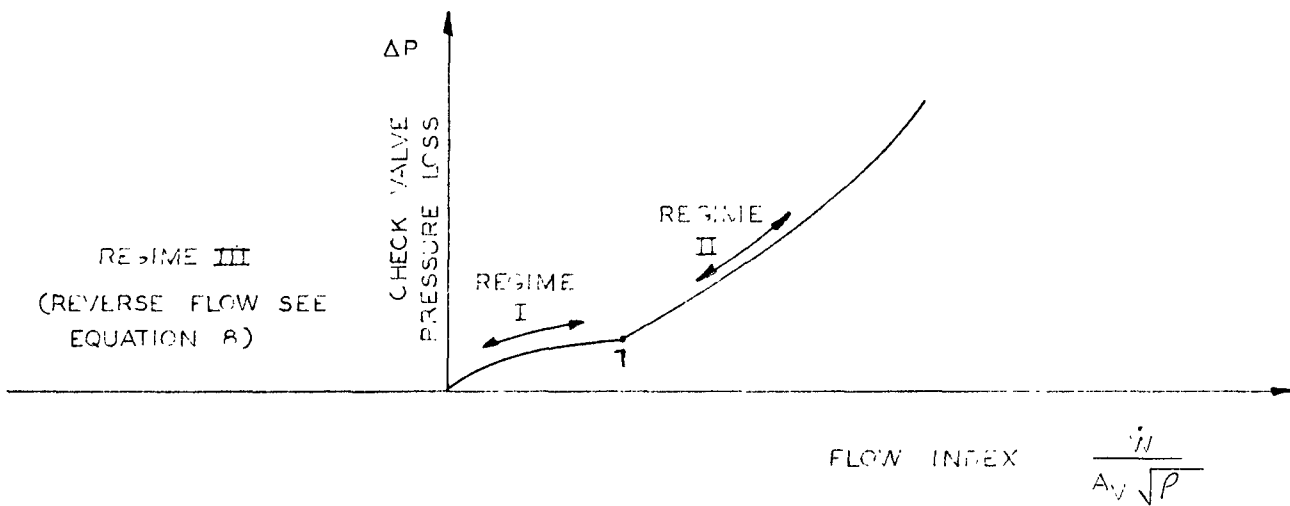
Other constants in the fluid term, B, C, F, and G, depend upon the fluid density and the valve disk geometry. These constants can be evaluated with the use of figure 3 in reference (3).

Calculation of the check valve pressure loss is accomplished by two different methods. Selection of one method of pressure loss calculation over the other depends upon the flow direction. Using Figure XII.10, the pressure loss is divided into three regimes. In regime I the flow is in the forward direction with the valve disk between the full closed and the full open position. The check valve pressure loss is obtained from Figure XII.10 between the origin and point 1 after the flow index has been calculated. In regime II the flow is still in the forward direction, and the valve disk is at the full open position. The check valve pressure loss is obtained from Figure XII.10 either at point 1 or the portion of the curve above point 1 depending upon the flow index value. It should be noted that the flow may be decreasing in the forward direction and still fall in regimes I or II. Regime III represents reverse flow, and the

ΔP versus flow index curve is not used in this case. The pressure loss for reverse flow is calculated from the equation

$$\Delta P = \frac{C_D}{2gc} \left(\frac{A}{H^3} \right) \frac{w_1 w_1}{D} \quad (19)$$

The drag coefficient in equation (19) is for flow past disk, and it remains at a value of approximately one over a large range of Reynold's number. This method of pressure loss calculation for a check valve under reverse flow conditions represents an arbitrary selection.



CHECK VALVE PRESSURE LOSS CURVE

FIGURE XII.10

3) List of Symbols

A = valve disk area, FT^2

A_o = dashpot orifice area, FT^2

A_p = dashpot piston area, FT^2

A_v = maximum free port area for check valve, FT^2

B, C, F, G = coefficients for fluid moment terms which depend upon valve disk diameter, shape, and fluid density, $\frac{LB_f SEC^2}{FT}$

C_D = drag coefficient for a disk, dimensionless

D = valve disk diameter, FT

g_c = gravitational constant, $\frac{LB_m}{LB_f} \frac{FT}{SEC}$

H^3 = valve port area, FT^6

I = valve disk moment of inertia, $LB_f FT SEC^2$

K = valve disk radius of gyration, FT

K_d, K_f = experimental coefficients, dimensionless

L = distance from valve disk center of gravity to pivot point centerline, FT

P = $(\int r^3 dA/A)^{1/3}$

Q = $(\int r^2 dA/A)^{1/2}$

R = $(\int r dA/A)$

R_B = pivot pin bearing radius, FT

r = distance from valve disk centerline to some arbitrary point on valve disk, FT

\bar{r} = distance from valve disk centerline to point which contacts dashpot arm, FT

S = torsional spring constant, $\frac{FT LB_f}{RAD}$

U = fluid velocity in check valve at point of minimum cross section, $\frac{FT}{SEC}$

3) List of Symbols (Continued)

\dot{W} = mass flow rate, $\frac{\text{LBm}}{\text{SEC}}$

\bar{W} = average mass flow rate through dashpot orifice, $\frac{\text{LBm}}{\text{SEC}}$

W_s = submerged valve disk weight, LB_f

α = $\frac{\theta}{2}$ at the time the valve disk contacts the dashpot arm, RAD

ΔP = check valve pressure loss, $\frac{\text{LB}_f}{\text{FT}^2}$

θ = valve disk angle (positive toward open position), RAD

$\dot{\theta}$ = valve disk angular velocity (positive toward open position), $\frac{\text{RAD}}{\text{SEC}}$

$\ddot{\theta}$ = valve disk angular acceleration (positive toward open position), $\frac{\text{RAD}}{\text{SEC}^2}$

(e) Secondary Loops Hydraulics

The secondary loop hydraulics simulation method is the same as the method used for the primary loops: the equation (equation 11) is written for each segment of piping and components.

Pressure drops out of the final equation for $\dot{\omega}_s$ when the individual equations are summed.

With our assumption of incompressible flow, the mass flow into and out of the secondary loop's surge tank are the same and, hence, the level change in the tank is due only to temperature changes.

(f) Tertiary Air System Hydraulics

The fluid's inertial term is neglected because the coolant mass is small. Hence, hydraulic behavior is determined by an algebraic equation which equates input energy (fan and natural draft of off gas stacks) to flow resistance (DHX tube bundle, throttling air vanes, ducts, etc.), kinetic, and potential energy changes:

$$\frac{g}{g_c} Z_1 + \frac{V_1^2}{2g_c} + \int_2^1 v dp + W_e = \frac{g}{g_c} Z_2 + \frac{V_2^2}{2g_c} + \text{Frictional losses.}$$

Isothermal expansion and the perfect gas law are assumed for the air system. Frictional losses are calculated for an average specific

volume over each segment of the system:

$$\text{losses} = m\bar{v}^2 + \text{air vanes pressure loss}$$

$$\text{where } m = \Sigma \left(\frac{4fL}{D} + K \right) \frac{w|w|}{2g_c A^2}$$

For a perfect gas,

$$Pv = \frac{RT}{MW} \text{ or } \frac{P}{\rho} = RT$$

Integration gives,

$$\frac{RT}{MW} \ln \frac{P_1}{P_2} = \frac{g}{g_c} (Z_2 - Z_1) + \frac{1}{2g_c} (V_2^2 - V_1^2) + M\bar{v}^2 - W_e + \text{air vanes pressure loss}$$

Stack draft is computed as follows:

$$D_r = .52 P_{ATM} H \left[\frac{1}{460+T_{ATM}} - \frac{1}{460+T_h} \right], \text{ in. H}_2\text{O}$$

The fan pressure is then,

$$FAN_p = W_e - D_r', \text{ in consistent units.}$$

The air rate is determined by the intersection of the fan pressure/capacity curve and the system demand curve for a given fan speed. The demand curve continually shifts (1) due to the change in system resistance brought about by the changing air vane position to modulate the air rate as required by a process controller or overriding trip switch, and (2) due to the continually varying DHX exit air temperature. The calculation of the air rate can be done in the digital code via a four dimensional tabulation involving air rate, system pressure loss, inlet vane position and DHX exit air temperature for a fixed inlet air temperature.

3. Sodium Pumps and Drives

Variable speed pumps are simulated. Eddy current clutch and wound rotor drives have been simulated, but this discussion is confined to the wound rotor, liquid rheostat type.

a. Pump Speed

Pump and drive speed is determined by a torque balance around the pump equating the rotational mechanical torque of the pump and drive assembly to the difference between the input torque from the drive and the torque consumed by the pump.

$$\frac{\pi I}{30g} \dot{\omega} = T_M - T_P$$

where

I = moment of inertia of pump and drive assembly lb-ft²

ω = speed, rpm

T_M = torque delivered to pump from drive assembly lb-ft

T_P = torque consumed by the pump as hydraulic torque and torque losses, lb-ft

b. Drive Characteristics

The drive torque may be from the main or pony motors, and friction and windage losses are accounted for:

$$T_M = K_{MM} T_{MM} + K_{PM} T_{PM} - T_{F\&W}$$

K_{MM} = control integer of 0 or 1: 0 if main motor disconnected;
1 if connected

T_{MM} = main motor input torque, lb-ft

T_{PM} = pony motor input torque, lb-ft

K_{PM} = pony motor shaft torque, lb-ft

$T_{F\&W}$ = friction and windage torque losses, lb-ft (about 3% of input electrical torque to main motor at design speed)

Motor torque is a function of speed and the amount of rotor plus external resistance in series with the rotor resistance as illustrated in Figure XII.11. The family of curves can be described by an equation of the form:

$$T = \frac{aRS}{b(S)^2 + cR^2}$$

where

T = normalized input torque

R = normalized external rotor resistance ratio, where

R is given as sum of rotor resistance plus external resistance divided by rotor resistance

S = normalized motor slip

$$= \frac{1200 - \omega}{1200} \text{ for 1200 rpm}$$

synchronous speed

a, b, c = constants which are dependent on rated speed and maximum torque developed.

$$T_{MM} = T \times T_{MM,D}$$

$T_{MM,D}$ = main motor rated design torque, which is obtained from the design load torque as follows:

$$T_{MM,D} = \left[\frac{(\text{Hydraulic Design HP})5250}{\omega_D} \right] e$$

where ω_D is design speed

e is factor to account for friction and windage in drive assembly (equal about 1.03)

The normalized resistance R is a function of the process controller which modulates pump speed (see below).

Pony motor torque is a function of speed for a squirrel cage type motor. A typical torque curve is shown as follows:

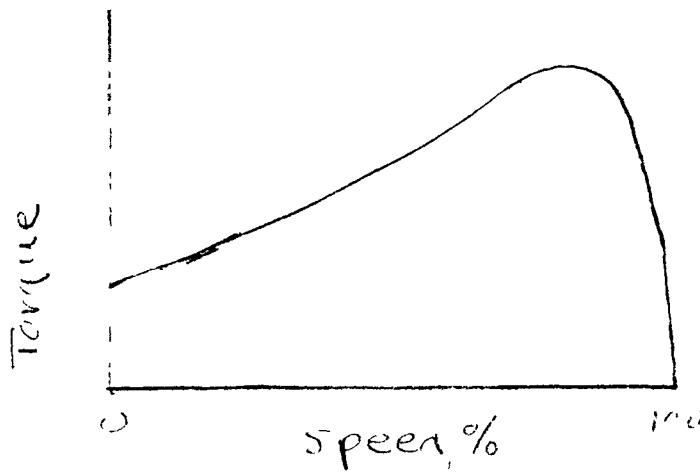


FIGURE XII.12

Friction and windage torque is taken as being proportional to the speed.

c. Liquid Rheostat Positioning

Variable speed is obtained by varying the electrical resistance external to the motor rotor. This is done by varying the electrode position in the drive's liquid rheostat.

A cubic relationship is assumed for relating the position of the electrodes to normalized resistance. Typically,

$$R = 200 \left(1 - \frac{Z}{100}\right)^3 + 1$$

Z = electrode position, % of full stroke

The coefficient of 200 is related to the maximum practical speed turndown, which is about 3:1.

The position is determined by a process controller output (control flow by varying pump speed). A second order process is assumed.

Hence,

$$\ddot{Z} = KX - CZ - \delta\dot{Z}$$

where

K, C, S = input constants to characterize the system (δ is the damping factor)

X = controller input, % full scale.

d. Pump Characteristics

We simulate pump operation for all practical zones of pump operation as described by the Karman Knapp circle diagram shown in Figure XII.13. In practice only zones A (normal pump), H (energy dissipation) and G (turbine operation) need be simulated. Operation within these abnormal zones is possible following check valve failure to close accidents. Our digital codes include these abnormal zones, but only the normal zone is currently simulated on the hybrid.

The pump characteristics are shown in the more usual fashion in Figures XII.14 and XII.15. The normal zone is shown in XII.14. The zones of turbine and energy dissipation operation are shown XII.15. Normalized characteristics are used as follows:

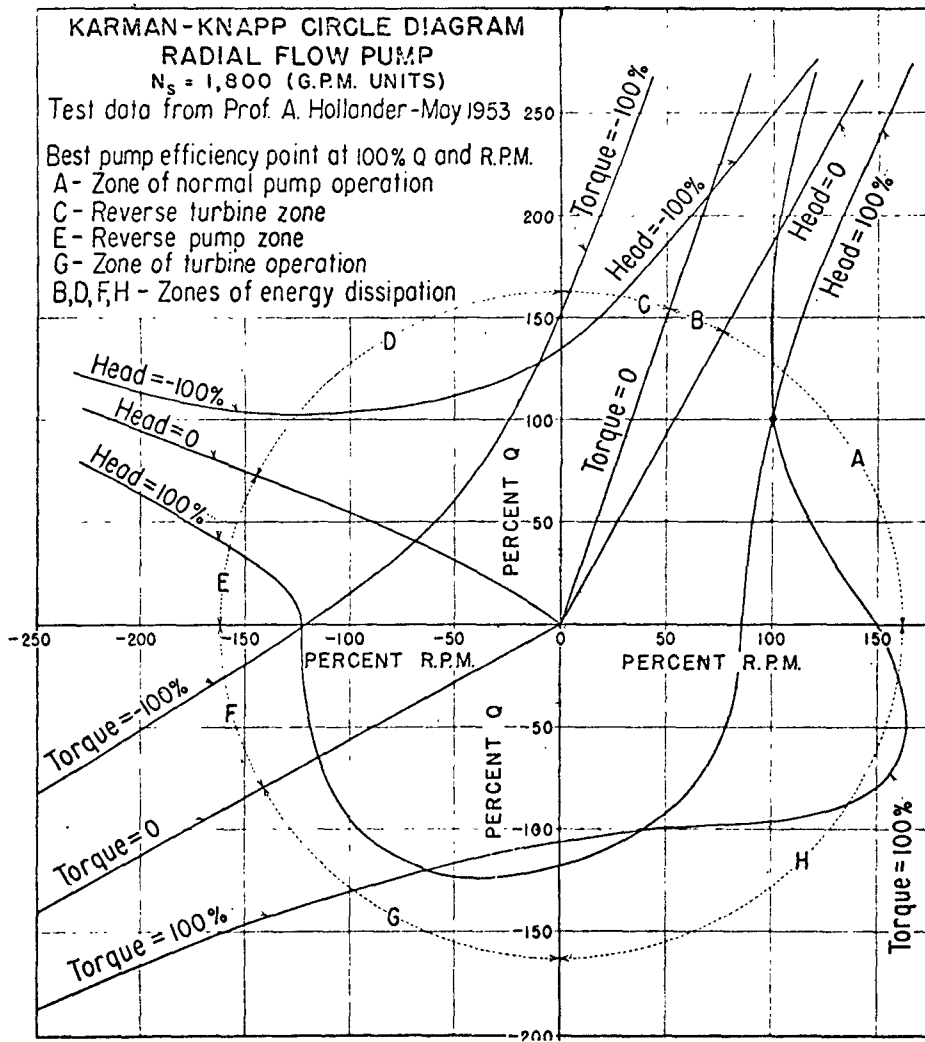
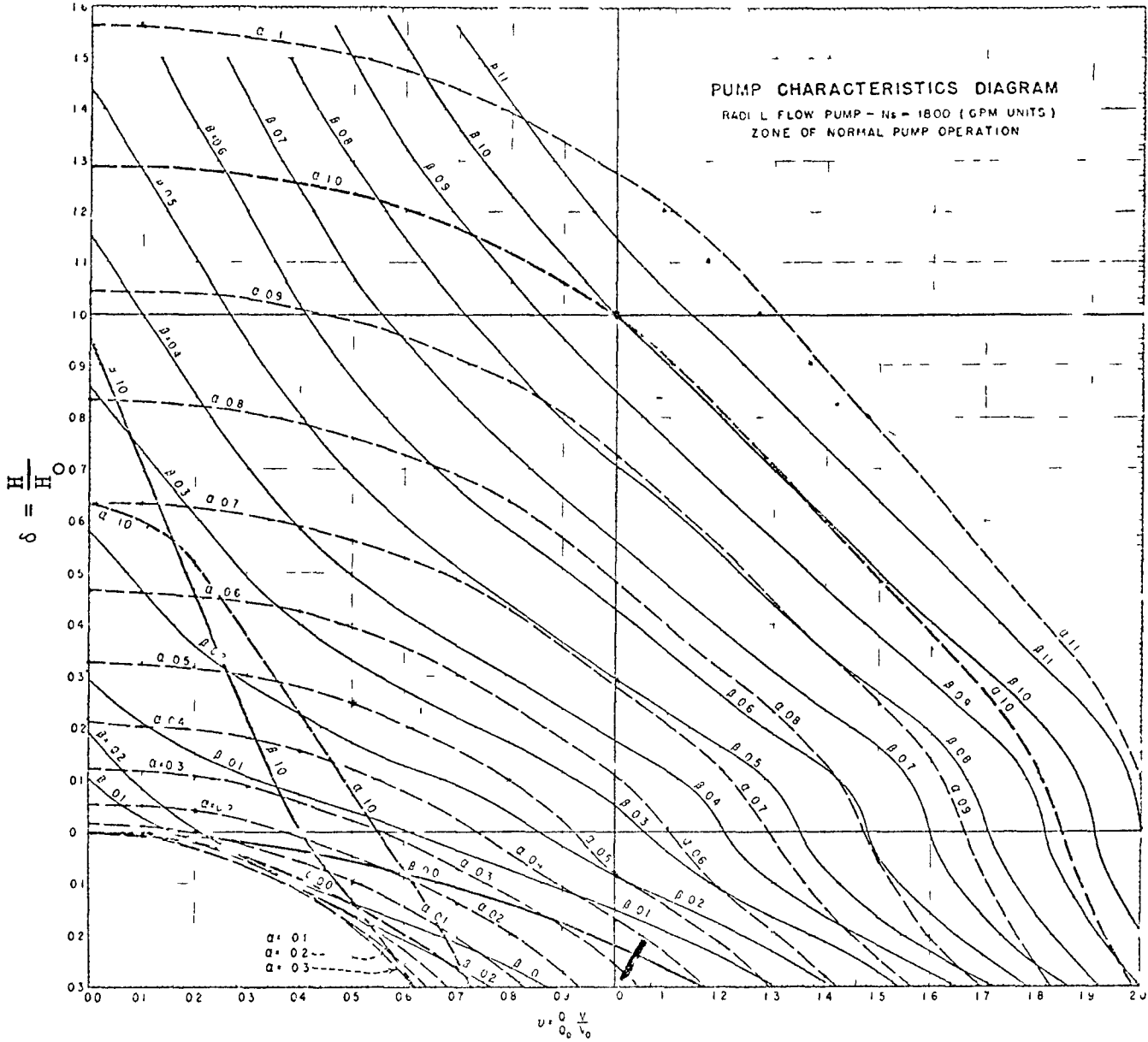
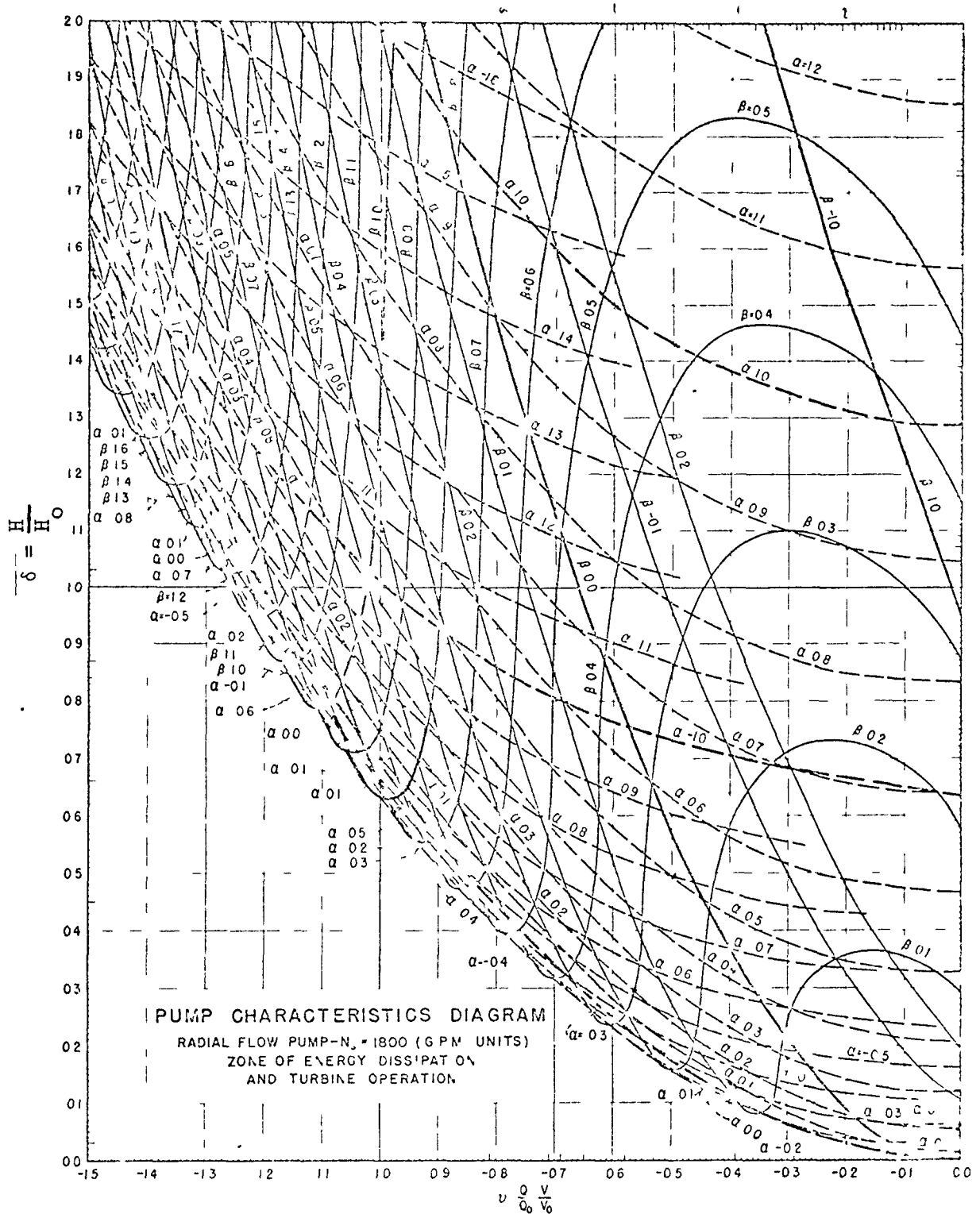


FIGURE XII.13

Fig. XII.14



XII.61
Fig. XII.15



v = normalized volumetric flow rate = Q/Q_D

α = normalized speed = ω/ω_D

β = normalized torque = T/T_D

δ = normalized head = H/H_D

subscript D refers to design value.

Characteristics are determined as follows:

$$\delta = f(\alpha, v)$$

$$\beta = f(\alpha, v)$$

with normalized speed obtained from the integration of the torque balance equation and normalized flow from the integration of the equations of motion.

The curves shown in Figure XII.14 and XII.15 do not account for a change in pump efficiency with speed. The curves account only for the efficiency as a function of capacity. Thus, the pump torque must be corrected as follows for this additional efficiency consideration:

$$T_p = r_T \rho \beta / e_2$$

where

r_T = normalization constant

$$= \frac{Q_D H_D}{\frac{\pi}{30} \omega_D^2 e_D}$$

ρ = density coolant at pump

$$e_2 = f(\omega)$$

XII.63

Note that the pump head is a feedback to the equations of motion and that the pump torque is a feedback to the pump speed torque balance equation.

4) Intermediate Heat Exchanger

a. Introduction

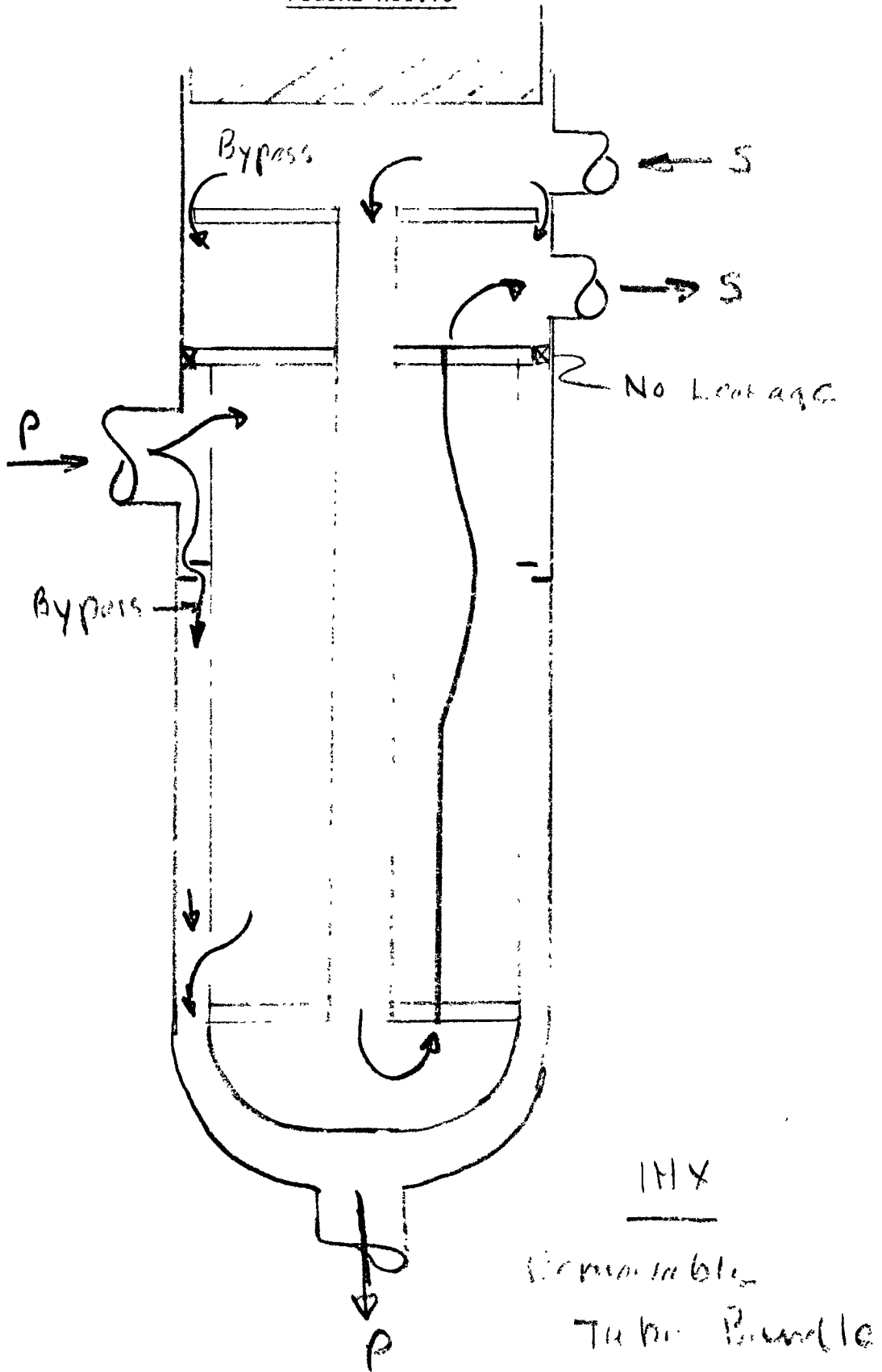
The intermediate heat exchanger (IHX) is an extremely important part of the FFTF heat transport system, as the response characteristics of the IHX are felt directly by both reactor and dump heat exchanger (DHX). For hybrid system simulation, an IHX model is needed which will perform well for a wide range of conditions, including severe temperature ramps, flow coastdowns, and unbalanced flows. Such a model may be a "black box" approach, with primary and secondary outlet temperatures responding appropriately to flow and inlet temperature changes, and internal parameters.

Several IHX models have been used to date by workers in reactor system simulation, mostly variations on discretizing the space dimension (i.e., breaking the IHX into segments or nodes). Two basic approaches are used: (1) performing a series of heat balances on well-defined segments of the IHX length, with the outlet of a node becoming the inlet of the next, and (2) solving the partial differential equations of heat transfer at the nodal boundaries, with various assumptions of temperature distribution in order to achieve separation of variables. The first approach has been used by Westinghouse in its proprietary code, IANUS. General Electric, BNWL, and the British have used the other approach. For steady-state conditions with balanced flows, each of the techniques is equivalent; however, extreme differences in model response appear when inputs change markedly. Hence, a definitive statement is needed for the selection of an IHX model suitable for the FFTF hybrid simulation.

The following pages present the results of comparing several IHX models using the DYNASAR program, applied to the FFTF IHX design of March, 1969. IHX models are described, models are compared for a wide spectrum of flow and temperature transients, and conclusions are drawn as to the best model for FFTF hybrid simulation.

A schematic diagram of an FFTF intermediate heat exchanger is shown in Figure XII.16. Mathematical models should make provisions for shell and tube side bypassing and mixing at the inlets and outlets in addition to the heat transfer within the tube bundle. Heat storage in the shells is also a consideration.

FIGURE XII.16



b. Model Descriptions

For the purposes of comparing IHX models, several basic features were present in each model: (1) eight (8) axial nodes, (2) variable material properties and heat transfer coefficients for each node, (3) bypass flow streams for both primary and secondary, (4) ideal mixing plenums at the inlet and outlet of each coolant stream, and (5) separation of radial regions, accounting for tube coolant, tube metal, shell coolant, and vessel wall. Each model employed the design data for the FFTF IHX design of March, 1969.

1) General Model

Figure XII.17 shows the overall picture of the IHX model, basic to each of the particular models described later.

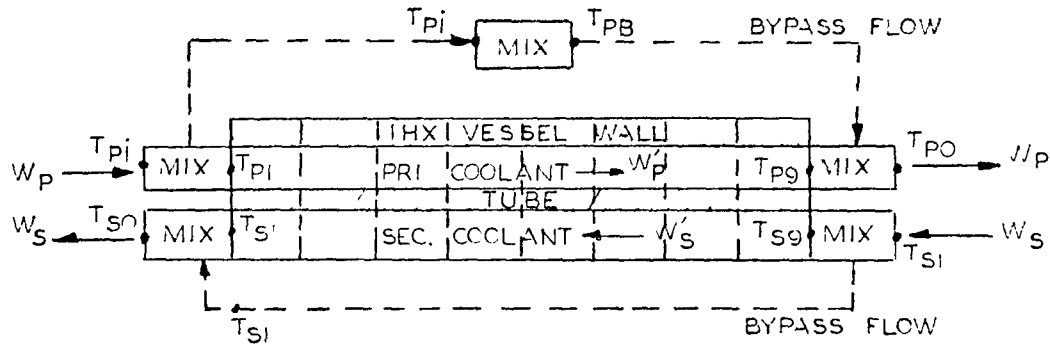


Figure XII.17 General Model, 3-Node FFTF IHX

Equations (19) through (25) define those parts of the model common to all the modeling approaches.

$$W'_p = (1 - \beta_p)W_p \tag{19}$$

$$W'_s = (1 - \beta_s)W_s \tag{20}$$

where β_p and β_s are the primary and secondary bypass fractions, respectively.

$$(\rho VC)_{PB} \frac{dT_{PB}}{dt} = \left(\frac{\beta_p}{1 - \beta_p} \right) C_{PB} [W_p'] [T_{Pi} - T_{PB}] \quad (21)$$

where the subscript PB refers to properties of a large mixing volume for primary bypass sodium between inlet and outlet.

$$(\rho VC)_{Pi} \frac{dT_{Pi}}{dt} = [W_p'] C_{Pi} [T_{Pi} - T_{Pi}] \quad (22)$$

$$(\rho VC)_{Po} \frac{dT_{Po}}{dt} = [W_p'] C_{Po} [T_{Pg} - T_{Po}] + \left(\frac{\beta_p}{1 - \beta_p} \right) C_{Po} [W_p'] [T_{PB} - T_{Po}] \quad (23)$$

$$(\rho VC)_{Si} \frac{dT_{Si}}{dt} = [W_s'] C_{Si} [T_{Si} - T_{Si}] \quad (24)$$

$$(\rho VC)_{So} \frac{dT_{So}}{dt} = [W_s'] C_{So} [T_{S1} - T_{So}] + \left(\frac{\beta_s}{1 - \beta_s} \right) C_{So} [W_s'] [T_{Si} - T_{So}] \quad (25)$$

where the ρVC 's denote properties of the respective mixing plena, as defined by the plenum outlet temperature. It remains to describe the models used in computing the coolant outlet temperatures from the tube bundle zone, i.e., T_{Pg} and T_{S1} .

2. Nodal Heat Balance Technique

Considering a single node of the IHX as shown in Figure XII.17, a heat balance is performed on it per Figure XII.18 and the following equations:

$$(\rho VC)_{Vj} \frac{dT_{Vj}}{dt} = (UA')_{Vj} [T_{Pjj-1} - T_{Vj}] \quad (26)$$

for $j = 2 \dots 9$

$$(\rho VC)_{Pjj-1} \frac{dT_{Pj}}{dt} = \frac{W_p' C_{Pjj-1}}{\Delta X} [T_{Pj} - T_{Pj-1}] - (UA')_{Vj} [T_{Pjj-1} - T_{Vj}] - (UA')_{Pj} [T_{Pjj-1} - T_{Tj}] \quad (27)$$

for $j = 2 \dots 9$

$$(\rho V \dot{C})_{Tj} \frac{dT_{Tj}}{dt} = (UA^-)_{Pj} [T_{Pj-1} - T_{Tj}] - (UA^-)_{Sj} [T_{Tj} - T_{Sj-1}] \quad (28)$$

for $j = 2 \dots 9$

$$(\rho V \dot{C})_{Sj+1} \frac{dT_{Sj}}{dt} = \frac{W_s C_{Sj+1}}{\Delta X} [T_{Sj+1} - T_{Sj}] + (UA^-)_{Sj+1} [T_{Tj+1} - T_{Sj+1}] \quad (29)$$

for $j = 1 \dots 8$

and

$$T_{Pj-1} = (T_{Pj} + T_{Pj-1})/2 \quad (30)$$

$$T_{Sj+1} = (T_{Sj} + T_{Sj+1})/2 \quad (31)$$

As noted previously, the $\rho V \dot{C}$'s are computed as functions of their respective temperatures. Heat transfer coefficients are computed as functions of flow and temperatures, with nodal average coolant temperatures (equations 30 and 31) being used. This model is represented in Figure XII.18.

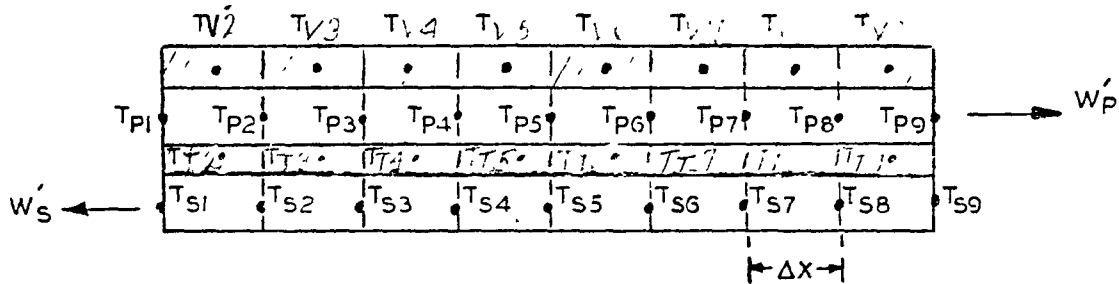


Figure XII.18 Tube Bundle Model, Nodal Heat Balance

The basic assumption inherent in the above equations is the equating of the outlet temperature derivative to the average temperature derivative for each node. This approach avoids the traditional problem of erroneous outlet temperature response to inlet temperature perturbations and becomes better as the number of nodes is increased.

3) Differencing Techniques

With a finite differencing approach, the basic heat balance equation for the coolant temperature at a mesh point, j , is

$$(\rho VC)_j \frac{dT_{Cj}}{dt} = - WC_j \frac{\partial T_{Cj}}{\partial X} - (UA)_j [T_{Cj} - T_{Tj}] \quad (32)$$

where the symbols are the standard ones. The basic question then becomes how to represent the axial temperature gradient, $\frac{\partial T_{Cj}}{\partial X}$. In general, equation (32) may be represented as

$$(\rho VC)_j \frac{dT_{Cj}}{dt} = - WC_j \left(\frac{\Delta T_{Cj}}{n\Delta X} \right) - (UA)_j [T_{Cj} - T_{Tj}] \quad (33)$$

The selection of ΔT_{Cj} 's and n 's may be done in a variety of ways. Figure XII.19 shows the nodal temperatures for the differencing approach.

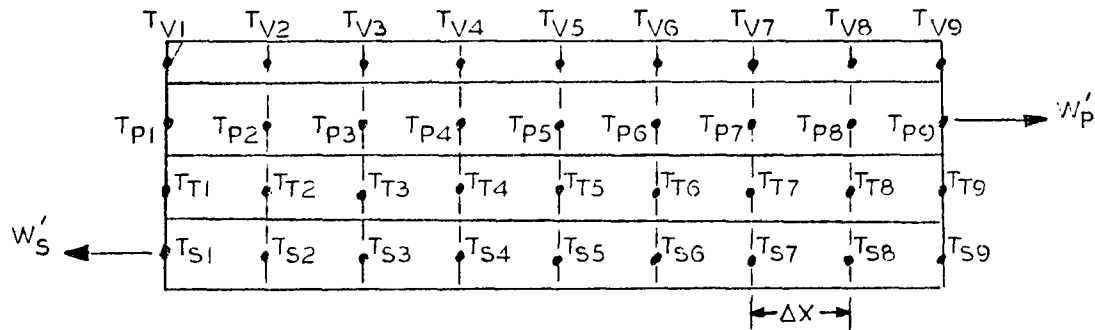


Figure XII.19 Tube Bundle Model, Finite Difference Approach

Equations (26) through (29) are rewritten as follows:

$$(\rho VC)_{Vj} \frac{dT_{Vj}}{dt} = (UA)_{Vj} [T_{Pj} - T_{Vj}] \quad (34)$$

for $j = 1 \dots 9$

$$\begin{aligned}
 (\rho V \dot{C})_{Pj} \frac{dT_{Pj}}{dt} &= - \frac{W_p \dot{C}_{Pj}}{n \Delta X} [\Delta T_{Pj}] - (UA')_{Vj} (T_{Pj} - T_{Vj}) + \\
 &\quad - (UA')_{Pj} [T_{Pj} - T_{Tj}] \\
 &\text{for } j = 2 \dots 9 \quad .
 \end{aligned} \tag{35}$$

$$\begin{aligned}
 (\rho V \dot{C})_{Tj} \frac{dT_{Tj}}{dt} &= (UA')_{Pj} [T_{Pj} - T_{Tj}] - (UA')_{Sj} [T_{Tj} - T_{Sj}] \\
 &\text{for } j = 1 \dots 9 \quad .
 \end{aligned} \tag{36}$$

$$\begin{aligned}
 (\rho V \dot{C})_{Sj} \frac{dT_{Sj}}{dt} &= \frac{W_s \dot{C}_{Sj}}{n \Delta X} [\Delta T_{Sj}] + (UA')_{Sj} [T_{Tj} - T_{Sj}] \\
 &\text{for } j = 1 \dots 8 \quad .
 \end{aligned} \tag{37}$$

4) Two-Point Backward Difference: With this approach, the temperature gradient at point j is approximated by assuming it to be equal to a linear distribution along the previous node (i.e., backward with respect to flow direction). The assumption holds for both primary and secondary. Two-point backward expressions for ΔT_j become

$$\Delta T_{Pj} = T_{Pj} - T_{Pj-1} \tag{38}$$

$$\Delta T_{Sj} = T_{Sj+1} - T_{Sj} \tag{39}$$

for which $n = 1$.

5) Three-Point Backward Difference: A three-point backward difference utilizes the temperatures at the point j and the two points upstream. The expressions become

$$\Delta T_{Pj} = 3T_{Pj} - 4T_{Pj-1} + T_{Pj-2} \tag{40}$$

$$\text{for } j = 3 \dots 9$$

$$\Delta T_{Sj} = 3T_{Sj} + 4T_{Sj+1} - T_{Sj+2} \tag{41}$$

$$\text{for } j = 1 \dots 7$$

and for which $n = 2$. The first-computed temperature in the coolant stream must use a central or two-point backward approximation, as three temperatures are not available. Central differences were selected and the expressions become

$$\Delta T_{P2} = T_{P3} - T_{P1} \quad (42)$$

$$\Delta T_{S8} = T_{S9} - T_{S7} \quad (43)$$

6) Central Difference: This approach uses a temperature on each side of the calculated temperature to get the gradient, but reserves a three-point backward calculation for the outlet temperature of each coolant stream. The equations become

$$\Delta T_{Pj} = T_{Pj+1} - T_{Pj-1} \quad (44)$$

for $j = 2 \dots 8$

$$\Delta T_{Sj} = T_{Sj+1} - T_{Sj-1} \quad (45)$$

for $j = 2 \dots 8$

and for which $n = 2$. The ΔT -expressions for the outlet temperatures become

$$\Delta T_{P9} = 3T_{P9} - 4T_{P8} + T_{P7} \quad (46)$$

$$\Delta T_{S1} = -3T_{S1} + 4T_{S2} - T_{S3} \quad (47)$$

7) Mixed Difference: After initial check runs with the central and three-point backward difference techniques, a composite approach was attempted, alternating the differencing technique such that the inlet uses central and the outlet uses the three-point formula. Only an even number of nodes will work with this approach. The equations become

$$\Delta T_{Pj} = T_{Pj+1} - T_{Pj-1} \quad (48)$$

$$\Delta T_{Sj} = T_{Sj+1} - T_{Sj-1} \quad (49)$$

$$\text{for } j = 2, 4, 6, 8$$

$$\text{and } \Delta T_{Pj} = 3T_{Pj} - 4T_{Pj-1} + T_{Pj-2} \quad (50)$$

$$\text{for } j = 3, 5, 7, 9$$

$$\Delta T_{Sj} = -3T_{Sj} + 4T_{Sj+1} - T_{Sj+2} \quad (51)$$

$$\text{for } j = 1, 3, 5, 7$$

In all the above differencing approaches, materials properties and heat transfer coefficients are computed at each mesh point, in similar fashion to the nodal heat balance approach.

Heat transfer film coefficients are functions of flow and temperature as illustrated by Figures XII.20 and XII.21 where the film coefficient, h , is obtained from the Nusselt Number:

$$Nu = \frac{hD}{K} .$$

The flow data for Reynolds numbers are obtained from the integration of the equations of motion. The temperature data for physical properties are feedbacks from the integrations of the IHX energy balance equations.

FIGURE XII.20 INTERMEDIATE HEAT EXCHANGER TUBE-SIDE
FILM COEFFICIENT FUNCTION

UNCLASSIFIED

XII.74

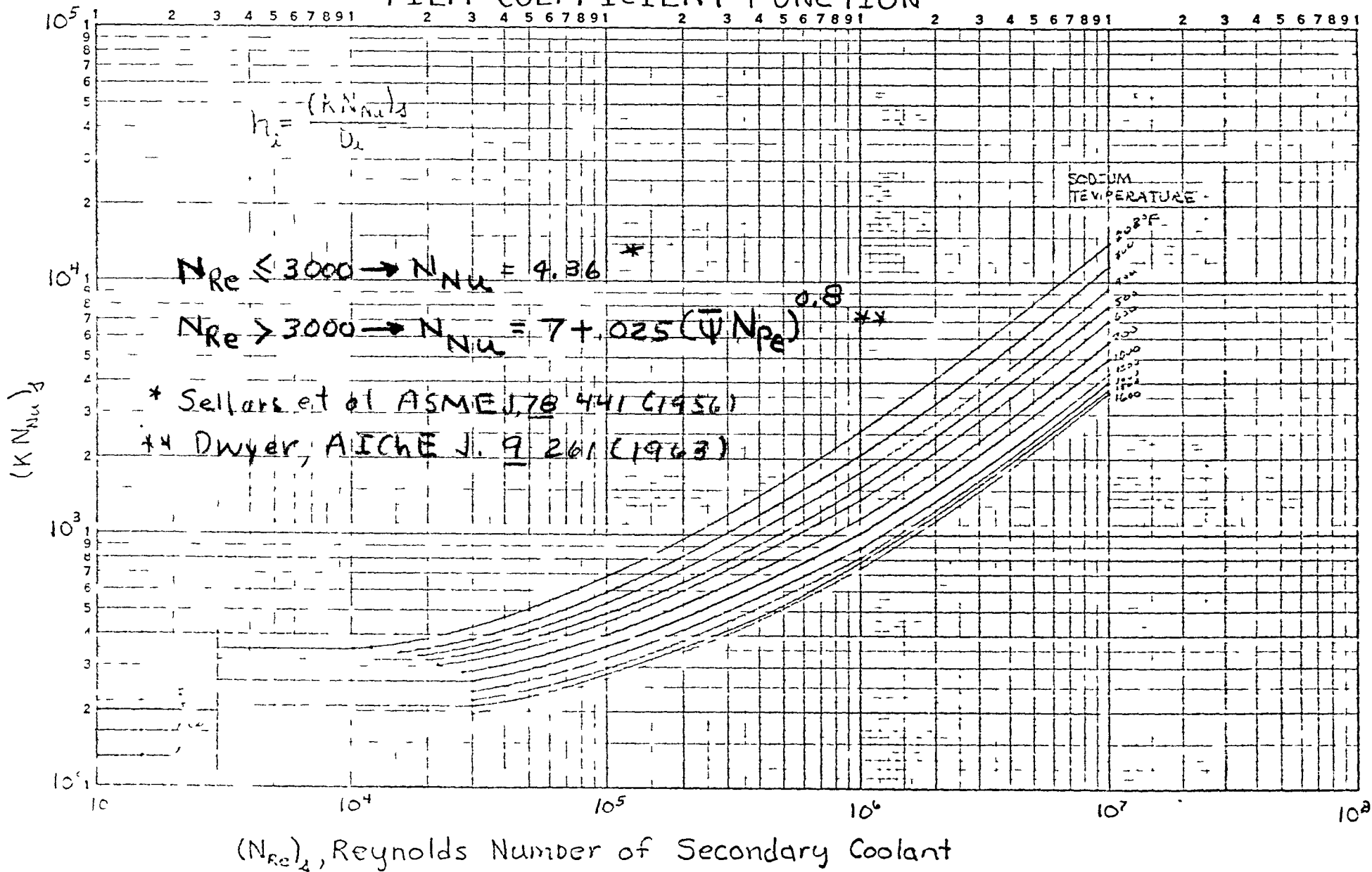
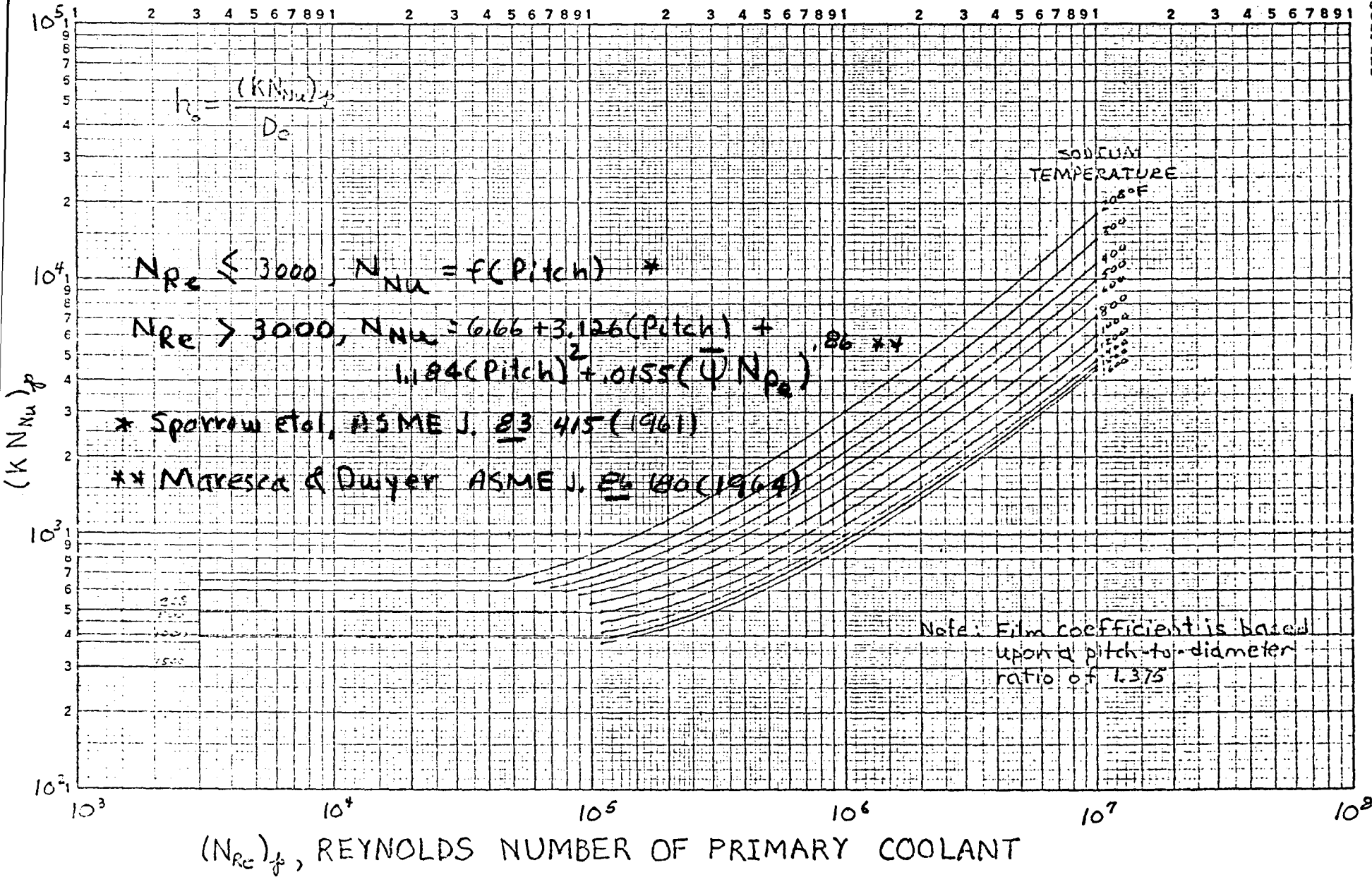


FIGURE XII.21 INTERMEDIATE HEAT EXCHANGER SHELL-SIDE FILM COEFFICIENT FUNCTION

UNCLASSIFIED

XII.75



8) Model Comparison

To check the relative responses of the foregoing models, transients representative of those expected on the FFTF were used as inputs. Flow decay characteristics for the loss of pump motor power were used for both primary and secondary sodium flows. Calculation of the flow decay assumed process system data consistent with the example IHX (Appendix A), with low-inertia pumps and pony motors coming on-line automatically. Temperature inputs were used as ramp functions, with transient rates and total temperature changes indicative of the most severe expected transients. Flow increases were also treated as ramps to full flow.

Only typical results are presented here to support the conclusion that the mixed difference technique is preferred. Shown in Figures XII.22 and XII.23 are comparative data for a ratio of primary to secondary flow of 10:1. Temperature response data are shown in Figure XII.22. Temperature profile data are given in Figure XII.23. Heat balance data are included in Table XII.6. The temperature response data and heat balance data indicate little difference between the mixed difference and nodal heat balance models. However, the mixed difference model is selected because of a more reasonable temperature profile (see Figure XII.23).

Data have been obtained to support the following model simplifications:

- (1) There is no need to simulate the shell or to provide separate tube wall nodes. The error in neglecting heat storage in the shell is

negligible, and almost exact results are obtained by lumping the metal wall of the tube as equivalent sodium (1/2 to secondary and other half to primary). In this way the number of differential equations and each mesh point is reduced from 4 to 2.

- (2) There is no need to use local temperatures for calculating physical properties and heat transfer coefficients. The error introduced by using average temperatures across the length of the IHX for determining physical properties and heat transfer data is insignificant.

FIGURE XII.22 IHX MODEL RESPONSE, SECONDARY FLOW TO 10 %

- NOTES: A= NODAL HEAT BALANCE MODEL
 B= MIXED DIFFERENCE MODEL
 C= CENTRAL DIFFERENCE MODEL
 D= 3-POINT BACKWARD DIFFERENCE MODEL
 E= 2-POINT BACKWARD DIFFERENCE MODEL

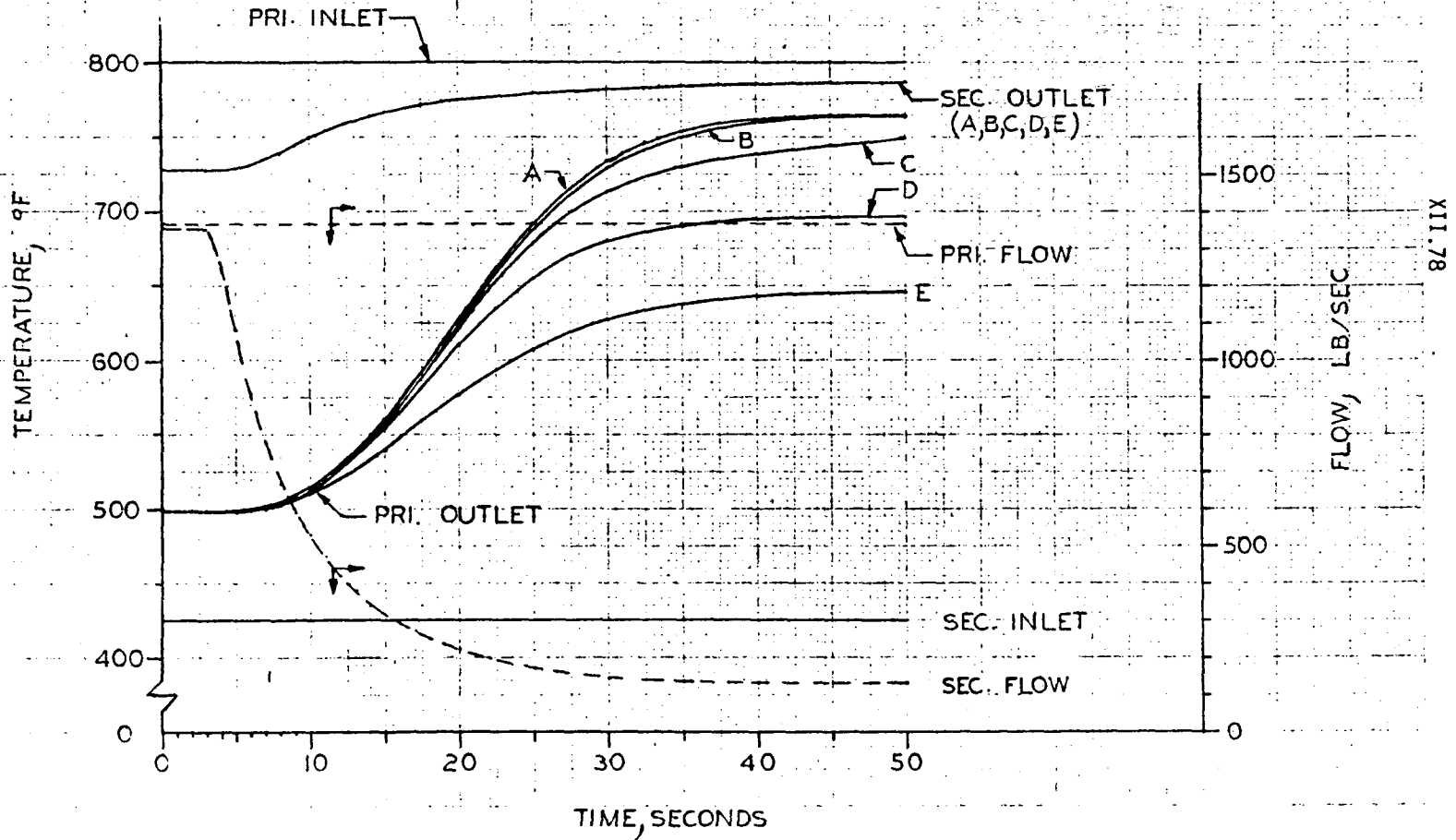
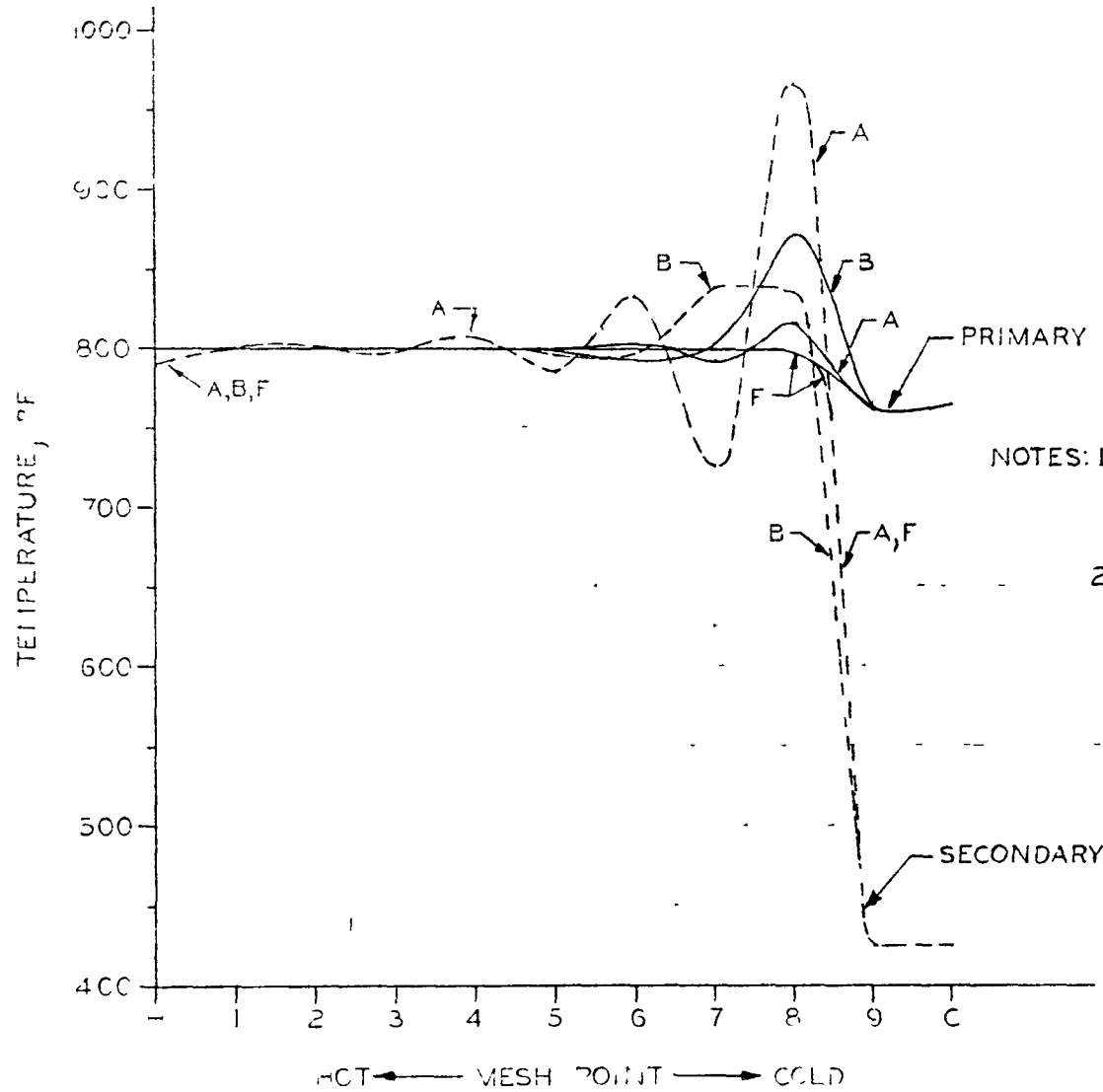


FIGURE XII.23 IHX TEMPERATURE DISTRIBUTION, UNBALANCED FLOWS WITH 10 % SECONDARY FLOW



NOTES: 1. A=NODAL HEAT BALANCE MODEL
 B=MIXED DIFFERENCE MODEL
 F=EXACT CALCULATION
 2. PRIMARY FLOW=1365 LB/SEC
 SECONDARY FLOW=130 LB/SEC

XII.79

HOT ← MESH POINT → COLD

Table XII.6 Heat Balance Results, 10:1 Primary and Secondary Flow Ratio

Model	Pri. Inlet (°F)	Pri. Outlet (°F)	Sec. Inlet (°F)	Sec. Outlet (°F)	Pri. Pwr. (MW)	Sec. Pwr. (MW)
Exact Solution	800	764.5	425	790.4	15.57	15.57
3-Point Backward	800	697	425	789	45.23	15.47
Central Difference	800	763.1	425	809.5	16.21	16.35
Mixed Difference	800	765.1	425	790.6	15.32	15.54
Nodal Heat Balance	800	765.0	425	790.0	15.37	15.52

Primary Flow = 1365 lb/sec; Secondary Flow = 130 lb/sec

Heat Balance Results, 10:1 Secondary - Primary Flow Ratio

Model	Pri. Inlet (°F)	Pri. Outlet (°F)	Sec. Inlet (°F)	Sec. Outlet (°F)	Pri. Pwr. (MW)	Sec. Pwr. (MW)
Exact Solution	800	443.0	425	459.6	15.83	15.83
3-Point Backward	800	443.7	425	536.3	15.85	50.32
Central Difference	800	424.6	425	462.4	16.70	16.91
Mixed Difference	800	443.8	425	460.6	15.84	16.09
Nodal Heat Balance	800	444.6	425	459.8	15.81	15.73

Primary Flow = 136 lb/sec; Secondary Flow = 1352 lb/sec

5. Dump Heat Exchanger

a. Problem Statement

Since comparison of calculated DHX results with test results is not possible, a means of determining the accuracy and appropriateness of the DHX simulation models is desired. A very detailed mathematical model would provide the desired reference simulation to which other more simple methods (using the computer code DYNASYAR) could be compared. From this study would come a determination of how detailed models are required to be to obtain the necessary accuracy in transient analysis.

b. Reference DHX Simulation

Investigation of available methods and various references led to the selection of the Thermal Analyzer Program (the designation TAP will be used hereafter) for the reference. TAP was developed by AI and has been converted for use on our facilities.

TAP simulates heat transfer processes by the commonly used method of electrical analogy. Heat flow and geometry are represented by a network of equivalent admittances, Y , and capacitances, C , and source terms, Q . The admittances are analogous to the UA terms in heat transfer, the capacitance C to the $\rho V c_p$ terms, and through some manipulation the flow of fluids can also be represented in terms of equivalent admittances.

In order to simplify the model as much as possible without sacrificing the desire for detail, the following assumptions were made:

- (1) Each tube of the DHX was assumed to be identical to every other tube. Thus, only one tube of n passes was modeled.
- (2) Though the DHX which was assumed has only one tube row per pass, and thus the sodium flow path would be somewhat staggered, we assumed an air flow that likewise was staggered. In effect, we straightened out the flow path but did not change geometry. The assumption is

illustrated in the sketch, Figure XII.24. The diagram is not to any scale.

- (3) Since this type of analysis cannot reflect a constantly changing DHX, the study was based on the unit which resulted from the initial operation conditions of 400 MW_t , a vessel inlet temperature of 500 F and a vessel outlet of 800 F with an IHX LMTD of 85 F . The description of the DHX simulated is given in Table XII.7.

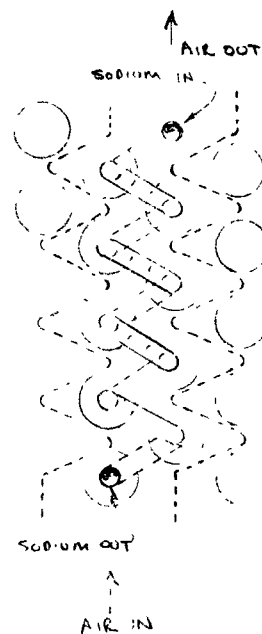


Figure XII.24

TABLE XII.7 DHX DIMENSIONAL DATA

Number of Passes	10
Outside Tube Diameter, in.	1.9
Height of Fins, in.	0.109
(Outside Diameter of Fins, in.	3.40)
Tube Pitch, Triangular, in.	3.775
Fin Thickness, in.	0.050
Number of Fins Per Foot	60
Axial Tube Length, ft.	18.
Effective Tube Length	15.
Fouling Factor, Sodium	0
Fouling Factor, Air Side	0.003
Number of Tubes Per Pass (N_T)	258
Tube Material	314 S.S.
Fin Material	410 S.S.

The single tube which is typical of all the tubes in the DHX was divided into 30 representative sections of equal length and the air stream flowing past this tube was divided into three equal flow streams. This is illustrated in Figure XII.25 within each of these five feet sections. The thermal processes were assumed to be represented by a single fin located midway through the section. The TAP code is so constructed that the temperatures computed for each node are assumed to be the arithmetic average of each node. Each of these centrally

located fins were assumed to be symmetrical about the center plane of the fin. Thus, we finally have described in detail only one six-hundredth of each of the 30 sections. Each of these half fins was divided into eight circumferential nodes plus two associated fluid nodes. The arrangement of nodes and the network of admittances is given in Figure XII.26.

The admittances were computed generally as follows:

a. Metal to metal nodes and adjacent air nodes not in the direction of flow.
$$Y = \frac{\bar{A}k}{L} \quad (52)$$

b. Metal to sodium
$$Y = \left[\frac{L}{k\bar{A}} + \frac{1}{h_i A} \right]^{-1} \quad (53)$$

c. Metal to air
$$Y = \left[\frac{L}{k\bar{A}} + \frac{1}{h_f A} \right]^{-1} \quad (54)$$

d. Flowing fluid nodes
$$Y = 2Wc_p \quad (55)$$

Where:

\bar{A} = Logarithmic mean area

L = Path length

A = Area

k = Thermal conductivity

c_p = Specific heat

W = Weight flow rate per given path

h_i = Heat transfer coefficient, sodium to metal

h_f = Heat transfer coefficient, metal to air

FIGURE XII.25 DIAGRAM OF DHX TUBE SECTIONS

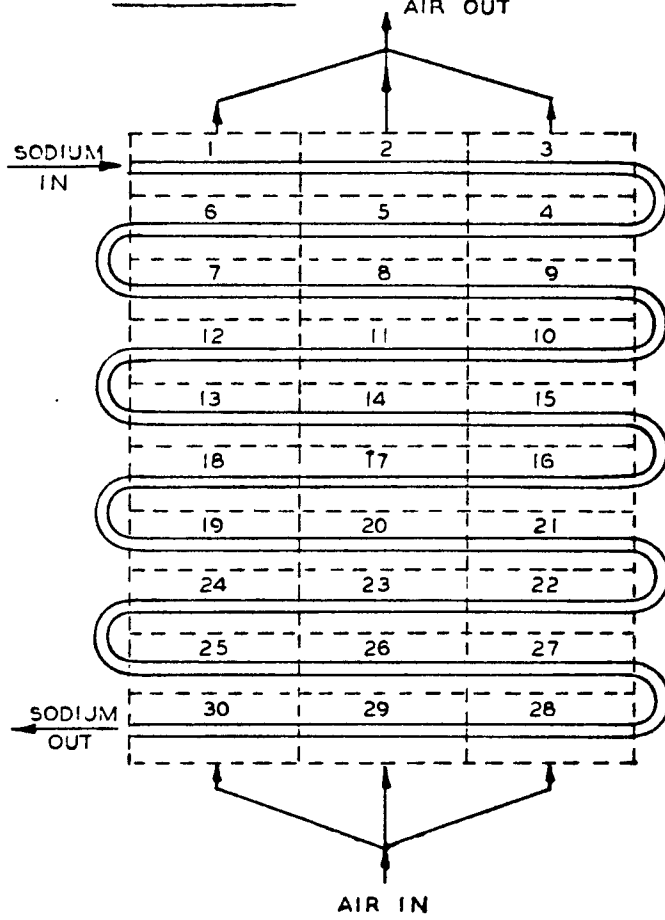
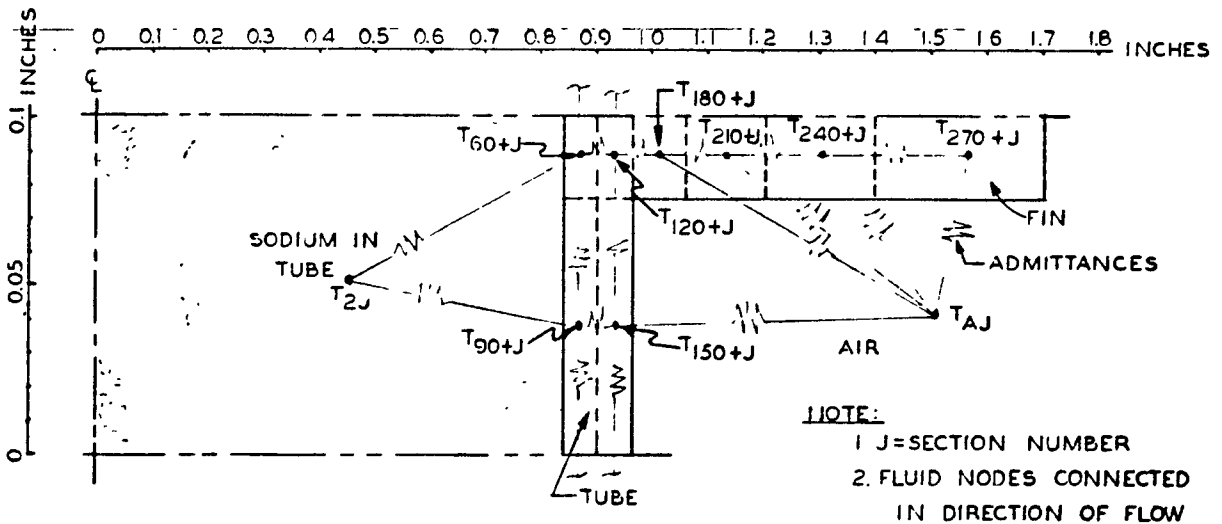


FIGURE XII.26 NODAL ARRANGEMENT - TYPICAL FOR EACH SECTION



The heat transfer coefficients are computed as in Kern's Process Heat Transfer. A summary of the method is given below.

1) Sodium to metal:

$$h_i = \frac{k}{D_i} N_{Nu} \quad \text{where } D_i = \text{inside diameter} \quad (56)$$

$$N_{Nu} = \text{Nusselt Number}$$

$$N_{Nu} = A + 0.025 (\psi N_{Pe})^{0.8} \quad \text{where} \quad (57)$$

$$N_{Pe} = \text{Peclet Number}$$

ψ = correction factor = $f(N_{Re})$

$A = 5.0$ for sodium

$$\psi = 1 - \frac{1.82}{N_{Pr} \left(\frac{\epsilon_m}{v}\right)_{\max}^{1.4}} \quad (58)$$

where

N_{Pr} = Prandtl Number

$\left(\frac{\epsilon_m}{v}\right)_{\max}$ is obtained from Dwyer's
work = $f(N_{Re})$

2) Metal to air:

The Sieder-Tate relationships are used where a j factor is defined as:

$$j = \frac{h_o D_e}{k N_{Pr}^{1/3}} \quad \text{where } h_o = \text{metal to air heat transfer} \quad (59)$$

coefficient without fouling

D_e = equivalent diameter

The j factor is also a function of Reynold's number.

$$j = 13.44 \left(\frac{N_{Re}}{10^3} \right)^{0.72322} \quad (60)$$

So that

$$h_o = \frac{j k N_{Pr}^{1/3}}{D_e} = \frac{13.44 \left(\frac{N_{Re}}{10^3} \right)^{0.72322} k N_{Pr}^{1/3}}{D_e} \quad (61)$$

In the above relationships

$$D_e = \frac{2 A_F}{\pi \lambda} \quad \text{where } A_F = \text{free flow area} \quad (62)$$

$\lambda = \text{projected perimeter}$

The air-side fouling resistance, R_f , is included so that

$$h_f = \frac{h_o/R_f}{h_o + 1/R_f} \quad (63)$$

The heat storage terms, or in TAP the capacitances - $\rho V c_p = C$ terms - for the air side are neglected. This was done to obtain a reasonable time increment for transient analysis and is, furthermore, quite reasonable as $\frac{C_{\text{sodium}}}{C_{\text{air}}} \doteq 400$ and $\frac{C_{\text{metal}}}{C_{\text{air}}} \doteq 1700$. This is a fairly common assumption as well.

An extensive check of this simulation was made resulting in the attainment of excellent agreement with the steady state predictions of the ADOPT computer code. Assuming the coolant flow rates and temperatures which result from a specified DHX unit

capacity of 133.33 MW_t. This TAP model predicts a heat transfer rate of 135.53 MW_t, a difference of slightly over 1.6%. This is well within the accuracy of the correlations and methods used.

In connection with this check, the exact solution of the radial temperature distribution in the fin was obtained by solving the equation:

$$Y_r \frac{d^2T}{dr^2} + \frac{Y_r}{r} \frac{dT}{dr} + \frac{dY_r}{dr} \frac{dT}{dr} - \frac{h}{k} T = 0 \quad (64)$$

which, for rectangular fins becomes the modified Bessel equation of order $n = 0$:

$$\frac{d^2T}{dr^2} + \frac{1}{r} \frac{dT}{dr} + (N^2 i^2 - \frac{n}{r^2})T = 0 \quad \text{where } r = \text{radius} \quad (65)$$

$T = \text{temperature}$
 $i = \sqrt{-1}$
 $N^2 = \frac{h}{kY_b}$

which has a solution of the form:

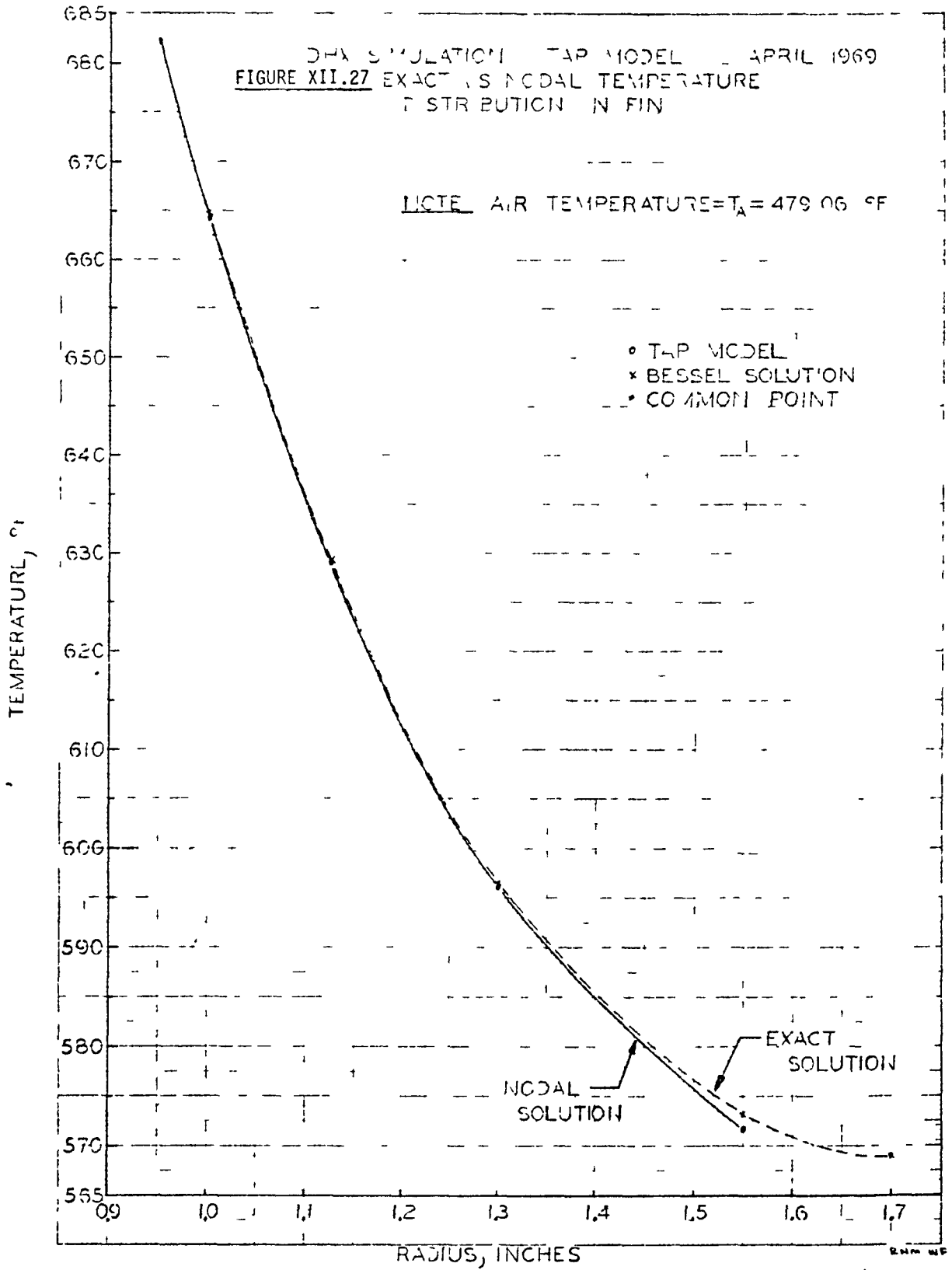
$$T = C_1 J_0(iN_r) + C_2 Y_0(iNr) \quad (66)$$

Figure XII.27 shows this temperature distribution compared with the TAP results for one typical location.

Also coincident to this check was the determination that the 10 pass DHX cross-flow exchanger behaves sufficiently like a

DNA SIMULATION TAP MODEL - APRIL 1969
 FIGURE XII.27 EXACT AND NODAL TEMPERATURE
 DISTRIBUTION IN FIN

NOTE: AIR TEMPERATURE = $T_A = 479.06$ °F



BHM WF

counterflow exchanger that a correction to the log mean temperature difference is not required.

c. Simplified DHX Simulations

When we speak of simplified simulations we mean the representation of the DHX by a set of differential equations which may then be set up for solution using the dynamic systems analysis code, DYNASYAR.

To obtain the set of representative equations, the same DHX as described in Table XII.7 was used. Each of the sodium tubes of 10 passes, we assume, is straightened out and the air is assumed to flow in a truly counterflow manner. The following assumptions were then made:

- (1) Three radial nodes were used, one each for air, sodium and metal.
- (2) Initially, the thermophysical properties and heat transfer coefficients were computed on the basis of local temperatures.
- (3) Initially, six longitudinal nodes were used.
- (4) No plenum effects at the inlet or outlet will be considered initially. These will be added once the model to be used is determined.
- (5) Heat transfer in the fins was represented through the vehicle of fin efficiency.

The sketch, Figure XII.28, illustrates the model:

Since the code cannot handle spatial derivatives they must be expressed by difference techniques. The technique of alternating central differences with 3-point backward differences will be used. Thus, equations (67), (68), and (69) become for each mesh point (j) indicated:

$$\frac{dT_{S_j}}{dt} = - \left(\frac{U}{\rho C}\right)_{S_j} \left(\frac{A'}{V'}\right)_S [T_{S_j} - T_{F_j}] - \begin{cases} \left(\frac{3}{L_x V'_S}\right) \left(\frac{W_S}{\rho S_j}\right) [T_{S_{j+1}} - T_{S_{j-1}}] & j=2,4,6 \\ \left(\frac{3}{L_x V'_S}\right) \left(\frac{W_S}{\rho S_j}\right) [3T_{S_j} - 4T_{S_{j-1}} + T_{S_{j-2}}] & j=3,5,7 \end{cases} \quad (70)$$

$$\frac{dT_{F_j}}{dt} = \left(\frac{U_{S_j}}{\rho_{F_j} C_{F_j}}\right) \left(\frac{A'_S}{V'_F}\right) [T_{S_j} - T_{F_j}] - \left(\frac{U_{T_j}}{\rho_{F_j} C_{F_j}}\right) \left(\frac{A'_T}{V'_F}\right) [T_{F_j} - T_{T_j}] \quad (71)$$

A11 j

$$\frac{dT_{T_j}}{dt} = \left(\frac{U}{C}\right)_{T_j} \left(\frac{A'}{V'}\right)_T [T_{F_j} - T_{T_j}] + \begin{cases} \left(\frac{3}{L_x V'_T}\right) \left(\frac{W_T}{\rho T_j}\right) [-3T_{T_j} + 4T_{T_{j+1}} - T_{T_{j+2}}] & j=1,3,5 \\ \left(\frac{3}{L_x V'_T}\right) \left(\frac{W_T}{\rho T_j}\right) [T_{T_{j+1}} - T_{T_{j-1}}] \end{cases} \quad (72)$$

where:

A'_S = heat transfer area per unit length inside tubes

A'_T = heat transfer area per unit length outside tube and fins

V'_S = sodium volume per unit length (inside tubes)

V'_F = tube and fin metal volume per unit length

V'_T = air side volume per unit length

The heat transfer coefficients U_{Tj} and U_{Sj} were determined as follows. The metal temperatures T_{Fj} were taken as the fin base temperature as this is the temperature on which the fin efficiency is based. Then:

$$U_{Sj} = \left[\frac{1}{h_{ij}} + \frac{D_i \ln(D_o/D_i)}{2k_{FTj}} \right]^{-1} \quad (73)$$

where

D_i = inside tube diameter

D_o = outside tube diameter (diameter at location of T_{Fj})

k_{FT} = thermal conductivity of tube

h_i = inside heat transfer coefficient.

The coefficient h_i is computed exactly as outlined for the TAP model. The outside U-factor is next:

$$U_{Tj} = \left[\Omega A'_{fj} + A'_{tj} \right] \frac{h_{fj}}{A'_{Tj}} \quad (74)$$

where

Ω = fin efficiency

A'_{fj} = fin surface area exposed to air per unit length

A'_{tj} = tube surface area exposed to air per unit length

$$A_{T_j}^c = A_{f_j}^c + A_{t_j}^c$$

h_f = outside heat transfer coefficient.

The coefficient h_f is determined exactly as outlined for the TAP model. The fin efficiency, Ω , is a function of geometry, h_f and T_{F_j} and is the ratio of actual heat transfer to the heat transfer which would take place if the entire fin surface were at the temperature of the fin base.

During the check of the model we determined that for the six-node simulation there was negligible difference between the heat transfer coefficients computed based on local temperatures and average coefficients. Since the latter almost halved the computer time, it was quickly adopted.

The initial six-node model was both expanded and contracted so that we have examined five models:

- (1) 12-node, average coefficients (12N-ave.)
- (2) 6-node, average coefficients (6N-ave.)
- (3) 4-node, average coefficients (4N-ave.)
- (4) 4-node, local coefficients (4N-L)
- (5) 4-node, both average coefficients and average material properties (4N-L)

Up to this time we have examined the above five models for five different conditions.

- (1) Balanced flow rates, temperature of fluid vs location. Figures XII.29 and XII.30 present the results for all six cases. Similar data for unbalanced flows (10:1 and 50:1) are shown in Figures XII.31-34.
- (2) Beginning at a balanced flow steady state condition a rapid ramp to a moderately unbalanced flow condition; transient response of coolant outlet temperatures. This case was for high secondary, low tertiary flow (3.48:1). Figure XII.35 presents the comparison of the 4N-min. Simulation with the same transient computed via TAP. The steady state end points are indicated at the right side of the curves. Only the 4N-min case is shown as all other simplified models are almost identical to this one.
- (3) The spatial temperature distribution in the fluids at the steady state end points of the preceding transient are given in Figure XII.36. Again the comparison is for the 4N-min vs the TAP reference simulation.

FIGURE XII.29 DHX SIMULATION SODIUM TEMPERATURE VS DISTANCE IN DHX JULY 1969

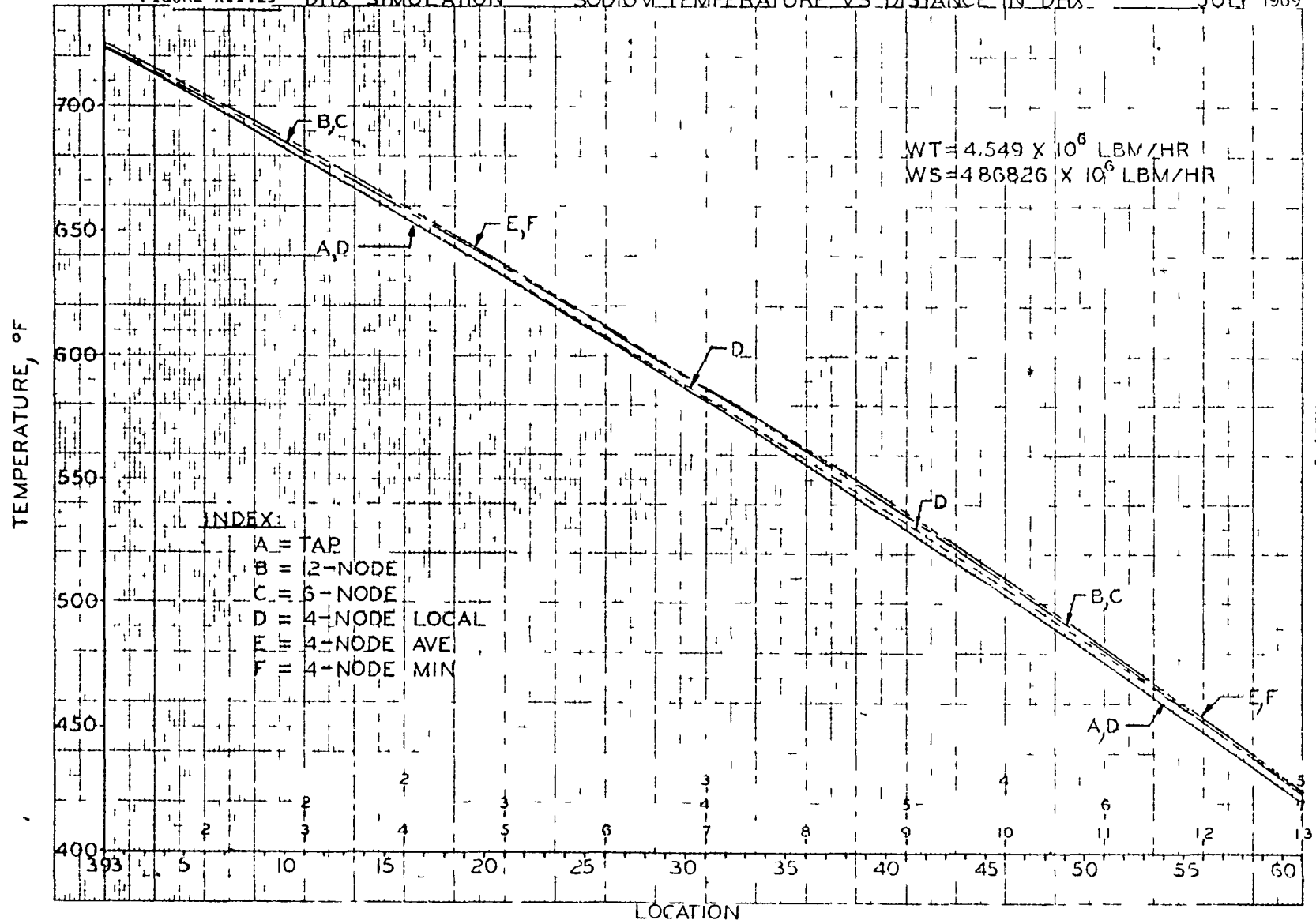
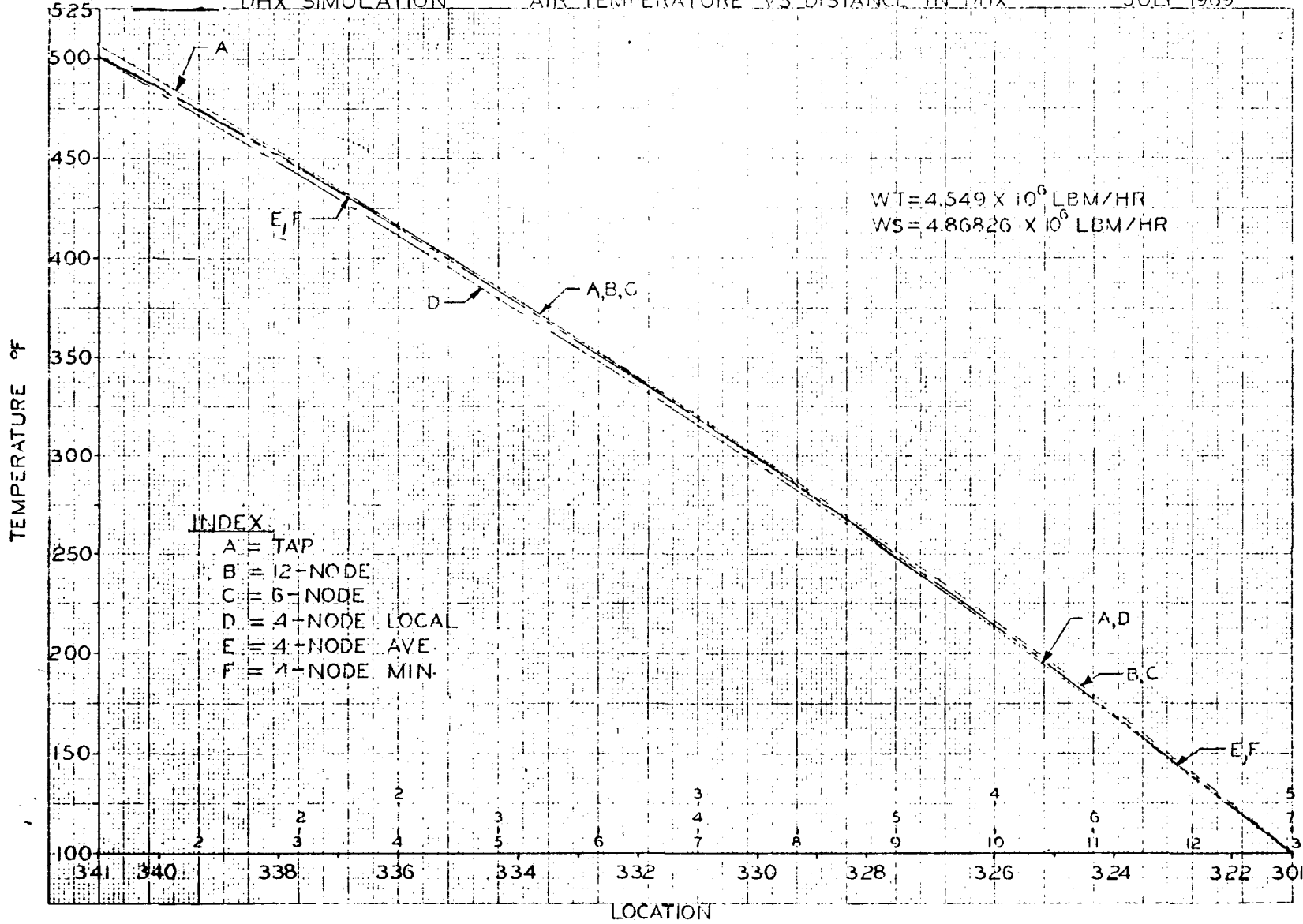


FIGURE XII.30

DHX SIMULATION

AIR TEMPERATURE VS DISTANCE IN DHX

JULY 1969



XII.97

FIGURE XII.31

XII.98

DHX SIMULATION TAP-4N-MIN AUGUST 1969
TEMPERATURE DISTRIBUTION FOR UNBALANCED FLOW
HIGH SECONDARY-LOW TERTIARY FLOW (100%-10%)

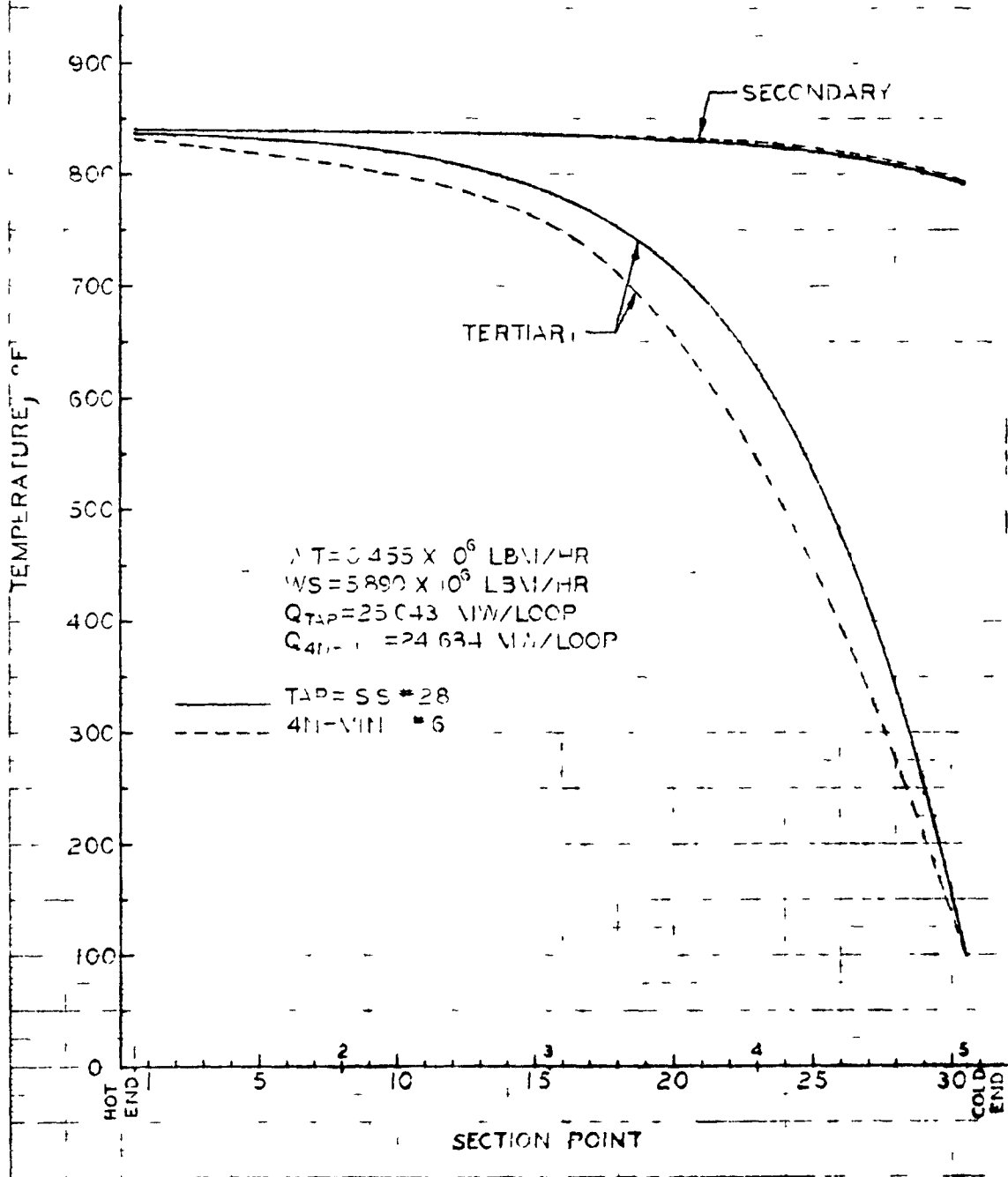


FIGURE XII.32

XII.99

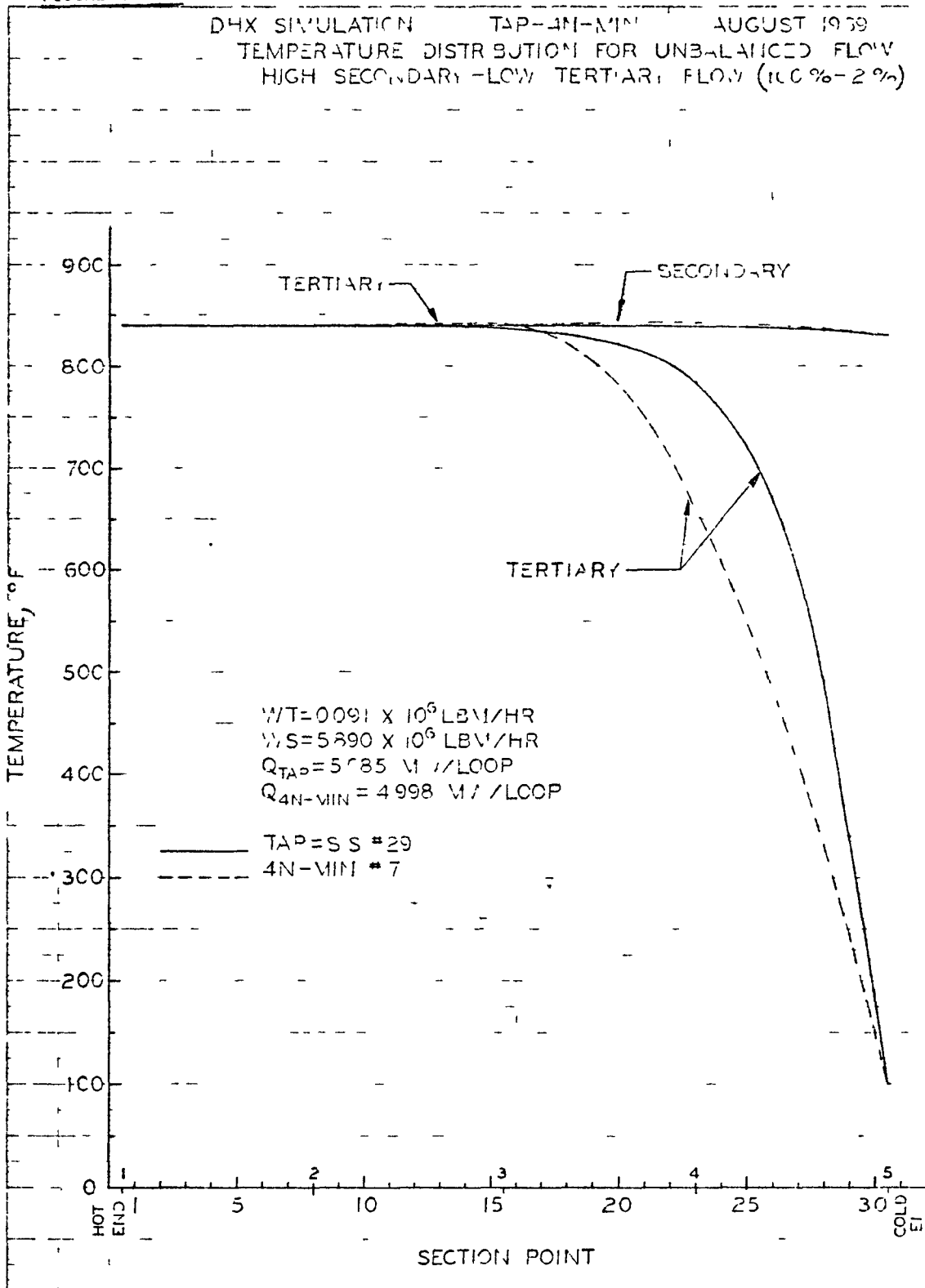


FIGURE XII.33

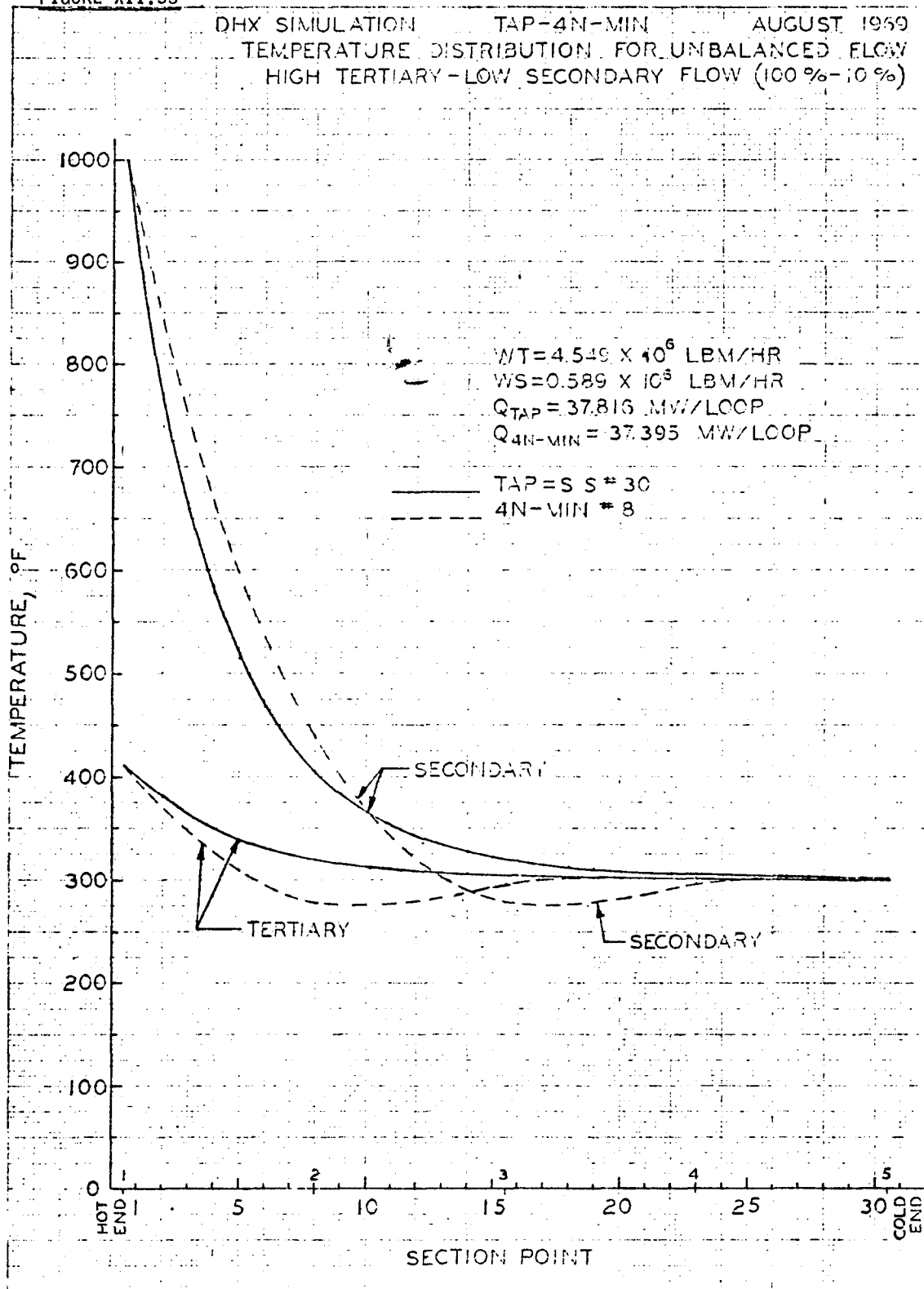
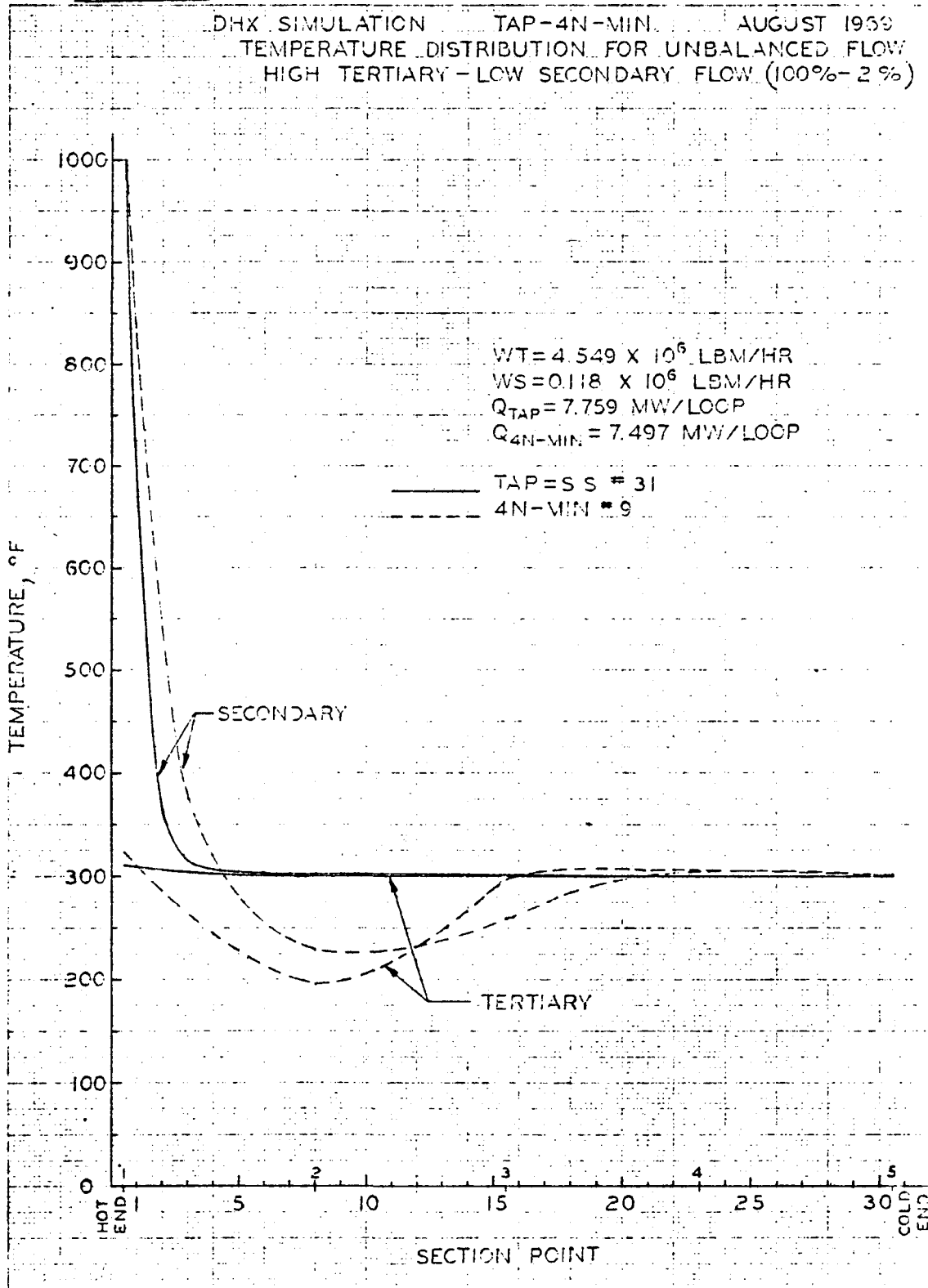


FIGURE XII.34

XII.101



DHX SIMULATION

AUGUST 1969

FIGURE XII.35 4-NODE MIN. TRANSIENT SIMULATION COMPARED WITH
TAP DHX REFERENCE SIMULATION
HIGH SECONDARY-LOW TERTIARY FLOW (3.48:1.0)

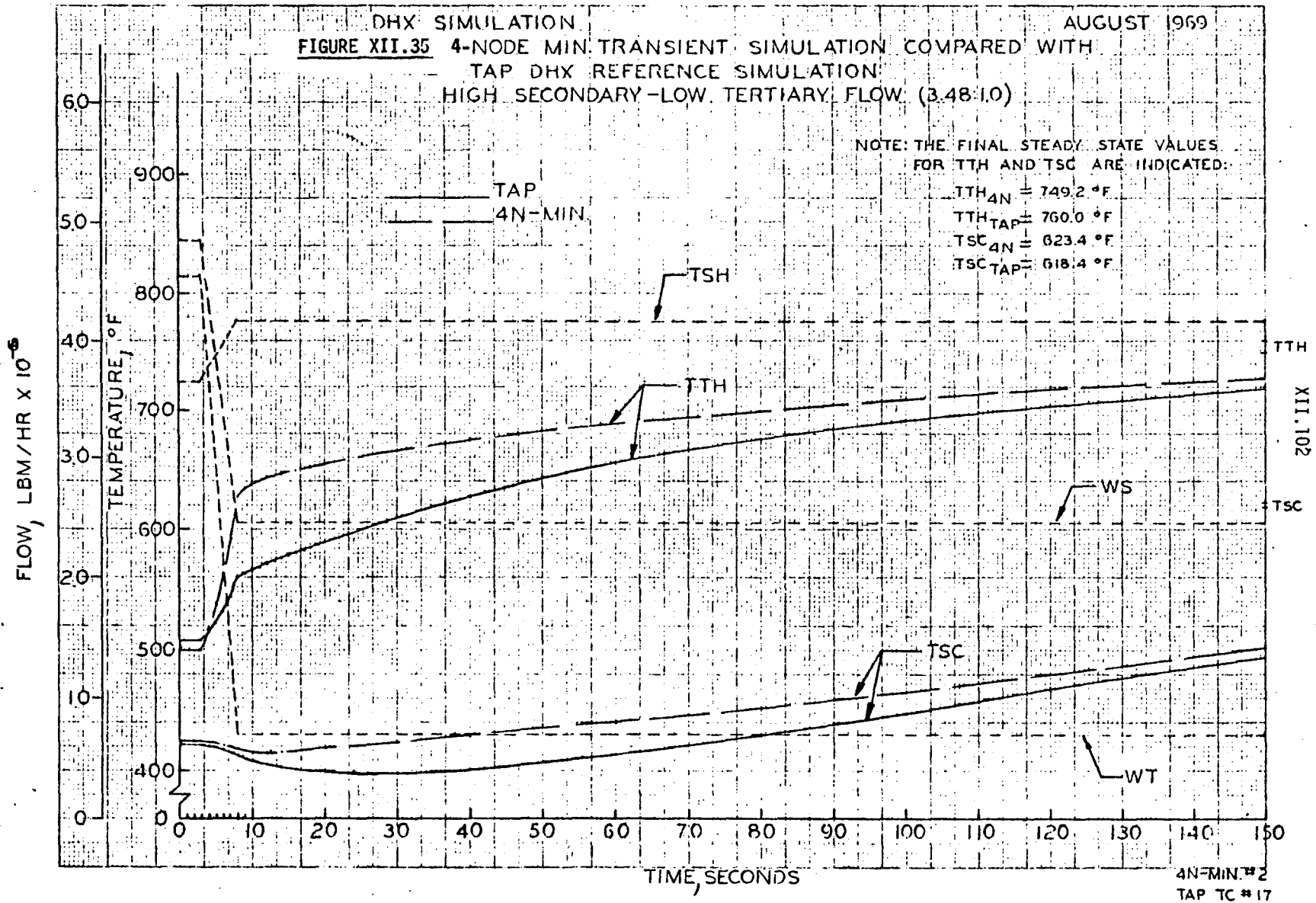
NOTE: THE FINAL STEADY STATE VALUES
FOR TTH AND TSC ARE INDICATED:

$$TTH_{4N} = 749.2 \text{ } ^\circ\text{F}$$

$$TTH_{TAP} = 760.0 \text{ } ^\circ\text{F}$$

$$TSC_{4N} = 623.4 \text{ } ^\circ\text{F}$$

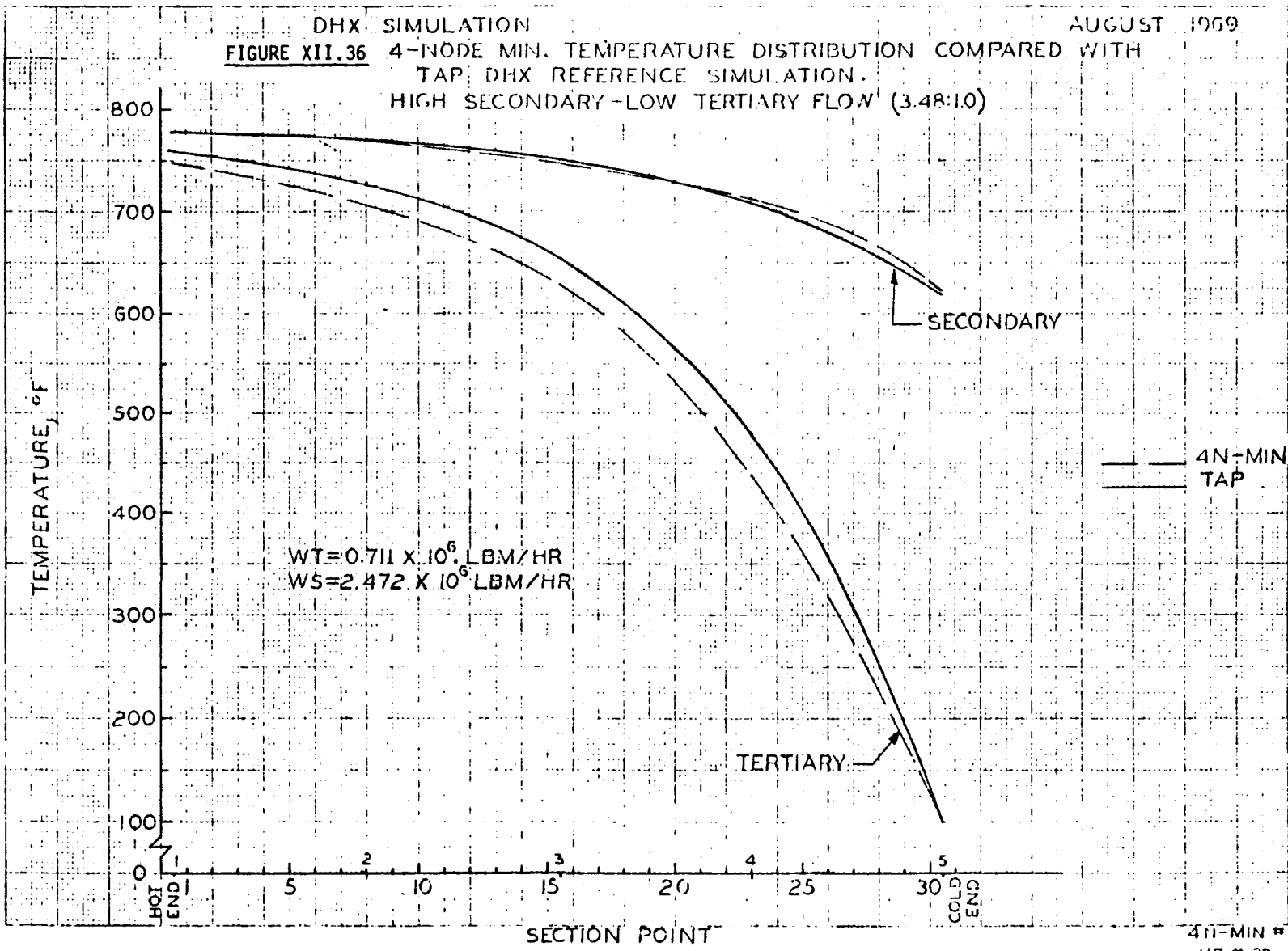
$$TSC_{TAP} = 618.4 \text{ } ^\circ\text{F}$$



XII.102
TTH
TSC

DHX SIMULATION
 FIGURE XII.36 4-NODE MIN. TEMPERATURE DISTRIBUTION COMPARED WITH
 TAP DHX REFERENCE SIMULATION.
 HIGH SECONDARY-LOW TERTIARY FLOW (3.48:1.0)

AUGUST 1969



4N-MIN #3
 UB # 20

- (4) Figure XII.37 presents the transient responses of coolant outlet temperature for a rapid ramp to a moderately unbalanced flow in the opposite direction to the above.
(Tertiary:Secondary = 3.06:1)
- (5) Finally, Figure XII.38 shows the spatial fluid temperature distribution at the steady state end points for the preceding transient.

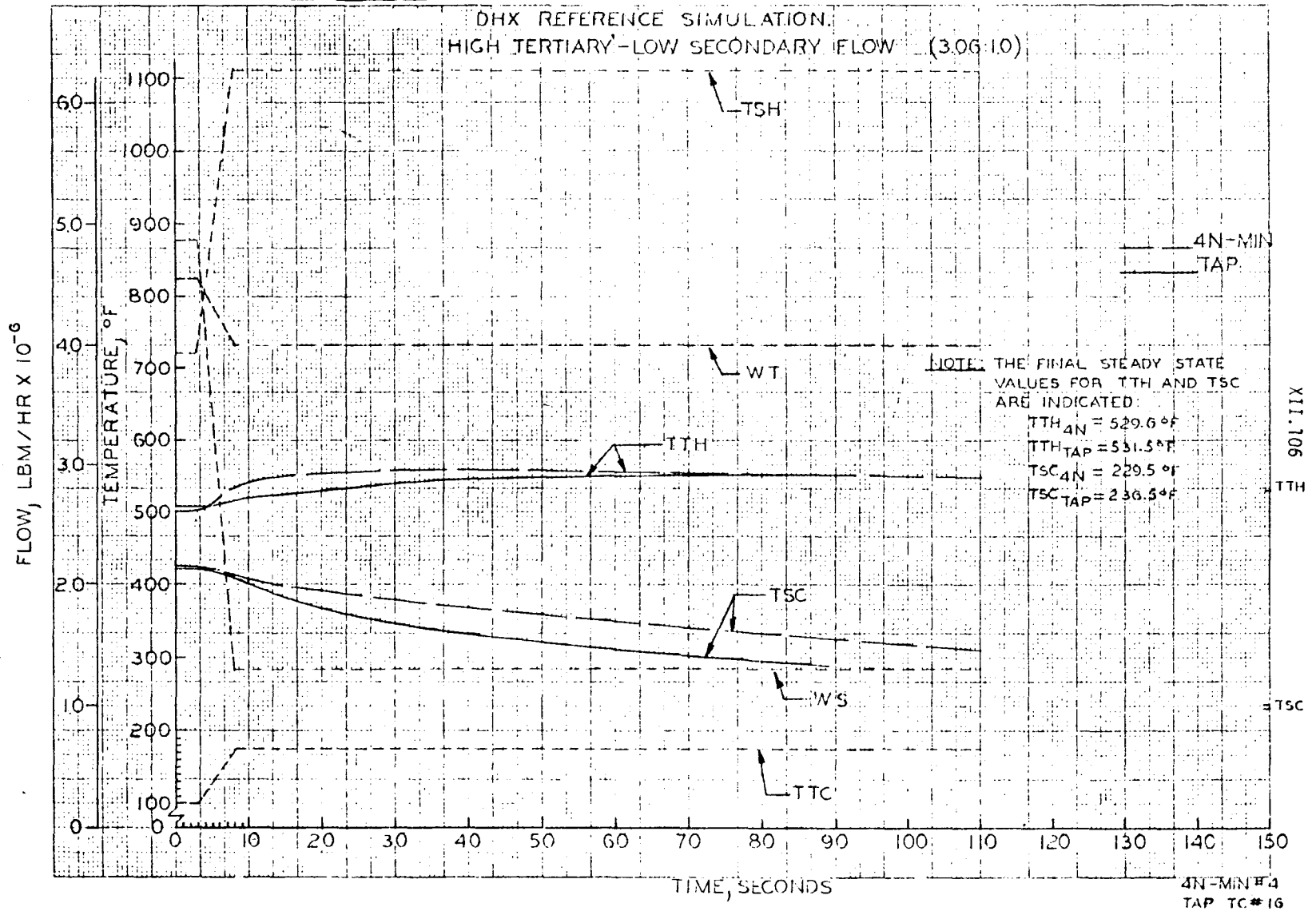
The results so far indicate that good accuracy is obtained for steady state with balanced and moderately unbalanced flows using the most simple 4-node model. Transient analyses with the simplified models seem to give a higher rate of temperature change for the sodium and a lower rate of change for the air.

Analysis and comparison is still proceeding and we will next investigate behavior in extremely unbalanced flow conditions. When a final model determination has been made the effect of manifold mixing will be included using the assumptions of perfect mixing. The equations which will be programmed are:

$$\rho V c_p \frac{d\bar{T}}{dt} = W c_p (T_i - \bar{T}) \quad (75)$$

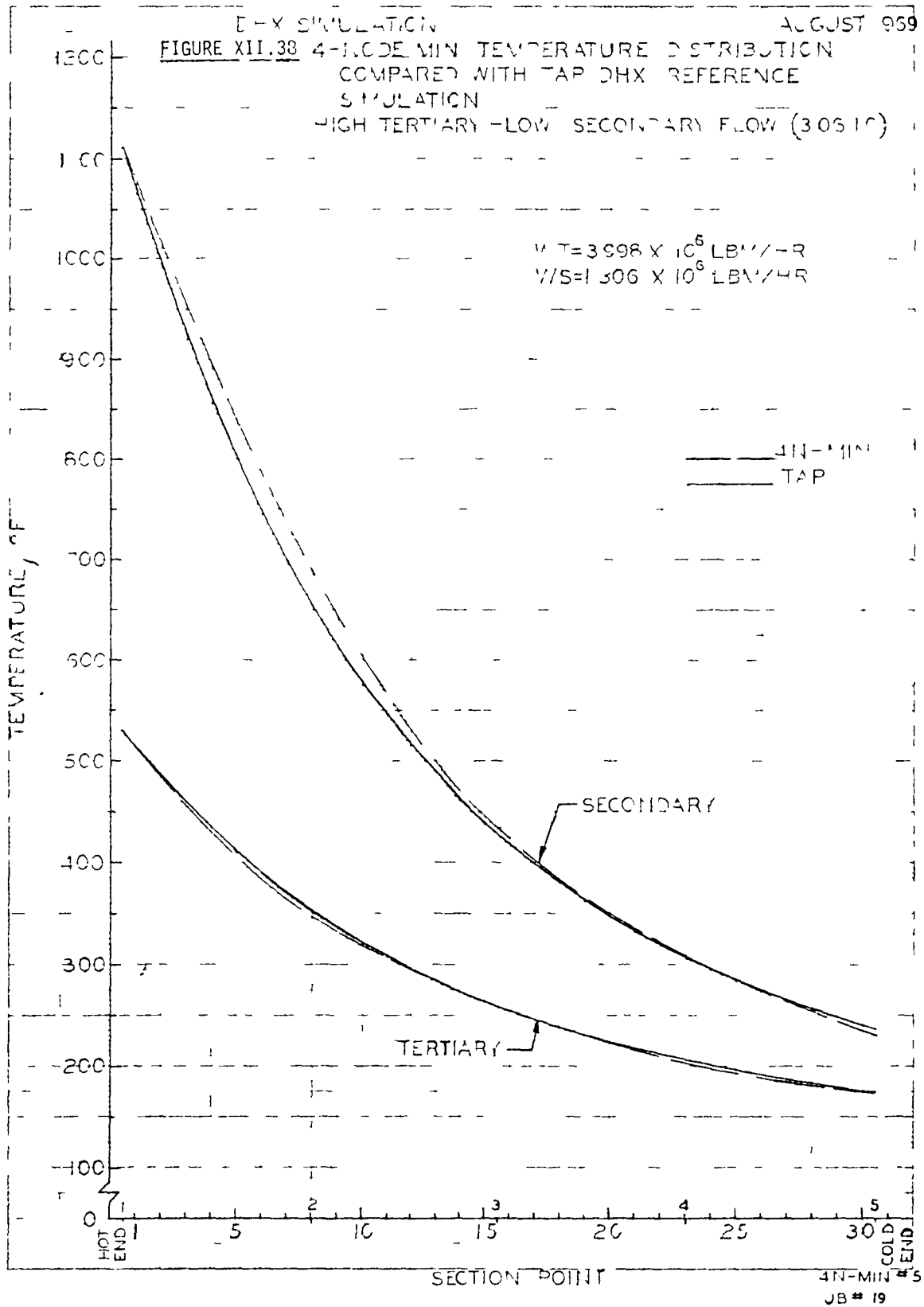
where ρ = fluid density
 V = mixing plenum volume
 c_p = specific heat capacity
 W = weight flow rate
 T_i = fluid inlet temperature to plenum
 \bar{T} = temperature leaving plenum and entering the average tube.

FIGURE XII.37 4-NODE MIN. TRANSIENT SIMULATION COMPARED WITH TAP



AUGUST 1959

E-X SIMULATION
FIGURE XII.38 4-INCH DE MIN TEMPERATURE DISTRIBUTION
COMPARED WITH TAP DHX REFERENCE
SIMULATION
HIGH TERTIARY - LOW SECONDARY FLOW (30610)



6. Sodium Piping

The coolant's transport time between components is important in transient analysis work. In work to date, we have neglected heat storage in pipe walls. As shown later, a small increase in simulation accuracy can be achieved by accounting for the stored heat.

a. Pure Transport Delay

The transport time is given by the following equation:

$$\int_{t-\tau}^t Q(t) dt = V$$

where

$Q(t)$ = coolant volumetric flow rate

t = time

τ = transport time

V = volume of pipe section

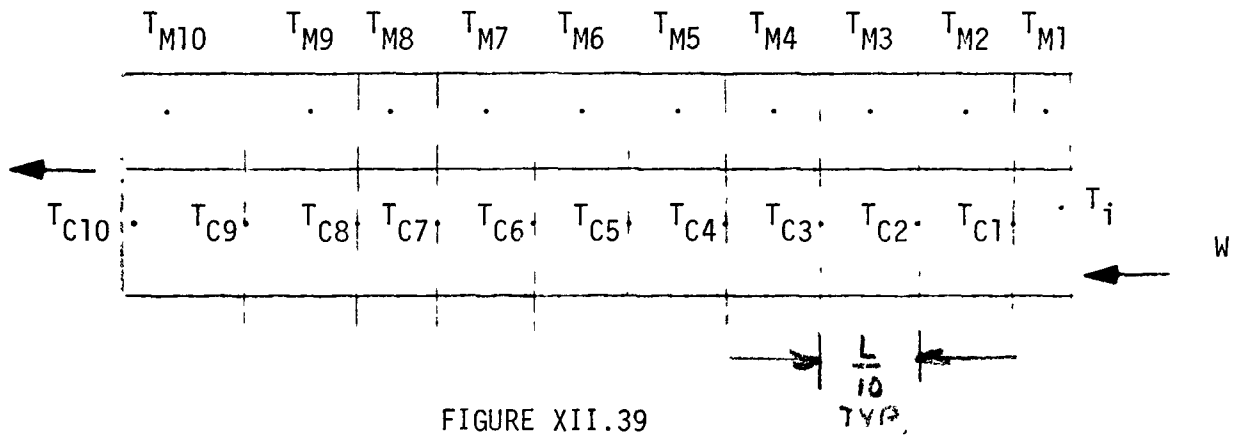
Coolant entering the pipe section at a temperature T at time $t-\tau$, exits at time t at temperature T .

In this case, pipe wall stored heat and heat losses through the wall and insulation are neglected. No mixing of coolant within the pipe is assumed.

The flow rate is obtained from the integration of the equation of motion for that pipe run. The coolant density for conversion of the weight flow to a volumetric flow varies with time and is the average of the coolant at the inlet and exit points.

b. Transport Allowing For Stored Heat In Pipe Wall

The pipe section is modeled as shown in Figure XII.39 for ten nodes:



The system can be described by the following equations if we neglect heat losses from the insulated pipe to the ambient and if we assume perfect mixing in each node of the model:

General Equations:

$$\text{Metal: } (\rho V \hat{c})_{mj} \frac{dT_{mj}}{dt} = - (UA')_j \left(T_{mj} - \frac{T_{cj} + T_{cj-1}}{2} \right) \quad \dots (76)$$

$$\text{Sodium: } (\rho V \hat{c})_{cj} \frac{dT_{cj}}{dt} = - (WC)_{cj} \frac{(T_{cj} - T_{cj-1})}{\Delta x} + (UA)_j \left(T_{mj} - \frac{T_{cj} + T_{cj-1}}{2} \right) \quad \dots (77)$$

Take sodium properties based on average nodal temperature.

These equations are similar to the nodal heat balance model equations described for the IHX. That is, the node outlet temperature time derivative is equated to the nodes average temperature derivative.

c. Comparison of Modeling Techniques

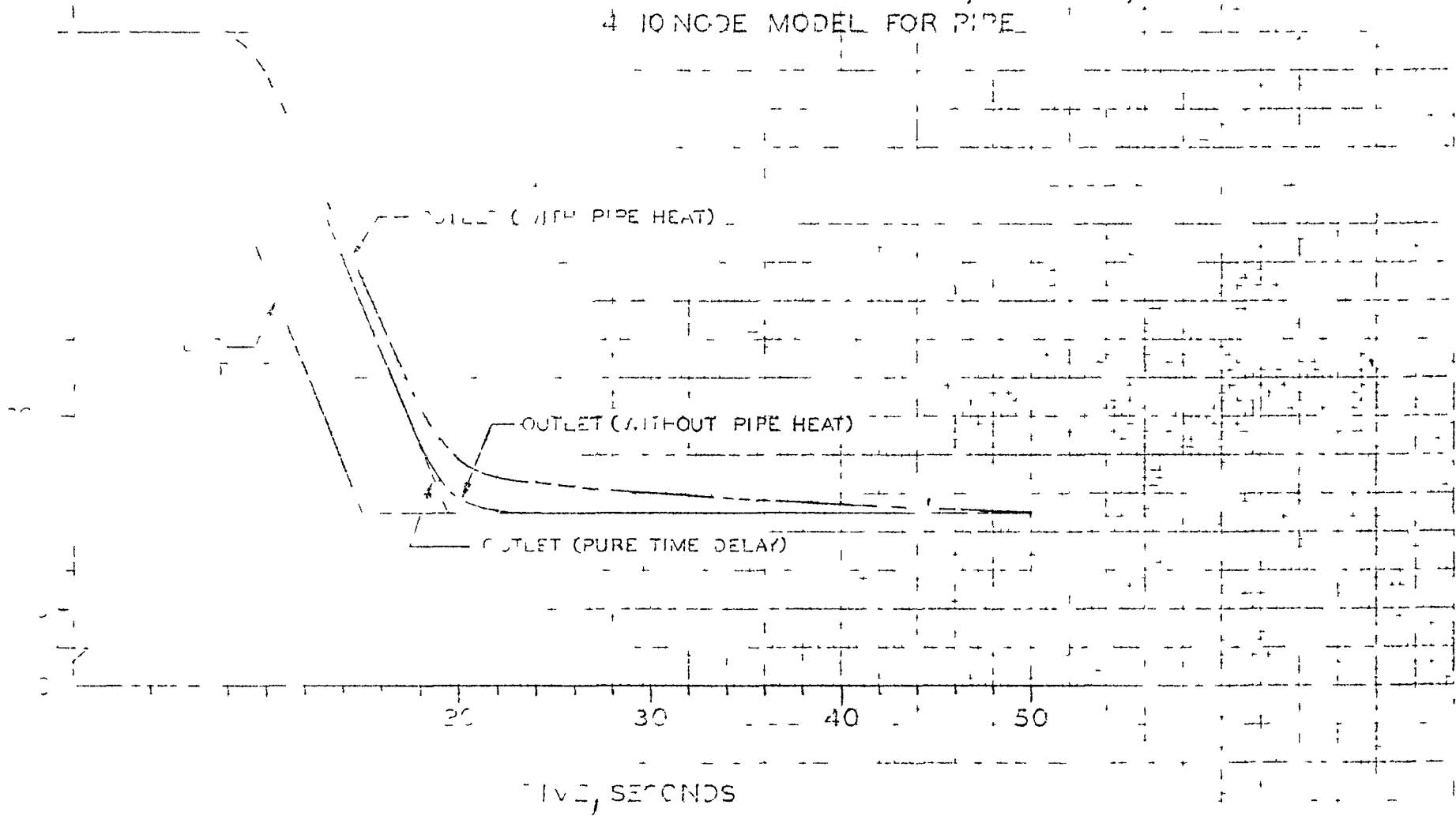
Results are presented in Figure XII.40 for an inlet temperature ramp at constant coolant flow rate. Cases with varying flow rates, with and without varying inlet temperatures, have been studied, but are not reported here. The results shown are typical in that the maximum rates of temperature change are quite similar for the two methods. For final process control and safety analysis work, it would be best to account for stored heat, but for conceptual design work the use of the worst case method (pure transport delay) is certainly justified. The pure transport delay model is preferred from the programming standpoint because of its relative simplicity, especially if four or more nodes are needed in the stored heat model.

FIGURE XII.40

COOLANT THERMAL TRANSIENT

AUG 69

- 1 INLET TEMPERATURE RAMP OF $25^{\circ}\text{F}/\text{SEC}$
- 2 CONSTANT SODIUM FLOW OF $1600 \text{ LB}/\text{SEC}$
- 3 PIPE SIZE 100 FT LONG, $\text{O.D.} = 9 \text{ IN}$, $\text{I.D.} = 8.25 \text{ IN}$
- 4 10 NODE MODEL FOR PIPE



XII.111

7. Tertiary Air Fans and Flow Control

a. Supply Fans

Constant speed fans are assumed. The fan supply curve is then programmed only for the design speed as:

$$\text{Fan pressure} = f(\text{fan air rate})$$

The pressure and rate are determined by the simultaneous solution of this equation and the hydraulics equations for the air side of the DHX (see p. 52).

b. Air Flow Control

The air rate is modulated by changing the position of inlet vanes at the fans. The rate is related to the valve's pressure drop as follows:

$$\omega = c \sqrt{\frac{P\Delta P}{T+460}} \quad , \text{ lb/sec}$$

where P = line pressure

ΔP = pressure drop across vanes

T = temperature of air, °F

c = coefficient of flow (includes conversion factors).

c is a function of vane position which is varied depending on a process controller output.

The air flow vane pressure loss is an input into the hydraulics equations

c. Fan Coastdown

The coastdown of the air rate following a deenergization of the fan motors can be approximated by:

$$\frac{Q(t)}{Q_0} = \frac{1}{1 + \frac{t}{a}}$$

where

Q = air rate

t = time after deenergization

$$a = \frac{N_0 I \omega_0^2}{g \rho_0 \Delta P_0 Q_0}$$

N = fan efficiency

I = inertia of fan and drive

ω = speed

ρ = density

ΔP = fan pressure

subscript 0 refers to initial values.

The coastdown equation neglects inertia in the air and assumes that the static pressure terms are small compared to the other losses. It also assumes the frictional losses are proportional to flow squared and that air flow rate is proportional to the fan speed.

8. Process Control

Process Controllers with gain plus reset actions are simulated. A controller time constant and the time constant of the sensing element and its transmitter are included.

a. Sensors and Transmitters

These functions are combined and represented by a first order process:

$$\tau_s \frac{dX}{dt} + X = Z$$

or in transfer function notation

$$\frac{\hat{X}}{\hat{Z}} = \frac{1}{\tau_s s + 1}$$

where

X = measured variable (output)

Z = process input (i.e., coolant temperature, flow rate, speed, etc.)

τ_s = time constant of measuring system.

The output is compared to the controller setpoint to create the error signal for the controller to act upon (see paragraph b).

b. Controllers

The controller output is represented by:

$$\frac{dX}{dt} = \frac{K_g K_r}{60\tau_c} \int_0^t \epsilon dt + \frac{K_g}{\tau_c} \epsilon - \frac{X}{\tau_c} + \frac{X_0}{\tau_c}$$

where

X = controller output, % and $0 < X < 100$

K_g = gain

K_r = reset, repeats/minute

τ_c = controller time constant

ϵ = error signal

= measured variable - setpoint

X_0 = initial output corresponding to steady state setpoint.

The first term on the right hand side of the equation is usually limited to 100%.

c. Actuators for Manipulated Variables

The following process conditions have been controlled.

- (1) Primary coolant flow rate by varying pump speed.
- (2) Secondary coolant flow rate by varying pump speed.
- (3) Reactor power (this is a special control problem which was discussed in the Reactor Model Description paragraphs,
- (4) Sodium temperature at DHX exit or IHX exit by throttling DHX inlet air vanes.

The kinetics of the liquid rheostat for pump speed control is discussed under Pumps and Drives . The kinetics

of the air inlet vanes for DHX air flow regulation is similar to that for valves and is treated as a first or second order process, depending on the actuator.

Programs are flexible. For example, we can easily substitute reactor outlet temperature control by modulating pump speed for primary coolant flow control. Also rate action can be added to the controllers if required.

9. Trip Switches

On/off actions are simulated as required. For example, automatic actuation of a scram trip can be simulated by comparing a measured temperature against a fixed trip point high temperature:

$$T_{tP} - T_m < 0, \text{ rods latched}$$

$$T_{tP} - T_m > 0, \text{ rods unlatched.}$$

Of course, model logic is such that the rods remain unlatched after the trip point is reached even if the temperature difference again becomes < 0 .

T_{tP} = fixed trip point temperature

T_m = measured temperature

Time dependent trips are also used. Pump coastdown has been delayed a fixed amount of time after the reactor scram trip. Logic to identify the time of the scram trip is required if the scram is initiated automatically.

10. Interfaces With "Other" Systems

The reactor and heat transport systems have important interfaces with the inert gas, sodium supply, and cell ventilation systems.

To date we have simply held the gas space pressures in the reactor vessel and pump barrels, and building spaces surrounding the equipment at zero gauge in spite of the fact that these pressures will vary in practice. If needed, these pressures can be simulated. We will probably assume the perfect gas law applies, if and when these equipment pressures are added.

Concerning sodium supply, we have taken the worst case approach in that no make-up sodium is assumed. Logic could be added to introduce make-up sodium as a function of reactor vessel coolant level and/or as a function of a loss of coolant accident trip switch.

Actually, our current models are arranged for adding make-up sodium and for varying equipment and cell gas space pressures as known functions of time. These features were added with the idea that useful parametric studies could be made during the conceptual design phase.

FFTF Hybrid Simulation

a. Reactor Vessel

The reactor vessel model is shown schematically in Figure XII.41. Two heat transport loops (A and B) dump cold primary sodium into the inlet plenum where a single mixing lag term computes the inlet temperature to the core and other vessel internals. Similarly, the outlet plenum is simulated with a single mixing lag, with inputs from fuel to be coolant, leakage coolant, reflectors and vessel wall coolant. Several assumptions were made in order to fit the model on the computer:

- (1) No axial heat conduction.
- (2) Constant properties with respect to temperature.
- (3) Heat transfer between vessel wall bypass and outlet plenum coolant only.
- (4) Single axial region.
- (5) Control rod coolant response the same as reflector response.
- (6) Fuel cladding response the same as tube coolant response.

Equations are shown on following pages. The simplified model has been checked against the detailed digital reactor model (REMOD) programmed on the DYNASAR code and found to provide adequate response characteristics at the vessel outlet.

b. Process System

Two coolant circuits are simulated, as shown in Figure XII.2. As noted, each circuit has a primary loop, a secondary loop, pumps for each,

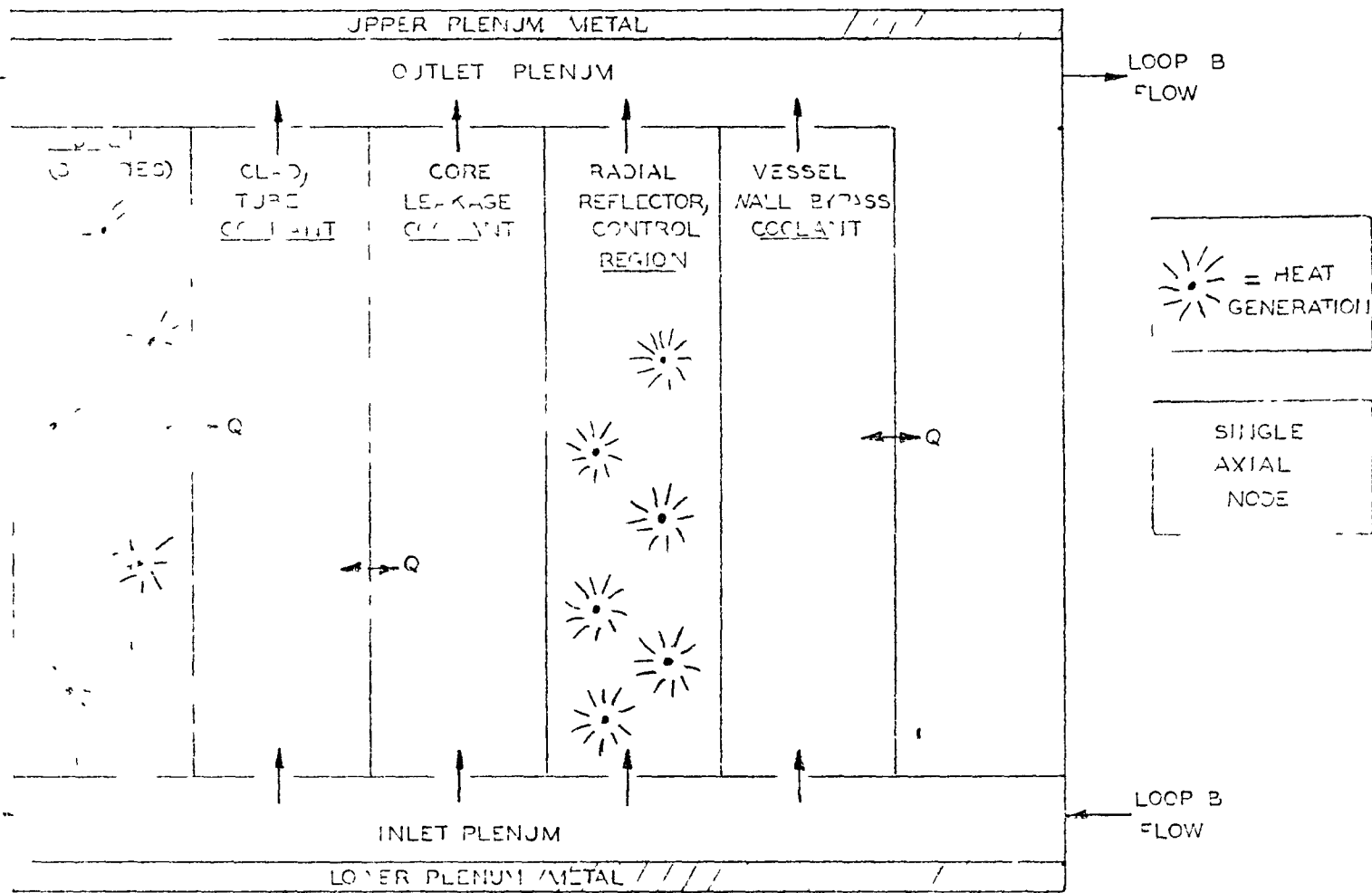


FIGURE XII.41 SCHEMATIC OF REACTOR VESSEL MODEL, HYBRID SYSTEM SIMULATION

variable transport delays for each, an intermediate heat exchanger (IHX) and a dump heat exchanger (DHX). The IHX and DHX are simulated as 4-node counterflow devices, with metal lumped with coolant, and with variable heat transfer coefficients. Mixing volumes are provided at the sodium inlet and outlet of each device. The heat transfer model for each uses a finite difference approach to the temperature distribution, with alternating central and three-point backward approximations.

Sodium pumps are simulated by solving the dynamic equations for pump speed and torque. Flows are computed from a dynamic equation with terms for natural convection, loop pressure loss, and pump head. Air flow is simulated simply by an "on-off" function generator for fan response, with natural convection added.

MODEL SUMMARY (HYBRID): REACTOR VESSEL

... Based on FFTF Concept 5A (SK-3-14540)

Heat Generation:

$$PL_{TOT} = PL_N + PL_{FP} \quad (78)$$

$$PL_{CL} = \gamma_{CL} PL_{TOT} \quad (79)$$

$$PL_{RR} = \gamma_{RR} PL_N \quad (80)$$

$$PL_F = PL_{TOT} - PL_{CL} - PL_{RR} \quad (81)$$

$$\left\{ PL \text{ into main HTS} = (1 - \gamma_{CL}) PL_{TOT} \right\}$$

Kinetics:

$$PL_N = \left[\frac{1}{\beta - \delta k} \right]_{i=1}^3 \gamma_i \lambda_i C_i \quad (\text{algebraic}) \quad (82)$$

$$\frac{dC_i}{dt} = \frac{\beta_i}{\lambda_i} (PL_N) - \lambda_i C_i \quad (83)$$

Reactivities: (subscript Z is reference temperature)

$$\begin{aligned} \delta k = & \alpha_C (T_{ACTR} - T_{ACTRZ}) + && (\text{Na expansion}) \\ & + \alpha_D (T_{AFR} - T_{AFRZ}) + && (\text{Doppler-linear}) \\ & + \alpha_E (T_{ACTR} - T_{ACTRZ}) + && (\text{Core expansion}) \\ & + \alpha_B (T_{CTR} - T_{CIP}) + && (\text{Bowinq}) \\ & + \gamma_{FE} (T_{AFR} - T_{AFRZ}) + && (\text{Fuel expansion}) \\ & + \delta k_S + && (\text{Scram}) \\ & + \delta k_C && (84) \quad (\text{Control}) \end{aligned}$$

Fission Product Power:

$$\frac{d(PL_{FP1})}{dt} = \lambda_{FP1} (\beta_{FP1} PL_N - PL_{FP1}) \quad (85)$$

$$\frac{d(PL_{FP2})}{dt} = \lambda_{FP2} (\beta_{FP2} PL_N - PL_{FP2}) \quad (86)$$

$$\frac{d(PL_{FP3})}{dt} = \lambda_{FP3} (\beta_{FP3} PL_N - PL_{FP3}) \quad (87)$$

$$PL_{FP} = PL_{FP1} + PL_{FP2} + PL_{FP3} \quad (88)$$

Reactor Thermal Model:

$$\text{Flows: } W_{TR} = B_{TR} W_R \quad (89) \text{ (fuel)}$$

$$W_{LR} = B_{LR} W_R \quad (90) \text{ (leakage)}$$

$$W_{RR} = B_{RR} W_R \quad (91) \text{ (shield control)}$$

$$W_{VR} = B_{VR} W_R \quad (92) \text{ (vessel)}$$

$$B_{TR} + B_{LR} + B_{RR} + B_{VR} = 1 \quad (93)$$

$$W_R = N_A W_{PA} + N_B W_{PB} \quad (94)$$

Number of loops represented by simulated loop A and B.

Input Plenum:

$$\frac{dT_{CIP}}{dt} = \frac{W_R C_{CIP}}{(\rho VC)_{IP}} (T_{CIR} - T_{CIP}) - \frac{(UA)_{LSR}}{(\rho VC)_{IP}} (T_{CIP} - T_{LSR}) \quad (95)$$

Lower Support Structure:

$$\frac{dT_{LSR}}{dt} = \frac{(UA)_{LSR}}{(\rho VC)_{LSR}} (T_{CIP} - T_{LSR}) \quad (96)$$

Outlet Plenum:

$$\begin{aligned} \frac{dT_{COR}}{dt} = & \frac{W_R C_{COR}}{(\rho VC)_{COR}} (B_{TR} T_{CTR} + B_{LR} T_{CLR} + B_{RR} T_{CRR} + \\ & + B_{VR} T_{CVR} - T_{COR}) - \frac{(UA)_{USR}}{(\rho VC)_{COR}} (T_{COR} - T_{USR}) - \\ & - \frac{(UA)_{VR}}{(\rho VC)_{COR}} (T_{COR} - \frac{T_{CVR} + T_{CIP}}{2}) \end{aligned} \quad (97)$$

Upper Support Region Metal:

$$\frac{dT_{USR}}{dt} = \frac{(UA)_{USR}}{(\rho VC)_{USR}} (T_{COR} - T_{USR}) \quad (98)$$

Vessel Coolant:

$$\frac{dT_{CVR}}{dt} = \frac{(UA)_{VR}}{(\rho VC)_{VR}} (T_{COR} - \frac{T_{CVR} + T_{CIP}}{2}) - \frac{W_{VR} C_{CVR}}{(\rho VC)_{VR}} (T_{CVR} - T_{CIP}) \quad (99)$$

Radial Reflector Coolant: (includes control rods)

$$\frac{dT_{CRR}}{dt} = \frac{b PL_{RR}}{(\rho VC)_{RR}} - \frac{W_{RR} C_{CRR}}{(\rho VC)_{RR}} (T_{CRR} - T_{CIP}) \quad (100)$$

Leakage Coolant: (for hydraulic holddown)

$$\begin{aligned} \frac{dT_{CLR}}{dt} = & - \frac{W_{LR} C_{CLR}}{(\rho V C)_{CLR}} (T_{CLR} - T_{CIP}) + \\ & + \frac{N_{ER} (UA')_{TR}}{(\rho V C)_{CLR}} \left(\frac{T_{CTR} - T_{CLR}}{2} \right) \end{aligned} \quad (101)$$

Fuel-Coolant: use 3 radial fuel nodes

Tube Outlet Coolant:

$$\begin{aligned} \frac{dT_{CTR}}{dt} = & - \frac{W_{TR} C_{CTR}}{N_{ER} (\rho V C)_{CTR}} (T_{CTR} - T_{CIP}) + \\ & + \frac{(UA')_{TR}}{(\rho V C)_{CTR}} (T_{F3} - T_{ACTR}) - \\ & - \frac{(UA')_{TR}}{(\rho V C)_{CTR}} \left(\frac{T_{CTR} - T_{CLR}}{2} \right) \end{aligned} \quad (102)$$

NOTE: Primed parameters (A' , V') are per driver element.

Average Coolant Temperature:

$$T_{ACTR} = \frac{T_{CTR} + T_{CIP}}{2} \quad (103)$$

Fuel Temperatures (equal volume nodes);

$$\frac{dT_{F1}}{dt} = \frac{b \alpha_1 P L_F}{N_{ER} (\rho V C)_{F1}} - \frac{(UA')_{1-2}}{(\rho V C)_{F1}} (T_{F1} - T_{F2}) \quad (104)$$

$$\begin{aligned} \frac{dT_{F2}}{dt} = & \frac{b\alpha_2 PL_F}{N_{ER} (\rho V^* C)_{F2}} + \frac{(UA^-)_{1-2}}{(\rho V^* C)_{F2}} (T_{F1} - T_{F2}) - \\ & - \frac{(UA^-)_{2-3}}{(\rho V^* C)_{F2}} (T_{F2} - T_{F3}) \end{aligned} \quad (105)$$

$$\begin{aligned} \frac{dT_{F3}}{dt} = & \frac{b\alpha_3 PL_F}{N_{ER} (\rho V^* C)_{F3}} + \frac{(UA^-)_{2-3}}{(\rho V^* C)_{F3}} (T_{F2} - T_{F3}) - \\ & - \frac{(UA^-)_{3-C}}{(\rho V^* C)_{F3}} (T_{F2} - T_{ACTR}) \end{aligned} \quad (106)$$

Average Fuel Temperature:

$$T_{AFR} = \frac{T_{F1} + T_{F2} + T_{F3}}{3} \quad (107)$$

References

1. BNWL-878, SIMPL-I Simulation Implementing Machine Programming Language - Version 1, R. D. Benham, et. al., August 1968.
2. Goss, C. L., Engineers Manual on Fortran IV Version of Dynamic Systems Analyzer (Dynasyar), DUN-M-17, March 1968.
3. Pool, E. B., et. al., Prediction of Surge Pressure From Check Valves for Nuclear Loops, ASME 62-WA-219, November 1962.
4. Pool, E. B., Minimization of Surge Pressure From Check Valves for Nuclear Loops, ASME 62-WA-220, November 1962.

XIII. REACTOR PROTECTION SYSTEMS

C. L. Fies

A. Introduction

There are three items which cause people to pay attention to protection systems:

1. They cost too much. Most instrumentation systems are quite extensive. They require ample redundancy, must meet single failure criteria, and must be tested. The actuators provided must be very reliable, must be tested, and are very expensive.
2. The reactor shutdown scram system tends to shut down the reactor when it is not wanted. This tends not only to cost money, but upsets the management of the facility because the plant was not designed to be shut down, but rather to be run for a specific purpose, whether it be to test fuel or to produce power.
3. Failure of the protection system can be disastrous. Not only is the danger to public exposure increased, but the economic consequences of an accident such as a partial core meltdown can be severe. One does not want to invest \$100 - 200 million dollars in a nuclear facility and have it destroy itself.

B. Definitions

Various definitions exist as to what constitutes the scope of a plant protection system as shown in Figure XIII.1. Until very recently, plant protection systems were limited solely to instrumentation. For example, in IEEE-279,⁽¹⁾ Nuclear Power Plant Protection System is defined as,

"That system encompassing all electrical and mechanical devices and circuitry (from sensors to actuation device input terminals) involved in generating those signals associated with the protective function."

In other words, only the instrumentation was considered part of the protection system, and all actuators were considered part of their respective individual systems. During the past year work has been in progress on supplementary criteria for reactor plant protection systems.⁽²⁾ In these supplementary criteria the definition of protection systems has been extended to include not only the instrumentation, but the actuators. In the latest draft copy of the supplementary criteria, plant protection system is defined as follows:

"Those active devices, with the associated equipment necessary to initiate their action, which function to (1) prevent plant variables or conditions from reaching their respective safety limits, and (2) to mitigate the consequences of exceeding safety limits."

The reason for extending the definition of protection systems to include the actuators is to take into account the fact that one must have completion of

XIII.3

action to complete the job that the protection system is called upon to do. It does not make sense to design a very reliable redundant safe instrumentation system and to connect this system up to the set of actuators with marginal construction. Both the instrumentation and the actuators must work as a unit to meet the performance requirements set down by design.

A third definition of what constitutes a protection system can be expressed in terms of failures as shown on Figure XIII.2.

If a failure of a component or system could cause the loss of one of the three barriers providing protection against the release of radioactive material, these systems or components are part of the protection system.

The three barriers we are concerned with here are the cladding, reactor vessel and primary system, and the containment. By this definition, any component or system whose failure could result in breach of the cladding, such as instrumentation to detect high power or low flow, along with the actuator systems such as control rods or boron injection would be part of the protection system. If a containment building is provided, closure of ventilation valves is required to prevent release of radioactive material. The containment valves themselves and the instrumentation providing a signal to close the valves would be part of the protection system. The items normally considered as part of the protection system are as follows:

1. A fast shutdown system - reactor trip system - scram system
2. Containment isolation systems
3. Containment cleaning systems
4. Containment cooling systems

5. Emergency core cooling
6. Emergency power systems

C. Basic Requirements

There are two basic requirements which all protection systems must meet. First, the protection system must be free from failures. The modes of failure of the plant and the protection system can be explained with the aid of Figure XIII.3.⁽³⁾ There are four basic modes to be considered. In the first mode both the protection system and the plant are within safe limits. This is the normal operating condition. Mode 2 is a situation where the plant is within safe limits, but for some reason the protection system is actuated. This is the item that the availability people and reactor operators are very concerned about; having the plant shut down by the protection system when it is not wanted. Mode No. 3 is strictly a safety consideration, and the one that causes the most worry. The plant is outside the safe limits and the protection system is not actuated. It can be seen that Modes 1 and 4 are essentially normal operation; whereas Modes 2 and 3 are failures. Mode 2 type failures are safe failures that one analyzes if one is interested in plant unavailability. Mode 3 failures are unsafe failures that are concerned with safety. The discussion today will concentrate on the subject of unsafe failures. When analyzing the probability of failure of protection systems, one normally considers random failures only. The reason for this is that the information, in some cases, is available on random failures for various components. One can look up the mean time between failure of a relay that is going to be installed in the system. The mean time between the failure of an amplifier

can be taken from a handbook. These are then combined with some probabilistic mathematical expressions to come up with the probability of failure of the system.

The second requirement of the protection system is that it must perform as designed. Its basic function is twofold, it is either a no go or a go system. The reactor is either operating normally below its trip point or a shutdown irreversibly. The containment building is either a passive structure being cooled by ventilation or the valves must be closed. The emergency cooling system is either on standby and not used, or the emergency cooling system must work to prevent overheating of the core in the event of the loss of outside power. For all these protective functions, a speed of response is required. The rods must be inserted a certain amount in a certain time. The containment system valve must close in a certain time to prevent the release of radioactivity. The emergency cooling system must come on line and be fully operational within a certain period of time. When considering what we might call performance failures, we should be looking at things that are non-random. As will be explained later, these are the things that cause accidents. The reactor shutdown system cannot perform because a number of identical relays in the safety circuit cannot function due to the sticking of contacts, a number of identical rods in the reactor cannot be inserted because of crud accumulated in the control rod channels. These are examples of performance failures. Something has been overlooked in the design which causes the environment to change and prevents the protection system from doing its job.

D. Probability of Random Failure

I would now like to go into a brief treatment of how one analyzes the probability of failure of protection systems due to random failures. In the

XIII.6

supplementary plant protection system criteria,⁽²⁾ which I mentioned earlier, there is a quantitative requirement which states that, as a guide, the probability of failure for any protection subsystem should not exceed 1×10^{-5} . When doing probability of failure calculations due to random failures, one is forced to make a number of assumptions about the system being analyzed, as shown on the next figure (XIII.4).⁽³⁾

1. Each channel or component is assumed to be either perfect or failed - there is no in-between.
2. The failure probability is constant. There is no aging or wear-out and the failure occurs randomly distributed in the time interval.
3. All identical channels or components in the system are identical with respect to failure. A random failure has an equal probability of affecting any channel.
4. All failures can be detected by testing. This particular one causes big problems, as one has a difficult time testing sensors in their true environment. Also, it is very difficult to test actuators such as control rods in the environment which they must operate in to perform correctly; for instance, full power and full temperature.
5. One assumes that repairs made on the system are perfect and do not allow for the unhappy instrument technician with a warped screwdriver or the man that goes about and adjusts all the instruments wrong, causing a failure of all instruments.

XIII.7

6. It is assumed that failures of redundant or multiple channels are independent of each other and of the need for protection system action. If one has four redundant channels, the failure affecting one will have no influence on the others. This tends to be unrealistic, as experience has shown that there are failures which can wipe out all channels.

When analyzing the probability of failure of a set of components or a system, one uses various mathematical expressions. The next figure (XIII.5) shows some of the equations one uses in calculating probability of failure.⁽⁴⁾ These expressions actually show the probability of success of the set of components which is one minus the probability of failure. The approximations shown in the right hand column are obtained from the expressions on the left by series expansion of the exponentials. To obtain an understanding of the meaning of these expressions, I would like to consider the three items shown on the next figure (XIII.6).

1. The failure rate of a particular component.
2. The testing interval involved, where one attempts to detect any failures which have occurred.
3. When considering coincidence or redundancy, the number of individual components which must fail before the system cannot act.

The probability of failure Q is then, simply, the failure rate multiplied by the test interval taken to the power of the number of components which must

XIII.8

fail. The next figure (XIII.7) shows some very simple examples to illustrate this calculation. Consider a system composed of one channel. In this case, only one item need fail to cause failure of the system. Assume a failure rate of one failure per 100 hours. If we ask ourselves what is the probability of this system failing, assuming a test interval of 100 hours, one can see that the answer is simply 1. If we shorten the test interval to 10 hours, the probability is .1. If we consider the same failure rate and same test interval and apply it to a redundant system where two failures are needed to prevent the desired action, we see the result on the next figure (XIII.8). If one were to carry this treatment to the extreme and apply it to a reactor shutdown actuators, wherein most cases only one rod need be inserted out of a substantial number, one can see that the probability of failure can get quite low, as one keeps raising the product of failure rate times test interval to the correspondingly higher and higher exponents. If one wants to apply a probability of failure to the complete system, this can be done by simply adding up the probabilities of failures of the equipment that must work in series, as shown on the next figure (XIII.9). To consider a simple example, assume that we have an instrument system involving four channels where two-of-the-three channels work in coincidence to provide a trip signal. This trip signal, in turn, is passed through redundant strings of relays where either string can cause release of the actuators or rods in the system. Assume further, that the rod system for the particular accident which we are considering must have one-of-the-six safety rods inserted into the core at its design rate. The criterion of 10^{-5} is meant to be applied to a subsystem such as the one illustrated.

E. Performance Failures

The treatment of random failures and probability of failure is sometimes called the numbers game by people who tend to feel that one is wasting his time in calculating these numbers. These people, in many cases, feel that there is an advantage to doing these types of calculations for comparison purposes, but that one tends to get too involved in the mathematics and does not come up with any number that approaches reality. There is a basic reason for this skepticism. That reason is that a random failure has never, repeat never, caused a reactor accident.⁽³⁾ It appears that what we have done is used redundancy in such a way that it is very successful in protecting against random failures. By putting redundant instruments in systems of 1 of 2, 2 of 3, 2 of 4, we have completely protected ourselves against random failures. On the other hand, the accidents that do happen are caused by performance type failures. The heat transfer reactor experiment (HTRE-3 Excursion and Reactor Meltdown) is an example of this type of failure.⁽⁵⁾ This reactor had the usual complement of neutron sensing chambers, including three uncompensated safety chambers in the scram circuit. Because of electronic noise which was thought to be picked up in the connecting cables, the circuit for these uncompensated ion changers was modified by putting in a resistance capacitance network. This modification, as it turned out, placed a series resistor in the circuit such that the current was limited so that it could never be as high as the trip value. In this case an experiment was run, the control system malfunctioned, the power protection failed to work, and the reactor was destroyed.

Another case which has not been very highly publicized and which, in turn, did not cause a reactor accident, but only because an accident was not present, concerned the problems with the control rods at the Piqua Nuclear Power Facility. At Piqua the usual procedure was to operate as a load following plant with large swings in power which necessitated movement of control rods at rather short time intervals. However, at one time during operation, it was decided to base load the plant and, in this case, the plant had operated for several days with very little movement of control rods. With organic coolant radiation breakdown of the coolant caused coking around those control rods which were in a position in the core where they could add negative reactivity. Because of coking problems in the core, the temperature went up in some of the thermocouples in the safety circuit and reactor scram was called for. In this case, when the scram was given, the rods which could add negative reactivity were frozen in position and could not move. In this case, the facility was shut down by taking advantage of the temperature coefficient raising the temperature and lowering the power which, in turn, allowed the xenon effect to take over and decrease the power. After this, the reactor operator was able to use the drive mechanisms on the rods to break the rods loose from the coking and gradually work them into the core. This is an example where identical rods were used and something had been overlooked in the design, causing a common failure of the rods. If an accident had occurred during this period of time, it could have had disastrous consequences.

Another performance type accident occurred at the Windscale No. 1 pile in England.⁽⁵⁾ This accident resulted in permanent shutdown of this plutonium production reactor. In this case, a standard procedure was to shut off the

air flow and raise the power level to a certain level to allow the annealing process to take place in the graphite. The thermocouples which were supposed to shut down the reactor in the event of high temperature were located in the section of the core that was normally hot, monitoring the temperature of the air once that it had flowed through the pile. With the air shut off, however, the hot spot was on the opposite end of the pile. This resulted in thermocouples being located in the incorrect area to provide protection. A fire started in the graphite and, as a last resort, water was used to quench the fire and consequently the reactor was destroyed.

Protection systems have even been designed in such a manner that they succeed in blowing up a reactor if they do work. This happened on an Oak Ridge critical assembly in 1956.⁽⁵⁾ This critical experiment involved a homogeneous critical mass in a flat geometry at the bottom of the barrel-like structure. Parts were used to make the level fluctuate and create a critical situation when enough liquid was injected into the tank. As an added safety measure, a cadmium plate was positioned above the tank which, in the event of an excursion, was to drop into the liquid pool. When the reactor was scrammed, however, and the cadmium plate was dropped, a wave motion was set up in the pool which caused a secondary excursion which overrode the effect of the poison that was inserted. This is an example of how something was overlooked in the design which caused the accident.

E. P. Epler has performed a study of ORNL experience with common failures based on approximately 100 reactor years of experience at Oak Ridge.⁽⁶⁾ During this time 14 simultaneous failure incidents occurred involving protection

systems. The next figure (XIII.10) shows a categorization of the causes of failure. Examples of each class of failure can be outlined as follows:

1. Change in characteristics of the system being protected -
Oak Ridge Research Reactor: Beam holes were flooded in accordance with procedures. This cut off the neutron beam and shielded the neutron detection.
2. Unrecognized dependence on a common element - Low Intensity Test Reactor: Ionization chambers were purged continuously with gas from a common bottle. Contaminated gas caused most chambers to fail.
3. Disabled by accident - Aberdeen Pulse reactor: When the reactor was pulsed at ORNL, the high ionization current destroyed the field-effect transistors in the flux amplifiers.

ORNL is not unique in its experience with common failures. The next figure (XIII.11) shows a list of incidents related to plant protection system performance involving failures of safety circuits.⁽⁷⁾ Because experience indicates that random failures are not a problem and that performance failures are, it has been suggested that what we have is essentially a graph of diminishing returns as is shown on the next figure (XIII.12). This shows the probability of failure Q plotted against failures required. What it shows is that if one considers only random failures, multiple redundancy can achieve a very low Q or probability failure. Based on the ORNL data, however, Q appears to be approximately 10^{-3} .

XIII.13

The probability of failure can be made very low, due to random failures but, below a certain level, the interaction or systematic failures take over. What this means, in effect, is that in calculating the probability of failure, one cannot multiply the testing interval and the failure rate and take this product to the power of the number of elements that have to fail. There is an interaction coefficient that should be used to adjust this power to take into account the fact that in some cases the failures of redundant and coincident channels are not independent and to take into account the fact that common failures do occur. Since we are taking a rather small number and raising it to some power, the power that we raise it to has a tremendous effect on the final result. There are many ways in which interaction can occur. There is a common element which may be a set of identical detectors; the logic devices can be identical, test instrumentation can malfunction and incorrect setpoints can affect all channels. Mode switches are used to switch to various modes of operation which cause interaction among the channels. Bypass switches cause independence to decrease. There is also common environment. All instrumentation is involved with the same reactor. Control rooms tend to bring so-called independent channels together. Cable trays can cause interaction between both control channels and protection channels and between redundant protection channels. An illustration of how probability of failure is combined with accident frequency is shown on the next figure (XIII.13). If we assume that the frequency of a potentially destructive accident is 1 per year and the design life of a reactor is 20 years, then the chance of reactor destruction during its design life is 1 in 5000 for random failures and 1 in 50 for common failures.

F. Defense Against Common Failures

What, then, are the ways that one can prevent common failures? About the only defense which has been thought of to date is diversity. Diversity is an extension of redundancy in such a way that the possibility of the common failure is minimized. This is accomplished, for example, by using flux and pressure trips for a rod withdrawal accident. What we hope is that whatever affects the flux trips, in terms of the common failure, will not affect the pressure. This may take care of the diversity of sensors; however, in the protection logic, unless one designs for independent logic strings involving relays for one set of sensors, and, for example, solid state logic for another set of sensors, one is vulnerable to a common failure in the logic.

The actuators are another area where one can get into problems because of a common fault. As was mentioned before, usually one or two control or rod elements inserted into the core out of a number such as 10-20 elements are sufficient to shut down the reactor, at least for a short time. If one applies the random failure probability calculation, one comes out with a tremendously small number. However, this is completely ridiculous. Interaction between control elements, when these control elements are designed as identical units, is bound to be somewhat larger than such a small number. Thus, diversity is also needed in the actuators.

The problem is that it is difficult to design against something that is unknown and this is essentially what a common failure is. If one is aware of a particular type of failure that is going to invalidate all his equipment, he will certainly design against it. However, it is the maintenance man, the

improper installation of equipment, or some test that was run that causes a set of identical elements to fail. There seems to be no way of guarding against this other than to provide diverse equipment which has a somewhat better chance of surviving a common failure.

References

- (1) Proposed IEEE Criteria for Nuclear Power Plant Protection Systems No. 279, Institute of Electrical and Electronic Engineers, Nuclear Science Group, Standards Committee.
- (2) Draft Tentative RDT Supplementary Criteria for RDT Reactor Plant Protection Systems, Revision A, June 10, 1969.
- (3) S. H. Hanaver and C. S. Walker, "Design Principles of Reactor Protection Instrumentation Systems," ORNL-NSIC-51, UC-80, NSIC.
- (4) Reliability Stress and Failure Rate Data for Electronic Equipment, Military Standard Handbook, MIL-HDBK-217A, December 1965.
- (5) T. J. Thompson, Accidents and Destructive Tests, The Technology of Nuclear Reactor Safety, MIT Press, Cambridge, Mass., 1964.
- (6) E. P. Epler in "Nuclear Safety," Volume 10, Number 1, Technical Progress Review, Nuclear Safety Information Center, ORNL, January - February 1969.
- (7) Reactor Operating Experience (ROE) Reports, Division of Operational Safety, USAEC.

PROTECTION SYSTEM DEFINITIONS

IEEE-279

THAT SYSTEM ENCOMPASSING ALL ELECTRICAL AND MECHANICAL DEVICES AND CIRCUITRY (FROM SENSORS TO ACTIVATION DEVICE INPUT TERMINALS) INVOLVED IN GENERATING THOSE SIGNALS ASSOCIATED WITH THE PROTECTIVE FUNCTION.

SUPPLEMENTARY CRITERIA

THOSE ACTIVE DEVICES, WITH THE ASSOCIATED EQUIPMENT NECESSARY TO INITIATE THEIR ACTION, WHICH FUNCTION TO (1) PREVENT PLANT VARIABLES OR CONDITIONS FROM REACHING THEIR RESPECTIVE SAFETY LIMITS AND (2) TO MITIGATE THE CONSEQUENCES OF EXCEEDING SAFETY LIMITS.

PROTECTION SYSTEM DEFINITION

IF A FAILURE OF A COMPONENT OR SYSTEM COULD CAUSE THE LOSS OF ONE OF THE THREE BARRIERS PROVIDING PROTECTION AGAINST THE RELEASE OF RADIOACTIVE MATERIAL, THESE COMPONENTS OR SYSTEMS ARE PART OF THE PROTECTION SYSTEM.

Fig. XIII.2

MODES OF PLANT AND PROTECTION SYSTEM OPERATION

		PROTECTION SYSTEM	
		SYSTEM QUIESCENT	SYSTEM ACTUATED
PLANT	WITHIN SAFE LIMITS	MODE 1 SAFE	MODE 2 FALSE ACTUATION
	OUTSIDE SAFE LIMITS	MODE 3 UNSAFE	MODE 4 PROTECTED

Fig. XIII.3

ASSUMPTION IN RELIABILITY CALCULATIONS

1. EACH COMPONENT IS PERFECT OR FAILED
2. FAILURE PROBABILITY IS CONSTANT
3. ALL CHANNELS OR COMPONENTS ARE IDENTICAL
4. ALL FAILURES CAN BE DETECTED BY TESTING
5. ALL REPAIRS ARE PERFECT
6. CHANNEL OR COMPONENT FAILURES ARE INDEPENDENT OF EACH OTHER.

OPERATIONAL REDUNDANCY EQUATION APPROXIMATIONS

Situation	Formula	Approximation
1 unit of 2 must be working for success	$2e^{-x} - e^{-2x}$	$1-x^2$ or e^{-x^2}
1 unit of 3 must be working for success	$3e^{-x} - 3e^{-2x} + e^{-3x}$	$1-x^3$ or e^{-x^3}
1 unit of 4 must be working for success	$4e^{-x} - 6e^{-2x} + 4e^{-3x} - e^{-4x}$	$1-x^4$ or e^{-x^4}
1 unit of n must be working for success	$\sum_{a=1}^n (-1)^{a+1} \binom{n}{a} e^{-ax}$	$1-x^n$ or e^{-x^n}
2 units of 3 must be working for success	$3e^{-2x} - e^{-3x}$ $3e^{-2x} - 2e^{-3x}$	$1-3x^2$ or e^{-3x^2}
3 units of 4 must be working for success	$4e^{-3x} - 3e^{-4x}$	$1-6x^2$ or e^{-6x^2}
n-2 units of n must be working for success	$ne^{-(n-1)x} - (n-1)e^{-nx}$	$1 - \binom{n}{2} x^2$ or $e^{-\binom{n}{2} x^2}$
2 units of 4 must be working for success	$3e^{-4x} - 8e^{-3x} + 6e^{-2x}$	$1-4x^3$ or e^{-4x^3}
3 units of 5 must be working for success	$6e^{-5x} - 15e^{-4x} + 10e^{-3x}$	$1-10x^3$ or e^{-10x^3}
n-2 units of n must be working for success	$\sum_{a=0}^2 (-1)^a \binom{n}{a} e^{-nx} + \sum_{a=1}^2 (-1)^a \binom{n}{a} e^{-(n-1)x} + \binom{n}{2} e^{-(n-2)x}$	$1 - \binom{n}{3} x^3$ or $e^{-\binom{n}{3} x^3}$
m units of n must be working for success	$\left[\sum_{a=0}^m (-1)^a \binom{n}{a} \right] e^{-nx} + \left[\sum_{a=1}^m (-1)^a \binom{n}{a} \right] e^{-(n-1)x} + \left[\sum_{a=m}^n \binom{n}{a} \right] e^{-(n-m)x}$	$1 - \binom{n}{m-1} x^{n-m+1}$ or $e^{-\binom{n}{m-1} x^{n-m+1}}$

$$1 - \sum_{k=1}^{n-1} \binom{n}{k} e^{-kx} (1 - e^{-x})^{n-k}$$

STANDBY REDUNDANCY EQUATION APPROXIMATIONS

Situation	Formula	Approximation
1 unit of 2 must be working for success	$e^{-x} + xe^{-x}$	$1 - \frac{x^2}{2}$ or $e^{-\frac{x^2}{2}}$
1 unit of 3 must be working for success	$e^{-x} + xe^{-x} + \frac{1}{2} x^2 e^{-x}$	$1 - \frac{x^3}{6}$ or $e^{-\frac{x^3}{2}}$
1 unit of n must be working for success	$e^{-x} + xe^{-x} + \frac{1}{2} x^2 e^{-x} + \dots + \frac{1}{(n-1)!} x^{n-1} e^{-x}$	$1 - \frac{x^n}{n!}$ or $e^{-\frac{x^n}{n!}}$

NOTES:

1. The errors associated with the use of some of these formulae are shown in Table VIII-IV.
2. e^{-x^2} is a more accurate approximation than $1-x^2$.
3. It should be noted that these approximations cannot be used indiscriminately.
4. Substitute λt for X in all equations.
5. The expression $\binom{n}{k}$ refers to the combinatorial formula (i.e. $\binom{n}{k} = \frac{n!}{k!(n-k)!}$)

PROBABILITY OF FAILURE

Q IS THE PROBABILITY OF FAILURE

λ IS THE UNSAFE FAILURE RATE

T IS THE TESTING INTERVAL

N IS THE NUMBER OF COMPONENTS WHICH MUST
FAIL TO HAVE AN UNSAFE FAILURE

$$Q = (\lambda T)^N$$

Fig. XIII.6

EXAMPLE 1 - FAILURE ASSURED

λ = UNSAFE FAILURE RATE = 1 PER 100 HOURS = 0.01

T = TEST INTERVAL = 100 HOURS

N = NUMBER OF FAILURES REQUIRED = 1

$$Q = (0.01 \times 100)^1 = 1$$

EXAMPLE 2 - EFFECT OF TEST INTERVAL

λ = 0.01

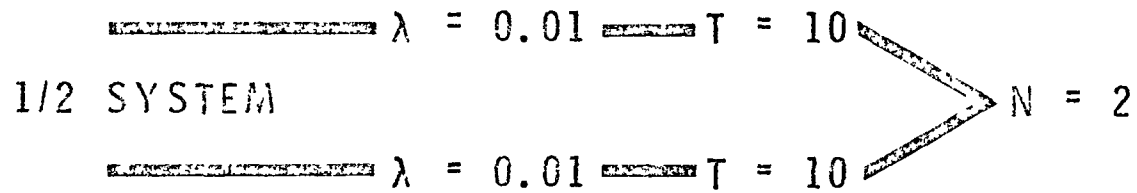
T = 10 HOURS

$$Q = (0.01 \times 10)^1 = 0.1$$

Fig. XIII.7

EXAMPLE 3 - EFFECT OF REDUNDANCY

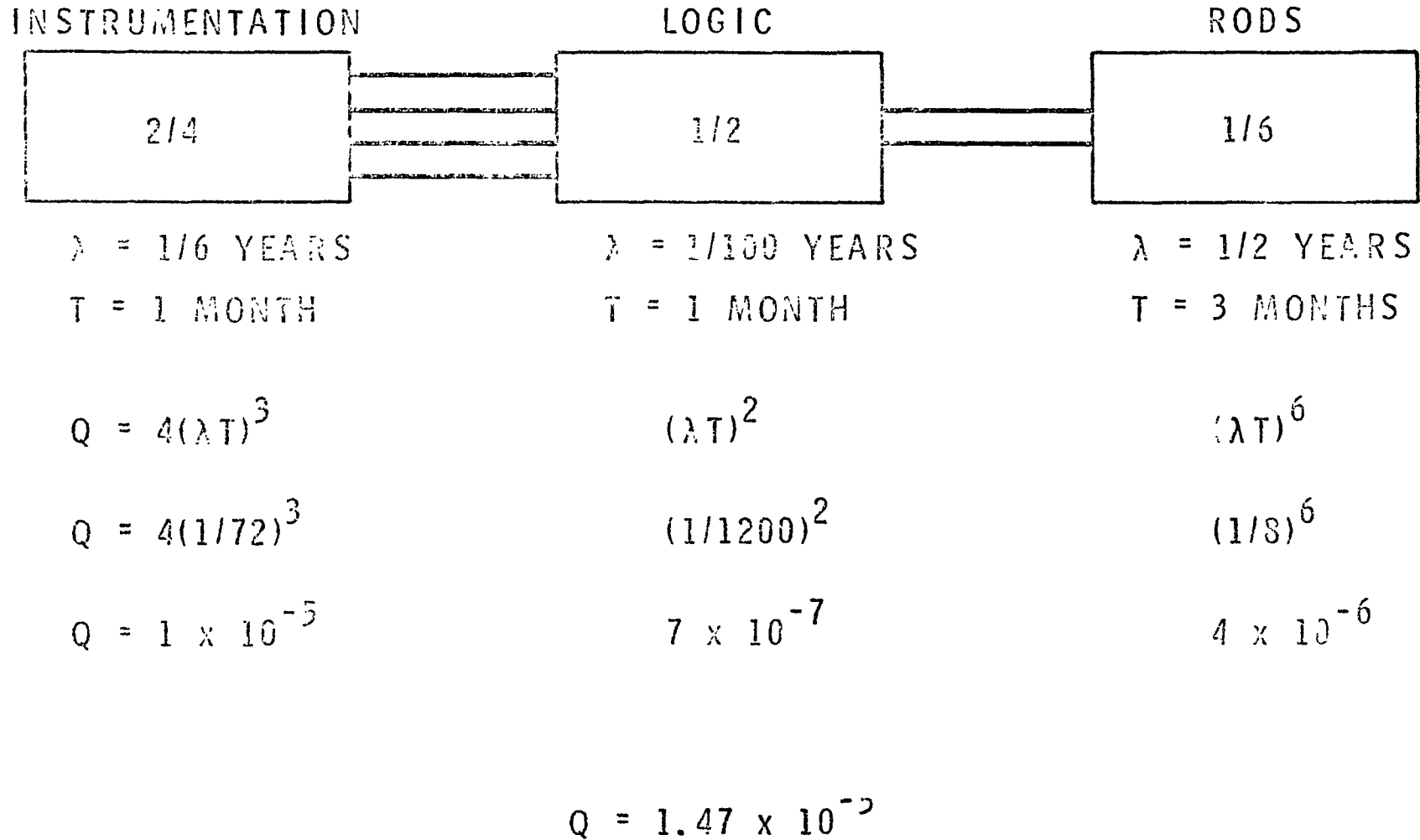
TWO COMPONENTS ARE PROVIDED AND BOTH MUST FAIL TO HAVE SYSTEM FAILURE.



$$Q = (0.01 \times 10)^2 = 0.01$$

Fig. XIII.8

SUBSYSTEM PROBABILITY OF FAILURE



XIII.25

Fig. XIII.9

ORNL COMMON FAILURE STUDY

<u>CAUSES OF FAILURE</u>	<u>NO. OF CASES</u>
CHANGE IN CHARACTERISTICS OF SYSTEM BEING PROTECTED	3
UNRECOGNIZED DEPENDENCE ON A COMMON ELEMENT	7
DISABLED BY THE ACCIDENT BEING GUARDED AGAINST	2
COMMUNICATIONS (HUMAN) ERROR	2

Fig. XIII.10

List of Incidents Related to Plant Protective System Performance

Disarmed Safety Circuits

ROE:64-6, Failure of Safety Rods to Scram at K Reactor (SR)
Short and fusing of wires in cable tray held power to safety circuit. No scram action possible and unknown until attempted scram at end of operating cycle.

ROE:65-15, Bypassing of ML-1 Reactor Ultimate Shutdown Device by Factory Installed Snipping Hardware
Spring used in shipment was left in (3 years) which prevented the secondary shutdown system (chemical poison injection) from ever working.

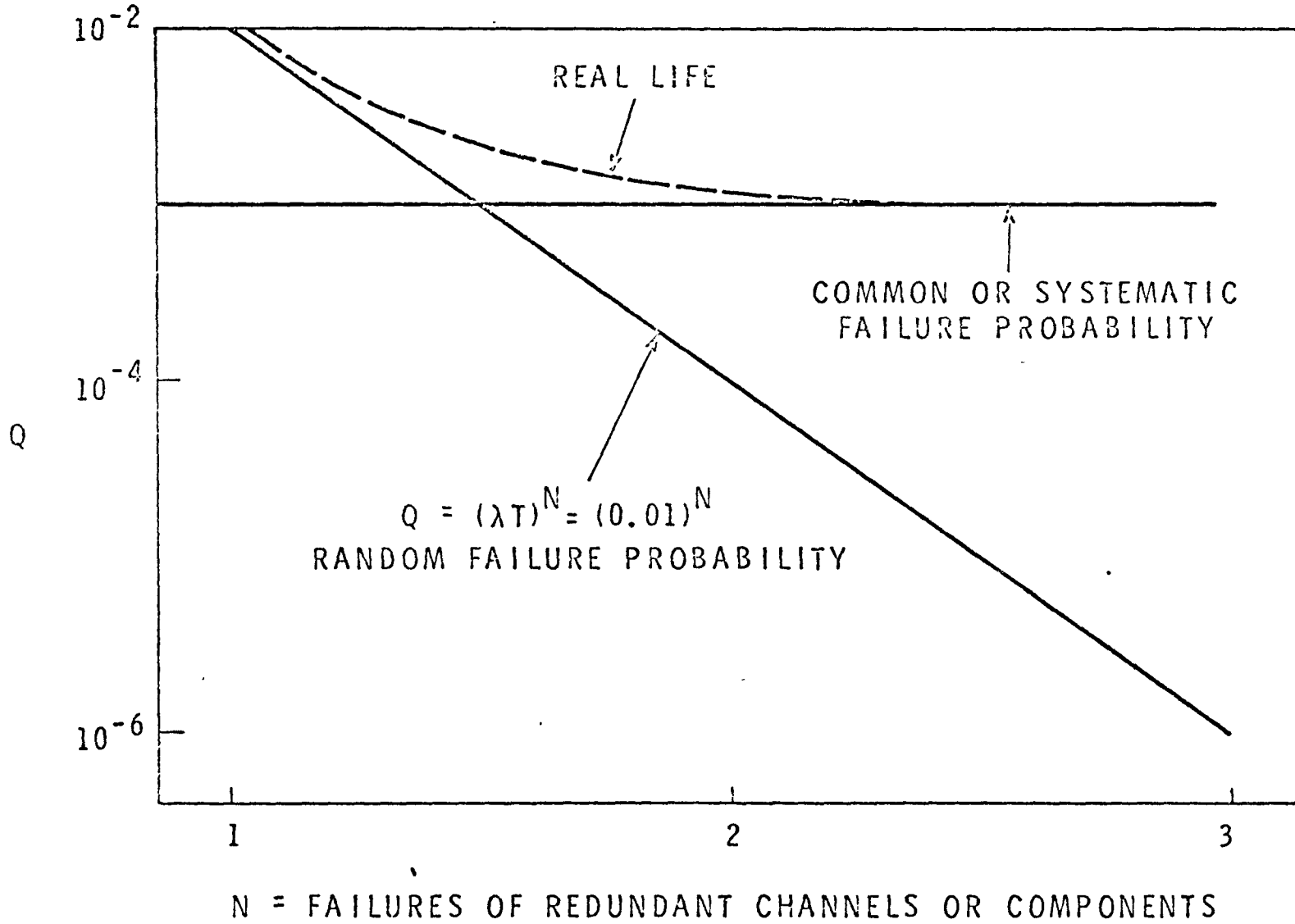
ROE:65-3, Failure of Automatic Shutdown Protection at AEC-Owned Reactor (SR)
Scram relays held closed by stray capacitance leakage paths, therefore, scram action ineffective. Found during prestart checkout.

ROE:68-6, Inadvertent Disarming of Safety Circuit Instrumentation
An instrumentation test signal was not removed and later caused a scram. Serious plant damage could have occurred.

I.43, General Atomic, TRIGA
Startup with one neutron level still bypassed (whole function, I think).

ROE:69-16, Detection of Potential Disabling of Safety System
Design deficiency in shutdown relay power supply--single malfunction could have rendered 6 auto. shutdown circuits inoperable.

PLOT OF DIMINISHING RETURNS



XIII.23

Fig. XIII.12

PROBABILITY OF FAILURE AND ACCIDENT FREQUENCY

<u>FREQUENCY OF POTENTIALLY DESTRUCTIVE ACCIDENT</u>	<u>DESIGN LIFE OF REACTOR</u>	<u>Q</u>	<u>PROBABILITY OF PLANT DESTRUCTION DURING LIFETIME</u>	<u>CHANCE OF DESTRUCTION DURING LIFE</u>
1 PER YEAR	20	10^{-5}	2×10^{-4}	1 IN 5000
1 PER YEAR	20	10^{-3}	2×10^{-2}	1 IN 50

XIII.29

Fig. XIII.13

XIV. PROTECTIVE INSTRUMENTATION

R. E. Peterson

A. Introduction

Having heard a description of potential protected accidents in the preceding two or three lectures, it is logical to next discuss protection against these accidents afforded by various instruments in conjunction with the plant protective system. This lecture is the second of a two-part series; the first dealt with aspects of the protective system, while this lecture deals with types of protection, criteria, and the sensors involved. Although there are many other interesting topics in instrumentation relative to accomplishing the testing program associated with the FFTF, it is the objective here to consider only that instrumentation which functions in a safety capacity.

B. Types of Protection and Criteria

There are three basic categories of accidents against which protection is sought. These are overpower, loss of coolant and fuel failure (which may or may not be related to the other two). In the case of overpower, heat generation in the reactor exceeds the cooling capability normally provided to carry away that heat. The accident is normally initiated with an accidental input of reactivity. The reactor instrumentation responds to introduce negative reactivity via the control system to counteract the increased reactivity, reducing the reactor power until it again matches or drops below the cooling capability. The instruments that are effective in sensing the initial increase in reactor power are either nuclear or thermal types.

Loss of coolant, on the other hand, is characterized by an accidental decrease in coolant flow below that required to remove the normal heat generation

XIV.2

of the reactor core. The accident may be initiated by flow blockage, loss of pumping power, breaks in the coolant system boundary or gas bubbles. In this case the reactor instruments also respond to introduce negative reactivity and reduce the reactor power until cooling is adequate to remove the heat. Fuel failure is considered to be distinct from the previous two reactor accidents in that the failure may be purely mechanical in nature. That is, fuel cladding can fail due to undetected defects or deterioration in normal service conditions. In this case, instrumentation is desired that detects the failure and shuts down the reactor so that the defected fuel can be replaced. It is presumed that continued operation with defected fuel would lead to more severe failure and eventual loss of coolant to part of the fuel.

In order to establish the sensors and their characteristics needed to protect against the above accidents, it is first necessary to establish failure modes and criteria. Since the first barrier to escape of fission products to the environment is the fuel cladding, it is the failure of cladding that must be guarded against. In addition, if the fuel in the interior of the pins is allowed to become molten, rapid relocation becomes possible with accompanying reactivity changes that can trigger an overpower accident. Therefore, criteria have been formulated relating to clad failure and fuel melting failure modes. These criteria have been discussed to some extent in previous lectures and are shown again in Figure XIV.1. Fuel failure mechanics and physical properties that form the bases for these criteria were discussed in Lecture X.

C. Sensors and Characteristics

Before relating sensor types with specific accidents, it is desirable to learn something about the characteristics of the various sensors available. Four basic types will be discussed: Nuclear Sensors, Flow Sensors, Thermal Sensors, and Failed Fuel Detection.

1. Nuclear Sensors

Nuclear sensors are those devices that are sensitive to the neutron flux environment in or near the reactor core. Since they provide a measure of the neutron flux, either as pulses or as current flow, these sensors give an indication that is also in direct relation to the operating power level. It is therefore possible to obtain a flux (or power) level and a rate of change or period measurement. It is important to note that these sensors and their associated electronics must span a very wide dynamic range from flux levels corresponding to the shutdown reactor to as high as several times the design flux level. Typically, this might be a factor of 10^{12} or so.

Because of the wide dynamic range required of the neutron sensors, it is usual design practice to divide the system into three channels: low level, intermediate range and high range. Because overlap is required, the dynamic range of the first two is about 6 to 8 decades each, while the high range spans only about 3 decades. This power coverage is illustrated in Figure XIV.2.

A variety of commercial chambers is available to perform these sensor functions. However, in a fast reactor the high gamma background relative to the neutron flux can constitute a problem, which will be discussed later. The neutron sensors proposed for use in the FFTF are summarized in Table XIV.1. There are numerous characteristics that are of interest but beyond the scope

FFTF PROTECTIVE SYSTEM NEUTRON SENSORS

<u>CHANNEL</u>	<u>SENSOR</u>	<u>DYNAMIC RANGE</u>	<u>LOCATION</u>
LOW LEVEL	U-235 FISSION COUNTER OR B-10 PROPORTIONAL	6-8 DECADES ($\sim 5 \cdot 10^6$ cts/SEC)	IN-VESSEL AND OUT-OF-VESSEL POSITIONED
INTERMEDIATE RANGE	γ COMPENSATED, B-10 LINED ION CHAMBERS	6-8 DECADES ($\sim 10^3 - 10^{10}$ mv)	OUT-OF-VESSEL SHIELD
HIGH RANGE	γ COMPENSATED, B-10 LINED ION CHAMBERS	3 DECADES ($\sim 10^8 - 10^{11}$ mv)	OUT-OF-VESSEL SHIELD

XIV.3a

Table XIV.1

of this lecture. It is sufficient to state that for our purposes the sensor response to changes in reactor power is essentially instantaneous. Delays are encountered in the remainder of the protective system, however.

2. Flow Sensors

The measurement of liquid flow is based on a rather long developmental history. However, flow measurement in liquid metal systems is of more recent origin and is associated with unusual problems related to the severe operating environment of such systems.

Flowmeters operating on various principles have been applied to liquid metal systems. These are magnetic, differential head, transit time and turbine types, to name several. Because of the more immediate interest to FFTF, only the magnetic types will be discussed here.

The principal governing magnetic flowmeter operation is electromagnetic induction, discovered by Faraday, namely, that a potential is developed across a conductor which is moving in a magnetic field. The potential is proportional to both the velocity of the conductor and the strength of the magnetic field and is developed at right angles to both the magnetic field and the direction of motion of the conductor. Thus, when the conductor is a liquid metal (sodium) and so arranged to flow through a magnetic field, a voltage is developed across the flow stream as shown in Figure XIV.3.

There are three ways in which a signal can be derived from the magnetic flowmeter:

- Induced voltage
- Force
- Magnetic field distortion.

XIV.5

The first method involves simply measuring the induced voltage with electrodes across the pipe wall. In the second case, eddy currents that are induced in the fluid interact with the magnetic field and exert forces on the fluid and on the magnetic field which can be translated to a force on the magnet structure. The force is proportional to fluid conductivity, B^2 , fluid velocity and pipe radius cubed. Finally, magnetic field distortion is based upon the fact that eddy currents, which are produced by the magnetic field gradient near the ends of the field, in turn give rise to a field that reinforces the imposed field at the downstream end and opposes it at the upstream end. Thus, the imposed magnetic field appears to be dragged downstream by the moving fluid. This distortion is a function of fluid velocity and conductivity.

In addition, the imposed magnetic field may be supplied by a permanent magnet or by ac or dc electromagnets. In the FFTF, it is proposed that each fuel channel utilize an eddy current, field shift probe flow sensor. In this device field excitation is provided by an ac current to a coil. Two adjacent coils on either side of the exciting coil are connected series opposing so that a signal is obtained only for the flowing or shifted field condition. Flow in the process piping is to be measured by means of magnetic flowmeters of the permanent magnet dc type. Typical problems with flow instrumentation include:

- Temperature sensitivity
- Radiation effects
- Temperature distortion of components, and
- Calibration (distribution of flow).

Calibration under test conditions before installation is often unsatisfactory because of material and environmental differences in actual use.

3. Thermal Sensors

By far the majority of temperature sensors used in liquid metal reactor technology are thermocouples. These devices are relatively rugged, occupy little volume and are sufficiently accurate for a wide range of application. Where higher precision is desired, wire resistance thermometers are used at some penalty in physical size. Many other techniques for temperature measurement have been and are being considered. For example, optical, acoustic and microwave devices are proposed in a variety of forms.

Thermocouples operate on the principle that whenever the junctions of two dissimilar homogeneous materials are exposed to a temperature difference, an emf will be generated which is dependent on that temperature difference and also on the temperature level and materials involved. The resulting emf is measurable either by means of a millivolt meter or potentiometer. A typical thermocouple circuit is shown in Figure XIV.4.

Although a great many combinations of metals and alloys will provide a thermal emf, not a great number are used in practice. Chromel/alumel thermocouples are preferred for monitoring in-vessel coolant streams in the FFTF and much of the process system as well.

Thermocouples for use in contact with liquid metal, as in the core outlet for example, are sheathed in a metal jacket for protection and stability. The thermocouple leads are insulated from the sheath and from each other by a ceramic packing. The junction itself may be grounded or ungrounded as shown

in Figure XIV.5. Speed of response of the thermocouples depends on their sheathed size and whether grounded or ungrounded. Grounded thermocouples provide faster response but their expected life is substantially reduced over the ungrounded type. Grounded thermocouples of 1/16 in. OD have a time constant (63% response to step change) of about 0.2 seconds. Larger sizes ~1/8 in. OD have a grounded response of about 1 second and ungrounded of about 2 seconds or less.

4. FEDAL

Failed element detection and location (FEDAL) requires different types of sensors, depending upon the approach taken. It is generally accepted that fission products entering the coolant stream will shortly appear in the reactor cover gas. Thus, a significant fuel pin failure can be detected by monitoring the cover gas activity. However, having detected a pin failure in this manner, one is then faced with the problem of locating the defected pin from amongst the many thousands of pins in the core. It is the location problem that is particularly difficult and it is this function that introduces most of the complexity into FEDAL.

The approaches taken to solve this problem may be classified as:

- Coolant sampling
- Noise measurement, and
- Tagging

The technique that has been considered conceptually for FFTF is the first.

Coolant sampling involves the extraction of a sample of coolant exiting from the fuel subassembly and transporting of this sample to a counter where

analysis is made for characteristic evidence of fission products, i.e., noble gases or delayed neutrons. Because the volumetric quantity of released fission products is small relative to the volume of coolant, it is necessary to enrich the coolant sample taken by means of a separator such as a vortex generator. If each subassembly is to be monitored, the system requires a coolant sampling line from each core position to some point external to the reactor vessel, a disengaging device and a return line. For the size of sample line that will not plug easily, a rather substantial volume of liquid metal must be transported.

In the second approach, noise analysis, several techniques have been explored on a limited basis, particularly in the United Kingdom. Concepts of this type based on acoustic signals have been investigated. The acoustic characteristic is associated with bubble collapse from a localized boiling condition. Acoustic wave guides immersed in the sodium pool coupled to transducers provide signals that can be used to triangulate the location of the boiling. Neutron fluctuations associated with bubble formation have also been investigated.

Perturbations in the magnetic field of a flowmeter-like device caused by bubbles in the coolant have been measured. Also noise developed in thermal sensors has been explored. The degree to which these techniques can be refined for use in a practical FEDAL system is largely unknown at the present time and the problems are formidable.

Tagging consists of inserting identifiable (either radioactively or mass spectrometrically) isotopes into the filling gas of a fuel pin at the time it is manufactured. By using previously established ratios of stable

isotopes such as Xe^{124} , Xe^{126} and Xe^{129} , it is possible to determine the location of the released tag. The amount of Xe involved is of the order of $1 \text{ cm}^3(\text{STP})$. Obviously, the isotopes must be chosen so as not to be subject to significant change in concentration by fission product yield of the same isotopes.

D. Interrelationship of Parameters

In considering the protection against the two fundamental conditions that place the reactor in jeopardy, namely:

- (1) Power exceeds cooling capability
- (2) Cooling capability falls short of power generation

there are a number of key parameters that affect the ability of the reactor to survive credible accidents. These are generally shown in Figure XIV.6. Fuel failure may either be a cause or a consequence of these conditions. Within a safe operating regime defined for the reactor (i.e., a definition of what the fuel is designed to survive), there must exist a consistent set of these parameters. It is perhaps obvious that there are a great many sets that can fulfill this requirement and an optimum must be sought. For example, a low control strength may be offset by a high "g" rod or large inherent safety parameters.

As a part of the safety system design effort, it is important to understand the interrelation and significance of these parameters as they affect fast reactor safety. This is perhaps best accomplished by examining protected accident studies that appear to be significant.

Since the potential failure of fuel is closely related to temperature conditions in the core, it is desirable to first indicate what these are

and where they occur. The peak fuel temperature occurs at the centerline of a fuel pin and at an elevation corresponding to the equatorial plane of the core. The peak cladding temperature, on the other hand, occurs at the top of the active zone where the exiting coolant is also hottest.

In the FFTF design it is a goal to maximize the power density within safeguards constraints to achieve the highest neutron flux per megawatt of power dissipated. This in turn dictates high linear pin powers and thus high fuel pin centerline temperatures. Since the melting point of mixed oxide fuel is near 4850°F (corresponding to a linear pin power of ~18 kW/ft), it is necessary to operate at some margin below this value. Typically, we have used a linear power margin of 20%. Although the overpower margin has been investigated parametrically, it will not be discussed further here.

E. Power Excursions

1. Ramp Reactivity Excursions

There are some characteristics in relation to ramp reactivity excursions that should be pointed out. These are illustrated in Figure XIV.7, where the peak fuel temperature and associated average coolant temperature are shown as a function of time for a 2\$/sec ramp and no protective action. While this is an extremely large ramp, it serves to illustrate the following:

- (1) The time scale for instrument sensing and protective action is very small -- a few tenths of a second at most.
- (2) Melting of the fuel occurs before any appreciable rise in coolant temperature is noted.
- (3) The Doppler ΔK to melting is about 15¢.

Factors, other than those associated with the protective system, in addition to the Doppler coefficient, are the sodium coefficient and fuel expansion. The sodium coefficient, even if it were entirely negative, is seen to be delayed in time. Similarly, expansion is also delayed and it has not been conclusively demonstrated to be reliable in oxide fuels. Thus, of the inherent mechanisms, the Doppler coefficient appears most likely to be of importance for reactivity accidents. We have investigated the sensitivity of fuel melting to the magnitude of the Doppler. Some of the results are shown in Figure XIV.8.

In this graph the limiting effect on fuel centerline temperature is shown for a 4\$/sec ramp and Doppler constants of -0.002, -0.004, and -0.008, respectively.

Other assumptions include:

$$\text{Scram Initiated at } \frac{P}{P_0} = 1.2$$

Scram Rods = 20\$, 1g acceleration, 10 cm above core

Time delay = 158 msec.

On the order of 150°C decrease is obtained for a factor of two Doppler increase. It is concluded from this and similar studies that the Doppler effect will be helpful but not strongly influential in limiting centerline fuel temperatures for ramps in the \$/second range.

Therefore, to achieve protection against credible accidents in the dollar/second range, the greatest assurance stems from a fast, reliable plant protection system. Interrelationships for designed parameters are shown in Figure XIV.9. Shown on this graph are curves of safety system rod worth as a

function of ramp reactivity insertion for time delays of 10, 25, 50, and 100 msec. Each curve represents a rod acceleration and initial position combined with the inherent parameters of the reactor which are held constant for all cases to just reach incipient melting.

The final question, relative to reactivity accidents is: What likely ramps must the instruments protect against? In Figure XIV.10, a series of single channel meltdown accidents is shown. This is perhaps the most severe reactivity input accident that can reasonably be protected against. It is seen that the maximum ramp shown is 4.4 $\$/\text{sec}$ for a total of 1\$. Without protection the resulting excursion may lead to explosive disassembly of the core.

Recalling the previous figure for a moment, the elements of optimization are rod strength, acceleration, initial rod position and protection system delay. The latter, of course, is made up of the sensor delay, signal conditioning and relaying and the rod unlatching time. Without discussing the other constraints, a total delay of 100 to 200 msec is all that can be tolerated for reactivity accidents of a severe nature. Since most of this time is taken up in the remainder of the protection system, the sensor must respond nearly instantaneously. Thus, it is concluded that:

- For overpower accidents in the maximum credible range, all sensors except nuclear instruments are precluded from protection capability.
- Inherent parameters are not significantly effective in limiting these accidents.

This perhaps reinforces the concern in the previous lecture about diversity in the plant protection system. Little diversity of sensors exists in this area.

2. Design Problems - Nuclear Sensors

Since reliance on nuclear sensors for overpower accidents is essentially total, it is of interest to indicate some of the potential problems. Perhaps the most significant problem is the high gamma background. The gamma field affects the sensitivity of counters and ion chambers and furthermore, it is not proportional to the reactor power level. The source consists of $\sim 10^6$ R/hr (n- γ), $\sim 10^5$ R/hr (Na^{24} and Na^{22}) and decay gammas from other materials. Potential problems with cables in a high temperature environment and electronics are fairly standard concerns and will not be discussed here.

F. Loss of Flow

Loss of flow can occur in a number of ways. We wish to consider particularly the time available for protective action with each to determine the sensor that can best provide protection.

1. Flow Coastdown

In event of a total power loss to the primary pumps, the flow begins to decrease and the core outlet temperature begins to rise. Unless the core power is reduced accordingly, a boiling situation will develop. Protective action may be taken on loss of power, low flow or high ΔT . These cases are shown in an example in Figure XIV.11. The first thing to note is the relatively long time scale for these cases compared with reactivity accidents. Several seconds are available before the boiling point is reached. Probably the most

rapidly acting sensor in this case would be a cycle counter on the primary pump power supply or a revolution counter. In the example, a rather generous allowance of 0.75 seconds is assumed for this. Scram on low flow from a magnetic flowmeter in the primary loop occurs in about 2 seconds and finally high bulk ΔT occurs in another second. An interesting point in this example is that Doppler feedback is assumed to reduce the power as the core heats up. In the real situation, the controller (manual or automatic) would be tending to counteract this loss of power until the trip occurs. Thus, a more optimistic and even unrealistic case is presented. Rates are slow enough that no large response would be expected from the nuclear instrumentation. However, sufficient other diversity of sensors exists in this type of accident that there is little cause for concern.

2. Primary System Breaks

A severe break in the primary system boundary can divert a large quantity of coolant in a short time, starving the core and giving rise to a boiling condition. Such a case is shown in Figure XIV.12 for a double-ended pipe break in the high pressure inlet to the reactor vessel. Although scram action is taken (arbitrarily 2 seconds after the break), temperatures climb very rapidly at the core outlet and exceed boiling in the hot channel. Flowmeters are essentially the only sensors likely to signal a break of this size rapidly enough. In-core flowmeters, if connected to the trip system, would probably act in less time than shown. However, the bulk flowmeter in the affected loop may indicate a flow increase so that either a high flow or a rate trip would be required. Admittedly, a break of the size assumed is extremely unlikely.

3. Channel Blockage

While pipe breaks in the primary system are very nearly catastrophic, blockage to channels in the core are envisioned to result in even worse consequences if taken to the extreme. Two cases are considered here. The first is that of partial blockage to a subassembly and the second is total blockage such as occurred in the Fermi accident, both at startup and at power. As previously, the focus will be on the time available for protection and the sensors likely to be of greatest benefit.

Calculations of the core outlet temperature for various degrees of partial inlet blockage, with and without scram, are shown in Figure XIV.13. The dashed lines represent scram 70% and 80% reductions and the solid lines show the no-scram temperatures for 50, 60, 70, 80, and 90%. The interesting result from this work is that blockages up to about 50% at the inlet in this case could be tolerated, even if no scram occurred. Sensors triggering scram action were useful in prevention of boiling up to about 70% blockage. Above this point no instrumentation was useful. While this window (50 - 70%) is variable, depending upon other parameters, it remains narrow, so that partial blockages at power are not highly protectable events from a safety point of view. Obviously, it is desirable to protect the core against any blockage, since some fuel damage will result and this in itself may become a hazard and certainly an economic issue.

For a completely blocked channel, radial and axial steady-state temperatures were calculated as a function of power level. The significant result here is that at a reactor power of 2 MW, the coolant temperature within the subassembly is above boiling while no apparent change has occurred at the outlet

of the affected subassembly or its nearest neighbors. Therefore, in-core temperature sensors are not adequate to detect a complete blockage and a flow monitor for each channel appears to be the only acceptable sensor for this condition.

In the event total channel blockage occurs at full power, rather violent consequences may result. A study recently completed by the General Electric Company gives the time sequence of events based on one model. The sequence is illustrated in Figure XIV.14. At about 0.8 seconds, boiling and vaporization begins at about the mid-plane of the core, the sodium is expelled upward rapidly while the lower half continues to vaporize until it dries up. Pressures developed are insufficient to expell the coolant downward. At about 2.5 seconds, partial reentry occurs from the top and a re-expulsion takes place.

Energy absorption capability of the duct wall is shown in Figure XIV.15 as a function of time. At about 2.5 seconds, very little energy absorption capability remains in the affected assembly and most of the first reentry pulse energy must be absorbed by the adjacent duct wall. Thus, the model gives some feeling (though perhaps little more) of how rapidly propagation might occur. A model predicated on melt-through would proceed more slowly. For an accident of this type, slightly more time for protective action appears possible than heretofore thought. It is now believed that an in-core flowmeter would be useful in terminating a propagation accident of this type. At present such phenomena are poorly understood and perhaps even thermal sensors may be adequate.

4. Subchannel Blockage

Small blockages occurring in subchannels of the fuel subassembly can result from localized failure or foreign objects lodging in the small clearances between fuel pins. A graphical portrayal of several such blockages is shown in Figure XIV.16. Temperatures developed immediately above such a blockage involving 6 subchannels at mid-core are shown in Figure XIV.17 for different mixing parameters. The point of this example is that temperatures attenuate very rapidly above the blockage. In this case, little temperature difference is seen only 0.15 in. above the blockage. At the end of the fission gas plenum, blockages of single subchannels have been shown to be virtually undetectable. Very marginal thermal detection capability is obtained for blockages of 6 subchannels, again depending on the degree of mixing. Similar conclusions are reached for detection of flow perturbations. Thus, subchannel blockages remain of concern and protection against potential consequences of a small number of pin failures must be obtained by means other than thermal or flow sensors. At the present time, a failed element detection system is believed to be the best protection against onset of pin failure, whether from local blockage or other causes.

G. Summary

In attempting to achieve protection by means of in-core instrumentation, one is confronted with a decision of what action should be taken on signals from these sensors. For example, if it is established that in-core sensors will trip the protection system on a preset condition, then inherent in this decision is a certain penalty in availability occasioned by spurious trips.

XIV.18

Thus, reliability and redundancy are strong factors in weighing such a decision. Further, it is important to establish just what degree of protection is obtained if protective action is taken as opposed to some other action such as power setback or annunciation and operator action. This was done in a study, the results of which are given in Figure XIV.18 for in-core flowmeters and thermocouples.

Each curve on the graph represents the demarcation between safe and unsafe fuel channel coolant temperatures for flow loss accidents. Boiling is the criterion assumed for this purpose. Each point on a curve is a unique combination of total flow loss and flow loss rate that will just prevent boiling if protective action is taken from the indicated sensor. The area lying above a given curve represents a region of protection while that area below is unprotected.

In the case of thermocouples, the significant parameters are time delay and trip or limit setting. The horizontal line for $\tau = \infty$ is consistent with prior flow blockage analyses that indicate boiling does not result, even with no protective action for blockage as high as 60%. It is interesting to note that the degree of protection afforded by a very rapidly acting thermocouple (1 second or less) is not significantly greater than one that responds in more reasonable times (say $\tau = 2$ sec). This result is significant in that the tradeoff for higher reliability at the expense of response time can be made with small penalty.

The other parameter indicated is the trip setting. The sensitivity of protection to this parameter is shown in Figure XIV.19 for a flow loss rate of 32%/sec to a final flow of 20% and no time delay in the thermocouple. In

this case a trip setting of 30 °F above the nominal coolant outlet is about as "loose" as one would consider. This corresponds to about 10% of the core delta T.

Flowmeters are seen to afford substantially greater protection than thermocouples, especially for a "tight" trip setting. Thus, it appears highly beneficial to develop a reliable in-core flowmeter.

The state-of-the-art of in-core instrumentation today is such that it may not be used to initiate scram action. This is especially the case for flowmeters. However, power set-back action can be nearly as beneficial when one considers that the higher probability accidents are those that are associated with lower rates of flow loss. A survey of in-core instrumentation that exists in contemporary fast reactors, either under construction or in operation, is shown in Table XIV.2. It is interesting to note that the protection is far from being ideal in any case. It is probable that this picture reflects the general dissatisfaction with sensor development and their use in a fast reactor environment rather than any philosophy that the protection afforded does not warrant their inclusion.

Table XIV.2

SURVEY OF SUBASSEMBLY TEMPERATURE, FLOW, AND
FUEL FAILURE INSTRUMENTATION

<u>Reactor</u>	<u>Design Power (MWT)</u>	<u>Outlet Temp. (°F)</u>	<u>Coolant</u>	<u>Fuel Failure</u>		<u>Subassembly</u>		<u>Comments; Status</u>
				<u>Detection</u>	<u>Location</u>	<u>Coolant Temperature</u>	<u>Flow</u>	
EBR-II	62.5	900	Na	Yes	No	26 of 47 (Above Sub-assemblies)	No	In operation.
FERMI	200	800	Na	Yes	No	25 Percent (Above Subassemblies)	No	In operation.
FARET	50	1200	Na			Yes (On Some, Subassemblies)	No	Cancelled
SEFOR	20	820	Na	No	No	On 6 of 109 Sub-assemblies	For 6 of 109 Subassemblies	Not yet in operation.
DFR (Dounreay)	60	700	NaK	Yes	No	6 TC's for 342 Elements (Bulk Coolant)	No	In operation.
PFR	600	1200	Na	Yes	Yes	Majority	On 3 Dummy Subassemblies	Under construction.
Rapsodie	10	1000	Na	Yes	No	Yes, For All	No	In operation.
Phenix	600	1000	Na	Yes	Yes (At Least Partial)	Yes, For All	No	Under construction.

OXIDE FUEL DAMAGE CRITERIA
FOR THE FFTF ACCIDENT SEVERITY LEVELS

ACCIDENT SEVERITY LEVELS	FUEL MATRIX DAMAGE CRITERIA				CLADDING DAMAGE CRITERIA
	CROSS-SECTIONAL AREA $\geq T_{MELT}$		PEAK FUEL TEMPERATURE		PEAK TEMPERATURE
	NEW FUEL	IRRADIATED	NEW FUEL	IRRADIATED	IRRADIATED
DESIGN BASIS ACCIDENT					
DISRUPTIVE ACCIDENT					
MAJOR ACCIDENT	70%	50%			1600°F
MINOR ACCIDENT	20%	20%			1300°F
OPERATIONAL INCIDENT	0	0	5100°F	4950°F	1200°F
NORMAL OPERATING ZONE					

XIV.21

Fig. XIV.1

NUCLEAR SENSOR POWER COVERAGE PROTECTION SYSTEM

REACTOR POWER LEVEL

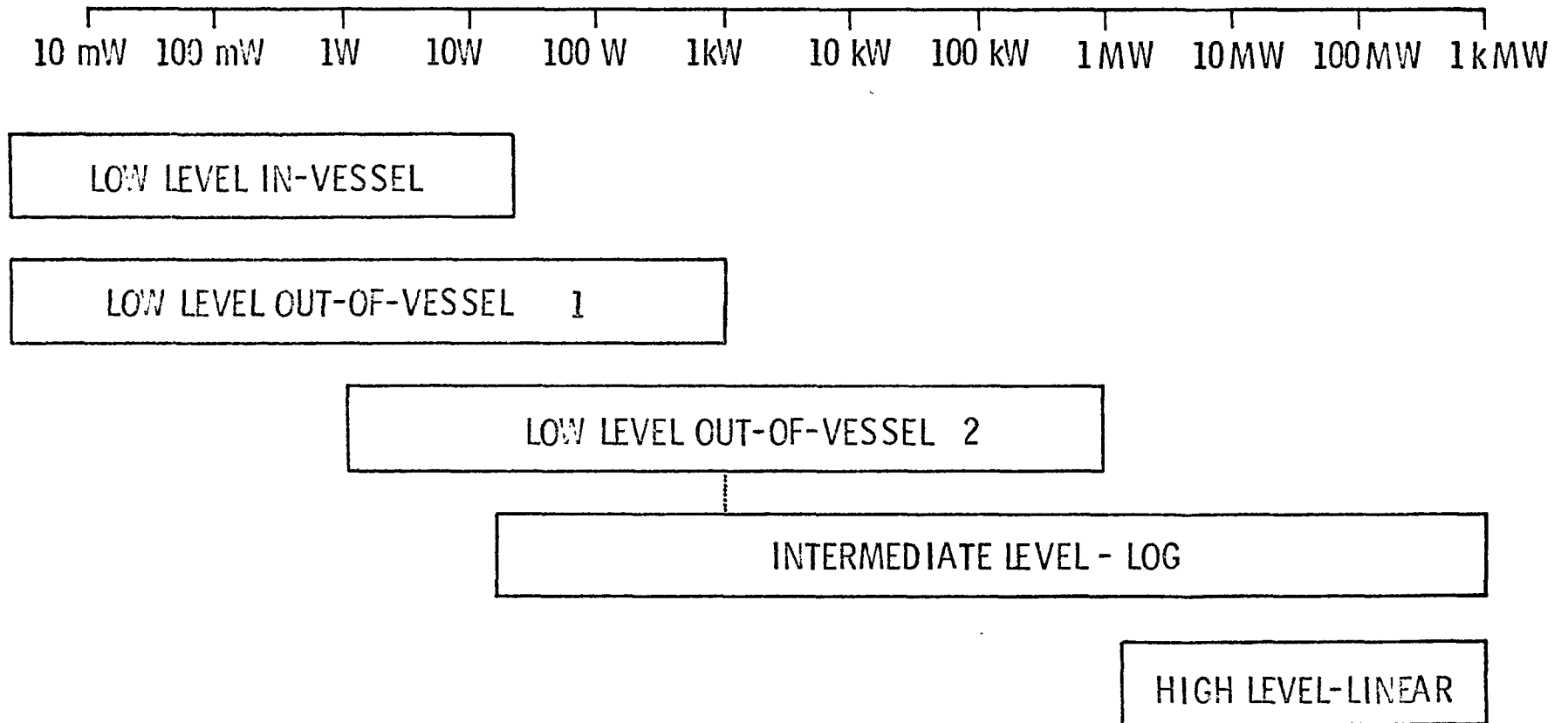


Fig. XIV.2

MAGNETIC FLOWMETER PRINCIPLE

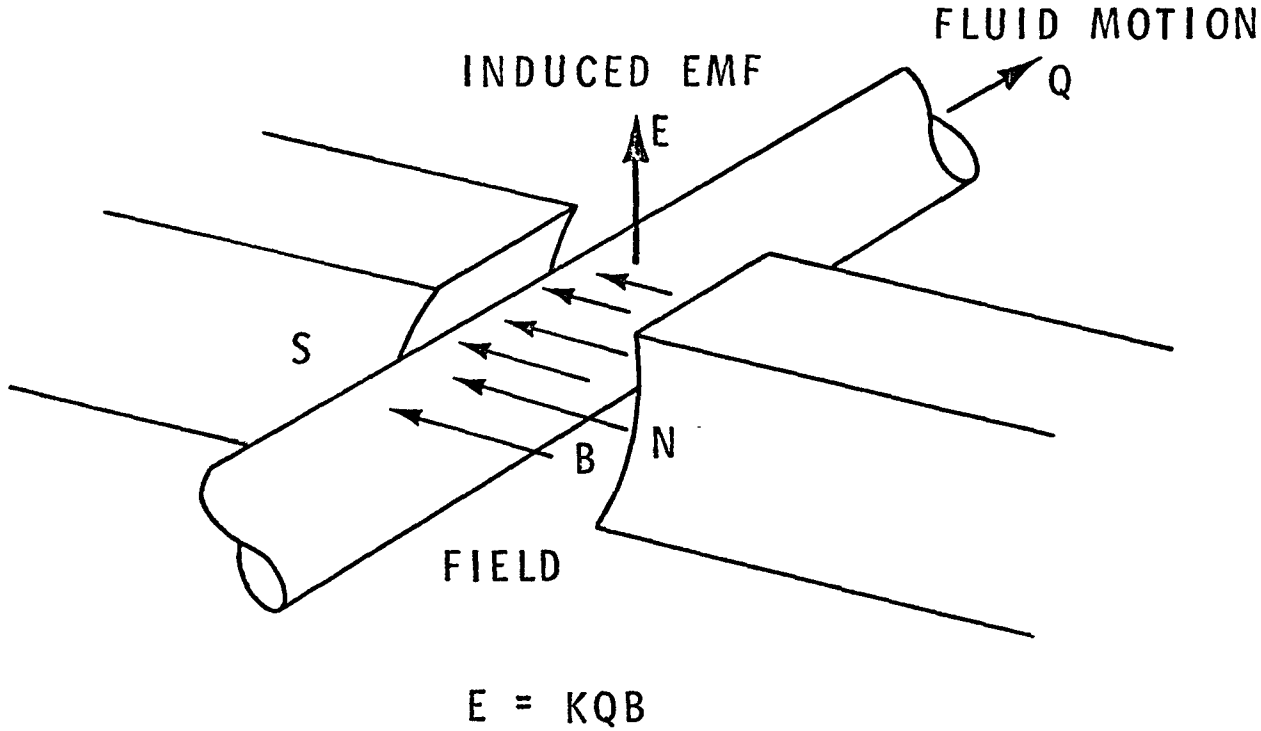
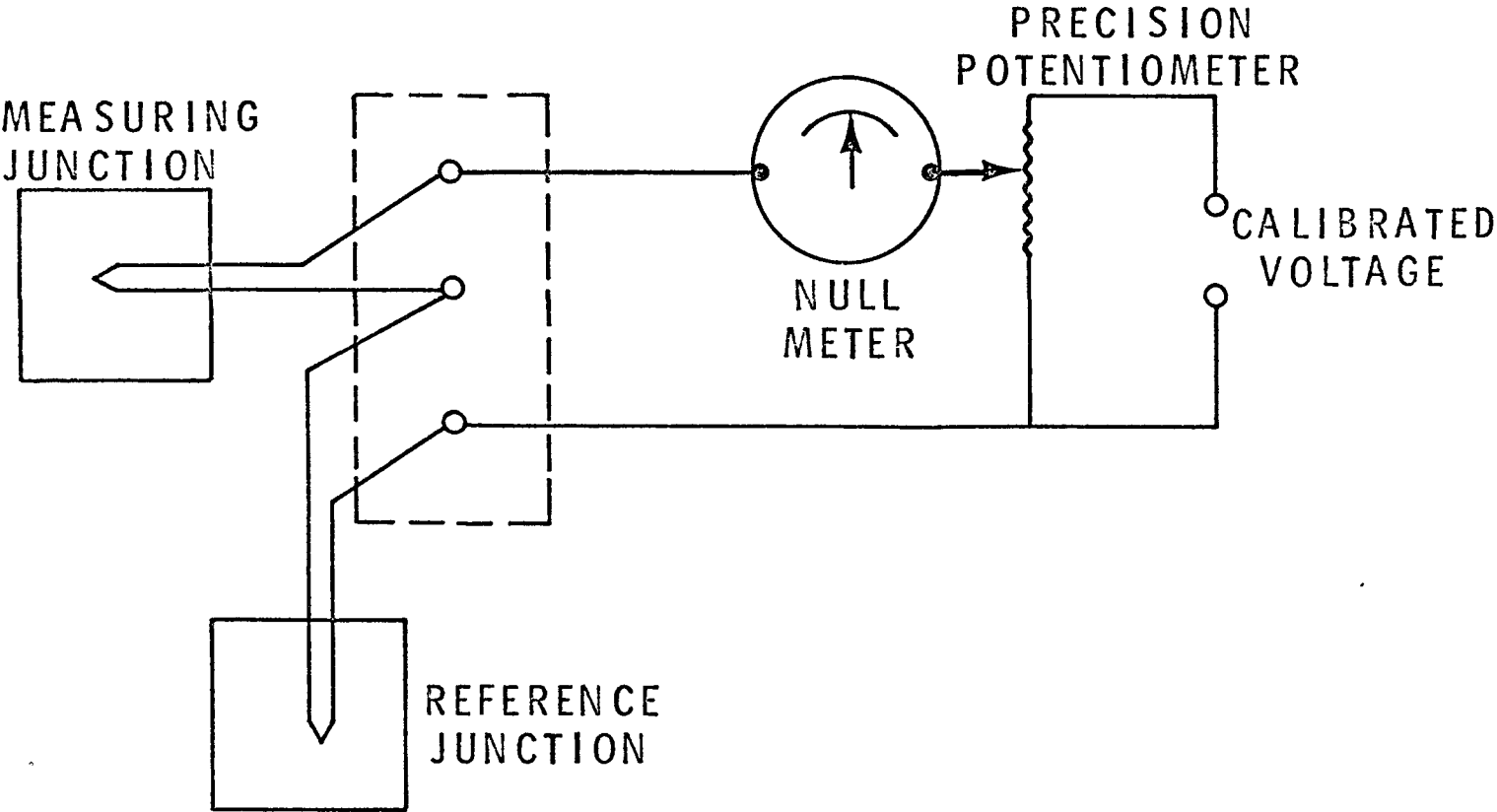


Fig. XIV.3

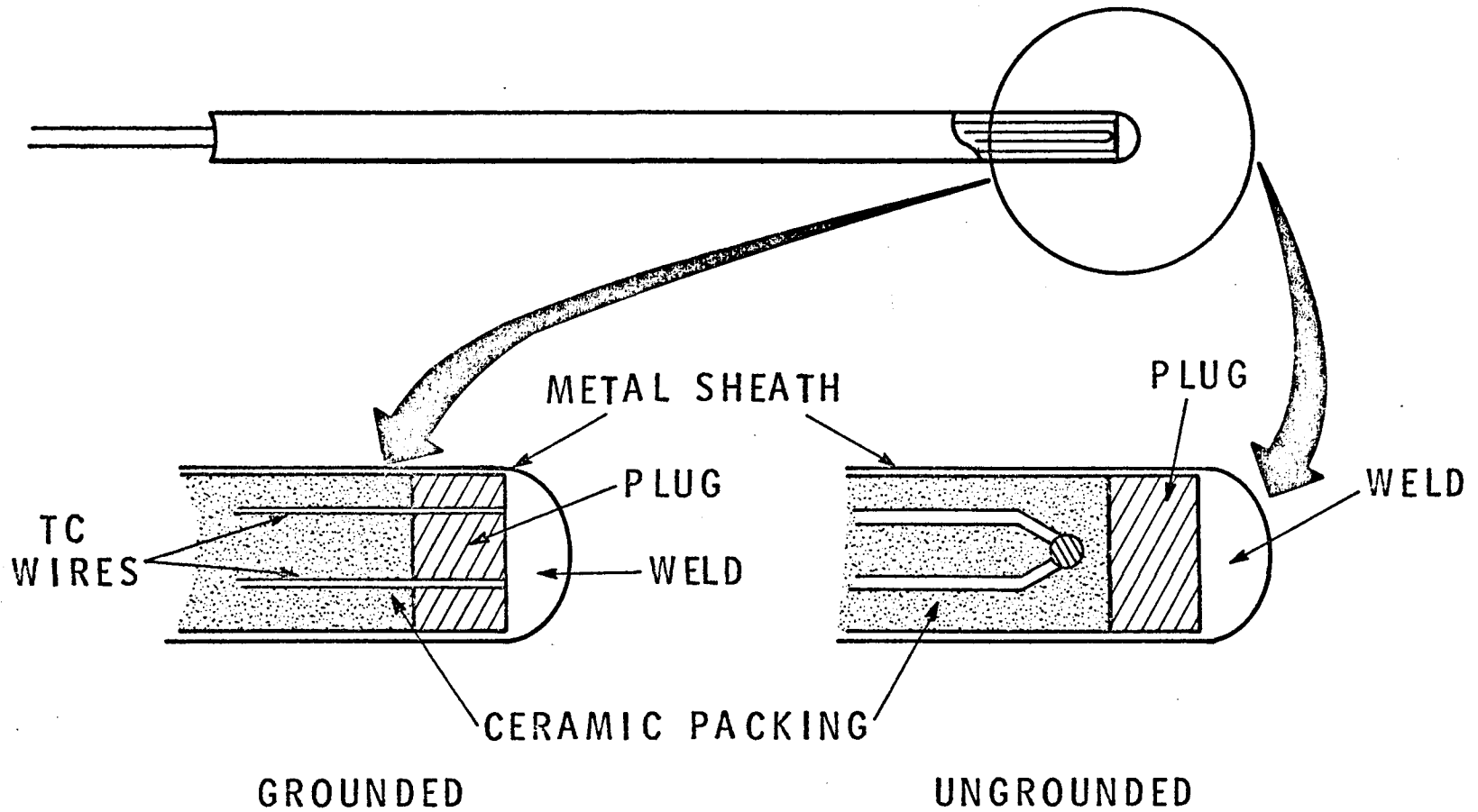
THERMOCOUPLE CIRCUIT



XIV.24

Fig. XIV.4

SHEATHED THERMOCOUPLE



XIV.25

Fig. XIV.5

SAFETY PARAMETERS

<u>INHERENT</u>	<u>DESIGNED</u>
DOPPLER COEFFICIENT	CONTROL STRENGTH
Na COEFFICIENT	CONTROL ACCELERATION
EXPANSION	DELAY TIMES
DELAY TIMES	OVERPOWER FACTOR

Fig. XIV.6

TEMPERATURES FOR RAMP REACTIVITY INSERTION OF 2\$/sec

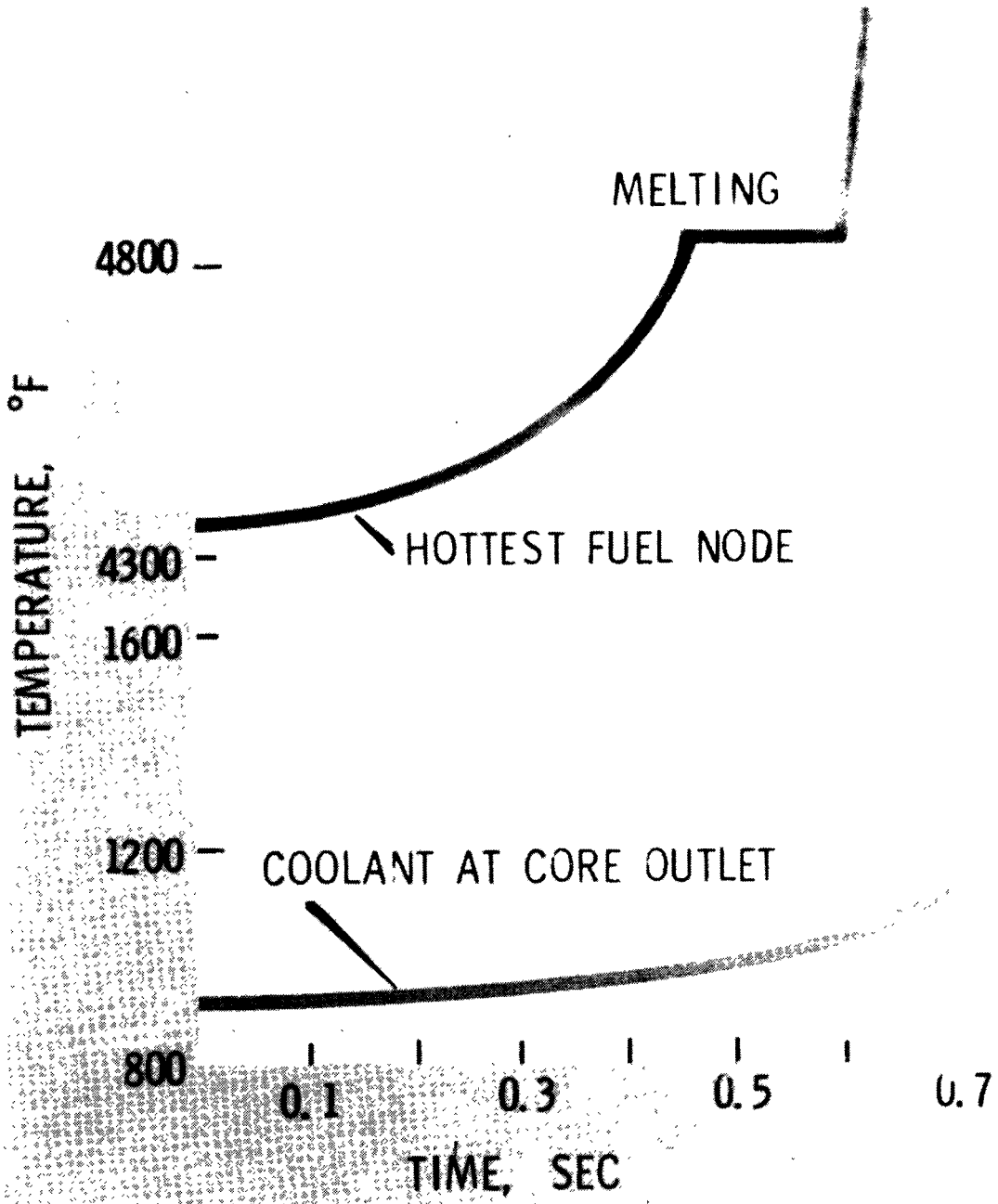


Fig. XIV.7

EFFECT OF DOPPLER COEFFICIENT

(4\$/sec Reactivity Input)

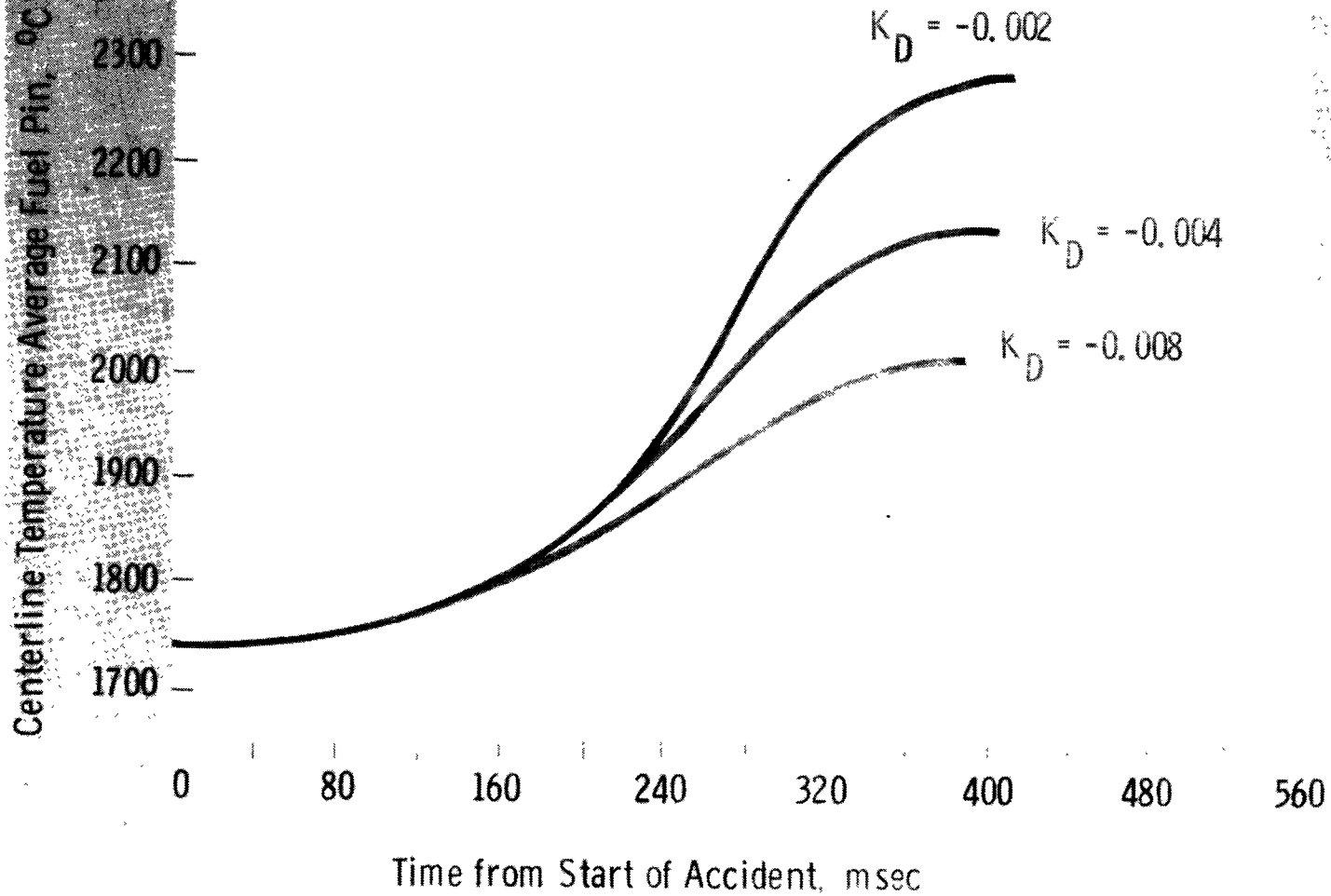
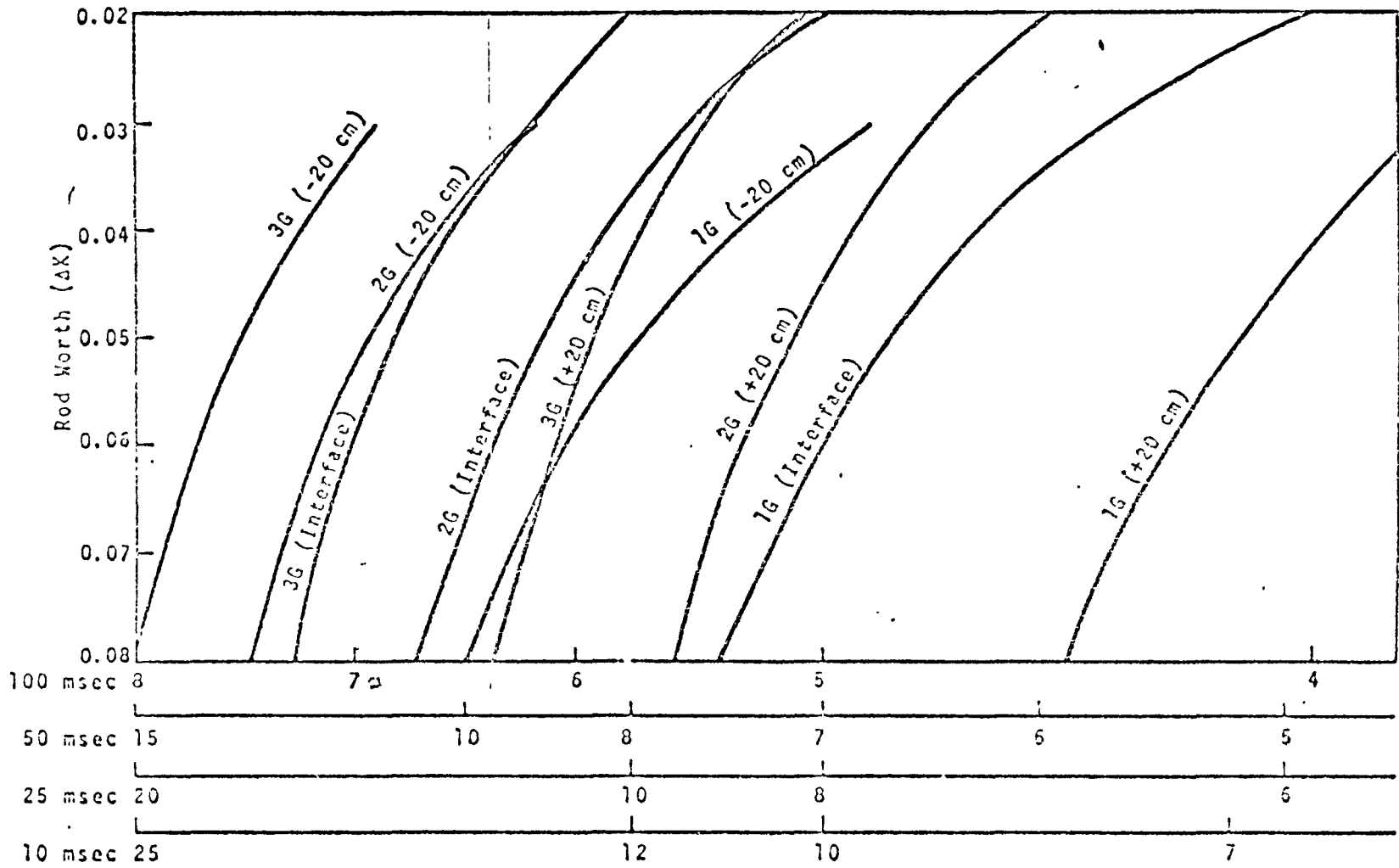


Fig. XIV.6



Reactivity Insertion ($\$/\text{sec}$) to Incipient Fuel Melting for Instrument Time Delays of 10 to 100 msec.

Rod Worth Versus Reactivity Insertion Ramp Rate for Varying Acceleration, Time Delay, and Rod Position

Fig. XIV.9

FUEL COMPACTION ACCIDENTS

<u>FUEL IDENT.</u>	<u>FISSILE INV(Kg)</u>	<u>RAMP RATE(\$/SEC)</u>	<u>TOTAL REACTIVITY(\$)</u>
<u>DRIVER FUEL</u>			
ZONE I	6	2.8	0.60
ZONE II	8	2.6	0.56
ZONE-II ZONE I	8	4.0	0.90
<u>CLOSED LOOP TEST</u>			
2.2 MW	0.82 U, 1.8 Pu	1.4	0.26
4.4 MW	3.35 U, 1.8 Pu	2.7	0.57
5.7 MW	4.78 U, 1.8 Pu	3.4	0.74
<u>OPEN LOOP TEST</u>			
8 MW	6.5	3.0	0.64
9 MW	7.5	3.7	0.83
10 MW	8.4	4.4	1.00

Fig. XIV.10

TEMPERATURE RESPONSE TO FLOW COASTDOWN

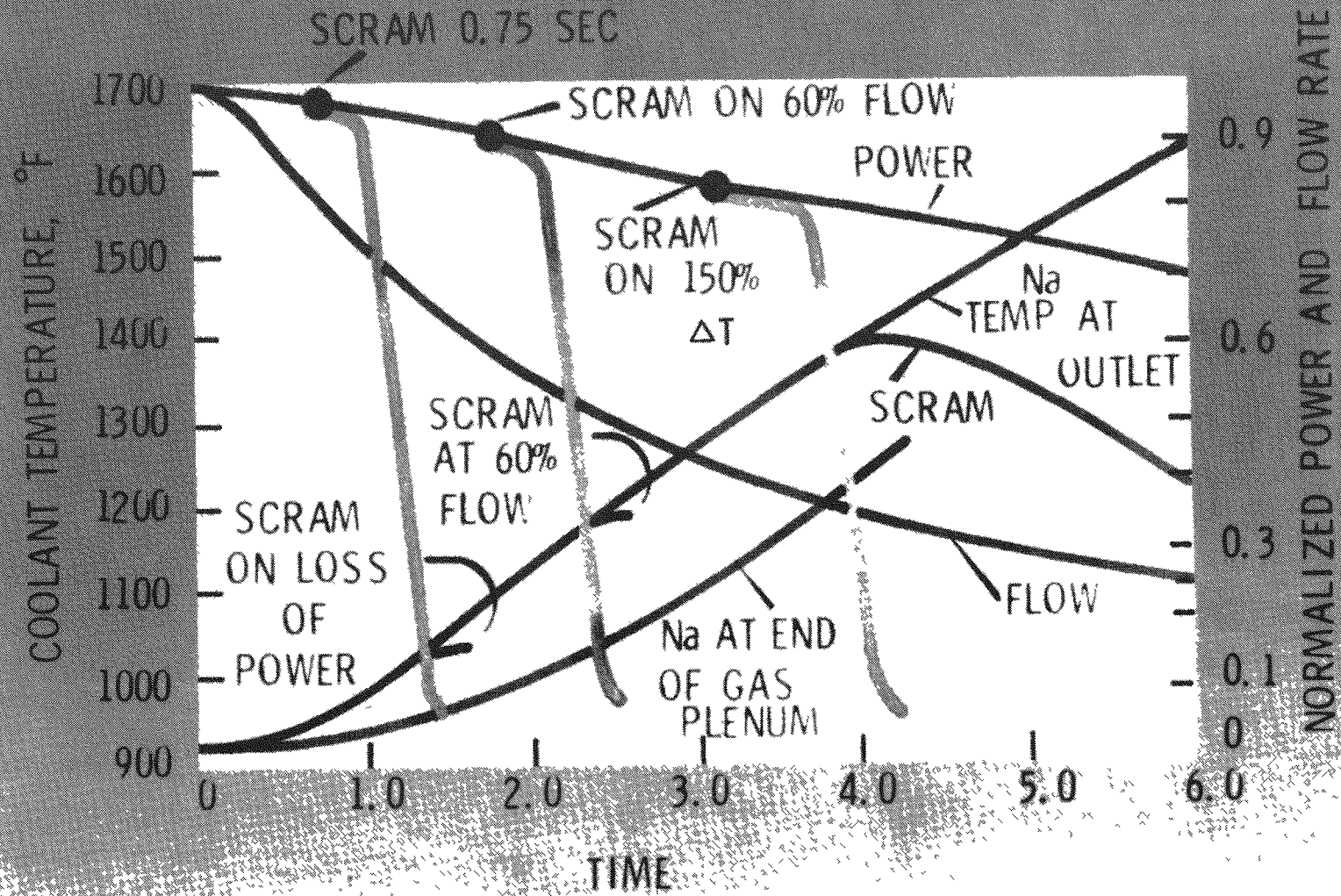


Fig. XIV.11

PUMP AND REACTOR INLET. INLET NOZZLES AT ABOUT 8 FT BELOW CORE

- NOTES:**
1. Coolant from break fills 1.0 ft³/ft x 30-ft standpipe.
 2. Reverse flow resistance to break of 1/2 velocity head provided at each inlet nozzle.
 3. 1g, 15% scram, 2 sec after break.
 4. Flow cooldown initiated 1 sec after scram.
 5. Hot channel factor = 1.4.
 6. Initial core, 400 MW, 600/900 °F, 3 loops.

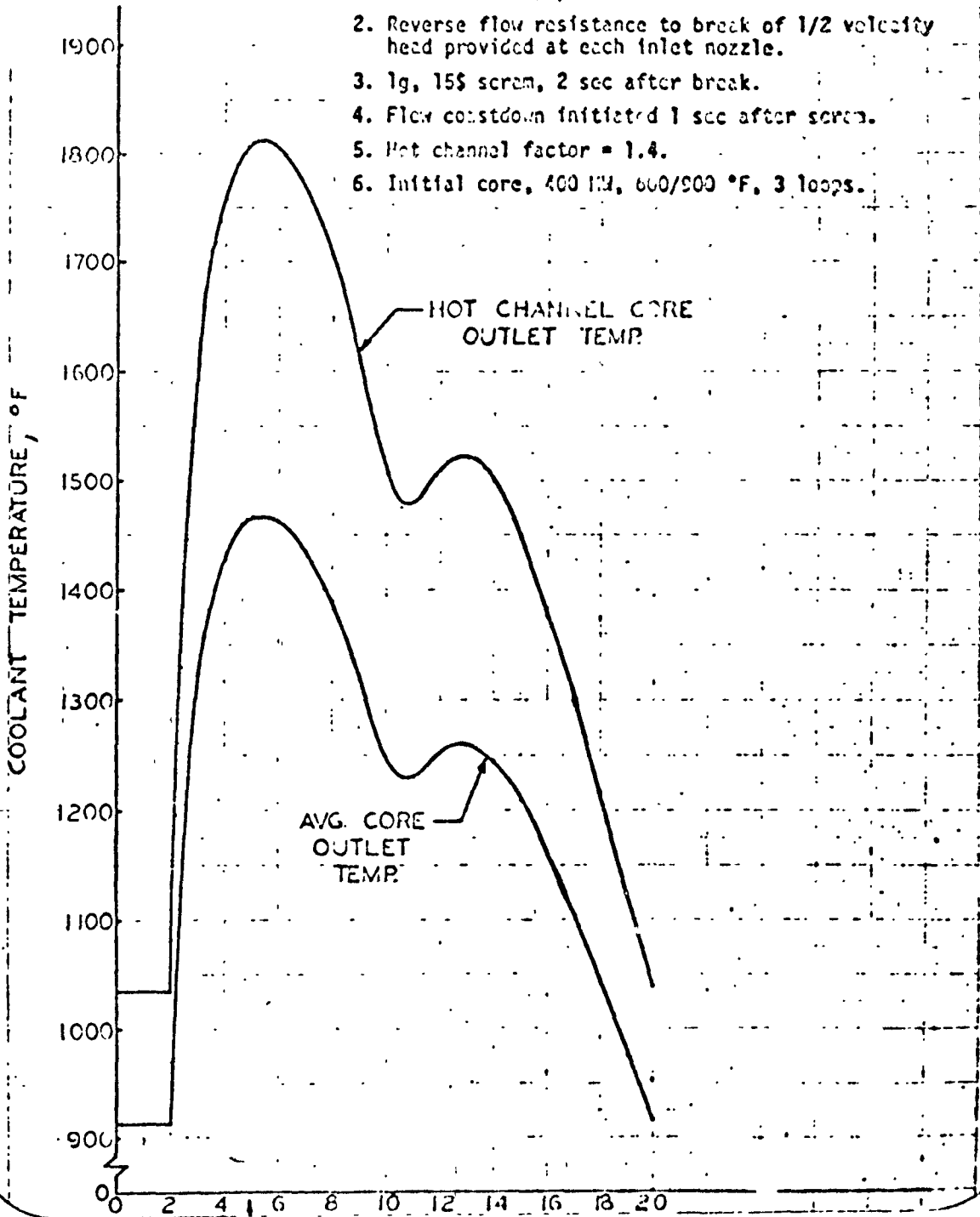


Fig. XIV.12

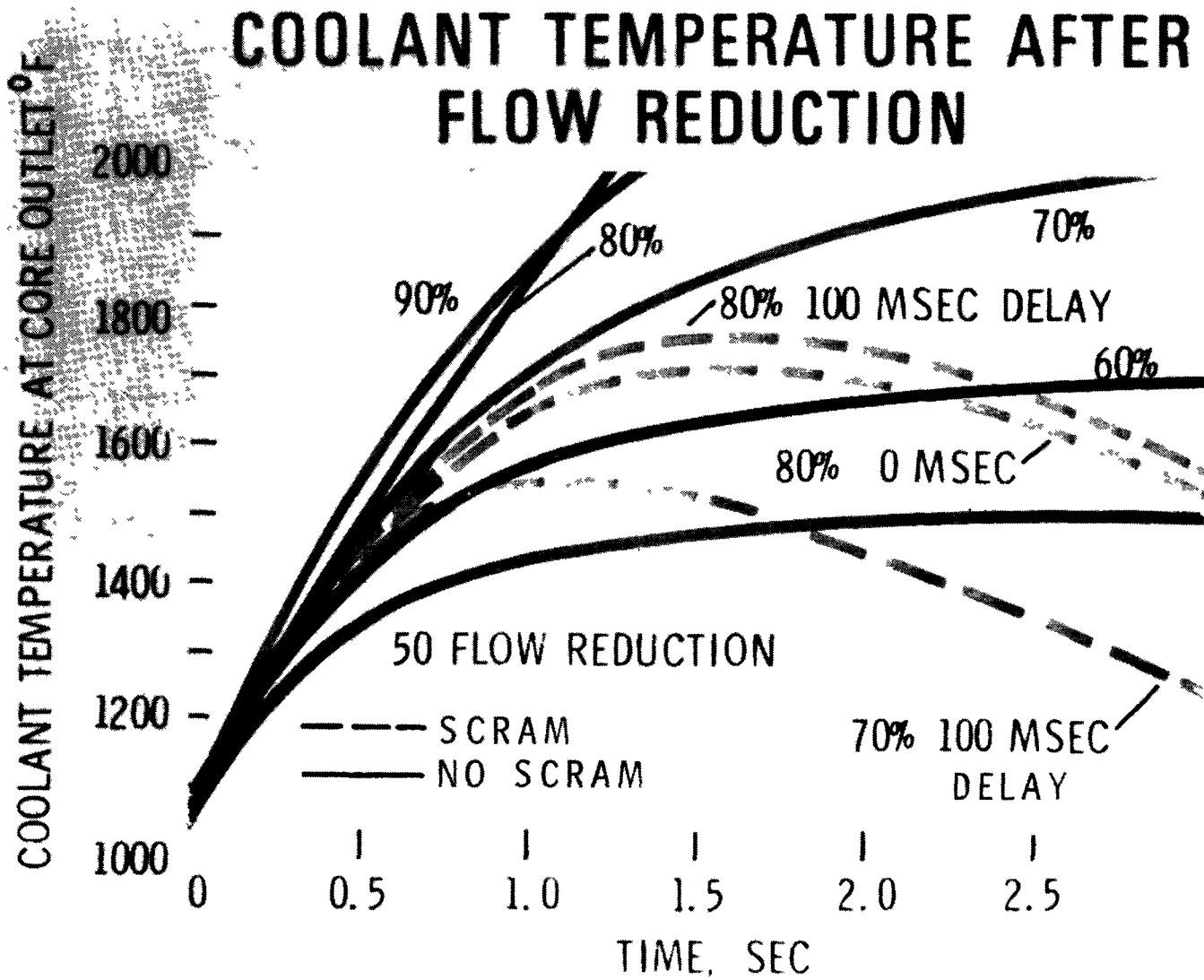
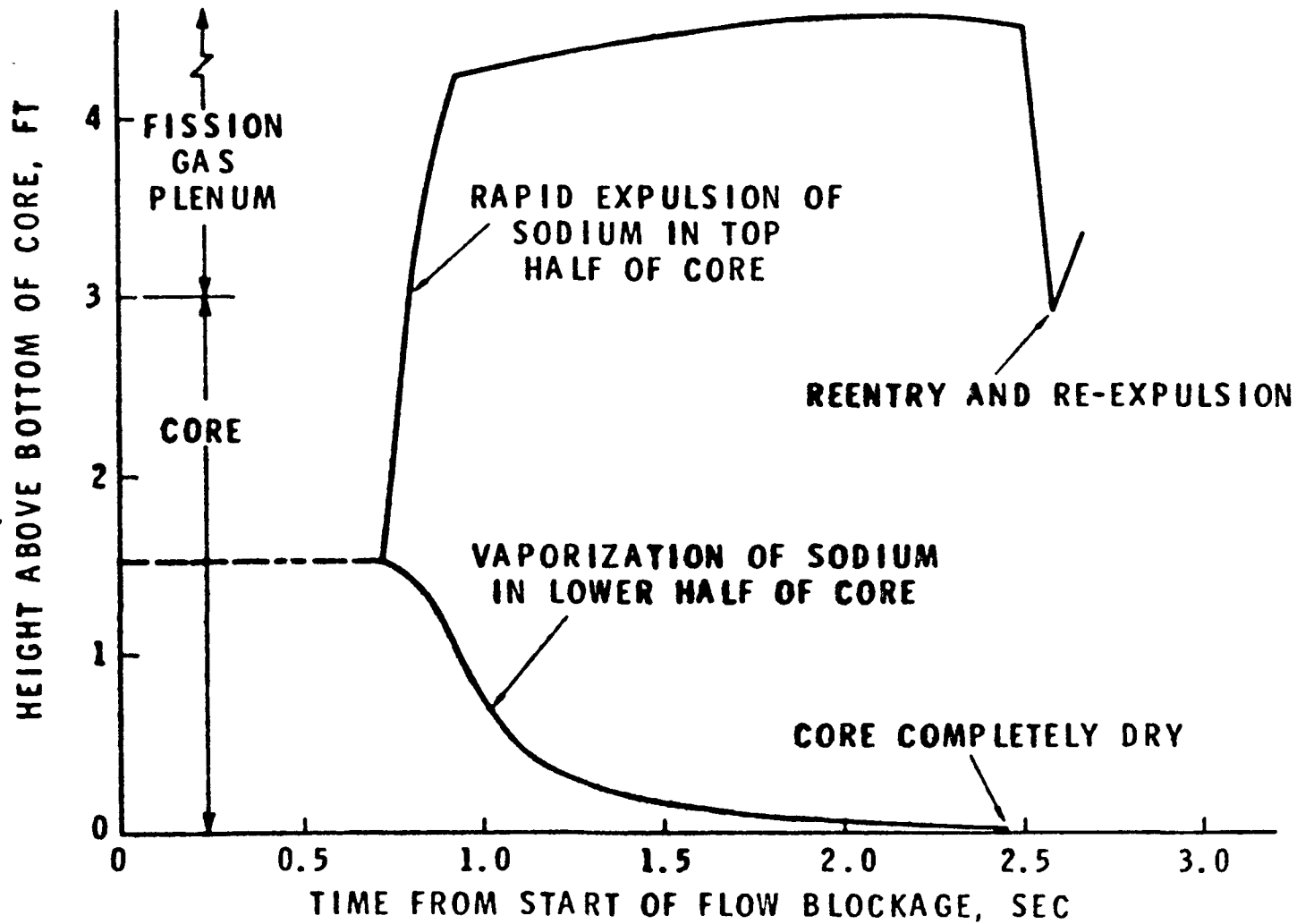


Fig. XIV.13

SODIUM VOIDING AND REENTRY FOR INSTANTANEOUS COMPLETE SUBASSEMBLY BLOCKAGE



XIV.34

Fig. XIV.14

ENERGY ABSORPTION CAPABILITY OF DUCT WALL

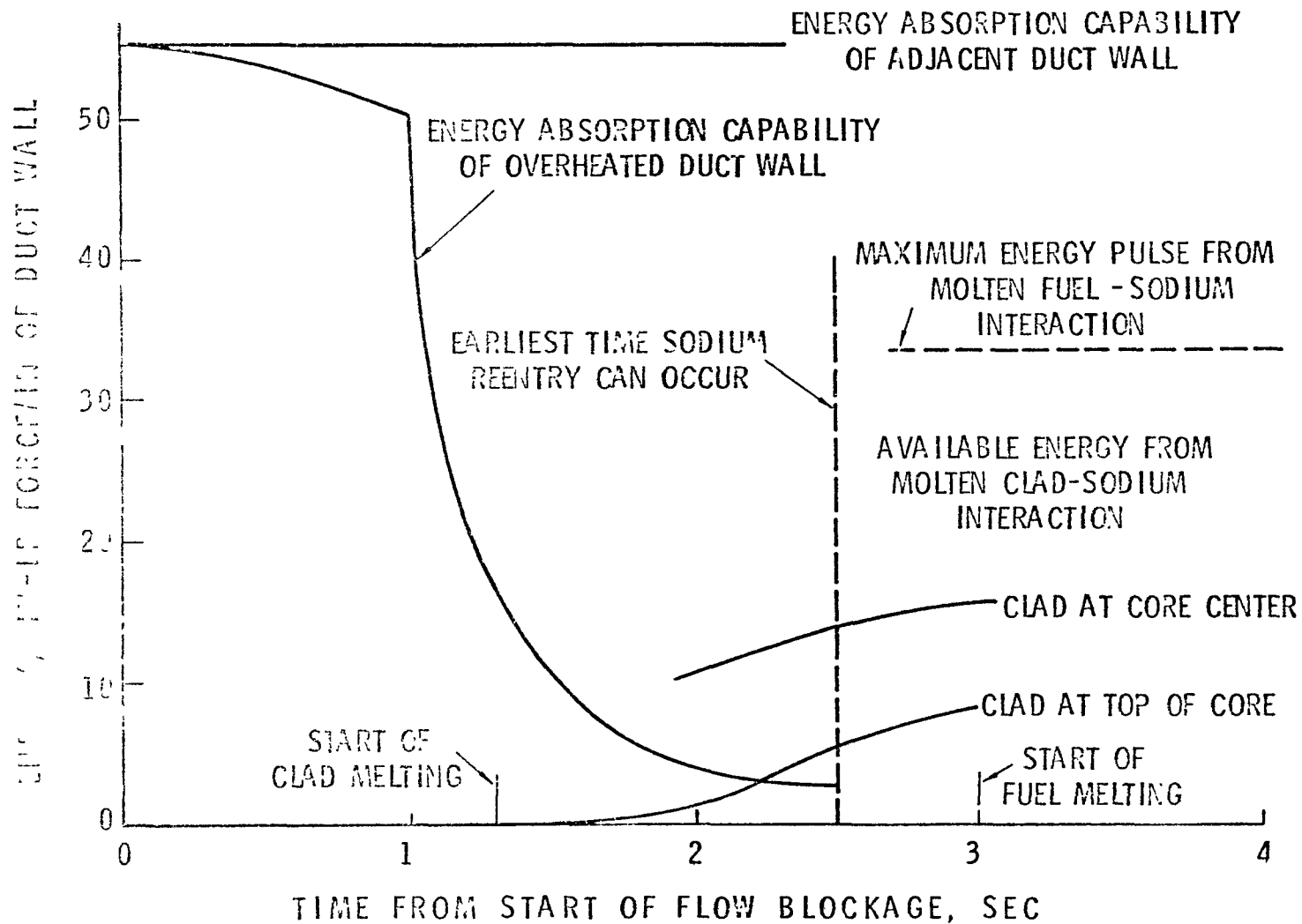


Fig. XIV.15

XIV.35

TYPES OF SUBCHANNEL BLOCKAGES

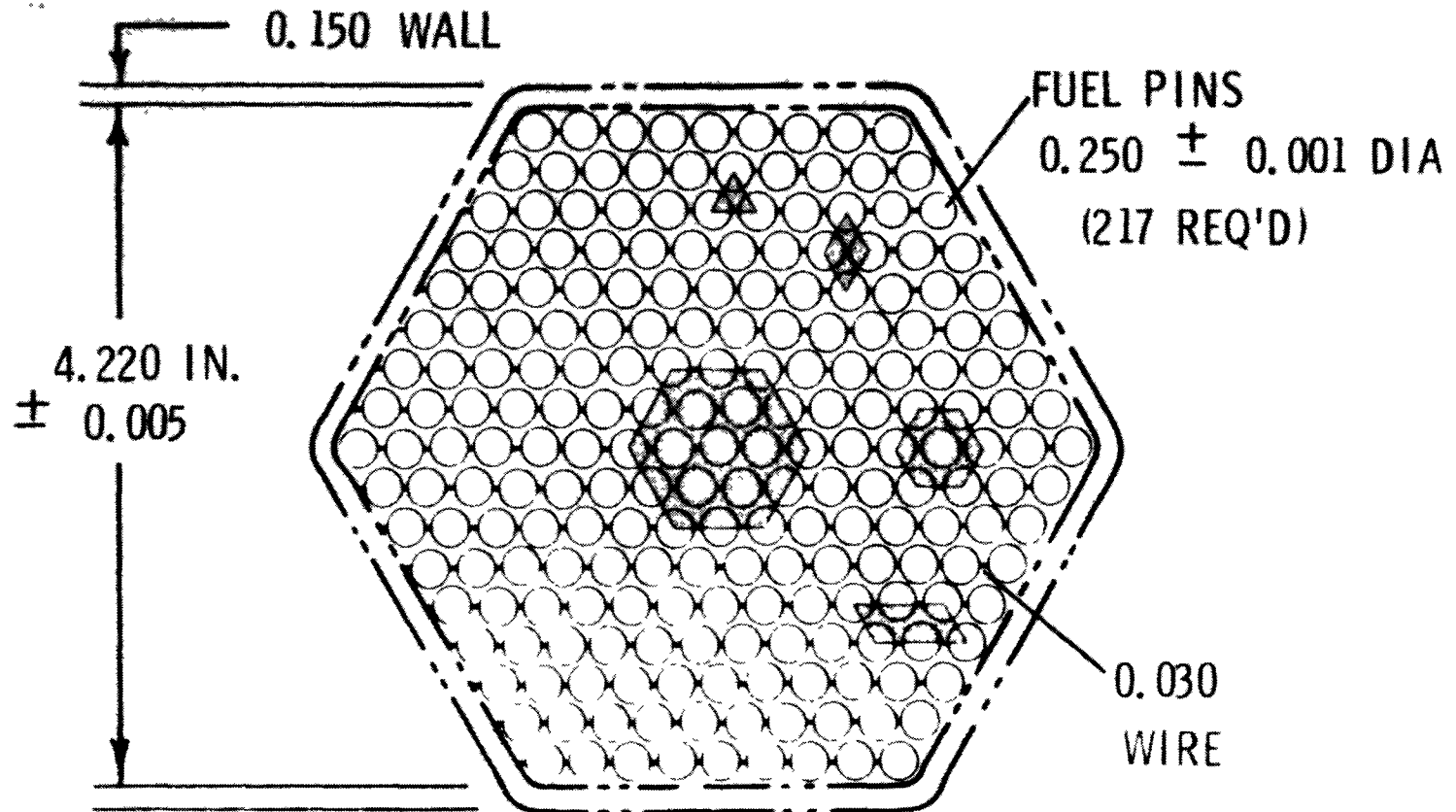


Fig. XIV.16

EFFECT OF TURBULENT MIXING ABOVE BLOCKAGE

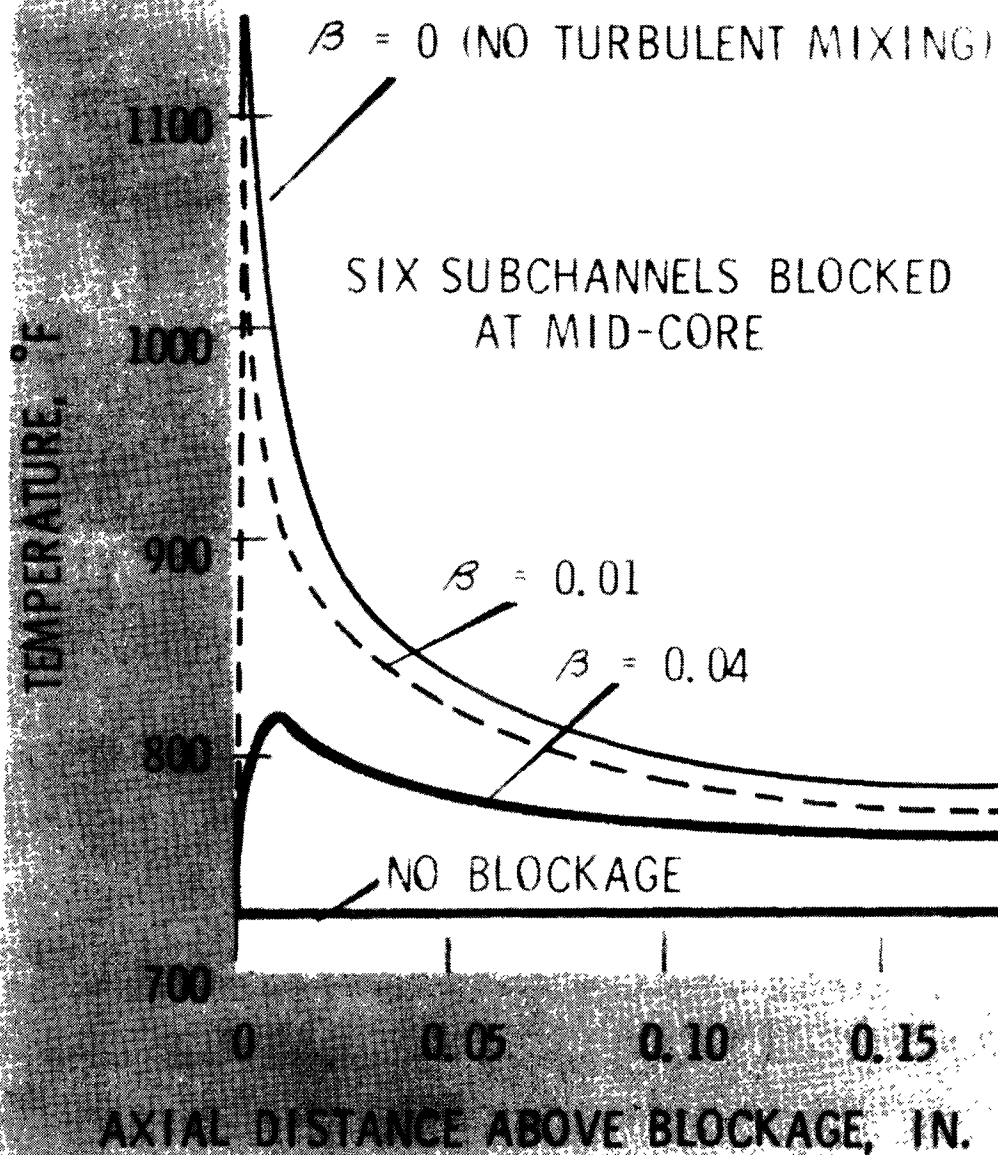
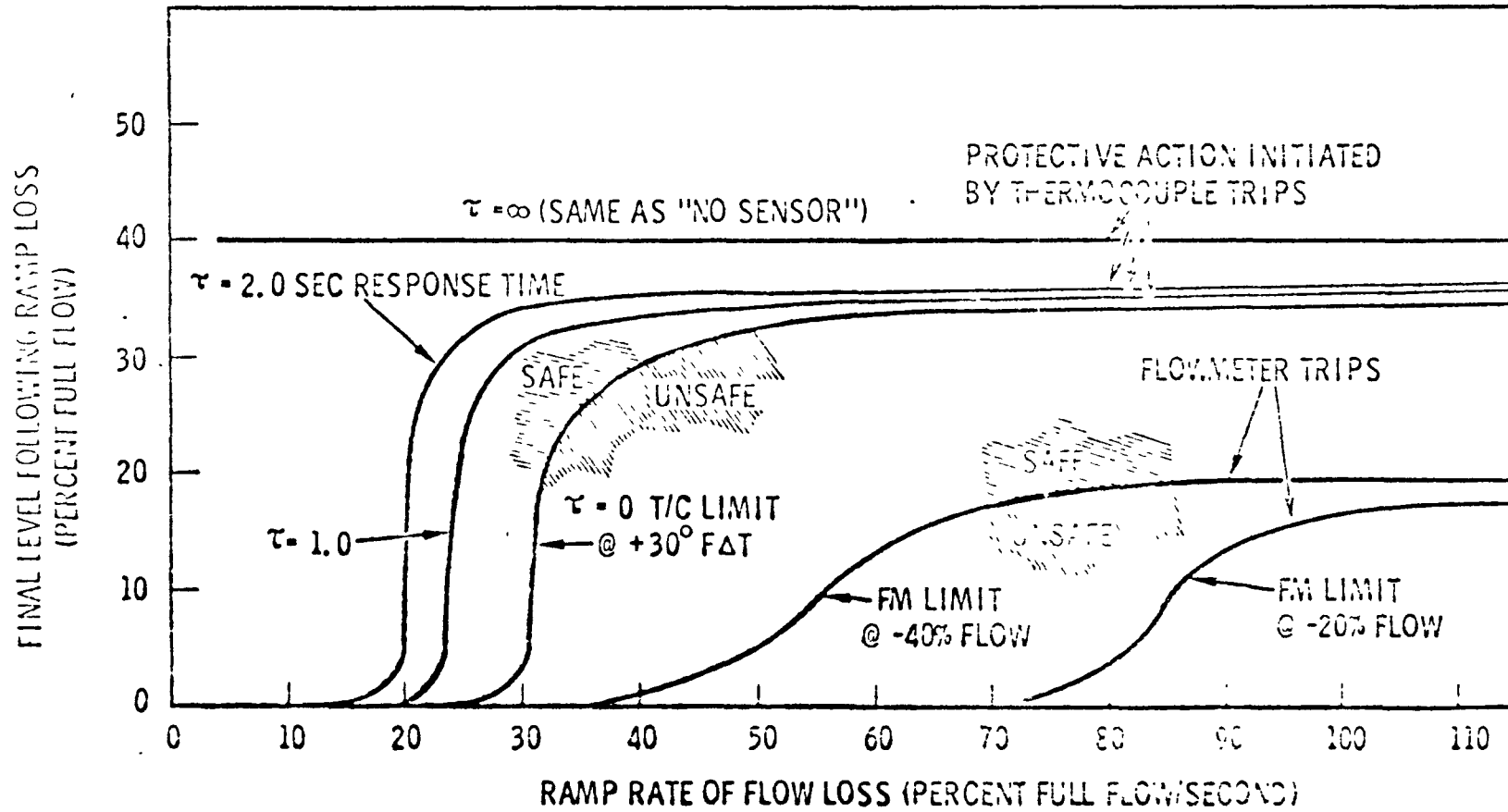


Fig. XIV.17

PROTECTION AGAINST COOLANT BOILING FURNISHED BY IN-CHANNEL INSTRUMENTATION



XIV.36

Fig. XIV.18

SENSITIVITY OF CHANNEL BOILING TO T/C TRIP SETTING

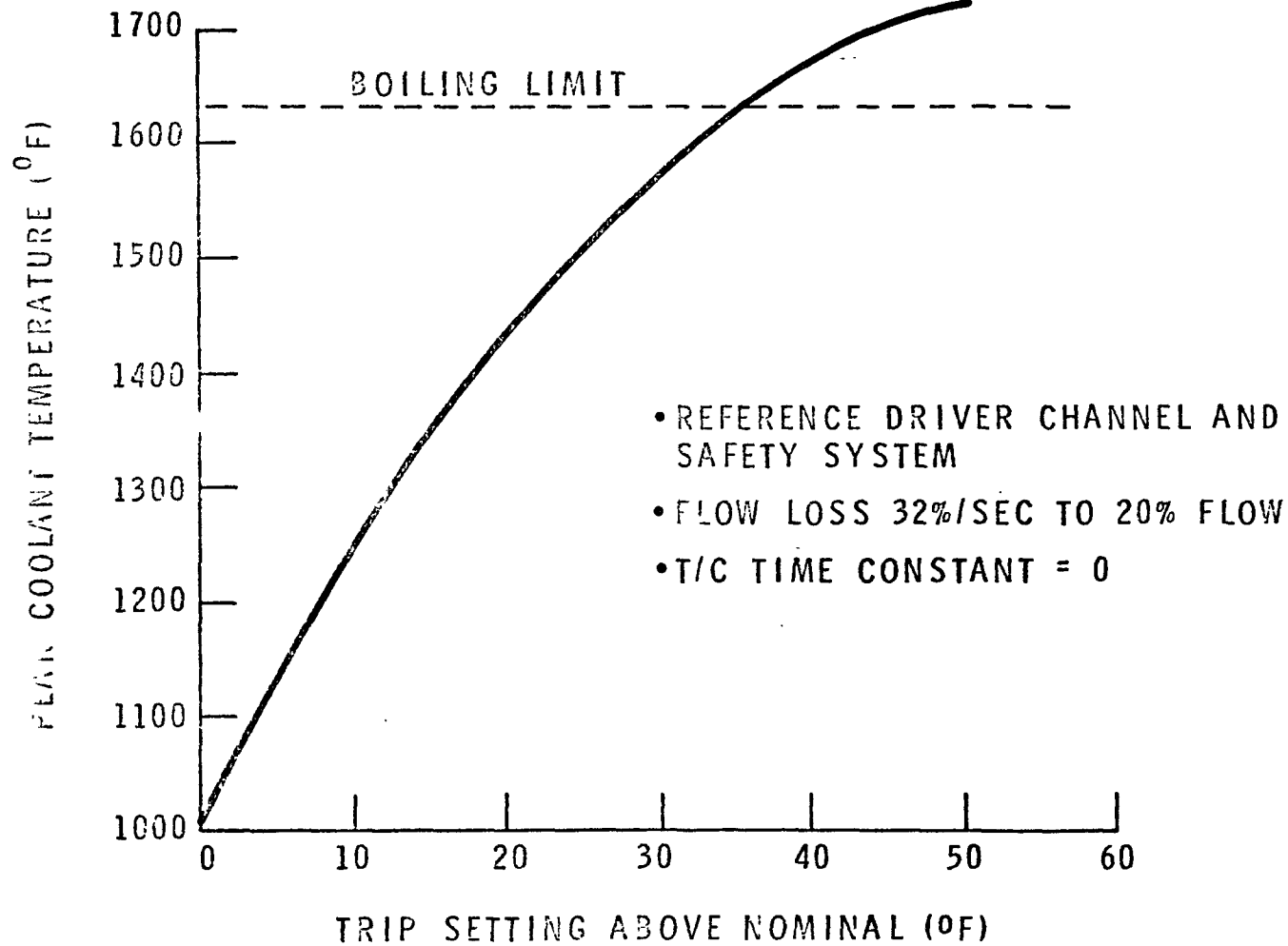


Fig. XIV.19

XV. MATHEMATICAL MODELS OF REACTOR POWER EXCURSIONS

A. E. Waltar

A. Introduction

As the construction of large sodium-cooled fast reactors approaches reality, increased efforts are being focused on methods to better understand core behavior under postulated accident conditions.^(1,2,3,4,5) In a broad sense, there are perhaps two basic questions regarding accident studies: 1) Can conditions ever arise to allow potentially large accidents to start and propagate unchecked?, and 2) If so, what is the course of the transient? Reactor designers and builders are virtually unanimous in their strong conviction that the answer to the first question is no! Fast reactors are designed to be and, in fact, are stable machines. A tremendous amount of effort is expended on each new design to be assured that the reactor is inherently stable and that adequate safety systems are available to successfully terminate any unexpected accident condition prior to reaching major damage proportions. Nevertheless, the second question is continually asked to allow the designer to provide engineered safeguards for protection of both the plant and the public even in the limiting, or hypothetical situation. It is the philosophy of providing safeguard features for a less than perfect system.

Although the first question has a highly speculative flavor, both are heavily laden with technical content. In the discussion to follow, however, the entire emphasis will be on question number two, i.e. given an accident initiating condition what is the course of the transient. This is done because of interest in its own right, but also because an investigation of uncontrolled accidents can provide significant information on possible techniques to provide successful arrest and, further, may help to illustrate the extreme

set of conditions which must be postulated in order to arrive at results of concern.

B. The Approach

Given the task of analyzing the course of a fast sodium-cooled reactor transient from accident inception to its logical termination, the problems become immediately evident. The sheer number of the possible types of interactions which might occur render the analysis procedure complex. Many assumptions have to be made regarding failure mechanisms which are, for the most part, poorly understood. The interaction of Doppler, sodium voiding, and fuel relocation reactivity effects--particularly near prompt critical--can greatly influence the consequences of major accidents. Because of the importance of proper coupling, especially for fast reactors containing a sodium void worth which is highly spatially dependent, a multi-axial, multi-channel core description is deemed mandatory.

No known methods currently exist which are capable of characterizing core conditions in the detail desirable, nor will such methods exist for several years to come. Basic experimental data is often missing upon which to build meaningful models. Further, the programming effort--even if such models could presently be built--would be gigantic and it is doubtful that such programs would fit into even the largest of present day computers or execute in a time anyone could afford. Hence, choices must be made in order to learn something about the problems now.

The approach taken at BNW has been to construct a flexible, fast running code initially containing several rather simplified yet fairly realistic models in order to provide a reasonable basis for assurance that all major feedback mechanisms, and their interaction, can be accounted for. This involves the simultaneous computation of fuel temperatures at numerous core locations in

order that the proper sequencing of spatial feedback effects can be treated. In order to keep the running time to acceptable limits for parametric use, however, substantial simplifications within the fuel pin were necessitated. The emphasis, however, is to contain sufficient detail to be reasonably assured that the gross behavior is correctly understood and then improve the sensitive areas as better analytical models become available.

An early version of the code developed, entitled MELT-II, is presently being used to analyze severe accidents up to the point where fuel temperatures approach the point where substantial core disassembly pressures are attained. At that point the calculations are transferred to a disassembly code as described in the following lecture. Current emphasis, therefore, will be focused on the methods and to characterize core behavior only up to the point of disassembly. A reasonable description of core condition at that time, however, is extremely important because of the pronounced influence on the total energy release exercised by the initial conditions of a disassembly calculation.

Discussion in the present lecture will center almost exclusively on the MELT-II program, developed at BNW as an early generation code to study global core response in the pre-disassembly phase. It is well recognized, however, that within recent years other laboratories have made significant advances in formulating computational models to analyze similar accidents. Hence, wherever appropriate, an intercomparison of techniques will be made.

The core model itself will first be given, followed by a discussion of the methods used to solve the kinetics and heat transfer equation. Discussions will then shift to the real crux of the matter--the methods used to calculate various feedback phenomena. Examples of core response to actual

power transient and loss of flow accidents will then be given to illustrate the type of interactions possible. Finally, a brief review of other current computational tools will be attempted.

C. Core Model

The core geometry assumed by the MELT-II code is illustrated in Figure XV.1. As indicated, the model allows the core to be divided into a maximum of 10 radial regions (channels or rings) and 20 axial segments. Within each channel, power density and temperatures are calculated for one pin which is considered to be characteristic of all fuel pins within the channel. The fuel region within the pin may be divided into a maximum of 15 radial nodes, and the gap (or sodium bond), cladding and coolant are each assigned a single node.

D. Neutronics Model

1. General Formulation

The core power is assumed to be space-time separable in which the time dependence is characterized by the lumped parameter kinetics equations;

$$\frac{dP}{dt} = \frac{\rho - \beta}{\Lambda} P + \sum_{i=1}^G \lambda^i C^i \quad , \quad (1)$$

and

$$\frac{dC^i}{dt} = \frac{\beta^i P}{\Lambda} - \lambda^i C^i \quad , \quad (2)$$

where:

ρ = Reactivity

P = Power density (W/cm^3)

C^i = Precursor density for group i (W/cm^3)

λ^i = Decay constant for group i (sec^{-1})

β^i = Delayed neutron fraction for group i

β = Total delayed neutron fraction

Λ = Neutron generation time (sec)

G = Number of precursor groups.

The method of solution utilizes a variable time step march-out algorithm developed by Little^(6,7). Basically, the method is built around the exponential nature of the neutron and precursor densities. In determining a new time step, two approximations to the power density are calculated and compared to see whether a specified error criterion is satisfied.

Explicitly, the method proceeds as follows. First, one defines approximations to the instantaneous period at time mesh j for the power density and precursor densities, i.e.,

$$\omega_j = \frac{\rho_j - \beta}{\Lambda} + \frac{1}{P_j} \sum_1^G \lambda^i c_j^i \quad (3)$$

$$\gamma_j^i = \frac{\beta^i P_j}{\Lambda c_j^i} - \lambda_i \quad (4)$$

Now if $-\omega P(t)$ and $-\gamma_j^i c^i(t)$ are respectively subtracted from both sides of Equations (1) and (2), integration from t_j to t_{j+1} yields

$$P_{j+1} = e^{\omega_j h} \left[P_j + \int_0^h d\xi \left\{ \frac{\rho(\xi) - \rho_j}{\Lambda} P(\xi) e^{-\omega_j \xi} + \sum_1^G \lambda_j^i \left(c^i(\xi) - c_j^i \frac{P(\xi)}{P_j} \right) e^{-\omega_j \xi} \right\} \right], \quad (5)$$

and

$$c_{j+1}^i = e^{\gamma_j^i h} \left[c_j^i + \int_0^h d\xi e^{-\gamma_j^i \xi} \left\{ \frac{\beta^i}{\Lambda} \left(P(\xi) - \frac{P_j}{c_j^i} c^i(\xi) \right) \right\} \right], \quad (6)$$

where: h = mesh spacing
 j = time index.

To evaluate the integrals in Equations (5) and (6) the first approximations

$$P(\xi) = e^{\omega_j \xi} P_j \quad (7)$$

and

$$C_j^i(\xi) = e^{\gamma_j^i \xi} P_j \quad (8)$$

are placed in the integrals, and the integration is performed using the trapezoidal rule. This leads to the final (second approximation) march-out algorithm

$$P_{j+1} = e^{\omega_j h} \left[P_j \left(1 + \frac{h}{2\Lambda} \left\{ \rho_{j+1} - \rho_j \right\} \right) + \sum_1^G \lambda^i C_j^i \cdot \left. \left\{ \frac{e^{h(\gamma_j^i - \omega_j)} - 1}{\gamma_j^i - \omega_j} - h \right\} \right] \quad (9)$$

$$C_{j+1}^i = e^{\gamma_j^i h} \left[C_j^i + \frac{P_j \beta^i}{\Lambda} \left\{ \frac{e^{h(\omega_j - \gamma_j^i)} - 1}{\omega_j - \gamma_j^i} - h \right\} \right]. \quad (10)$$

The variable time step, h , is determined by the requirement that the first approximation for P_{j+1} , Equation (7), agree with the second approximation, Equation (9), with a prescribed tolerance. That is,

$$\frac{P_{j+1}^{(2)} - P_{j+1}^{(1)}}{P_{j+1}^{(1)}} \leq \epsilon, \quad (11)$$

where epsilon is an input parameter.

The spatial power distribution, $PS(r,z)$, is computed by the relationship

$$PS(r,z) = P_j N(r,z) \quad (12)$$

where

$$N(r,z) = \text{Input spatial distribution.}$$

In order to evaluate the new power P_{j+1} in expression (9), the reactivity ρ_{j+1} at the end of the new time step must be known. But it cannot be computed until the new power is available since it depends upon new temperatures. Hence, an extrapolation procedure is used to obtain a guess for ρ_{j+1} and after Equation (11) is satisfied, the new temperatures and resulting feedback are computed. The power is then recomputed and if it differs from the original calculation by more than a preset value, the entire time step computation is recycled.

It is worth noting that the convergence criterion of Equation (11) does not restrict the fractional power increase which can occur during a time step. When the reactivity is high and changing slowly, the power is nearly exponential in shape and very large time steps are possible. No geometric constraints are attached to the magnitude of the time step because an implicit scheme is used for the temperature calculations. For low values of net reactivity, however, the power varies slowly and the method, as outlined above, requires very small time steps for convergence. To offset this difficulty, a zero neutron lifetime method, as outlined below, was developed to perform the neutronics calculations for relatively slow portions of the transient.

2. Zero Neutron Lifetime Approximation

As suggested in Lecture No. VII, for reactivities less than about 90¢ a useful approximation to Equation (1) and (2) is

$$P = \frac{\sum \lambda_i C_i}{\beta - \rho} \quad (13)$$

and

$$\dot{C}_i = \beta_i P - \lambda_i C_i \quad (14)$$

where here $\hat{c}_i = \Lambda C_i$.

The important gain in using this formulation is that the very short lifetime is removed from the equation and the time step is governed by the slowly changing precursor densities. Working through by analogy to Equation (3) ff, the final march out algorithm becomes, in this case,

$$c_{j+1}^i = e^{\gamma_j^i h} \left[c_j^i + \frac{\beta^i h}{2} \left\{ \frac{\sum_m \lambda_m c_j^m e^{(\gamma_j^m - \gamma_j^i) h}}{\beta - \rho_{j+1}} - \rho_j \right\} \right] \quad (15)$$

and a similar convergence criterion is used.

For convenience, a "mixed mode" option is available in the code which allows the zero neutron lifetime method to be used so long as the net reactivity is below a specified value and so long as the precursors are within a specified fraction from equilibrium with the power density. This option has been particularly useful for loss of flow transients and for certain power transients when the net reactivity is held relatively low during certain portions of the transient.

E. Heat Transfer Model

1. General Formulation

The general core geometry used is illustrated in Figure XV.1. A more detailed view of the radial pin geometry in the nodal approach used, however, is illustrated in Figure XV.2. All radii (including the central void) can be specified arbitrarily. Likewise the cladding node can be connected to a coolant node located at any axial position within the node. Axial heat conduction is ignored, although all axial positions are linked via heat convection through the coolant channel.

As pointed out earlier, an implicit scheme is used to solve the heat conduction equations, i.e. all nodal temperatures along one axial level are solved for simultaneously. Hence, a variable time step scheme, as governed by the neutron kinetics, can be effectively used to reduce problem running time.

Mathematically, the nodal approximation to the fundamental heat conduction equation takes the forms shown below. Within fuel node X (see Figure XV.2):

$$\begin{aligned}
 \frac{V\rho C_p}{d\theta} \left[T_X^{\text{New}} - T_X^{\text{Old}} \right] &= \frac{Q_{\text{OLD}}}{2} + \frac{Q_{\text{NEW}}}{2} & (16) \\
 &+ \frac{U_{X-1}^{\text{New}}}{2} \left[T_{X-1}^{\text{New}} - T_X^{\text{New}} \right] + \frac{U_{X-1}^{\text{Old}}}{2} \left[T_{X-1}^{\text{Old}} - T_X^{\text{Old}} \right] \\
 &- \frac{U_X^{\text{New}}}{2} \left[T_X^{\text{New}} - T_{X+1}^{\text{New}} \right] - \frac{U_X^{\text{Old}}}{2} \left[T_X^{\text{Old}} - T_{X+1}^{\text{Old}} \right]
 \end{aligned}$$

in which the LHS represents the time rate of change of energy in node X, the Q's represent the average power deposited in the node during the present time step, and the U's represent thermal admittances. "New" and "Old" represent conditions at the end and at the start of the time step, respectively. Since variable conductivity and specific heat are allowed in the code, temperature extrapolations must be made to determine properties at the end of the new time step before the actual temperatures can be completed. A check is then made to assure validity of the original extrapolation. If the test is not passed, the entire calculation is done over. Normally the recycle procedure is only used extensively while the fuel is undergoing melting. This results because of the fictitious C_p used during the fusion process.

Within the coolant node:

$$\begin{aligned} \frac{V\rho C_p}{d\theta} \left[T_{\text{coolant}}^{\text{New}} - T_{\text{coolant}}^{\text{Old}} \right] &= \frac{Q_{\text{OLD}}}{2} + \frac{Q_{\text{NEW}}}{2} \quad (17) \\ &+ \frac{U_{\text{Clad}}^{\text{New}}}{2} \left[T_{\text{Clad}}^{\text{New}} - T_{\text{Coolant}}^{\text{New}} \right] + \frac{U_{\text{Clad}}^{\text{Old}}}{2} \left[T_{\text{Clad}}^{\text{Old}} - T_{\text{Coolant}}^{\text{Old}} \right] \\ &- \frac{1}{2} (\omega C_p)^{\text{New}} \left[T_{\text{down}}^{\text{New}} - T_{\text{up}}^{\text{New}} \right] - \frac{1}{2} (\omega C_p)^{\text{Old}} \left[T_{\text{down}}^{\text{Old}} - T_{\text{up}}^{\text{Old}} \right] \end{aligned}$$

where $T_{\text{Coolant}} = f(T_{\text{down}} - T_{\text{up}}) + T_{\text{up}}$

and the only other difference from Eq. (16) is the presence of the heat removal by fluid flow terms.

Although variable conductivity within the fuel and variable specific heat for fuel, cladding, and coolant can be specified, the present version of

the code requires constant gap and film coefficients. The local film coefficient, however, is automatically dropped to a specified value once local coolant channel voiding is incurred.

1. Intercomparison of Results

As stated previously, MELT-II was designed primarily to investigate those portions of the accident following the attainment of failure thresholds such as cladding rupture or coolant boiling. However, it is important that it be capable of reasonably characterizing steady state conditions since this has direct bearing on the time sequencing for approaching the various failure levels.

The code has been compared, therefore, to results obtained by the two established codes, FORE II⁽⁸⁾ and NUTIGER⁽⁹⁾, currently used at BNW for steady state and mild transient studies, and to SAS-IA⁽³⁾ which is being developed at Argonne to accomplish analysis in roughly the same domain as that intended for MELT-II.

a. MELT-II Comparison with FORE II and NUTIGER

The case chosen for comparison with FORE II and NUTIGER was a 1040 liter core divided into three equal-volume radial channels and seven equal-volume axial nodes. The three fuel pins representing their respective radial core regions consisted of a 0.230 in. (0.584 cm) OD, a clad thickness of 0.014 in. (0.036 cm), and a fuel pellet OD of 0.195 in. (0.495 cm). Variable fuel thermal conductivity was used along with the assumption that the conductivity is constant for temperatures greater than 1800 °C. No sintering, fuel swelling, or central void formation was assumed to occur for the fuel.

The steady-state axial temperature distributions of the fuel, clad, and coolant are compared in Figure XV.3 for the hottest (inner) radial

channel with the exact solution. The coolant temperatures calculated by MELT-II, FORE II, and NUTIGER agree well with the exact solution.

For this case, the centroid of the coolant nodes in MELT-II were assumed to be at the axial midpoint. As pointed out previously, MELT-II allows the centroid to be placed anywhere between the inlet and outlet of the node and for transient problems with low coolant flow rates the centroid should be placed near the outlet. However, the MELT-II output provides the coolant temperature at the outlet of the coolant node regardless of the location of the centroid. For FORE II the temperature of the coolant centroid is always taken as the arithmetic average of the inlet and outlet temperatures, but the coolant temperature, anywhere between the inlet and the outlet, assuming a linear temperature gradient, can be printed out. NUTIGER assumes that the centroid is always located at the outlet of the node.

The clad axial temperature distributions calculated by MELT-II and FORE II compare very well with the exact solution which assumes that the clad node should be connected to the average coolant temperature. Therefore, the NUTIGER clad temperatures are slightly higher because it assumes that the clad is connected to the coolant temperature at the outlet of the coolant node.

The fuel in each axial segment was subdivided radially into seven equally-spaced nodes, and the axial temperature distribution for the hottest (innermost) node is shown in Figure XV.3. MELT-II and FORE II agree quite well with the exact solution, but the NUTIGER temperatures are high due to the different connection between the clad and coolant. The effect has been aggravated because the fuel thermal conductivity decreases with temperature. That is, the slightly higher fuel temperatures at the outer edge of the fuel pellet results in slightly lower thermal conductivities which result in higher temperatures further in, etc.

The steady-state radial temperature distributions at the axial midpoint of the hottest channel is shown in Figure XV.4. As already shown in Figure XV.3, the coolant and clad temperatures are identical for MELT-II and FORE II and slightly higher for NUTIGER because of the connection between the clad and the coolant. The fuel temperatures for both MELT-II and FORE II tend to be higher than the exact solution near the outer surface of the fuel pellet and then lower than the exact solution near the center. This is characteristic of the nodal approach which lumps all of the physical properties of the node into the centroid. Also shown in Figure XV.4 are the fuel temperatures calculated by a finite-difference analysis. The temperatures are very close to the exact solution. The finite-difference analysis will be used later for comparison of transient results for which there is no exact solution as a basis.

The effect of a 6\$/sec reactivity ramp, without scram, on clad and fuel temperatures is shown in Figure XV.5 for the same axial level as in Figure XV.4. Although the clad temperatures for MELT-II and FORE II are initially identical, the slightly higher fuel temperatures in MELT-II causes its clad temperature to eventually rise faster than that of FORE II. The transient fuel temperatures for MELT-II, FORE II and NUTIGER have essentially the same shape and compare well with the results from the finite-difference analysis. Therefore, the difference in the time it takes to reach the melting point of the fuel is the result only of the different initial steady-state temperatures. For MELT-II, there is a slight (10 °K) rise in temperature as the fuel passes through melting because a variable specific heat model is used for the heat of fusion. The associated power calculation for the above case is shown in Figure XV.6.

A brief comparison of the UNIVAC 1108 computation time required by the three codes for the particular transient chosen is made in Table XV.1. The numbers given, however, are not completely revealing, since the codes use quite different methods for time step determination.

TABLE XV.1
Comparison of Running Time

Code	Comments	No. Time Steps	Total Run Time, sec (Including loading)	
MELT-II	{	Finite lifetime (very tight error criteria)	416	82 ←
		Mixed mode (very tight error criteria)	92	59
FORE II	{	5% power change per time step	112	79 ←
		1% power change per time step	468	157
NUTIGER	{	~4.5 msec time step (geometry determined)	65	126
		2 msec time step	145	240 ←

NOTE: *Arrows index the cases which are plotted*

NUTIGER and FORE II both require a geometric check on the largest permissible time step because they use explicit temperature calculation schemes. NUTIGER makes no other check and in order to insure accurate power calculations during super prompt critical conditions, the user must specify a short time step which is then held fixed throughout the transient. All reactivity feedback is one time step behind the power calculation. FORE II allows a variable time step which can be limited in size by the fractional power increase per time step. An extrapolation procedure is used to predict reactivity feedback effects in the new time step to enable reasonable power calculations to be made. No check is made, however, to determine whether

the estimated feedback corresponds to that actually occurring due to the new temperatures. MELT-II, as discussed previously, utilizes a variable time step procedure which is not numerically constrained by heat transfer considerations. An upper limit, of course, does arise regarding accuracy in accounting for rapid feedback terms. This is common to all codes.

From Table XV.1, it is noted that MELT-II and FORE II are comparable in running time, whereas NUTIGER is substantially longer, primarily because of the fixed time step procedure. The NUTIGER time step allowable from geometry considerations was not adequate for the neutronics calculations. Essentially, no difference in accuracy was detected for the two FORE II runs. The mixed mode approximation in MELT-II yielded a substantial savings in computer time over the rigorous method at the expense of a maximum error of only 12 °K in the peak fuel node and a 2% error in the power. In general, MELT-II is shown to compare quite favorably with the NUTIGER and FORE II codes up to the point of fuel melting.

b. MELT-II Comparison with SAS-IA

A brief comparison was likewise made between MELT-II and SAS-IA. Conditions selected were similar to those outlined above although a lower power rating, as well as a finer axial subdivision, was used. Figure XV.7 contains the steady state axial temperature comparison and Figure XV.8 illustrates the radial temperatures distributed in the hottest axial node. Since no exact calculations were performed it is difficult to infer which code is more accurate, but the differences are seen to be fairly small. One desirable feature of the SAS-IA code is its ability to expand the fuel and cladding radially upon heating from the cold to the at-power conditions. This is illustrated in Figure XV.8.

Figure XV.9 contains a comparison of the power level as calculated by the two codes for an unbounded, unprotected ramp rate of 5\$/sec with Doppler feedback only. The reason for the somewhat higher power, as calculated by SAS-IA, appears to be directly the result of a smaller Doppler feedback contribution. Again, no exact solution is available, but it is suspected that the MELT-II power trace is more accurate because of the six channel core representation used as opposed to the single hot channel representation utilized in the SAS-IA system. Even though the single pin representation in the SAS-IA system is substantially more advanced than that used in MELT-II, the multichannel feature of the latter system is believed to be extremely valuable in predicting Doppler feedback, which depends upon the temperature distribution of the entire reactor, as well as the sequencing of feedback due to sodium voiding and fuel relocation. No meaningful computer time comparisons were made between the MELT-II and SAS-IA codes.

F. Feedback Models

The difficult part of simulating major reactor excursions is in determining the feedbacks which might exist. As pointed out in Lecture VII, the problem is not so much that of determining the reactivity consequences as the result of fuel movement or coolant density change as it is in determining the physical movement of fuel or coolant in the first place. Simplified models which have been developed to approximate these phenomena in MELT-II comprise the subject matter for the present section.

At the end of each time step, the total reactivity is obtained by combining the input drive term with the feedback terms, i.e.,

$$\rho(t) = F_p(t) + \sum_i \rho_i(t) \quad (18)$$

where $F_p(t)$ is the programmed reactivity and the $\rho_i(t)$ terms represent the individual feedback terms. The feedback models are treated separately below.

1. Doppler

In a mixed oxide fast reactor, the Doppler effect is perhaps the only reliable prompt negative reactivity feedback mechanism. Hence, proper treatment of this phenomenon is of utmost concern. For oxide fueled cores, the assumption is normally made that $\frac{dk}{dT}$ remains constant over the temperature range of interest. However, simply applying this law to an average core temperature may not be adequate for at least two reasons. First, the temperature buildup during an excursion may not develop symmetrically and temperature changes at the core top may be significantly less important than for similar changes at the core center. Secondly, if and when sodium voiding

occurs, the local spectrum hardens and the local Doppler feedback effect is reduced. Hence, the formulation* of the Doppler effect in MELT-II allows for both local importance weighting and local spectrum changes in the following manner:

$$k_{\text{Doppler}} = \frac{K_D \sum_{i,j} W(i,j) V(i,j) \ln \frac{T(i,j)}{T_0(i,j)}}{\text{CORE VOLUME}} \quad \text{for } T_0 \leq T \leq T_1,$$

$$A + \frac{K_D \sum_{i,j} F W(i,j) V(i,j) \ln \frac{T(i,j)}{T_1(i,j)}}{\text{CORE VOLUME}} \quad \text{for } T_1 < T \quad (19)$$

where K_D = original whole core Doppler coefficient,
 $W(i,j)$ = local Doppler weighting factor,
 $V(i,j)$ = local nodal volume,
 $T(i,j)$ = local nodal fuel temperature,
 $T_0(i,j)$ = original local nodal fuel temperature,
 $T_1(i,j)$ = local nodal fuel temperature at the time local voiding occurs,
 F = effective normalized change in the Doppler coefficient for spectrum hardening due to sodium voiding,
 A = feedback value evaluated at $T = T_1$.

Figure XV.10 illustrates both the above mentioned effects. The particular example chosen is a guillotine pipe rupture accident in which the Doppler coefficient at the start of the excursion was assumed to be -0.005. Because

* A simple core average fuel temperature scheme may be exercised as a code option.

of the asymmetric fuel temperature rise (fuel temp. near the core top rising more rapidly than elsewhere due to the rapid increase in the coolant outlet temperatures), the effective Doppler coefficient drops off significantly. Here, the "effective Doppler" value is defined as the coefficient resulting if one were to simply use a core average fuel temperature for Doppler calculations. The second major drop is due to the spectrum hardening which results from coolant voiding. Approximately one half of the core was voided at the termination of the accident.

2. Sodium Density Change

Sodium reactivity feedback effects are separately computed in MELT-II for two types of situations--small density changes and complete voiding. This section describes the methods used to account for small coolant density changes associated with coolant temperature changes. Section (5) outlines the treatment for complete voiding.

One scheme used by the code to compute the coolant feedback is to simply combine an effective thermal expansion coefficient with the core average coolant temperature. Because of the marked spatial variation of sodium worth in fast reactors, however, a much more realistic computation is to combine the sodium worth curve with the actual local changes in sodium density caused by a changing temperature profile. Symbolically, the computation is performed as follows:

$$k_c = \sum_{i,j} w_c(i,j) [D_c^0(i,j) - D_c(i,j)] v_c(i,j) \quad (20)$$

where $W_c(i,j)$ = sodium void worth,
 $D_c(i,j)$ = local sodium density (temperature dependent),
 $D_c^0(i,j)$ = original local sodium density,
 $V_c(i,j)$ = local sodium volume.

Figure XV.11 contains coolant reactivity feedback results due to heating for two types of accidents. The solid lines correspond to a power transient (5\$/sec ramp) and the dashed lines correspond to a flow coastdown accident. In both cases curves are plotted for the simple single node thermal expansion approximation and for the spatial weighting scheme discussed via Equation (20) above. For the point model, a thermal expansion coefficient of $-1.5 \times 10^{-6} \delta k/^\circ\text{C}$ was used.

In both accident types considered, the point model yielded a substantial monotonically increasing value of negative reactivity. For the more accurate spatial model, however, the feedback calculated was significantly less and, in fact, in the case of the power transient the feedback was always positive. This was the result of coolant heating up in the core center (in the positive sodium void region) faster than at the core periphery. Although the most serious error in using the simple point model appears to occur for the power transient case, it is worth pointing out that the total coolant feedback computed by either model is here small compared to the Doppler feedback (the value of which is indicated, in parenthesis, on each curve at the time cladding failure or coolant boiling is reached). Hence, use of the spatial model is perhaps even more important when analyzing loss of flow transients. In any event, it appears better to ignore sodium density reactivity effects entirely rather than to use a single point thermal expansion model.

3. Axial Pin Expansion

The general feeling among reactor designers is that axial expansion is probably not a reliable negative feedback mechanism for oxide fueled cores. In contrast to metal fueled reactors, where a fairly strong axial feedback effect is available, oxide fuel tends to crack profusely and, particularly for high burnup fuel, it is not clear that the fuel column itself will effectively elongate during power excursions. Hence, relatively little emphasis has been attached to this mechanism in the modeling work. The only option presently available is to associate a linear expansion coefficient with the core average fuel temperature.

However, there is some interest in the possibility of segmenting the fuel column with mechanical plugs. If these plugs are rigidly attached to the cladding, it is possible that the fuel would be forced to move with the cladding during an excursion. A model has been developed to investigate this situation. Basically the model assumes the pins to be fixed at the core bottom and all axial expansion is in the upper direction. Local fuel worths are combined with calculated fuel density changes (caused by the elongating cladding) and the summation over all radial and axial core nodes is then performed to obtain the total effect. By simply replacing the cladding temperature with the fuel temperature in this calculation, a substantially improved method over that of the single node expansion discussed earlier would be available to assess the effects of fuel expansion -- should this mechanism be deemed realistic.

The effectiveness of moving the fuel with the cladding (assuming a good bond or the use of many axial segmenting plugs) is illustrated in Figure XV.12. The particular example chosen was a flow coastdown accident where the transient

is slow enough to allow the cladding to undergo a substantial expansion (a rapid power transient would not allow enough time for heat to be conducted to the cladding and the mechanism under discussion would be expected to be of insignificant magnitude). For the base case (solid lines) including Doppler feedback only, the core average temperature increased about 100 °K at the end of 5.4 seconds, the time corresponding to initial coolant boiling. The associated Doppler feedback caused the power drop as shown. Including the axial fuel feedback, due to expansion with the cladding, caused a substantial negative reactivity feedback to occur. This resulted in a faster drop in power and it just so happened that this rate of drop almost exactly balanced the heat removal capability of the decaying coolant system because the core average fuel temperature rose only about 5 °K at the end of 6.0 seconds. Doppler feedback was, therefore, almost zero. The net effect of including the cladding expansion feedback was to delay the onset of coolant boiling in the hot channel from 5.4 seconds to approximately 6.0 seconds. Although this is not completely negligible, both time lapses are sufficiently long to allow quite adequate time for normal scram action to occur. A similar analysis for a pipe rupture accident revealed that a feedback of this type based on cladding movement would allow relatively more time prior to the onset of boiling or cladding failure. This was primarily the result of rapid cladding heating, due to the low flow spike, early in the transient.

4. Fuel Relocation

One of the major concerns in the safety analysis of fast reactors is that fuel, in contrast to the situation found in thermal reactors, is characteristically not arranged in its most reactive configuration. Hence, there is at least the theoretical possibility that should an accident occur where

substantial amounts of molten fuel are generated, the molten fuel might compact in a fashion which could severely aggravate the accident. Early fast reactor safety analyses^(10,11) were based, to a large degree, on pessimistic models of gross molten fuel compaction. In EBR-II⁽¹⁰⁾, for example, the assumption was made that fuel in the central one third of the core melted and compacted into the lower one third, after which time the upper one third fell down and resulted in recriticality at a very large reactivity ramp rate. The analysis of FERMI⁽¹¹⁾ was based on instantaneous total loss of coolant (as well as loss of some fuel) attendant with a completely molten core condition. Uniform gravity core compaction was then assumed and, again, the reactivity ramp rates calculated were very large (several hundreds of dollars per second).

The approach at BNW has been to avoid these arbitrary assumptions by evaluating core temperature distributions resulting from the initiating accident and, thereby, having some basis for defending an incoherent fuel melting and relocation pattern. A basic difficulty still exists, however, in that even now there exist no models for fuel relocation which can be defended as being realistic. There are just too many unknowns and too little experimental data upon which to base reasonable models. Hence, the fuel movement models in MELT-II are very simple--far too simple to justify any claim of realism--yet plausible and flexible enough to lend confidence to the position that an upper bound to the problem can be computed.

a. Cladding Failure Thresholds

Although one might speculate that some molten fuel movement could occur prior to cladding rupture, due either to internal pressure gradients or to the existence of a central void, it is generally agreed that failure of the cladding must precede gross fuel motion. Both the axial position and time

of failure are of interest--not only because of subsequent fuel motion but also because such information helps determine the initial conditions for coolant expulsion.

For power transients, in which the cladding heats up slowly relative to the fuel, the cladding is expected to rupture due to thermal expansion of the fuel and/or high internal pressures due to hot fill gas or rapid release of fission gases. The fission gas release problem tends to become more severe with increasing burnup. For loss-of-flow transients, fuel behavior is relatively unimportant and the cladding failure mode is usually that of overheating. The analysis presented in Lecture X indicates that for irradiated fuel, cladding rupture would be expected to occur once roughly 50% of the fuel cross-sectional area is molten. For loss-of-flow excursions, cladding failure would be expected for temperatures around 1200 °K. The technique used in MELT-II to predict cladding failure is simply to monitor cladding and fuel temperatures and use the criterion stated above.

b. P n Collapse

In one of the fuel movement models developed, all of the fuel above the initial point of cladding failure is assumed to fall according to the following equation of motion:

$$\frac{d^2H}{dt^2} + \xi \frac{dH}{dt} = -G \quad (21)$$

where ξ represents a viscous factor and G is the driving function (normally the gravitation constant, although any value can be used). Below that failure point, however, local cladding failure must occur before fuel is allowed to slump. This model was chosen because FTR pins are supported from the bottom and are relatively unconstrained at the top. This model is

illustrated, for slumping versus time, in Figure XV.13. Perhaps a more graphic illustration of the model would be the analogy of holding a match near the center of a wax candle. As fuel moves, the reactivity consequences of such movement are computed by simply dropping the fuel through a pre-determined worth curve, i.e.

$$\rho_{\text{collapse}} = \sum_{i,j} [W(i,j) - W_0(i,j)] S(i,j) \quad (22)$$

where $W(i,j)$ = current fuel worth at position i,j ,
 $W_0(i,j)$ = original fuel worth at position i,j ,
 $S(i,j)$ = fuel mass at node i,j .

Naturally, if too much fuel movement takes place, perturbation theory is no longer valid and the whole model becomes meaningless. However, only a small amount of core movement (a few centimeters) need take place before substantial amounts of reactivity can be added.

c. Fuel Squirting

Although one is tempted to argue that gravity forces should provide an upper limit for the rate of fuel compaction which could occur, the fission gas pressure inside a pin at high burnup may approach 1000 psi. Some of the transients performed in the TREAT reactor have suggested that molten UO_2 is extremely mobile. Actual squirting of molten fuel has been observed under certain conditions. Although high internal pin pressures may serve to aid the shutdown process by squirting molten fuel away from the central hottest regions toward the cooler pin ends, the potential for fuel relocation into a more reactive configuration does exist.

In order to gain some insight into the consequences associated with fuel squirting due to high internal pin pressures, a simple model has been built which, upon cladding failure, allows the full fission gas pressure to act on an assumed molten fuel column and the fuel enters the coolant channel. By using a geometric ratio of coolant-to-fuel area, the amount of molten fuel progressing in both directions in the coolant channel can be determined. As would be expected, the very conservative model, if parametrically tested for extreme conditions, can give rise to very rapid additions of reactivity.

5. Sodium Voiding*

In large fast reactors, the rate of sodium voiding from the core during an accident is of major importance because of the associated reactivity effects. Three possible voiding mechanisms have been identified in the analysis of both power excursions and loss of flow accidents: (1) sodium boiling, (2) release and expansion of fission gases, and (3) a molten fuel-sodium interaction. These three voiding mechanisms have been incorporated into the MELT-II accident analysis code.

During loss-of-flow accidents (e.g., flow coastdown, pipe rupture, complete blockage at subassembly inlet), conditions for sodium boiling are attained within several seconds depending on the severity of the flow decrease and the incipient-boiling superheat. Experimental observations with alkali metals such as sodium and potassium and with fluids simulating alkali metals such as freon have shown that the rate of vapor growth can occur as a single bubble which grows and occupies the entire channel and then expands in a piston-like manner. Hence, a simplified expulsion model assuming a slug-type flow regime, as illustrated in Figure XV.14 has been developed.

*The material for this section was contributed by Dr. A. Padilla, Jr.

The equation of motion and for ejection of liquid coolant is as follows:

$$\rho \frac{D\bar{V}}{Dt} = - \bar{\nabla}P - [\bar{\nabla} \cdot \bar{\tau}] + \rho \bar{g} \quad (23)$$

which may physically be described as

$$\text{mass x acceleration} = \begin{matrix} \text{pressure} \\ \text{force} \end{matrix} + \begin{matrix} \text{viscous} \\ \text{force} \end{matrix} + \begin{matrix} \text{gravitational} \\ \text{force} \end{matrix} .$$

Assuming one-dimensional flow and integrating from Z_1 to Z_2 , this relation can be expressed as

$$\dot{m} = \frac{1}{\int_{Z_1}^{Z_2} \frac{dZ}{A}} \left[(P_1 - P_2) - (\Delta P_m + \Delta P_f) - \rho g(Z_2 - Z_1) \right] \quad (24)$$

- where
- \dot{m} = rate of change of mass flow rate
 - A = cross sectional area of liquid column
 - Z_1 = local axial level
 - Z_2 = axial level at slug extremity
 - P_1 = local driving pressure
 - P_2 = pressure at slug extremity
 - ΔP_m = momentum losses
 - ΔP_f = friction losses
 - ρ = liquid density
 - g = gravitation constant

The momentum and friction loss terms are obtained from steady state pressure drop calculations and a functional relationship to the mass flow rate is used in Equation (24). By solving for the mass flow rate in the upper and lower liquid slug at the end of each time step, the motion of the upper and lower void-liquid interface boundaries can be computed as a function of time. Reactivity feedback resulting from these voiding patterns is then computed according to the expression

$$P_{\text{void}} = \sum_L \left[\left(\int_{Z_D}^{Z_V} W_C(Z,L) dZ \right) (M_C) \right] \quad (25)$$

where Z_V = upper void-liquid interface
 Z_D = lower void-liquid interface
 W_C = sodium void worth (per unit mass basis)
 M_C = mass of sodium voided.

a. Coolant Boiling

The conditions for coolant boiling are specified by a boiling temperature which includes both the assumed saturation temperature and the superheat. Whenever the sodium temperature reaches the boiling point, the driving force for expulsion of the sodium from the core is obtained by using the cladding temperature at the point of boiling initiation to calculate a pressure (P_1) according to the sodium vapor pressure equation. This essentially assumes the presence of a thin liquid film existing for the duration of the expulsion process. The rate of rise of the cladding temperature, and hence the pressure for sodium expulsion, can be controlled within certain limits by an adjustable parameter.

Further analytical studies are currently in progress to assess the accuracy of this simplified sodium boiling model--particularly to determine whether coolant vaporization from the liquid-void interface can significantly add to the driving pressure.

b. Gas Release

The boiling temperature for loss-of-flow accidents may be above 1200 °K even if no superheat is assumed. At these temperatures, the cladding is relatively weak and may rupture before sodium boiling conditions are attained. If the rupture takes place at the top of the core, which would be the expected location except for a complete flow blockage, the release of fission gases from the plenum above the core could be very rapid because the gases do not have to diffuse through the fuel to reach the cladding rupture. If the accident takes place near the end of life of the fuel, the pressure in the fission gas plenum will be of the order of several hundred psi and the expansion of the released fission gases could result in much faster voiding rates than sodium boiling, depending on how many pins rupture at the same time.

Figure XV.15 contains a comparison of voiding rates, using FTR fuel subassembly geometry and operating conditions, for the above two models during a flow coastdown accident. Voiding is assumed to start at the top of the core where the peak coolant and cladding temperatures occur. The voiding in the downward direction takes longer because the initial momentum of the coolant flow at the start of voiding has to be overcome. It is seen that the fission gas release, assuming that all the pins are ruptured simultaneously, results in a voiding rate approximately seven times faster than sodium boiling assuming 100 °C superheat.

c. Molten Fuel-Coolant Interaction

For rapid power excursions (e.g., reactivity insertions of the order

of 2\$/sec or more), fuel melting will occur prior to sodium boiling. If cladding rupture also occurs, it is possible for the molten fuel to be expelled into the coolant flow channel and be mixed with the sodium. It has been postulated that the violent boiling process could result in a vapor explosion which would give extremely rapid expulsion of the remaining coolant from the core. In the expulsion model for the molten fuel-sodium interaction, it is assumed that the heat transfer rates are so rapid that thermal equilibrium between the molten fuel and the sodium is attained. It is further assumed that the relative amounts of molten fuel and sodium are such that the sodium in one axial layer of the MELT-II simulation of the core is heated to the melting point of the fuel (approximately 3040 °K). At this supercritical temperature, the pressure of the sodium is approximately 700 atm. The decrease in pressure as the sodium volume increases due to voiding is determined from a thermodynamic analysis of an adiabatic expansion process.

It is possible that a molten fuel-sodium interaction may not take place even though molten fuel is expelled into the coolant flow channels. Recent experiments using a sodium autoclave in the TREAT reactor have indicated that the fission and/or fill gas contained within the fuel region can blanket the molten fuel particles from the sodium and prevent the rapid energy transfer. The expansion of this gas could also be sufficient for expelling the sodium from the core. However, it is difficult to determine how much gas is available within the core region and whether the gas in the fission gas plenum would also be available.

Figure XV.16 compares the voiding rates for the molten fuel-sodium interaction and fission gas release during a large reactivity insertion accident. The voiding is assumed to start near the center of the core since

the maximum amount of fuel melting occurs at that location. The sodium expansion following the molten fuel-sodium interaction gives a 40% faster voiding rate than the fission gas release even though all of the fission gas in the plenum was assumed to be available for expansion. If a molten fuel-sodium interaction could originate from the center of a large core, the extremely rapid voiding rate (approximately 12 milliseconds) would result in a very large rate of reactivity insertion.

G. Progression of a Power Transient

The primary purpose of this lecture is to outline models and methods rather than to present results. Because of the number of interactions which can occur during a transient, however, it is perhaps worthwhile to present the results of a few selected cases to illustrate how the various models tie together. No attempt will be made, however, to present a parametric study.

For the examples given, the pertinent core parameters used are those summarized below.

TABLE XV.2

Core Parameters used for Transient Analysis

Core Height	91.4 cm
Core Radius	60.0 cm
Core Volume	1034 liters
Core Density	5.5 g/cm ³
Fuel Density	3.0 g/cm ³
Fuel Loading	3100 kg
Initial Neutronics Power Level	380 MW
Delayed Neutron Fraction	0.0030
Neutron Generation Time	5 x 10 ⁻⁷ sec
Doppler Coefficient (T dk/dT)	- 0.005
Central Fuel Worth	2.8 x 10 ⁻⁴ δk/kg
Central Sodium Void Worth	16 x 10 ⁻⁵ δk/kg
Worth of Voiding "Dome"	3.30 \$
Worth of Total Core Voiding	0.65 \$
Worth of Voiding Core Plus Upper & Lower Axial Reflectors	- 1.40 \$

The core was geometrically subdivided, for analytical purposes, into six channels (rings) -- each corresponding to an actual ring of subassemblies as indicated in Figure XV.17. This was deemed to be a reasonable division since one would expect flow patterns, at least on a gross scale, to behave

similarly throughout a particular subassembly but not necessarily between adjacent subassemblies. The basic assumption made, therefore, was that flow and power may vary independently between radial subassemblies but remain uniform in subassemblies at the same radial distance from the core center. Eighteen axial nodes within the active core region were used. The set of sodium void worth curves used is shown in Figure XV.18.

1. 5\$/sec Ramp Case

A 5\$/sec ramp rate accident, although quite severe in a real sense, is normally considered mild when one contemplates Design Basis Accident candidates. Clearly the only real concern for this case arises from possible reactivity feedback effects which could aggravate the accident. Since power transients of this magnitude or higher will almost certainly result in cladding rupture prior to coolant boiling, the concern really centers around the manner in which molten fuel will move under these conditions and, perhaps more importantly, the way sodium might be ejected.

Since potential methods of positive reactivity feedback are the main issue for this case, the axial position of cladding rupture is quite important. The hottest pins in the reactor will have an inner void, prior to the transient, extending nearly the full length of the pin. Therefore, as melting progresses and fission products are released, one might expect the entire molten region occupying the original void space to be at nearly the same pressure throughout. Since the peak cladding temperature occurs near the top of the pin, one might logically expect the cladding to fail at that point. Reactivity due to voiding at this location would be initially negative--quite the opposite from the situation arising should cladding rupture occur at the axial center. For the case investigated, however, the predicted time of failure of the cladding

near the top of the core relative to the center of the core was quite small. Hence, for the sake of conservatism, failure at the center was assumed.

Figure XV.19 contains the reactivity balance which developed for this case. At the point where the net reactivity nears one dollar (the prompt critical point) the fuel temperatures rise rapidly and the resulting Doppler feedback holds the net reactivity just below one dollar until the point of initial cladding rupture is attained. For the example given, a molten fuel-sodium interaction was assumed to occur at the time of cladding rupture and, as can be seen, the reactivity feedback due to sodium expulsion was extremely rapid. Figure XV.20 contains an enlargement of the net reactivity as well as the void and collapse reactivity feedback terms starting at the point of initial cladding rupture. Also sketched in on the figure is the time at which fuel temperatures rose to the point where a negative feedback due to core disassembly should be included. The rate of reactivity feedback due to sodium voiding is noted to be in the range of 400 $\$/\text{sec}$ whereas the feedback due to fuel collapse, assuming the gravity slumping model, is completely negligible. This is simply due to the fact that the rapid sodium feedback elevates core temperatures so fast that very little time is available for collapse to occur prior to reaching the core disassembly condition.

It should be clearly noted, at this point, that the accident sequence just described by no means completes the analysis. As will be shown in the following lecture, wherein the disassembly phase will be described, core conditions at the point of transfer to the disassembly phase are quite important in determining the final nuclear energy generated in the overall excursion. For the case just discussed, for example, the 400 $\$/\text{sec}$ ramp rate does not cause undue concern because sodium yet remains in most of the core and this substantially mitigates the magnitude of the overall energy generated.

2. Sodium Bubble

One of the accidents often considered as a DBA candidate for fast reactors is that of a large bubble (void) passing the core at normal coolant flow velocity. To provide an upper bound to the reactivity consequences of such an event, the passage of a bubble of such size as to envelop just the region of the core corresponding to the exact size of the positive sodium dome was considered.

As the bubble first enters the lower reflector region the reactivity effect is negative and the power level drops (see Figures XV.21 and XV.22). Since an effectively zero film coefficient is assumed for those coolant regions which are voided, there is a tendency for fuel temperatures to rise. However, the power drop more than offsets this effect and the resulting lower fuel temperatures actually result in a small positive Doppler feedback. Eventually the bubble enters the positive sodium void dome region and reactivity is gained. As liquid sodium re-enters the lower reflector an additional positive reactivity insertion is obtained and the moving bubble induced reactivity ramp rate at the time core disassembly conditions are established is nearly 80\$/second.

For all bubble type accidents which generate a substantial amount of molten fuel, clad rupture and subsequent spewing of molten fuel into the coolant channel is a definite possibility. The relevant question, as discussed in a previous section, relates to the location of cladding failure and the type of fuel motion which follows. A molten fuel-sodium interaction is difficult to imagine if the rupture point is enveloped by the bubble, particularly if the bubble contains a high void fraction. Rupture near the core top, although perhaps occurring in a region still containing all liquid sodium, could only result in negative reactivity effects due to voiding.

The compaction of molten fuel near the core center, should cladding rupture occur at that place, could present a problem. Perhaps the main concern arises near end-of-life conditions where the large internal fission gas pressure could theoretically squirt the molten fuel into the coolant channel at a very rapid rate. However, the resistance to flow caused by frozen fuel in the immediate vicinity, the potentially obstructed path interfering with efficient communication between the driving pressure and the molten fuel, and the availability of relatively cold cladding which could provide an efficient heat sink for fuel resolidification, all provide cogent arguments to support a molten fuel squirting rate to be far less than its theoretical upper limit.

In order to get some feeling for the sensitivity of the results to the possible rapid insertion of reactivity due to fuel relocation, the very conservative (and, perhaps totally unrealistic) fuel squirting model was employed as a complication to the case just considered. The reactivity ramp rate at the time of disassembly was augmented to nearly 300\$/sec. However, because of the extremely conservative squirting model used this case is not considered to be of significant interest.

H. Progression of a Loss of Flow Transient

Because of the basically different nature of a loss-of-flow type accident, relative to the power transients discussed above, it is perhaps of interest to briefly consider the sequence of events which might occur for such excursions. Figure XV.23 contains the flow reduction versus time assumed for the flow coastdown and pipe rupture accidents to be described.

1. Flow Coastdown

Transient analyses on the flow coastdown accident (loss of power to the pumps) reveal that both coolant and cladding temperatures peak at the top core-reflector interface and failure would be expected at that axial location. There is a question as to whether the initial failure mechanism will be sodium flashing and subsequent coolant expulsion, or cladding rupture and release of fission gas -- which could also result in coolant expulsion. Fuel temperatures are far too low to be of direct concern from a failure mechanism standpoint. For this case, however, the transient appears to be sufficiently slow that even for an assumed superheat of 100 °K, prior to flashing, the cladding is cool enough to retain its integrity. Hence, sodium flashing is assumed to be the mechanism for coolant expulsion.

Figure XV.24 illustrates the transient response calculated. As noted from the graph, voiding began in the hottest channel at about 5.4 seconds after loss of power to the pumps. Because of the incoherence associated with coolant flashing in the remaining radial channels, the total reactivity due to voiding never exceeded 1.50 dollars. Ultimately the entire core plus both axial reflectors voided (in about 7 seconds after the start of the accident) and the net reactivity dropped to nearly -2.00 dollars. Eventually, if the coolant were to remain outside of the core, fuel melting would propagate to

the outer region of the fuel column and core collapse could possibly cause a secondary excursion. The rate of collapse, under the conditions, would almost certainly be bounded by gravitational forces, since all hydraulic and internal pin forces would be absent. However, for the case considered, fuel melting did not propagate completely across the fuel column in the hottest pin until nearly 11 seconds. Coolant re-entry would almost assuredly occur prior to this time.

2. Pipe Rupture

A massive pipe rupture in one of the three feeder pipes could result in a sudden depressurization of the inlet plenum and an immediate drop in flow to about 10 percent. As the stand pipe begins to fill, however, flow is reestablished to about 30% of full flow and a gradual coastdown is expected thereafter. This explains the flow versus time curve depicted in Figure 16 23.

The much faster drop in flow for this case, relative to the flow coastdown accident, causes initial failure to occur much earlier, i.e. about 1.3 seconds. Further, calculations indicate cladding failure will likely precede coolant boiling. Hence, the coolant ejection mechanism was assumed to be the sudden release of fission product gases into the coolant channel. Expulsion rates, due to this mechanism, have been computed to be approximately seven times faster than that due to coolant flashing at 100 °K superheat. This faster voiding rate is evident from the transient response curve shown in Figure XV.25.

As in the flow coastdown accident, however, the incoherence of radial channel voiding patterns held the peak reactivity due to voiding to well under 2.00 dollars and the entire core plus both axial reflectors voided

prior to the attainment of fuel temperatures high enough to exert a significant ,
disassembly force within the core.

I. Review of Current Fast Reactor Accident Analysis Codes

To conclude this lecture, perhaps brief mention should be made of parallel work being conducted at other laboratories. Certainly those codes mentioned here are not inclusive, but they may serve to indicate the type of activity and interest developing in the field. Finally, only those codes dealing with the predisassembly phase will be here mentioned; disassembly codes will be discussed in Lecture XVI.

Perhaps the accident code system into which the most effort has been expended is the SAS-IA system developed at Argonne. The emphasis in this code has apparently been to mock up a single fuel pin with considerable detail at the expense of limiting the code model to that of a single channel. Fuel is allowed to expand radially and flow axially within the cladding prior to cladding rupture. Pressure within the fuel pin, due to thermal expansion, is correlated with cladding strength to determine the location of cladding failure. In the original code, internal pressure resulting from the release of fission gases was not included, although it is believed that such a capability is presently being incorporated. Sodium voiding models include an annular flow as well as a slug flow. A modified version of the MARS disassembly code is available as a subroutine so that an excursion can be followed through the nuclear disassembly phase. Most, if not all, of the feedback mechanisms discussed for MELT-II are available in the code although, because of the limitation to a single channel, feedback incoherence is difficult to model.

General Electric at Sunnyvale is currently developing a multichannel meltdown code entitled FREADM. Because it is apparently still in the active development stages, not enough information has yet been published to allow

full assessment of its utility. The code appears to have a smaller nodal capacity than MELT-II but efforts have apparently been made to couple the coolant channels hydraulically and to reduce computer running time by minimizing the frequency of performing detailed heat transfer calculations. Both of these features appear attractive.

A computer program entitled TART has been written at Babcock and Wilcox in which a spatial kinetics package can be used to replace the point kinetics routine. As in the case of FREADM, the code is quite new and not enough information has yet appeared to provide basis for significant comment.

References

1. A. E. Waltar, R. A. Harris and A. Padilla, Jr., "Considerations of Sodium Conditions and Molten Fuel/Sodium Interactions for Fast Reactor Excursion Calculations," Trans. Am. Nucl. Society, 11, 694 (1968).
2. A. E. Waltar, MELT-I, A Simplified Meltdown Code for Fast Reactor Safety Analysis, BNWL-944, Battelle-Northwest, Richland, Washington, December 1968.
3. G. J. Fischer et al., "Fast Reactor Accident Study Code SAS-1A," Conf. Effective Use of Computers in the Nuclear Industry, Oak Ridge National Laboratory, (April 20-23, 1969).
4. D. D. Freeman, "Coupling of Dynamics Calculations in the FREADM Code", Conf. Effective Use of Computers in the Nuclear Industry, Oak Ridge National Laboratory (April 20-23, 1969).
5. M. G. Stevenson and B. E. Bingham, "TART, An LMFBR Transient Analysis Project," Conf. Effective Use of Computers in the Nuclear Industry, Oak Ridge National Laboratory (April 20-23, 1969).
6. W. W. Little, Jr., K-III, A Three Region Kinetics Code in FORTRAN-IV, BNWL-252, Battelle-Northwest, Richland, Washington, June 1966.
7. K. F. Hansen, B. V. Koen, and W. W. Little, Jr., "Stable Numerical Solutions to the Reactor Kinetics Equations," Nucl. Sci. and Eng., Vol. 22, pp. 51-59 (May, 1965).
8. J. N. Fox, B. E. Lawler, and H. R. Butz, "FORE II: A Computational Program for the Analysis of Steady-State and Transient Reactor Performance," GEAP-5273, September 1966.
9. "FFTF Monthly Informal Technical Progress Report - December 1966", BNWL-CC-973, Battelle-Northwest, Richland, Washington.
10. L. J. Koch et al., Hazard Summary Report - Experimental Breeder Reactor -II (EBR-II), ANL-5719, Argonne National Laboratory, May, 1957.

See also

L. J. Koch et al., Addendum to Hazard Summary Report - Experimental Breeder Reactor-II (EBR-II), ANL-5719 (Addendum), Argonne National Laboratory, June, 1962.

11. Enrico Fermi Atomic Power Plant, Technical Information and Hazard Summary Report, Part B, Vol. 7, NP-11526, available from clearinghouse for Federal Scientific and Technical Information, Springfield, Virginia, 1961.

MELTDOWN MODEL

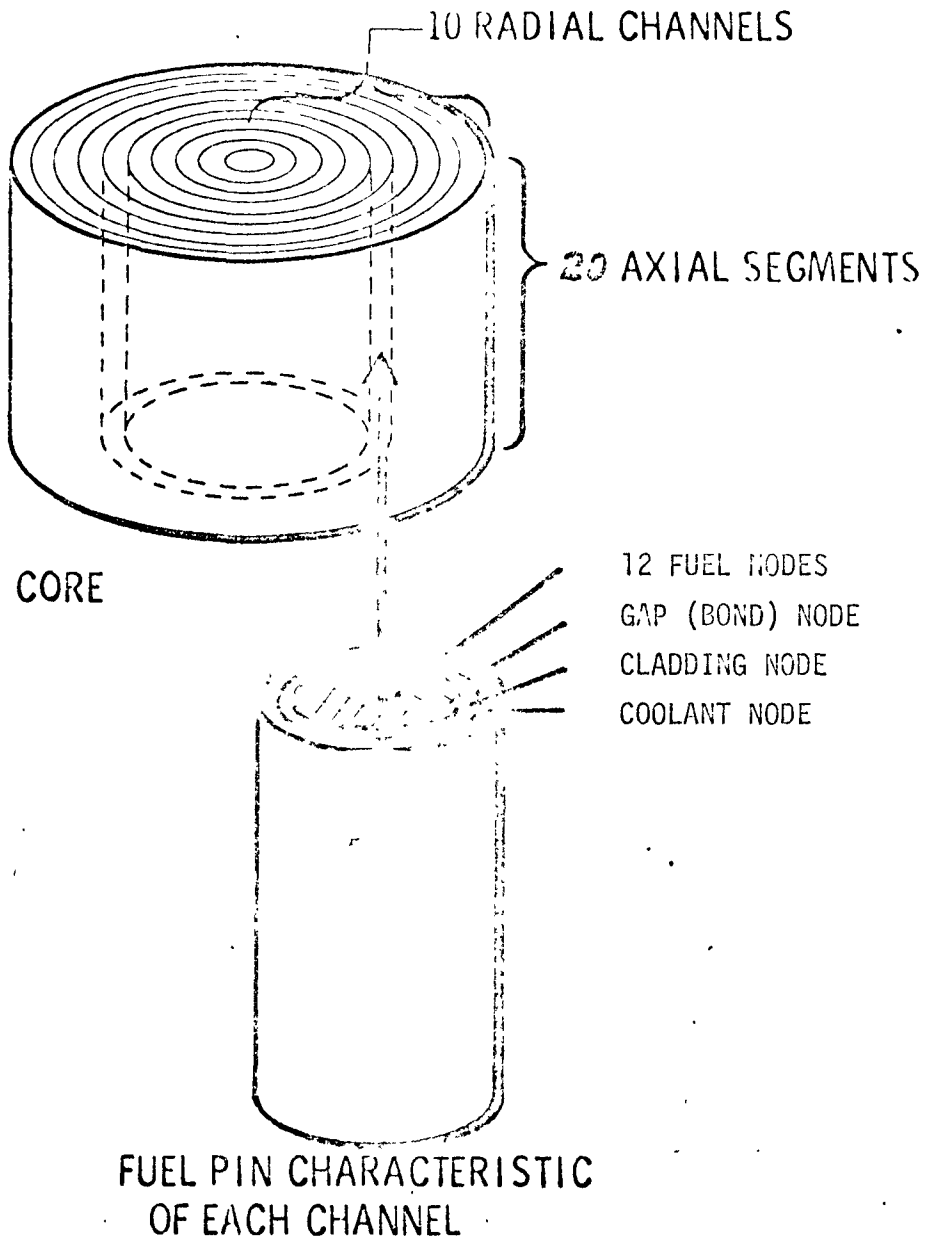


Fig. XV.1 Core Geometry Used in the Meltdown Model

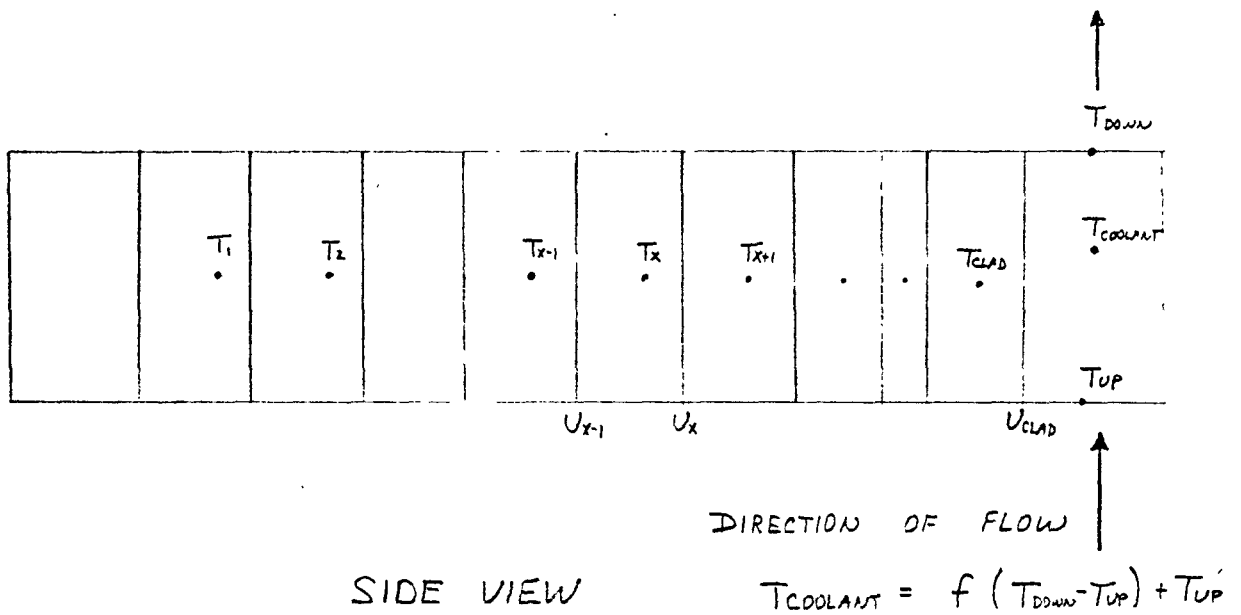
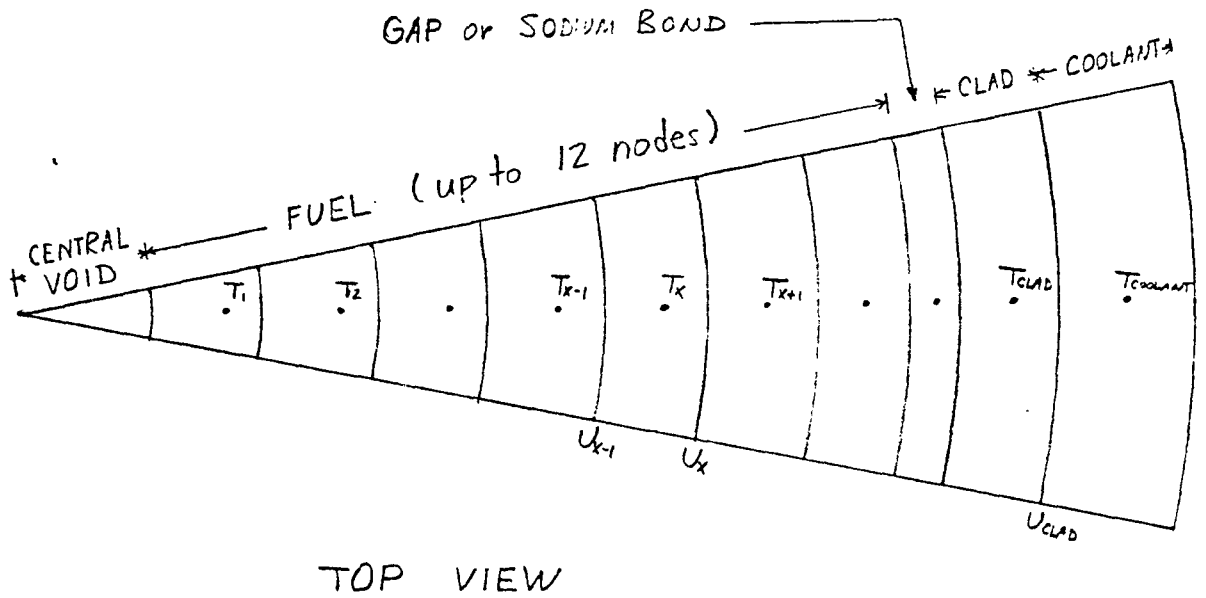


Fig. XV.2 RADIAL PIN GEOMETRY USED IN HEAT TRANSFER CALCULATIONS

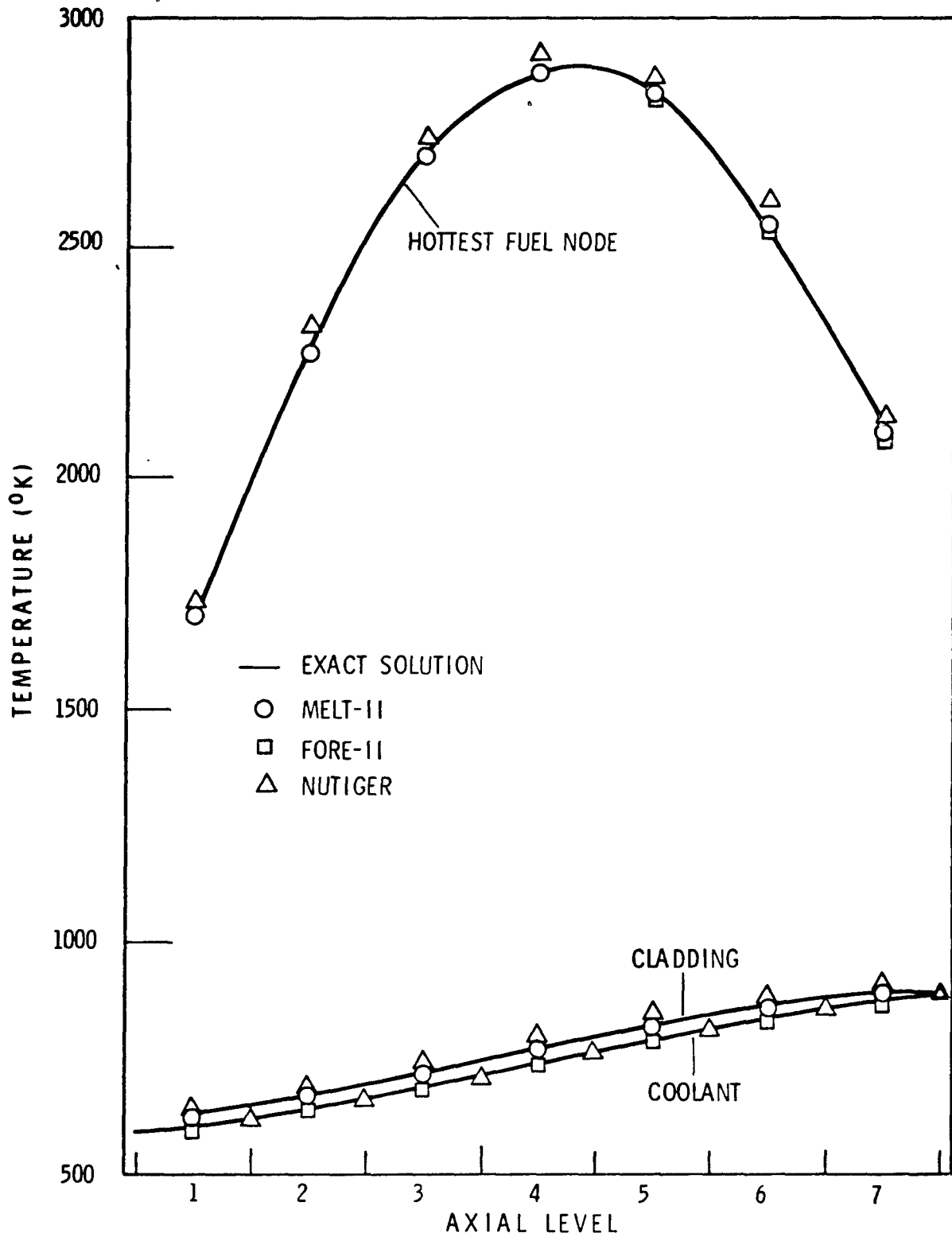


Fig. XV.3 Comparison of Steady-State Axial Temperature Distribution

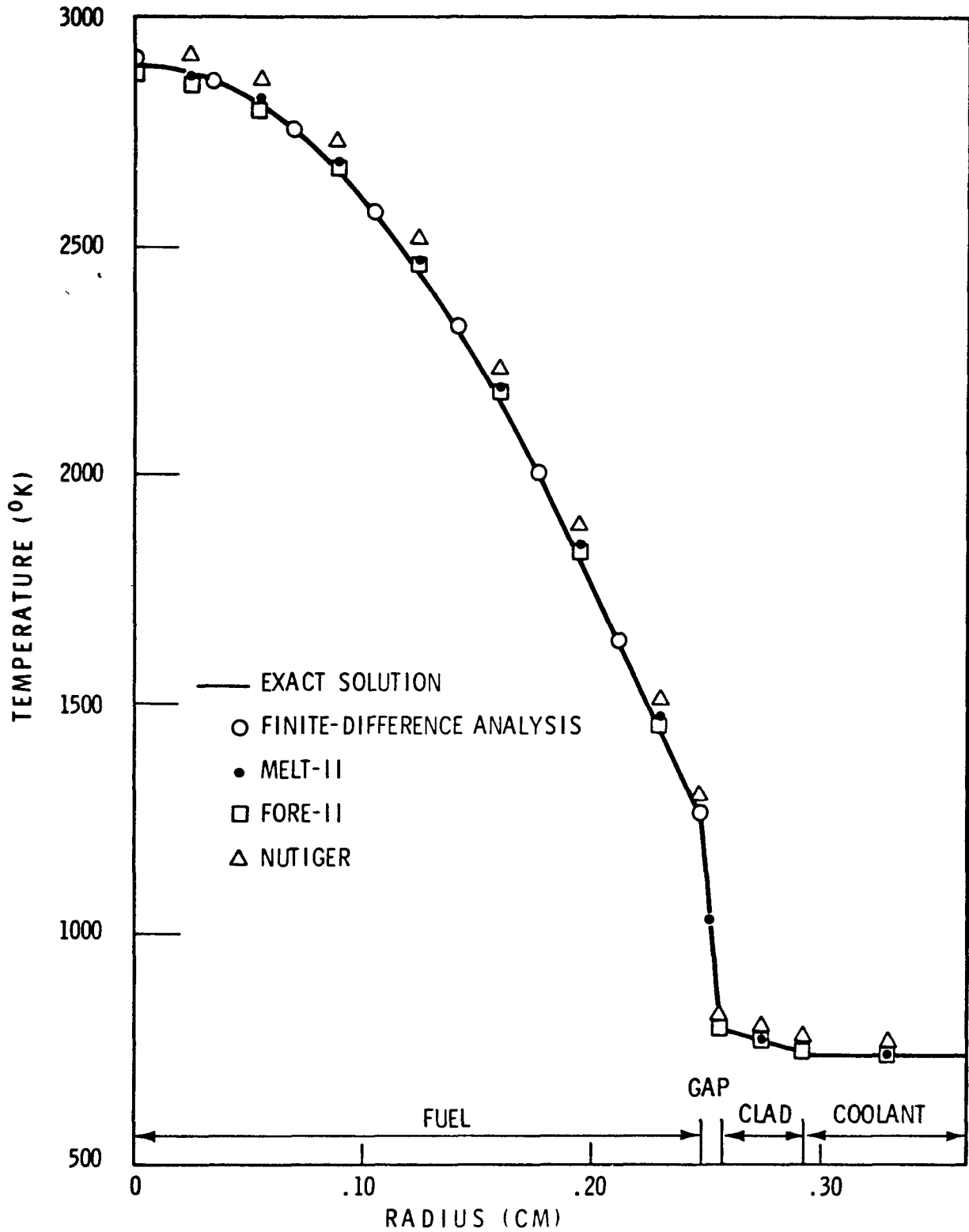


Fig. XV.4 Comparison of Steady-State Radial Temperature Distributions

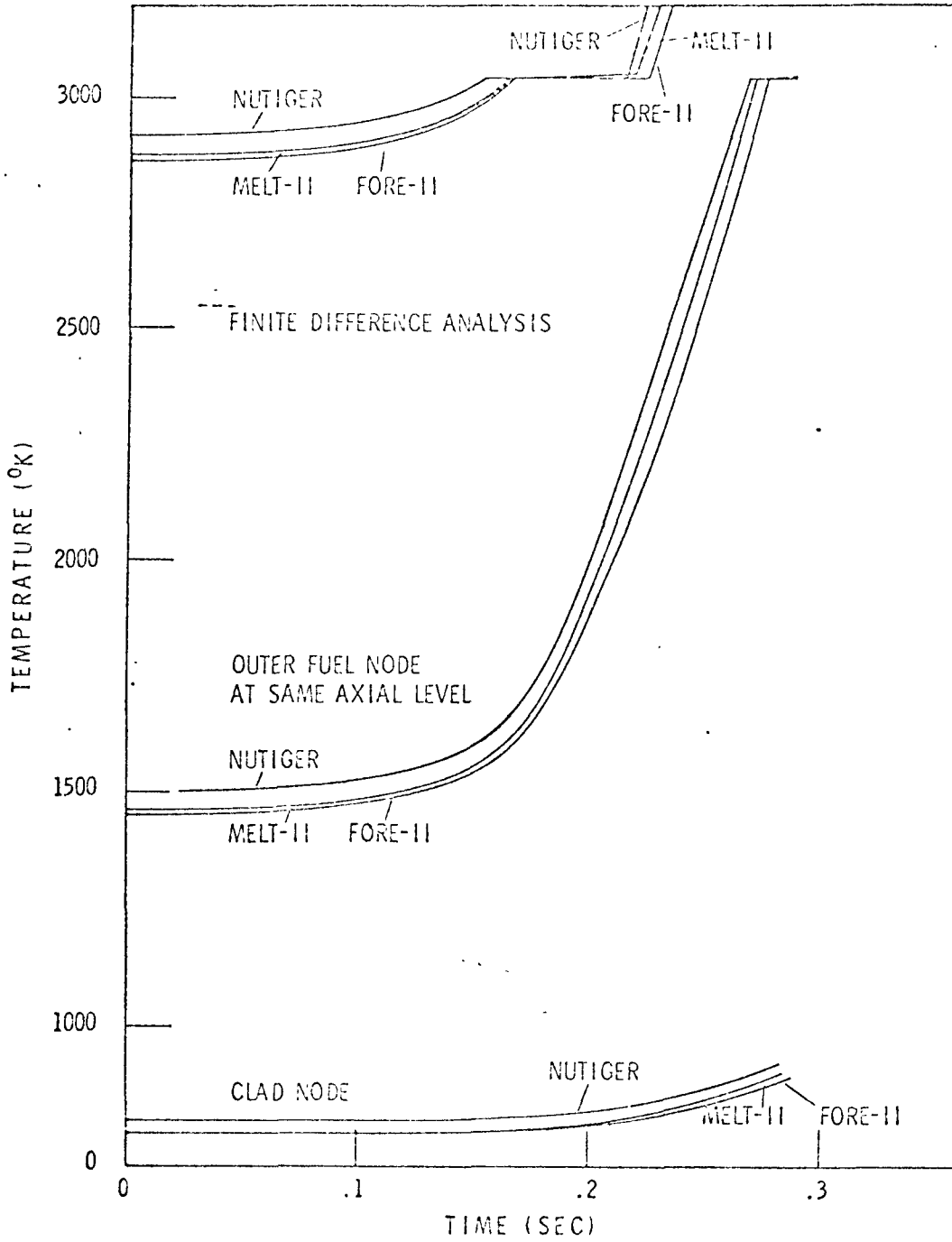


Fig. XV.5 COMPARISON OF TRANSIENT TEMPERATURES (6\$/SEC RAMP)

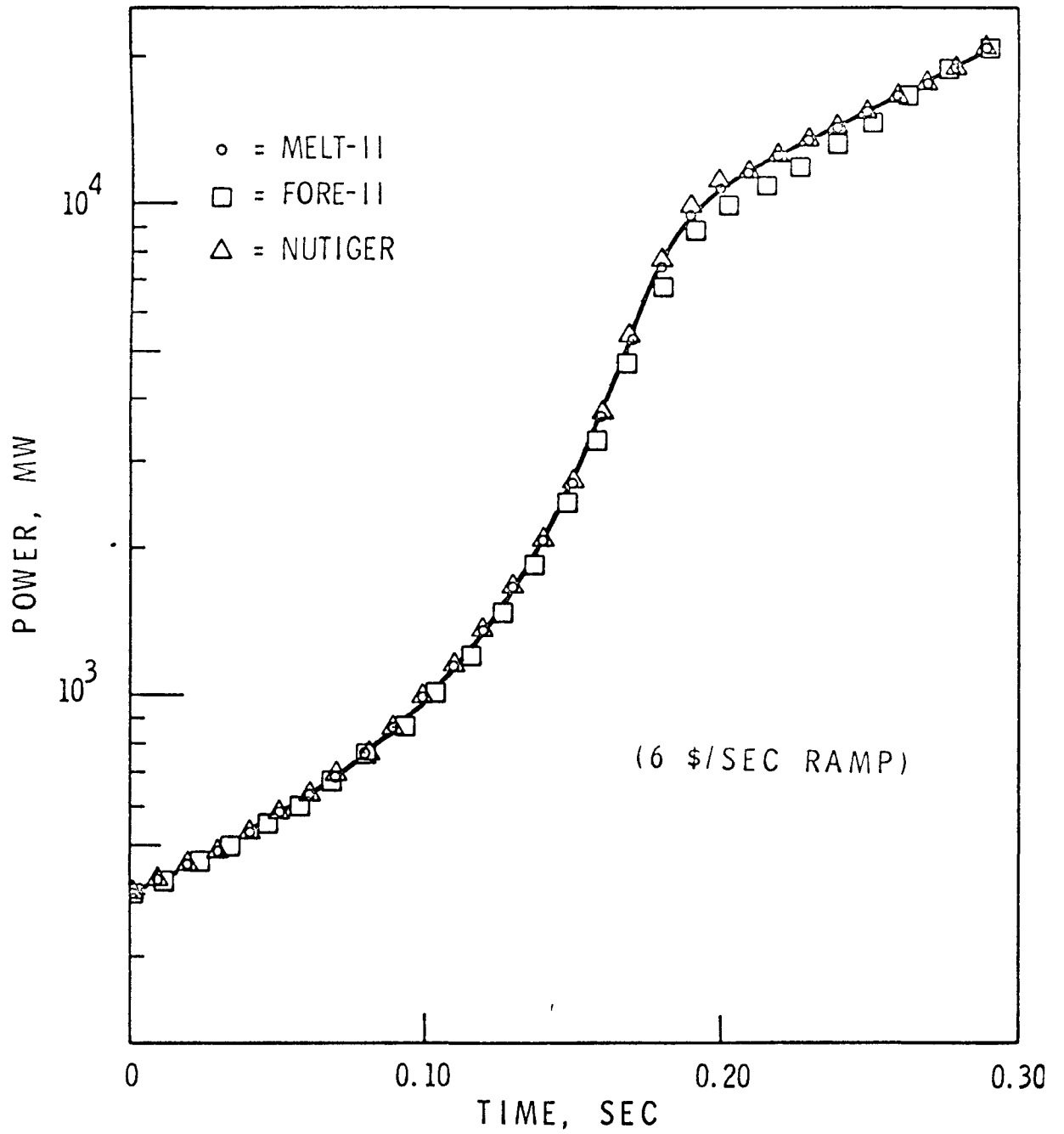


Fig. XV.6 COMPARISON OF POWER GENERATION (6\$/SEC RAMP)

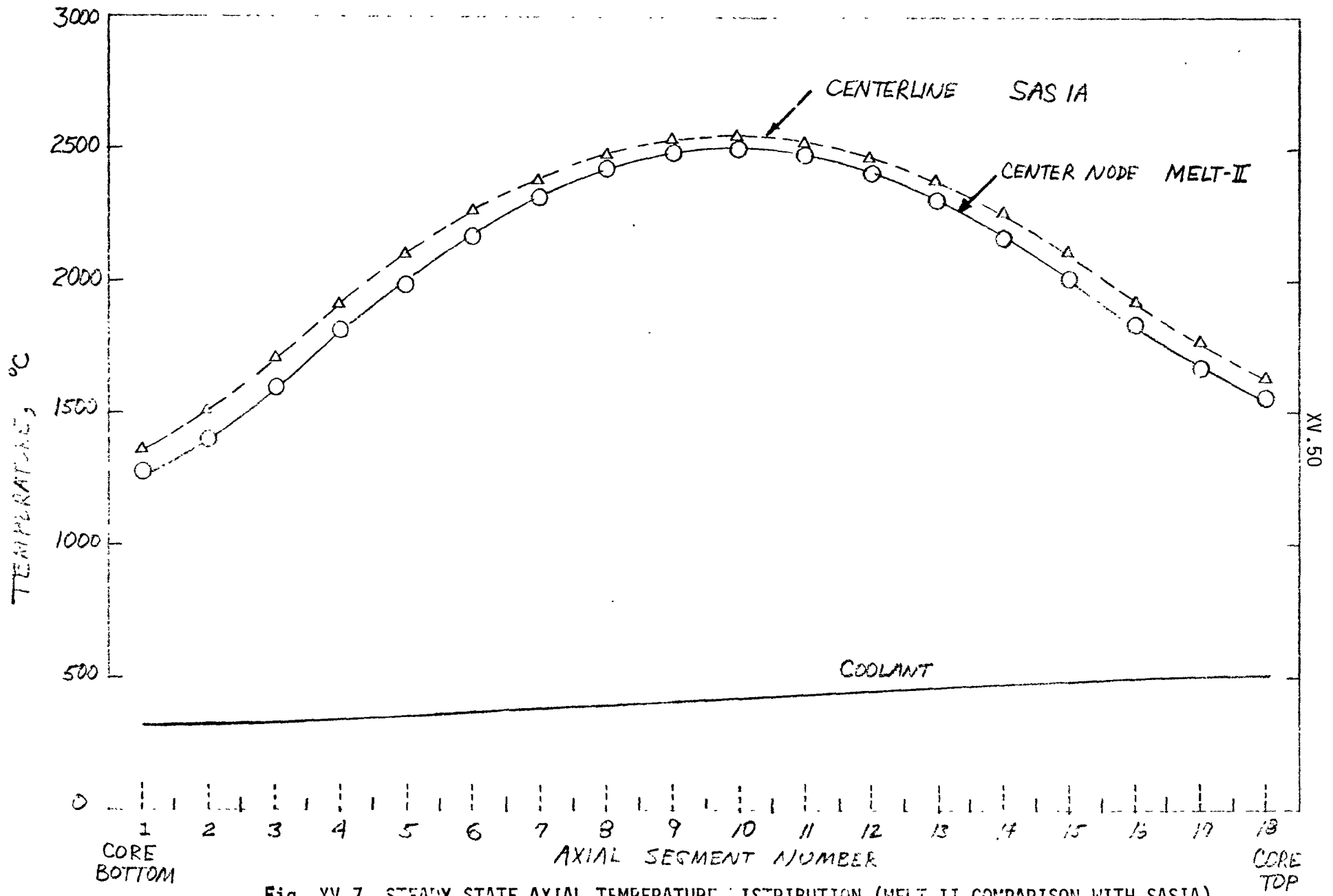


Fig. XV.7 STEADY STATE AXIAL TEMPERATURE DISTRIBUTION (MELT-II COMPARISON WITH SASIA)

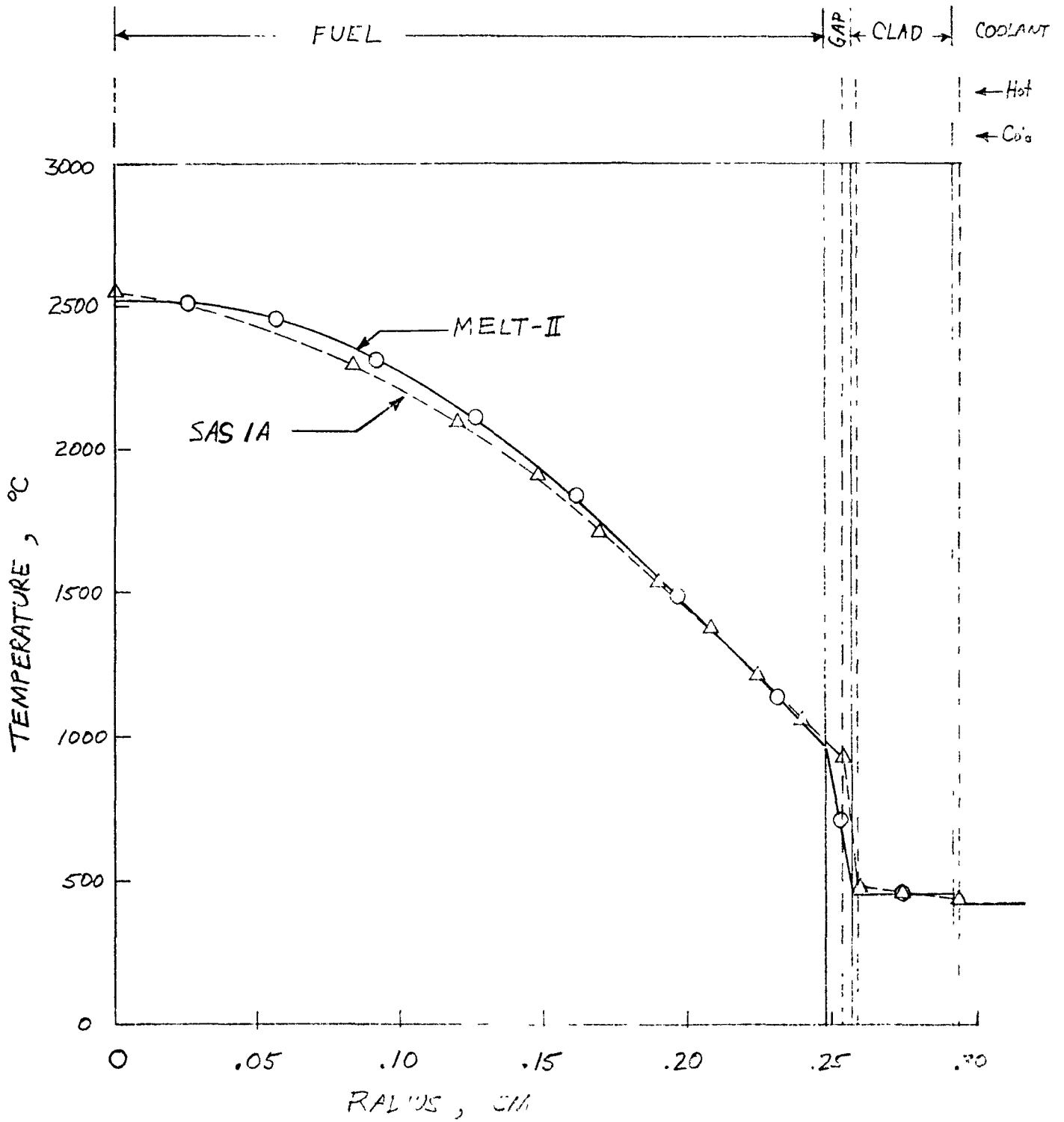


Fig. XV.8 STEADY STATE RADIAL TEMPERATURE DISTRIBUTION (MELT-II COMPARISON WITH SASIA)

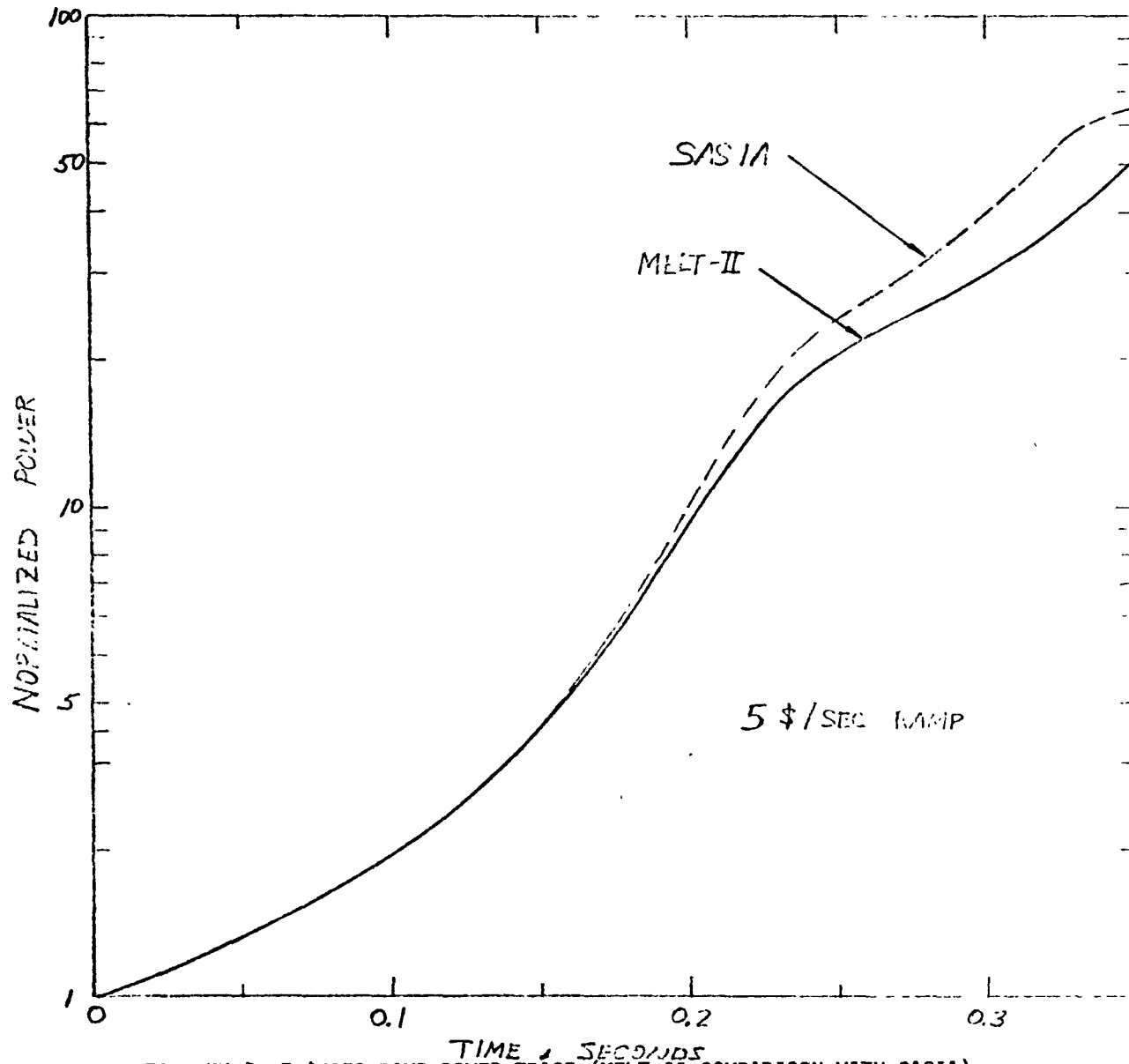


Fig. XV.9 5 \$/SEC RAMP POWER TRACE (MELT-II COMPARISON WITH SASIA)

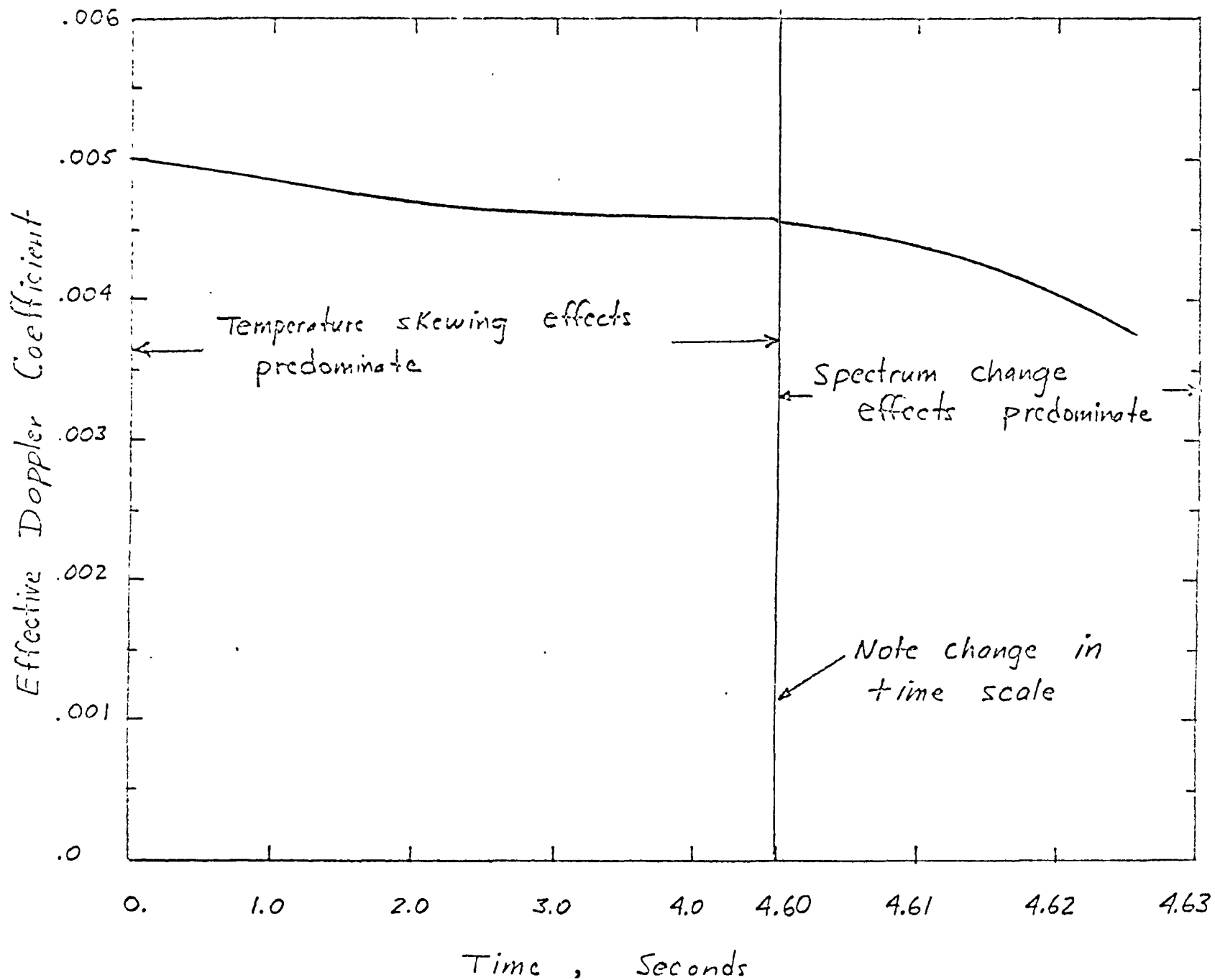


Fig. XV.10 CHANGES IN THE EFFECTIVE DOPPLER COEFFICIENT DURING A HYPOTHETICAL PIPE RUPTURE ACCIDENT

XV.54

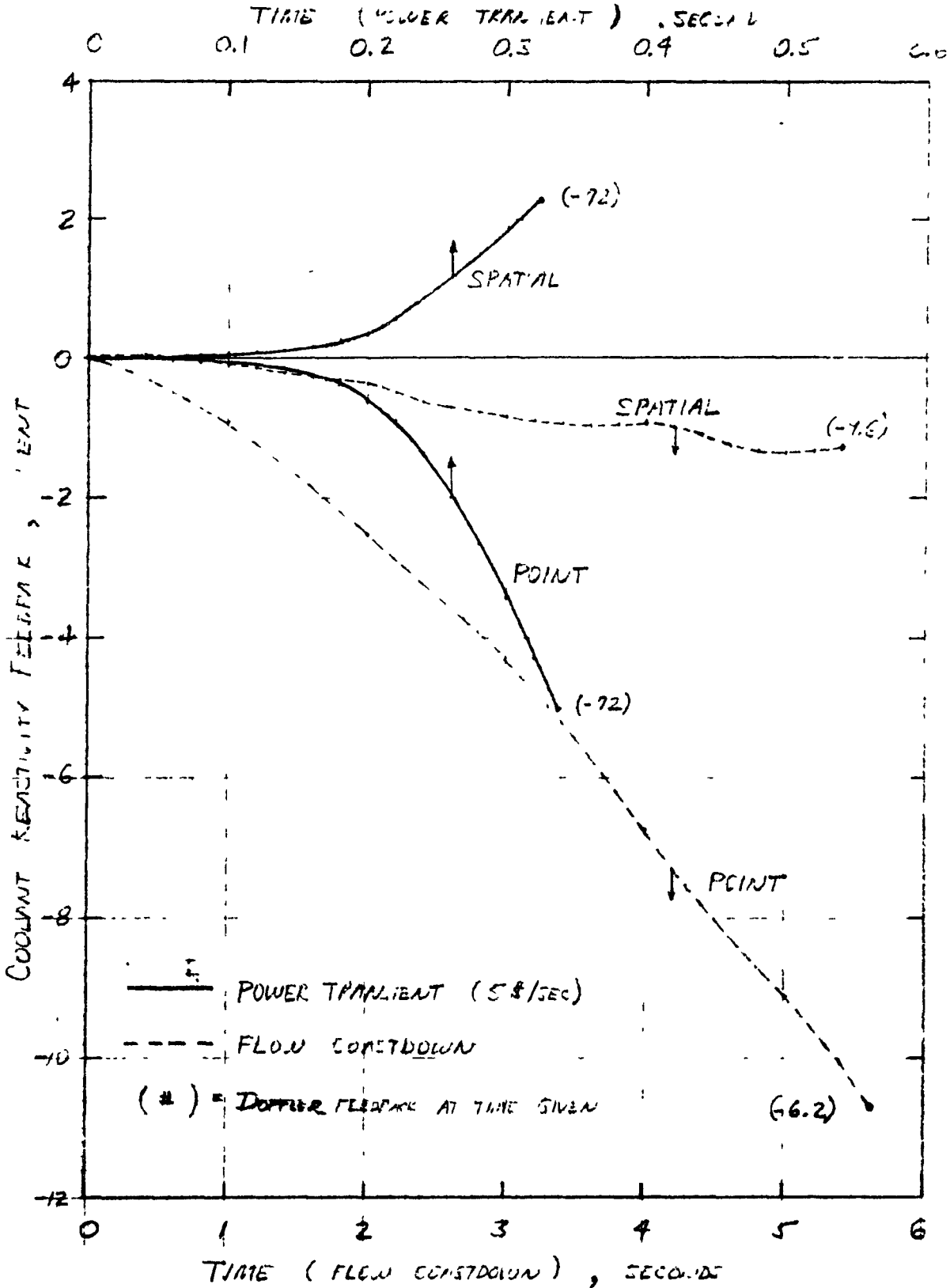


Fig. XV.11 COOLANT REACTIVITY FEEDBACK FOR POWER TRANSIENT AND FLOW COASTDOWN ACCIDENT (COMPARISON OF SPATIAL VERSUS LUMPED TREATMENT)

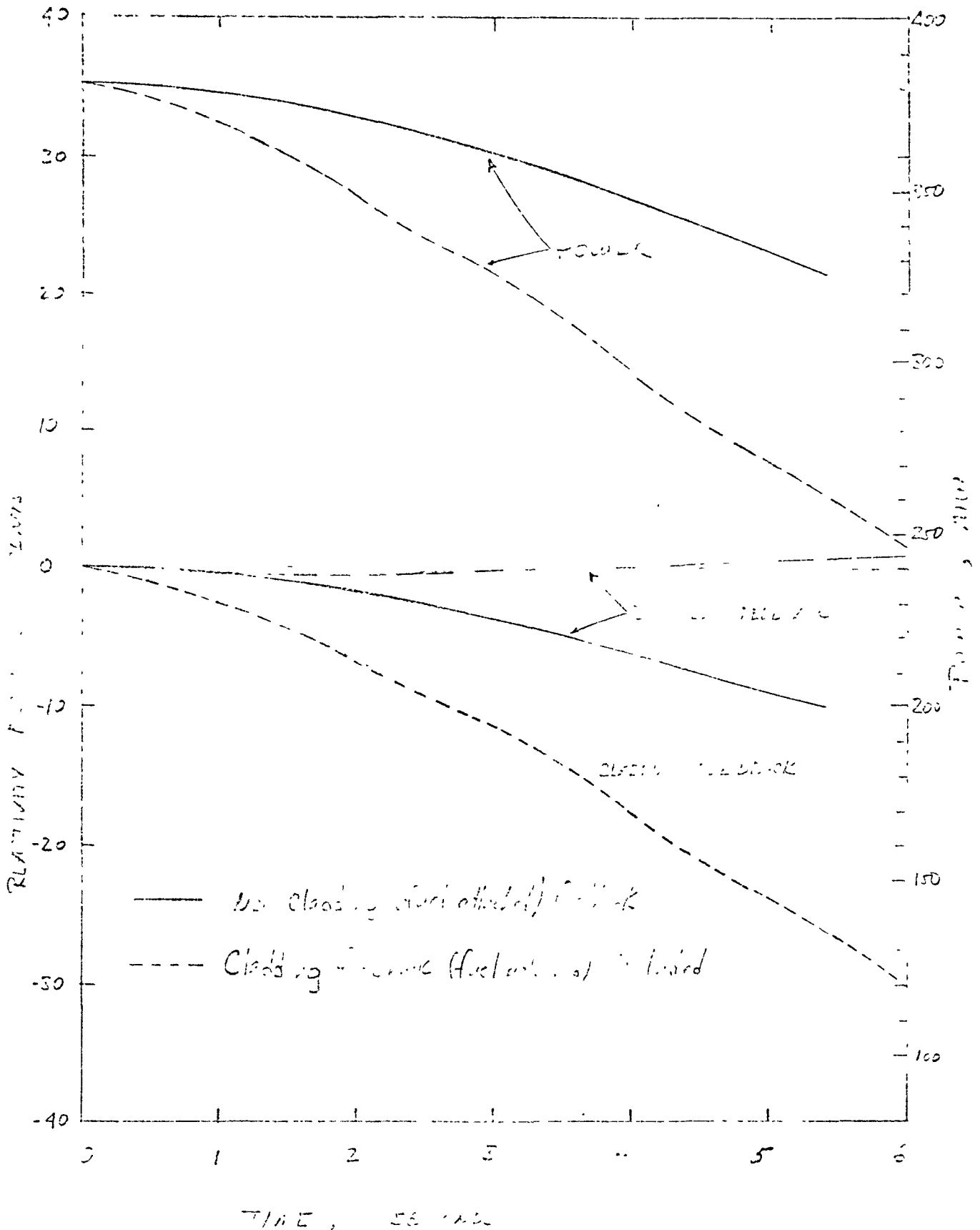


Fig. XV.12 FEEDBACK FROM AXIAL FUEL EXPANSION DUE TO CLADDING ELONGATION FOR A FLOW COASTDOWN ACCIDENT

PIN SLUMPING MODEL

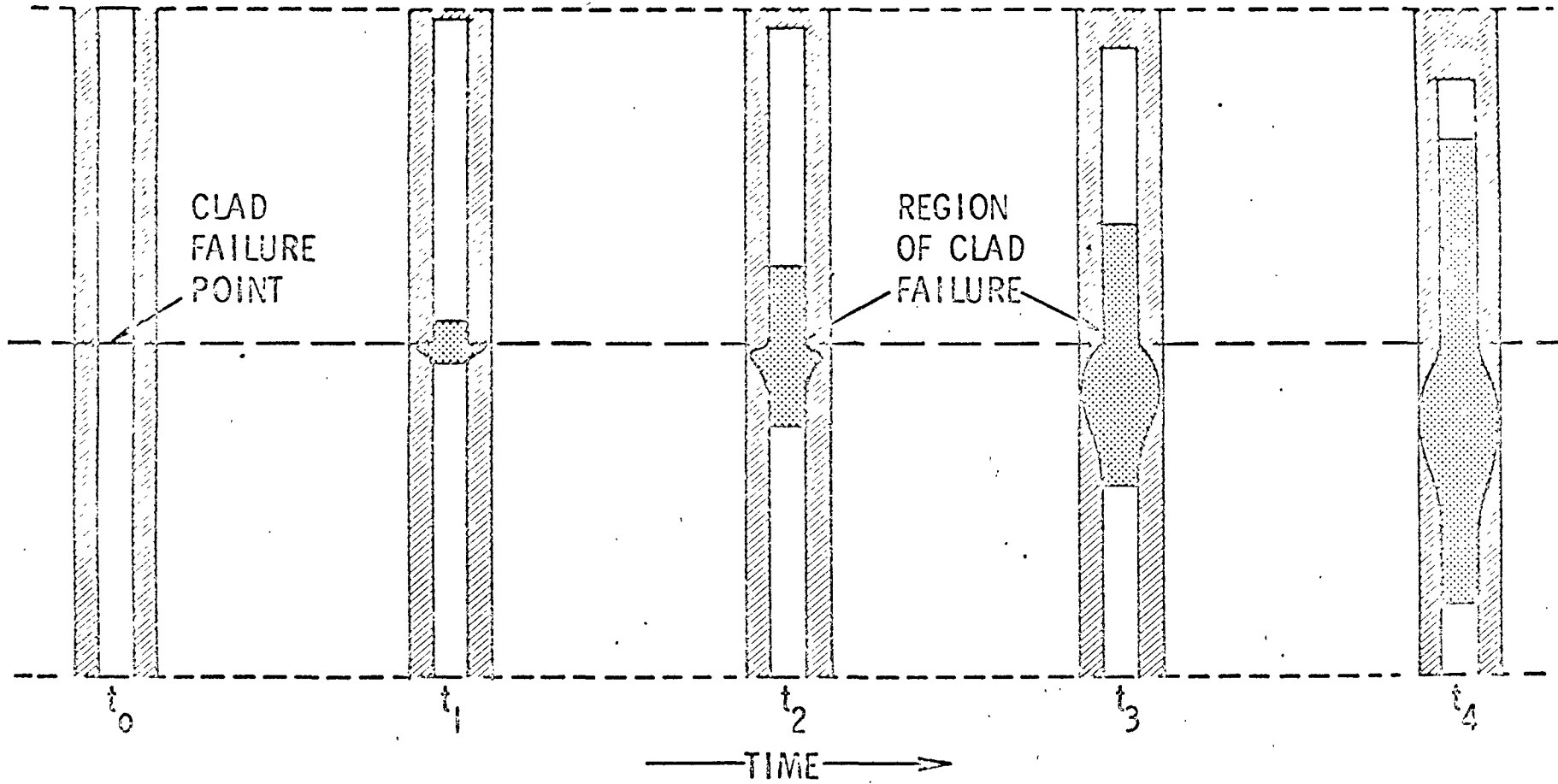


Fig. XV.13 PIN SLUMPING MODEL

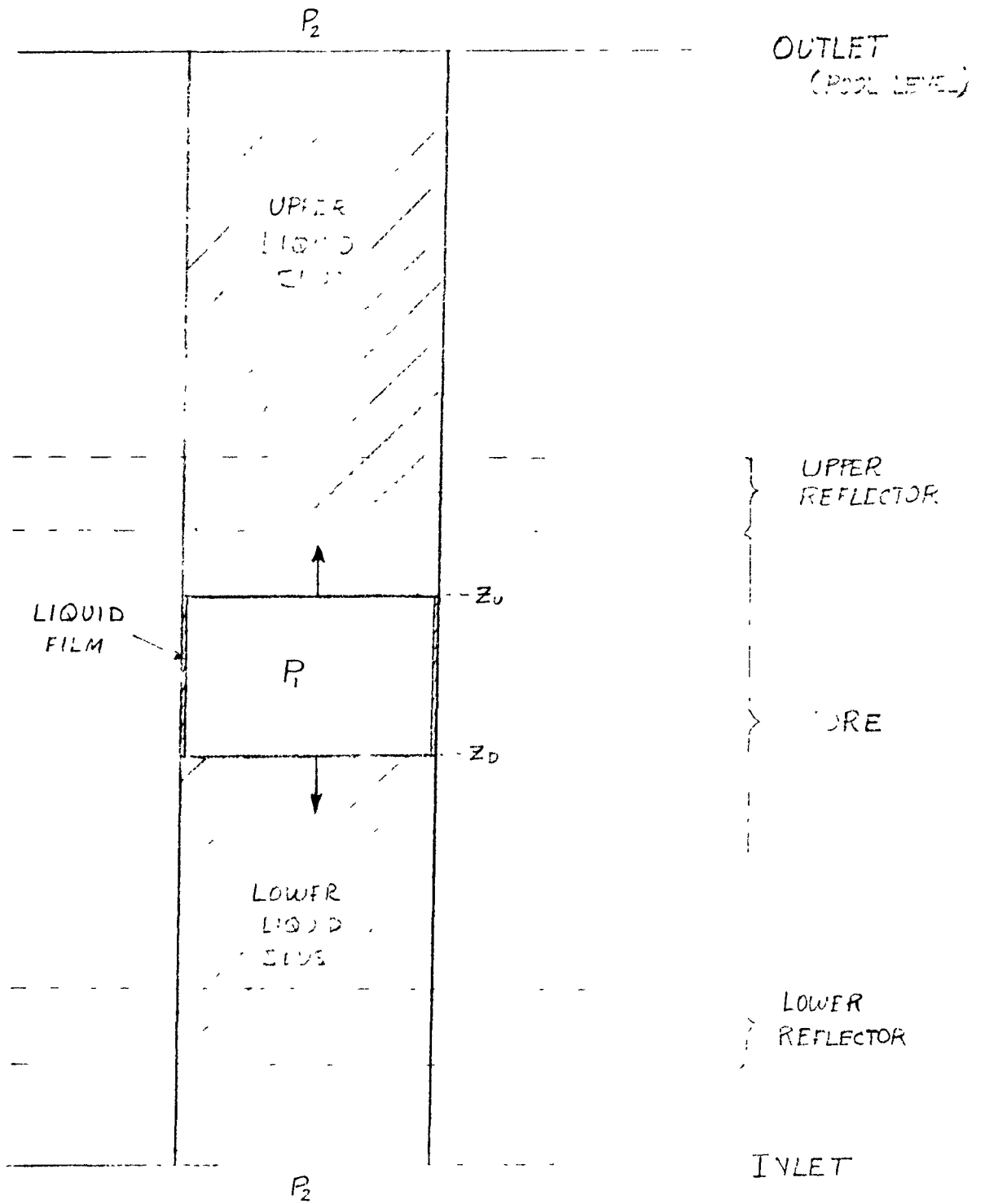


Fig. XV.14 SODIUM VOIDING MODEL

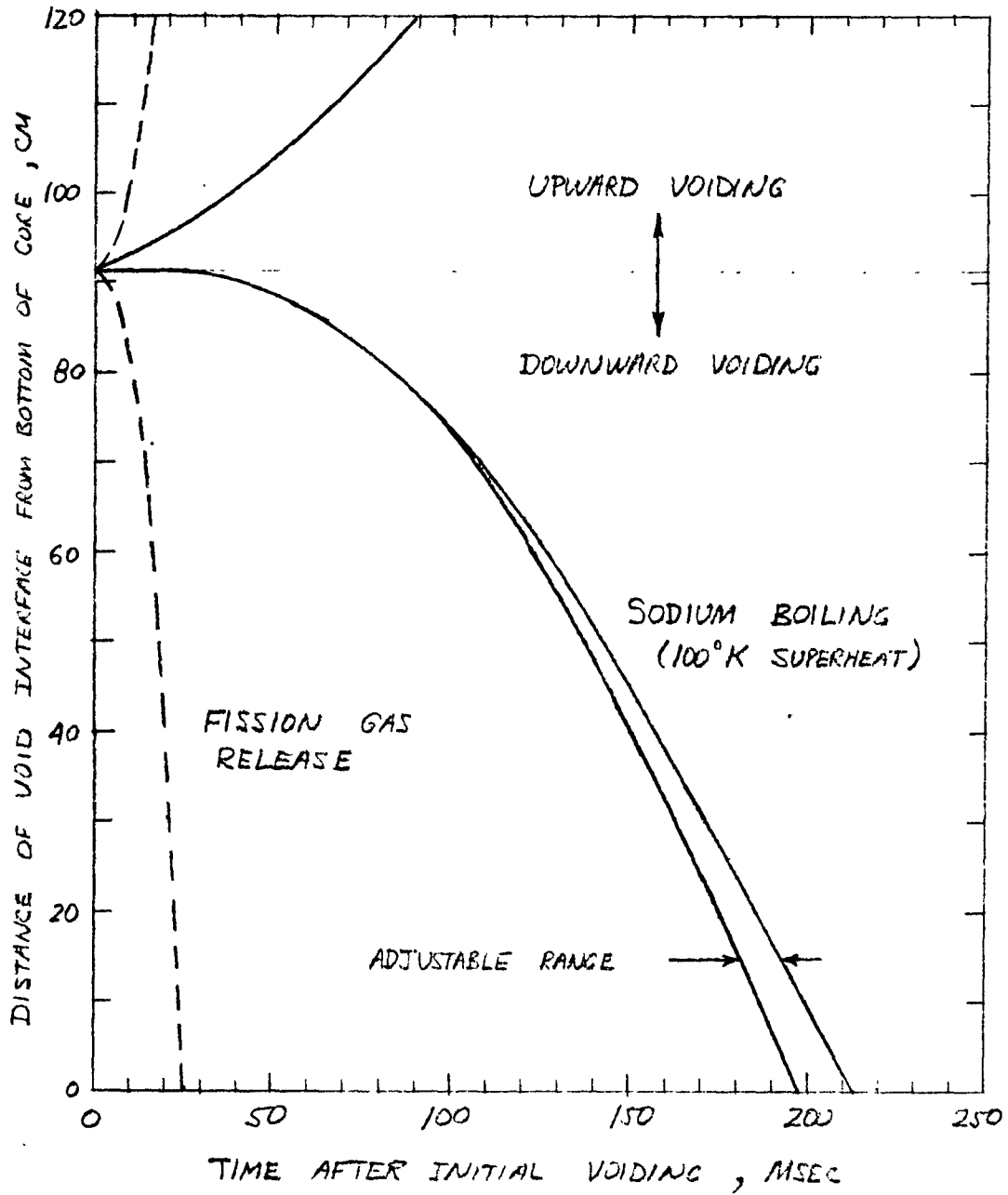


Fig. XV.15 COMPARISON OF SODIUM VOIDING RATES FOR BOILING AND GAS RELEASE FOR FLOW COASTDOWN ACCIDENT

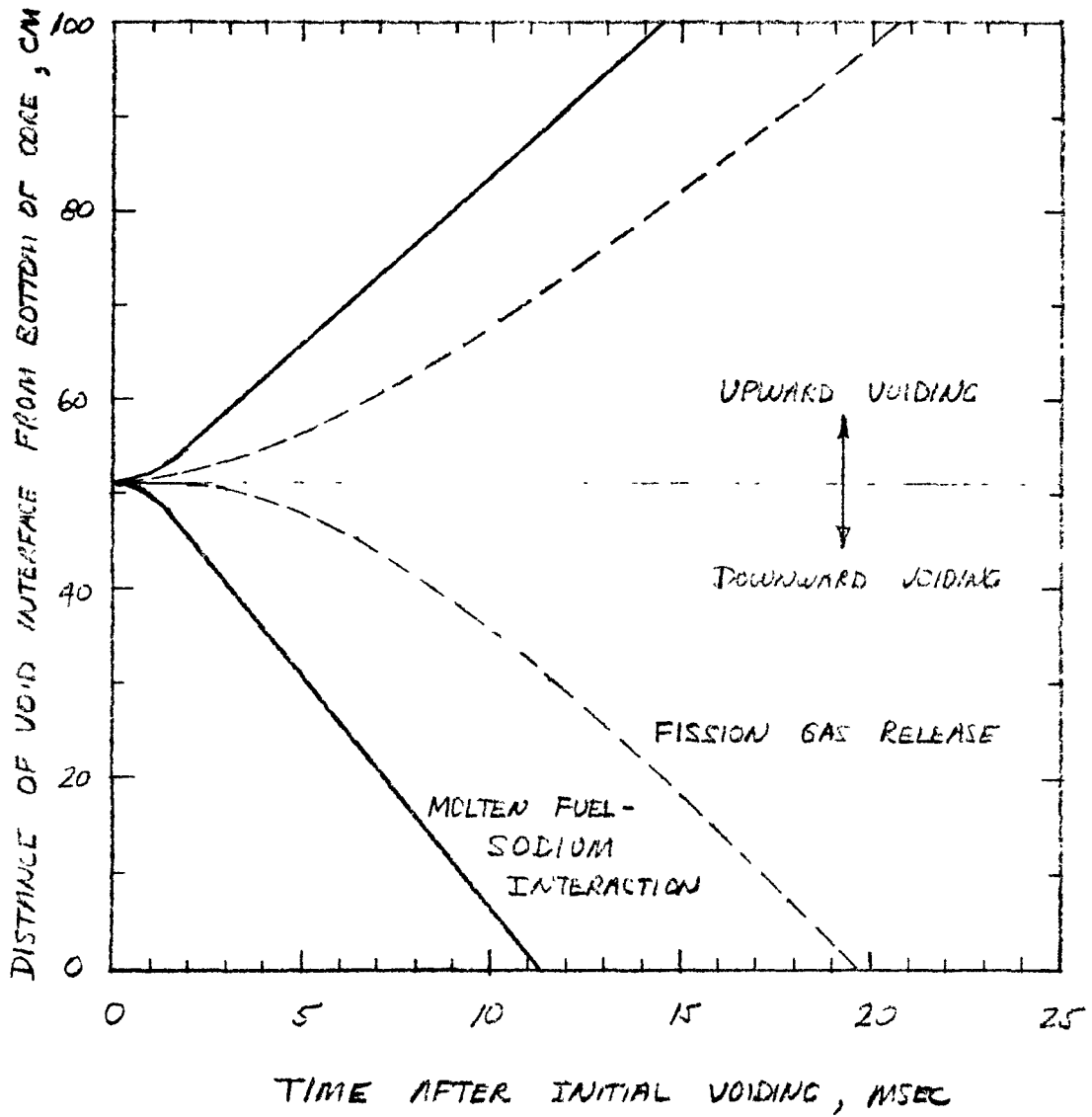


Fig. XV.16 COMPARISON OF SODIUM VOIDING RATE FOR GAS RELEASE AND
MOLTEN FUEL-SODIUM INTERACTION FOR A POWER TRANSIENT

-  Open Loops - 3
-  Closed Loops - 6
-  Control/Safety Rods - 6
-  Peripheral Control Rods - 15
-  Reflectors - 111
-  Drivers - 76

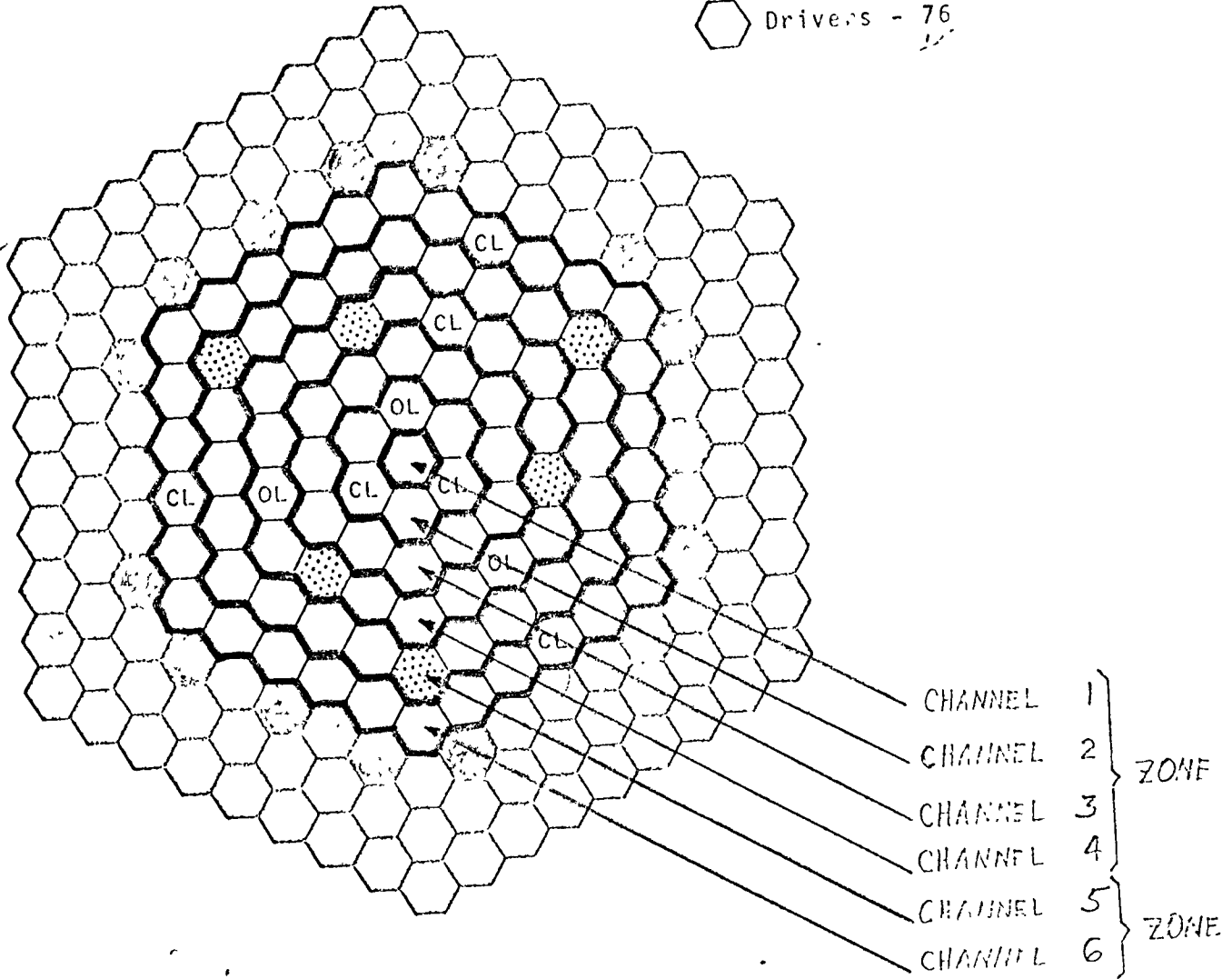


Fig. XV.17 RADIAL CORE SUBDIVISION USED IN TRANSIENT ANALYSES

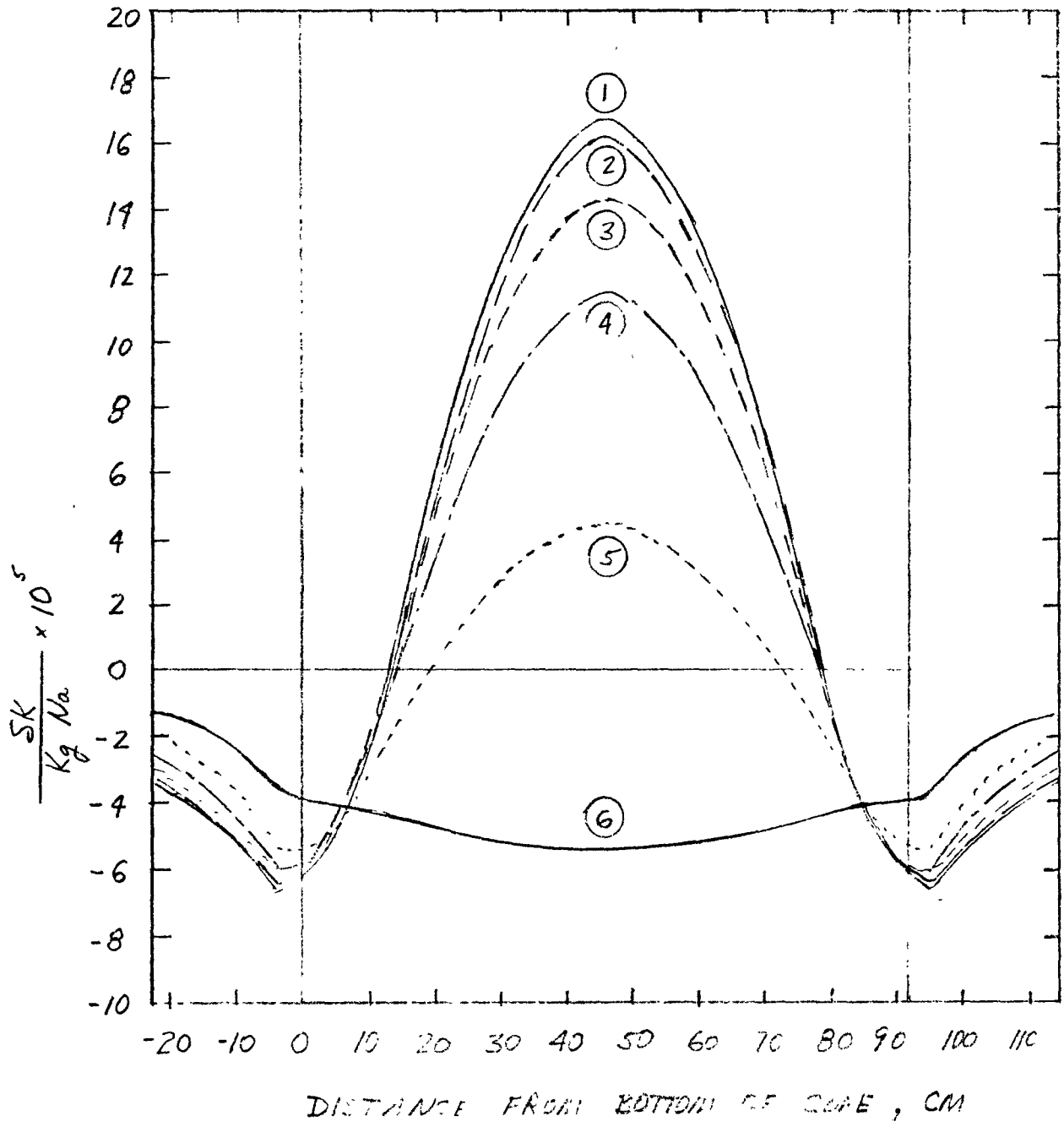


Fig. XV.18 SODIUM VOID WORTH CURVES

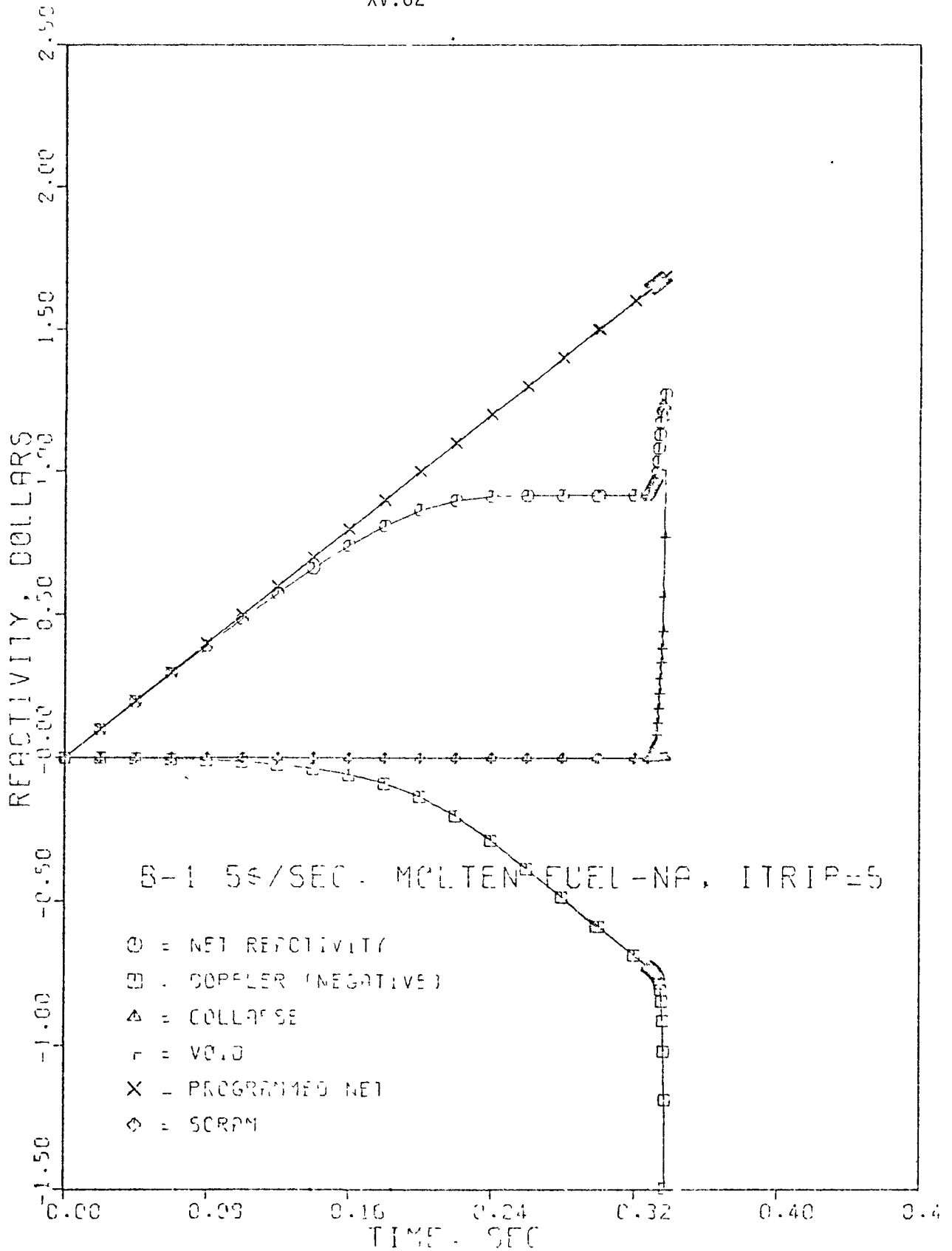


Fig. XV.19 REACTIVITY BALANCE FOR 5\$/SEC RAMP CASE
(MOLTEN FUEL-SODIUM INTERACTION)

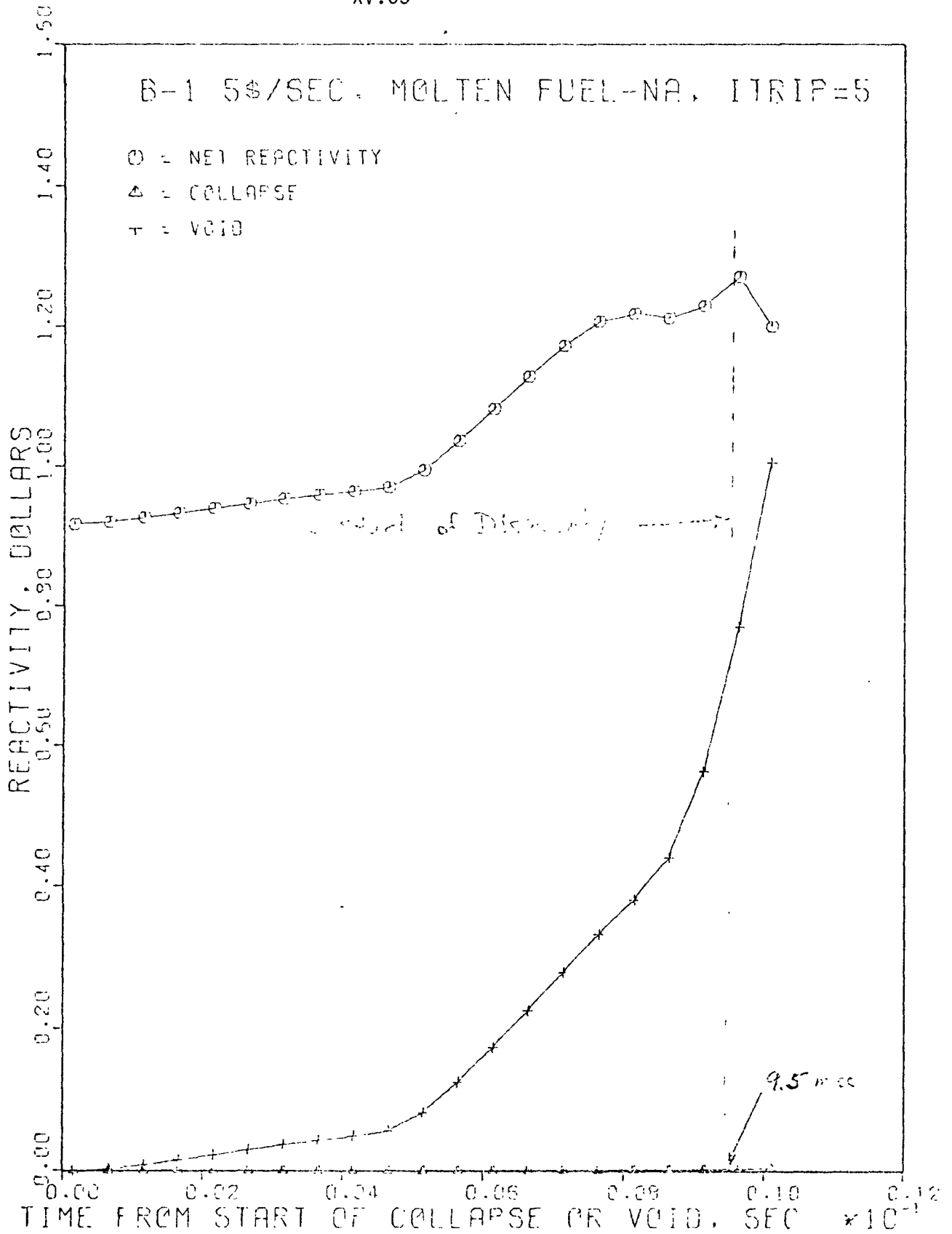


Fig. XV.20 ENLARGEMENT OF REACTIVITY BALANCE AFTER START OF VOIDING (5\$/SEC RAMP CASE, MOLTEN FUEL-SODIUM INTERACTION)

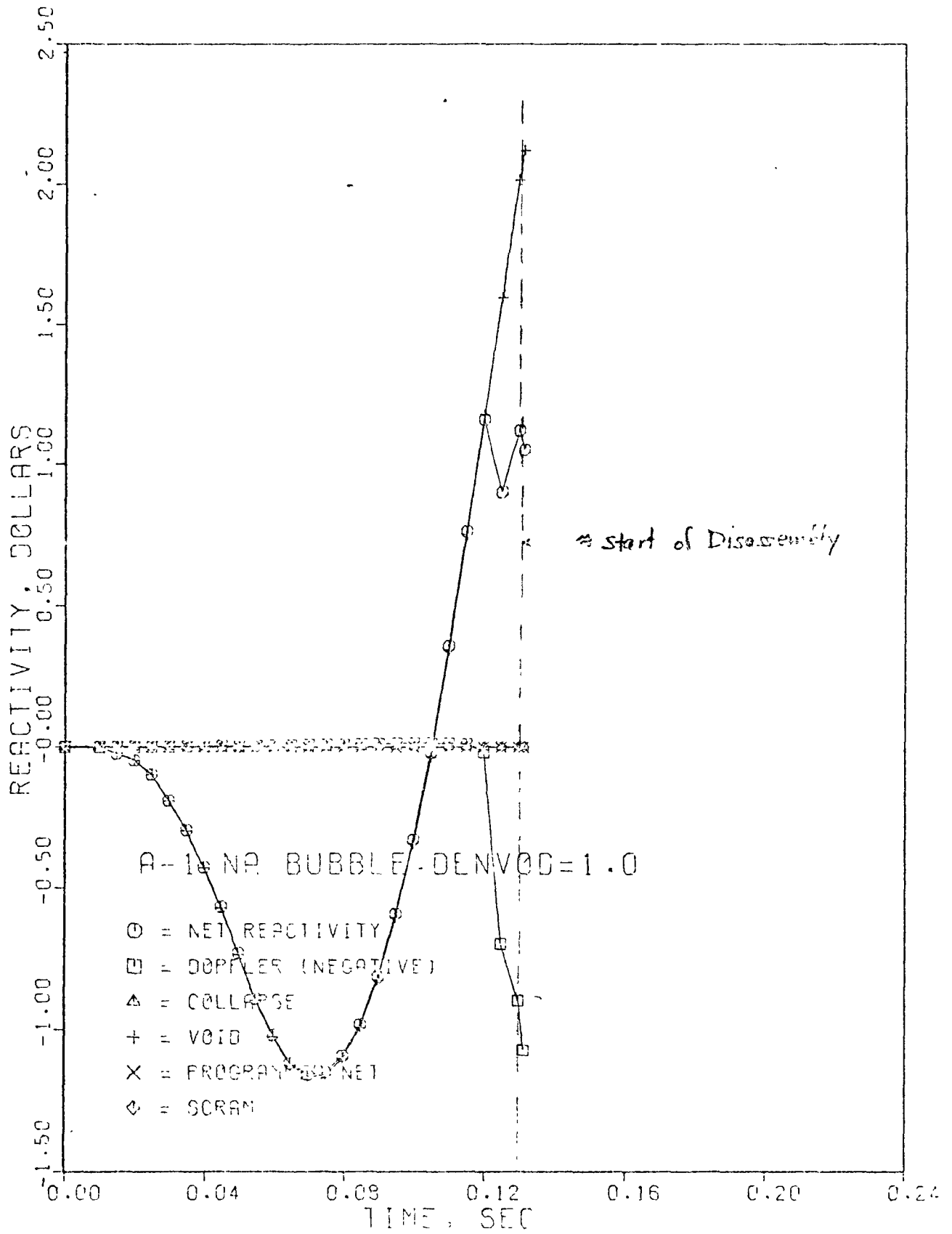


Fig. XV.21 REACTIVITY BALANCE FOR SODIUM BUBBLE PASSING THROUGH CORE.

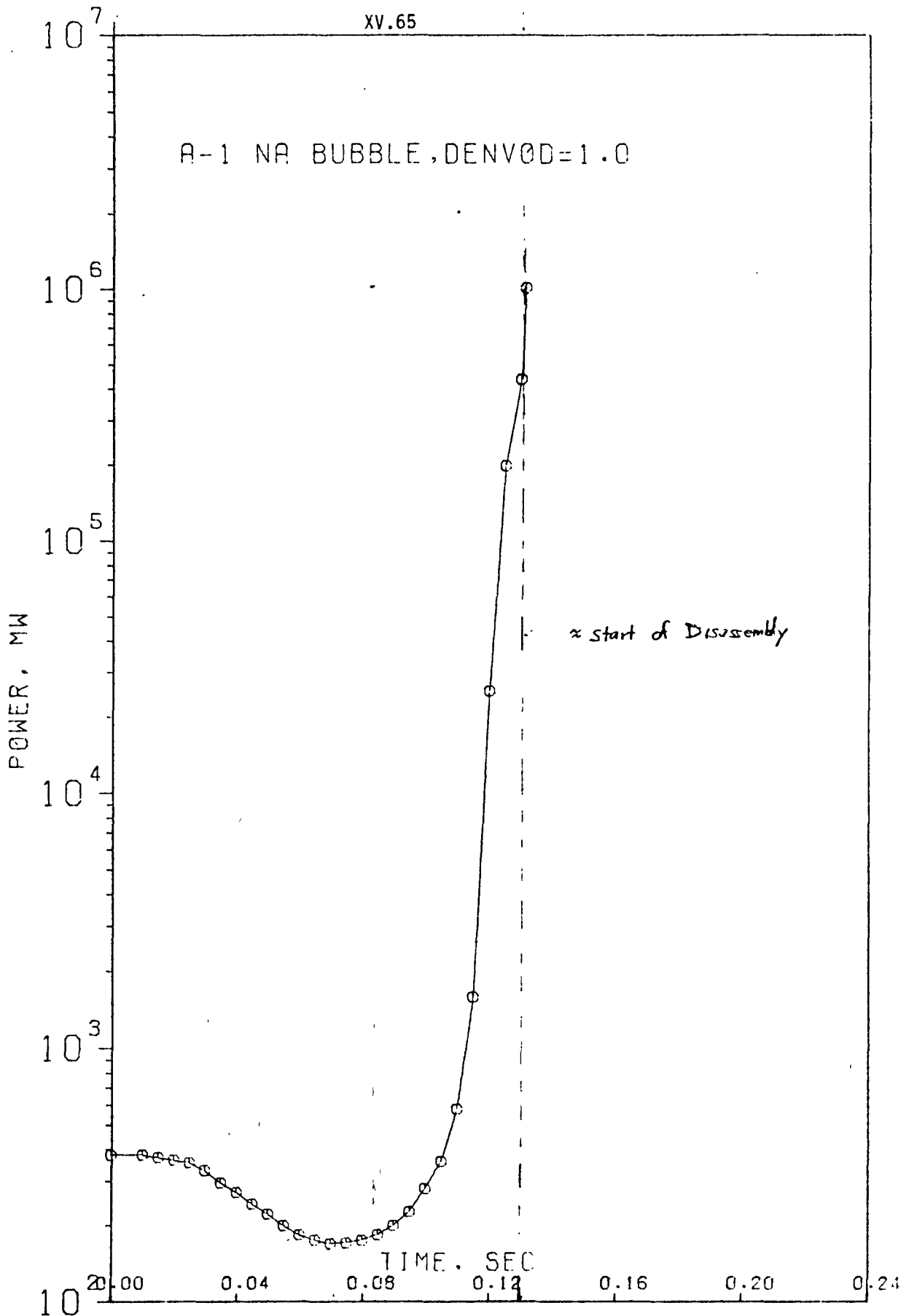


Fig. XV.22 POWER TRACE FOR SODIUM BUBBLE PASSING THROUGH CORE.

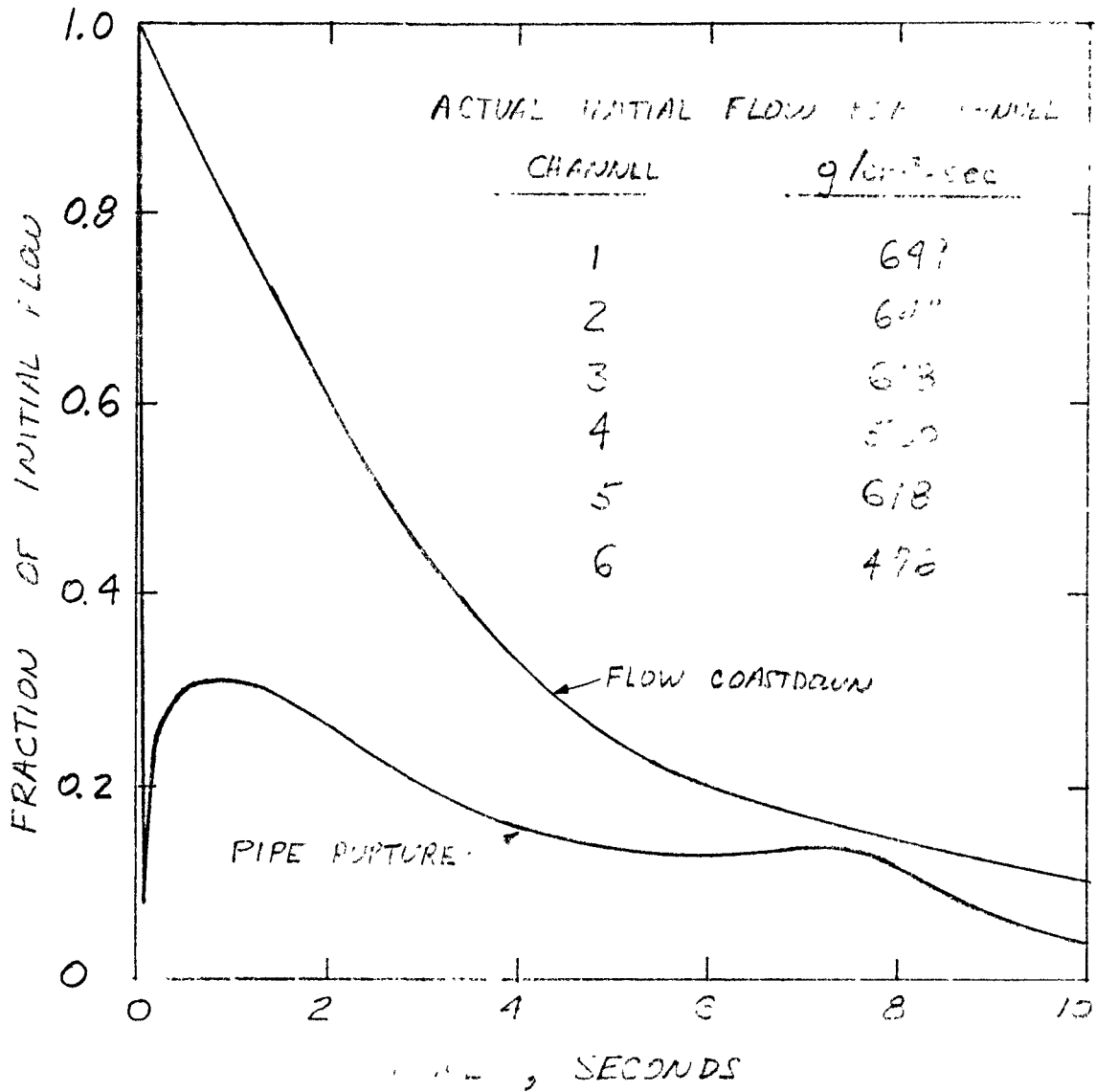


Fig. XV.23 ASSUMED FLOW VERSUS TIME FOR FLOW COASTDOWN AND PIPE RUPTURE ACCIDENT.

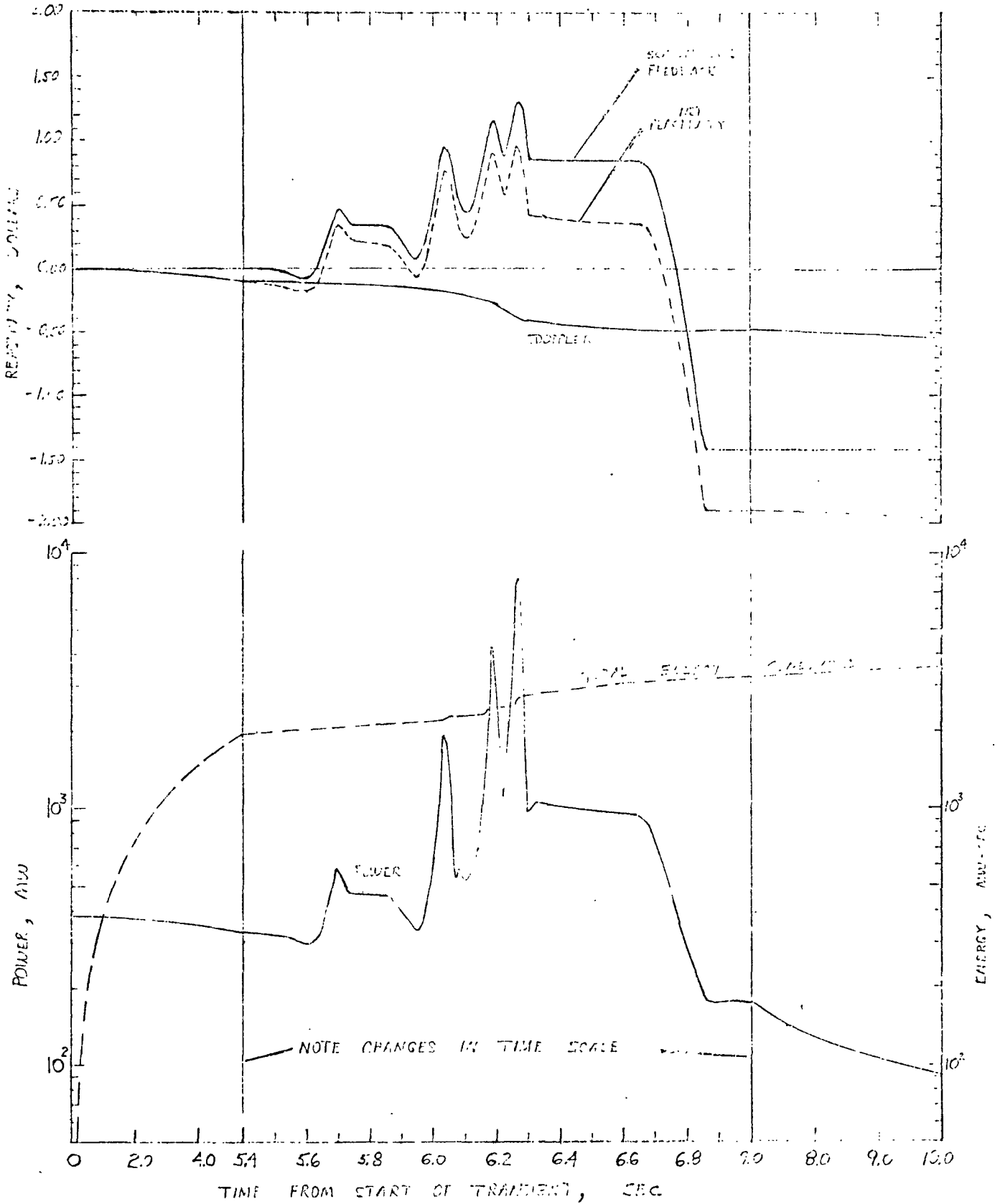


Fig. XV.24 TRANSIENT RESPONSE FOR FLOW COASTDOWN ACCIDENT.

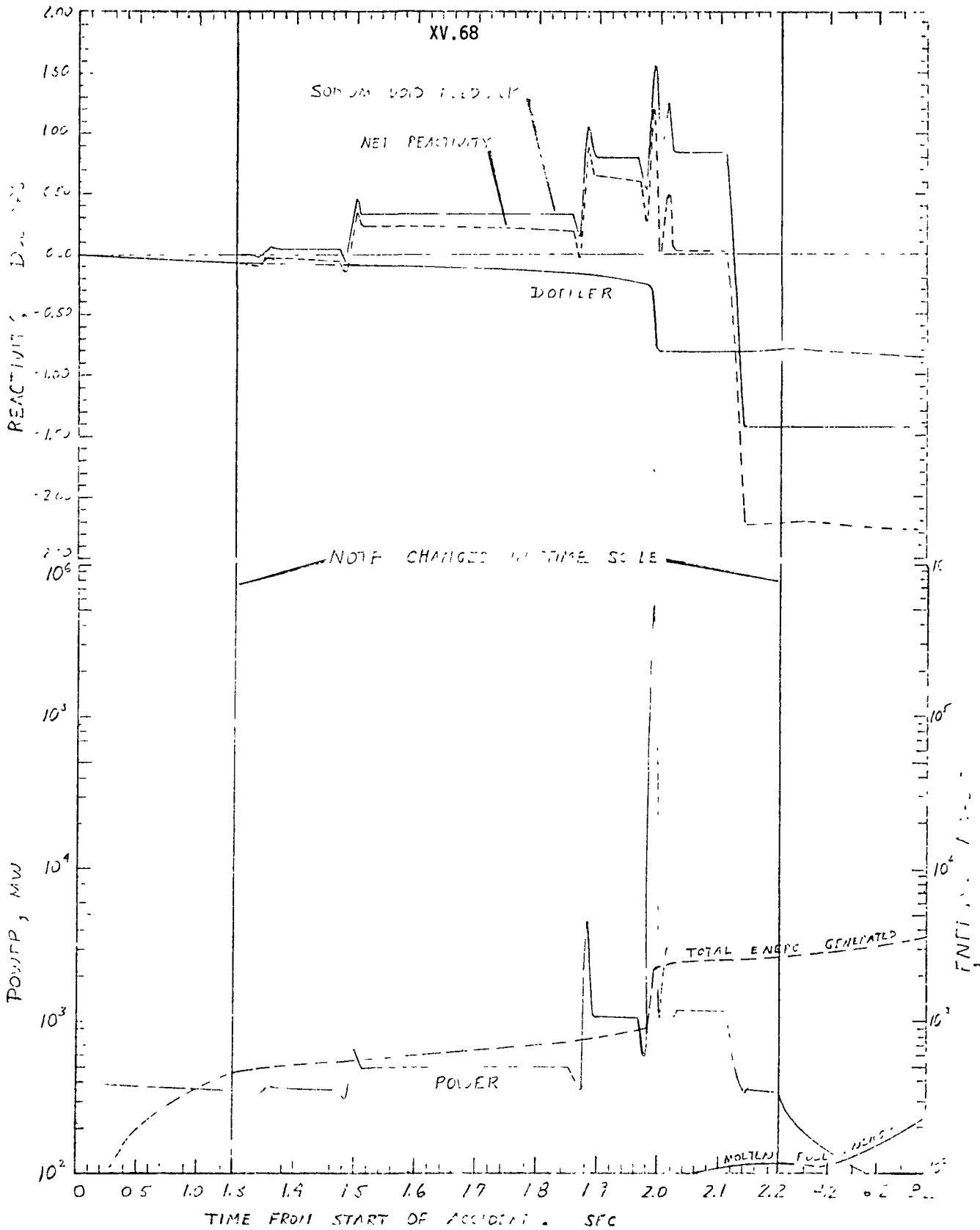


Fig. XV.25 TRANSIENT RESPONSE FOR PIPE RUPTURE ACCIDENT.

XVI. MATHEMATICAL MODELS OF REACTOR DISASSEMBLY

A. F. Walter

A. INTRODUCTION

Very early in the history of fast reactor development concern was expressed over the possibility of core meltdown and subsequent compaction into a more reactive configuration. Although the probability for such an event is considered to be exceedingly small, there exists a definite interest to establish an upper bound to the energy which might be generated -- given extremely pessimistic accident conditions -- in which physical core disassembly is assumed to be the ultimate shutdown mechanism. Calculations of this type are useful in providing a semi-quantitative basis for containment design such that public protection can be guaranteed beyond any reasonable doubt.

The purpose of the present lecture is to discuss techniques which have been developed to analyze core disruptive-type accidents. Brief mention will be made of the historical evolution of such techniques and of the fundamental ideas involved, but the main thrust will be focused on current methods -- particularly those being developed and utilized at BNW. Mention will be made, whenever appropriate, of computational tools being used elsewhere.

B. HISTORICAL EVOLUTION

Most of the early literature regarding fast reactor safety was addressed to the low probability, large energy release type of accident. This should not be surprising for it is precisely in the area of major accidents where the safety analysis of fast reactors differs most markedly from that of thermal systems.

1. Bethe-Tait

Without doubt, the earliest classic to appear on the topic was a paper by Bethe and Tait⁽¹⁾, which appeared in 1956 entitled "An Estimate of the Order of Magnitude of the Explosion when the Core of a Fast Reactor Collapses". This method, although improved significantly by other contributors since its original publication, provides the basis for most of the computational efforts being currently used.

Despite its importance, no attempt will here be made to analytically thread through the Bethe-Tait method. Perhaps the main reason for not doing so is that the closed solution, which can (in a sense) be obtained, is not very revealing, i.e. there is no way to see an explicit variation of total energy generation versus the parameters of interest. This is primarily because the problem is complex and it cannot be characterized in a simple, concise fashion. It is believed to be worthwhile, however, to write down the basic equations used. This will help to articulate the approximations made and set the stage for obvious refinements to follow.

Following Nicholson⁽²⁾, we write the following set of coupled equations:

Kinetics (no delayed neutrons)

$$\frac{d^2 Q}{dt^2} = \frac{k-1-\beta}{\ell} \frac{dQ}{dt} \quad (1)$$

where

$$Q(t) = \int_0^t p(\xi) d\xi \quad , \quad (2)$$

i.e. energy = integral of power.

Energy Distribution

$$E(\underline{r}, t) = N(\underline{r}) Q(t) \quad (3)$$

Reactivity

$$k(t) = k_0 + k_p(t) + k_D(t), \quad (4)$$

i.e. net = initial + programmed + disassembly feedback

Disassembly Feedback

$$k_D(t) = \int_V \underline{U}(\underline{r}, t) \cdot \nabla D(\underline{r}) dV \quad (5)$$

where

$\underline{U}(\underline{r}, t)$ = material displacement

$\nabla D(\underline{r})$ = gradient of the worth distribution

Hydrodynamics

$$\frac{d^2 \underline{U}(\underline{r}, t)}{dt^2} = -\frac{1}{\rho} \nabla P(\underline{r}, t) \quad , \quad (6)$$

i.e. mass acceleration = negative pressure gradient/density

Equation of State

$$P(\underline{r},t) = f(E(\underline{r},t)) \quad (7)$$

where here the pressure buildup is assumed to be proportional only to the energy buildup (see Figure XVI.1). The functional form used by Bethe and Tait was to assume zero pressure generation prior to the point where fuel expanded sufficiently to fill up the space vacated by sodium. This point was defined as Q^* . Upon differentiating Equation (5) twice, substitution of Equation (6) results in

$$\ddot{k}_D(t) = -\frac{1}{\rho} \int_V [\nabla P(\underline{r},t)] \cdot [\nabla D(\underline{r})] dV \quad (8)$$

or, for spherical geometry,

$$\ddot{k}_D(t) = -\frac{f(Q(t))}{\rho} \int r^2 \frac{dN(r)}{dr} \frac{dD(r)}{dr} dr$$

where $N(r)$, from Eq. (3), is the radial power distribution.

One general observation can be made at this point. If either the power distribution, $N(r)$, or the fuel worth distribution, $D(r)$, are flat across the core, the disassembly feedback term will be zero and the energy release is, therefore, mathematically infinite. However, Equation (8) can be extended beyond the core surface to include the abrupt change in power in a surface term. Hence, even the calculated value would never be infinite, but the generalization that flat power and worth distributions are bad from an energy release standpoint is still true.

In order to solve the coupled set of equations, Bethe and Tait divided up the problem into two phases -- Phase I characterized the first time interval in which the reactivity insertion was emphasized (a molten core collapsing freely under gravity was the assumed insertion mechanism). Phase II dealt mainly with core disassembly and the associated negative reactivity feedback.

Although the method as developed was perhaps adequate for a first cut, several rather serious approximations were made to render the problem tractable to hand solution. Among the approximations were the neglect of the effect of fuel vapor pressure as a disassembly force, neglect of any Doppler feedback, neglect of delayed neutrons, the neglect of a density dependence in the equation of state, and the restriction to spherical geometry.

Nicholsen⁽²⁾ removed the most serious of these approximations, namely the neglect of fuel vapor pressure and the neglect of Doppler feedback, by formulating the problem for digital computation. Inclusion of the Doppler feedback and fuel vapor pressure were both shown to significantly reduce the magnitude of the excursion.

Basically the reason is as follows. Without a negative feedback mechanism, power builds up very rapidly beyond the point of prompt critical. This is due to the very short prompt neutron lifetime associated with fast reactors. Since negative feedback due to disassembly is an inertial controlled process, even very large internal core pressures are required to act for a relatively long time (relative to the rate of power increase) prior to significant core movement. A negative Doppler feedback tends to hold the net reactivity and, therefore, the power level, down so that pressures which do exist have sufficient time to start the disassembly process. Likewise, fuel vapor pressure -- even though it may be small in magnitude -- begins to be felt

early in the transient and the core disassembly process can be started early enough to result in a substantial overall reduction in the total energy generated.

2. Current Approaches

In recent years, attempts at describing core disassembly have been almost exclusively formulated for digital computation. The activity, and it has been rather intensive, has been increasingly geared toward two-dimensional models and to consideration of a density dependent equation of state. All current methods of interest account for Doppler feedback and include vapor pressure in the equation of state.

Another factor which has come under discussion within the past five years or so concerns the working fluid assumed for conversion of the heat energy generated into energy available to do work on the system. Originally, the core fuel material was assumed to be the working fluid, and work energy was normally computed to be bounded by an adiabatic expansion of the "fireball" to one atmosphere. However, at one atmosphere the temperature of UO_2 is approximately 3000 °K. Hence, if there is any sodium in the vicinity it is possible for sodium to be heated beyond its boiling point and the subsequent sodium expansion phase could accomplish more work on the system. Furthermore, for situations in which a large percentage of the normal sodium inventory is present during the nuclear excursion, it is even possible that the molten fuel could transfer most or all of its heat to the sodium prior to any fuel expansion and the sodium could be the effective working fluid throughout the post nuclear expansion process. Because of the large interest which is currently developing in methods for characterizing available work energy, the entire topic is reviewed separately in the following lecture.

C. THE ROLE OF DOPPLER FEEDBACK

As pointed out earlier, Doppler feedback plays a very significant role in core disassembly calculations.^(3,4) To reiterate, the primary reason for the reduction in energy release attendant with increasing negative Doppler feedback is that the net reactivity is kept relatively low, preventing a rapid energy generation, long enough to allow the core pressures to begin expanding the core. Once the disassembly process starts, negative feedback due to fuel density reduction is very rapid. A typical energy versus Doppler curve is shown in Figure XVI.2 for two constant ramp rate conditions. As noted from the logarithmic scale used, a "knee" appears in the curve somewhere in the vicinity of $T \frac{dk}{dT} = -0.002$ for the example given, i.e., for a Doppler coefficient smaller than this magnitude the total energy generated increases very rapidly. Hence, the argument for a strong Doppler coefficient.

One interesting feature of both curves in Figure XVI.2 is their oscillatory nature. Perhaps an explanation of this effect, since questions always seem to arise over this point, is in order. We shall consider the 100 \$/sec ramp case and focus attention on the two Doppler coefficient values of -0.0045 and -0.005. Total energy generation is seen to be larger for the latter value. Figure XVI.3 contains the power traces for the two cases. As noted from this figure, the power in the first peak is larger for the case of -0.0045. This, of course, is a direct result of less Doppler feedback. As noted from Figure XVI.4, however, the fuel temperature rise is fairly small (the core was assumed initially to be shutdown at approximately room temperature) and fuel pressures are well below the point of being significant for core disassembly. Reactivity is assumed to be added constantly by the external 100 \$/sec ramp and, therefore, the net

reactivity, as illustrated in Figure XVI.5, exceeds prompt critical and a second power pulse is generated. Again, the power peak is larger for the -0.0045 case and the resulting fuel temperature rise is larger. This process repeats until fuel temperatures are elevated to the point where significant disassembly pressures are generated. For the case of -0.0045, this point is reached at the fourth power pulse. For the case of -0.005, however, another power pulse is required to elevate temperatures to the core disassembly point. It is the energy generated in the fifth pulse that is responsible for the larger energy generation associated with the larger (more negative) Doppler coefficient. For a Doppler value slightly higher than -0.005, however, sufficient fuel temperatures are generated in five pulses to disassemble the core. Hence, the decrease in energy generation versus Doppler coefficient -- up to the point where, again, the process explained above causes a situation where $N + 1$ pulses are required.

Despite the sensitivity of energy generation versus Doppler to the fine details of the calculation, an envelope can be drawn which clearly has a knee shape and the argument for a large (highly negative) Doppler coefficient to reduce the magnitude of a core disassembly accident remains valid.

D. THE EQUATION OF STATE

One of the prime unknowns in performing reactor disassembly calculations is the equation of state. Once fuel temperatures are known, the equation of state provides the vital link to determining the forces which tend to disassemble the core.

As mentioned in Section B, the original attempt⁽¹⁾ was to assume zero disassembly pressure until the fuel-expanded (via density reduction) to the point where all volume available to the fuel was filled, at which time pressures rose rapidly -- characteristic of a heated, confined liquid. The next major improvement⁽²⁾ was to account for fuel vapor pressure which, although low, early in the transient, could act over a relatively long period of time and, thus, be significant in affecting early core disassembly. Later refinements allowed for vapor pressure to act up to the point of a completely liquid phase at which time pressures could build up rapidly as in the original method. A substantial improvement in the disassembly code itself was necessary, however, since large pressures would tend to move molten material rapidly, and even a small change in volume could cause the effective pressures to revert back to the two phase (liquid-vapor equilibrium) domain. Neglect of this expansion, as made in all the early disassembly codes, could cause a sizeable overestimate of disassembly pressures, and therefore, an underestimate of the energy release.

Finally, recognition was given to the possibility of large amounts of sodium residing in the core at the time of disassembly. This results in the generation of large pressures much earlier in time and, hence, provides a much more severe test on the ability of the disassembly code to handle large local pressure fluctuations.

Figure XVI.6 schematically illustrates the increasing range of complexity associated with various degrees of sophistication in describing the equation of state. Case IV, which considers sodium in the core, contains all the complexity of Case III (density dependent) in addition to changing slopes for a given density as a result of sodium compressibility. The point to be made, from the figure, is that pressures are generated relatively early for the sodium-in case.

1. Fuel Vapor Pressures

Although agreement is essentially unanimous that fuel vapor pressure is significant in providing a driving force for disassembly calculations, there is little agreement as to the actual vapor pressure existing for a given fuel temperature. Experimental data, even for pressures orders of magnitude below one atmosphere, is scant. To the knowledge of the author, there is presently no experimental data for UO_2 in the one atmosphere range. We are, of course, mainly interested in mixed oxide fuel, but the assumption is almost universally made that if a reasonable equation of state for pure UO_2 can be specified, this will also be reasonable for use with mixed oxide systems. Fortunately, if the Doppler feedback term is fairly large the the sensitivity of the calculated energy release to the particular vapor pressure curve chosen is not too critical.

Because there exists no experimental data on the pressure, energy and temperature relationships for mixed oxide fuels in the temperature and pressure range usually encountered in disassembly accident calculations, it has been the practice to estimate these properties of the fuel by extrapolating or otherwise utilizing what little data is available at low temperatures. The data most often used in this procedure are the vapor pressure

measurements of Ackermann⁽⁵⁾ and Ohse⁽⁶⁾ and the density measurements of Christensen⁽⁷⁾. These data were all obtained for UO_2 .

The method most often employed to estimate the high pressure-high temperature equation of state is the principle of corresponding states.⁽⁸⁾ This principle states that all materials behave similarly if put in terms of the reduced variables of state. These reduced variables are the ratios of the normal variables to the corresponding values at the critical point (i.e., reduced temperature = actual temperature/critical temperature). If a few properties (estimated from low temperature data) of a material are known, all of the required properties including the available work-energy content relationship can be determined using this principle. It is well known that several materials deviate significantly from this principle.⁽⁹⁾ However, in the absence of any obviously better method, the procedure does provide at least an estimate of the quantities desired.

Hougen, et al.⁽⁸⁾ have generated tables for applying the corresponding states principle based on measurements of several different materials. The procedures for using these tables, as outlined by Meyer⁽¹⁰⁾, require that several characteristics of the material and system under consideration be specified. These include:

- (a) The critical constants (i.e., temperature at the critical point),
- (b) The specific heats at constant pressure and volume of an ideal gas composed of the fuel material,
- (c) The melting and boiling temperatures,
- (d) The latent heats of vaporization at both the melting and boiling points, and
- (e) The specific volume of the fuel material in the system under consideration.

The choice of critical constants can appreciably alter the equation of state derived from the corresponding states principle. Both Miller⁽⁹⁾ and Robbins⁽¹¹⁾ have investigated the possible range of constants and obtained quite large limits for their values. For illustrative purposes, however, examples will here be presented using the "probable" values obtained by three investigators.^(10, 13, 9) All used different approaches; however, some "reduced relationships" (corresponding states principles) were utilized in each instance and the low temperature data discussed above were taken into account. In general, the results compare reasonably well for the accuracy one would expect from their separate methods. These critical constants are shown in Table XVI.1.

TABLE XVI.1

Critical Constants of UO₂

	<u>Menzies</u> ⁽¹³⁾	<u>Miller</u> ⁽⁹⁾	<u>Meyer</u> ⁽¹⁰⁾ <u>et al.</u>
Critical Pressure (atm)	2000	1230	1915
Critical Temperature (°K)	8000	9115	7300
Critical Volume (cm ³ /mole)	90	170	85

Although making a choice between the constants shown in the above table may appear to be merely academic, several properties of the Menzies constants have been shown⁽¹²⁾ to make them the most desirable. Perhaps the main reasons are that in utilizing Menzies constants, 1) the vapor pressure agrees well with the data at low pressures, and 2) the specific heat at constant volume, as calculated from the Hougen and Watson tables⁽⁸⁾, appears reasonable.

Vapor pressure curves, using the reduced vapor pressure equation of Riedel⁽⁸⁾, were generated⁽¹²⁾ for the Miller and Menzies critical constants (the Meyer constants yielded values quite similar to those of Menzies) and are shown in Figure XVI.7 along with the analytical fits to the data of Ackermann⁽⁵⁾ and Ohse.⁽⁶⁾ As was found by APDA⁽¹⁴⁾, the Miller constants yield vapor pressures much lower than the measured data when extrapolated to lower pressures. The vapor pressure curve for the Menzies constants, however, agrees quite well. It should be noted that the experimental curves are extrapolations of the measured vapor pressure of the solid. The curves should be corrected slightly to reflect the vapor pressure of the liquid (reduced slope).

The range of data and functional fits, using critical constants as referenced, is seen to span a rather wide range, i.e. the boiling temperature is seen to vary as much as 1000 °K. However, as suggested earlier, even these large differences do not cause vast differences in the final energy generation -- primarily because most of the shutdown comes from the Doppler feedback effect.

2. Density Dependent: Sodium Out

A fuel vapor pressure equation of state, even if known accurately, is not sufficient to characterize disassembly pressures once fuel expands to the point that all the available volume is filled. Pressures beyond that point become characteristic of a heated, confined liquid and the rate of pressure buildup with increasing temperature (or energy) is exceedingly rapid.

Menzies⁽¹³⁾ was perhaps the earliest contributor to derive a set of density dependent pressure-energy curves and analytically fit the set for

use in a disassembly code. A similar set, derived in BNWL-760⁽¹²⁾ for FTR use, is shown in Figure XVI.8. The energy base, for the curves, is the melting point in the liquid phase. The sharp breaks in the pressure versus energy curve as a function of density (or reduced specific volume) occur when the liquid has expanded enough to fill the available volume. As a point of reference, if sodium is assumed to be completely voided from the core, the reduced volume is of the order of 0.6. Hence, the excursion is nearly over before the local energy density (or fuel temperature) becomes high enough for the departure point to be attained. In this event, the density dependence allowed for in the equation of state is not very significant in the final analysis. For higher density systems, however, the departure points can become quite important. This is precisely the case encountered when a large sodium inventory exists.

The functional fit to the set of curves illustrated in Figure XVI.8 is as follows:

$$P_v = 42870 \exp \left\{ \frac{-5968}{E + 1271} - \left(\frac{4358}{E + 1271} \right)^2 \right\} \quad (9)$$

$$P_\ell = \left\{ 99.2 + 163.4 V_r - 466 V_r^2 \right\} \left(E + 10730 - 49740 V_r + 49830 V_r^2 \right) \quad (10)$$

where P_v = vapor pressure (atm)
 P_ℓ = confined liquid pressure (atm)
 E = energy above the melting point in the liquid phase (joules/g)
 V_r = relative volume.

The larger of the two pressures as calculated above is assumed as the effective disassembly force.

3. Density Dependent: Sodium-In

It is possible to use the results of Figure XVI.8 for sodium-in conditions by simply specifying a high density system, i.e. the effective smeared fuel density would now be computed on the basis of a much smaller available volume -- smaller by the volume percent of sodium present. However, Figure XVI.8 was obtained for a temperature domain significantly higher than that of interest for sodium-in situations. Hence, the equation of state for sodium-in conditions was rederived in BNWL-760 Supplement #1⁽¹⁵⁾ to better reflect the temperature range of interest and to account for sodium compressibility.

Sodium compressibility can be a rather significant factor when evaluating the energy generated in an excursion for a core containing a substantial amount of sodium. By ignoring compressibility, the very high pressures computed for a heated, confined liquid can only be relieved by volume expansion of the fuel. But such pressures can also be relieved by sodium compression and a neglect of this effect leads to an under-estimation of the energy release.

The method used in BNWL-760 Supplement #1 emphasized the temperature-density data available⁽⁷⁾ for UO_2 at and slightly above the melting temperature, i.e. this data was used to establish the point at which the system departs from the vapor pressure curve. Table XVI.2 contains the low temperature data used. Christensen⁽⁷⁾ found that the melting temperature, liquid density at the melting point, and linear coefficient of expansion at the melting point of UO_2 were 3070 °K, 8.74 g/cm³, and 3.5×10^{-5} °K⁻¹,

respectively. From this data, it was estimated that the volumetric coefficient of expansion (α) was about $1.05 \times 10^{-4} \text{ }^\circ\text{K}^{-1}$. Disregarding any pressure dependence, the liquid density was then estimated to be

$$\begin{aligned} \rho &= \rho_0 [1 - \alpha(T - T_0)] \\ &= 8.74 [1 - 1.05 \times 10^{-4} (T - 3070)] \text{ g/cm}^3. \end{aligned} \quad (11)$$

This equation can be used to determine the departure temperature for a given fuel system by letting ρ equal the density of the fuel in its available volume. Thus,

$$\begin{aligned} T_d &= \left(1 - \frac{\rho}{\rho_0}\right) \frac{1}{\alpha} + T_0 \\ &= \left(1 - \frac{\rho}{8.74}\right) \frac{1}{1.05 \times 10^{-4}} + 3070 \text{ }^\circ\text{K} . \end{aligned} \quad (12)$$

The temperature dependence of the liquid fuel density, as described above is shown in Figure XVI.9.

TABLE XVI.2

*Low Temperature Data Used in Sodium-In
Equation of State Determination*

Parameter	Value	Reference
Melting temperature	$T_0 = 3070 \text{ }^\circ\text{K}$	Christensen (7)
Liquid density at melting point	$\rho_0 = 8.74 \text{ g/cm}^3$	Christensen (7)
Volumetric Coefficient of expansion at melting point	$\frac{1}{\rho} \left(\frac{\partial \rho}{\partial T}\right) = -\alpha$ $\cong -1.05 \times 10^{-4} \text{ }^\circ\text{K}^{-1}$	Christensen (7)
Vapor pressure at melting point	$P_{vp} \cong 0.06 \rightarrow 0.01 \text{ atm}$	Ackermann (5) (extrapolated)

The extrapolated data relationship is shown as a straight line even though it should have a downward curve (at least near the critical point). Miller⁽⁹⁾ utilized Christensen's data and the "law of rectilinear diameters" to construct a temperature-density relationship up to the critical point. From his plot, it was estimated that a linear temperature-density relationship was quite adequate over the temperature range of interest. In any event, any downward curve in the relationship would cause departure to occur at lower temperatures, and thus, the linear relationship would be conservative.

Once the fuel system has entered the pure liquid region, it was assumed that the slope of the pressure temperature curve was a constant for a given fuel density, i.e.,

$$\left. \frac{\partial P}{\partial T} \right)_{\rho} = f(\rho) \quad .$$

An estimate of the $f(\rho)$ was obtained from the corresponding states tables of Hougen et al.⁽⁸⁾ The plot (for an assumed critical compressibility of 0.27) in Figure XVI.10 indicates that the straight line approximation is quite adequate. The vapor pressure plotted in the curve is a fit to the high temperature data of Ackermann⁽⁵⁾ (for sodium-in cases the vapor pressure relationship assumed is not too significant since departure into the single phase region is the major pressure mechanism). An analytic fit to this figure is

$$\left. \frac{\partial P_r}{\partial T_r} \right)_{\rho_r} = \rho_r \exp[2.0958 + 0.430(\rho_r - 0.832)^2] \quad (13)$$

where P_r = reduced pressure,
 T_r = reduced temperature, and
 ρ_r = reduced density

or,

$$\left(\frac{\partial P}{\partial T}\right)_\rho = \frac{R \rho 0.27}{M} \exp[2.0958 + 0.430(\rho_r - 0.832)^2] \quad (14)$$

where P = pressure,
 T = temperature,
 ρ = density,
 M = molecular weight of fuel, and
 R = gas constant.

If a critical density (ρ_c) of 3.0 g/cm^3 , as obtained from Menzies⁽¹³⁾ critical constants, is assumed,

$$\left(\frac{\partial P}{\partial T}\right)_\rho = \rho 0.666 \exp[0.048(\rho - 2.5)^2] \quad (15)$$

The pressure-temperature relationship in the liquid fuel region can thus be written as,

$$P = \left(\frac{\partial P}{\partial T}\right)_\rho (T - T_d) + P_d \quad (16)$$

where

$\left(\frac{\partial P}{\partial T}\right)_\rho$ is given by Equation (15)

T_d is given by Equation (12), and

P_d is the pressure of the fuel vapor at the temperature T_d .

If sodium is assumed to be incompressible, Equation (16) can be evaluated explicitly for any temperature-density condition. However, in considering the effects of sodium compressibility, the problem becomes significantly more complicated. To consider this effect consider a small core volume element initially containing M grams of fuel, $V_{\text{Na}_0} \text{ cm}^3$ of

sodium, and V_{ss_0} cm³ of inert material. The inert material (i.e., stainless steel) is assumed to be incompressible. If the initial volume of the element is V_{T_0} , the initial density of the fuel in its available volume is:

$$\rho_0 = \frac{M}{V_{T_0} - V_{Na_0} - V_{ss_0}} \quad (17)$$

As the accident progresses, however, the total volume and the volume occupied by the sodium will change. The fuel density then will be

$$\rho = \frac{M}{V_T - V_{Na} - V_{ss_0}} \quad (18)$$

where V_T and V_{Na} are time-dependent values. V_{Na} can be determined if the sodium adiabatic compressibility (β_s) and the pressure (P) are known:

$$V_{Na} = V_{Na_0} \exp[-\beta_s(P - P_0)] \quad (19)$$

As will be discussed in the following section, the mass of material in each element of a Lagrangian coordinate system disassembly code remains constant during the transient and the current volume occupied by the element and current fuel temperature are monitored. The volume occupied by the sodium is not calculated explicitly and, therefore, must be inherent in the equation of state of the fuel material. If the sodium has a finite compressibility, Equation (18) becomes a function of pressure and Equation (16) can only be solved for pressure by iteration. In order to avoid iterations in the disassembly code, it would be desirable to have an equation similar to Equation (16) in which $\left(\frac{\partial P}{\partial T}\right)_\rho$ is replaced by $\left(\frac{\partial P}{\partial T}\right)_{V_T}$, and $\left(\frac{\partial P}{\partial T}\right)_{V_T}$, T_d , and P_d become functions only of the current volume occupied by the volume element (V_T). The resulting equation, if it can be found, would, of course, be a

function not only of the fuel properties but also of the reactor composition and adiabatic compressibility of sodium.

In BNWL-760 Supplement 1⁽¹⁵⁾ iterative solutions to Equations (15), (18), and (19) have been obtained and the feasibility of assuming $\left(\frac{\partial P}{\partial T}\right)_{V_T}$ to be a function only of V_T has been demonstrated. The details will not be repeated here. Since the total nodal volume, V_T , is always monitored in the Lagrangian disassembly codes used at BNW, the approach discussed above, i.e. avoiding iterations on pressure, can be utilized at a great savings in computation time.

For calculational purposes, the functional fit to the curves presented in Figure XVI.10 are

$$P_V = \exp \left\{ 55.455 - \frac{78847}{T} - 4.2808 \ln T \right\} \quad (20)$$

and Equation (15) is used for evaluation of $\left(\frac{\partial P}{\partial T}\right)_\rho$. In order to get

$\left(\frac{\partial P}{\partial T}\right)_{V_T}$ as indicated above to be desirable, a rather lengthy (but straightforward) scheme is used. Figure XVI.11 illustrates the sequence used.

- 1) P' is selected to be some large pressure near the upper range of interest (~ 2000 atm),
- 2) T_d and P_d are evaluated for zero pressure from (12) and (2'), respectively,
- 3) $\left(\frac{\partial P}{\partial T}\right)_{\rho_0}$ is evaluated from Equation (15),
- 4) T_1 is obtained knowing 2) and 3) above,
- 5) ρ' is evaluated from the equation

$$\rho' = \frac{\rho_f \rho_0}{\frac{\rho_f \rho_0}{\rho_f} - \rho_0 e^{-\beta_s \rho'} - \rho_0}$$

where ρ_f = current fuel smeared density,
 ρ_{fo} = initial fuel smeared density,
 f_0 = initial volume fraction sodium,
 g_0 = initial volume fraction structure,
 β_s = adiabatic sodium compressibility.

6) T' is evaluated by assuming sodium always had the volume it occupies at pressure P' , i.e.

T_d' , P_d' , $\left. \frac{\partial P}{\partial T} \right|_{\rho}$, are evaluated by (12), (20) and (15), respectively.

7) $\left. \frac{\partial P}{\partial T} \right|_{V_T}$ is then evaluated since P' , T' , and T_1 are known. Hence, P can be evaluated directly.

Although this appears cumbersome, the method avoids iteration on pressure, allows ease of changing core compositions, and is believed to be reasonably accurate.

To give some indication of the sensitivity of the energy generation to the main parameters of interest, a few examples from BNWL-760 Supplement 1 will be given. For this study, the reference value assumed an adiabatic compressibility of sodium to be $3 \times 10^{-5} \text{ atm}^{-1}$. The molten fuel energy generated versus the sodium compressibility is illustrated in Figure XVI.12. Figure XVI.13 illustrates the energy contained in molten fuel versus the percent of original sodium remaining in the core. The knee shape of this curve arises because of the following. For the particular example chosen, sodium volume fractions below approximately 60% were such that fuel vapor was sufficient to begin the disassembly process, whereas for higher volume fractions of sodium, departure point temperatures were encountered relatively

early in the transient. As noted from the curve, such temperatures were encountered very early in the transient for sodium volume fractions in excess of about 80% and the associated energy release values were quite low.

E. LAGRANGIAN COORDINATE SYSTEM

In the discussions on the equation of state, several references were made to the fact that large internal core pressures can be relieved when core movement takes place. All of the early disassembly codes used Eulerian coordinate systems wherein the boundaries of the system were fixed in time and, hence, pressure relief to fuel movement could not be accounted for. In considering only sodium voided cases, i.e. low density systems, the neglect of pressure relief (neglect of the density dependence in the equation of state) was usually adequate if the primary interest was computing energy release. For sodium-in cases, however, account must be taken of the pressure relief due to fuel movement and sodium compressibility.

The remainder of the discussion of the present section is, therefore, confined to those codes constructed with a Lagrangian coordinate system, i.e. a spatial mesh structure which moves with the fluid. In such systems, no mass crosses the mesh boundaries. Hence, as nodal pressures build up the nodal volumes expand and the fuel density, as well as the "mesh" density (used in the hydrodynamics equations), decreases. This scheme explicitly allows the density dependent equations of state, as formulated in the previous section, to be utilized.

1. MAX⁽¹⁶⁾

The first rapid and flexible disassembly program written in a Lagrangian coordinate system was a code entitled MAX⁽¹⁶⁾. Although this program is limited to one-dimension and to most of the other assumptions characteristic of the Bethe-Tait method (i.e. perturbation theory, point kinetics, etc.) the ability of the code to compute disassembly reactivity feedback by actual core movement was found to be extremely useful -- especially for investigating

excursions in a core assumed to have a large percentage of its normal sodium inventory still present. Another feature of the code is the flexibility for providing input. Zone dependent equations of state can be specified as well as an initial temperature distribution wherein some of the fuel nodes are partially or totally frozen.

After successful initial intercomparison with the established Eulerian code WEAK⁽¹⁷⁾, MAX was used exclusively for the preliminary analysis⁽¹²⁾ of postulated maximum accidents for the FFTF.

2. Venus^{(18)*}

Despite the utility of MAX, the limitation to one dimension severely limits the possibility of accomplishing a direct coupling to MELT-II, used at BNW for the pre-disassembly phase of the analysis. The VENUS program, developed over the past few years at Argonne, is essentially a two-dimensional version of MAX and is proving to be a very useful tool. A brief outline of the models essential to the code is given below.

a. Neutronics

The point kinetics model with up to six groups of delayed neutrons is used. In its original form, the method for solving the kinetics equation was that formulated by Kaganove⁽¹⁹⁾, which is basically an improved Runge-Kutta technique. Time steps are controlled by a specified change in power allowable within the time step. Although this method appears to be adequate, the entire kinetics package in the VENUS version at BNW has been replaced by the one described in Lecture XV. This was done mainly to accomplish a smoother transition between the MELT-II and VENUS phases.

*The author gratefully acknowledges the cooperation of Drs. G. J. Fischer and W. T. Sha, of Argonne National Laboratory, for releasing to BNW an early version of the code and for their assistance in helping to make the program operable.

The reactivity is computed as the sum of the programmed reactivity plus reactivity feedbacks due to Doppler broadening and the motion of reactor material.

b. Hydrodynamics

The motion of the reactor materials is assumed to satisfy the equation of motion of a compressible, nonviscous fluid. Conservation of mass requires that

$$\rho = \rho_0 \frac{V_0}{V} \quad (21)$$

where ρ_0 is the original density and V_0 and V represent the initial and the current volumes, respectively. The momentum equations are as follows:

$$\dot{u} \equiv \dot{r} = - \frac{1}{\rho} \frac{\partial P}{\partial r} \quad (22)$$

$$\dot{v} \equiv \dot{z} = - \frac{1}{\rho} \frac{\partial P}{\partial z} \quad (23)$$

where $P = p + q$; p and q are the pressures calculated from the equation of state and the pseudo-viscosity pressure respectively (the pseudo-viscosity pressure term represents an approximation technique developed by Von Neumann and Richtmyer⁽²⁰⁾ to numerically smear a shock wave over several mesh points and render stability to a program of this type).

Several possible methods for selecting a finite difference representation of the spatial derivative in the momentum equation have been reviewed by Herrmann⁽²¹⁾. The difficulty, or arbitrariness, of the selection is exemplified in Figure XVI.14. In setting up problems of this type, quantities such as distance, velocity, and acceleration are assumed to be known at the mesh interstices whereas mass, density, and pressure are normally associated with the mesh centroids. In solving for acceleration of one of the mesh corners,

therefore, one has to know the pressure gradient in both R and Z directions. It is not clear how to obtain these quantities.

The method used in VENUS is to establish $P_5 = \frac{1}{2} (P_1 + P_2)$, etc. and then express P_5 , as well as the other "midpoint" pressures in terms of a Taylor's series about P_0 . Expressions for mesh areas, required for volume determination, is likewise somewhat arbitrary and, as would be expected, all methods break down once the mesh becomes badly distorted.

Reactivity feedback, due to fuel motion, is calculated by perturbation theory using Equation (5) in cylindrical coordinates.

c. Equation of State

VENUS is now programmed to handle any of the equations of state discussed in the previous section. In particular, VENUS was recently tested⁽²²⁾ with the Sodium-In equation of state outlined in Section D.3 above. Figure XVI.15 illustrates a typical pressure-density behavior resulting from the use of a temperature-density-dependent equation of state. The particular example chosen was a rapid power excursion in an FTR type core. Values indicated are for the node in the core center after the transient reaches the disassembly phase. If the compressibility of sodium is ignored, the solid lines indicate a sharp rise in pressure when the fuel density drops to the point where all the void space available to the fuel is filled. Nodal expansion quickly follows, causing a density decrease. This relieves the liquid pressure allowing the pressure buildup in adjacent nodes to cause recompression. High pressures again follow and the process oscillates until enough overall core expansion has occurred to terminate the excursion. If sodium compressibility is taken into account, peak pressures are lower because of the increased volume available to the fuel.

A comparison of two 50 \$/sec cases was carried out in VENUS to note the differences in the transient for sodium-out and sodium-in conditions. The reactivity plot and the associated power curves for the sodium-out case are shown in Figures XV.146 and XVI.17, respectively. Doppler feedback, assumed to be $\beta \frac{dk}{dT} = -0.005$, was sufficiently strong to cause three power pulses prior to disassembly, the latter of which occurred at approximately 51 msec. Figure XVI.18 shows the core distortion at 50.73 msec and Figure XVI.19 shows the degree of core distortion at 51.41 msec, the point where the net reactivity dropped below zero. These latter two illustrations contain the R-Z spatial mesh hookup where the core is comprised of the central 11 x 18 (RxZ) nodes. The peripheral 5 nodes are reflector nodes. The point to be made is that with no sodium in the core, a substantial amount of core movement was required in the central regions and at the interface between Zone I and Zone II to effect core shutdown. Some implosion is noted from the power peak of Zone II.

The identical case except for a sodium-in equation of state is shown in the next series of figures, namely Figures XVI.20, XVI.21, and XVI.22. The excursion is over for the latter case in 49.35 msec -- the relatively earlier disassembly resulting from the higher pressures generated due to the sodium inventory. As illustrated in Figure XVI.22, the pressures were more nearly uniform for the sodium-in case and core shutdown was effected more by total core expansion, as opposed to the localized expansion for the sodium-out case.

F. MELT-II -- VENUS COUPLING

In order to analyze large nuclear excursions, from inception through core disassembly, it has been found desirable to accomplish a fairly tight coupling of the MELT-II and VENUS codes. The accident sequence is followed in MELT-II until fuel temperatures are elevated to the point where sizable disassembly pressures are attained. At this time the fine structure fuel temperature information is volume averaged over the R-Z nodal structure used in VENUS and this information, along with the power level and all reactivity components, is used directly as the starting point for the disassembly phase in VENUS. In addition, the core is scanned to determine which regions are void of sodium, and this information is used to establish whether a sodium-in or a sodium-out equation of state should be employed at a particular VENUS nodal point. This same core search on the sodium inventory is used to establish the effective Doppler coefficient to be used in the disassembly phase. Figure XVI.23 illustrates the type of information generated in each phase and indicates the type of information which must flow between MELT-II and VENUS in order to accomplish a smooth transfer.

Lecture XV contained a core subdivision used in the MELT-II calculations of FTR transients. This subdivision meshes directly with the grid utilized in VENUS, the latter of which is illustrated in Figure XVI.24. Within the core, the same 18 level axial structure is used as in MELT-II and the radial structure is constructed of simply a further subdivision of the 6 channel dimensions.

1. Test Case

Before embarking directly into the study of large accidents, using the coupled MELT-II - VENUS system, a check case was computed in which a 50 \$/sec,

unbounded ramp was imposed on the MELT-II - VENUS system and upon VENUS only, where, in both cases, an initial steady state operating condition of 380 MW neutronic power was assumed. The Doppler coefficient was assumed to be -0.005 and Doppler weighting was used in both codes. Figure XVI.25 contains the power and energy traces of the two cases. As noted from the figure, the coupled case yielded a work energy value of 304 MW-sec whereas the core utilizing VENUS for the entire excursion yielded a value of 339 MW-sec. The core average fuel temperature was 2709 °K at the time of transfer and the hottest fuel temperature in MELT-II was 4090 °K. Using 2806 °K and 4300 °K for the respective average and peak fuel temperature, i.e., delaying the time of transfer, the energy value obtained from the coupled system was 309 MW-sec. Waiting still longer, to obtain average and peak temperatures of 2917 and 4564 °K, the computed work energy was 325 MW-sec. Although this tends to indicate that core conditions corresponding to the latter transfer time better specify initial conditions for the disassembly phase than those used earlier, it might be noted that complete agreement between MELT-II and VENUS was not obtained up to the time of transfer, as can be seen from Figure XVI.25. The slight differences accrue mainly from a small discrepancy in the Doppler feedback. Although the difference has not completely been accounted for, the main difference is believed to be associated with the adiabatic assumption in VENUS. Even in this rapid power transient, some heat is in reality carried away by the coolant, and MELT-II accounts for this whereas VENUS cannot. The slightly smaller Doppler feedback, resulting from the slightly lower temperatures, would be expected to result in a power trace relative to VENUS as shown on the graph. Hence, because of the particular timing of the power pulses, VENUS, if used for the entire excursion, tends to overestimate the energy generated.

Therefore, the transfer time used in Figure XVI.25, or perhaps the next increment tried, is probably fairly close to the time for specifying initial conditions for the disassembly phase. Perhaps the most comforting result is that the timing for the exact point of transfer is not too crucial.

2. 5 \$/sec Power Transient with Molten Fuel-Sodium Interaction

Lecture XV contained the transient results up to the start of disassembly for a 5 \$/sec power transient which was assumed to be aggravated by a violent molten fuel-sodium interaction. Figure XVI.26 contains a continuation of this analysis through the disassembly phase. As noted from the figure the transition from the MELT-II to the VENUS phase is accomplished smoothly.

For the case shown, Channel 1 was about 2/3 voided in the core and Channel 2 was voided for a central axial distance of about 40 cm at the time of transfer to VENUS. Hence, that portion of the core was specified to have a sodium-out equation of state whereas a sodium-in equation of state was used elsewhere in the reactor.

Because of the very rapid increase in the reactivity ramp rate due to sodium expulsion, the exact timing for the transfer to VENUS was suspected to be fairly critical in this case. A sensitivity study, however, indicated that although the transfer should be accomplished earlier than for an all sodium-out case (the reason, of course, being that departure temperatures are attained fairly early with sodium in the core), again the timing is not too crucial. A difference of only $\pm 4\%$ in the energy release was calculated for an average fuel temperature at the time of transfer ranging from 2500 °K to 3000 °K. For a few of the cases investigated, a nodal pressure of 100 to 200 atmospheres was included for those nodes void of sodium. This was done to partially account for the disassembly effect of sodium vapor pressures which were assumed effective in ejecting the liquid sodium.

3. Sodium Bubble

Lecture XV also contained a few pre-disassembly transient results for the case of a large sodium bubble passing through the core. Figure XVI.27 contains the continuation of this analysis through the disassembly phase. Again, the transfer is noted to be accomplished smoothly.

In this instance, the sodium bubble had only moved up into the lower region of the core by the time sufficient reactivity had been added to disassemble the core. Hence, a fairly asymmetric equation of state mix was used in VENUS. Because of the large, relatively low pressure region associated with the sodium bubble, some core implosion was actually observed to occur. Net core movement, however, was in the direction of negative reactivity and a rapid nuclear shutdown was accomplished.

G. Review of Current Fast Reactor Disassembly Codes

Numerous fast reactor disassembly codes are now in existence and in active use at essentially all major nuclear reactor laboratories throughout the world. Because of the sheer magnitude, no attempt will be made to describe or even list all of them here. Rather, a few key codes will be mentioned which are believed to be representative of a large class of such programs.

Perhaps the program used most widely for early survey work in fast reactor disassembly analysis was the Weak Explosion Program⁽¹⁷⁾ (WEAK or WEP). This program, formulated by Nicholson, was the first program to include the effects of fuel vapor pressure and Doppler feedback. Perhaps the major liability of the code, for present consideration, is its intrinsic tie to a vapor pressure functional relationship for the equation of state. This prevents any straightforward way to even attempt utilizing a density dependent equation of state.

MARS⁽²³⁾ is essentially a two-dimensional version of the one-dimensional WEAK program. The equation of state in this program, although of the same vapor pressure functional form as in WEAK, can be specified differently for each material region. However, formulation of a density dependent equation of state is still not possible.

AX-1⁽²⁴⁾ is a one-dimensional disassembly code which uses a transport theory neutronics package rather than the simpler point kinetics formulation and associated perturbation theory. For most cases, however, this added complexity has been found unnecessary in addition to being quite unwieldy.

As mentioned in the notes earlier, MAX⁽¹⁶⁾ was the first disassembly code (one dimensional) written in a Lagrangian coordinate system. This allowed direct use of a density dependent equation of state. VENUS, discussed fairly extensively above, was written quite recently and also utilizes a Lagrangian coordinate system. It is a two-dimensional (R-Z) code and is probably the most advanced tool in current use for investigating core disassembly accidents.

References

1. H. A. Bethe and J. H. Tait. An Estimate of the Order of Magnitude of the Explosion when the Core of a Fast Reactor Collapses, RHM(56)/113. Atomic Energy Research Establishment, Harwell, Berks, England, 1956.
2. R. B. Nicholson. Methods for Determining the Energy Release in Hypothetical Reactor Meltdown Accidents, APDA-150. Atomic Power Development Associates, Inc., December 1962.
3. E. P. Hicks and D. C. Menzies. "Theoretical Studies on the Fast Reactor Maximum Accident," Proceedings of the Conference on Safety, Fuels, and Core Design in Large Fast Power Reactors, October 11-14, 1965, ANL-7120. Argonne National Laboratory.
4. R. A. Meyer, B. Wolfe, and N. F. Friedman. "A Parameter Study of Large Fast Reactor Meltdown Accidents," Proceedings of the Conference on Safety, Fuels, and Core Design in Large Fast Power Reactors, October 11-14, 1965, ANL-7120. Argonne National Laboratory.
5. R. J. Ackermann et al. "High Temperature Thermodynamic Properties of Uranium Dioxide," J. of Chem. Phys., Vol. 25, No. 6, p. 1089. 1956.
6. R. W. Ohse. High Temperature Vapor Pressure Studies of UO₂ by the Effusion Method, EUR-2166-E. European Atomic Energy Community, 1964.
7. J. A. Christensen. Thermal Expansion and Change in Volume on Melting for Uranium Dioxide, HW-75148. Available from Clearinghouse for Federal Scientific and Technical Information, Springfield, Virginia, 1962.
8. O. A. Hougen et al. Chemical Process Principles Vol. II, Thermodynamics, 2nd Edition, John Wiley and Sons, 1959.
9. D. Miller. "A Critical Review of the Properties of Materials at the High Temperatures and Pressures Significant for Fast Reactor Safety," Proceedings of the Conference on Safety, Fuels, and Core Design in Large Fast Power Reactors, October 11-14, 1965, ANL-7120. Argonne National Laboratory.
10. R. A. Meyer et al. Fast Reactor Meltdown Accidents Using Bethe-Tait Analysis, GEAP-4809. General Electric Company, January 1967.
11. E. J. Robbins. Limits for the Equation of State of Uranium Dioxide, TRG-Report-1344(R). Technical Research Group, New York, 1966.
12. D. E. Simpson, J. W. Hagan, A. E. Waltar, R. A. Harris, A. Padilla and G. L. Fox, Jr. Preliminary Analysis of Postulated Maximum Accidents for the FFTF, BNWL-760, Battelle Northwest, Richland, Washington, November 1968.

13. D. C. Menzies. The Equation of State of Uranium Dioxide at High Temperatures and Pressures, TRG-Report-1119(D). Technical Research Group, New York, 1966.
14. G. L. Ball, A. E. Klickman, D. B. Wehmeyer, and C. S. Yeh. Two-Dimensional Hypothetical Accident Investigation of a Mixed Oxide Core Design for the Fast Test Reactor, APDA-209. Atomic Power Development Associates, Inc., June 1968.
15. R. A. Harris. Preliminary Analysis of Postulated Maximum Accidents for the FFTF, Supplement 1 - Additional Calculations for Sodium-In Conditions, BNWL-760, Supplement 1, Battelle Northwest, Richland, Washington, December 1968.
16. W. W. Little, Jr. MAX-A One-Dimensional Maximum Hypothetical Accident Code in FORTRAN-IV, BNWL-612. Pacific Northwest Laboratory, Richland, Washington, March 1968.
17. J. W. Stephenson, Jr. and R. B. Nicholson. Weak Explosion Program, ASTRA 417-6.0. Astra, Inc., Raleigh, N. C., 1961.
18. W. T. Sha, T. H. Hughes, and P. Margel, "VENUS - Two Dimensional Neutronic-Hydrodynamic Power Excursion Computer Program," (to be published ANL-) 1969.
19. J. J. Kaganove. Numerical Solution of the One-Group Space-Independent Reactor Kinetics Equation for Neutron Density Given the Excess Reactivity, ANL-6132, Argonne National Laboratory, Argonne, Illinois, (1960).
20. J. Von Neumann and R. D. Richtmyer, J. Appl. Physics, 21 (1950).
21. W. Herrmann. Comparison of Finite Difference Expressions Used in Lagrangian Fluid Flow Calculations, MIT Technical Report No. WL-TR-64-104 (1964).
22. Alan E. Waltar and William T. Sha. "Fast Reactor Disassembly Calculation Utilizing a Temperature-Density-Dependent Equation of State," to be presented at the American Nuclear Society Meeting, Nov. 30 - Dec. 4, 1969, San Francisco, California.
23. N. Hirakawa. MARS, A Two-Dimensional Excursion Code, APDA-198, Atomic Power Development Associates, Inc., June 1967.
24. D. Okrent, J. M. Cook, D. Satkus, R. B. Lazarus, and M. B. Wells, AX-1, A Computing Program for Coupled Neutronics-Hydrodynamics Calculations on the IBM-704, ANL-5977, Argonne National Laboratory, Argonne, Illinois, (1959).

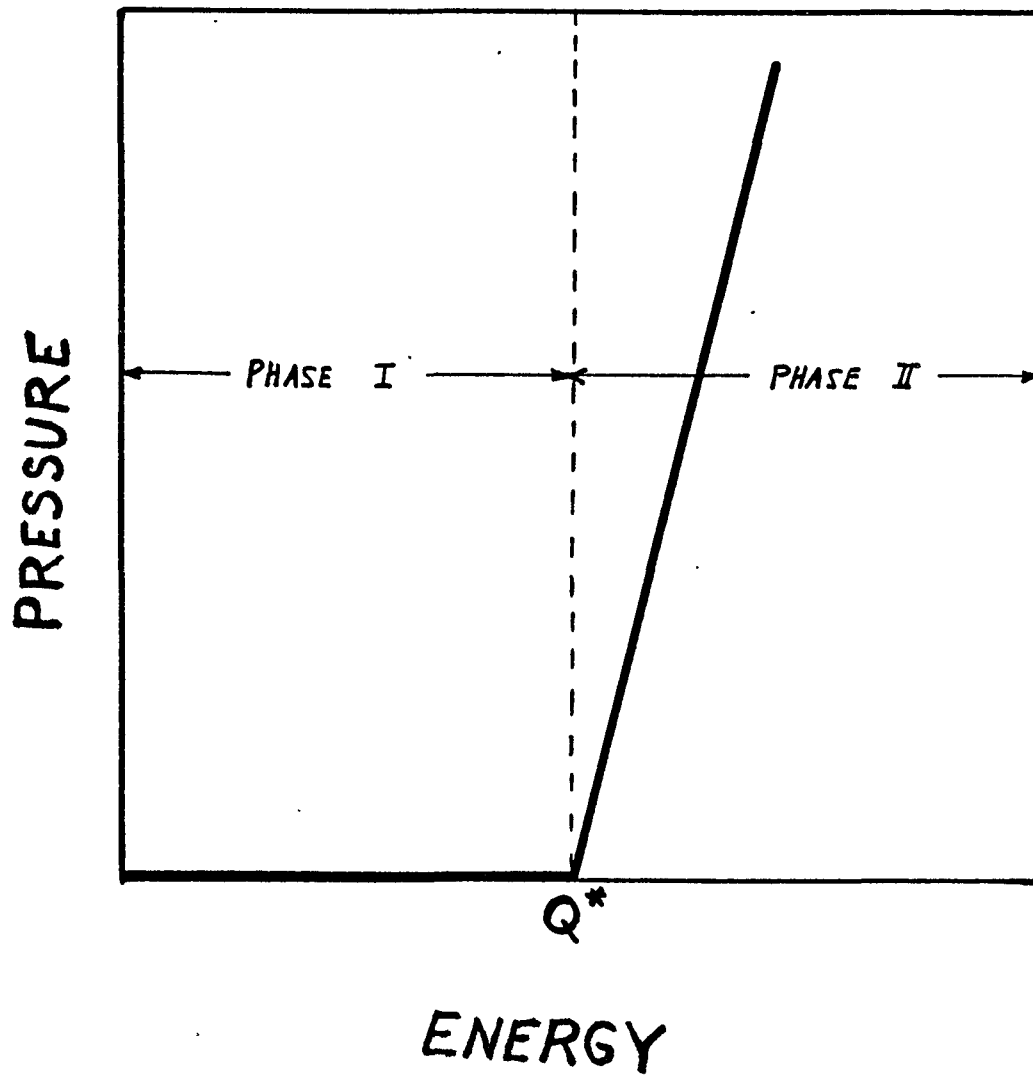


Figure XVI.1 Threshold Type Equation of State Used in Original Bethe-Tait Method

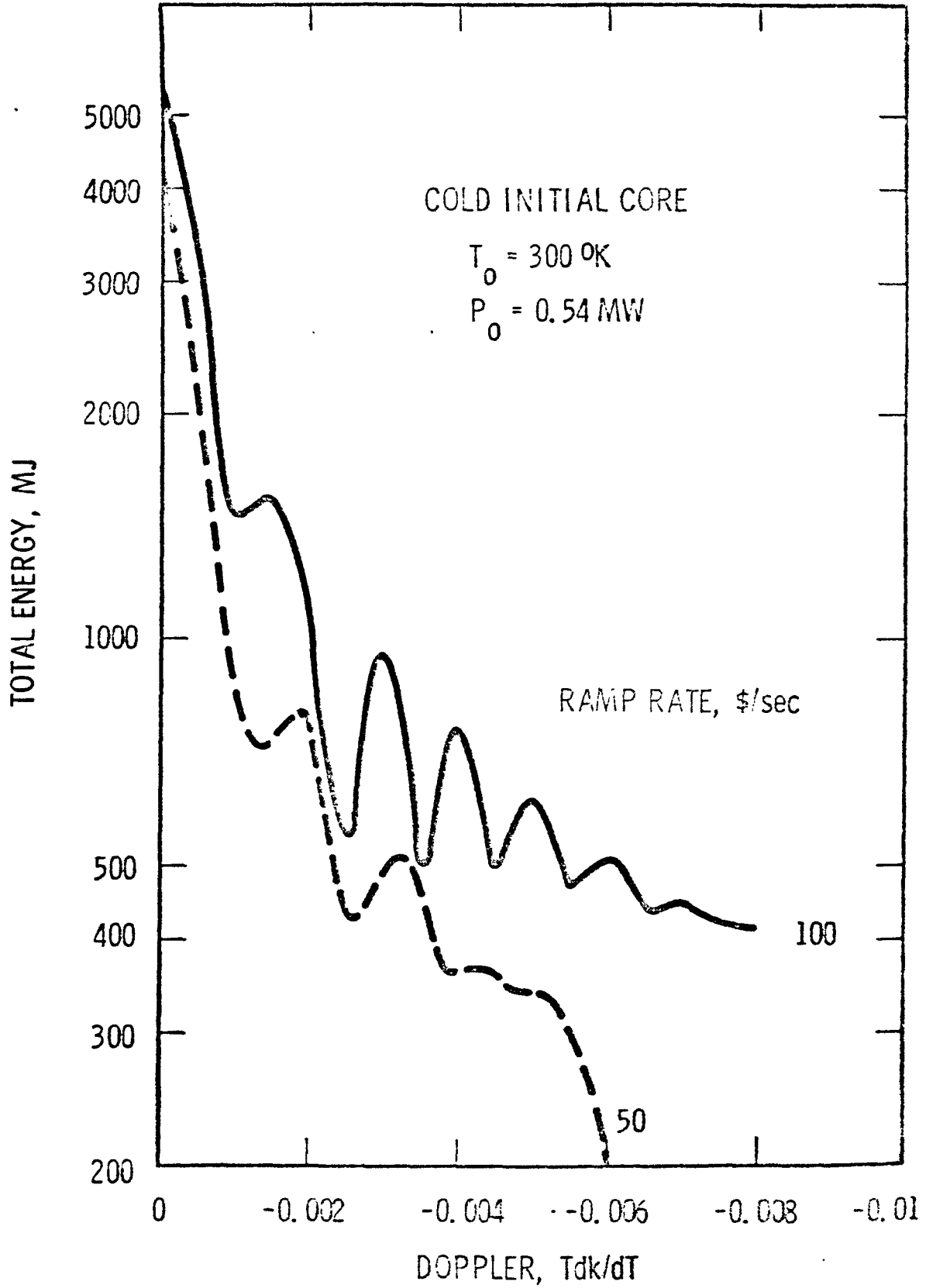


Figure XVI.2 Typical Energy Release versus Doppler Coefficient

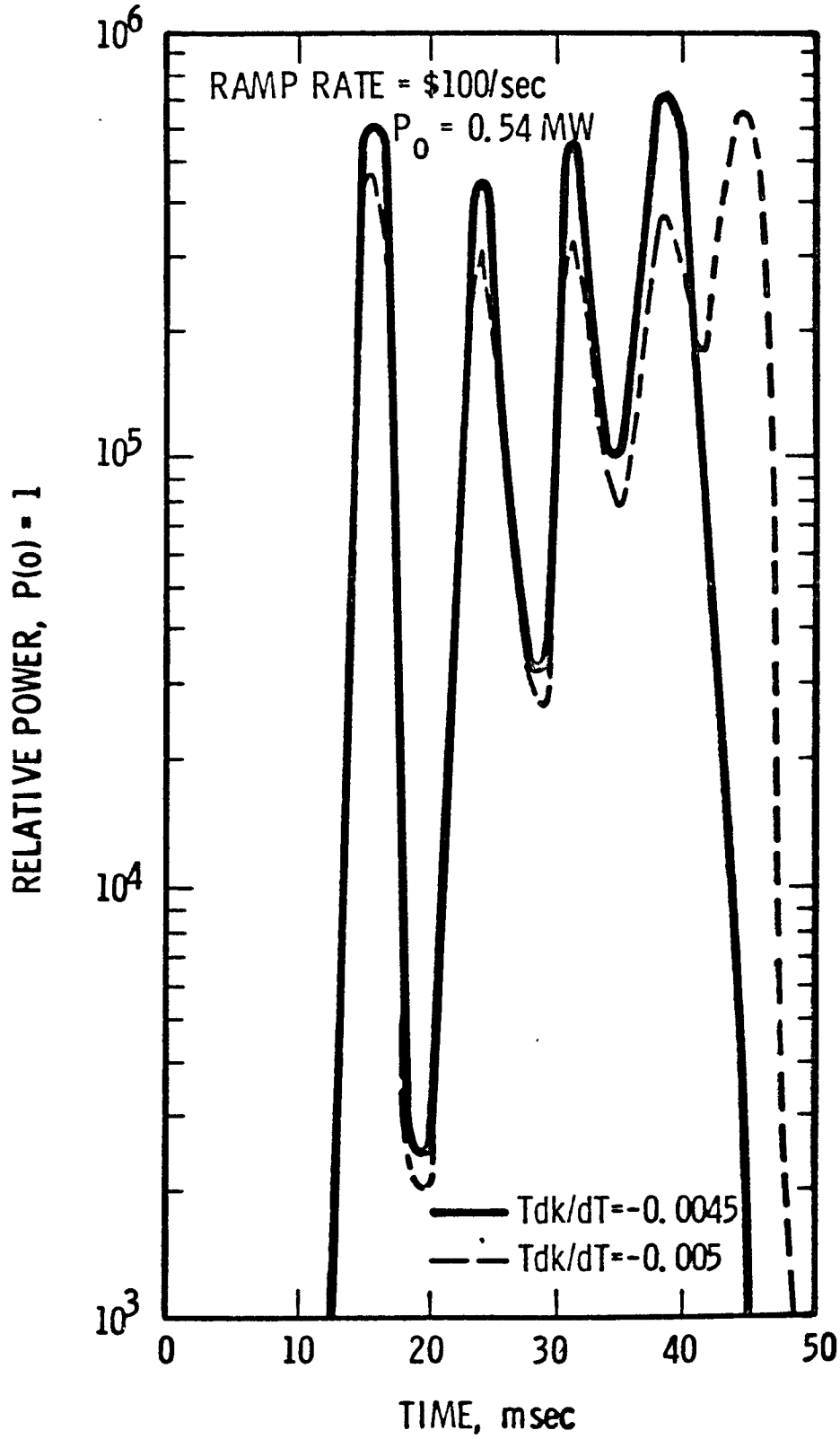


Figure XVI.3 Power Traces for Doppler Coefficients of -0.0045 and -0.005 .

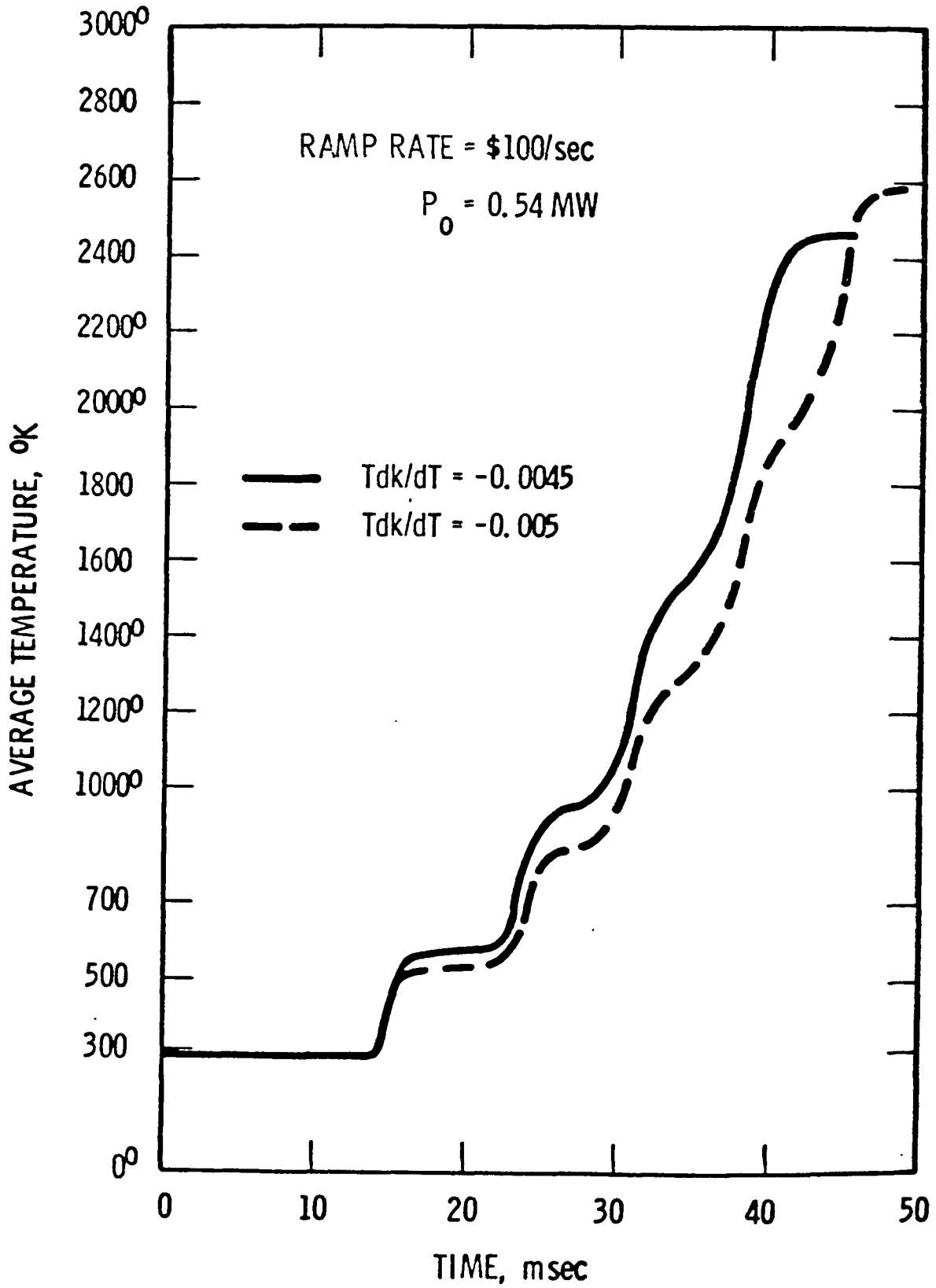


Figure XVI.4 Temperature Buildup for Doppler Coefficients of -0.0045 and -0.005 .

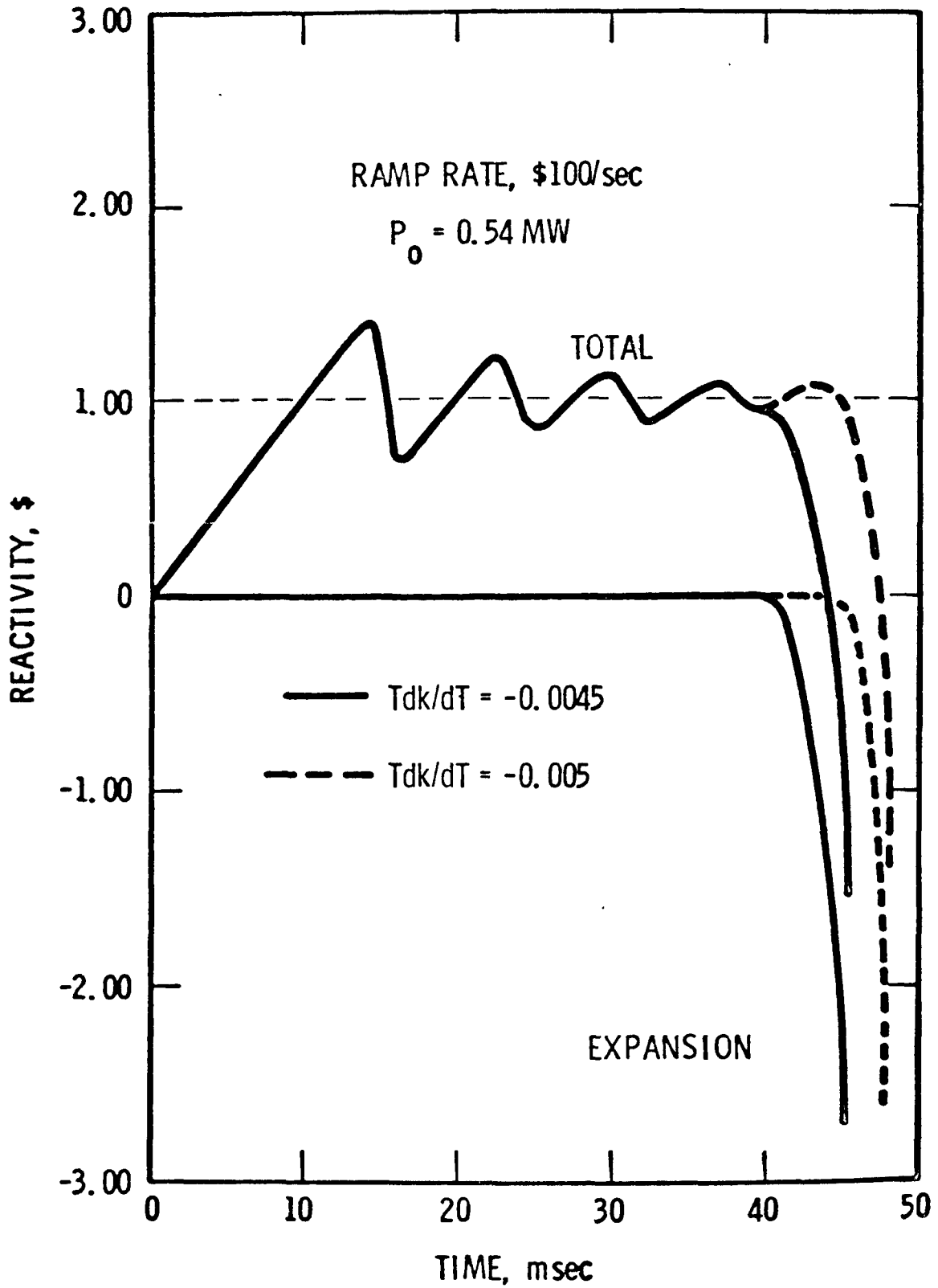


Figure XVI.5 Net Reactivity Traces for Doppler Coefficients of -0.0045 and -0.005 .

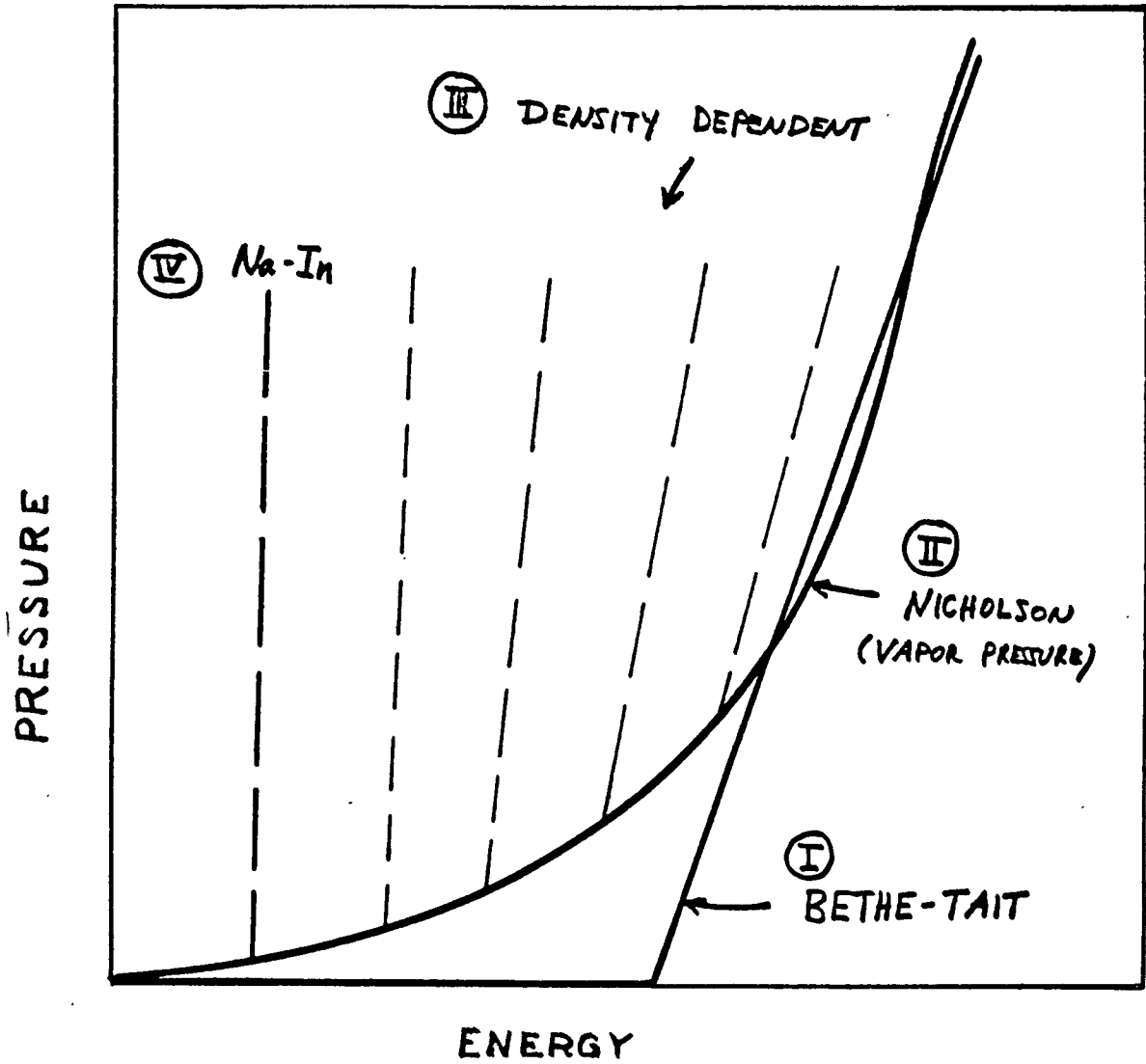


Figure XVI.6 Various Degrees of Sophistication Used in Formulating an Equation of State.

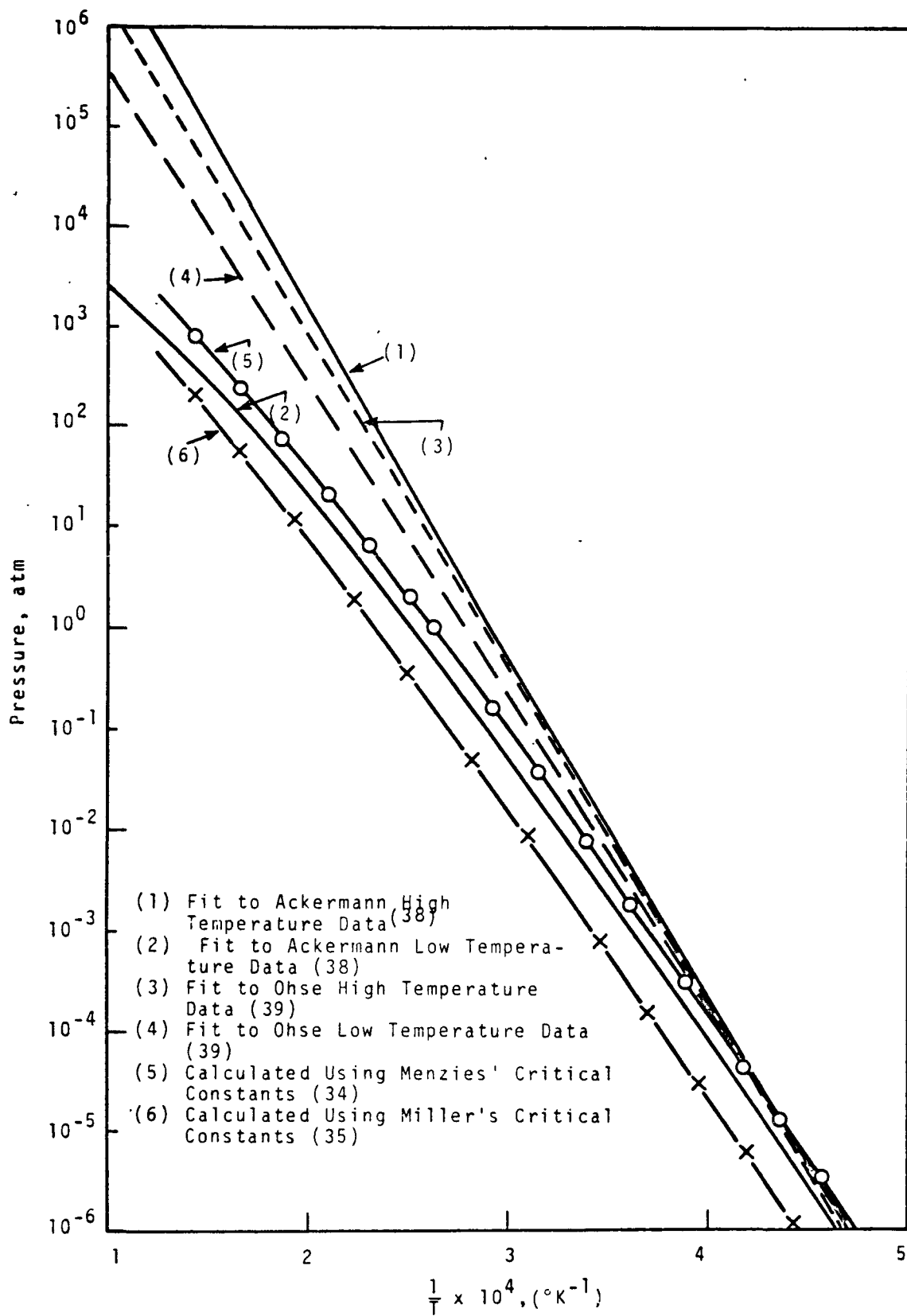


Figure XVI.7 Calculated and Measured Vapor Pressure Curves.

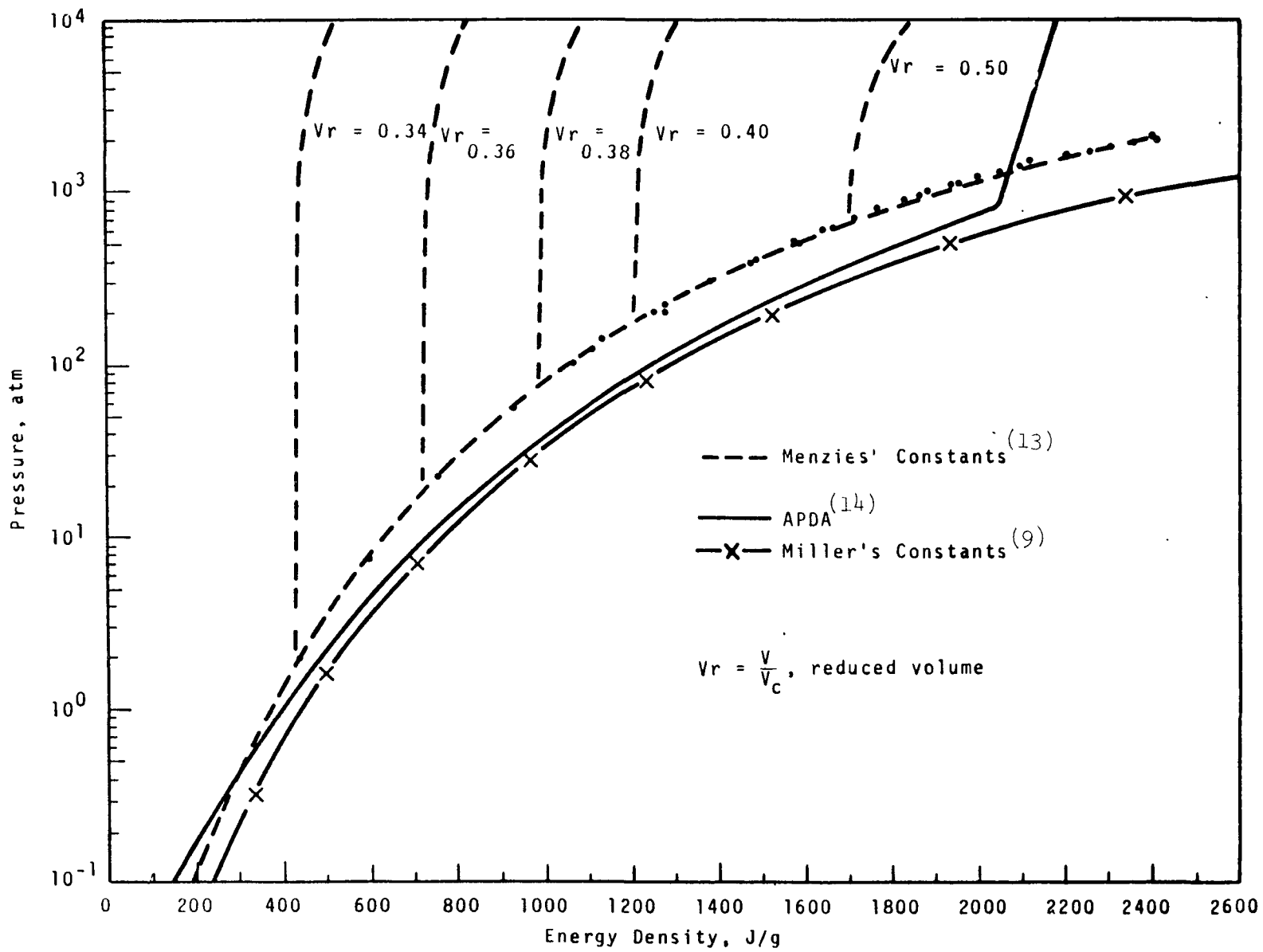


Figure XVI.8 Pressure-Energy Relationships for Sodium-Out.

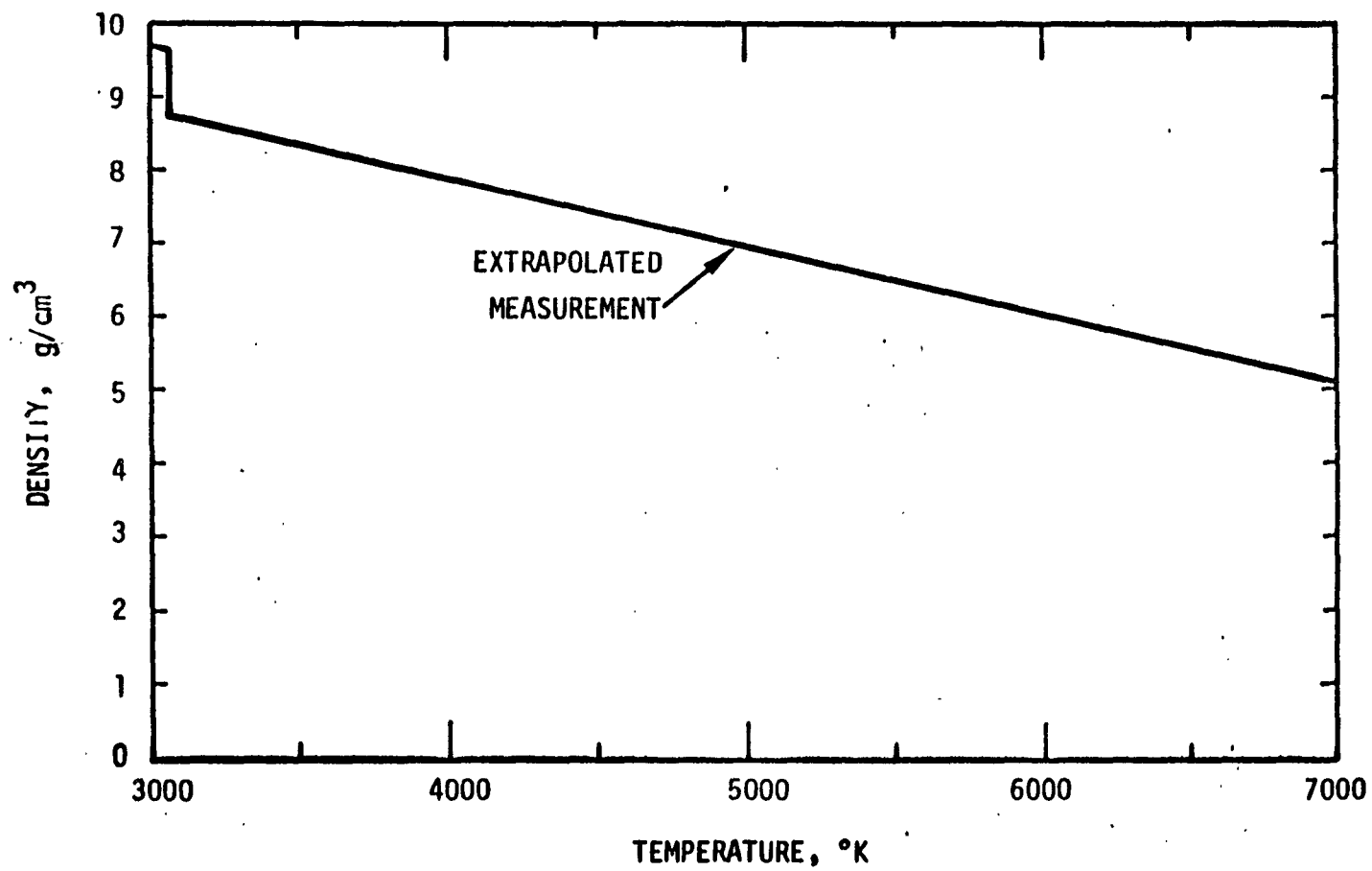


Figure XVI.9 *Liquid Density of UO_2 .*

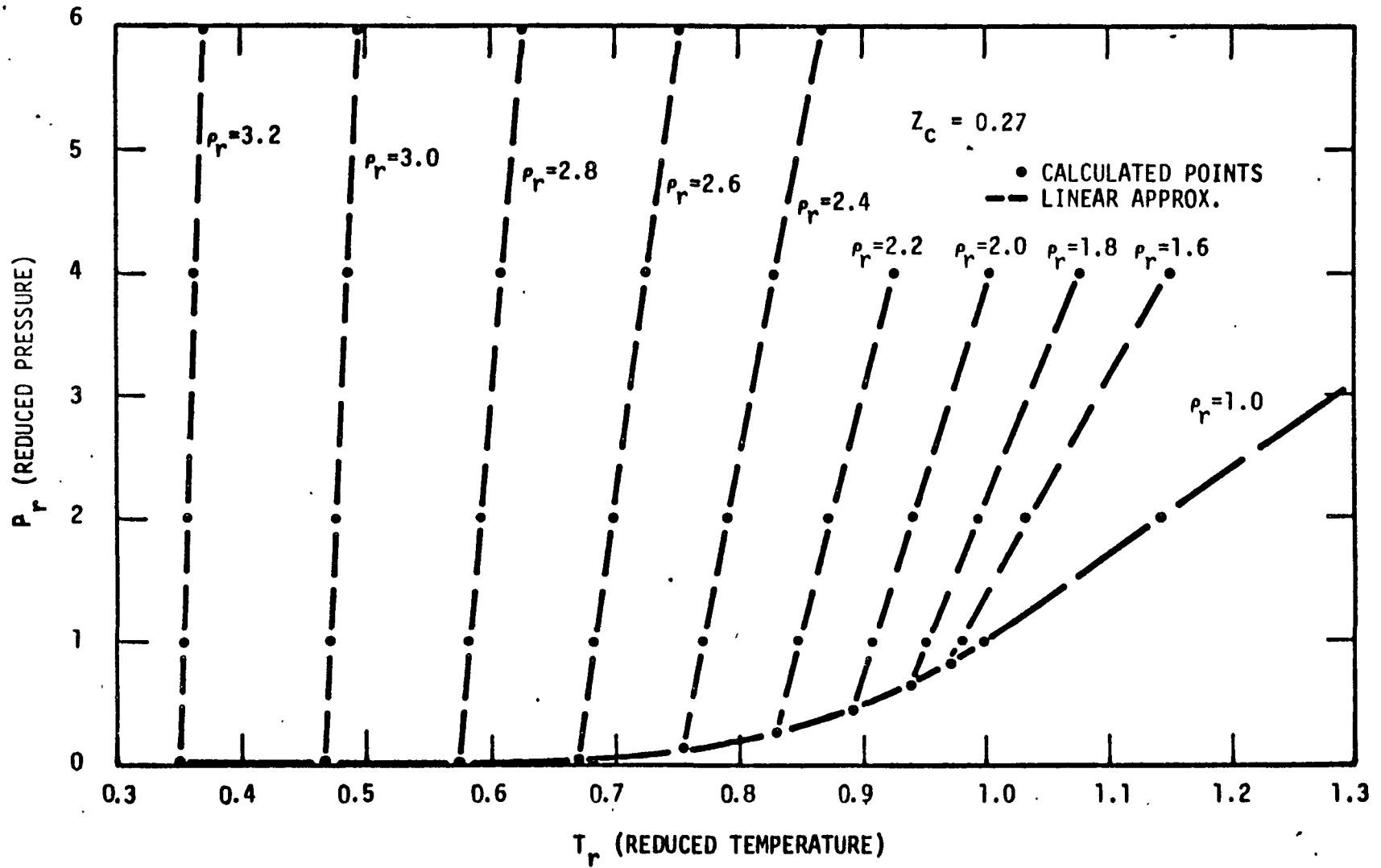


Figure XVI.10 Pressure-Temperature Relationship for Sodium-In Case.

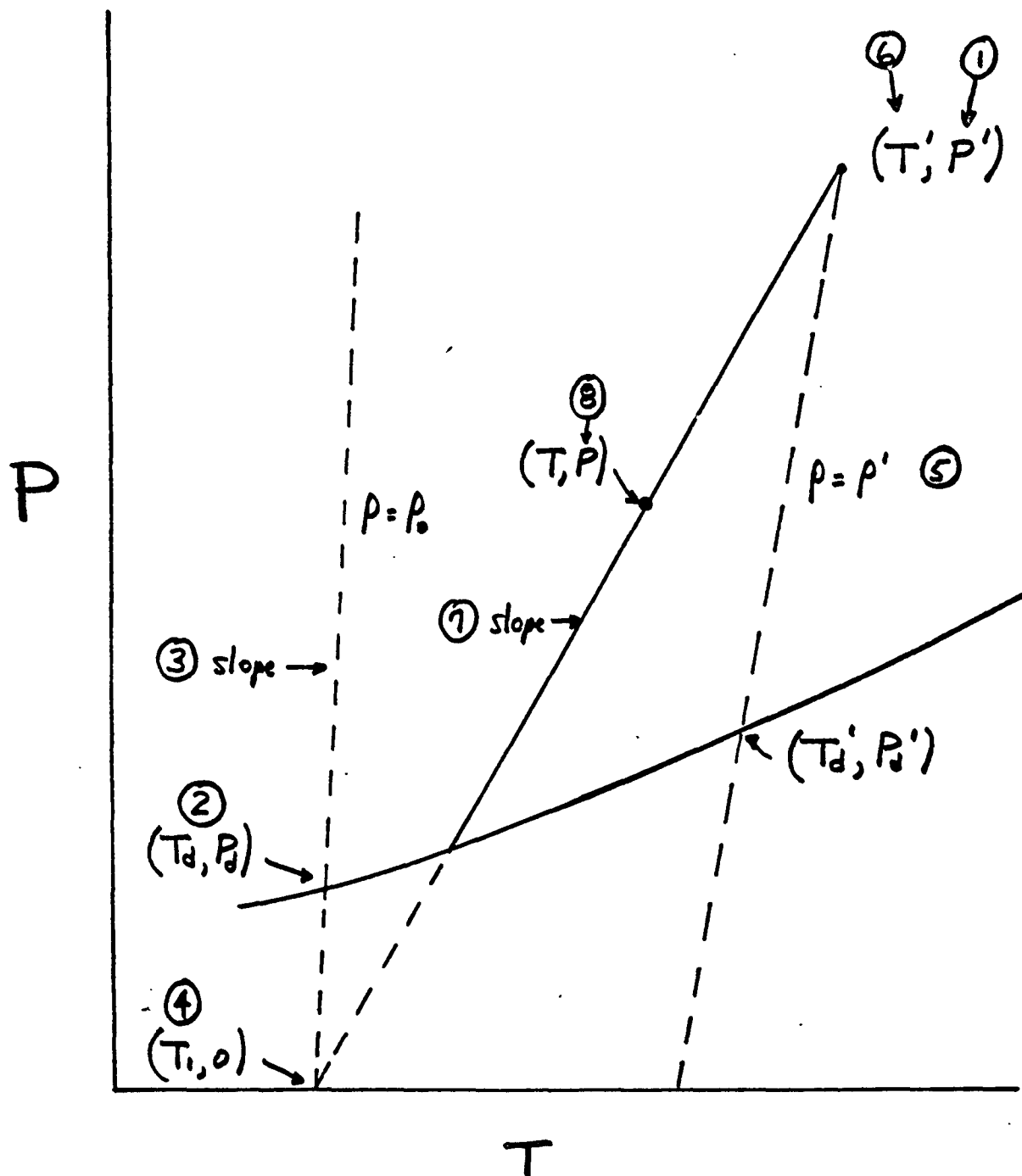


Figure XVI.11

Schematic of Computational Procedure used to Evaluate Slope of P-T Curve for Compressible Sodium.

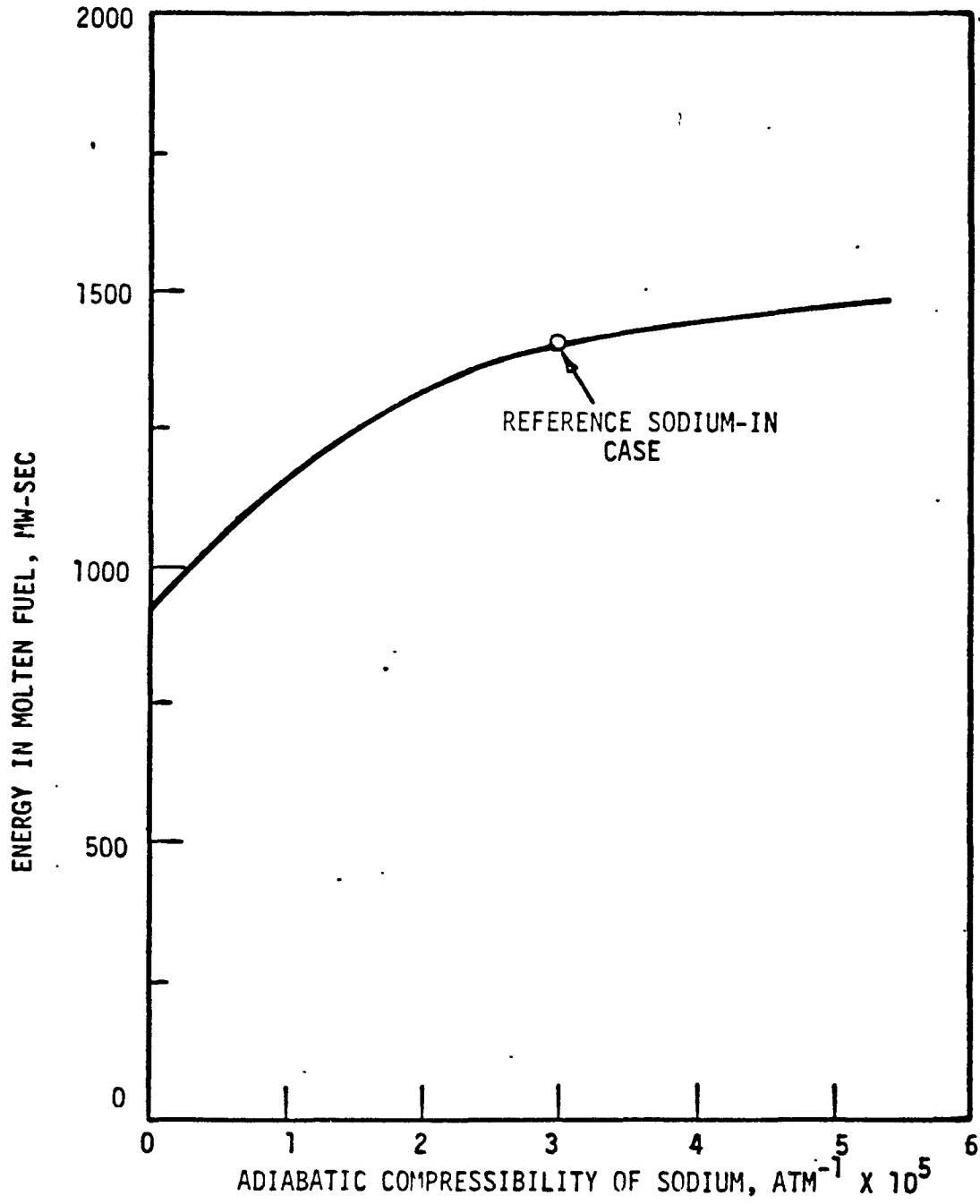


Figure XVI.12 Sensitivity of Molten Fuel Generated to Sodium Compressibility.

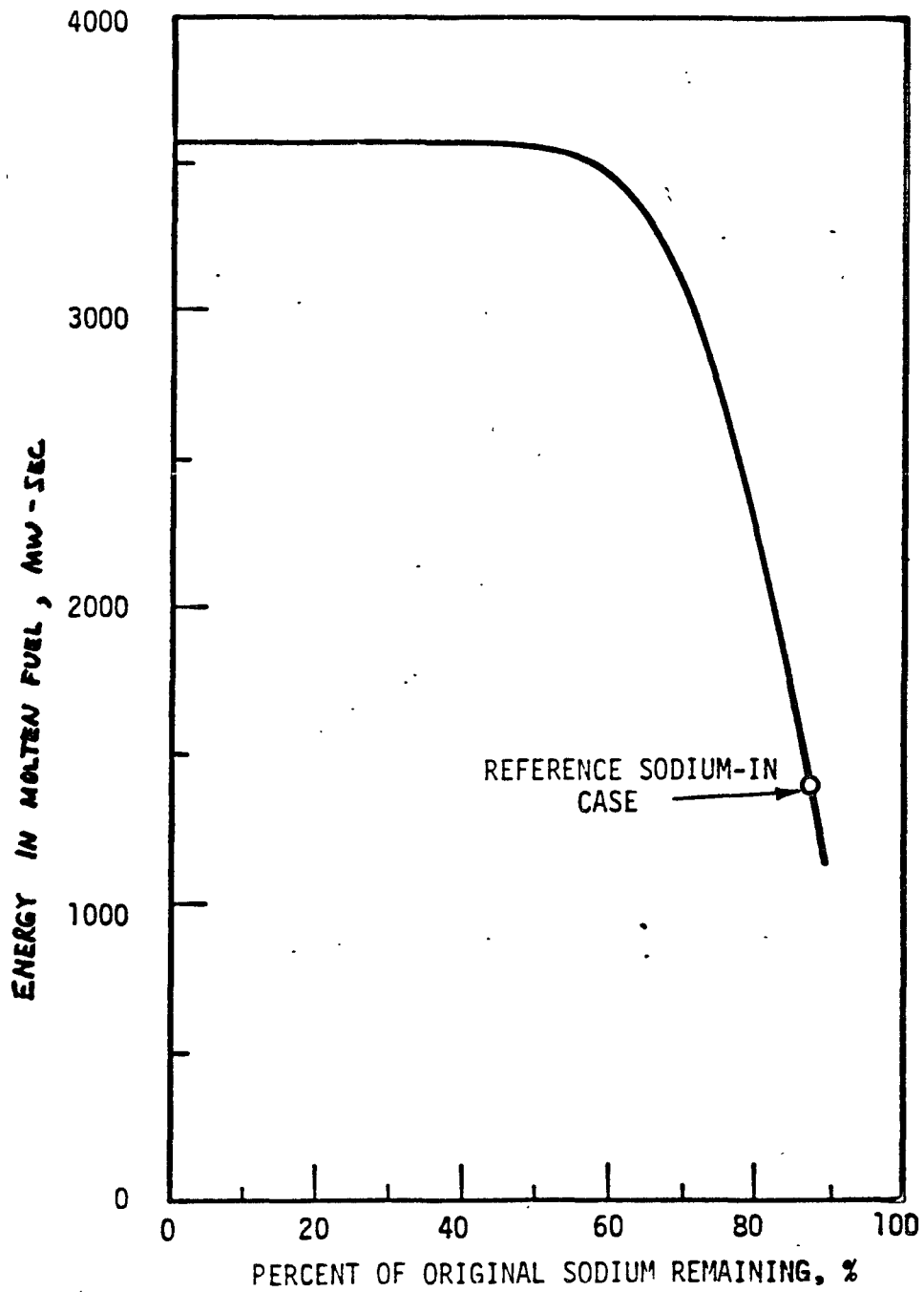


Figure XVI.13

Sensitivity of Molten Fuel Generated to Percent of Sodium in Core (Homogeneous Distribution).

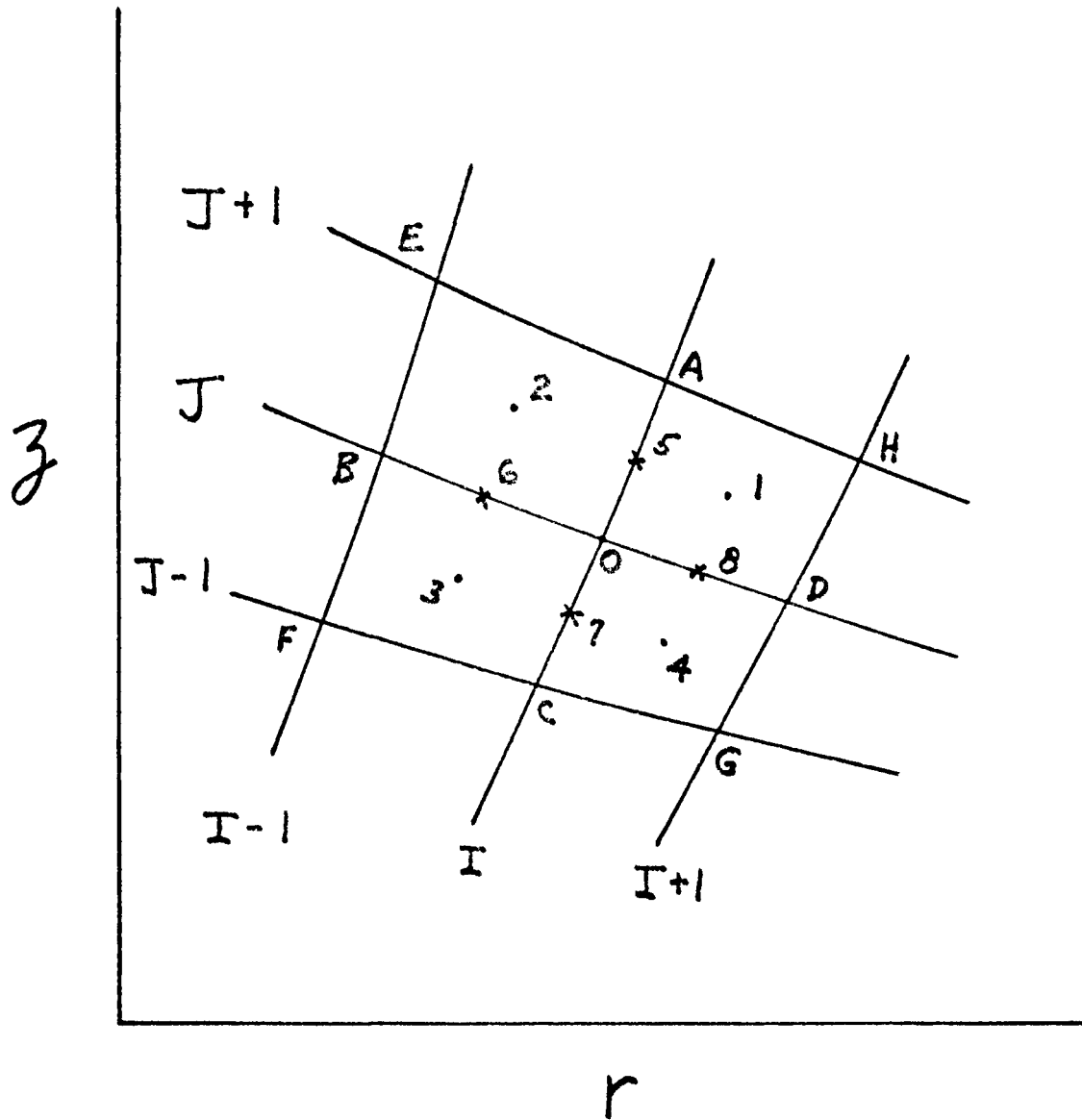


Figure XVI.14 Finite Difference Mesh Set-up Used in VENUS.

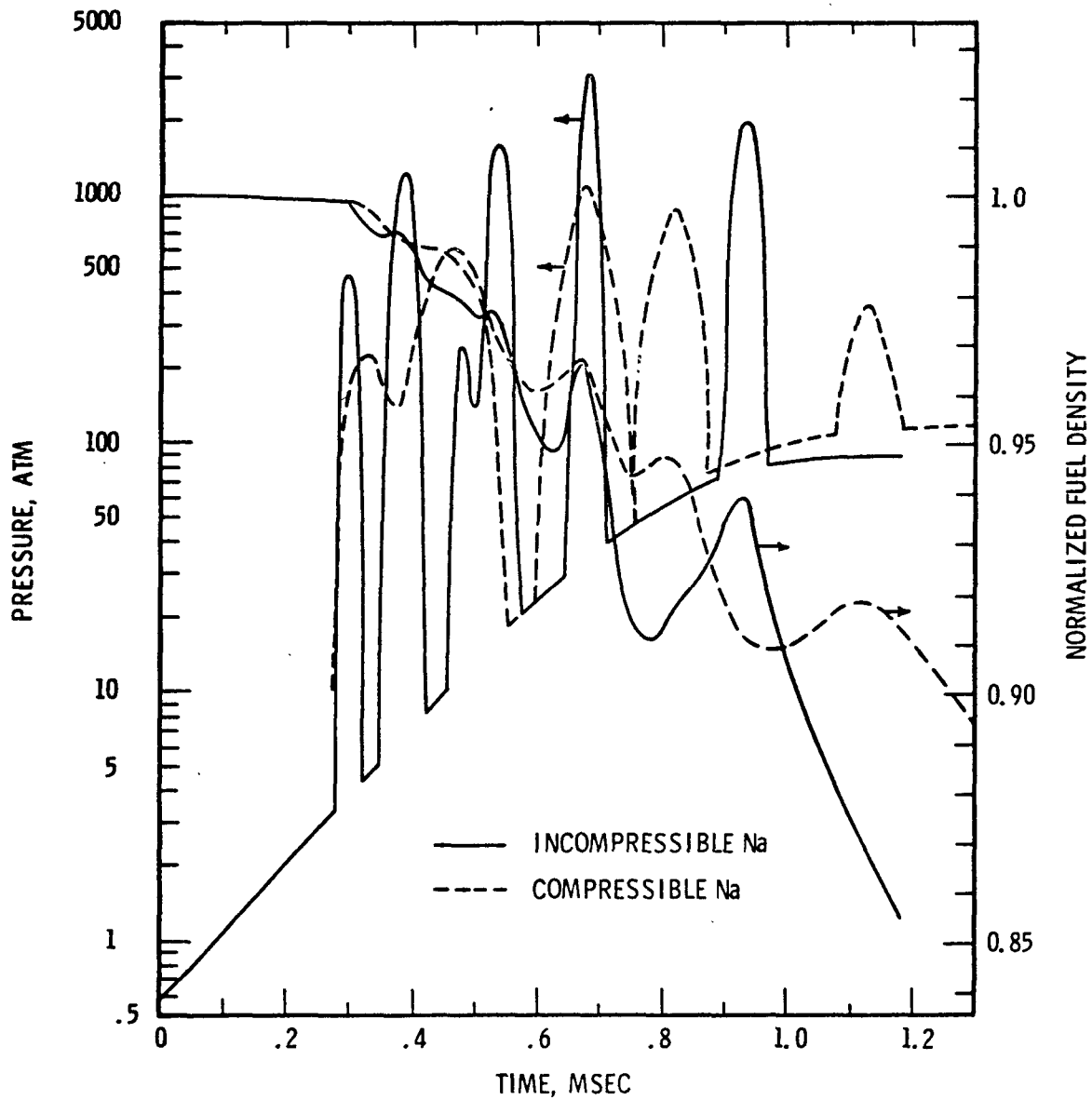


Figure XVI.15

Pressure-Density Variations in the Core Central Node as a Function of Sodium Compressibility.

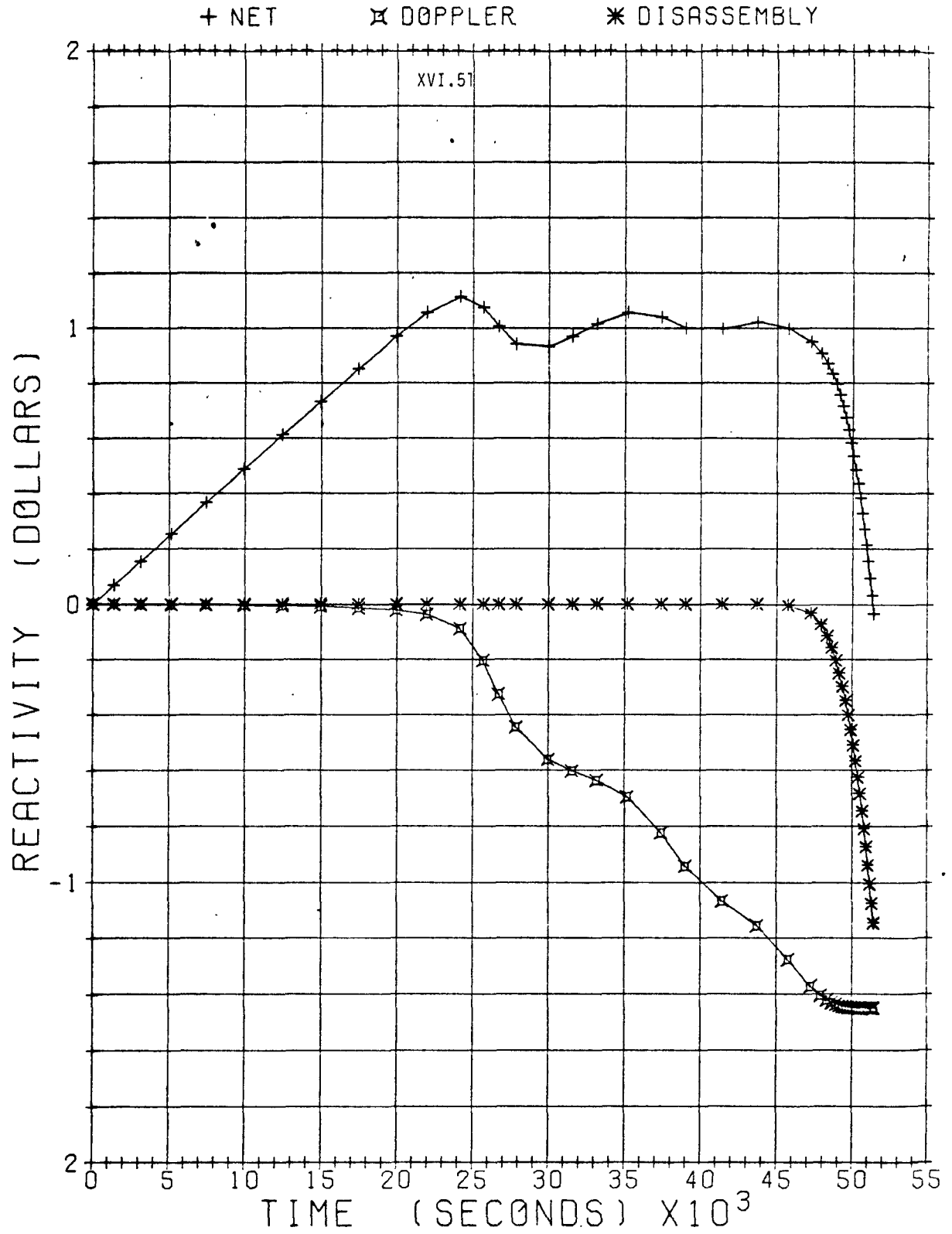


Figure XVI.16 Reactivity Plot for 50 \$/sec Sodium-Out Case.

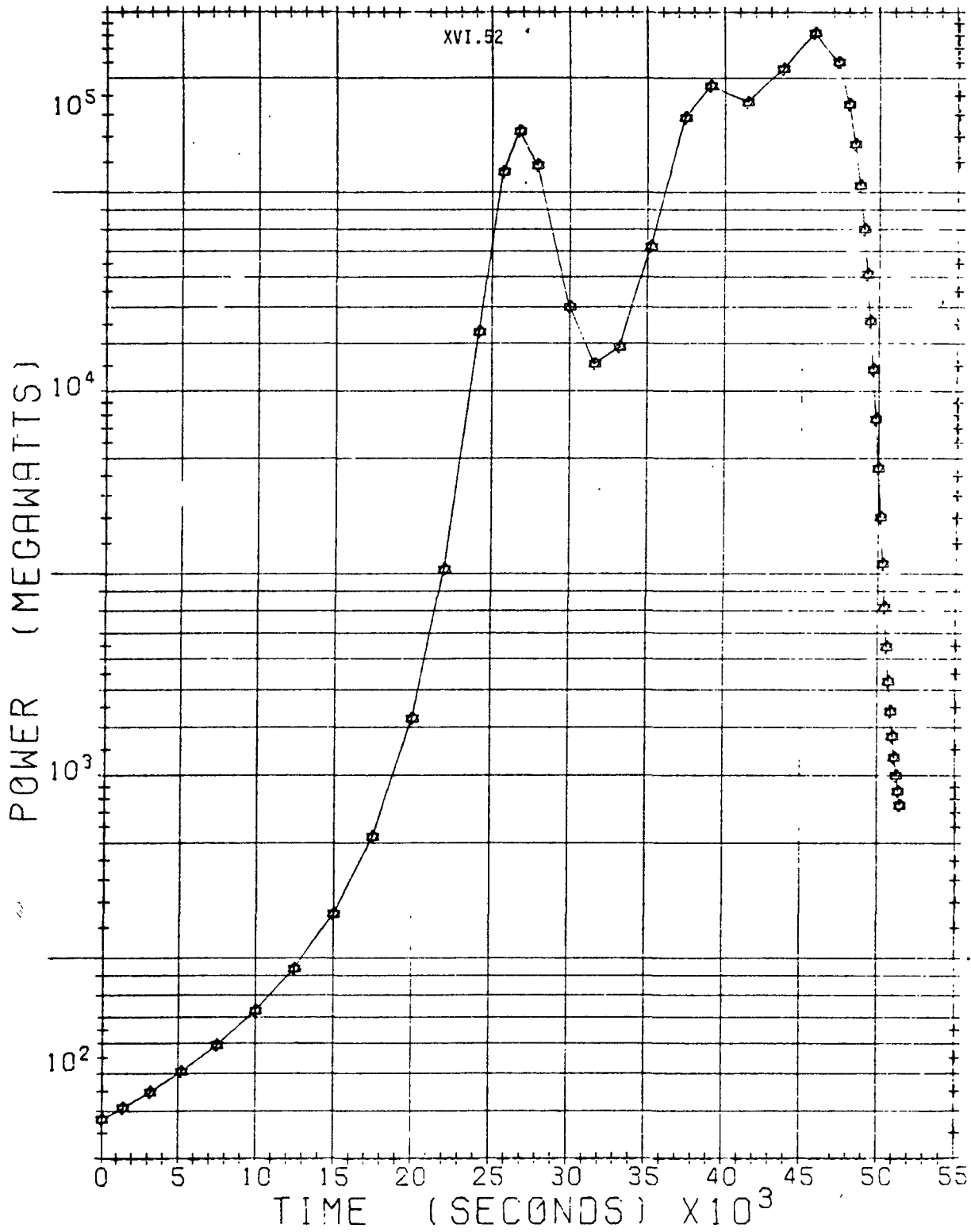


Figure XVI.19

Power Trace for 50 \$/sec Sodium-Out Case.

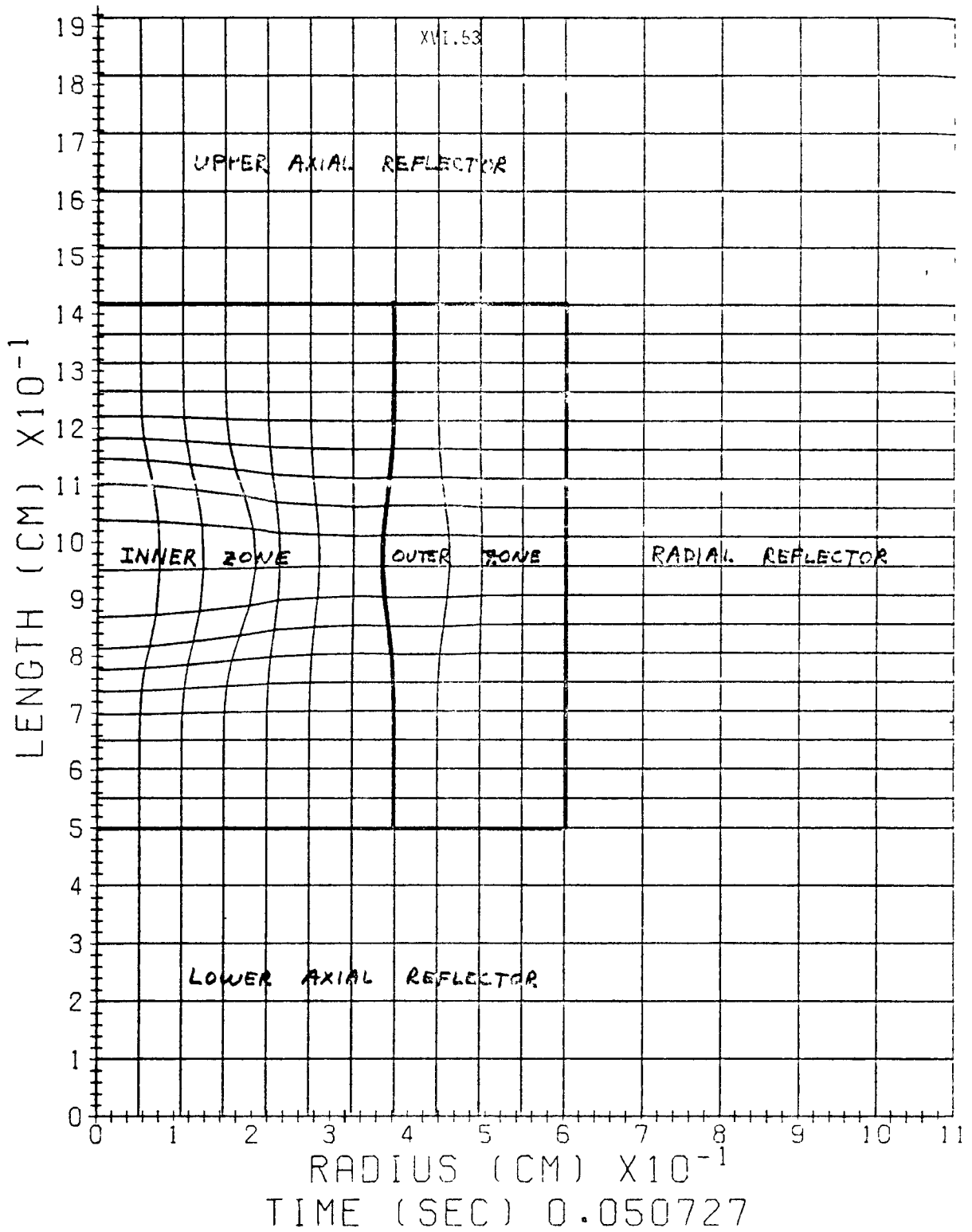


Figure XVI.1 - Core Distortion for 30 g/sec Sodium-Out Case at 50.727 msec.

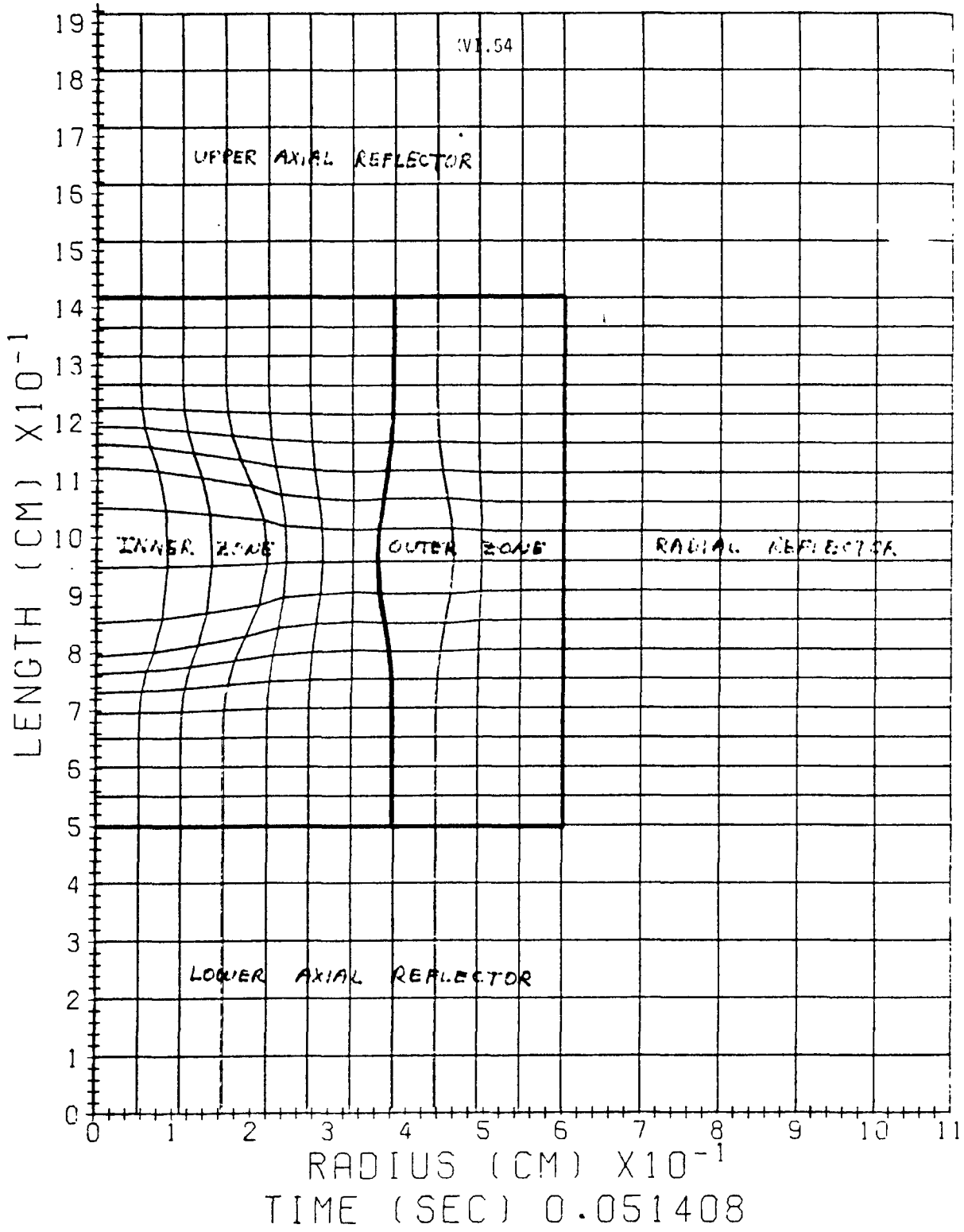


Figure VII.19 Core Distortion for 50 \$/sec Sodium-Out Case at Nuclear Termination Point.

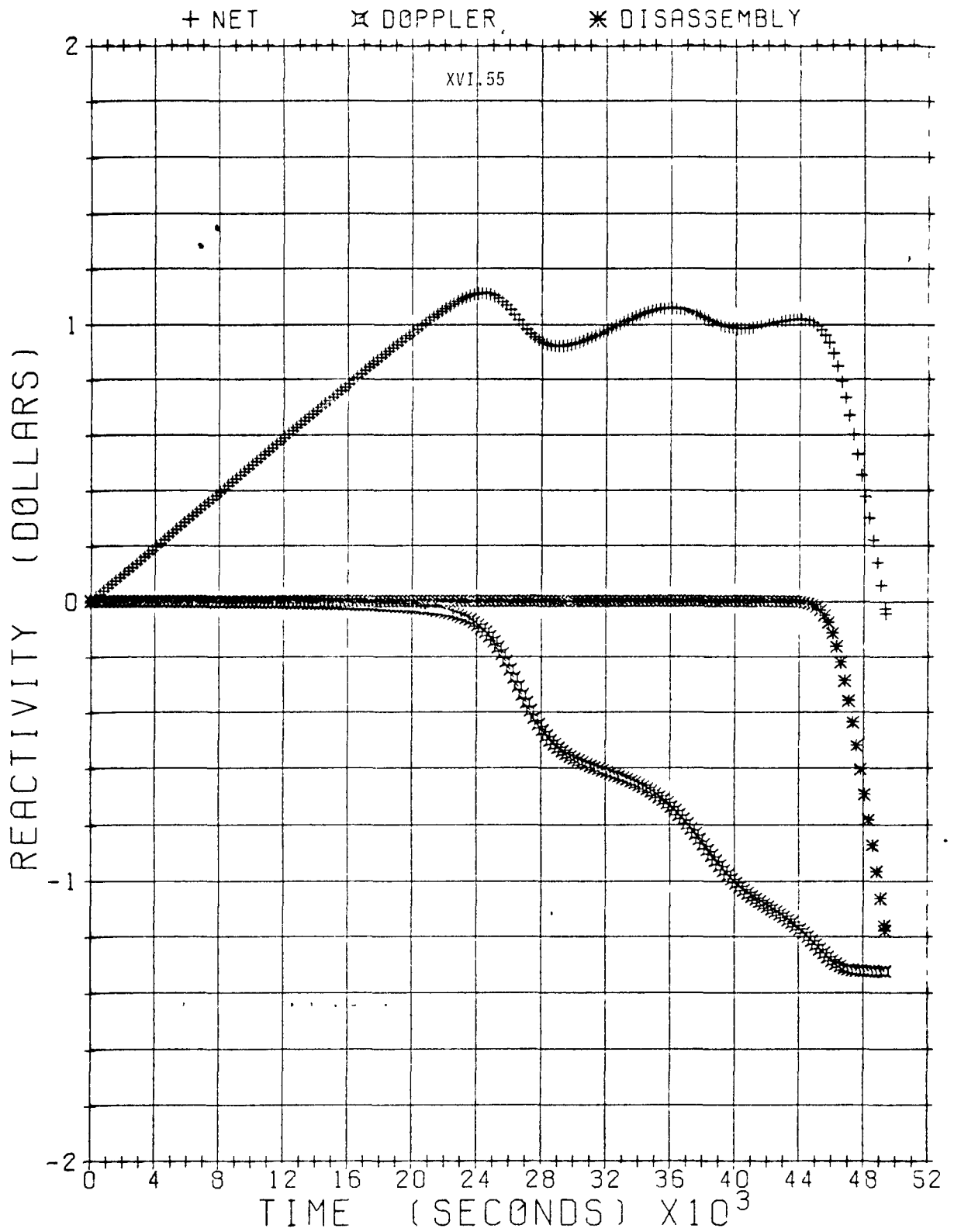


Figure XVI.55 Reactivity Plot for 50 \$/sec Sodium-In Case.

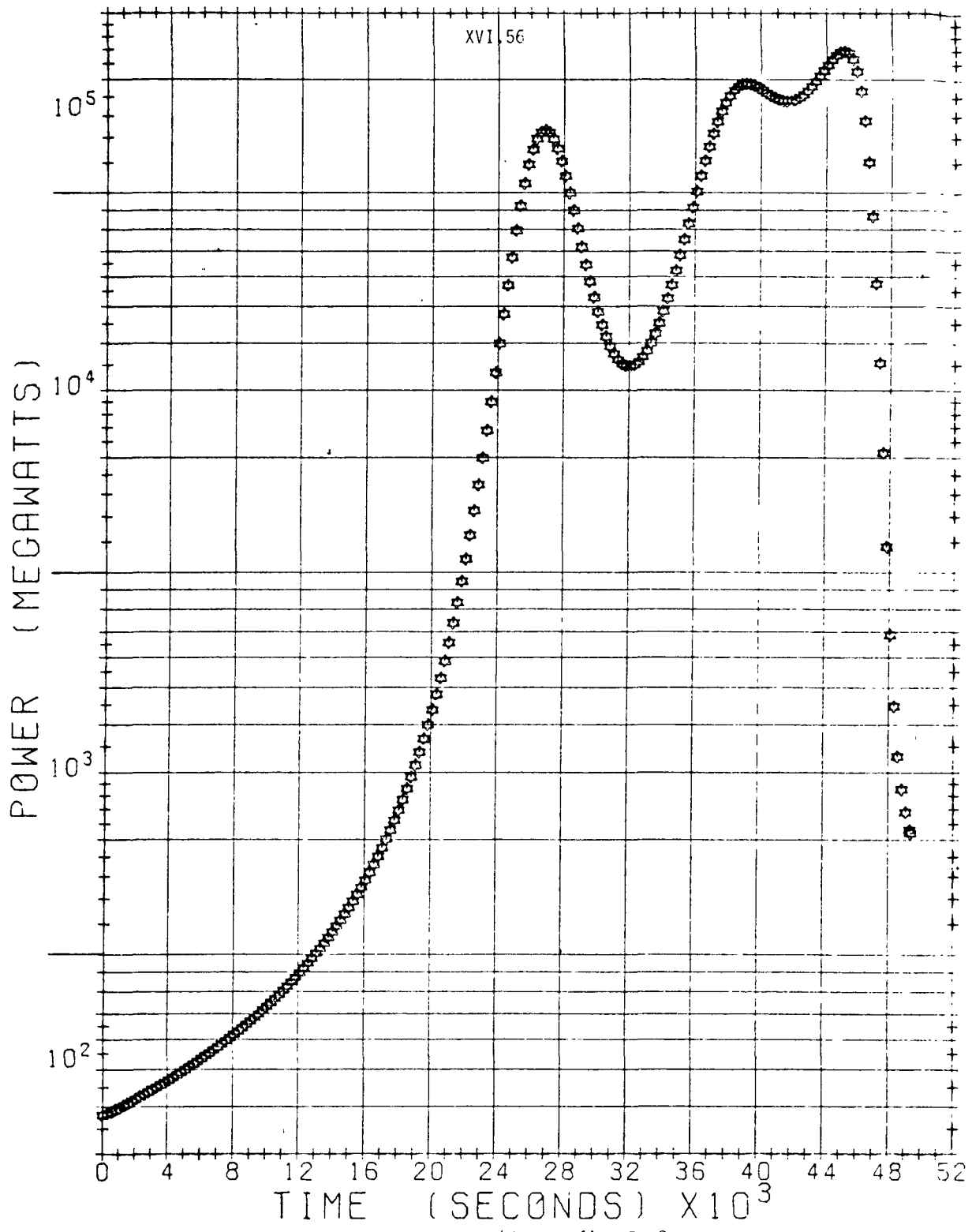


Figure XVI.21 Power Trace for 50 \$/sec Sodium-In Case.

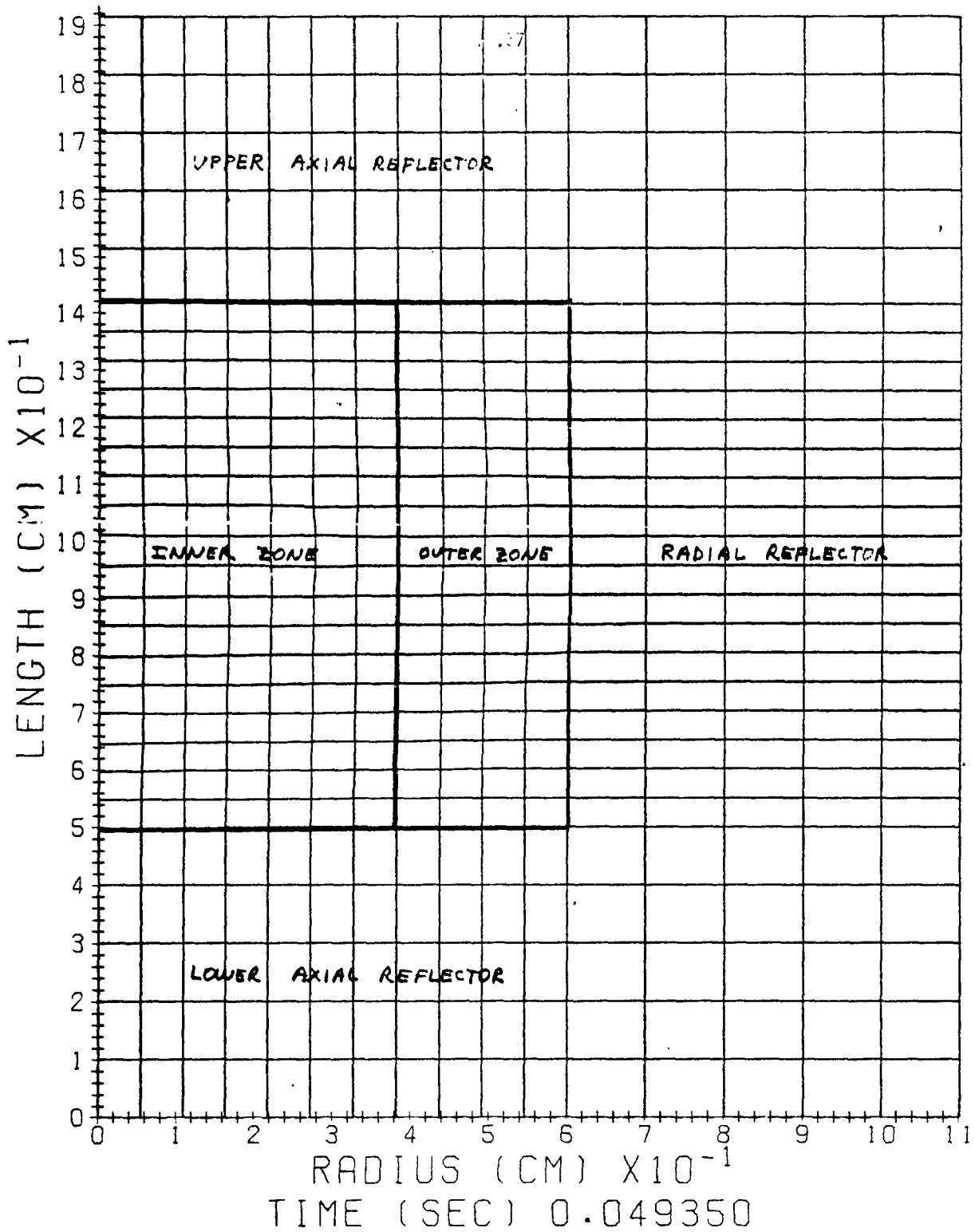
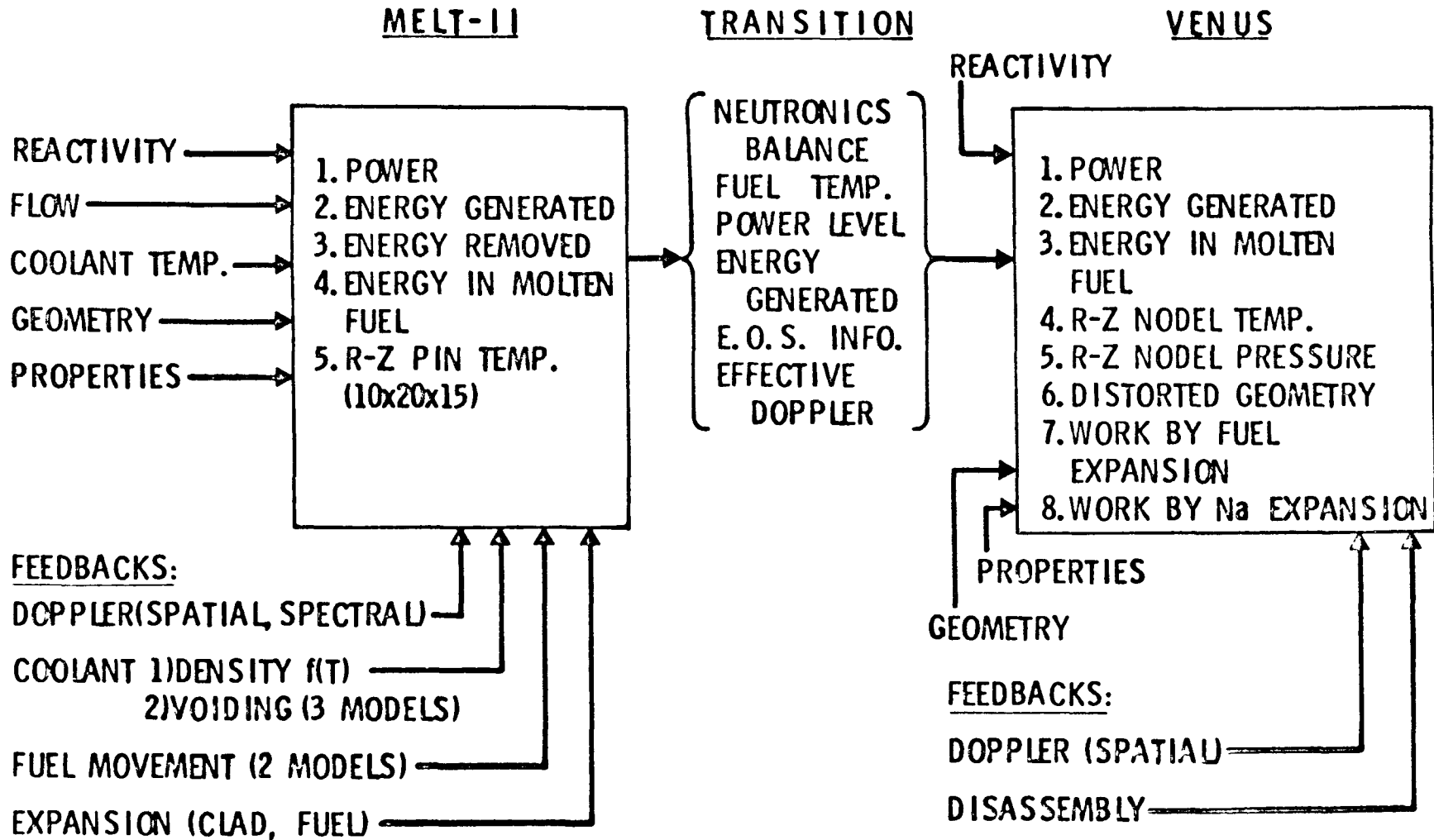


Figure XVI.22 Core Distortion for 50 \$/sec Sodium-In Case at Nuclear Termination Point.

MELT-II - VENUS COUPLING



XVI.58

Figure XVI.23 Information Flow in MELT-II - VENUS Coupling Scheme.

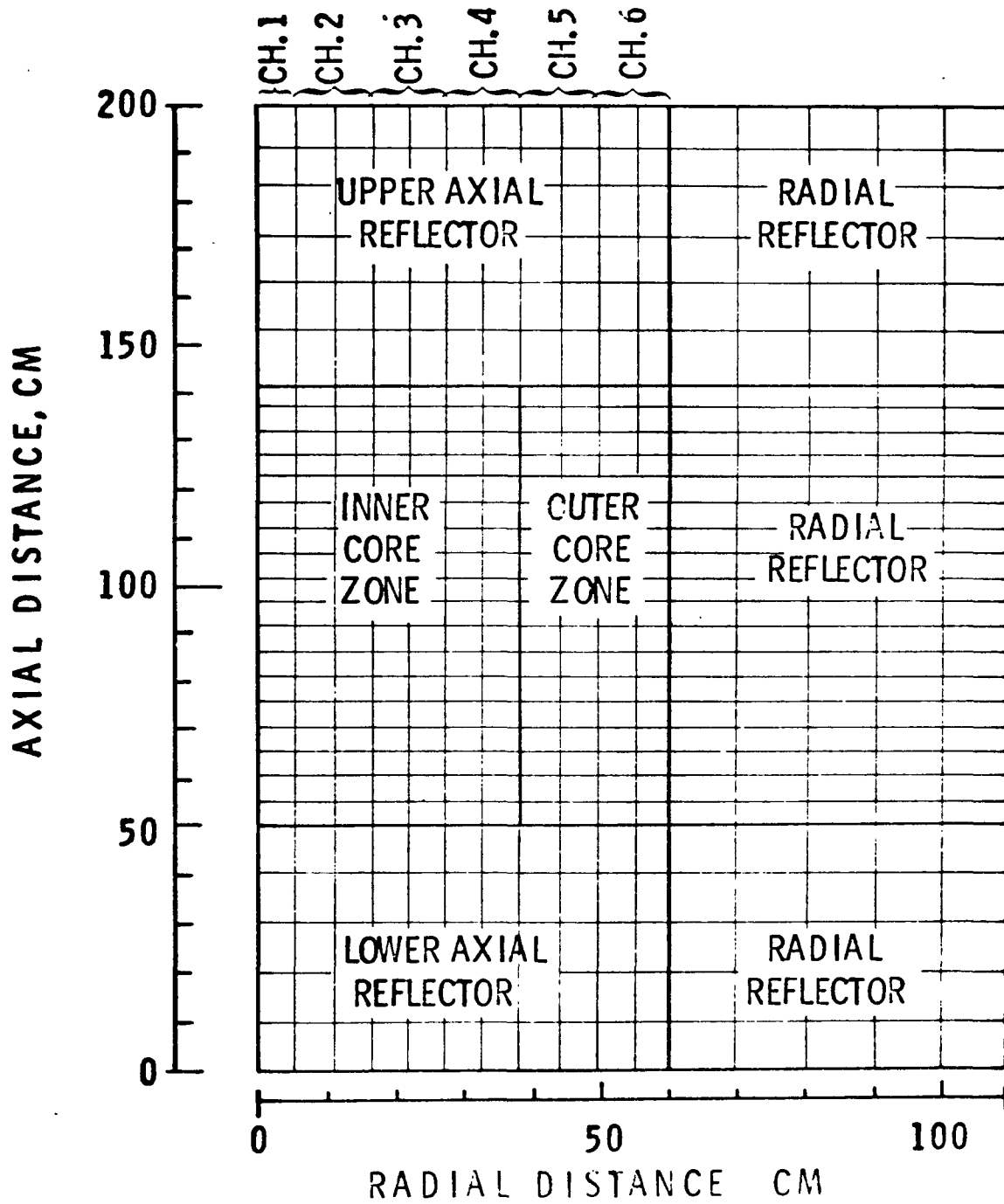


Figure XVI.24 k-Z Spatial Grid Used in VENUS Calculations.

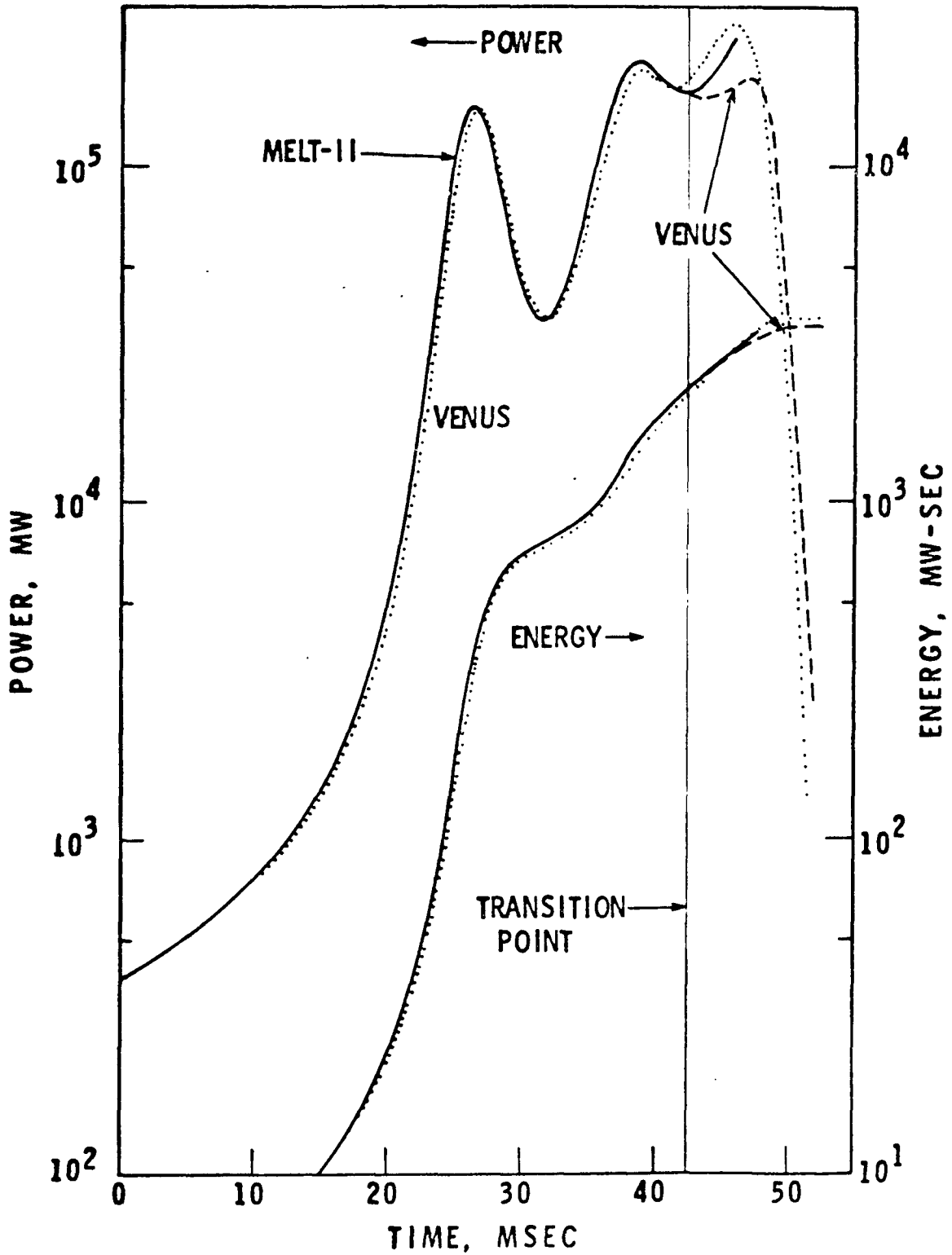


Figure XVI.25 Comparison and Coupling of MELT-II and VENUS.

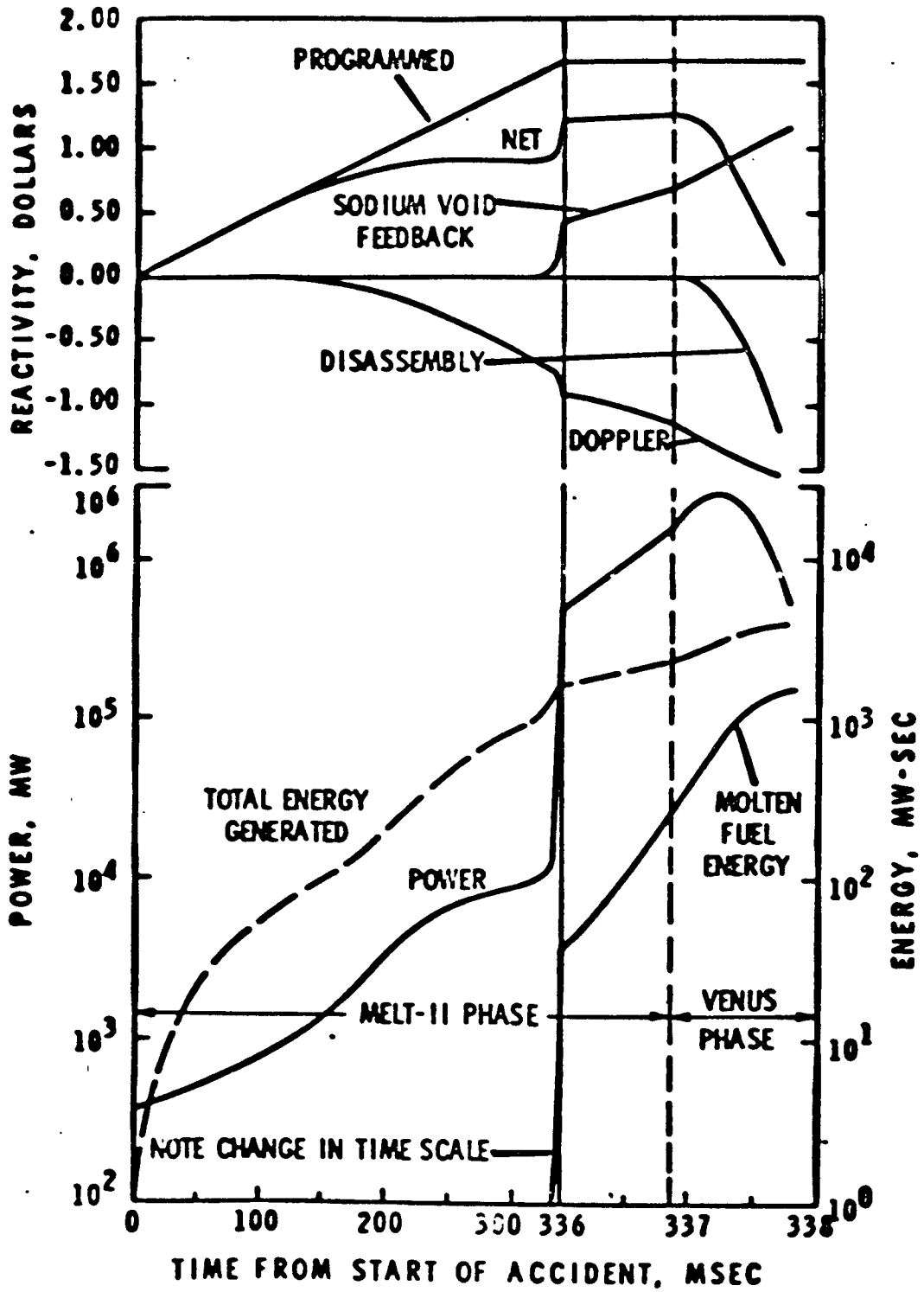


Figure XVI.26 Transient Response for 5 \$/sec Ramp Accident Aggravated by Severe Molten Fuel-Sodium Interaction.

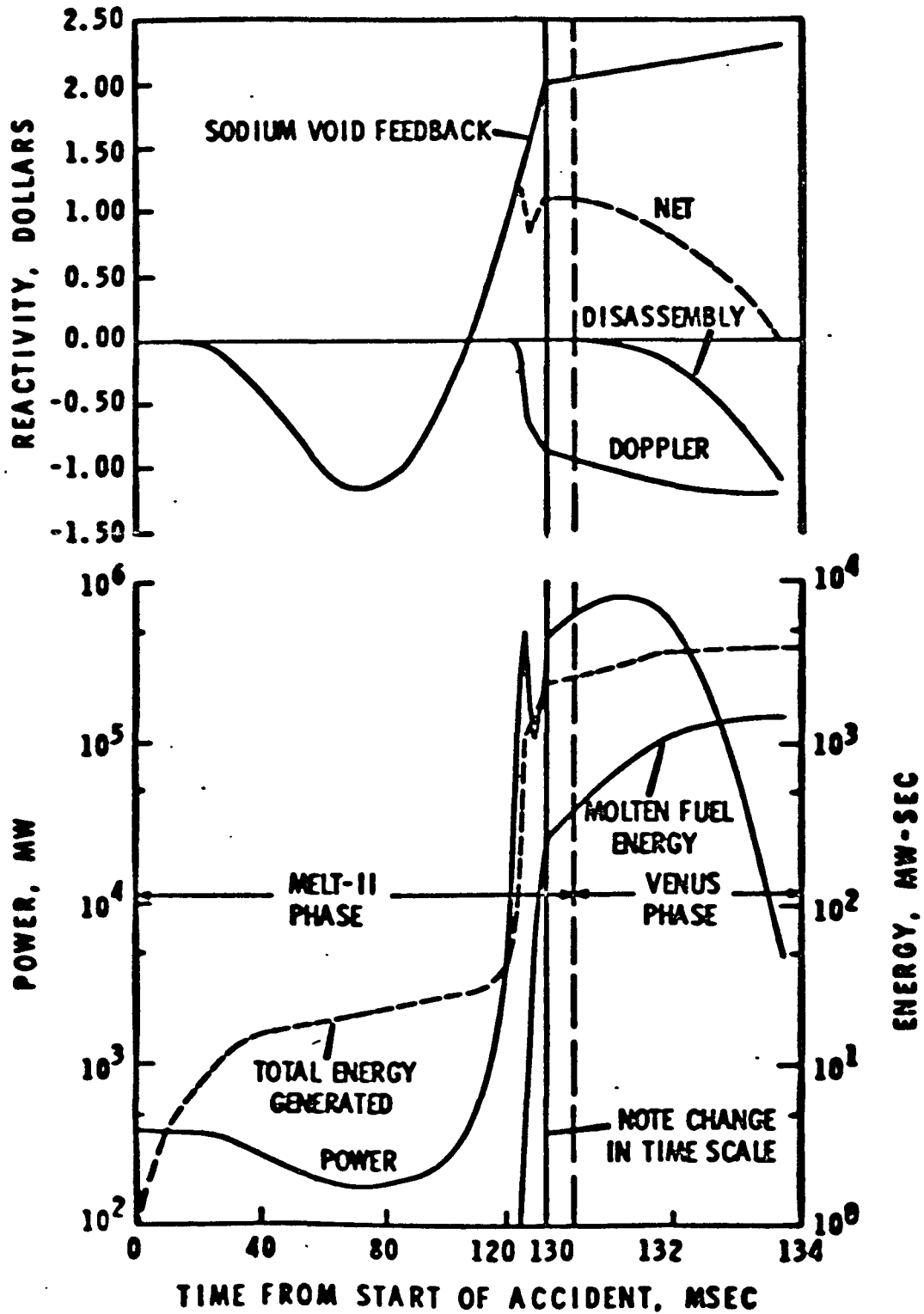


Figure XVI.27

Transient Response for Large Zero Density Bubble Passing Through Core

XVII. ENERGY RELEASE MECHANISMS

A. Padilla, Jr.

A. Introduction

During the course of hypothetical accidents involving the entire reactor core, a considerable amount of energy may have been generated and the rapid release of a portion of this energy may result in significant damage to the containment system. This rapid energy release can take two basic forms: shock energy and blast energy. The basic difference between these two energy forms is that the shock wave is a microsecond-time-scale phenomenon and blast is a millisecond-time-scale phenomenon.

This lecture deals with the methods of predicting the shock and blast energies resulting from a hypothetical disruptive accident. It is the link between the disassembly phase, treated in Lecture XVI, and the determination of actual damage to the containment system, which will be the topic of Lecture XVIII. The generation of additional energy due to a sodium fire is not discussed here, and will be the subject of subsequent lectures.

B. Assumed Factors

The fraction of the total energy generated which can be converted to destructive work can be estimated by assuming an efficiency factor. For example, in the safety analysis for the FARET reactor⁽¹⁾ this factor was chosen as 10% of the total energy generated during the disassembly phase. This particular value was estimated from calculations with the AX-1 disassembly code which calculated the kinetic energy of the displaced material and the volume-integrated pressure at the end of disassembly. The sum of these two quantities, which was slightly less than 10% of the total energy generated, was estimated to be the energy which could be converted to work.

The energy generated above some assumed threshold can also be used to estimate destructive work. In the safety analysis for the EBR-II reactor⁽²⁾, this threshold was taken as the threshold in the equation of state. In the analysis of the SL-1 accident⁽³⁾, this threshold was taken as the melting point of the fuel. In both cases, the energy above the threshold was converted to an equivalent amount of TNT and the characteristics of a TNT explosion used to estimate the potential destructive work.

C. Fuel Expansion

1. Introduction

When sodium is out of the core at the end of nuclear disassembly, expansion of the fuel may be the mechanism for obtaining destructive work. During the disassembly phase, the fuel melts and vaporizes as energy is added to it. When the fuel has expanded to fill all of the available core volume, it is entirely in the liquid phase and a slight increase in energy

causes a significant increase in pressure. It is this large pressure increase which causes sufficient core expansion to terminate the nuclear excursion.

2. Shock Energy

The transient pressures generated during the disassembly phase can be used to determine the shock energy. However, most of the disassembly codes which are available do not correctly account for the generation and propagation of shock waves because the density is assumed to be constant. The more recently developed disassembly codes such as FRAP⁽⁴⁾ and VENUS⁽⁵⁾ use the pseudo-viscous pressure term of Van Neumann and Richtmyer⁽⁶⁾ so that shock effects are calculated automatically whenever and wherever they arise.

In these disassembly codes, the clad and structure are treated as inert material (no heat generation) which occupy space and cause the available volume to be filled by the expanding fuel sooner.

3. Blast Energy

The blast energy can be estimated by expansion of the fuel in a thermodynamic process. If it is assumed that the expansion process is adiabatic and reversible, and therefore isentropic, then the maximum potential for work is obtained. One of the tenets of thermodynamics is that if any two state properties of a substance are known, then the rest of the state properties can be determined. Since internal energy and pressure at the end of disassembly are known, the entropy can be determined. Once the final pressure for expansion is chosen, the final conditions are determinate since the entropy is assumed to be constant for the process. The theoretical work of expansion is given by the difference in internal energy between the initial (at the end of disassembly) and the final (at the final pressure) conditions.

Figure XVII.1 shows the work energy obtained from expansion of the fuel to 1 atm for disassembly of the FTR⁽⁷⁾. Although three different equations of states are used for the fuel, all of the curves are quite similar. Another quantity of interest which can be determined from the expansion process is the relative amounts of liquid and vapor at the final conditions. This is easily determined from the final entropy and the entropies of the liquid and vapor. Figure XVII.2 shows the mass fraction of the fuel in the vapor state after expansion to 1 atm using the Menzies' critical constants for the corresponding states calculation. These results can be used as an upper limit on the amount of plutonium vapor which must be contained in a hypothetical disruptive accident.

D. Sodium Expansion

1. Introduction

In disassembly analyses, it is possible to assume that sodium is still in the core, as would be the case for a rapid power transient. However, the sodium is treated as an inert material which merely occupies volume although allowance for compressibility is sometimes made. If the intact core geometry no longer exists at the end of disassembly, it is difficult to preclude some sort of interaction between the sodium and fuel. For the "sodium-in" conditions, the amount of energy generated before fuel expansion causes sufficient core movement to terminate the nuclear excursion is much less than for "sodium-out" conditions. Consequently, the energy release obtained from fuel expansion is about an order of magnitude less than for the sodium-out case.

XVII.5

However, interaction between the fuel and sodium provide a mechanism for obtaining much higher energy releases. Since the critical temperature and pressure for sodium is substantially lower than that of the fuel, sodium is basically a more efficient working fluid for expansion. It will be shown that if it is possible to transfer a large amount of energy from the fuel to the sodium and allow the sodium to be the expansion fluid, much higher energy releases are obtained.

2. Equilibrium Models

a. Method of Hicks and Menzies

Hicks and Menzies⁽⁸⁾ were the first to postulate the expansion of sodium for calculating the energy release. They assumed that the mixing of fuel and sodium takes place at constant volume and that thermal equilibrium is attained before any expansion takes place. They derived an equation for the expansion of the sodium/fuel mixture assuming that thermal equilibrium exists at all times between the two materials.

Assuming constant physical properties, the energy lost by the sodium liquid and fuel goes into generation of sodium vapor:

$$(M C_{\text{Na}} + C_{\text{fuel}}) \frac{dT}{T} + \Delta H_{\text{vap}} d\left(\frac{x}{T}\right) = 0 \quad (1)$$

where M is the sodium/fuel mass ratio and x is the mass of sodium vapor.

Integrating equation (1) gives:

$$\Delta H_{\text{vap}} \frac{x}{T} = (M C_{\text{Na}} + C_{\text{fuel}}) \ln \frac{T_{\text{eq}}}{T} \quad (2)$$

where T_{eq} is the equilibrium temperature before expansion given by

$$T_{\text{eq}} = (M C_{\text{Na}} T_{\text{Na}} + C_{\text{fuel}} T_{\text{fuel}}) / (M C_{\text{Na}} + C_{\text{fuel}}) \quad (3)$$

where T_{Na} and T_{fuel} are the initial sodium and fuel temperatures before mixing. The work of expansion is given by the difference in internal energy:

$$W_1 = (M C_{\text{Na}} + C_{\text{fuel}}) (T_{\text{eq}} - T) - x (\Delta H_{\text{vap}} - RT) \quad (4)$$

This equation is valid until all of the sodium liquid is vaporized at temperature T_1 .

Assuming the ideal gas law for further expansion,

$$MR \ln \frac{P_{\text{sat}}(T_1)}{p} = (M C_{\text{vap}} + C_{\text{fuel}}) \ln \frac{T_1}{T} \quad (5)$$

The additional work done for the expansion of the vapor is given by:

$$W_2 = (M C_{\text{vap}} + C_{\text{fuel}}) (T_1 - T) \quad (6)$$

Hicks and Menzies found that the expansion work varied with the sodium/fuel mass ratio and that the maximum corresponded to complete vaporization of the liquid with insignificant superheating of the vapor. Figure XVII.3 shows their results for initial fuel and sodium temperatures of 3450°K and 1150°K, respectively.

The Hicks and Menzies approach can be extended to the case where further heat transfer between the fuel and sodium is prevented during the expansion process by vapor blanketing. Equations (1) and (4) are modified by omitting the fuel energy terms:

$$\Delta H_{\text{vap}} \frac{x}{T} = M C_{\text{Na}} \ln \frac{T_{\text{eq}}}{T} \quad (7)$$

$$W_1 = M C_{\text{Na}} (T_{\text{eq}} - T) - x (\Delta H_{\text{vap}} - RT) \quad (8)$$

For both the thermal equilibrium expansion and the adiabatic (vapor blanketed) expansion, the values of the sodium/fuel mass ratio to give the maximum energy release can be calculated. Figures XVII.4 and XVII.5 show the results obtained for the maximum energy release and the required sodium/fuel ratios for a final pressure of 100 atm.

The advantage of the Hicks and Menzies' method is that the concise solution in closed form permits rapid calculation of the energy release. Some of the disadvantages are:

- . The use of constant sodium properties does not allow the equilibrium temperature to exceed the sodium critical point.
- . The use of constant fuel specific heat does not allow for the solidification of the fuel during the mixing process and the thermal equilibrium expansion.

b. SOCOOL⁽⁹⁾

1) Description of Heating and Expansion Paths

In order to circumvent the disadvantages of the Hicks and Menzies' method, it was decided to completely specify the thermodynamic properties of the sodium and the fuel required for the calculation of energy release. The assumed processes are illustrated on an idealized temperature-entropy diagram for sodium shown in Figure XVII.6. When sodium is mixed with the fuel, it is assumed to be heated along the saturated liquid curve to the critical point and then to some equilibrium temperature and pressure T_{eq} , P_{eq} above the critical point along an extrapolated vapor pressure curve. The specific heat of the fuel, both liquid and solid, can be functions of temperature and the heat of fusion is taken into account. The sodium is allowed to expand during the process of heating up to thermal equilibrium. The result is that the expansion process following thermal equilibrium predicts only the blast energy and not the shock energy. The justification for assuming that the sodium is heated up as a saturated liquid is that the internal energy and entropy, at least below the critical point, are mainly a function of temperature and not pressure.

The expansion process depends on the equilibrium temperature in relationship to the fuel melting point and the sodium critical point. If the equilibrium temperature is above the fuel melting point, the thermal equilibrium expansion can be divided into three phases (curve A in Figure XVII.6):

- . expansion from thermal equilibrium T_{eq}, P_{eq} to the melting point of the fuel T_{fmp} involving heat transfer between the expanding sodium and liquid fuel
- . isothermal expansion at T_{fmp} as the fuel solidifies and transfers its heat of fusion to the expanding sodium
- . expansion from T_{fmp} to the final pressure P_f involving heat transfer between the expanding sodium and the solid fuel.

If the equilibrium temperature is below the melting point of the fuel but above the sodium critical point, the thermal equilibrium expansion is described by curve B which involves heat transfer between the expanding sodium vapor and solid fuel. If the equilibrium temperature is below the sodium critical point, the thermal equilibrium expansion can be divided into two phases (curve C):

- . expansion within the two-phase region until complete vaporization of sodium liquid and
- . expansion of superheated sodium vapor.

For the case of no further heat transfer between the sodium and the fuel during the expansion, the vapor-blanketed case in the Hicks and Menzies' method, it is assumed that the process is isentropic (adiabatic and reversible) and the expansion path is always described by a vertical line from thermal equilibrium to the final pressure.

The first law of thermodynamics is used for all the processes shown in Figure XVII. 6:

$$\begin{aligned}
 &\text{Energy added to system} = \text{Increase in internal energy of system} \\
 &+ \text{Work done by system on surroundings} \\
 &Q = \Delta U + W \qquad (9)
 \end{aligned}$$

In the heating up process, the energy added to the sodium by the fuel goes toward increasing the temperature of the sodium and, since the sodium is allowed to expand, doing expansion work against the surroundings. For the isentropic expansion of sodium, Q is zero and the energy release is the difference in internal energy between thermal equilibrium and the final pressure.

2) Prediction of Sodium Properties

Although much more thermodynamic data exists for sodium than for fuel, the highest temperature for which experimental data exists is approximately 1650 °K (2500 °F). The thermodynamic and transport properties for sodium have been summarized by Golden and Tokar.⁽¹⁰⁾ Beyond 2500 °F and up to the critical point, the heat of vaporization and vapor and liquid densities have been estimated by Miller.⁽¹¹⁾ The heat of vaporization for sodium was estimated from cesium data and expressed in the form:

$$\frac{\Delta H_{\text{vap}}}{RT} = 4.83 \left(1 - \frac{T}{T_c}\right)^{.377} \quad (10)$$

The vapor and liquid density for sodium was obtained by extrapolating low-temperature data according to the rectilinear diameter law and expressed in the form:

$$1 - \frac{\rho_{\text{vap}}}{\rho_c} = 1.422 \left(1 - \frac{T}{T_c}\right)^{.389} \quad (11)$$

$$\frac{\rho_{\text{liq}}}{\rho_c} - 1 = 3.982 \left(1 - \frac{T}{T_c}\right)^{.5435} \quad (12)$$

Use of Equations (10), (11), and (12) for extrapolating the sodium properties to the critical point still requires some approximations. In calculating the enthalpy, it was assumed that the curve of the average enthalpy (one-half the vapor plus liquid) could be extrapolated to the critical point. Figure XVII.7 shows the sodium enthalpy up to the critical point using Equation (10) and the critical constants suggested by Miller:

$$\begin{aligned} T_c &= 2733 \text{ }^\circ\text{K} \\ P_c &= 408.2 \text{ atm} \\ \rho_c &= .1818 \text{ gm/cm}^3 \\ Z_c &= .2302 \end{aligned}$$

In calculating the entropy, the curve of the average entropy (one-half the vapor plus liquid) is nearly vertical at the maximum range of the experimental data. Therefore, the average entropy was extrapolated as a vertical line to Miller's critical temperature. Figure XVII.8 shows the sodium entropy up to the critical point. The superheated vapor region between 2500 °F and the critical point is estimated from a virial equation of state suggested by Oldham,⁽¹²⁾

$$\frac{PV}{RT} = 1 + \frac{B}{V} + \frac{C}{V^2} + \frac{D}{V^3} + \frac{E}{V^4} \quad (13)$$

where B, C, D, and E are constants. Given the temperature and pressure, the enthalpy, entropy, specific volume, and specific heat can be calculated from thermodynamic relationships.

The sodium internal energy up to the critical point can be calculated from the thermodynamic relationship:

$$U = H - \frac{P}{\rho} \quad (14)$$

Since H and ρ have already been determined, the vapor pressure must be extrapolated to the critical point. Figure XVII.9 shows the vapor pressure plotted against the reciprocal of the absolute temperature. Extrapolation of the vapor pressure curve suggested in ANL-7323 does not pass through the critical temperature suggested by Miller. It was decided to empirically fit a curve between the experimental data and the critical point. The equation chosen was the reduced-vapor-pressure equation of Riedel which is used in corresponding states theory⁽¹³⁾.

$$\ln P_r = \alpha \ln T_r - 0.0838 (\alpha - 3.75) \left(\frac{36}{T_r} - 35 - T_r^6 + 42 \ln T_r \right) \quad (15)$$

$$\text{where } P_r = P/P_c$$

$$T_r = T/T_c$$

$$\alpha = \frac{1}{0.26} \left(\frac{1}{Z_c} - 1.90 \right)$$

If Z_c is taken as .2302 as suggested by Miller, Equation (13) does not blend into the low temperature experimental data. In order to obtain agreement with the data, it was found that Z_c should be .3114.

The theory of corresponding states⁽¹³⁾ along with Equation (13) is used for predicting the properties of sodium above the critical point. In addition to the critical constants, the thermodynamic properties of the ideal sodium gas are required for corresponding states calculations. The temperature at which these properties are specified is the critical point. Using the predicted sodium enthalpy and entropy at the critical point and the predicted departures from the ideal gas from the corresponding states tables, the enthalpy and entropy of ideal sodium gas can be calculated. By specifying the heat capacity of the ideal gas, the enthalpy and entropy at any other temperature can be determined. According to NASA SP-3001,⁽¹⁴⁾

the heat capacity at constant pressure for ideal sodium monatomic gas is essentially constant at 5 cal/mole-°K.

3) Analytical Results

Figure XVII.10 shows the effect of initial fuel temperature on the energy release for an initial sodium temperature of 672 °K (750 °F) and a sodium/fuel mass ratio of .085 for expansion to a final pressure of 1 atm. This mass ratio is obtained by mixing all of the fuel in the core with all of the sodium in the core for FTR conditions. For the adiabatic expansion, the energy release is constant over a wide range of initial fuel temperature since the equilibrium point is the same, the melting point of the fuel, and the energy remaining in the molten fuel is not available for the expansion process.

Figure XVII.11 shows the effect of increasing sodium/fuel mass ratio for initial fuel and sodium temperatures of 3800 °K and 672 °K, respectively, for expansion to a final pressure of 1 atm. There are two peaks in both the thermal equilibrium and the adiabatic expansion. The second peak, which appears to be the larger, is associated with equilibrium occurring at the sodium critical point. Some of the oscillations are due to the prediction of sodium properties near the critical point. Figure XVII.12 shows the adiabatic energy release per unit mass of sodium as a function of the equilibrium temperature and the two wiggles in the curve are indicative of the uncertainty in predicting the rapidly changing sodium properties near the critical point.

Figure XVII.13 shows the effect of the final pressure on the energy release. If the final pressure is 20 atm instead of 1 atm, the energy release is reduced by almost one-half for the thermal equilibrium expansion and almost 1/3 for the adiabatic expansion.

Since the sodium is not heated up at constant volume but allowed to expand during the approach to thermal equilibrium, the energy release calculated by SOCOOL is an estimate of the blast energy only. One possible consequence of this blast energy is the acceleration of the coolant above the core and impact of this coolant against the reactor head. The decrease in pressure as the sodium expands can be predicted from expansion process itself, realizing that the expansion is a reversible one and therefore infinitely slow. Figure XVII.14 shows the pressure as a function of increasing volume for the case where thermal equilibrium occurs at the melting point of the fuel with all of the fuel still molten. The isothermal expansion of an ideal gas has also been drawn for comparison and lies approximately between the thermal equilibrium and adiabatic expansion paths.

The energy releases calculated above from thermodynamic considerations are conservative for several reasons:

- . A reversible process gives the maximum theoretical work and any real process will give less work.
- . For realistic sizes of fuel particles mixed with realistic amounts of sodium, thermal equilibrium will not be attained before expansion of sodium starts.

c. Effect of Heat Transfer During the Expansion Process

From the preceding analytical results, it is seen that the energy release for the thermal equilibrium expansion is about three times that for the adiabatic expansion for a final pressure of 1 atm. Therefore, a substantial reduction in the upper limit for the energy release can be attained if it can be shown that very little heat transfer can occur between

the fuel and the sodium during the expansion. Intuitively, the expansion process would occur so fast that not enough time would be available for heat transfer.

As a basis for the analysis the results of a typical ASPRIN calculation for coolant slug impact against the reactor head⁽¹⁵⁾ was assumed. Figure XVII.15 shows the normalized pressure as a function of time and it is seen that the coolant slug impact occurs after 25 milliseconds. The analytical model used to calculate heat transfer was a spherical fuel particle with sodium in a concentric sphere. An Eulerian coordinate system with a moving boundary was used to describe the expansion of sodium. The fuel and sodium are initially at thermal equilibrium, which was chosen to be the liquid fuel at its melting point. Heat transfer is assumed to occur by conduction only.

A trial and error technique was used which involved matching the results of a SOCOOL calculation assuming a fictitious solid fuel specific heat and the results from the spherical heat transfer model such that the total amounts of heat transferred are equal. This criterion is somewhat artificial since the thermodynamic expansion using SOCOOL does not involve time.

As an example, consider the case where the radius of the fuel particle is 100 microns. The initial pressure is 700 atm corresponding to sodium at 3040 °K, the melting point of the fuel, and the final pressure is 27 atm according to the final normalized pressure at 25 msec in Figure XVII.15. For the SOCOOL calculation, it is assumed that the sodium will expand in thermal equilibrium with the solid fuel with an assumed specific heat of .05 joules/gm-°K. From the SOCOOL expansion from 700 to 27 atm, the total

energy transferred and the relationship between increasing volume, decreasing pressure, and decreasing temperature is obtained. This expansion path is then used as input for the actual heat transfer calculation. From the pressure-time relationship in Figure XVII.15, the increase in volume as a function of time along with the changes in sodium transport properties could be determined. Corresponding states was used to predict the variation in heat capacity⁽¹³⁾ and thermal conductivity⁽¹⁶⁾ with time. It was found that the total heat transferred in the spherical expansion and heat transfer model was less than that obtained from the thermal equilibrium expansion as long as condensation does not occur.

A dilemma is encountered when condensation occurs. The thermal conductivity of the sodium liquid is so large that if a mass-weighted average thermal conductivity is used, the heat transfer is substantially increased. The increased heat transfer would serve to vaporize the sodium liquid thus reducing the average thermal conductivity. For this reason, whenever the expansion path intersects the saturated vapor curve, further expansion may occur along the saturation line rather than extending into the two-phase region.

The results are summarized in Figure XVII.16. For a fuel particle radius of 100 microns the expansion follows the adiabatic expansion quite closely until the saturated vapor curve is reached. Beyond that point, the expansion is assumed to follow the saturated vapor line. For a fuel radius of 10 microns, the expansion path to give the same total heat transfer as the spherical expansion and heat transfer model results in an energy release approximately mid-way between the thermal equilibrium and adiabatic expansion. It appears that a fuel particle radius of 1 micron would correspond fairly closely to the thermal equilibrium curve.

Although the above gyrations may not be aesthetically pleasing, the conclusions obtained would not be expected to be grossly in error unless some dominant mechanism has been overlooked (for example, if convection heat transfer is significantly higher than conduction). More elegant formulations could possibly be devised. One promising idea is to use the techniques of irreversible thermodynamics to determine the rate of entropy generation from the rate of heat transfer, thereby eliminating the coupling of a finite-time rate process with an infinite-time thermodynamic process.

3. Expansion of an Ideal Gas

Instead of calculating the energy release by means of a complicated, theoretical thermodynamic process, it might appear more reasonable to use a simple gas expansion process. If it is assumed that the expansion process is adiabatic and that the ideal gas law applies, then

$$PV^\gamma = \text{constant} \quad (16)$$

where $\gamma = \frac{C_p}{C_v}$, the ratio of heat capacity at constant pressure to that at constant volume. For an isentropic expansion, the work can be easily derived and is given by:

$$W = \frac{RT_1}{\gamma-1} \left[1 - \frac{P_2}{P_1} \right]^{\frac{\gamma-1}{\gamma}} \quad (17)$$

Assuming that $\gamma = 5/3$, the theoretical value for a monatomic gas, the expansion work for an initial pressure of 700 atm and a final pressure of 1 atm is about 25% lower than the isentropic work calculated with SOCOOL. This is not surprising because the ideal gas expansion neglects the effect of condensation which is an energy source for doing more work.

However, an experimental value of 1.35 for γ has been obtained for flow of saturated sodium vapor through a nozzle. When this value is used in Equation (17), the expansion work calculated is 30% higher than the corresponding SOCOOL result.

If $\gamma = 5/3$ is used for expansion from 700 atm to 280 atm (approximately the point where the two-phase dome is encountered) and $\gamma = 1.35$ is used for expansion from 280 atm to 1 atm, the total expansion work is 10% higher than the SOCOOL result.

For any reversible expansion process of an ideal gas,

$$PV^\delta = \text{constant} \quad (18)$$

where δ does not have any theoretical significance compared to γ for the adiabatic process. No equation comparable to Equation (15) can be derived and the work must be evaluated from the more general relationship

$$W = \int_{V_1}^{V_2} P dV \quad (19)$$

4. Transient Models

It may be overly conservative to assume that the fuel and sodium can attain thermal equilibrium before expansion begins except for extremely small fuel particles intimately mixed with a small amount of sodium. When sodium comes into contact with the fuel, whether gentle boiling or the violent vapor explosion associated with a molten fuel/sodium interaction occurs depends on the time scale for heat transfer and the acoustic period of the system. This is illustrated in Figure XVII.17. The acoustic period of the system is the time it takes a shock wave to travel to the nearest free surface and back. If the time for heat transfer is small in comparison to the acoustic period, then the sodium is heated up extremely rapidly at

essentially constant volume. The tremendous pressures associated with heating a liquid in a confined volume thus prevent the sodium from boiling. The heated liquid is able to eventually expand against the unheated liquid thus relieving the large pressures. When the pressure in the heated region decreases to the saturation pressure associated with the temperature of the liquid, boiling can occur.

If the time for heat transfer is large compared to the acoustic period, then a pressure wave generated in the heated region has sufficient time to travel to the free surface and be reflected back as a rarefaction wave which then relieves the pressure in the heated region when it returns. Thus, there are no high internal pressures to prevent boiling when the saturation temperature is reached and boiling can occur normally.

a. Heat Transfer

The heat transfer is calculated by considering a unit cell of a single spherical fuel particle with sodium concentrically smeared around it. It is assumed that the sodium is heated up at constant volume and that there is no heat transfer between the heated and unheated liquid regions. Constant physical properties for the sodium and fuel are assumed. Since the thermal diffusivity for sodium decreases with temperature, this assumption results in higher heat transfer.

Figure XVII.18 shows the average sodium temperature as a function of time for a fuel particle diameter of 100 microns and sodium/fuel mass ratios of 0.1, 0.5, and 1.0. The initial fuel temperature is 3040 °K and a specific heat equal to the heat of fusion is used to account for fuel solidification. This assumption is reasonable only for a sodium/fuel mass ratio of 0.1 where the equilibrium temperature is at the fuel melting point. For the other two mass ratios, the actual equilibrium will be lower than 3040 °K. Figure XVII.19 shows the time to reach 90% of thermal equilibrium (assumed to

be 3040 °K) for various fuel particle sizes. The time for heat transfer is significantly less than the acoustic period based on 25 feet except for a fuel particle diameter of 1000 microns with sodium/fuel mass ratios of 0.5 and greater.

b. Pressure Generation

For a liquid heated in a confined region, the pressure increase is given by:

$$dP = \left(\frac{\partial P}{\partial T} \right)_V dT + \left(\frac{\partial P}{\partial V} \right)_T dV \quad (20)$$

$$dP = \gamma_V dT - \frac{1}{\beta_T} \frac{dV}{V} \quad (21)$$

where γ_V is the thermal pressure coefficient and β_T is the isothermal compressibility. Integrating Equation (21) gives:

$$P_2 - P_1 = \gamma_V (T_2 - T_1) - \frac{1}{\beta_T} \ln \frac{V_2}{V_1} \quad (22)$$

It is assumed that the temperature and pressure are uniform throughout the molten fuel/sodium region. The term $(T_2 - T_1)$ is obtained from the previous section. The increase in volume V_2/V_1 is obtained by assuming one-dimensional pressure wave propagation. The velocity of the interface between the heated and unheated liquid regions can be predicted by the particle velocity:⁽¹⁸⁾

$$u_2 - u_1 = \frac{P_2 - P_1}{\rho_o C_o} \quad (23)$$

where C_o is the sonic velocity of the unheated liquid. If A is the interface area between the heated and unheated liquid, the rate of increase of volume of the heated liquid is:

$$\frac{dV}{dt} = 2A u_{avg} = 2A \left(u_1 + \frac{P_2 - P_1}{2 \rho_o C_o} \right) \quad (24)$$

Integrating Equation (24) and rearranging gives:

$$\frac{V_2}{V_1} = 1 + \frac{2A}{V_1} \left(u_1 + \frac{P_2 - P_1}{2\rho_0 C_0} \right) \Delta T \quad (25)$$

Equations (22) and (25) are solved simultaneously by trial and error at each time step ΔT with the heat transfer results from the preceding section. The physical properties were obtained from ANL-7323⁽¹⁰⁾ and were assumed to be constant.

Figure XVII.20 shows the pressure in the heated liquid region for various fuel particle sizes using a sodium/fuel mass ratio of 0.1. Figure XVII.21 shows how the pressure varies for a fuel particle diameter of 100 microns with various sodium/fuel mass ratios. When the pressure in the heated liquid region drops to the saturation pressure corresponding to the temperature of the liquid, then boiling can occur. Figure XVII.22 shows that for a 1000 micron diameter fuel particle and a sodium/fuel mass ratio of 0.1, this condition is reached at 98% of thermal equilibrium. If the sodium/fuel mass ratio is increased to 1.0, only 49% of thermal equilibrium is attained before boiling can occur as shown in Figure XVII.23. The results are summarized in Figure XVII.24 which shows the fraction of thermal equilibrium attained as a function of fuel particle size and sodium/fuel mass ratio. Significant departure from equilibrium occurs only for particle sizes on the order of 1000 microns.

c. Shock Energies

Since the analytical model contains a single interface between the heated and unheated liquid, the shock energy can easily be calculated

from the compression of the unheated liquid by the heated liquid:

$$E = \int PdV = \text{Force} \times \text{Distance} \quad (26)$$

The force term is obtained from the pressure in the heated liquid region and the distance is obtained from the interface velocity.

Using the core volume inside of a single driver fuel subassembly, Figure XVII.25 shows the effect of fuel particle size and sodium/fuel mass ratio on the generation of acoustic energy. The maximum acoustic energy is about 70% of the blast energy or about 40% of the total (shock plus blast) energy.

References

- (1) J. D. Geier, "Fast Reactor Test Facility (FARET), Volume II - Summary of Preliminary Safety Analysis," ANL-7168, Argonne National Lab., April 1966.
- (2) L. J. Koch et al., "Hazard Summary Report - Experimental Breeder Reactor - II (EBR-II)," ANL-5719, Argonne National Lab., May 1957.
- (3) J. F. Proctor, "Adequacy of Explosion-Response Data in Estimating Reactor-Vessel Damage," NUCLEAR SAFETY, Vol. 8, No. 6, Nov.-Dec. 1967.
- (4) L. I. Moss and W. A. Rhoades, "A Method for the Study of Autocatalysis and/or Pressure Histories in Fast Breeder Reactor Excursions," Proceedings of the Brookhaven Conference on Industrial Needs and Academic Research in Reactor Kinetics, April 8-9, 1968, BNL-50117 (T-497).
- (5) W. T. Sha and A. E. Waltar, "Fast Reactor Disassembly Calculation Utilizing a Temperature-Density-Dependent Equation of State," Paper Presented at Winter ANS Meeting, San Francisco, Calif., December 1969.
- (6) J. Von Neumann and R. D. Richtmyer, "A Method for the Numerical Calculation of Hydrodynamic Shocks," JOURNAL OF APPLIED PHYSICS, Vol. 21, p. 232, 1950.
- (7) D. E. Simpson et al., "Preliminary Analysis of Postulated Maximum Accidents for the FFTF," BNWL-760, Pacific Northwest Laboratory, November 1968.
- (8) E. P. Hicks and D. C. Menzies, "Theoretical Studies on the Fast Reactor Maximum Accident," Proceedings of the Conference on Safety, Fuels, and Core Design in Large Fast Power Reactors, October 11-14, 1965, ANL-7160, pp. 654-670.
- (9) A. Padilla, Jr., "SOCOOL - A Computer Program to Predict the Energy Release Due to a Molten Fuel/Sodium Interaction," Pacific Northwest Laboratory (to be published).
- (10) G. H. Golden and J. V. Tokar, "Thermophysical Properties of Sodium," ANL-7323, Argonne National Lab., August 1967.
- (11) D. Miller, A. B. Cohen, and C. E. Dickerman, "Estimation of Vapor and Liquid Density and Heat of Vaporization of Alkali Metals to the Critical Point," Paper Presented at the International Conference on the Safety of Fast Breeder Reactors, Aix-en-Provence, France, September 19-22, 1967.
- (12) J. L. Oldham, "Thermodynamic Properties of Sodium and Potassium," UCID-15271, Lawrence Radiation Lab., February 1967.

- (13) O. A. Hougan, K. M. Watson, and R. A. Ragutz, Chemical Process Principles, Part II, Thermodynamics, John Wiley & Sons, Inc., New York, 1959.
- (14) B. J. McBride et al., "Thermodynamic Properties to 6000°K for 210 Substances Involving the First 18 Elements," NASA SP-3001, National Aeronautics and Space Administration, 1963.
- (15) G. L. Fox, Jr., Private Communication, Pacific Northwest Laboratory, June 17, 1969.
- (16) R. B. Bird, W. E. Steward, and E. N. Lightfoot, Transport Phenomena, John Wiley & Sons, Inc., New York, 1960.
- (17) L. J. Goldman, "Expansion and Flow Characteristics of Initially Saturated Sodium, Potassium, and Cesium Vapors," NASA-TN-D-3743, November 1966.
- (18) R. H. Cole, Underwater Explosions, Dover Publications, Inc., New York, 1948.

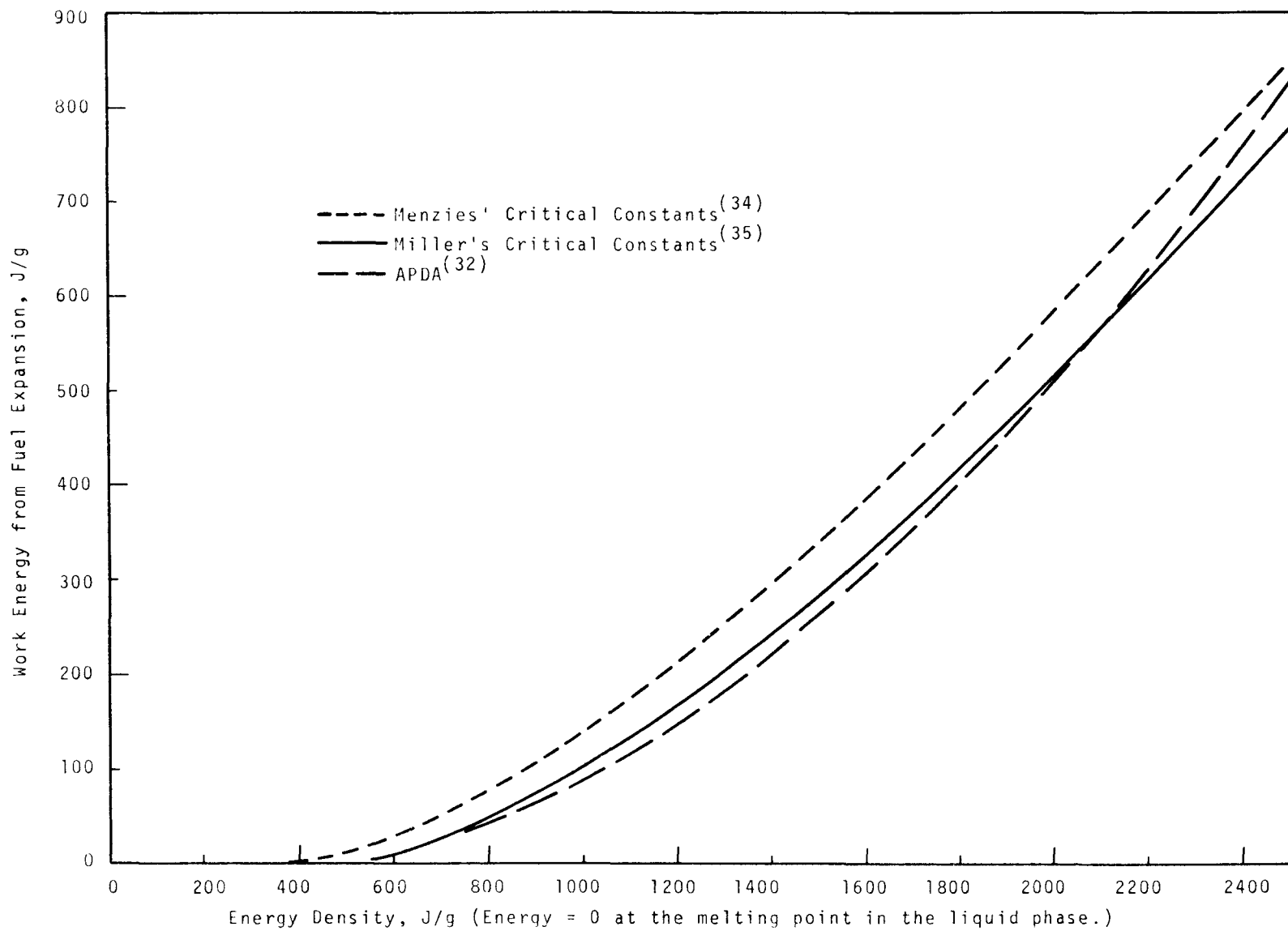


Figure XVII.1 *Maximum Work Energy from Fuel Expansion*

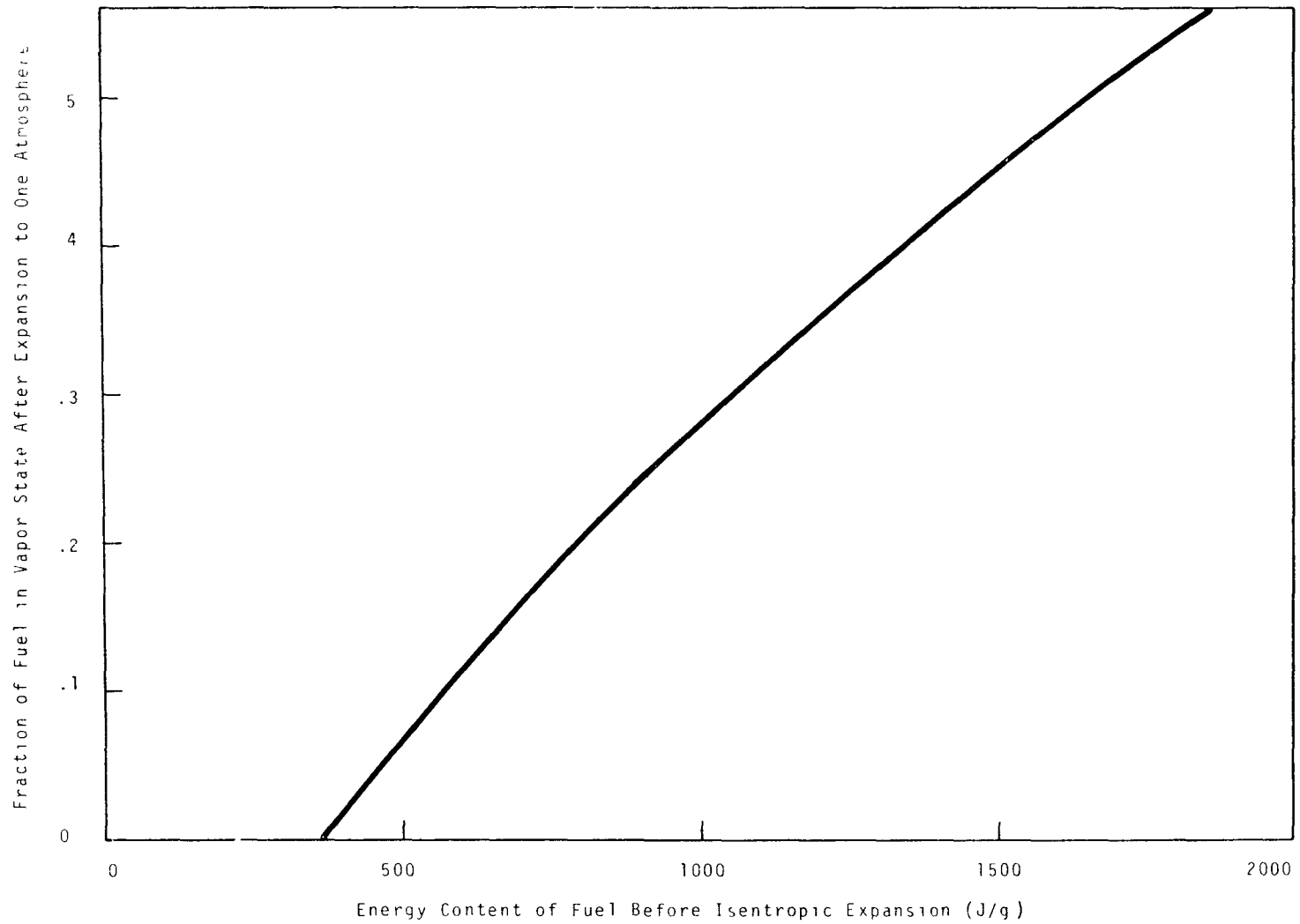
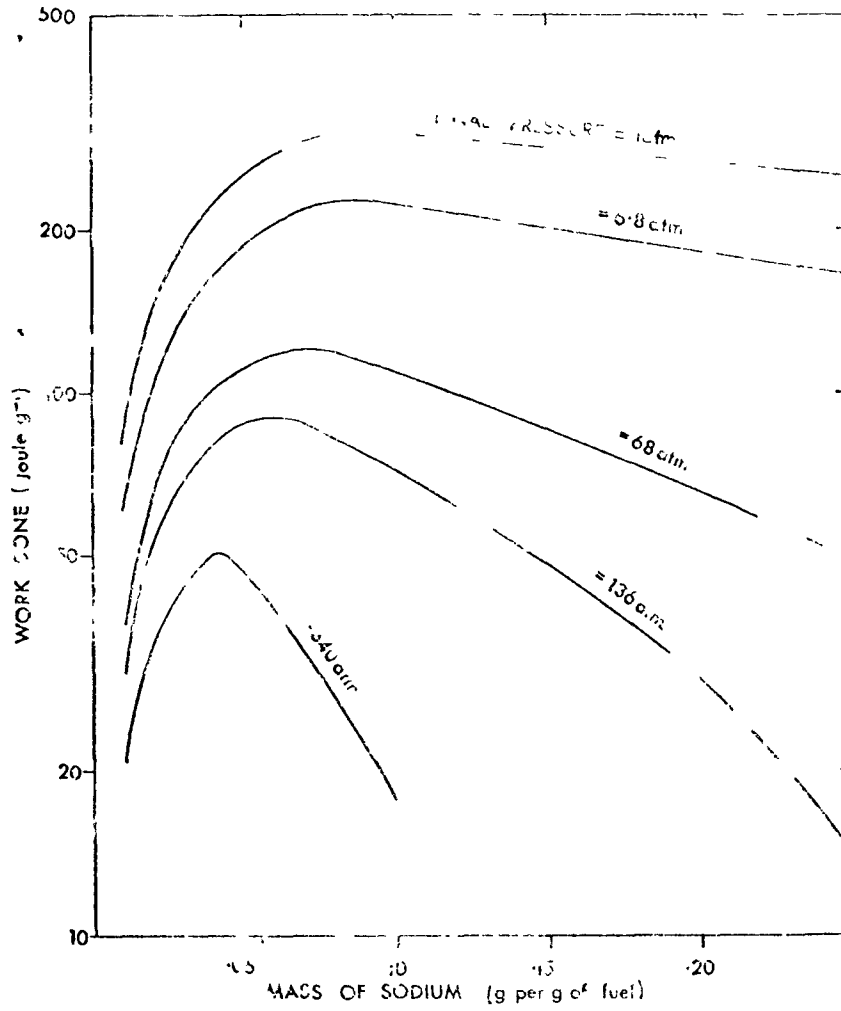


Figure XVII.2 *Final Fuel Vapor Fraction After Isentropic Expansion Using Mennies' Critical Constants*



The Work Done in a Spert-type Incident with Sodium and UO₂

Figure XVII.3

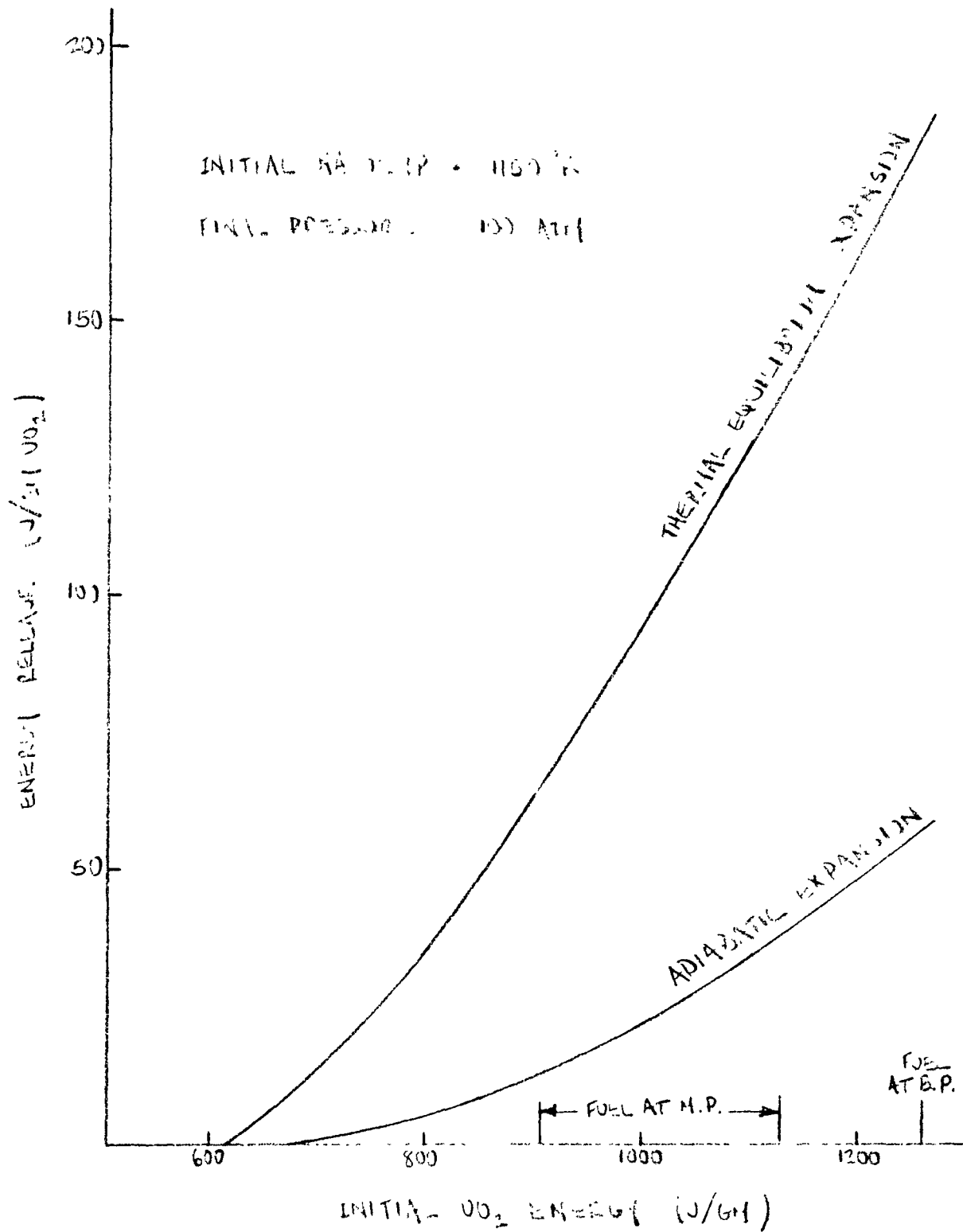
ENERGY RELEASE FROM CO_2/Na INTERACTION

Figure XVII.4

SODIUM/ UO_2 MASS RATIO REQUIRED FOR
OPTIMUM ENERGY RELEASE

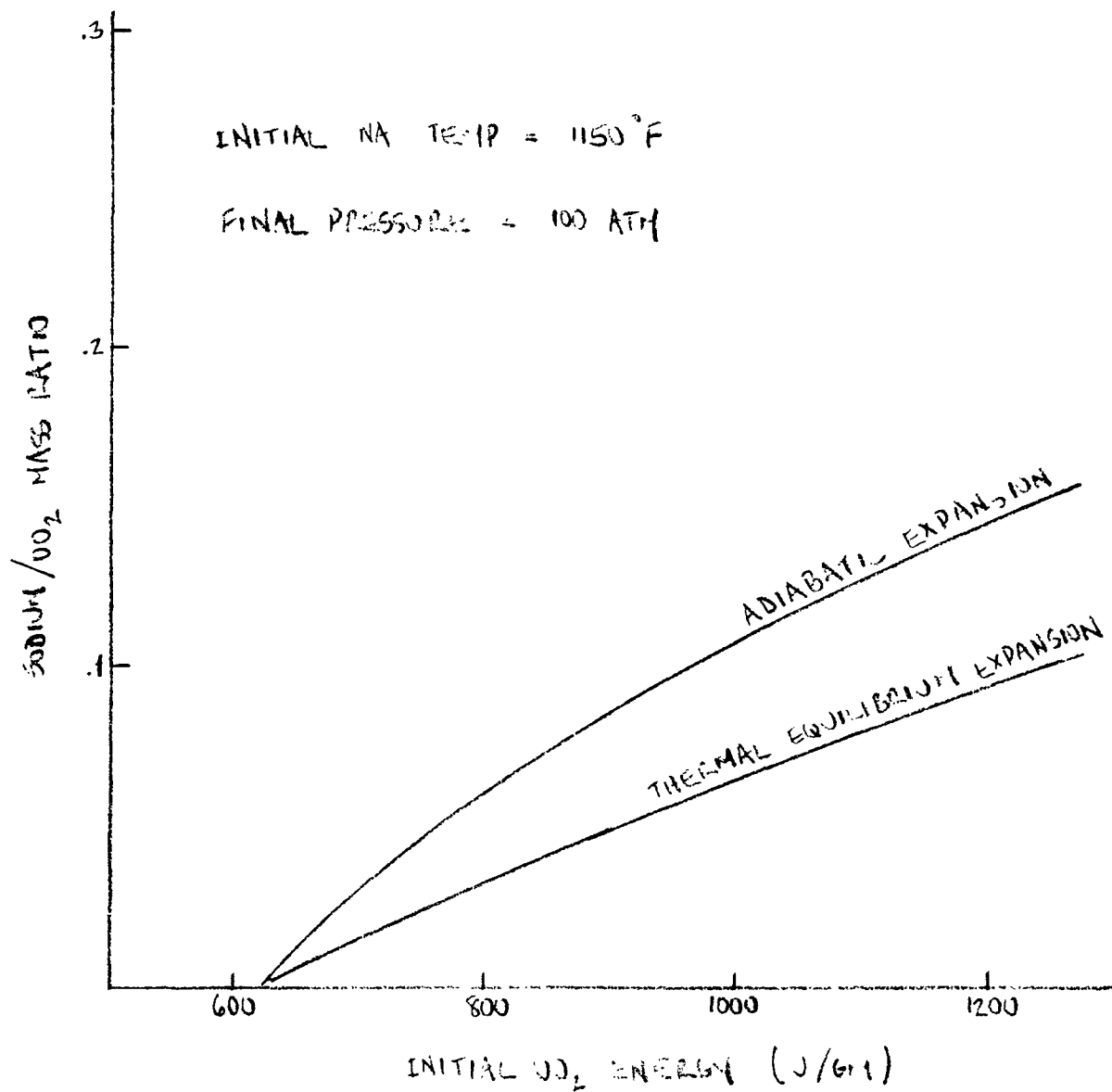
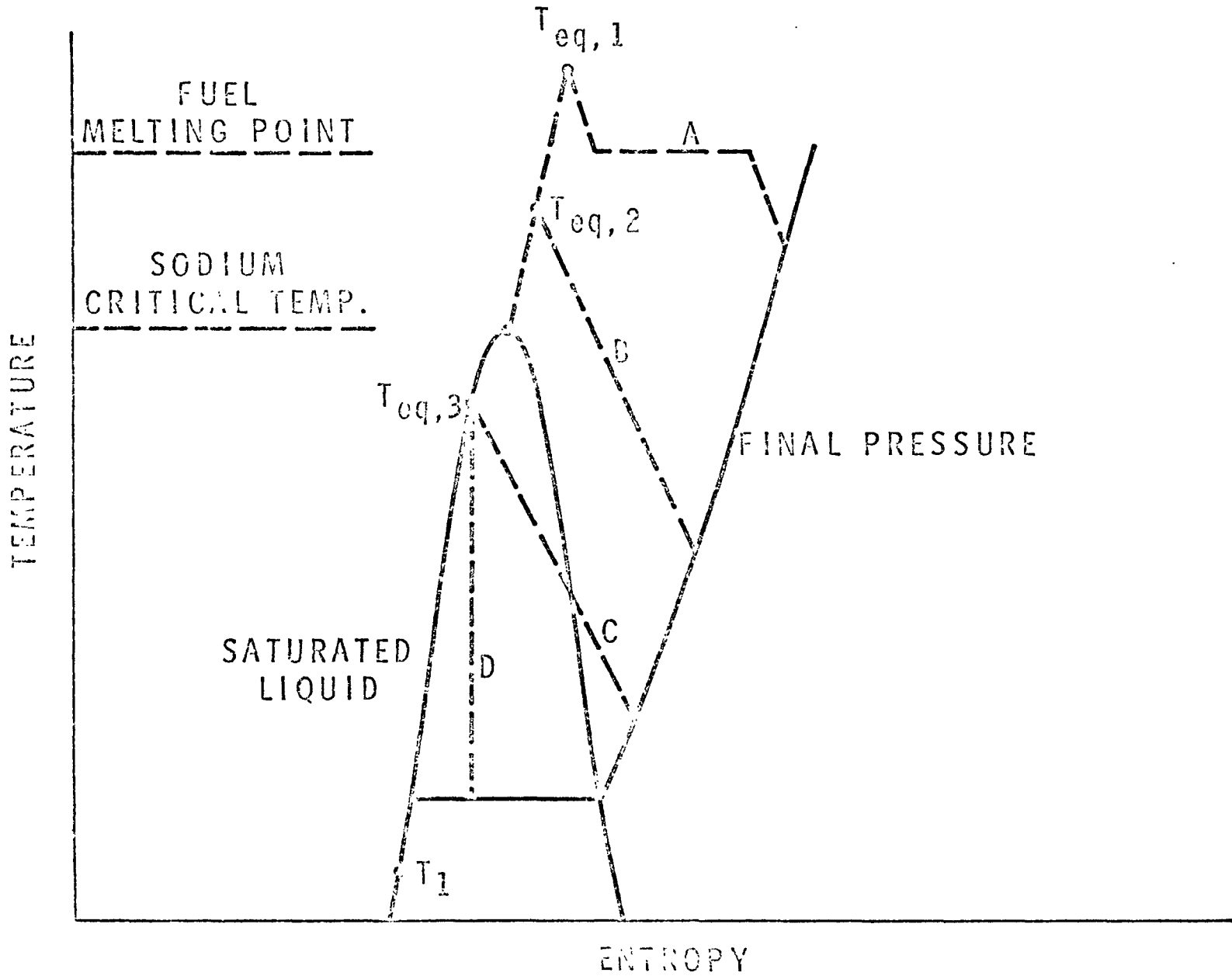


Figure XVII.5

THERMODYNAMIC PATHS FOR SODIUM EXPANSION



ENTROPY
Figure XVII.6

H-T DIAGRAM FOR SODIUM

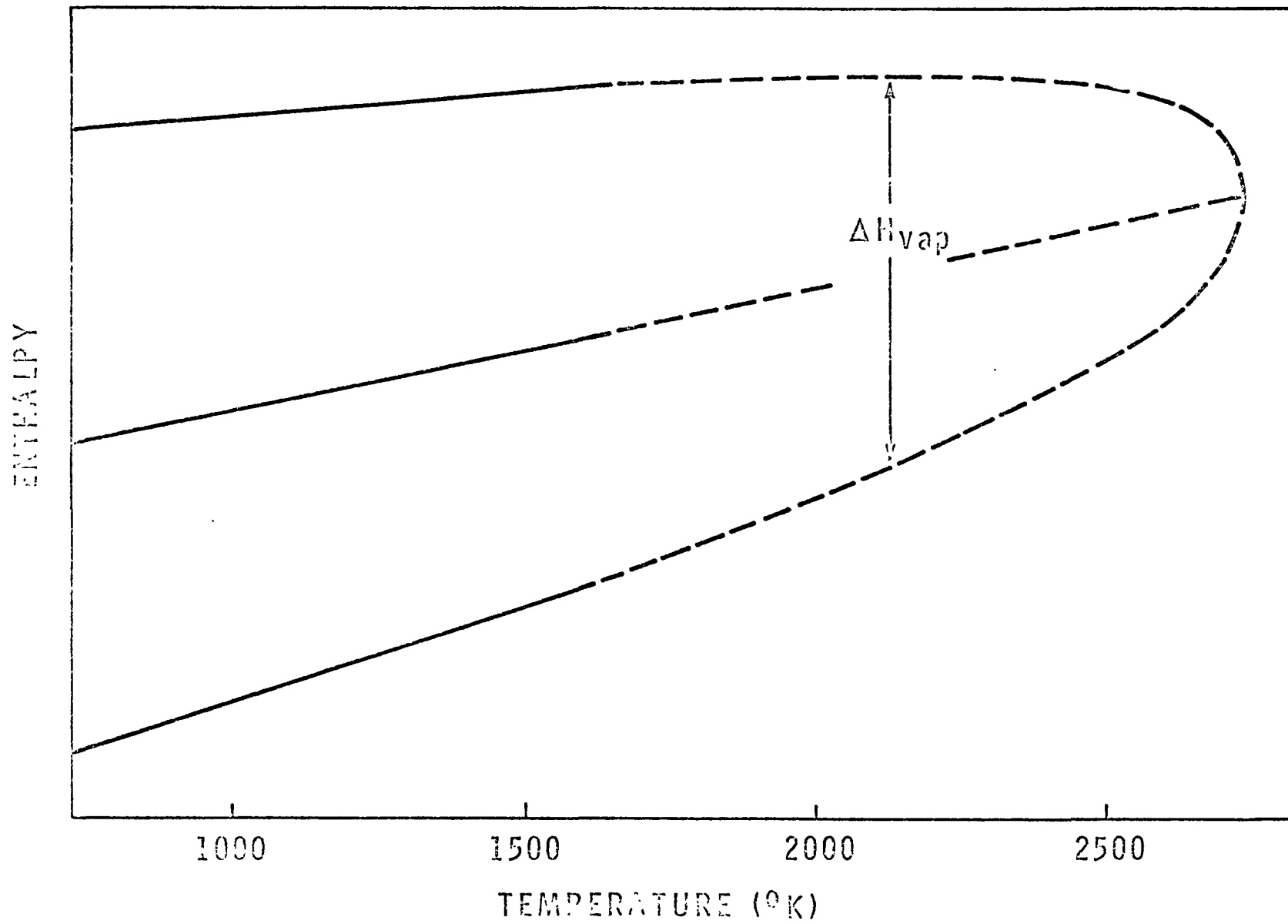
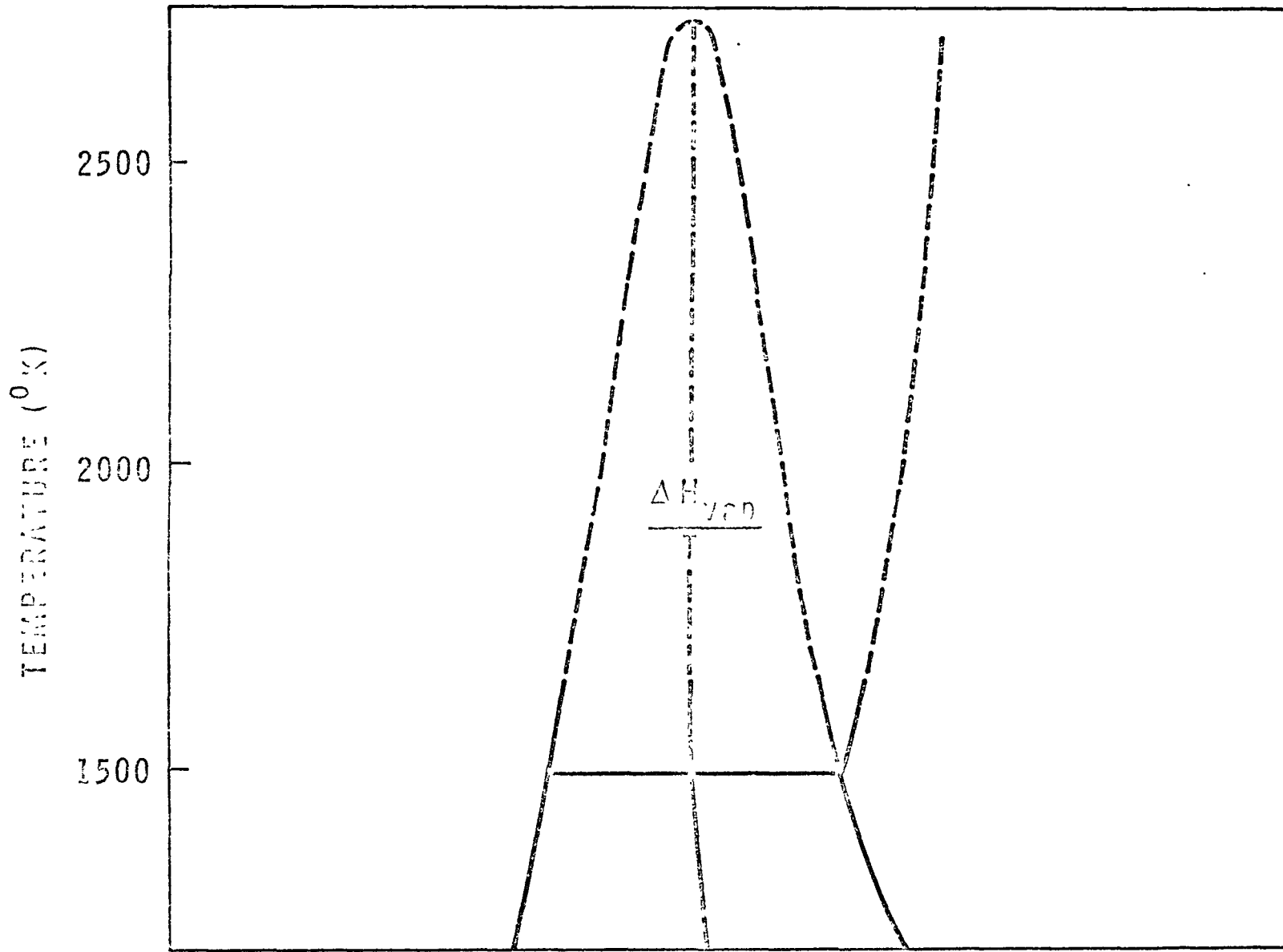


Figure XVII.7

T-S DIAGRAM FOR SODIUM



ENTROPY
Figure XVII.8

SODIUM VAPOR PRESSURE

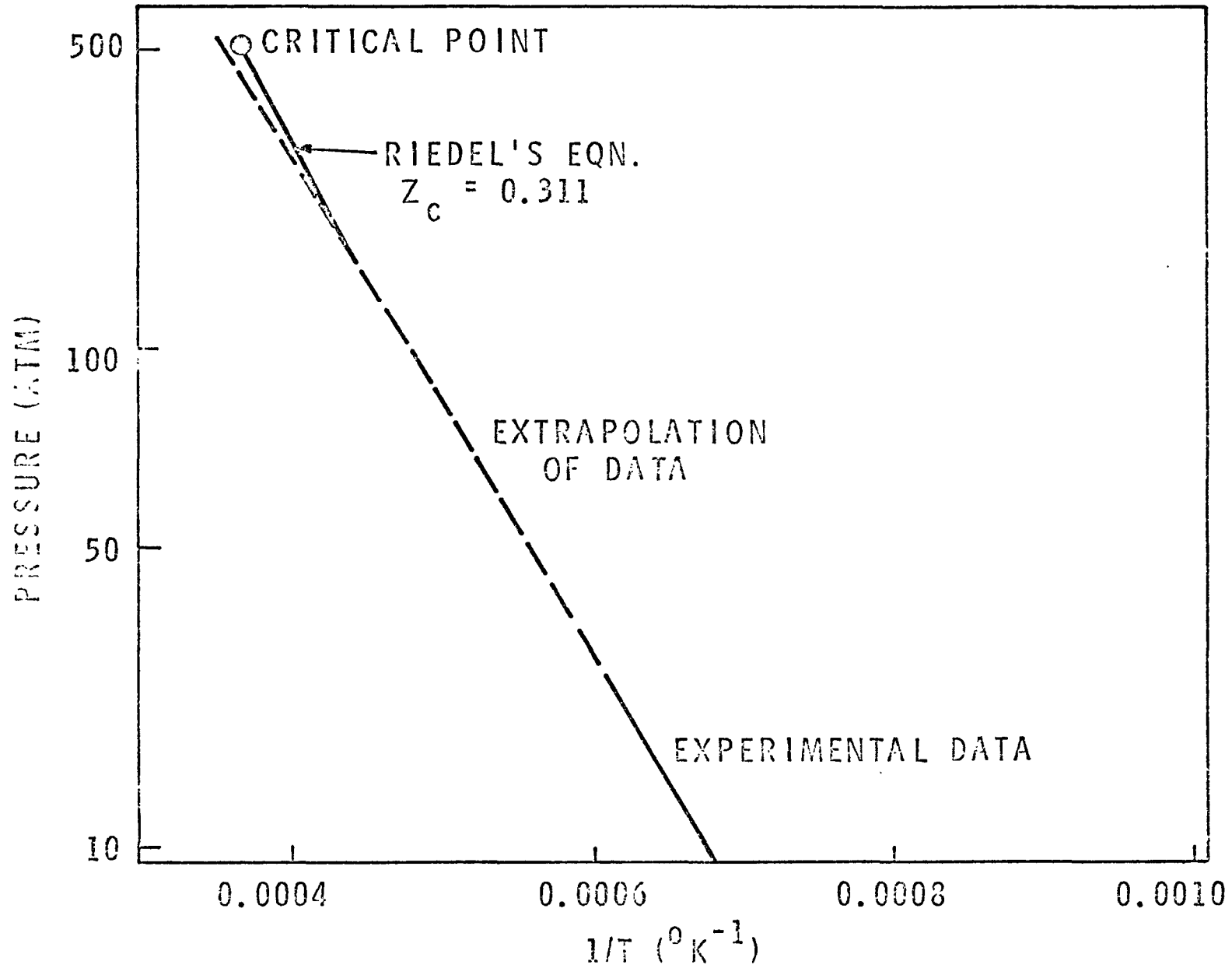


Figure XVII.9

EFFECT OF INITIAL FUEL TEMPERATURE ON ENERGY RELEASE

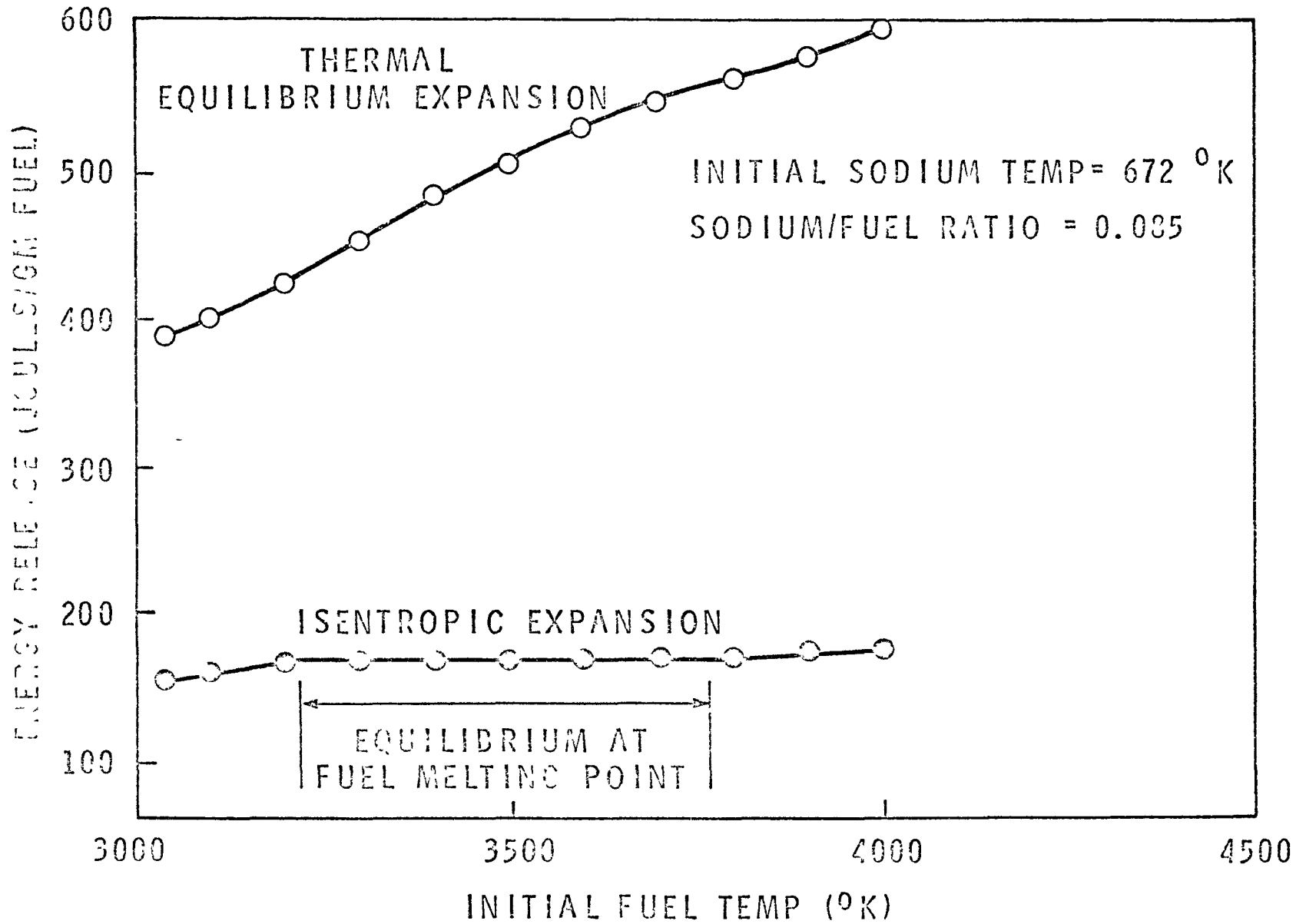


Figure XVII.10

EFFECT OF SODIUM/FUEL MASS RATIO ON ENERGY RELEASE

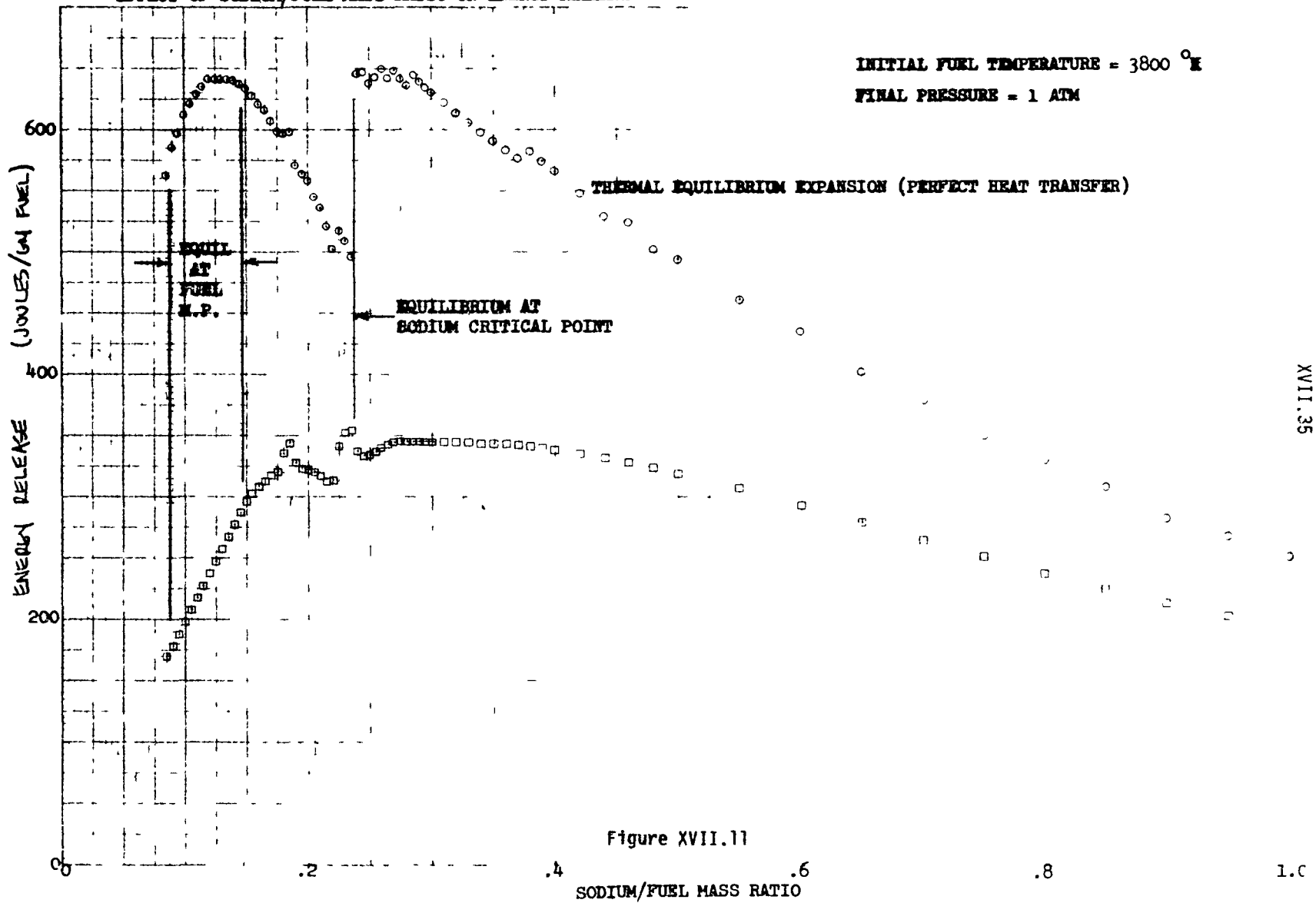


Figure XVII.11

XVII.35

1.0

ISENTROPIC EXPANSION OF SODIUM TO 1 ATM

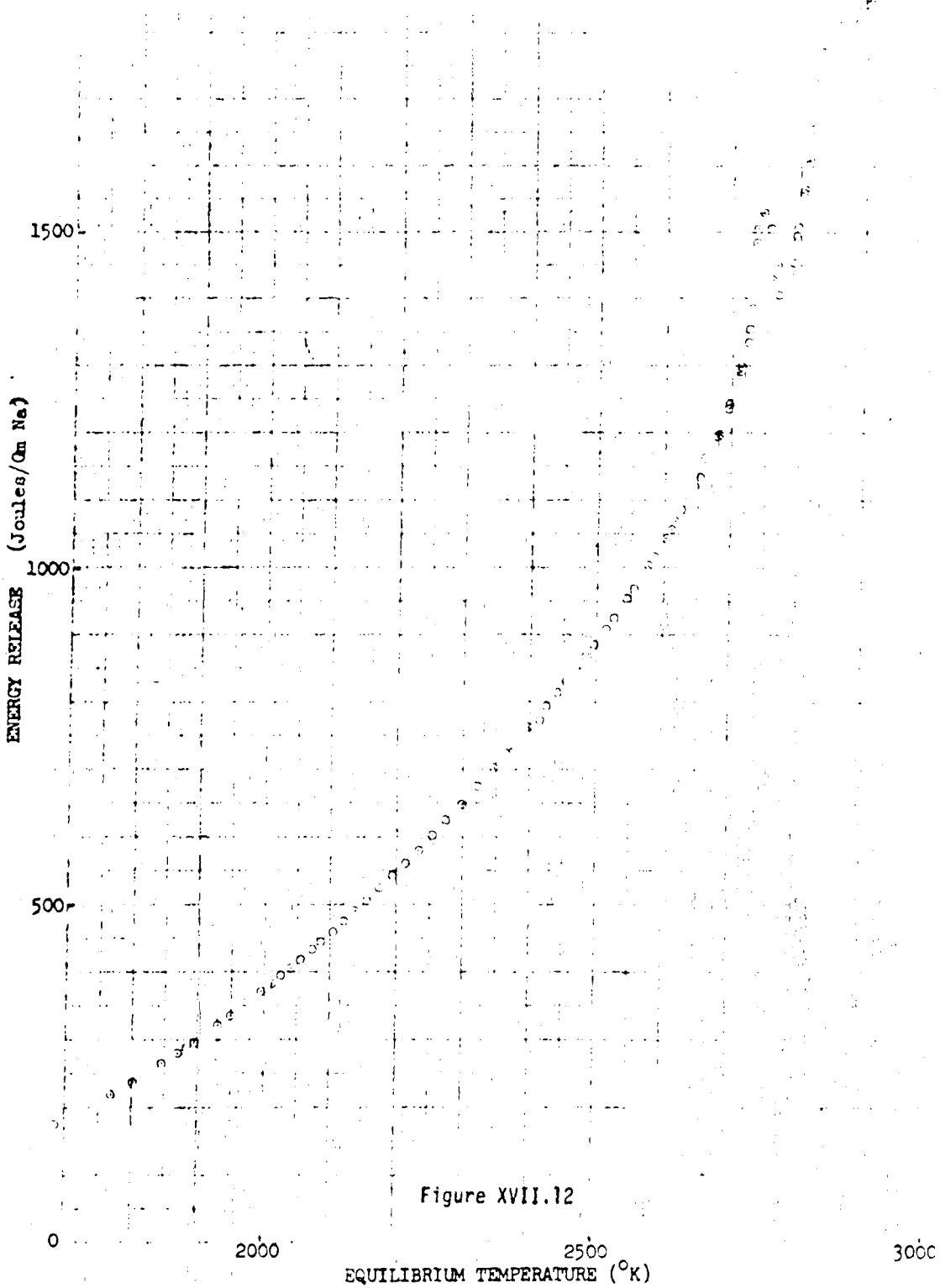
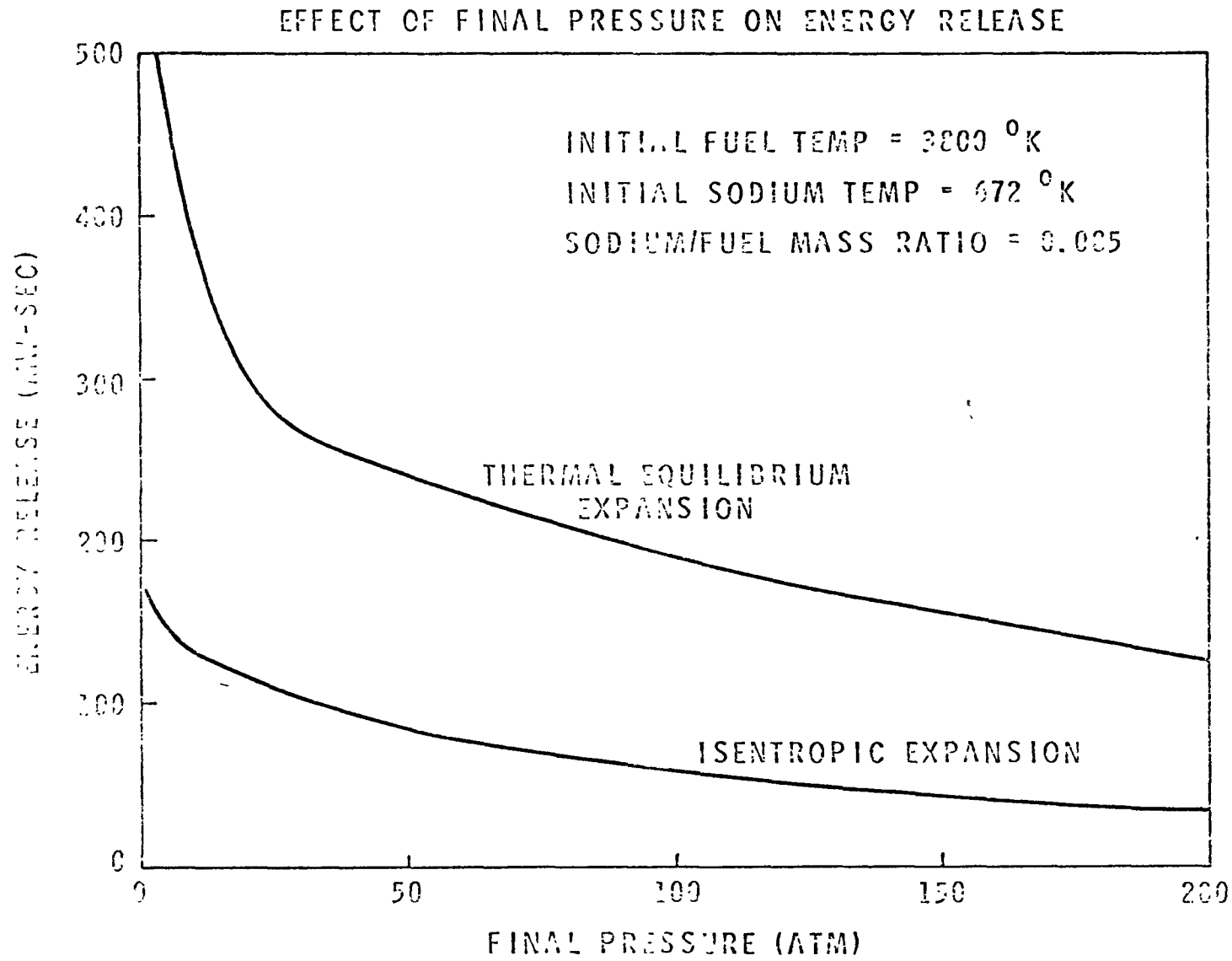


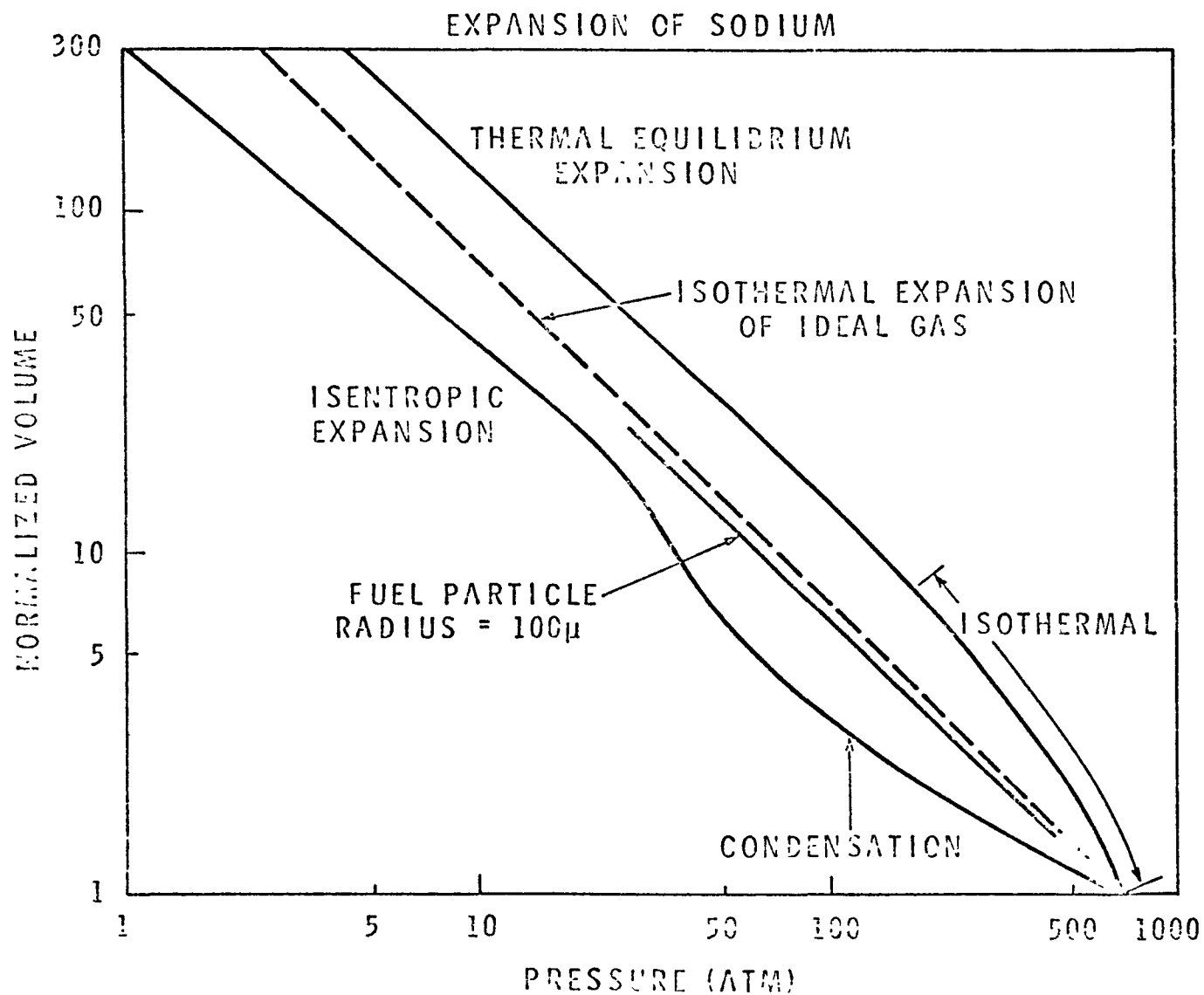
Figure XVII.12

Figure XVII.13



XVII.37

Figure XVII.14



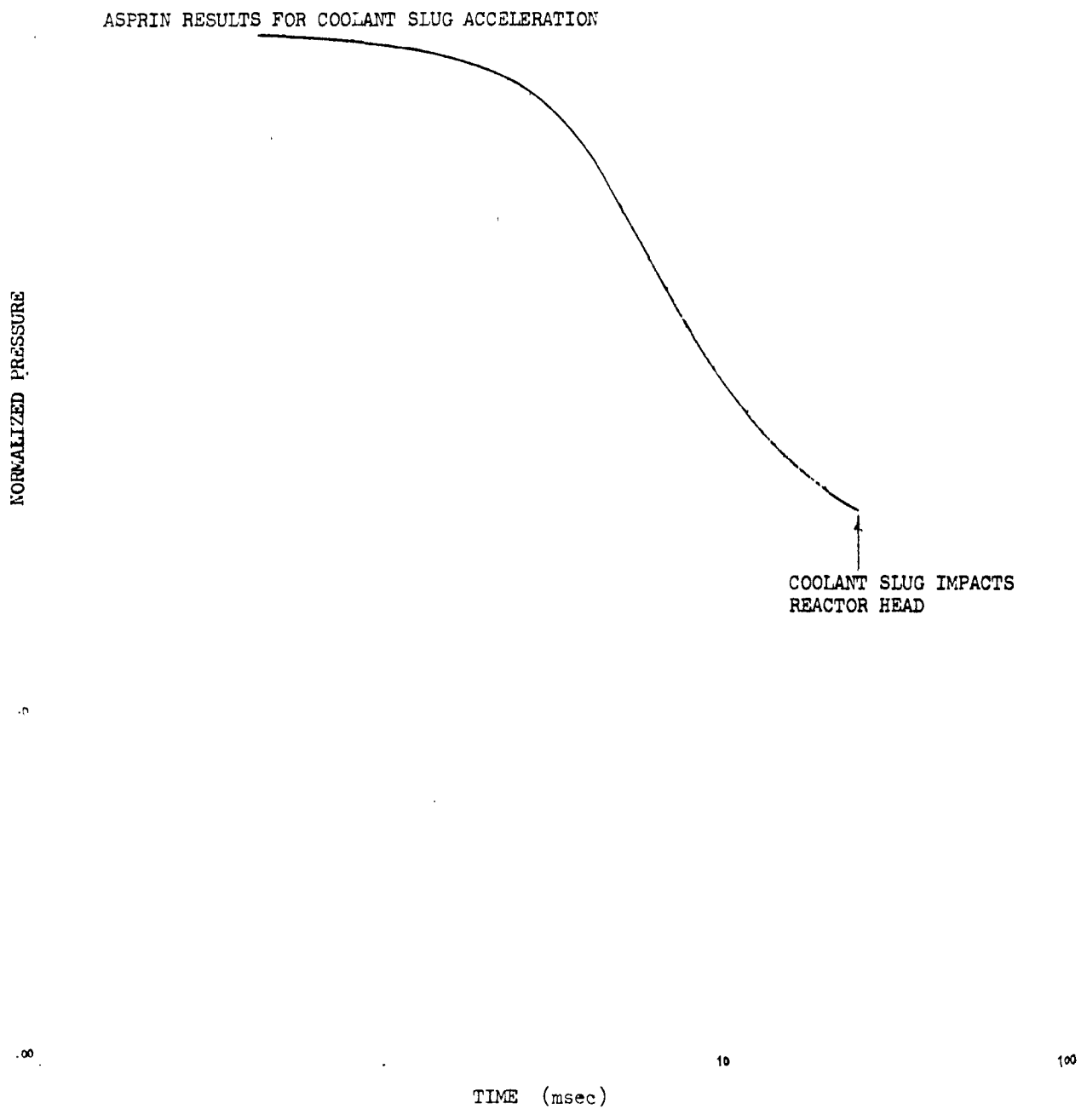
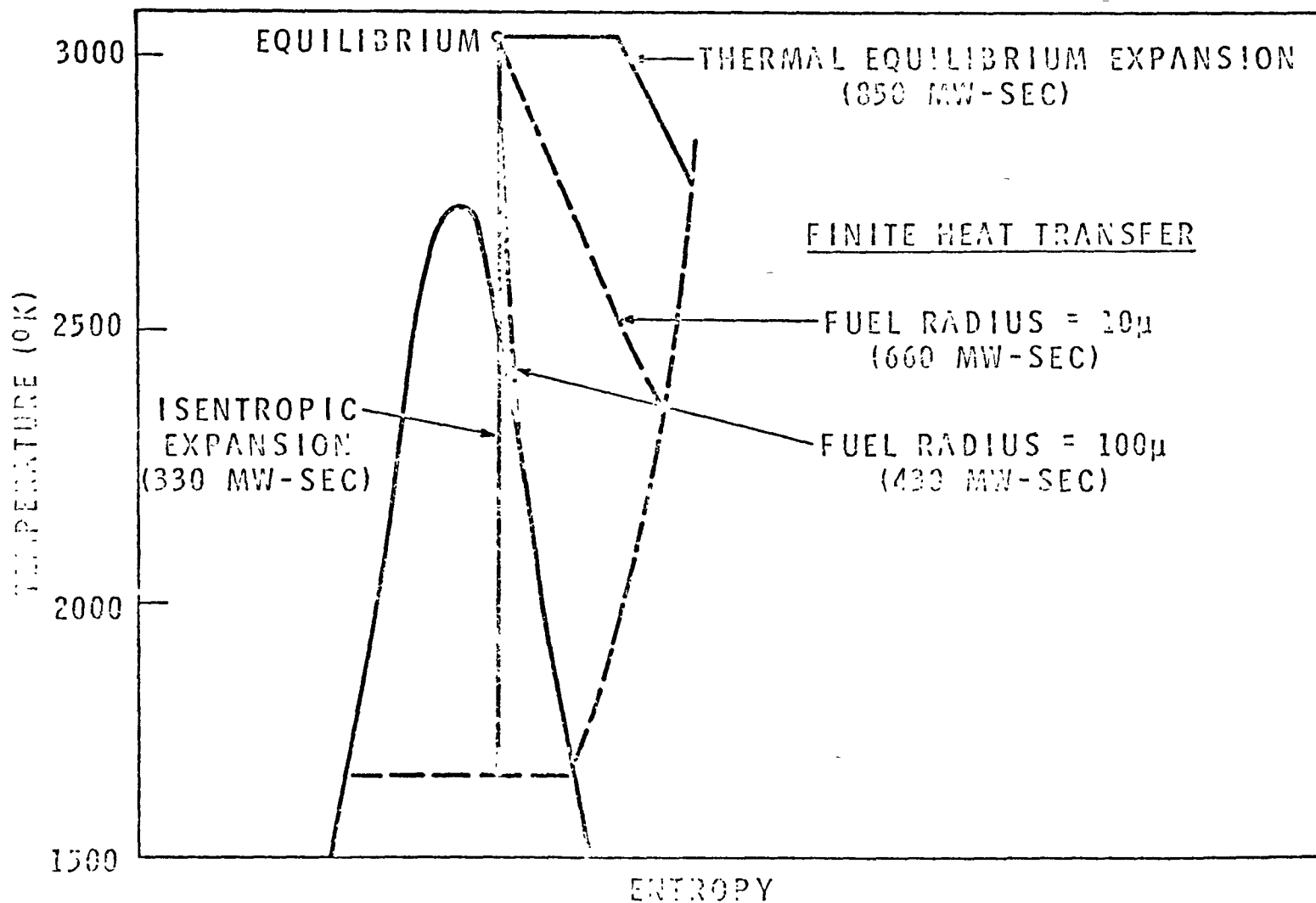


Figure XVII.15

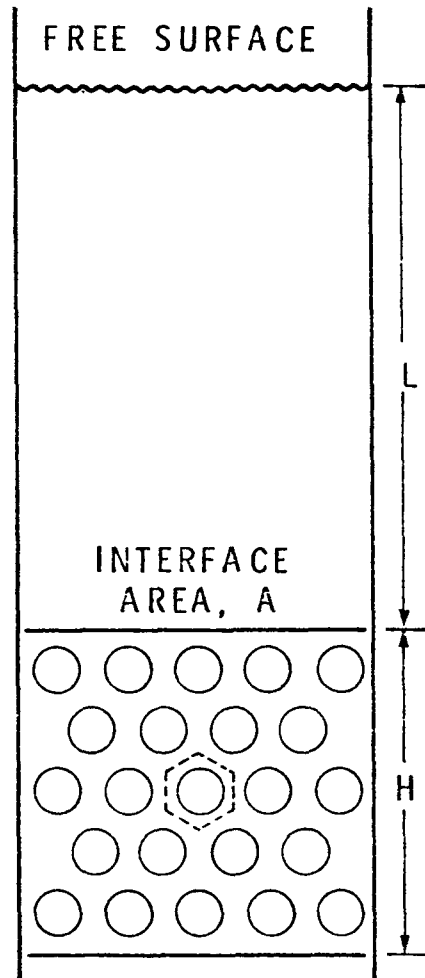
Figure XVII.16

EFFECT OF HEAT TRANSFER ON EXPANSION PROCESS



MODEL FOR MOLTEN FUEL/Na INTERACTION

Figure XVII.17



$$\tau_{\text{ACOUSTIC}} = \frac{2L}{C_0}$$

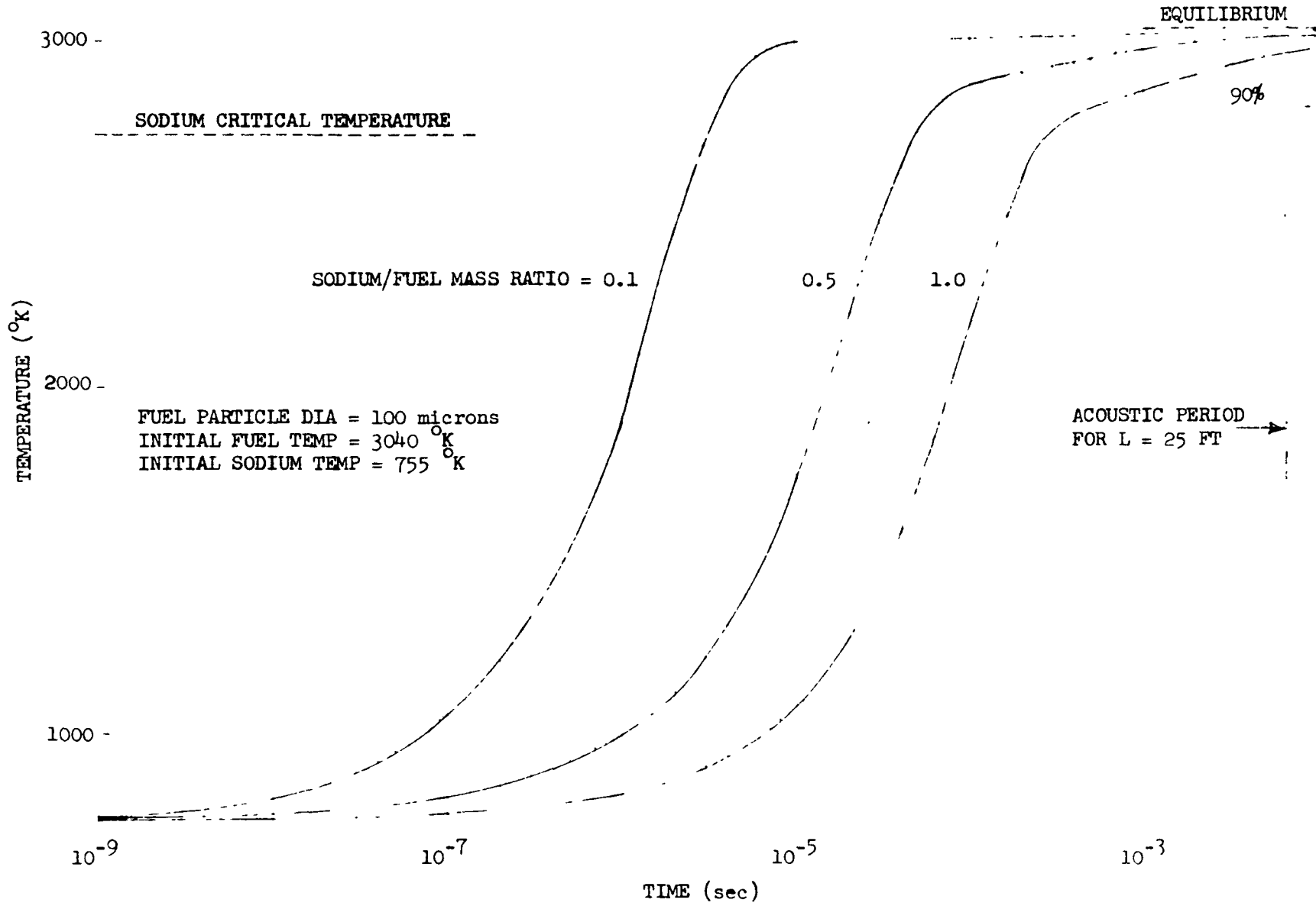
INERTIAL SYSTEM:

$$\tau_{\text{HEAT TRANS.}} \gg \tau_{\text{ACOUSTIC}}$$

ACOUSTIC SYSTEM:

$$\tau_{\text{HEAT TRANS.}} \ll \tau_{\text{ACOUSTIC}}$$

HEAT TRANSFER BETWEEN MOLTEN FUEL AND SODIUM - Figure XVII.18



XVII.42

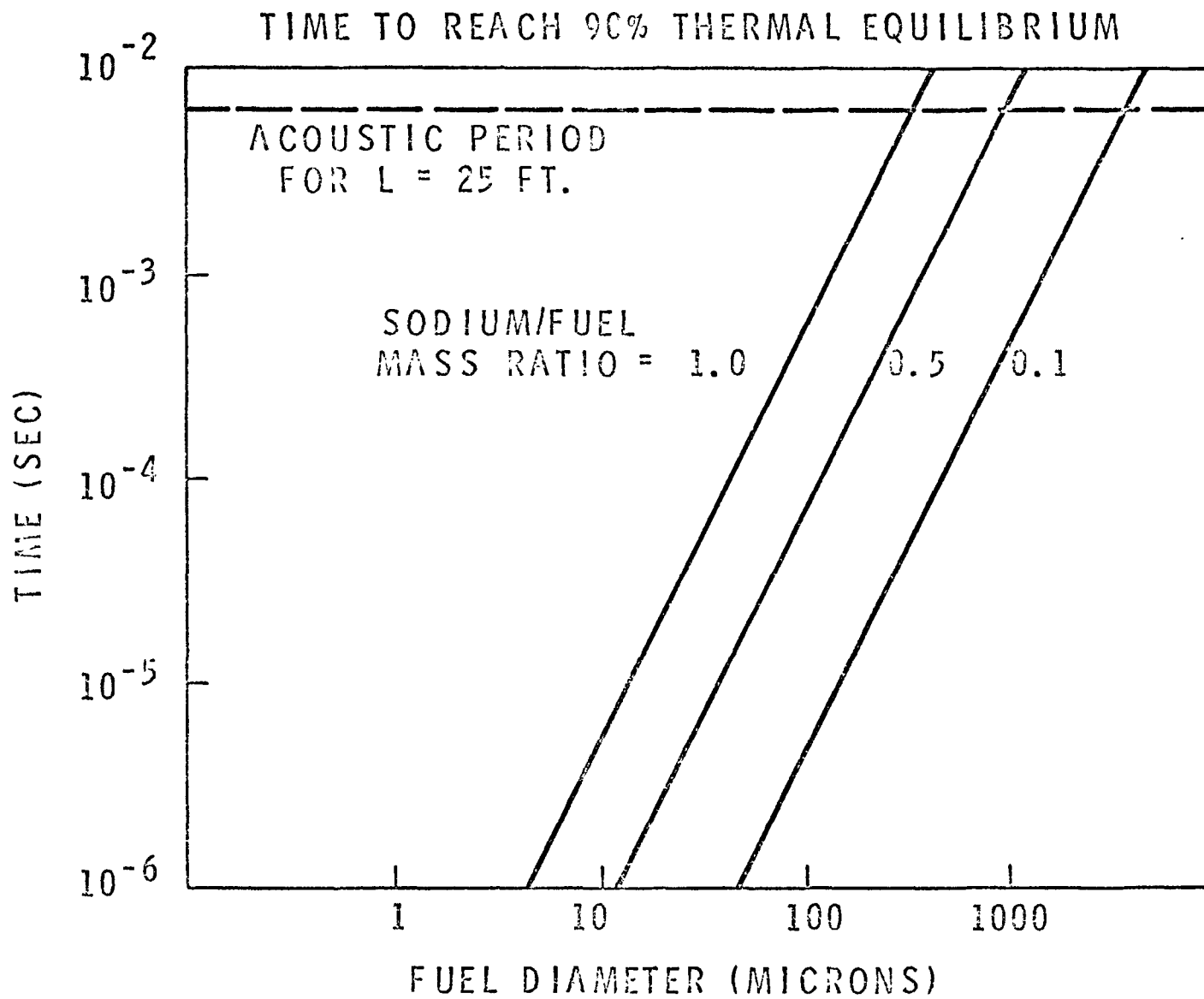
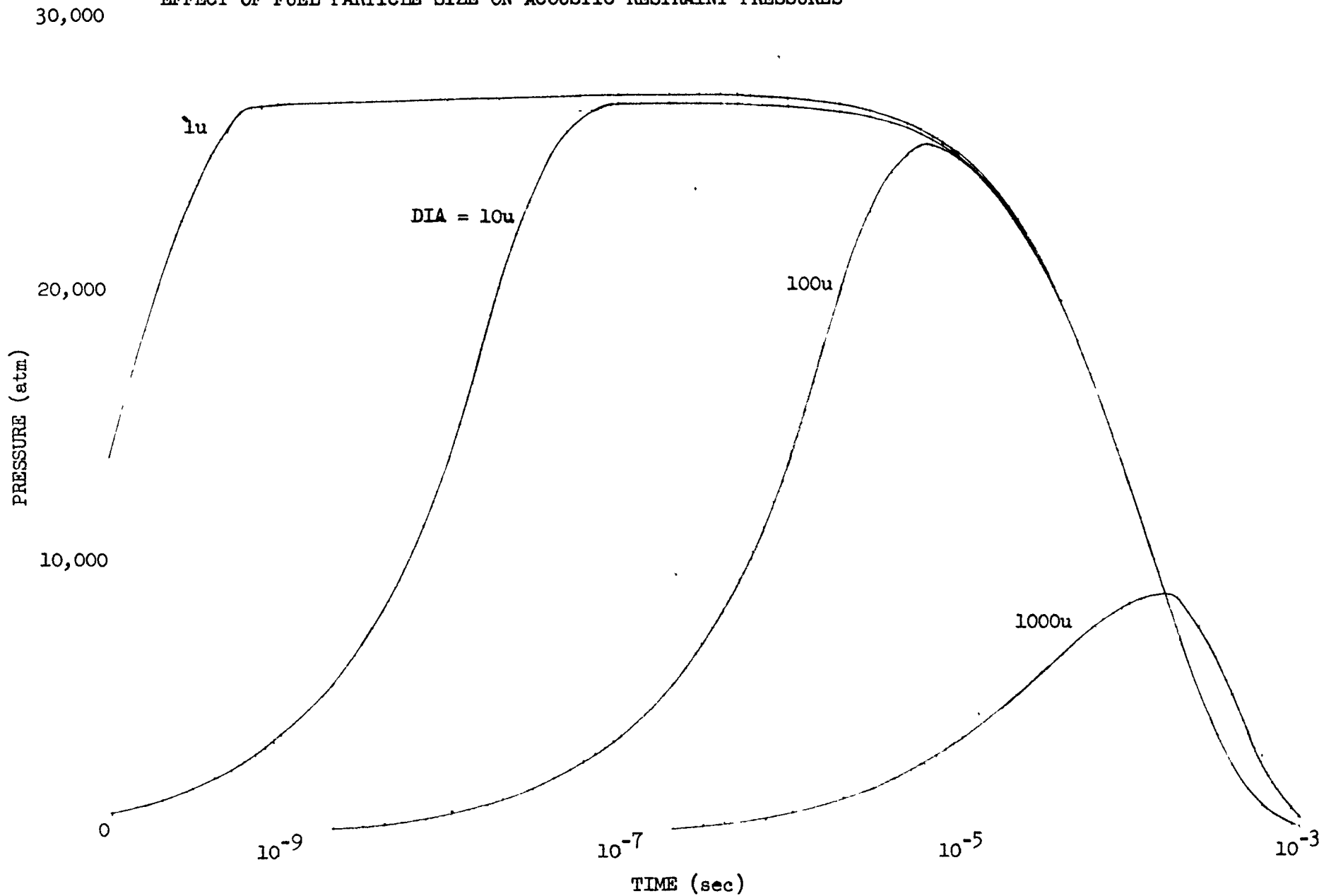


Figure XVII.19

Figure XVII.20

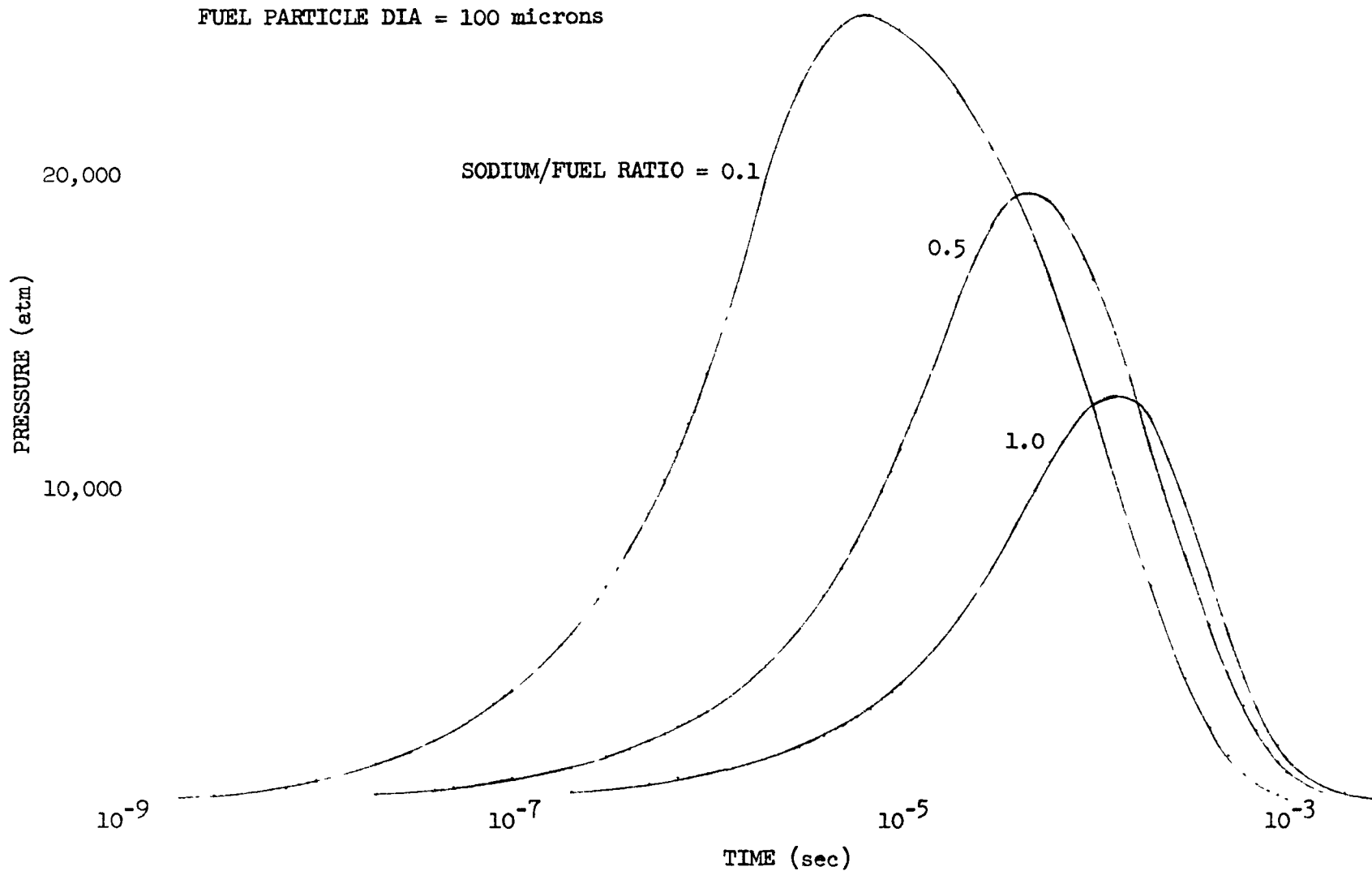
EFFECT OF FUEL PARTICLE SIZE ON ACOUSTIC RESTRAINT PRESSURES



30,000

EFFECT OF SODIUM/FUEL MASS RATIO ON ACOUSTIC RESTRAINT PRESSURES - Figure XVII.21

FUEL PARTICLE DIA = 100 microns



12,000

PRESSURES GENERATED DURING MOLTEN FUEL/SODIUM INTERACTION - Figure XVII.22

FUEL PARTICLE DIA = 1000 microns

SODIUM/FUEL MASS RATIO = 0.1

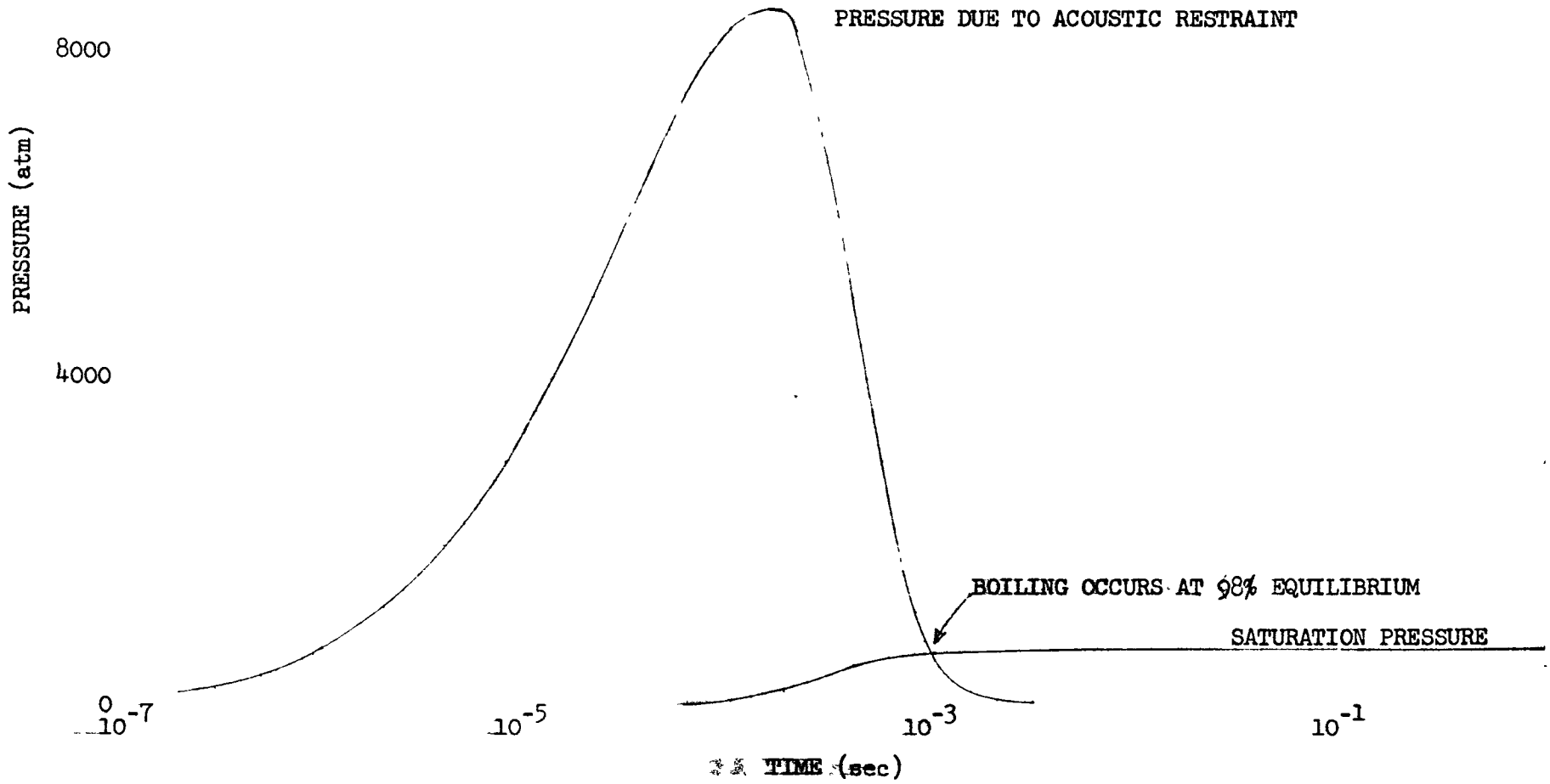
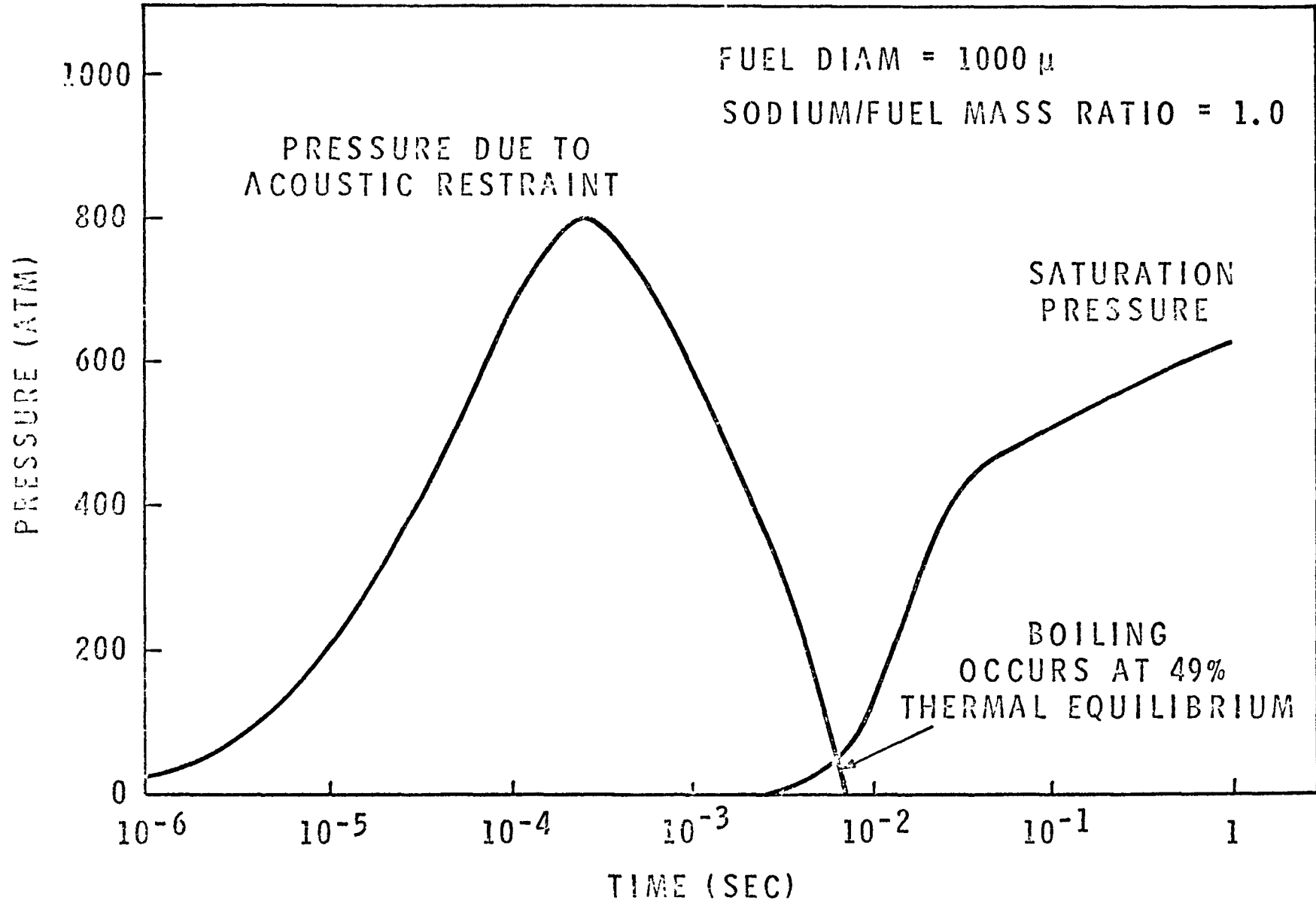


Figure XVII.23

PRESSURE GENERATED DURING MOLTEN FUEL/SODIUM INTERACTION



FRACTION OF THERMAL EQUILIBRIUM ATTAINED BEFORE BOILING

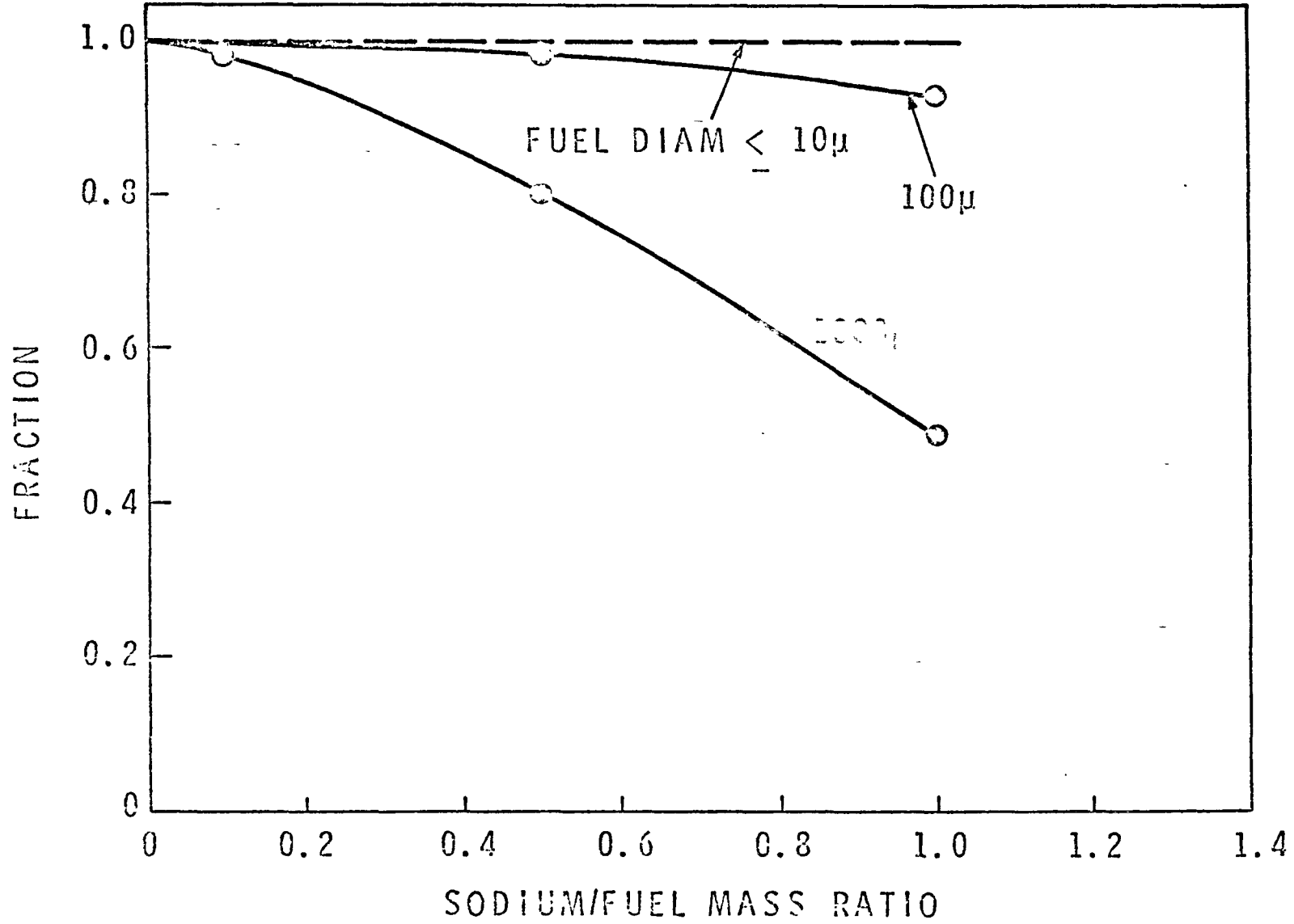
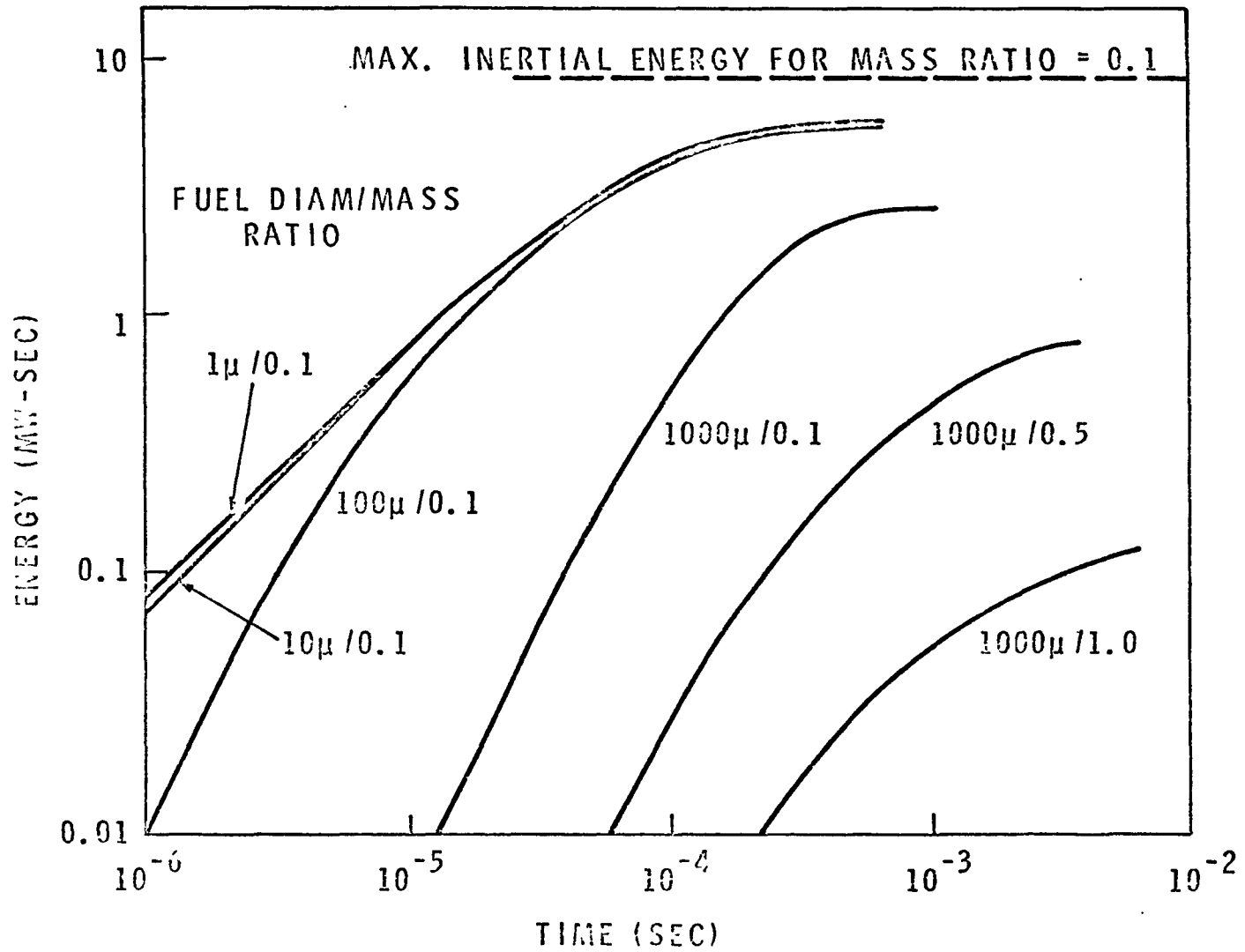


Figure XVII.25

GENERATION OF ACOUSTIC ENERGY



XVIII. EFFECTS OF REACTOR ACCIDENTS
ON REACTOR VESSEL AND HEAD

G. L. Fox

A. Introduction

The reactor accident is initiated by a rapid power excursion which melts the fuel and generates pressures which cause core disassembly. The molten fuel may mix with the reactor coolant and generate pressures which will cause further vessel damage. This reactor excursion has been discussed in Lectures XV and XVI. Energy release mechanisms were discussed in Lecture XVII. The part which will be discussed here will be what happens to the energy which is released within the reactor vessel.

B. Pressure Wave Effects in Fluids

First of all, it will be helpful to obtain background in what occurs in wave motion. A shock wave is a pressure discontinuity which will travel through sodium and react with surfaces or other boundaries at some distance from the source of the explosion. The figure, XVIII.1 shows what happens if a 1 kilobar step pressure rise is propagated in a sodium system. The thickness of the shock wave is of the order of 10^{-5} or 10^{-6} centimeters.⁽¹⁾ The conditions upstream of this pressure wave are zero velocity and pressure rise. On the downstream side of the shock wave, the pressure has jumped to the level of 1 kilobar and has a particle velocity of approximately 170 ft/sec in the direction of the shock wave. The temperature rise for this shock wave is extremely small, on the order of a degree Fahrenheit. The shock wave will propagate at approximately the acoustic velocity, or 7500 ft/sec for sodium

XVIII.2

at this temperature of 550°C. The shock wave is a dissipative process and the sodium entropy will increase. However, it has been found that the entropy increase for liquids is only significant for very intense shock waves of many thousands of atmospheres of pressure.

Now, consider what happens when the shock wave reaches different interface conditions. First, let the shock wave interact with a rigid boundary. In the acoustic approximation, the shock wave is reflected from the rigid boundary as a compression wave which will bring the particle velocity to zero. The compression wave compresses the fluid twice its previous pressure.

Next, let the shock wave react with a free surface which has a zero pressure boundary. The initial compression wave will reflect as a rarefaction wave which reduces the pressure to zero. The particle velocity will be doubled. These interface reactions are shown in Figure XVIII.2.

Now, apply the shock wave characteristics to the acceleration of a fluid column and compare with the Newtonian approximation. The specific example here assumes a column of sodium 15 ft long, has a free surface at the righthand boundary, and is under a pressure of 1 kilobar at the lefthand boundary. The shock wave propagates down through the sodium increasing the particle velocity to 170 ft/sec behind the wave as shown previously until it gets to the righthand boundary. The compression wave reflects as an expansion wave which doubles the particle velocity and leaves the fluid at a pressure of zero. This expansion wave will propagate back to the lefthand boundary at the initial pressure of 1 kilobar. At this point a compression wave of 1 kilobar will be superimposed on the system and this wave will propagate toward the righthand

boundary and raises the particle velocity to 510 ft/sec. This pressure wave propagates to the free boundary and is then again reflected as an expansion pressure wave and the particle velocity has been raised to 680 ft/sec.

Thus, the wave action continues back and forth from the constant pressure boundary to the free boundary and raises the velocity of the fluid column in steps. The acceleration of the fluid column is shown in Figure XVIII.3.

Figure XVIII.4 shows how the column velocity changes as a function of time for both the lefthand boundary and the righthand boundary. The Newtonian calculation is shown as a straight line from the origin. This line represents the acceleration calculated by dividing the pressure acting over a unit face area by the column mass. Thus, the acceleration is constant and the velocity is a linear function of time. For very short time periods it may be seen that the Newtonian calculation underpredicts the velocity of the lefthand face and overpredicts the velocity of the righthand face. However, after many reflections, the Newtonian calculation and the wave calculation give essentially the same results.

C. Characteristics of TNT Explosions

A TNT explosion will virtually instantaneously transform the TNT into an extremely hot, dense mass of gas at the original volume of the TNT. The temperature is approximately 3000°C with a pressure around 50,000 atmospheres.⁽¹⁾ The pressure immediately acts on the surrounding fluid, compresses it, causing it to accelerate away from the explosion center. As the wave propagates outward, the pressure level is decreased because of a spherical effect where the pressure decreases as $1/r$ for an acoustic wave. In addition, the TNT products expand, decreasing the pressure very rapidly in this region.

This causes the wave, as it moves out, to have a high peak pressure and rapidly tail-off to some lower value (see Figure XVIII.5). Thus, this pressure wave, as it propagates outward, will virtually instantaneously accelerate the fluid particles to a maximum velocity which will then decrease as the pressure decreases. However, in the case of a spherical explosion, the velocity will not return to zero as in the case of a cartesian coordinate system, but will retain a particle velocity which is dependent on the pressure history at that particular location. The pressure wave in water carried about 50% of the energy contained in the original TNT products. It has the capability of delivering an impulse to a surface. The impulse may be calculated as the integral of the surface pressure history over the time involved. Actually, when this wave strikes a surface, a portion of the energy is reflected and will not be absorbed, and so an efficiency factor must be considered.

A pressure spike has different characteristics than a step pressure increase. When the spike hits a free surface, it will be reflected as a rarefaction wave that causes a negative pressure in the system. The step jump pressure wave is also reflected as a negative pressure, but when it was superimposed on the original pressure, the sum resulted in zero pressure.

D. Experimental Data

We will now examine applicable experimental results and the SL-1 accident.

The U.S. Naval Ordnance Laboratory⁽²⁾ determined the amount of TNT that could be contained in cylinders. Their models were cylinders of different

XVIII.5

diameter and wall thickness which ranged from 5 inches to 20 inches in diameter and wall thickness of 0.06 to 1.03 inches. Examples of their test cylinders are shown in Figure XVIII.6. The main factors in their derivation of the containment law are shown in Figure XVIII.7. The equations for the impulse transmitted by the shock wave are coupled to the TNT equation, which resulted from prior knowledge of TNT similarity effects, and the material law equation, which represents linear strain hardening of the cylinder wall material. These three equations are combined into a form which shows the amount of TNT which would cause a cylinder to be strained to rupture and is shown on Figure XVIII.7 as the containment law. The values ψ_1 and ψ_2 are experimentally evaluated parameters which show the effect of strain hardening and efficiency factors for transmission of the impulse to the cylinder wall. The factors ψ_1 and ψ_2 were evaluated from many experiments and inserted in the law. The final form is shown on Figure XVIII.8. This shows the maximum contained TNT explosion is a function of the ultimate stress, ultimate strain, material density, wall thickness, and the internal and external radii. In addition, it was found that if one-third of the ultimate strain was used, the vessel would not fail from that amount of TNT. This is known as the amount of TNT which would be safely contained within this cylinder.

The results of the containment law are shown in Figure XVIII.9. The weight of TNT has been plotted as a function of the vessel radius and for wall thicknesses which range from 1 to 3 inches. The vessel material was 304 stainless steel with the indicated properties. Using a vessel radius of 8 ft and wall thickness of 2 inches, approximately 170 lbs of TNT can be safely contained and approximately 700 lbs of TNT is the maximum quantity which can be contained. (Both of these numbers depend on the ultimate strain of 40%.)

The Naval Ordnance Laboratory⁽³⁾ also performed scale model tests for the Enrico Fermi reactor. They exploded charges of TNT in the core region and measured the height to which the reactor cover was blown and the deformation of the vessel wall (Figure XVIII.10). Their tests confirmed that retaining the cover is a real problem (Figure XVIII.11). The cover jump appeared to be caused primarily by blast pressures, rather than shock waves. The cover received approximately 1.6% of the maximum hypothetical accident energies. NOL also found that since the cover acceleration occurred over a significant time period, there was considerable heat transfer from the blast products into the coolant and the reactor core structure. This reduced the energy which was available to accelerate the plug. Because of this heat transfer effect, the height of their plug jump was directly related to the initial temperature of the reactor coolant.

The United Kingdom Atomic Energy Authority⁽⁴⁾ performed an extensive series of tests for their PFR reactor. They used reactor models and set off simulated charges of 500 lbs of TNT and measured the vessel deformation and the energy to the reactor cover. Their measurements were over time spans of a few milliseconds, whereas the Naval Ordnance tests were over several hundreds of milliseconds. Thus, the British measured a very rapid transfer of energy to the cover. Their experiments did not show an effect if the coolant temperature was varied because there was not sufficient time for heat transfer to occur.

In this test series they also measured the effect of increasing the air gap between the top surface of the coolant and the reactor cover. They found that there was a gradual decrease of energy which the cover received because

XVIII.7

of the increasing air gap. This is shown in Figure XVIII.12. Note, also, on this figure that the cover received between 1 and 2% of the charge energy which is in agreement with the Naval Ordnance tests.

Joint experiments by the CEA-EURATOM⁽⁵⁾ and the UKAEA were carried out to compare the effect of using sodium or water as a coolant within a reactor. The results showed that there was considerable difference between the shock energy transferred using water or sodium. The impulse measured with sodium was approximately 1-1/2 times the value obtained in water. If one assumes that the energy transferred is proportional to the (impulse)⁽²⁾, this would mean that sodium should transfer 2.25 times as much energy. However, the results showed that the vessel damage from a given charge of sodium is less than that produced by twice the charge weight in water.

The SL-1 accident⁽⁶⁾ occurred in 1961 in Arco, Idaho and provided another set of data on what might occur in a reactor accident. Approximately 50 megawatts seconds of heat energy was released rapidly enough to simulate an explosion. The resultant blast pressures were sufficient to distort the vessel wall in the core region and to propel a coolant slug up toward the cover. When the slug impacted the cover, there was a transfer of kinetic energy from the coolant slug into the vessel walls and the cover. The walls distorted considerably in the upper vessel region as shown in Figure XVIII.13. The slug appears to have been accelerated to 159 ft/sec where it impacted the cover and transmitted enough energy to lift the vessel 11.4 ft. The significant point is the SL-1 accident established the importance of considering a coolant slug for the design basis accident in other reactor designs.

E. Design Basis Accident Characteristics

The actual pressure characteristics during the DBA are unknown. Important work is now being done by A. Padilla at BNW which characterizes this pressure history as a function of fuel particle size, fuel coolant ratio, and work energy involved. This work indicates that coolant acoustic pressures may be generated by the thermal expansion of the heated coolant and result in pressures in the range of 6000 to 10,000 atmospheres. The acoustic pressure wave may carry off as much as half the work energy. If the particle sizes are sufficiently large, the acoustic energy is small and the pressures will be in the order of the coolant vapor pressures or around 700 atmospheres. This compares with fuel vapor pressure during the DBA which is in the range of 600 to 1,000 atmospheres. These pressures are generally much smaller than the maximum TNT pressures which are in the order of 50,000 atmospheres. Defining the pressure history with certainty becomes dubious with the wide range of parameters involved. Eventually what may be done is to characterize the pressure history as a function of the DBA energy. Then it may be possible to optimize the vessel design, not to the maximum energy release, but to the most damage-producing type of energy release. The primary benefit of pressure history curves would be in analysis of the vessel cover. The fraction of energy it receives is directly related to this pressure history. At present, our models do not have the sophistication to take advantage of such pressure history curves. The maximum energy release is considered as a TNT charge to get the maximum shock wave effect. This maximizes the wall deformation in the core region and minimizes the loadings to the vessel cover. To obtain the other extreme, the energy release is considered to be a low

pressure blast wave. This has the ability to move a coolant slug and provide sustained high pressures on the vessel cover.

F. Shock Wave Effects

The maximum effect of the shock wave on the vessel walls is best approximated by the NOL containment laws. Various allowable wall strains may be substituted in the equation and the maximum weight of contained TNT can be calculated (for this analysis, one pound of TNT may be assumed equivalent to 2 megawatt-seconds of energy). This method ignores the effect of the structure within the reactor but, unless there is much energy absorption by plastic deformation in the core region, the deformation of the vessel walls is about the same. The results are shown in Figure XVIII.14.

Using the present vessel wall criteria of maintaining 10% ductility, about 95 MW-sec could be safely contained, and energies above 285 MW-sec would certainly cause rupture.

An estimate of the shock wave loading to the cover for a full reactor vessel may be obtained analytically.⁽⁷⁾ However, the results are not accurate because the explosion has occurred within a reactor vessel with all its constraints and is not a true spherical wave. Nevertheless, the energy magnitude is of interest.

The calculation details are not shown here. Pertinent physical values were:

Distance between cover and explosion center	20 ft
Cover Weight	550,000 lb
Cover Area	215 ft ²
TNT Weight	500 lb

The results showed a TNT explosion with 1000 MW-sec energy release transferred about 0.18% of the energy to the cover which would cause an unsecured cover lift of about 2.4 ft. Thus, the TNT type shock wave represents an inefficient mechanism for accelerating the vessel cover and may be disregarded.

G. Blast Wave Effects

The blast pressures may last many milliseconds. Therefore, it is feasible to approximate this motion with a Newtonian type model. This has been done in a computer code named ASPRIN. The analytical model has been previously described in much detail⁽⁸⁾ and only the major features will be described here.

The analysis is based on combinations of one dimensional Newtonian motion in the axial and radial directions (Figure XVIII.15). Wave phenomena are not considered and deformations are assumed to occur from the quasi-steady pressures in the core region. Output information from the code consists of gross vessel and cover displacements, velocities, stresses, strains and the DBA energy distribution. Predominant features of the analytical model for the code may be summarized as follows:

- A gas bubble in the core region provides the pressures and work energy predicted by molten fuel-coolant interaction.
- The dynamic wall motion in the core region results from the core bubble pressure, whereas the wall motion in the upper vessel region results from both the core bubble pressure and the slug impact pressure.
- The impact pressures, generated during the time period of energy transfer from the coolant slug to the vessel and

XVIII.11

cover, is approximated by a coolant mass balance and an energy balance. These pressures produce energy absorption in the upper vessel and cover structures.

- The cover is restrained by holddown bolts and/or the reactor vessel which undergo the elastic and plastic deformation. If the strain exceeds a prescribed value, the holddown structure ruptures, reducing the holddown force to zero.

The model was verified by comparing the predicted results with the data available from the SL-1 accident. The accident was simulated using ASPRIN with the proper geometry and mass conditions. A DBA work energy of 8.25 megawatt seconds was used, since this value is obtained from Proctor's work if the TNT products are expanded to one atmosphere. The vessel deformation pattern is shown also on Figure XVIII.13. Further details of the analysis may be found in Reference (4). Table XVIII.1 shows a comparison of the estimated energy absorption and generated pressures and are compared with the results predicted by ASPRIN. Note the estimated vessel velocity was approximately 29 ft per second, whereas ASPRIN predicted 31 ft per second and the vessel rise was 11.4 ft, whereas ASPRIN predicted 15 ft. The degree of correlation in Figure XVIII.13 and Table XVIII.1 is not the most important factor. A better correlation could be obtained by adjusting the work energy and varying the wall inertia parameters. This, however, is just data fitting and misleading. The important factor is that ASPRIN, as it is conventionally being used, underpredicts the vessel radial deformations and overpredicts the kinetic energy

Table XVIII.1

Comparison of SL-1 Conditions with Predictions by ASPRIN

<u>Parameter</u>	<u>SL-1 Conditions</u>	<u>ASPRIN Predictions 8.26 Mx-Sec Work Energy 200 Atm Max. Pressure</u>
Energy absorbed in lower vessel, ft/lb	1.85×10^6 Minimum	1.63×10^6
Energy absorbed in upper vessel, ft/lb	2.67×10^6	1.48×10^6
Maximum Slug Velocity, ft/sec	159	145
Impact Pressure, psi	10,000	6,000
Vessel Velocity, ft/sec	29	31
Vessel rise, ft	11.4	15

XVIII.11a

remaining in the coolant slug and cover system. This substantiates that the analytical model overpredicts the cover loadings which might occur as a result of a DBA.

ASPRIN has been applied to a "base case," parameter No. 1, liquid metal reactor design, and then selected parameters were varied to show their importance.

The reactor used for the "base case" was 17 ft in diameter with a 2-in. wall thickness. The inertia of a 3-in. thermal shield was included which reduces the energy dissipated in wall deformation. A distance of 20 ft was assumed from the top of the core to the vessel cover; however, only about a 12 ft height of sodium was used. This postulates that the sodium level could be reduced down to the outlet nozzles of the FTR during a pre-DBA condition. The DBA work energy was 1500 MW-sec with a peak pressure of 616 atm. A delay period of 3 msec was assumed before the gas bubble pressure acted on the vessel walls. A detailed listing of input variables for the base case is shown in Reference (8).

Only the highlights of the base case can be conveniently described here because of magnitude and variety of output. The slug is accelerated by the gas bubble to a velocity of 410 fps before impact occurs. The lower vessel walls have expanded 24 percent and did not surpass the rupture criteria of 25 percent. About 26 percent of the DBA energy is contained in the coolant slug mass of 3560 slugs. Upon impact, pressures of 31,000 psi are generated in the head region which accelerates the cover and upper vessel walls. The cover mass of 17,100 slugs is accelerated to a velocity of 64 fps in a few milliseconds and the upper vessel walls rupture about 5 msec later. The stainless-steel holddown bolts with a total area of 700 sq in. and a length

of 10 ft began decelerating the cover and stopped it after undergoing about 18 percent plastic strain.

It should be noted that the cover velocity of 64 fps compares very closely with the results from a completely inelastic collision which produces a velocity of 69 fps. Therefore, for approximate purposes, an inelastic collision is a reasonable assumption for wall thicknesses of a few inches.

The results of 13 parameter runs are shown in Figures XVIII.16 through XVIII.20. Only one parameter has been varied from the "base case" conditions for each run. The kinetic energy in the coolant slug and the vessel cover has been chosen as the most representative parameter which demonstrates the holddown problem. The total plastic strain produced in the holddown bolts is also included.

Figure XVIII.16 shows, with increasing wall thickness, a larger portion of the DBA is transmitted to the cover. The thicker walls not only provide more strength and inertia in the core region which shows as a larger slug kinetic energy before impact, but also prevent the upper vessel from rapidly distorting and absorbing energy. The steep line that signifies the energy decrease during the impact period is drawn only to connect before and after energy values.

Figure XVIII.17 shows the effect of increasing the gas gap between the cover and coolant slug. With larger gaps than shown here, there should be a point where the coolant slug mass becomes sufficiently small so that less energy is transmitted to the cover. That is, the increase in slug kinetic energy from expanding the gas bubble further does not compensate for the decrease in energy transferred because of the reduced slug mass.

Figure XVIII.18 shows that a larger cover mass is a very effective parameter for directing the slug kinetic energy into the vessel walls and not into the cover. The inertia of the cover prevents it from rapidly absorbing energy.

Figure XVIII.19 shows that a smaller DBA directs a larger percentage of the energy into the coolant slug. The walls more easily resist the gas bubble expansion since the pressure decreases more rapidly. However, an energy of 2000 MW-sec caused an early vessel rupture which reduced the cover loadings.

Figure XVIII.20 shows the effect of varying the maximum pressure used to characterize the DBA. The slug kinetic energy is rather insensitive to the initial pressure used.

When comparing the results of ASPRIN to TNT, an additional factor must be considered. A TNT explosion has initial shock wave pressures in the order of 50,000 atmospheres. This pressure is so intense that the deformations tend to move outward from the core region in all directions. Conversely, the sodium fuel interaction generates blast pressures around 700 atmospheres and the work energy may be channeled to a localized area. An example is the sodium slug above the core which may receive a large portion of the DBA energy as it is being accelerated toward the cover. This energy is concentrated in radial strain in the upper portion of the reactor vessel. The effect has been demonstrated by the results of the SL-1 accident which was shown in Figure XVIII.13. The damage from slug impact caused upper vessel strains several times those in the core region.

There is conservatism in the ASPRIN results because the original intent of the code was to underpredict the vessel deformation and, therefore, over-

predict the energy available to accelerate the vessel cover. So, the upper vessel deformation predicted by ASPRIN should not be considered upper limits, but indicative of the form of results.

ASPRIN was applied for the FFTF vessel with gas gaps of 0.5 and 8 ft between the top of the sodium pool and the vessel cover. The results are shown in Figures XVIII.21 and 22. The "Safe Level Limit" was selected at strains 1/3 of the ultimate strain similarly to the work of Proctor and Wise, NOL.* If failure of the upper vessel is selected as the criterion for vessel failure, the following energies may be obtained from the figures:

<u>Condition</u>	<u>Gross Vessel Rupture MW-sec</u>	<u>Safe Level Limit MW-sec</u>
ASPRIN Slug, 0.5 ft	160	23
ASPRIN Slug, 8 ft	58	13

The ductility of the upper vessel will undoubtedly be greater than the lower wall and perhaps one could construct a table based on different allowable strains for the upper and lower regions. However, the uncertainties do not warrant this refinement at present.

H. DBA Effects

This paragraph might be titled "What does the DBA do to containment design." First of all, both the TNT analysis and the blast wave analysis indicate there is a high probability that the vessel wall could fail. This

* The deformation criteria of 10% and 3.3% are presented here as logical extensions of the NOL TNT criteria and not valid vessel criteria for failure from blast loadings. Any significant plastic strain is a departure from pressure vessel code criteria and guaranteeing vessel integrity is extremely difficult.

means sodium coolant may be spilled in the reactor cavity and the designer must consider ways of handling the cooling loss. The blast wave analysis indicates that a considerable portion of the DBA energy may be transferred to the cover and will cause restrained cover lifts in the range of 1 to 2 ft for work energy release of 1000 MW-sec. This movement will cause openings to occur that will allow sodium to leak out of the reactor vessel for short periods of time. In addition, the bolts could cause cover decelerations of about 65 g's which must be considered for cover design. This deceleration force is distributed over the cover and may be considered as an effective cover pressure which is calculated to be 900 psi.

At this point it is necessary to discuss pressure design criteria for the vessel cover. Fundamental to this criterion is the assumption that the important cover stress is caused by the holding action of the holddown bolts. Pressure forces greater than the yield stress times bolt area will cause cover acceleration. The required cover strength to handle the DBA may be determined by two different criteria:

1. The cover and bolting system should be able to withstand slightly greater pressure levels than may be contained in the reactor vessel. The bolts should have sufficient length to absorb whatever energy is transmitted to the cover.
2. The bolting system will have sufficient energy absorbing ability to handle whatever energy is transmitted to the cover. The bolt forces will be less than the vessel maximum pressure capability times the cover area.

The first criterion provides system capability to withstand any DBA regardless of the pressure history. A very rapid pulse type pressure level will transmit low energy to the cover and rapidly accelerate the vessel wall causing it to rupture. A long pressure pulse will still accelerate the wall fastest because of its small inertia and also cause wall rupture. Thus, the first criterion has the advantage of being very simple to apply and decouples the cover design from the size of the DBA and analytical models for describing the DBA. The only requirement is that the holddown bolts provide sufficient energy absorbing capability to stop the cover motion.

The second criterion has the advantage of allowing the cover strength to be less than the vessel walls. This occurs because by applying a rapid DBA transient, one is able to substitute inertia of the cover for strength so the energy is primarily absorbed in the walls. A disadvantage is that this criterion depends heavily on the DBA energy and the analytical model for determining the energy transfer to the cover and the material properties of the holddown bolts. The first criterion is presently preferred, however, further analytical development may justify using the second criterion.

I. Future Work

The analysis just presented only represents a starting point in understanding DBA effects. Some areas for future work will be quickly outlined to point out needs.

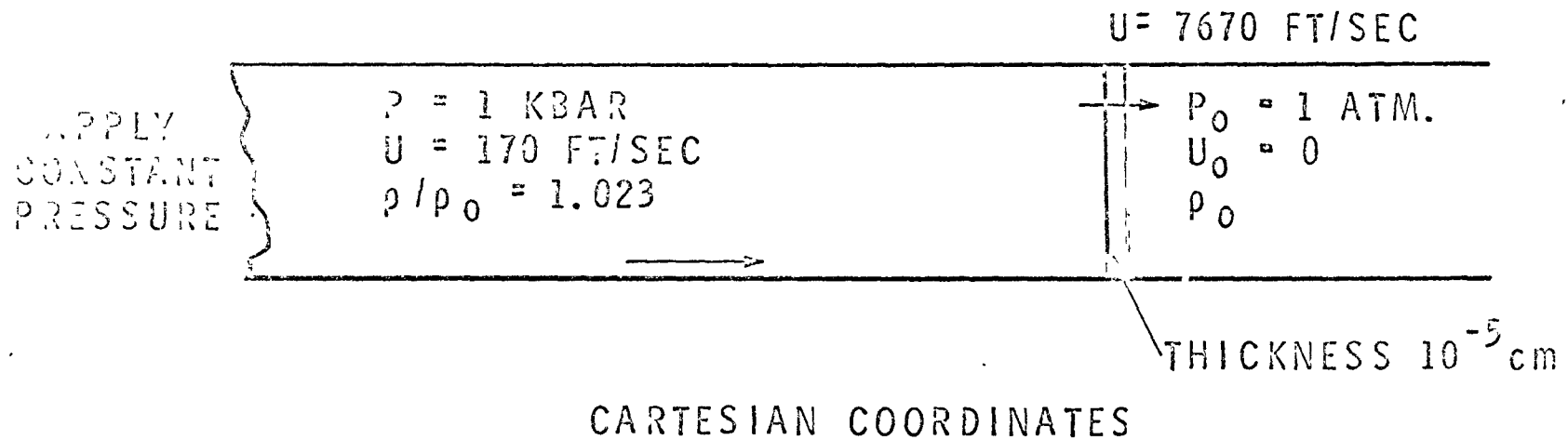
When the shock wave propagates outward in water, there is considerable energy loss through viscous dissipation. The details of energy transmission and loss through a sodium medium needs investigation.

When the slug impacts the cover, there is a rapid transfer of kinetic energy to the cover and upper vessel walls. A more sophisticated approach is needed than is currently included in ASPRIN. In addition, the small reactor core diameters within a large vessel may not generate a coolant slug with the same diameter as the vessel. The present description of the slug effect in ASPRIN may be too conservative and should be scrutinized.

Probably, two dimensional hydrodynamic models with wave action will be too cumbersome requiring extensive computer running times to provide the necessary analytical support for reactor DBA design. ASPRIN, using one dimensional Newtonian models, is adequate to handle most of the blast wave phenomena. The next step would be to develop combinations of one dimensional wave models which will simulate the shock wave and fast occurring phenomena.

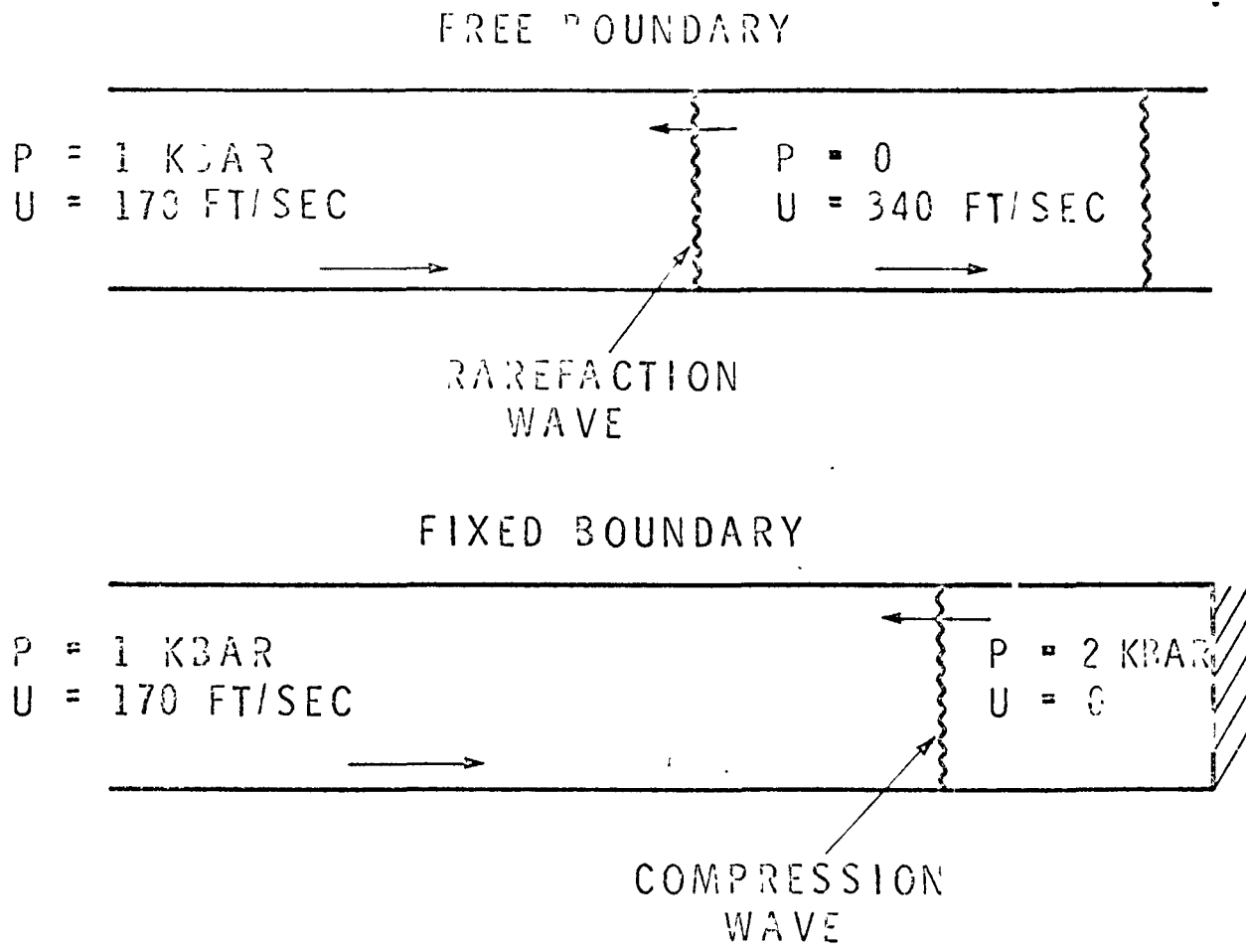
References

- (1) R. H. Cole, "Underwater Explosions," Dover Publication 1965.
- (2) W. R. Wise and J. F. Proctor, Explosion Containment Laws for Nuclear Reactor Vessels, U.S. Naval Ordnance Laboratory, NOLTR-63-140, October 1965.
- (3) W. R. Wise, Jr. et al., "Response of Enrico Fermi Reactor to TNT Simulated Nuclear Accidents," NOLTR 62-207.
- (4) N. J. M. Reese, "A Model Investigation of Explosion Containment in Single Tank Fast Reactors," ANL-7120.
- (5) G. A. V. Drevon et al., "Comparison of Pressure Loading Produced by Contained Explosions in Water and Sodium," ANL-7120.
- (6) J. F. Proctor, "Adequacy of Explosion Response Data in Estimating Reactor Vessel Damage," Nuclear Safety, Vol. 8, No. 6, November-December 1967.
- (7) Response of Enrico Fermi Reactor to TNT. Simulated Nuclear Accidents, pp B-1 to B-3, W. R. Wise, Jr. et al., NOLTR 62-207.
- (8) G. L. Fox, "Fast Breeder Reactor Vessel Analysis," ASME Winter Annual Meeting, November 1969 (ASME 69-WA-NE-23).



$$P - P_0 = \rho_0 C_0 (U - U_0)$$

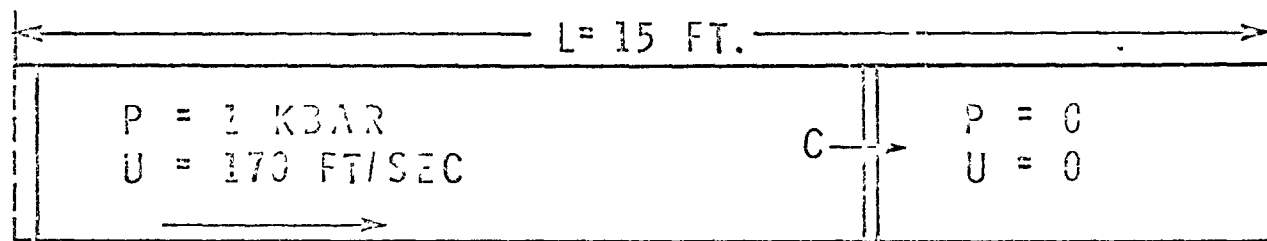
FIGURE XVIII.1 Shock Wave in Sodium 550 °C



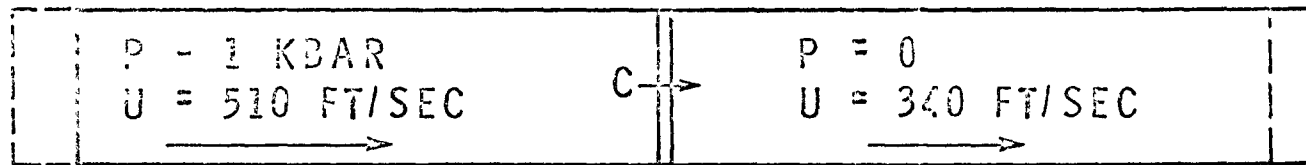
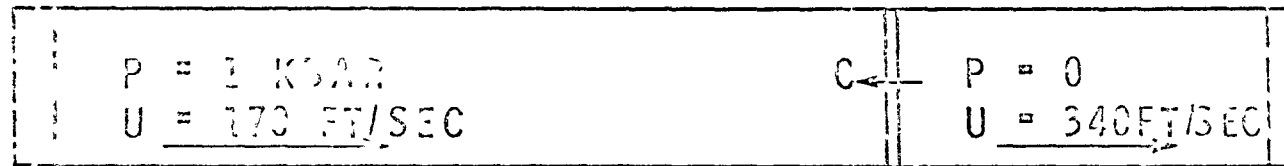
XVIII.21

FIGURE XVIII.2 Interface Conditions

APPLY
CONSTANT
PRESSURE



$C = 7500 \text{ FT/SEC}$



FREE SURFACE

FIGURE XVIII.3 Acceleration of Fluid Column

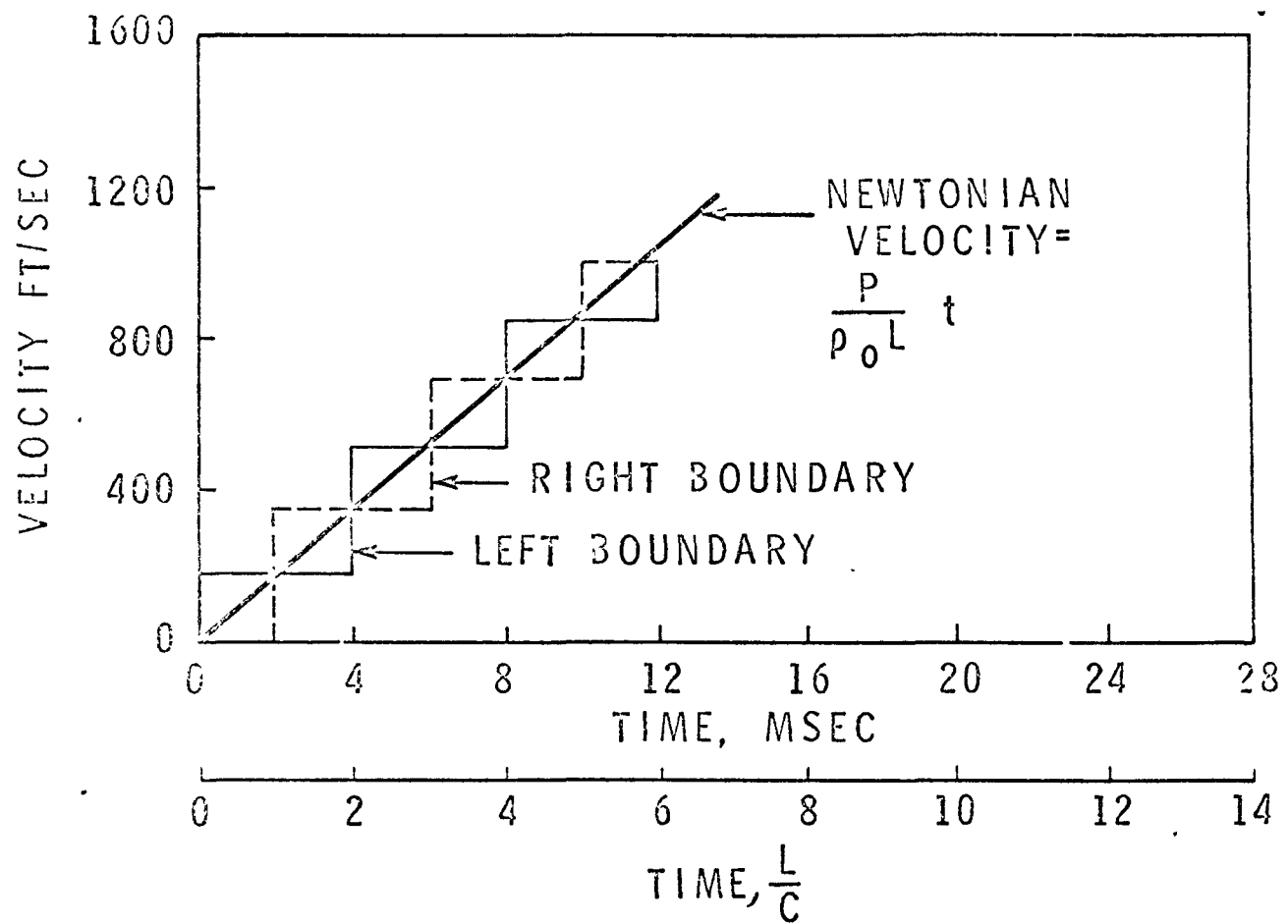
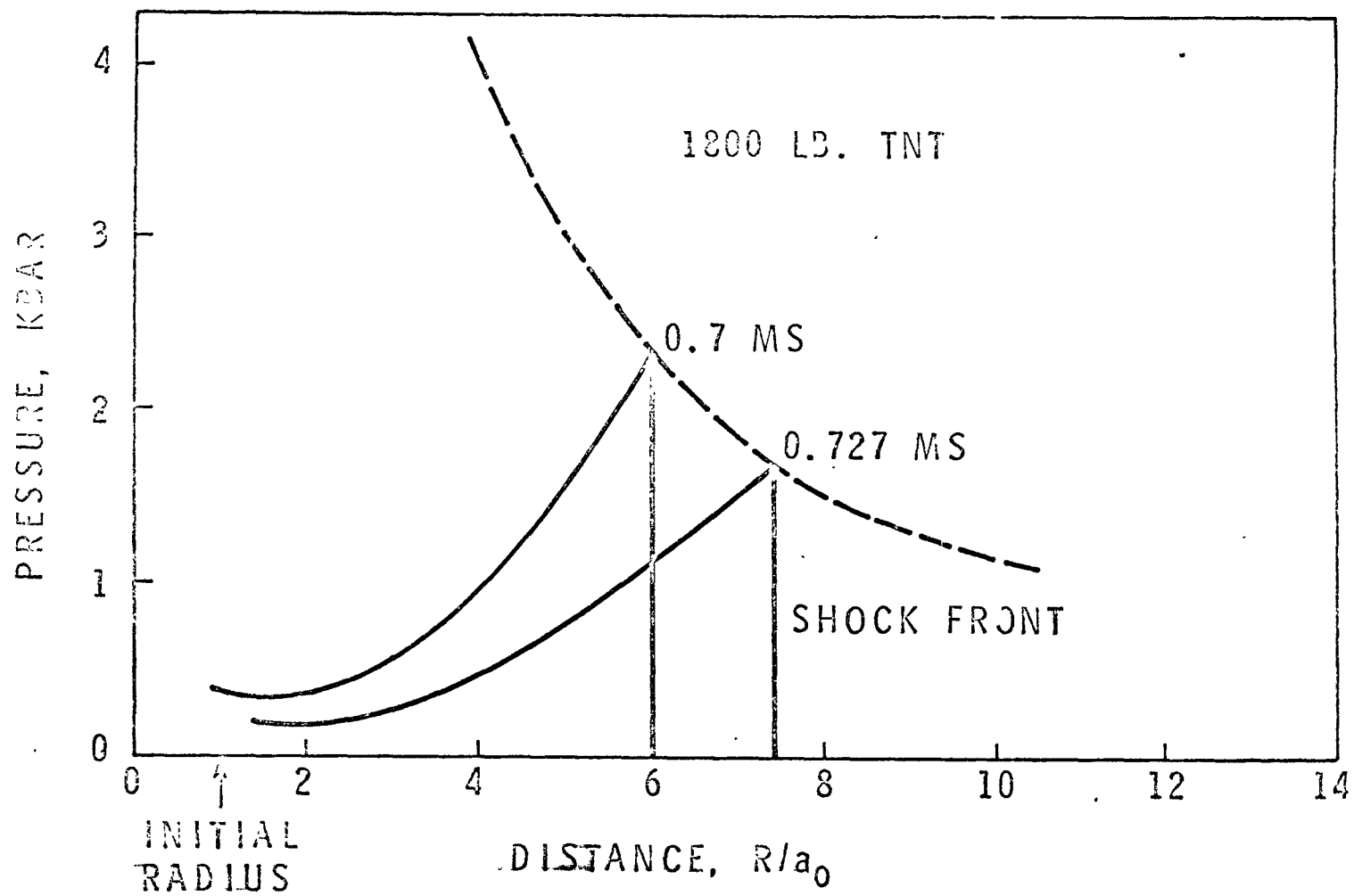


FIGURE XVIII.4 Column Velocity History

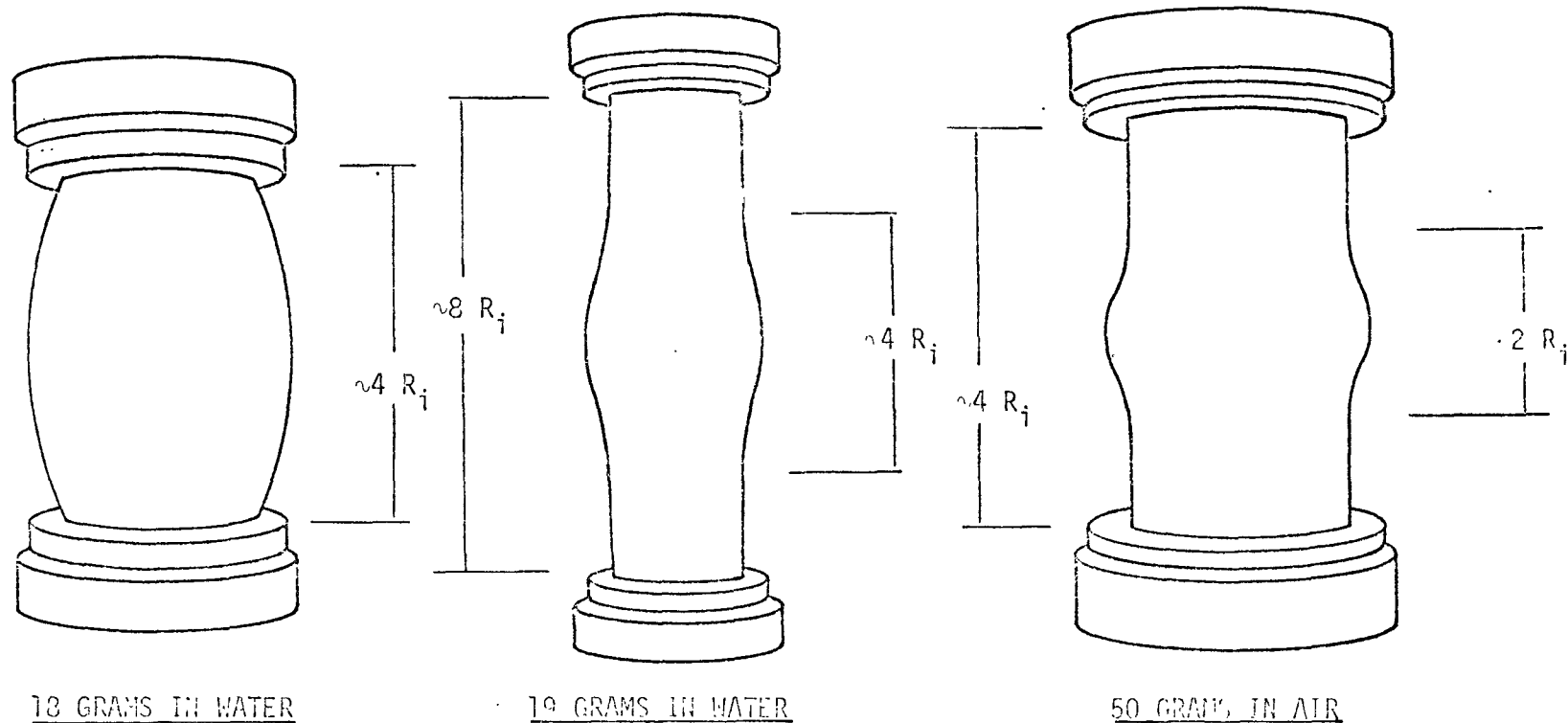


XVIII.24

FIGURE XVIII-5 ~~Pressure Propagation~~ Pressure Propagation from Spherical TNT Charge

R_i WAS INTERNAL RADIUS
PRIOR TO DEFORMATION

ALL CHARGES WERE DETONATED
AT THE CENTROID



VESSELS WERE ORIGINALLY RIGHT-CIRCULAR CYLINDERS, 5" ID, AND 1/8" WALL. INTERNAL LENGTH OF LEFT AND RIGHT VESSELS WAS 10"; THAT OF CENTER VESSEL WAS 20". ALL WERE CENTRIFUGALLY CAST FROM 304 STAINLESS STEEL.

Based on NOLTR 63-140

FIGURE XVIII.6 Localization Factors of Vessels Dilated with Pentolite in Air and Water

$$2 \pi R i \int_t P(t) dt = \frac{W}{g} \pi (R_e^2 - R_i^2) V_0$$

IMPULSE

$$I_f = K W^{1/3} \left(\frac{W}{R} \right)^{1/3} B$$

TNT EQ.

$$\sigma_t = \sigma_y + \left[\frac{\sigma_u (1 + \epsilon_u) - \sigma_y}{\epsilon_u} \right] \epsilon$$

MATERIAL LAW

$$D_h = \frac{W}{2g} V_0^2 = \sigma_t \epsilon \psi_1 (\dot{\epsilon})$$

ENERGY

$$W = \left[\psi_1 \psi_2 \mu \sigma_t (R_e^2 - R_i^2) \right]^{3/4}$$

LAW

FIGURE XVIII.7 Containment Law Derivation

$$W_{MAX} = \left[\frac{1.407 \sigma_u \epsilon_u (1 + \epsilon_u) (3.41 + 0.117 Ri/h_0) (R_e^2 - Ri^2)^{1.85}}{10^5 \omega^{-0.85} (1.47 + 0.0373 Ri/h_0)^{0.15} Ri^{0.15}} \right]^{0.811}$$

W = MAXIMUM WEIGHT OF CONTAINED TNT

σ_u = ULTIMATE STRESS

ϵ_u = ULTIMATE STRAIN

R_e = EXTERNAL RADIUS

R_i = INTERNAL RADIUS

ω = MATERIAL DENSITY

h_0 = WALL THICKNESS

FIGURE XVIII.8 Containment Law

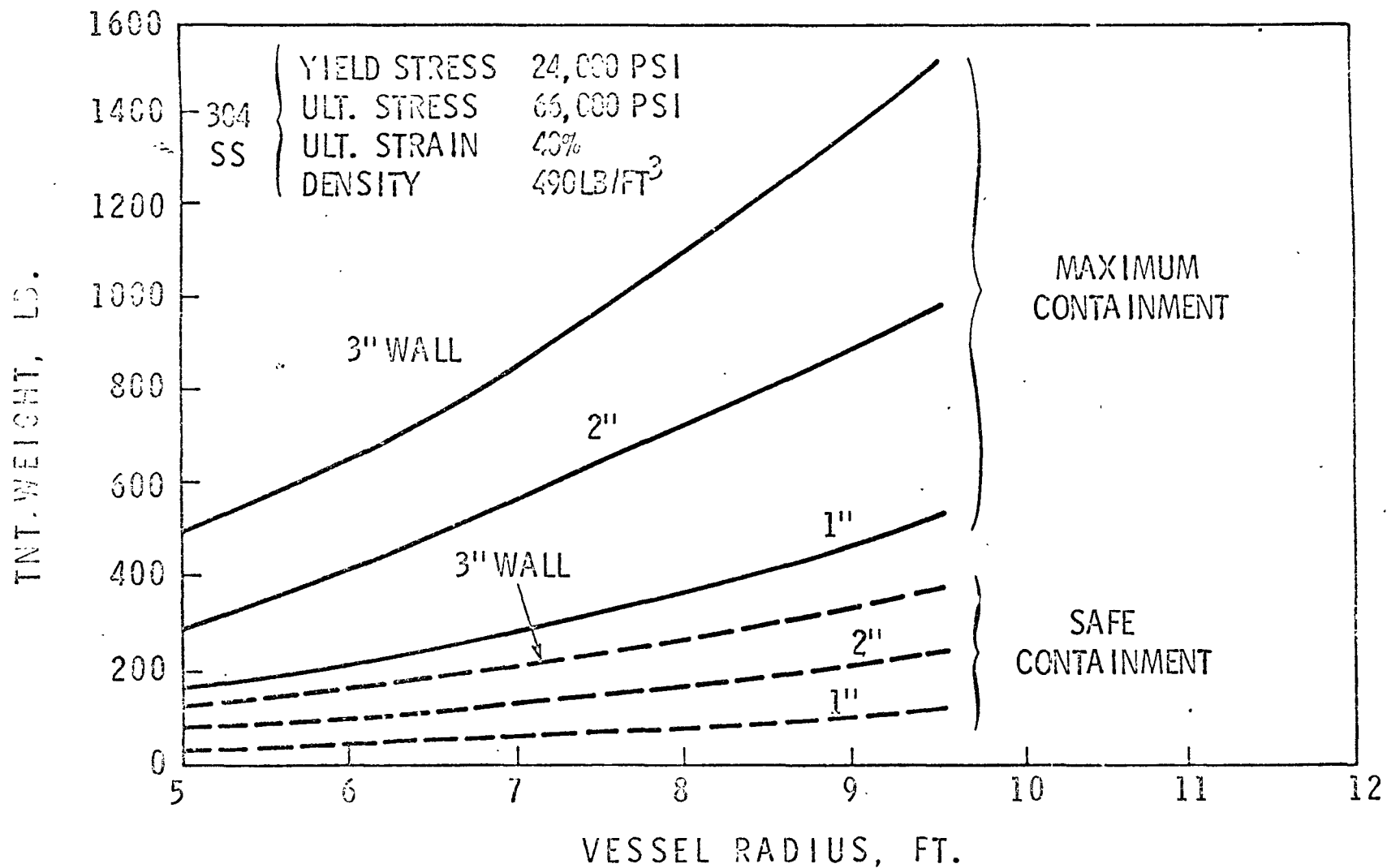
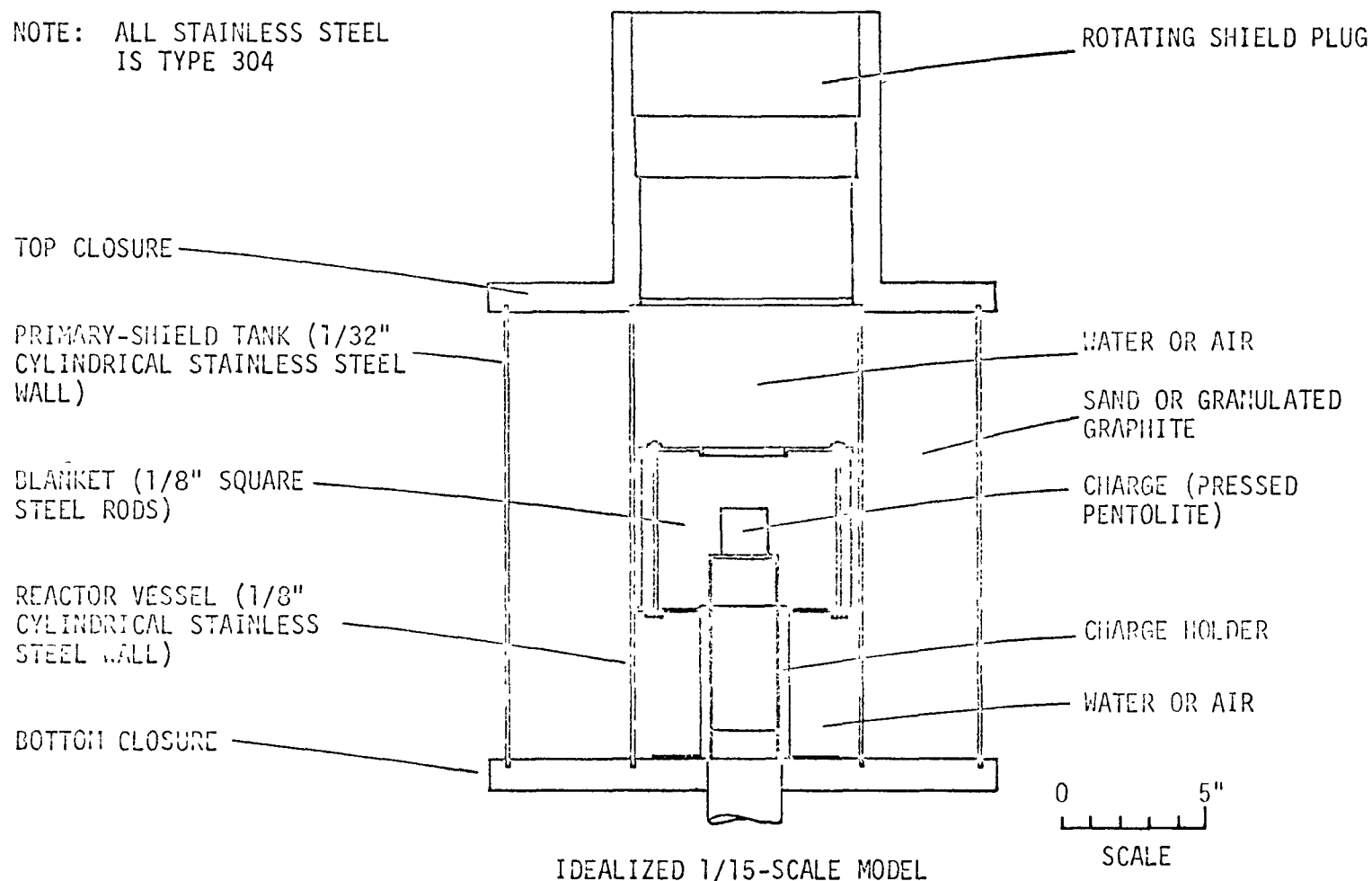


FIGURE XVIII.9 Containment Potential for Cylindrical Vessels

NOLTR 62-207

NOTE: ALL STAINLESS STEEL
IS TYPE 304



XVIII.29

FIGURE XVIII.10 Composite-Vessel Model (Diametral Section)

ENERGY RELEASE	CASE I MAJOR SODIUM LOSS, VESSELS RUPTURE, EVENT CONTAINED IN SECONDARY SHIELD	CASE II NO SODIUM LOSS, VESSELS RUPTURE, EVENT CONTAINED IN SECONDARY SHIELD	CASE III MAJOR SODIUM LOSS, EVENT CONTAINED IN REACTOR VESSEL	CASE IV NO SODIUM LOSS, EVENT CONTAINED IN REACTOR VESSEL
MtA	Ft	Ft	Ft	Ft
1000 lb TNT	~ 20	~ 20	101	102
Case V Magnitude of energy equivalent to 1000 lb TNT, but released at slower rate	< 20	< 20	< 101	< 102
Case VI Lesser accident e.g., 300 lb TNT	~ 6	~ 6	~ 30	~ 30

FERMI PLUG JUMP
(FT)

XVIII.30

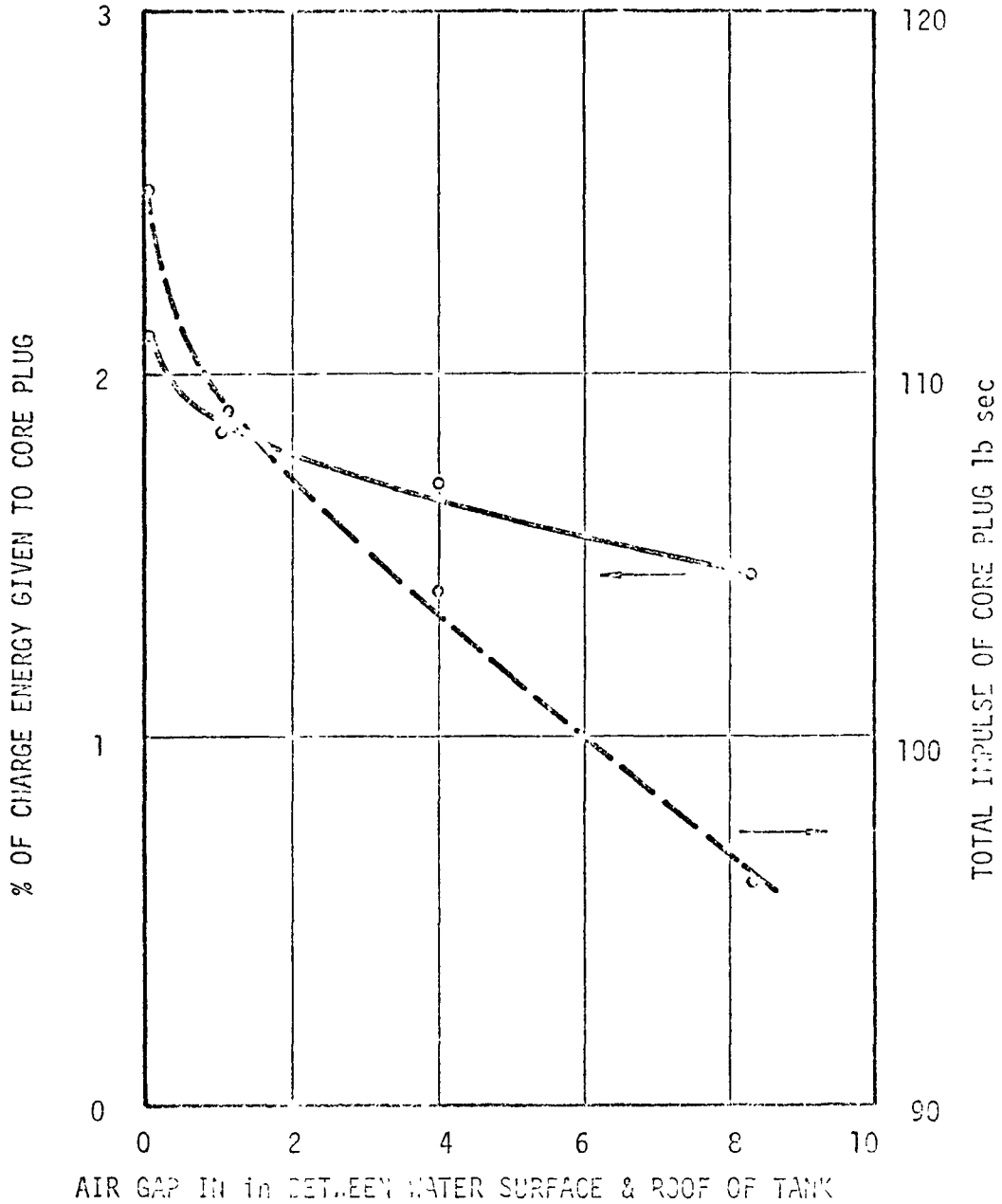
NOTE:

Results given in figure are based on maximum operating temperatures of various reactor components. If, at time of accident, temperatures are lower than maximum, resultant plug jumps for accident cases will be less than those listed in figure.

Based on NOLTR 62-207

FIGURE XVIII.11 Summary of Plug-Jump Accident Cases

MASS OF PLUG = 50 lb
 AREA OF PLUG = 47 in²



Based on Reference 4

FIGURE XVIII.12 Percentage of Charge Energy Imparted to Core Plug; also Total Impulse given to Core Plug versus Air Gap between Roof of Tank and Water Surface

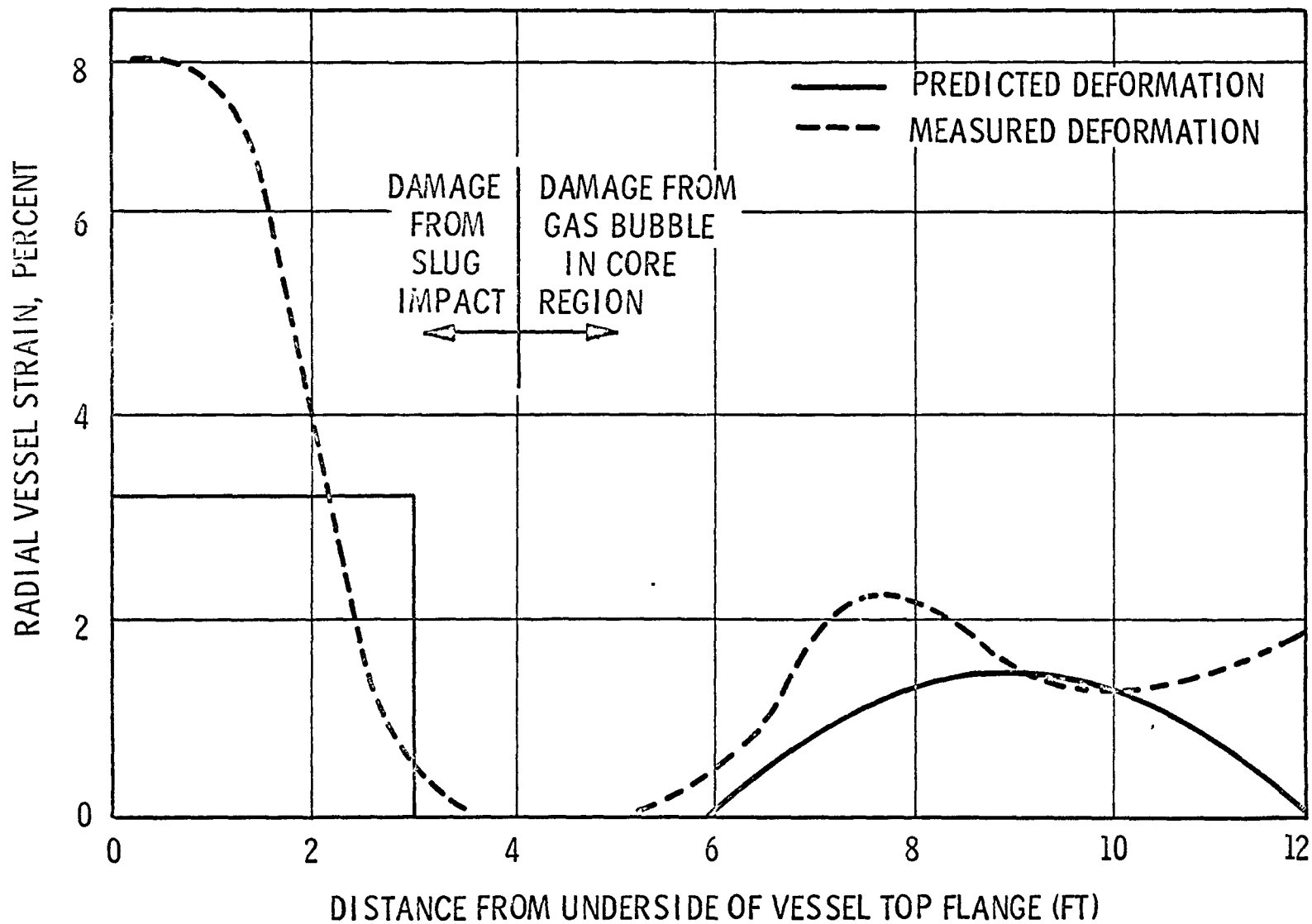


FIGURE XVIII.13 SL-1 Vessel Deformation Pattern

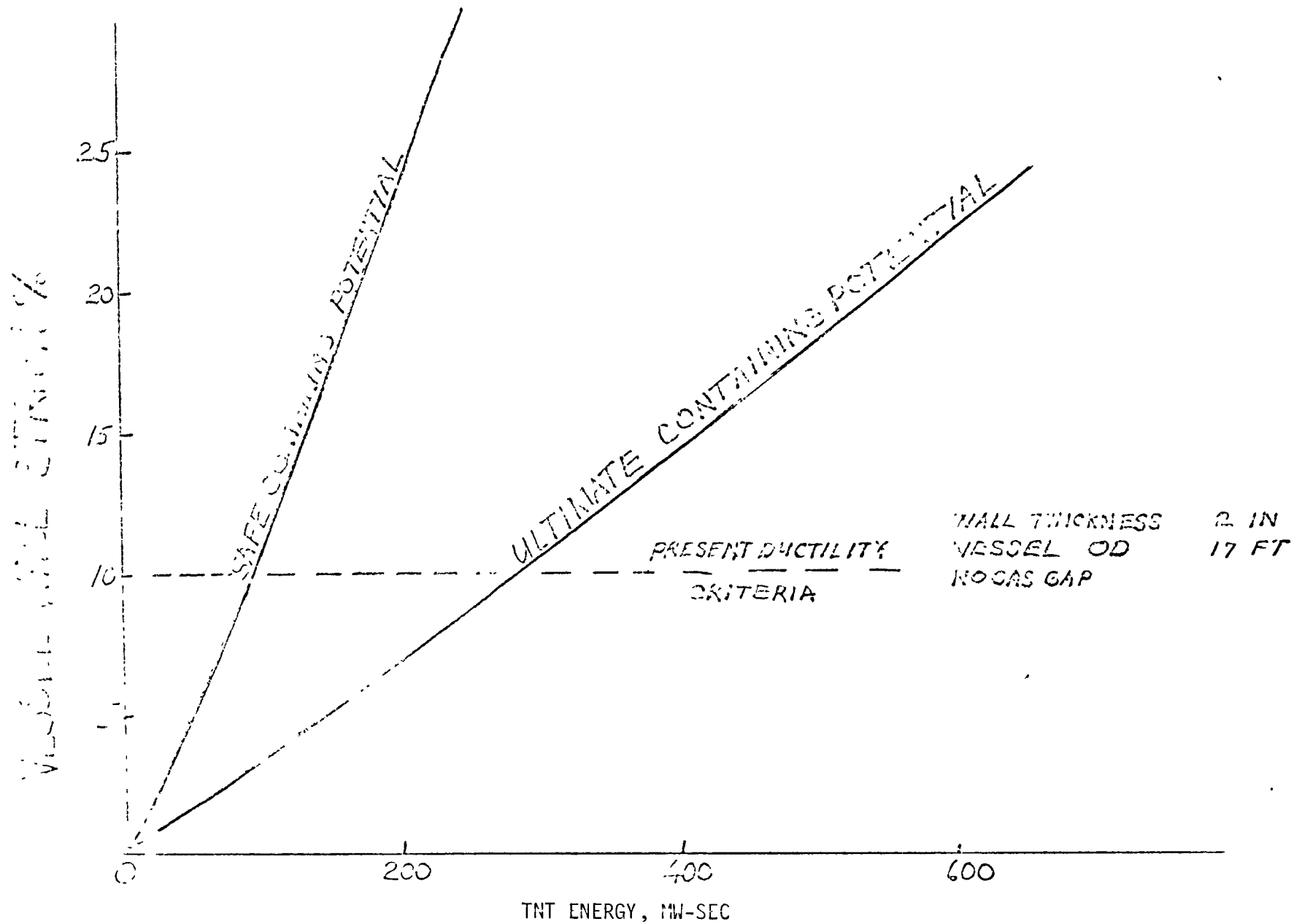


FIGURE XVIII.14 Containing Ability of Reactor Vessels (TNT)

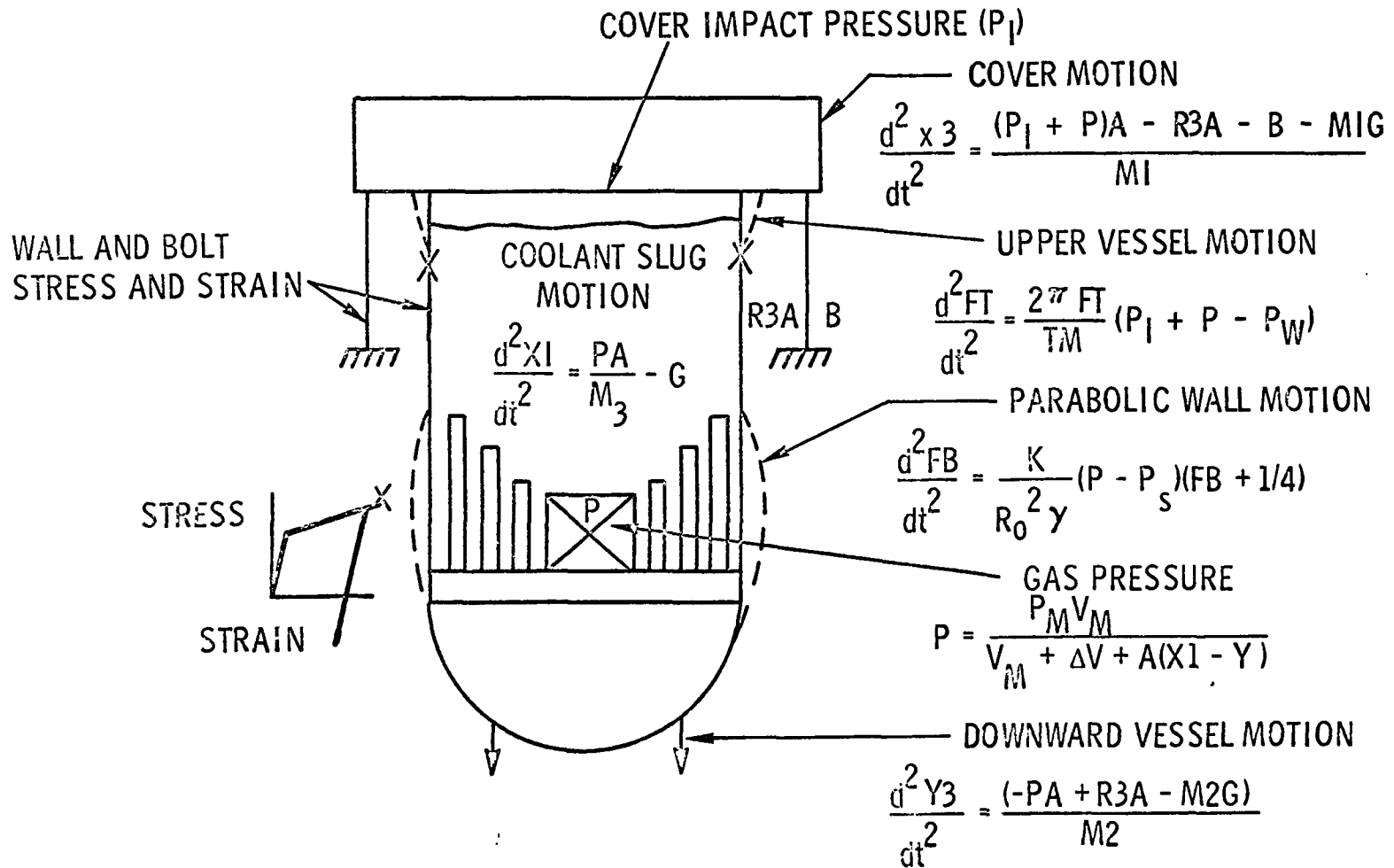


FIGURE XVIII.15 ASPRIN Analytical Model

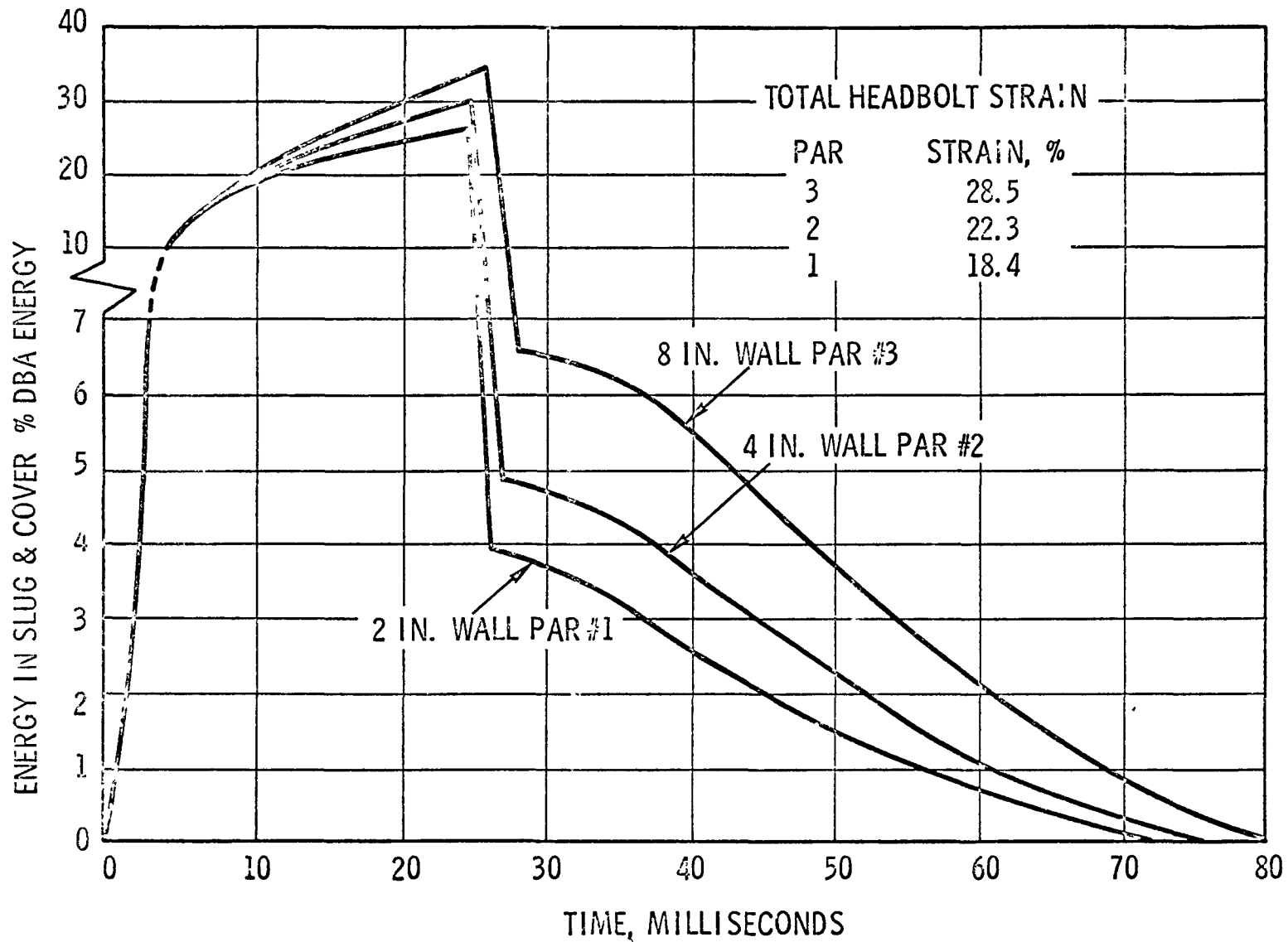


FIGURE XVIII.16 Effect of Vessel Wall Thickness for DBA

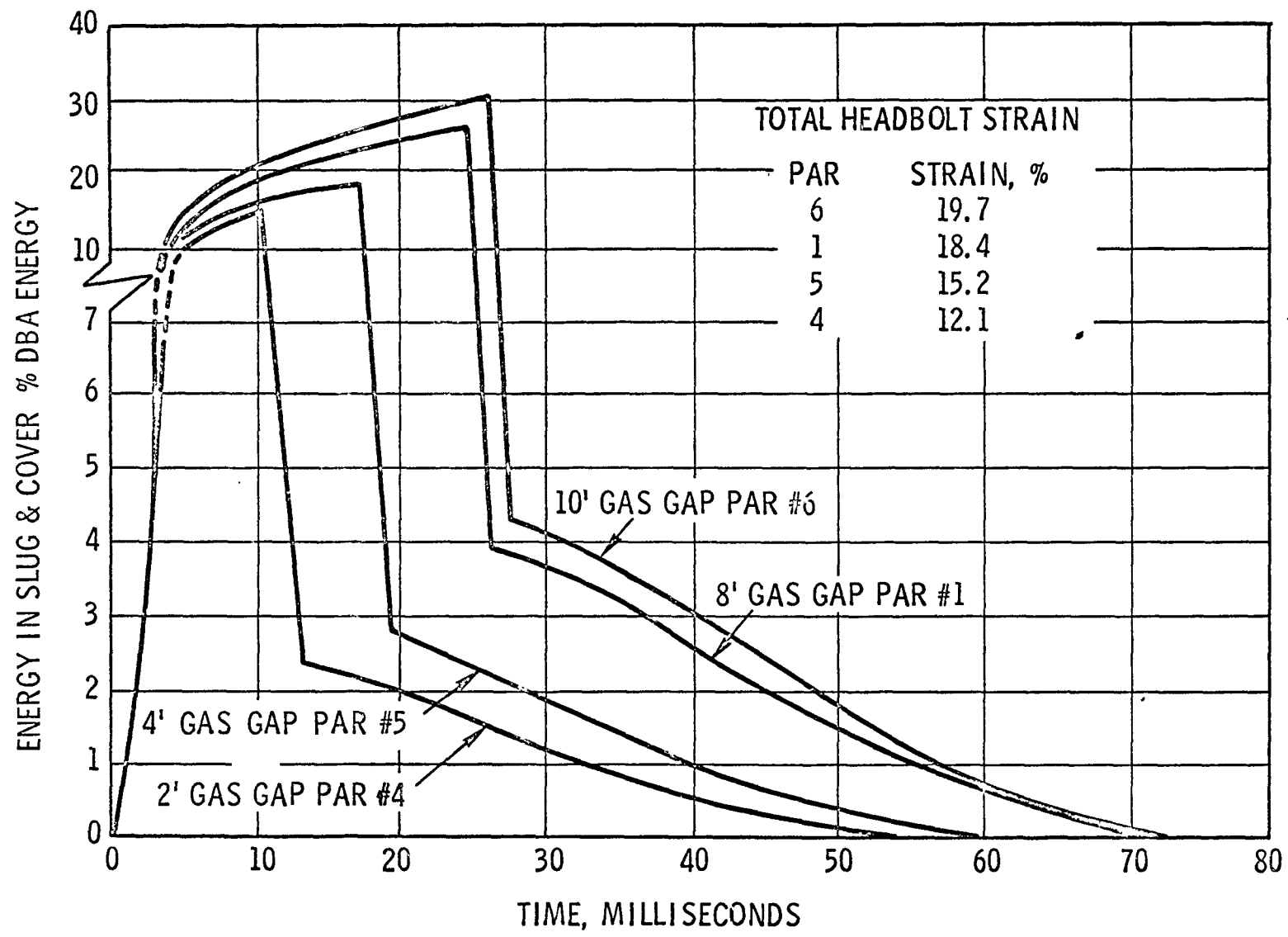


FIGURE XVIII.17 Effect of Variable Gas Gap Between the Core and Cover for DBA

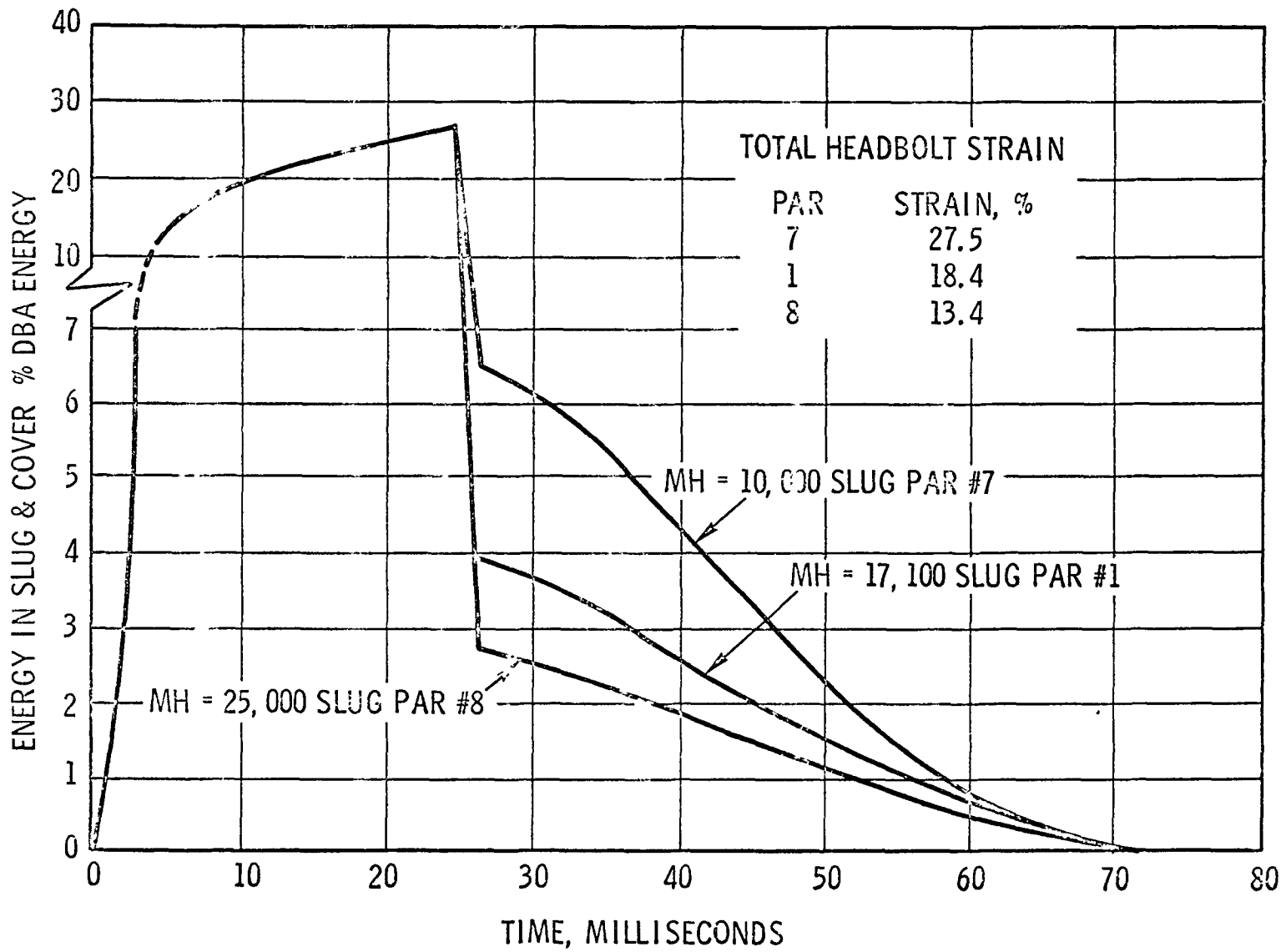


FIGURE XVIII.18 Effect of Cover Mass for DBA

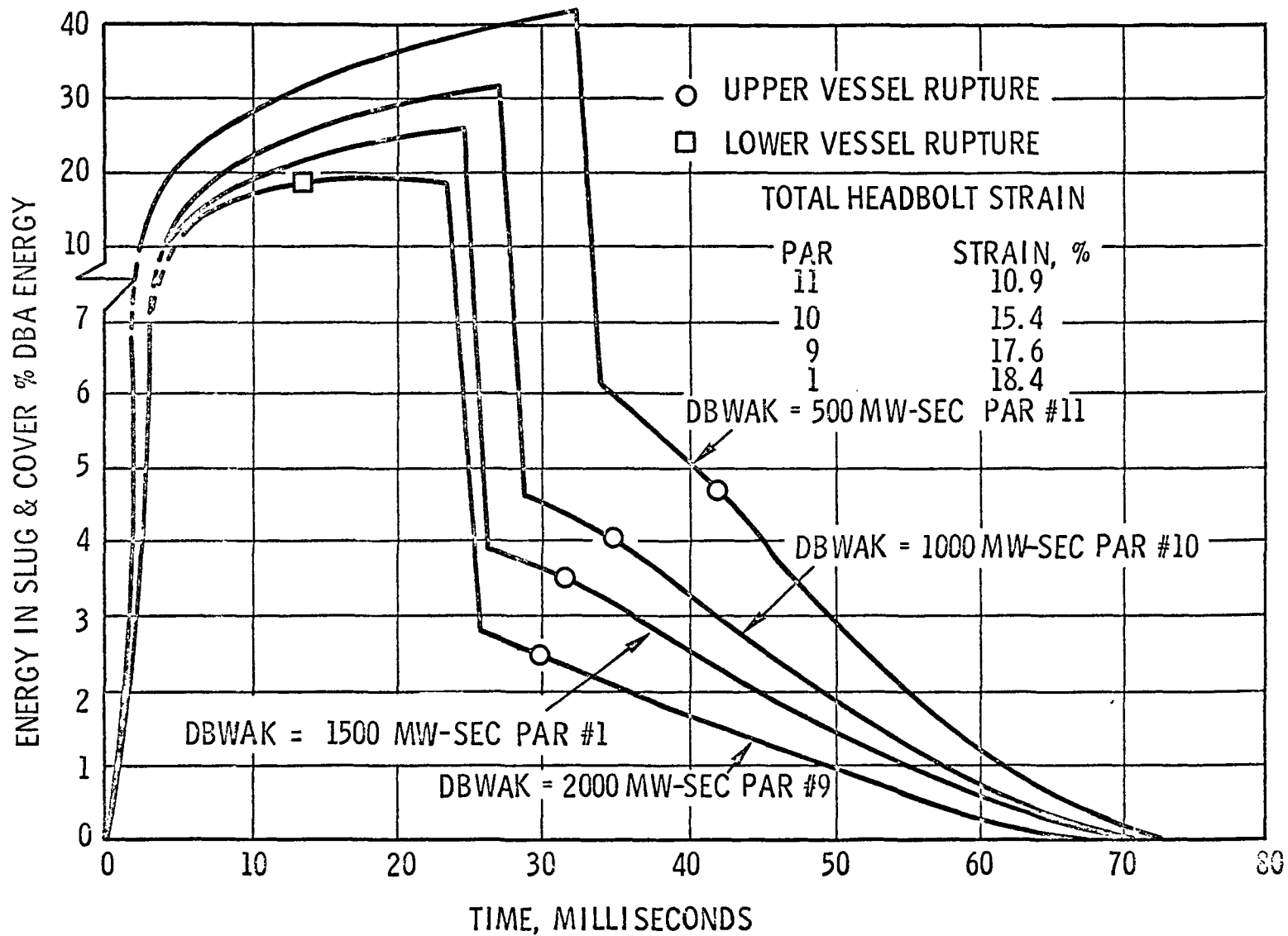


FIGURE XVIII.19 Effect of DBA Energy

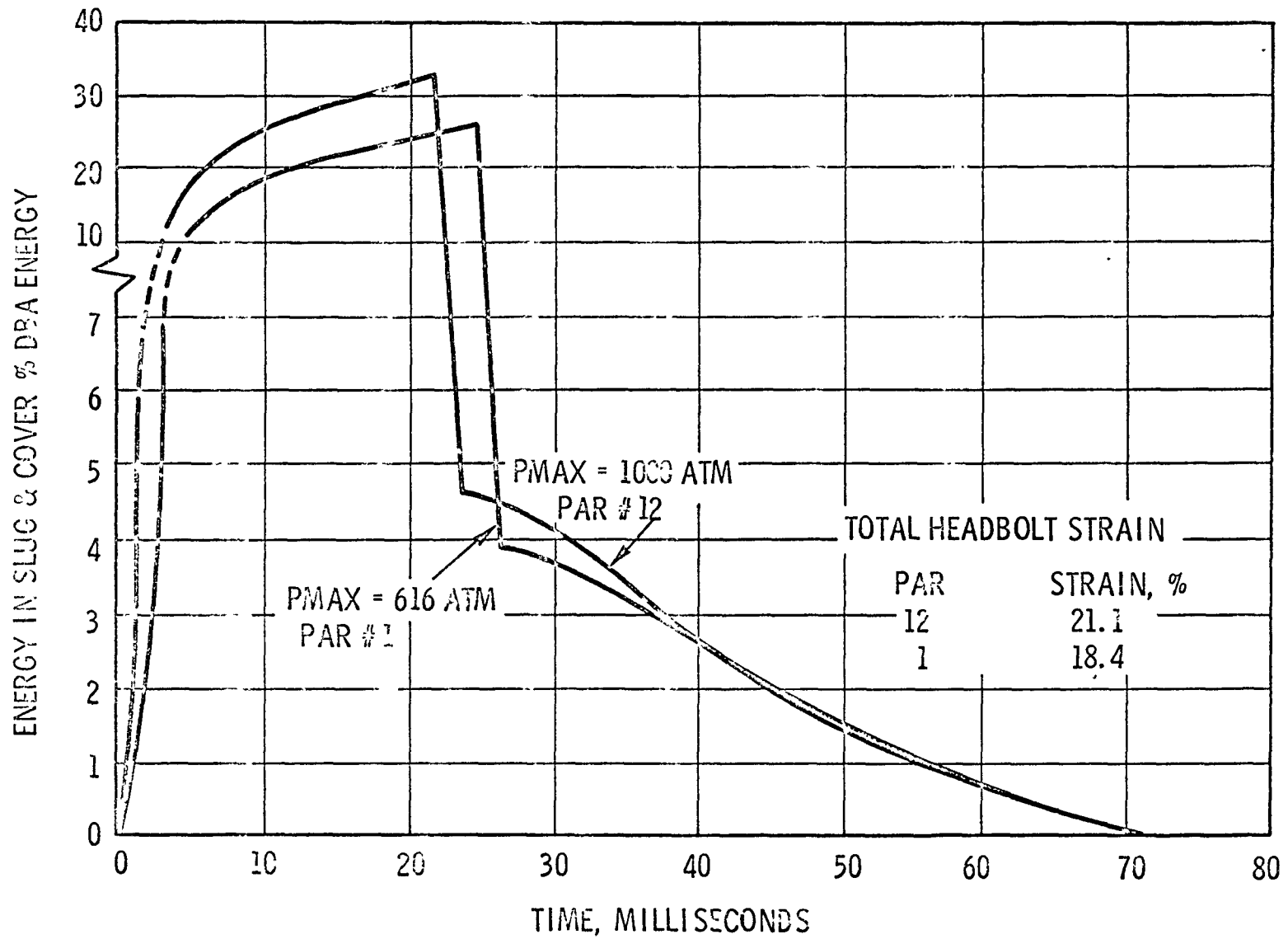
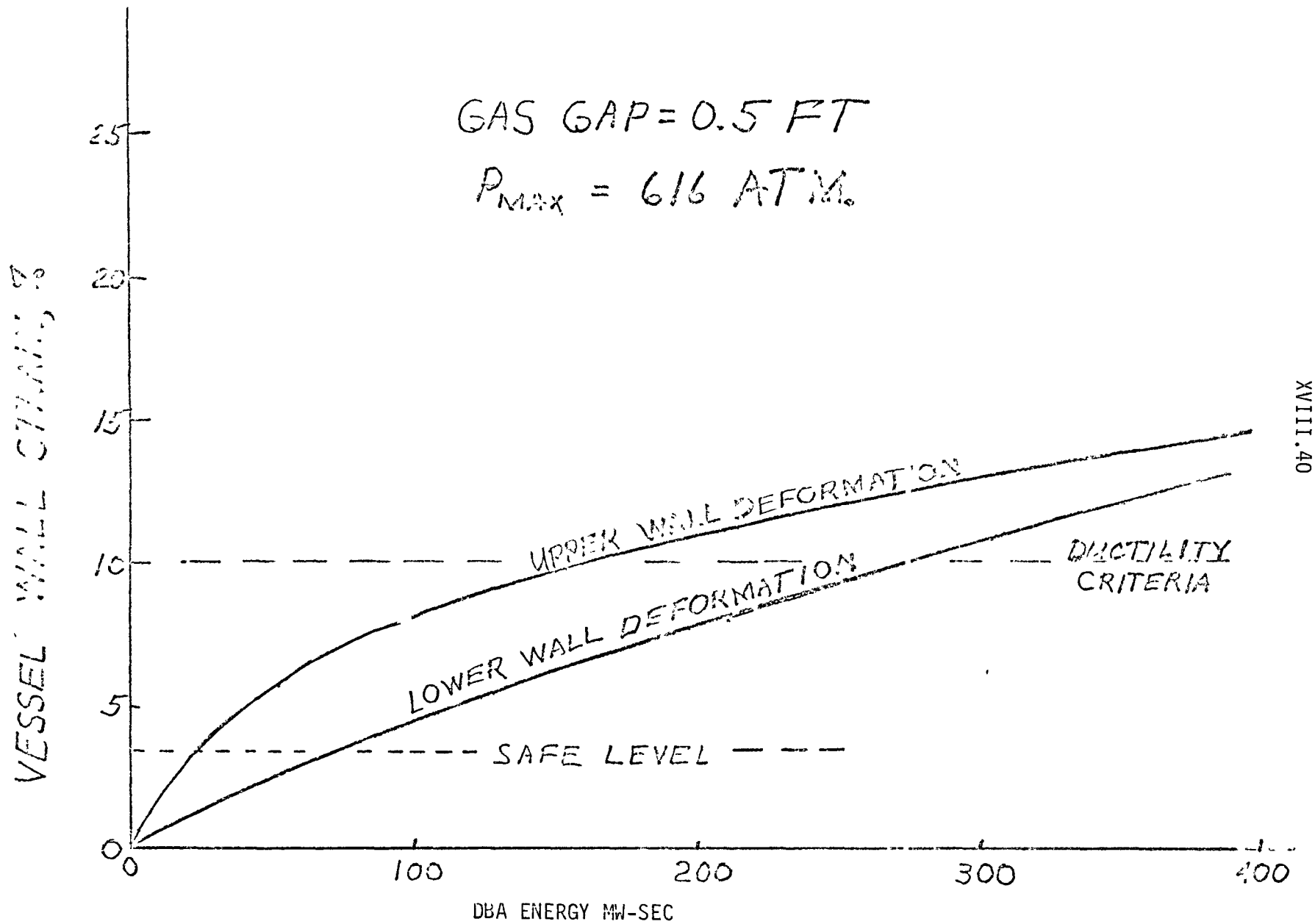


FIGURE XVIII.20 Effect of Maximum gas Bubble Pressure



XVIII.40

FIGURE XVIII.21 Vessel Wall Deformation (Slug Effect)

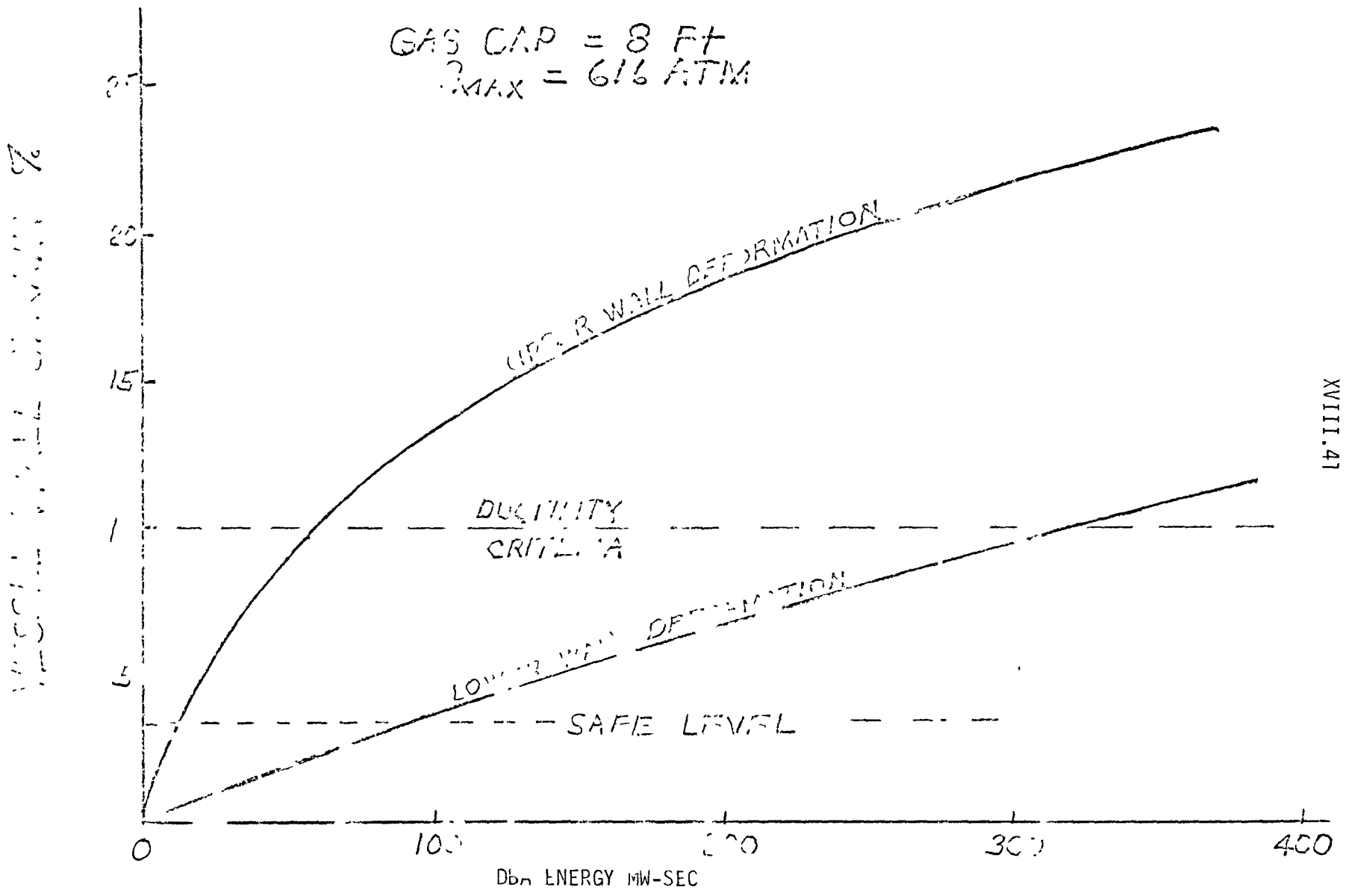


FIGURE XVIII.22 Vessel Wall Deformation (Slug Effect)

XIX. SODIUM FIRES

P. R. Shire

A. Introduction

Safety considerations require the enclosure of high temperature radioactive liquid sodium reactor coolant systems in a containment system. This containment structure must be capable of retaining scattered sodium under the temperature and pressure conditions which may result from an accident or failure of normal plant protection systems. The potential energy contributions of sodium chemical reactions constitute a major consideration for containment vessel requirements.

B. Sodium Reactions

Sodium reacts readily with many inorganic and organic compounds. Two reactions of particular concern for sodium-cooled reactor design are those that occur with oxygen and with water. Both of these reactants may be present in a reactor plant system. The heat of reaction is relatively large and the rate of evolution may be rapid. The goal in any sodium-cooled reactor design is to isolate sodium from oxygen, water, and any other potential reactants.

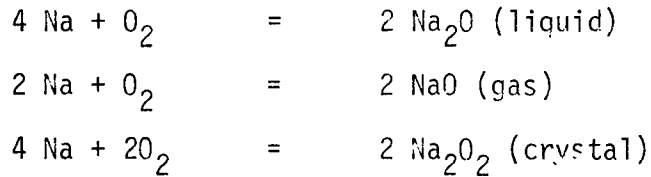
1. Oxidation

With the sodium-oxygen reaction it is necessary to consider the effects of various types of accidents involving the release of sodium into containment spaces. Sodium exposure to the containment atmosphere could occur in three ways: stagnant pool, pressurized spray, or an explosive ejection. Of these, the explosive ejection is potentially the most severe, followed in severity by the spray and the pool fire. This is due to the reaction rate

XIX.2

being proportional to the sodium surface exposure to oxygen, which is much greater for a small particle size and the same total sodium mass.

The most commonly occurring oxides of sodium for the ambient conditions prevailing are - disodium monoxide Na_2O , sodium monoxide NaO , and disodium dioxide Na_2O_2 :



These reactions and pertinent thermochemical calculations will be discussed in more detail in Section D.2.

a. Pool Fire

Pool oxidation is due to the reaction of the upper surface sodium with oxygen in the gas atmosphere. Dense clouds of sodium oxide smoke are generated above a high temperature flame when liquid sodium burns in air. No flame burning has been observed for oxygen concentrations of less than ~5% although oxidation is still present.

With pool oxidation the evolution of heat is slow enough that a significant amount is absorbed on containment surfaces. Pressure peaks occur on the order of 10 minutes to 15 hours, depending on the oxygen concentration and total amounts of sodium and oxygen present.

b. Spray Fire

A high pressure liquid sodium spray expulsion could occur under accident conditions in a sodium coolant system. The sodium-oxygen reaction would take place primarily while the sodium is in flight. Thus, the heat of reaction is

transferred directly to the gas atmosphere with little being lost initially to structures and containment walls. The heat of this reaction is utilized initially to raise the temperature and pressure of the cell or building atmosphere.

Under given initial conditions the sodium-oxygen reaction rate is a function of sodium surface exposure which depends on the mass rate and particle size of the sodium discharge. It is unlikely that a very large discharge rate and a fine particle dispersion could exist simultaneously; however, extensive work needs to be done to put the relationships into quantitative terms.

c. Explosive Ejection Fire

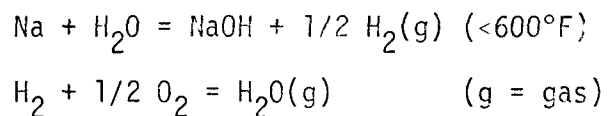
The only effective difference between the explosive ejection and the high pressure spray discharge is one of reaction rate with oxygen. With explosive ejection, optimum conditions are approached for the most severe reaction due to the large mass of finely dispersed sodium. For both explosive ejection and spray fires, the relative size and shape of the contained volume will have a marked effect on the mixing efficiency of sodium and oxygen before the liquid sodium comes to rest on containment surfaces. Perfect, instantaneous mixing is usually assumed for calculation of limiting pressures and temperatures.

2. Reaction with Water

If liquid sodium and liquid water are allowed to contact, as for example: in heat exchanger tube rupture, or sodium action on water of hydration in concrete, a high rate reaction will result in the formation of sodium hydroxide

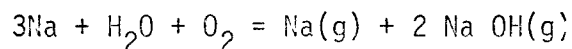
and hydrogen along with released steam and heat. Even when large quantities of the two liquids are mixed, the reaction is not very fast compared to a high explosive detonation. The heat transfer and heat capacity capabilities of both liquids are quite large so that much heat is dissipated to and through them. If the reaction takes place in a confined space, a quasi-static peak gas pressure will result. If oxygen is present (air or inert gas + nominal oxygen), it will react with the hydrogen, producing additional heat.

The reaction takes place in two stages:



In containment spaces water vapor may be present and if a sodium leak should occur, a combination sodium-oxygen-water reaction could result. Calculations for sodium sprayed into air⁽¹⁾ saturated with water vapor show that the adiabatic pressures are less than or equal to those obtained for dry air (Figure XIX.1). A peak pressure of 108 psia is attained when the sodium-oxygen molar ratio is 6:1 and sodium temperature is 800°F; this is ~10% less than the peak pressure for dry air.

The reaction goes according to the following equation if reactants are in stoichiometric ratio:



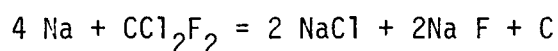
The same products are obtained in the case of sodium and water in 1:1 ratio in a calculation performed by Horton.⁽²⁾ The adiabatic calculation requires perfect spray mixing of both sodium and water with air, releasing

5700 Btu/lb of 800°F sodium. A comparison of adiabatic pressures for sodium-oxygen molar ratio <1.0 (in the range that Horton's calculations are valid) are shown in Figure XIX.2 for three cases: dry air, air saturated with water vapor, and sodium-water molar ratio = 1.00.

3. Other Reactions

Sodium reacts readily with halogen gases but is inert to noble gases. In general, sodium reacts readily with hydrogen- and oxygen-containing gases and hydrogen-containing liquids (i.e., water). Sodium is reactive with some halogen-containing liquids. It has been known to detonate with carbon tetrachloride. Sodium is not highly reactive with most metals but attacks practically all organic compounds.

The reaction of sodium with Freon-12 is of interest because of Freon utilized in containment ventilating and cooling systems. The most probable products are sodium chloride, sodium fluoride and carbon with a calculated energy release of 5600 Btu/lb of Freon-12:



A detailed summary of reactions of sodium is presented in the Liquid Metals Handbook.⁽³⁾

C. Accidents that Generate Sodium Fires in Sodium-Cooled Reactor Containment Systems

1. Pool Fires

It is generally accepted that the great percentage of possible accidents in a sodium coolant system will involve slow leakage of liquid sodium. Even in the case of a double-ended, guillotine pipe rupture, normal operating pressures

are low enough (< 100 psi) so that liquid sodium would probably issue in a solid stream. Since sodium operating temperatures are much lower than boiling (1617°F b.p. at atmospheric pressure), no flashing of sodium will occur. With a large pipe or equipment break, it is possible that a containment cell could fill to a depth of 1-3 feet with subsequent oxidation at the pool surface. If in a closed cell, oxidation will be terminated when either the sodium or oxygen is depleted.

A leak or pipe break may be nuclear in origin. A hypothetical and extremely unlikely nuclear accident occurring in the reactor may result in breakage of piping and/or equipment; a specific case is reactor vessel rupture or head lift. In this case, sodium coolant may contain heat from nuclear energy and decay heat from fission products as well as from sodium being radioactive itself. All of these conditions add thermal energy to the fire potential.

2. Spray Fires

The origin of accidents that may generate spray fires are similar to those that are responsible for pool fires. A possible way in which spray can be formed is for a high velocity discharge to impinge on piping or equipment, thereby breaking up into a liquid droplet spray.

The work of Krolikowski⁽⁴⁾ with small circular spray orifices suggests that high velocity or its requisite, high pressure combined with a small discharge opening may produce a fine particle dispersion. A possible way for this to occur as an accident is for a long longitudinal crack to develop in a straight pipe length; particle sizes range on the order of the crack width.⁽⁴⁾ By analogy with the orifice sizes investigated, a crack 15 ft long x .020" wide

and with 300 psi driving pressure (nuclear accident condition) may discharge ~ 200 lb/sec. If it is assumed that pipe lagging does not interfere with the discharge rate, a highly reactive spray could be produced.

In the work of Krolikowski,⁽⁴⁾ parameters were varied over a narrow range. The case posed here requires a reduction of oxygen concentration from 21% to 2% (in primary heat transport system cells) and velocity from 350 fps to 140 fps, both parameters are below the range for the work reported. However, the best estimate indicates an initial pressure rise rate of ~ 30 psi/sec in the 40,000 cu ft heat transport cell filled with inert gas ($\sim 2\%$ oxygen) for a fine particle discharge (.020" diameter). Since, in this case, oxygen is assumed to be completely burned, the average pressure rise rate can be estimated at one-half the initial rate or 15 psi/sec. The maximum room pressure, 33 psig, may be reached in ~ 2 seconds, assuming that adiabatic conditions prevail. Continued expulsion of sodium would reduce the gas temperature to the average sodium temperature in the limit.

Rupture of the reactor vessel may result in a large mass sodium spray expulsion to the reactor cavity following a nuclear accident. Another possible result of a nuclear accident is reactor head lift with large mass expulsion of sodium spray in the region above the vessel. If this region is enclosed (with a "machinery dome"), the result is reaction with 2% oxygen; if not enclosed, this expulsion would be directly to air in the outer containment vessel.

3. Explosive Ejection Fires

Extreme impact or very high pressures are required to instigate an explosive expulsion of sodium spray. Pressures of 1000-1500 psi have been utilized experimentally by Krolikowski⁽⁴⁾ as driving force for explosive-like expulsions, but such pressures are unknown in sodium coolant systems.

It may be possible to attain the impact force needed for explosive ejection with the fuel handling machine since it is mobile; however, the sodium cooled machine would contain a relatively small amount of sodium limiting the adiabatic pressure to a nominal value in the large air volume of the main containment sphere.

D. Theory of Sodium Explosive Ejection and Spray Fires

In 1958, Humphreys⁽⁵⁾ reported the results of chemical equilibrium calculations for the sodium-oxygen reaction, assuming instantaneous reaction with perfect mixing (spray fire). The calculated pressure was based on an adiabatic temperature rise. On the assumption of complete reaction, the maximum pressure and temperature for combustion in air was 138 psig and 6510°F at a sodium-oxygen molar ratio of 4:1; air was initially at room temperature and liquid sodium at 750°F. This effort was performed in support of experimental work and the hazard analysis for EBR-II (see Figure XIX.1).

In 1959, Garelis and Nims⁽⁶⁾ reported results of their calculated maximum theoretical pressures and temperatures for the sodium spray fire in air with sodium at 800°F. The maximum pressure was 129 psig at a Na/O₂ molar ratio of 7:1, while the maximum temperature of 3550°F occurred at a molar ratio of 5:1. This work was done in support of the Fermi reactor hazard analysis. Garelis used thermochemical data from several sources to calculate the temperature corresponding to internal energy balance of the system at equilibrium.

In 1965, Baker and Tevebaugh⁽⁷⁾ reported results of their calculations for sodium spray fires with 800°F sodium in support of FARET safety analysis. Initial condition of the air was room temperature at 12.2 psia corresponding

to the atmospheric pressure at NRTS. Again, a peak pressure of 82 psig occurred at a sodium-oxygen molar ratio of 7:1 and peak temperature of 3540°F occurred at a 5:1 molar ratio. The lower peak pressure resulted from the lower initial pressure 12.2 psia. In comparison with Humphrey's calculation, it was pointed out that the maximum temperature is limited by the thermodynamics of the system. At a 4:1 molar ratio, some Na_2O decomposes to NaO and uncombined oxygen.

In 1966, Leibowitz^(1,8) reported results for the sodium-oxygen reaction comparing favorable with those of Garelis and Nims⁽⁶⁾ (see Figure XIX.1) and also Baker and Tevebaugh⁽⁷⁾ (see Figure XIX.3). For room temperature air at 14.7 psia Leibowitz obtained a peak pressure of 119 psig at a 7:1 sodium-oxygen molar ratio and a peak temperature of 3610°F at a 5:1 molar ratio. The method of calculation to determine the equilibrium temperature was similar to two previous investigations^(6,7) with the addition of the method of free energy minimization^(9,10) to determine the equilibrium concentrations of products at the final temperature.

1. Variation of Equilibrium Pressure and Temperature.

a. Dependence on Sodium-Oxygen Ratio

This ratio is the molar ratio obtained by dividing the moles of liquid sodium by the moles of oxygen initially present as reactants. A mole of sodium is equivalent to 23 grams and a mole of oxygen occupies 22.4 liters at 0°C and one atmosphere pressure. Converted to engineering units, a 1:1 molar ratio is equivalent to 12.27 lb of sodium per 1000 cu ft of air at 80°F. This equivalence varies with the air temperature and the volume percent oxygen.

XIX.10

When plotted (see Figure XIX.1) vs molar ratio, the equilibrium or final pressure and temperature of the sodium-oxygen reaction characteristically increase to a peak value and then fall off asymptotically with excess sodium to the temperature of the liquid sodium and the air pressure corresponding to this temperature. At zero molar ratio, corresponding to no sodium present, the pressure and temperature will be that of the ambient gas condition. The peak temperatures and pressures do not necessarily occur at the same molar ratio due to the complex variation of gaseous product concentrations (see Figure XIX.4).

b. Dependence on Initial Temperature of Sodium

The equilibrium temperature and pressure is not strongly dependent on the initial temperature of sodium. The heat capacity of the liquid sodium above room temperature is a measure of the additional reaction energy to be attained. For room temperature air, this amounts to 5-10% of the total energy when compared with the heat of formation of the oxide. The variation in peak pressure at a 7:1 sodium-oxygen molar ratio is shown in Figure XIX.5; the increase in pressure with sodium temperature is <2% per 100°F.

c. Dependence on Initial Gas Temperature

There is a marked decrease in peak pressure for an increase in initial air temperature (see Figure XIX.6). For 80°F air and 1200°F sodium, the peak is 127 psig, while for an initial 500°F air, the peak is 70 psig. Since the initial pressure and the final temperature remain approximately constant (one atmosphere and 3150°F), the perfect gas law is a good approximation. Final pressure is inversely proportional to initial temperature.

d. Dependence on Initial Gas Pressure

If peak total pressure is plotted vs initial gas pressure, as is the case in Figure XIX.7 for 80°F air and 1200°F sodium, then a linear relationship is obtained. If the straight line is extrapolated downward to zero initial absolute air pressure (perfect vacuum), a final total pressure of - 13.7 psig (1 psia) is attained corresponding to the vapor pressure of sodium at 1200°F. Again, the relationship may be explained on the basis of the perfect gas law since the final equilibrium temperature remains approximately constant ~3150°F.

e. Dependence on Initial Oxygen Concentration

When the oxygen concentration in air (21 volume %) is reduced, the equilibrium pressures and temperatures are reduced. However, there is only a one-third reduction in pressure when oxygen is reduced by one-half (10 volume %). The relationship is shown in Figures XIX.8 and XIX.9. The molar ratio at which the peak pressure occurs varies with oxygen concentration: for air the peak occurs at a 7:1 molar ratio, at 10% oxygen the peak occurs at 5:1 ratio, and the peak occurs at 4:1 ratio for less than ~5% oxygen.

f. Dependence on Mixing Efficiency

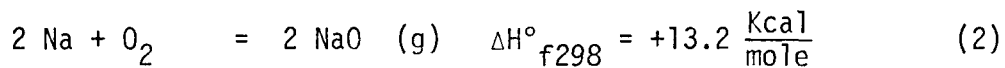
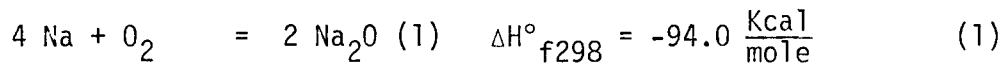
Under actual accident conditions, less than perfect mixing of expelled sodium spray with the gas atmosphere may be expected.

Figure XIX.10 shows the results of a parametric study on variation of mixing efficiency, 100%, 50%, and 10% for 1050°F liquid sodium sprayed into air at 80°F. For this study it was assumed that the chemical reaction occurred

within a limited part of the total volume as illustrated in Figure XIX.11. This figure shows results for mixing efficiencies in the specific case of 2.7 million cu ft (main containment sphere) with adiabatic pressure plotted vs quantity of sodium spray reacting.

2. Reaction Products Type and Final State

The stoichiometric reaction equations of Section B.1 are recalled:

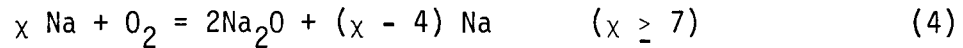


Equation (3) for the production of sodium dioxide is not important for sodium-oxygen molar ratios greater than 2:1 nor for final equilibrium temperatures exceeding 1700°F. For reaction in air, the production of Na_2O_2 will be limited to sodium-oxygen molar ratios of less than 1/2, since final temperatures exceed 1700°F when $\text{Na}/\text{O}_2 > 1/2$. The final temperatures attained in 2% oxygen are <1700°F so that production of Na_2O_2 is possible, but only for molar ratios $\text{Na}/\text{O}_2 \leq 2$, that is ≤ 2.25 lb per 1000 cu ft of gas. For molar ratios > 2 the sodium dioxide would be reduced by excess sodium to disodium monoxide Na_2O . Both Na_2O_2 and Na_2O are condensed at these temperatures, solid and liquid, respectively, so they are not contributing to the final total pressure.

For reaction in air the production of the gas sodium monoxide (NaO), Equation (2), peaks out at a sodium-oxygen molar ratio of 4:1, but the error

in omitting its partial pressure from the total is only a few percent. For low oxygen concentrations (<5%), the production of NaO is negligible due to the low temperature.

Product concentrations of Na₂O and NaO as well as excess oxygen and sodium are plotted vs initial sodium-oxygen molar ratio in Figure XIX.12. From this data it may be noted that the stoichiometric equation (1) is not a good representation for combustion in air. The differences are due to the existence of NaO and significant quantities of uncombined sodium and oxygen remaining as products. After passing the 7:1 molar ratio point, the relationship becomes less complex since Na₂O has reached a constant value of two moles, oxygen is completely consumed and NaO is negligible; therefore:



The dimer of sodium, Na₂ (gas), is not important at the temperature and pressure conditions existing at equilibrium. The fraction of Na₂ has been computed at <1% of the monomer, Na₁ (gas), for the reaction of 1200°F sodium in air.

3. Adiabatic Equilibrium Sodium-Oxygen Reaction Calculation Method at Constant Volume

Nomenclature

x_i	= No. of moles of the i th species.
$F(x_i)$	= Total free energy function of the system, dimensionless.
\bar{x}	= Total product moles of gaseous species.
m	= Total number of gaseous product species.
n	= Total number of condensed product species.

$k = m + n$	= Total number of product species.
w	= Total number of elements.
A_{ij}	= Number of atoms of the j th element in the i th species.
B_j	= Total number of atoms of the j th element.
R_c	= Gas constant, $1.987 \frac{\text{cal}}{\text{mole-}^\circ\text{K}}$
R_l	= Gas constant, $0.08206 \frac{\text{liter-atm}}{\text{mole-}^\circ\text{K}}$
T	= Final system temperature $^\circ\text{K}$.
P	= Pressure, standard absolute atmospheres.
V	= Volume of the system at initial conditions, liters.
$\frac{F^\circ - H^\circ_{298}}{T}$	= Free energy function $\frac{\text{cal}}{\text{mole-}^\circ\text{K}}$
ΔH°_{f298}	= Standard enthalpy of formation at 298°K $\frac{\text{K cal}}{\text{mole}}$
$E(x_j)$	= Total energy function of the system K cal .
$H^\circ_T - H^\circ_{298}$	= enthalpy difference between T and 298°K , K cal/mole .
T'_j	= Initial temperature of the j th reactant $^\circ\text{K}$.

Superscripts

c = condensed species

g = gaseous species

o = species in the standard state

Subscripts

f = heat of formation

T = ref. temperature

The calculation of the adiabatic equilibrium temperature is carried out in two steps:

- (1) Determine the equilibrium composition of the reaction mixture as a function of temperature, given several trial temperatures.
- (2) Determine the equilibrium temperature of the mixture from energy balance, utilizing the data from Step (1), Table XIX.1.

From thermodynamic considerations, the condition for chemical composition equilibrium is attained when the total free energy of the system is a minimum at a given temperature. Step (1) is realized by forming a table of sets of equilibrium concentrations as a function of temperature. Using the defining equations (5) and (7) calculate the total free energy of the system as a function of temperature by equation (8) assuming a constant volume process. This is subject to the chemical mass balance constraint equation (6).

To implement the NAFIRE⁽¹¹⁾ computer code, a feasible solution is determined for the mole fractions x_j in the chemical mass balance equation. As an example, this input data is shown in Table XIX.2 for the sodium-oxygen reaction with a 4:1 molar ratio in air. Any number (≤ 40) of product species may be suggested. Thermochemical data for the NAFIRE code is taken from the JANAF Tables.⁽¹²⁾

Given sets of $\{ x_j \}$, the equilibrium concentrations from Step (1), an energy summation is made on the heat required to raise the reaction products to temperature T , this will be equal to the chemical heat of reaction plus the enthalpy of the reactants, all referred to the reference temperature T_0 .

EQUATIONS FOR EQUILIBRIUM SODIUM-OXYGEN REACTION

STEP (1) COMPOSITION BY FREE ENERGY MINIMIZATION

$$\bar{X} = \sum_{i=1}^m X_i^g \quad (5)$$

$$\sum_{i=1}^k A_{ij} X_i = B_j, \quad j = 1, w \text{ AND } X_i \geq 0 \quad (6)$$

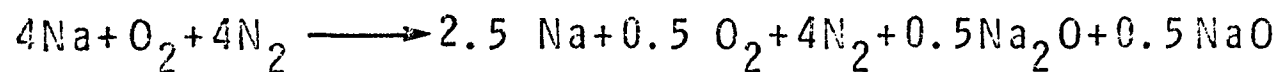
$$D_i = \left[\frac{F^0 - H_{298}^0}{R_c T} + \frac{1000 \Delta H_{f298}^0}{R_c T} \right]_i, \quad i = 1, k \quad (7)$$

$$F(X_i) = \sum_{i=1}^m X_i^g \left[D_i^g + \text{LOGE} \left(\frac{\bar{X} R_c T}{V} \right) - 1 + \text{LOGE} \left(\frac{X_i^g}{\bar{X}} \right) \right] + \sum_{i=1}^n X_i^c D_i^c \quad (8)$$

Table XIX.1

EQUILIBRIUM SODIUM-OXYGEN REACTION

FEASIBLE SOLUTION OF SET $\{x_j\}$ FOR CHEMICAL BALANCE:



$\{A_{ij}\}$ NO. OF ATOMS OF THE j^{TH} ELEMENT IN THE i^{TH} SPECIES.

ELEMENT	SPECIES				
	Na	O ₂	N ₂	Na ₂ O	NaO
Na	1	0	0	2	1
O	0	2	0	1	1
N	0	0	2	0	0

$\{A_{ij} \cdot x_j\}$ MOLES OF EACH ELEMENT IN PRODUCT SPECIES

Na	2.5	0	0	1	0.5	$\frac{3j}{4}$
O	0	1	0	0.5	0.5	2
N	0	0	8	0	0	8

Table XIX.2

This summation $E(x_i)$ is the total energy function of the system. The system equilibrium temperature is the value that makes the energy function equal to zero.

In Step (2), Table XIX.3, the heats of formation for the energy changes for each of the reactants and products, gaseous and condensed, are defined by Equations (9) through (14). The definitions of internal energy and energy increment are given by Equations (16), (17), and (18). Substituting the values for E and ΔE into the energy summation, Equation (15), the final equilibrium temperature is determined by iteration. Utilizing the equilibrium concentrations of gaseous products and the equilibrium temperature, Equation (19) gives the system pressure as the sum of the partial pressures of the gaseous products (see Figure XIX.12).

4. Adiabatic Equilibrium Sodium-Oxygen Reaction Calculation Method at Low Oxygen Concentration

At low oxygen concentration ($\sim 2\%$), the equilibrium system temperature for a sodium-oxygen reaction will be $< 1700^\circ\text{F}$ where the production of NaO is negligible, as explained in Section D.2. The two remaining oxides, Na_2O and Na_2O_2 , both are condensed species. The maximum release of heat will be realized for the stoichiometric sodium-oxygen molar ratio since no excess reactants are present to reabsorb the reaction heat. The stoichiometric reaction producing the Na_2O at a 4:1 molar ratio releases approximately 50% more heat than the production of Na_2O_2 at a molar ratio of 2:1. A product consisting entirely of Na_2O is obtained by the method of free energy minimization as shown on the accompanying calculation sheet (Table XIX.4).

EQUATIONS FOR EQUILIBRIUM SODIUM-OXYGEN REACTION

STEP (2) ENERGY BALANCE AND EQUILIBRIUM TEMPERATURE

CONDENSED

$$\Delta E^C = \Delta H_{f298}^0 \quad (9)$$

$$E_p^C = (H_T^0 - H_{298}^0) \quad (10)$$

$$E_r^C = (H_{T'}^0 - H_{298}^0) \quad (11)$$

GASEOUS

$$\Delta E^g = \Delta H_{f298}^0 - \frac{R_c(298)}{1000} \quad (12)$$

$$E_p^g = (H_{T'}^C - H_{298}^0) - \frac{R_c}{1000} (T - 298) \quad (13)$$

$$E_r^g = (H_{T'}^0 - H_{298}^0) - \frac{R_c}{1000} (T' - 298) \quad (14)$$

PRODUCTS

REACTANTS

$$E(X_i) = \sum_{i=1}^k [X_i (\Delta E_i + E_i)]_p - \sum_{j=1}^w [X_j (\Delta E_j + E_j)]_r \quad (15)$$

$$H = E + PV \quad (16)$$

ASSUMING PERFECT GAS LAW:

$$E = H - RT \quad (17)$$

$$\Delta E = \Delta H - \Delta(RT) \quad (18)$$

$$P = \sum_{i=1}^m P_i = \sum_{i=1}^m X_i^g \frac{R_g T}{V} \quad (19)$$

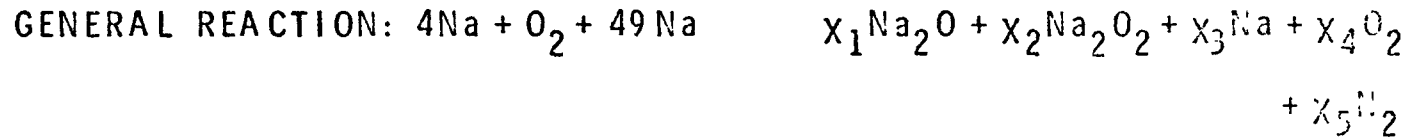
Table XIX.3

FREE-ENERGY MINIMIZATION, SODIUM-OXYGEN
REACTION AT LOW O₂ CONCENTRATION

$$f_i^g = D_i + \alpha + \ln \frac{x_i}{X}$$

$$f_i^c = D_i$$

$$T = 1000 \text{ } ^\circ\text{K}$$



$$f_4^g = -32.50 (\text{O}_2)$$

$$f_1^c = -63.98 (\text{Na}_2\text{O})$$

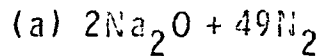
$$f_3^c = -8.56 (\text{Na})$$

$$f_5^g = -24.61 (\text{N}_2)$$

$$f_2^c = -79.20 (\text{Na}_2\text{O}_2)$$

$$F(x_i) = \sum_{i=1}^k x_i f_i$$

TWO LIMITING REACTIONS:



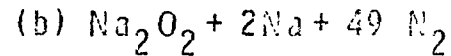
$$x_1 = 2 \quad x_5 = 49$$

$$x_2 = x_3 = x_4 = 0$$

$$F_a = x_1 f_1 + x_5 f_5$$

$$= 2(-63.98) + 49(-24.61)$$

$$F_a = -1333$$



$$x_2 = 1 \quad x_3 = 2 \quad x_5 = 49$$

$$x_1 = x_4 = 0$$

$$F_b = x_2 f_2 + x_3 f_3 + x_5 f_5$$

$$= 1(-79.2) + 2(-8.56) + 49(-24.61)$$

$$F_b = -1301$$

$F_a < F_b$ THEREFORE:

$$x_1 = 2; \quad x_2 = x_3 = x_4 = 0; \quad x_5 = 49$$

Table XIX.4

Since heat of formation vs temperature is available from the JANAF Tables,⁽¹²⁾ a further simplification of the calculation results if the reference temperature is chosen as the initial gas temperature. The energy balance is then given by Equation (20), Table XIX.5, which may be solved directly for the equilibrium temperature by Equation (21). The heat balance equates the reaction heat plus sensible heat in sodium liquid to the heat absorbed by Na_2O and nitrogen raised to the final temperature.

The heat of formation of Na_2O from sodium and oxygen is 3890 Btu/lb Na at room temperature. However, this value is for sodium in its standard state at room temperature which is the solid. To obtain the total heat of combustion, the enthalpy of the liquid above room temperature is added to the above value. Several values of heat of combustion as a function of liquid sodium temperature are shown in Table XIX.6. The tabular value of heat of combustion for liquid sodium may be utilized to estimate heat input to the sodium-oxygen reaction for the 4:1 Na/ O_2 molar ratio or 2.87 lb sodium per lb oxygen.

E. Theory of Sodium Pool Fires

1. Description of Burning Process

When liquid sodium is allowed to collect in a pool with an oxygen containing gas above it, oxidation will take place. The burning rate is determined primarily by pool surface exposure area, oxygen concentration and heat loss to the structural mass beneath the pool. Sodium atoms diffuse upward from the pool surface to the flame through the gas atmosphere. Heat transfer to and from the pool and flame by conduction, convection and radiation is determined by the flame temperature and a heat balance with the heat of

SODIUM-OXYGEN REACTION AT LOW O₂ CONCENTRATION

$$X_1 \Delta H_{fT_0}^0 + X_2 \Delta H_2 = (X_1 C_{p1} + X_3 C_{v3})(T - T_0) \quad (20)$$

$$T = \frac{X_1 \Delta H_{fT_0}^0 + X_2 \Delta H_2}{X_1 C_{p1} + X_3 C_{v3}} + T_0 \quad (21)$$

X₁ = 2 = MOLES OF Na₂O

X₂ = 4 = MOLES OF Na

X₃ = 49 = MOLES OF N₂ (MOLES OF O₂ = 1 = 2 VOLUME %)

ΔH_{fT₀}⁰ = HEAT OF FORMATION Na₂O(C) (ΔH_{f298}⁰ = 99.4 $\frac{\text{KCAL}}{\text{MOLE}}$)

ΔH₂ = ENTHALPY DIFFERENCE (T' - T₀) FOR Na LIQUID AT TEMP.
T' $\frac{\text{KCAL}}{\text{MOLE}}$

T₀ = REF. TEMPERATURE = INITIAL GAS TEMP. °K

T = FINAL SYSTEM TEMPERATURE °K

C_{p1} = SPECIFIC HEAT OF Na₂O(C) $\frac{\text{KCAL}}{\text{MOLE-°K}}$

C_{v3} = SPECIFIC HEAT OF N₂ AT CONSTANT VOLUME $\frac{\text{KCAL}}{\text{MOLE-°K}}$

Table XIX.5

HEAT OF COMBUSTION FOR LOW O₂ SODIUM-OXYGEN REACTION

$\Delta H_{f298}^0 = 99.4 \frac{\text{KCAL}}{\text{MOLE}}$ CONVERSION TO ENGINEERING UNITS:

$$99.4 \frac{\text{KCAL}}{\text{G-MOLE Na}_2\text{O}} \times 1800 \frac{\text{BTU}}{\#-\text{MOLE Na}_2\text{O}} \times \frac{2 \text{ MOLES Na}_2\text{O}}{4 \text{ MOLES Na}} \div 23 \frac{\#Na}{\#-\text{MOLE}} = 3800 \frac{\text{BTU}}{\#Na}$$

<u>T' LIQUID Na TEMP. (°F)</u>	<u>ΔT' (°F) ABOVE ROOM TEMP. (75 °F)</u>	<u>ΔH_{Na} = H_{T'}⁰ - H_{75F}⁰ BTU/# Na</u>	<u>HEAT OF COMBUSTION ΔH_{T'}⁰ = ΔH_{f298}⁰ + ΔH_{Na} BTU/# Na</u>
75	525	170	4000
200	725	230	4120
400	925	290	4180
1200	1125	350	4240

Table XIX.6

combustion of sodium. Heat transfer outward from the flame to the gas atmosphere is principally by convection and radiation.

Although an observable flame has not been detected for pool oxidation with <5% oxygen, the oxidation rates are not negligible in this region.

In an enclosure a pool fire will proceed at a decreasing rate due to oxygen depletion. With ~75% sodium consumed, a further decrease in burning rate is due to build up of oxide crust from the pool base, protruding through the pool surface and thereby reducing exposed surface area.

2. SOFIRE Computer Code⁽¹³⁾

This code is basically a short term (~1-50 hours) transient heat transfer calculation. The calculation of pressures, temperatures and other values of interest are determined by heat balances between the sodium and its environment. Sodium-to-flame and flame-to-gas heat transfer coefficients have been obtained from experimental work.⁽¹⁷⁾

The heat transfer model is shown in Figure XIX.13. The arrangement consists of a cell in which the fire takes place, with a ceiling vent or leakage path to a secondary volume (room above). If there is decay heat or Na²⁴ activity in the sodium, this is treated as an internal heat generation rate which results in self-absorption by the sodium pool. Heat may be removed by safeguard cooling systems in the cell and room. Inleakage or venting to the cell and room is variable, as is room exhaust. These venting and cooling terms, along with oxygen depletion and heating effect of the flame, cause a variable convective flow between the cell and room. Heat loss from the cell outward is through a three slab wall and floor. Heat transfer from the room is through a thick wall (concrete or insulation) and a thin wall (steel). An

additional heat absorbing mass may be located either in the cell or the room. The real time to be represented by a computer run may be controlled by any one of the following: low sodium temperature, oxygen depletion, sodium depletion, gas pressure less than 1/2 atmosphere, and maximum specified time limit. The phenomenon of oxide buildup is conservatively neglected by the program.

As an example of the use of the SOFIRE code, pressure and temperatures are plotted vs time in Figure XIX.14 for the following described accident.

A nuclear accident within the FTR reactor vessel may build up pressure and rupture piping in the three heat transport cells expelling 270 tons of 1050°F liquid sodium containing core debris with accompanying decay heat from full reactor power. It is postulated that the initial gas pressure buildup in cells due to sodium-oxygen reaction lifts shield plugs allowing the containment sphere air to vent into the cells. Assuming no ventilation or leakage from the sphere to the environment, the fire terminated in 37 hours due to oxygen depletion <.001% by volume. The initial decay heat input to the sodium pool was 30 million Btu/hr and decreased as a function of time.

F. Experimental Review

1. Explosive Ejection and Spray Fires

In 1956, Hines and Kelley⁽¹⁴⁾ reported results for spray oxidation in various oxygen concentrations 0.6 - 21%. Peak pressures ranged from 8 psig

at 0.6% to a maximum of 38 psig in air. This work in support of Fermi FBR utilized commercial nozzles and a drive pressure of 360 psi to inject 1 lb of sodium at 850°F into a 532 liter container. The sodium-oxygen ratio was 4.7:1 with 21% O₂ and the total time for injection was ~25 seconds.

In 1958, Humphreys⁽⁵⁾ reported results for rapid injection of varying amounts of sodium (0.5-4:1 Na/O₂ molar ratio) into air by the detonation of a hydrogen-oxygen gas mixture. The volume of the cylindrical reaction vessel was 2032 liters and sodium was 750°F. The maximum pressure, 85 psig, occurred for a molar ratio of 3:1, while a maximum of 75 psig occurred at a ratio of 4:1 (see Figure XIX.1). Sodium ejection times were on the order of 3-10 milliseconds. This work was in support of EBR-II.

In 1960, Gracie and Droher⁽¹⁵⁾ reported results on spray oxidation in low oxygen concentrations (0-5%) in a 48 cu ft rectangular chamber. One-half pound of liquid sodium at 1000°F and 50 psig drive pressure was injected through a slit ~.002" wide. Maximum pressure rise was 1.8 psig in 2% oxygen at a molar ratio Na/O₂ = 9:1. This work was performed in support of SRE.

In 1965, Charak and Smith⁽¹⁶⁾ (ANL) reported on a brief series of tests in which 1 or 2 gram quantities of sodium at 1200°F were fired from a revolver into an air-filled chamber where the Na/O₂ ratio was 4:1. The maximum pressure rise recorded was ~80 psig.

In 1965, Krolikowski⁽⁴⁾ reported results of sodium injection at high velocity, 1000-1500 psig drive pressure, into a 16.7 liter chamber. Ten grams of liquid sodium at 800°F was injected through a set of small orifices (.01 - .03" diam.) into various oxygen concentrations from 3.8 - 21% by volume. Maximum pressure rise in air was 45 psig at a Na/O₂ molar ratio of 3:1, while pressure rise was 3.8 psig in 3.8% oxygen at a molar ratio of 17:1.

2. Pool Fires

In continuing experimental work at Atomics International,^(15,17) considerable detail in observations⁽¹⁷⁾ has been obtained in order to provide constants for calculation procedures such as the SOFIRE code (Section E.2). Temperature readings in the sodium pool, the flame and the oxide cloud, along with heat balance has been utilized to determine heat transfer coefficients.

The following data from the LF-1 study⁽¹⁷⁾ is typical of experimental work on sodium pool fires. The sodium pool temperatures increased from the bottom of the 2 ft diameter pool to a maximum of $\sim 1100^{\circ}\text{F}$ at the surface. A jump in temperature to 1800°F to the flame immediately above the pool surface dropped off asymptotically to 500°F at 6 inches above the surface in the air atmosphere. In this test an average sodium burning rate of 6 lb/hr-sq ft was observed, the range was 3 to 10 lb/hr-sq ft over a 24 hour period before the effective surface was diminished by solid oxide buildup from the base of the pool.

For oxygen concentrations $< 5\%$ the average burning rate is 0.4 lb sodium/sq ft-hr per 1% oxygen concentration.

References

- (1) L. Leibowitz, "Sodium-Air Reactions," Fast Reactor Safety Studies, ANL-7225, Chemical Engineering Division Semiannual Report, January-June 1966, p. 201, Argonne National Laboratory (June 1966).
- (2) W. S. Horton, "Static Pressure Due to Sodium-Water Reactions in Closed Vessels," KAPL-722 (March 1952).
- (3) H. E. Johnson and N. K. Rumpf, "Chemistry" Liquid Metals Handbook, Sodium and NaK Supplement, Review Copy, 4th Edition, Liquid Metal Engineering Center (June 1967).
- (4) T. S. Krolkowski, "Violently Sprayed Sodium-Air Reaction in an Enclosed Volume," ANL-7472, Argonne National Laboratory (September 1968).
- (5) J. R. Humphreys, Jr., "Sodium-Air Reactions as they Pertain to Reactor Safety and Containment," Proc. Second International Conference on Peaceful Uses of Atomic Energy, Geneva (1958), Vol. 11, p. 177.
- (6) E. Garelis and J. B. Nims, "Sodium-Air Accident Study for a Sodium Cooled Reactor," AECU-4161 (July 1959).
- (7) L. Baker and A. D. Tevebaugh, "Sodium-Air Reaction Calculations," Reactor Safety, ANL-7055, Chemical Engineering Division Annual Report, January-June 1965, p. 208, Argonne National Laboratory (October 1965).
- (8) L. Leibowitz, "Calculations for the Sodium-Air Reaction," ANL-7230, Reactor Development Program Progress Report, June 1966, p. 70, Argonne National Laboratory (July 1966).
- (9) W. B. White, S. M. Johnson, and G. B. Dantzig, "Chemical Equilibrium in Complex Mixtures," Journal of Chemical Physics, Vol. 28, p. 751 (1958).
- (10) R. C. Oliver, S. E. Stephanou, and R. W. Baier, "Calculating Free-Energy Minimization," Chemical Engineering, Vol. 69, No. 4, p. 121 (February 19, 1962).
- (11) J. L. Anderson, "Chemical Equilibrium Calculations," Program B-194, Argonne National Laboratory (March 1966). (Converted to UNIVAC 1108 FORTRAN V as NAFIRE, November 1968)
- (12) "JANAF Thermochemical Tables," The Dow Chemical Company, Midland, Michigan (1965).
- (13) R. P. Johnson, "SOFIRE I-B Sodium Fires Code," TI-707-14-001, Atomic International (February 1969). (Converted to UNIVAC 1108 FORTRAN V as SOFIRE, October 1968 and July 1969.)

- (14) E. Hines and J. K. Kelley, "Determination of the Maximum Pressures Obtained During the Reaction of Sodium with Air in Closed Systems," NP-7320, Detroit Edison Company (February 1956).
- (15) J. D. Gracie and J. J. Droher, "A Study of Sodium Fires," NAA-SR-4383, Atomics International (October 1960).
- (16) I. Charak and F. A. Smith, "Preliminary Evaluation of a Technique to Study Expulsion of Sodium into Air," Proc. Conf. Safety, Fuel and Core Design in Large Fast Power Reactors, ANL-7120, p. 868, Argonne National Laboratory (October 1965).
- (17) G. N. Lauben, "Initial Experience with Large Sodium Fires Experiments (LF-1)," NAA-SR-12041, Atomics International (August 1966).

ADIABATIC PRESSURES FOR SODIUM-AIR REACTION

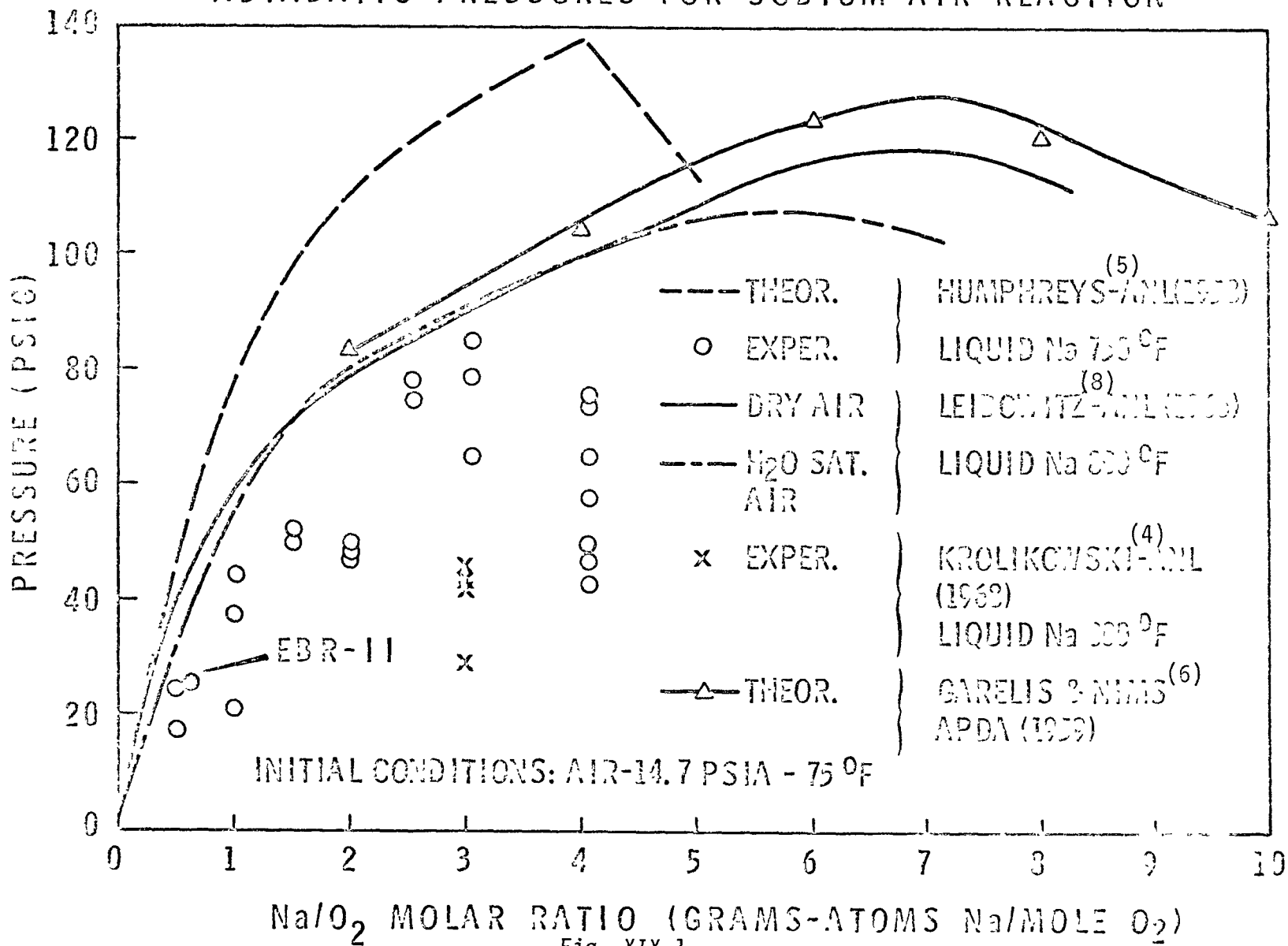


Fig. XIX.1

ADIABATIC PRESSURES FOR
SODIUM-AIR AND SODIUM-AIR-WATER REACTIONS

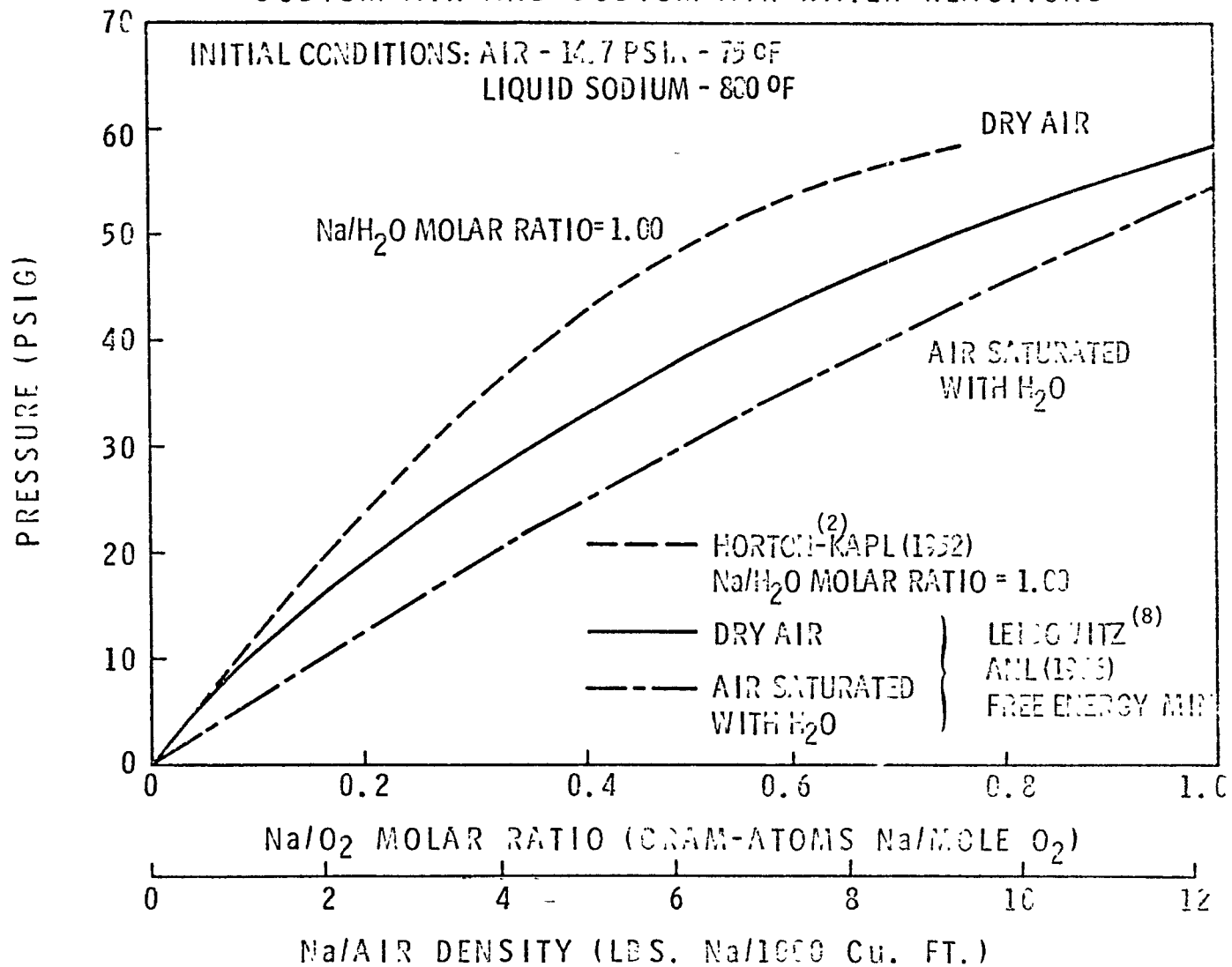


Fig. XIX.2

ADIABATIC PRESSURES FOR SODIUM-AIR REACTION

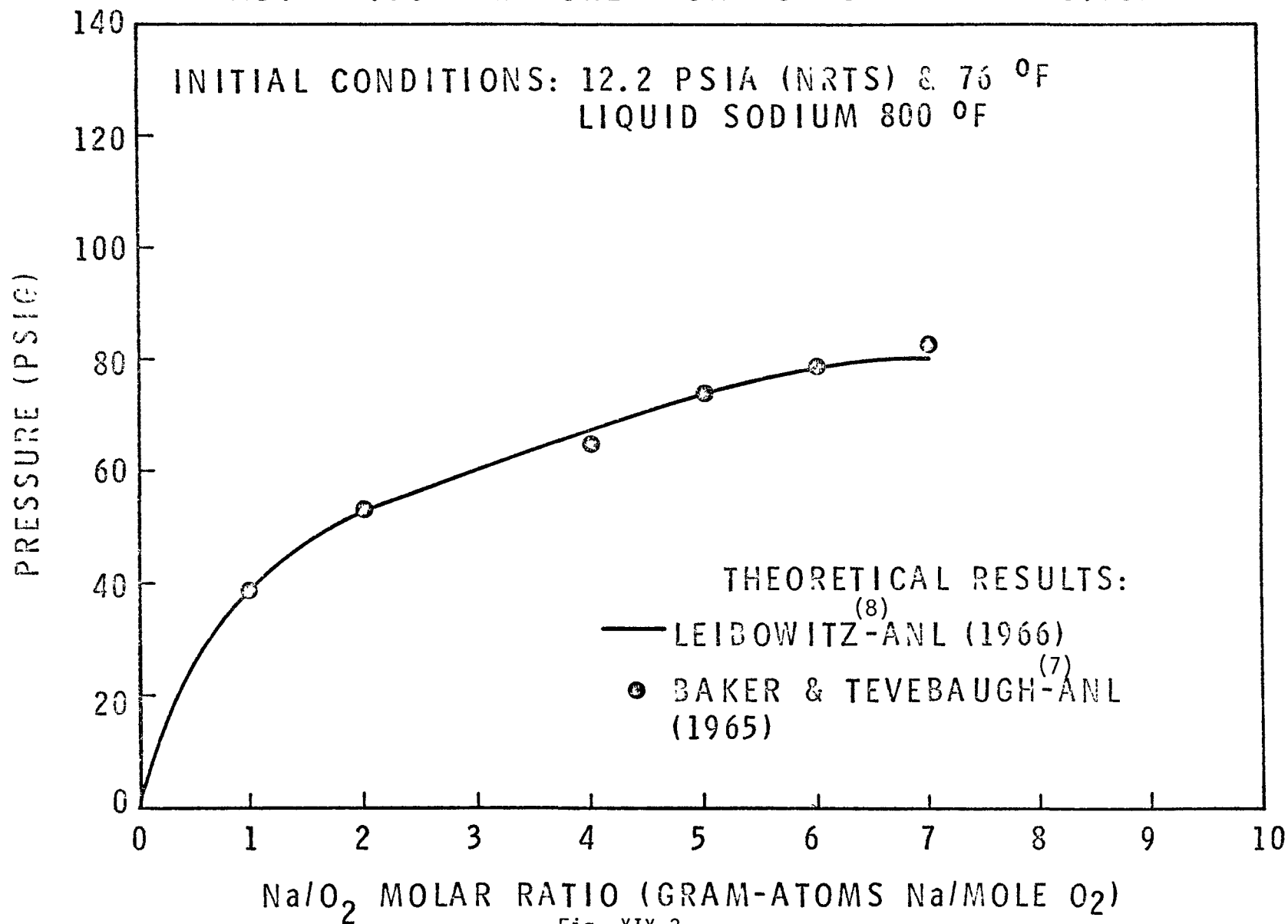


Fig. XIX.3

PRODUCT VERSUS REACTANT
CONCENTRATIONS FOR SODIUM-AIR REACTION

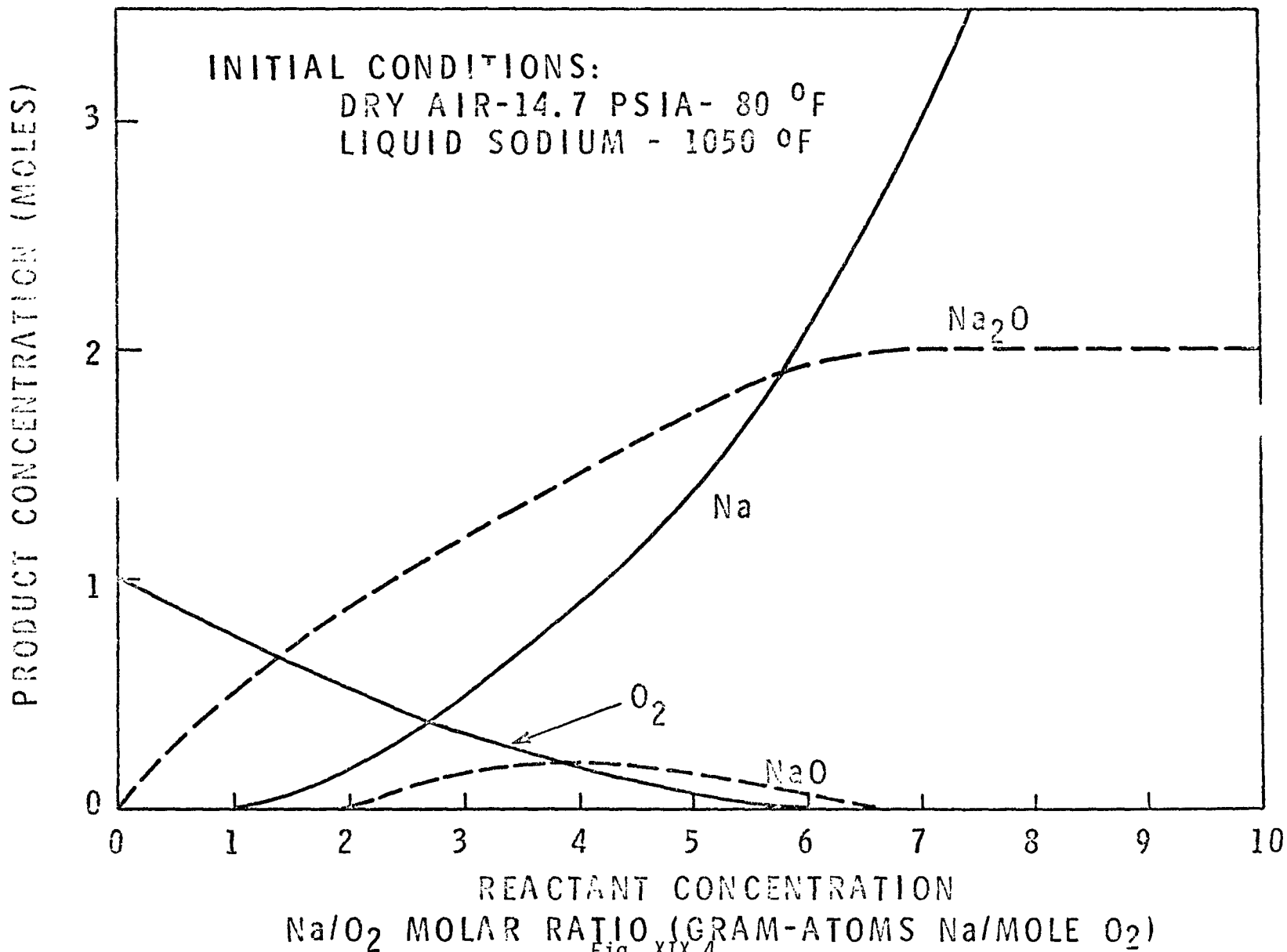


Fig. XIX.4

PEAK ADIABATIC PRESSURE VERSUS INITIAL
SODIUM TEMPERATURE SODIUM-OXYGEN REACTION

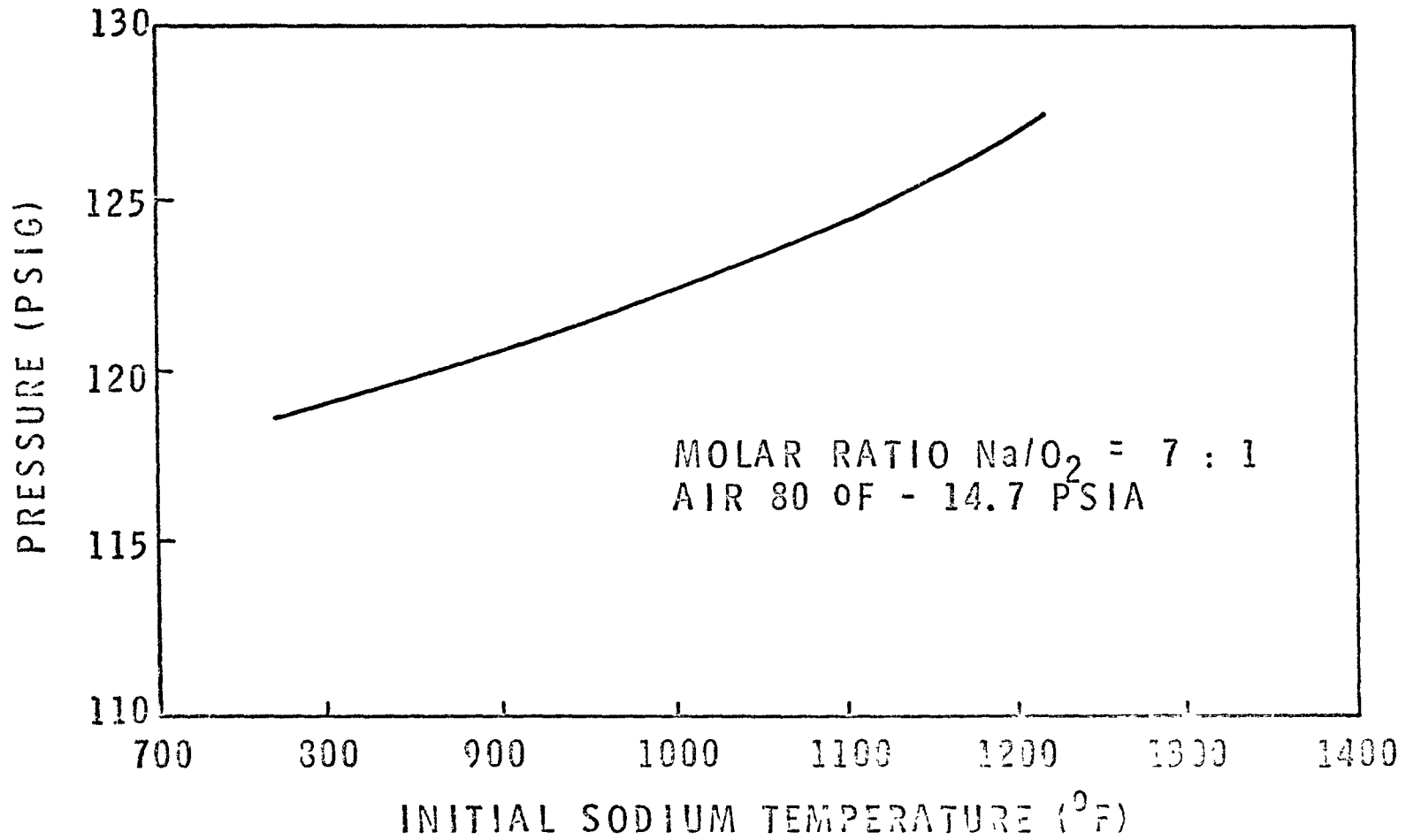


Fig. XIX.5

PEAK ADIABATIC PRESSURE VERSUS INITIAL
AIR TEMPERATURE SODIUM-OXYGEN REACTION

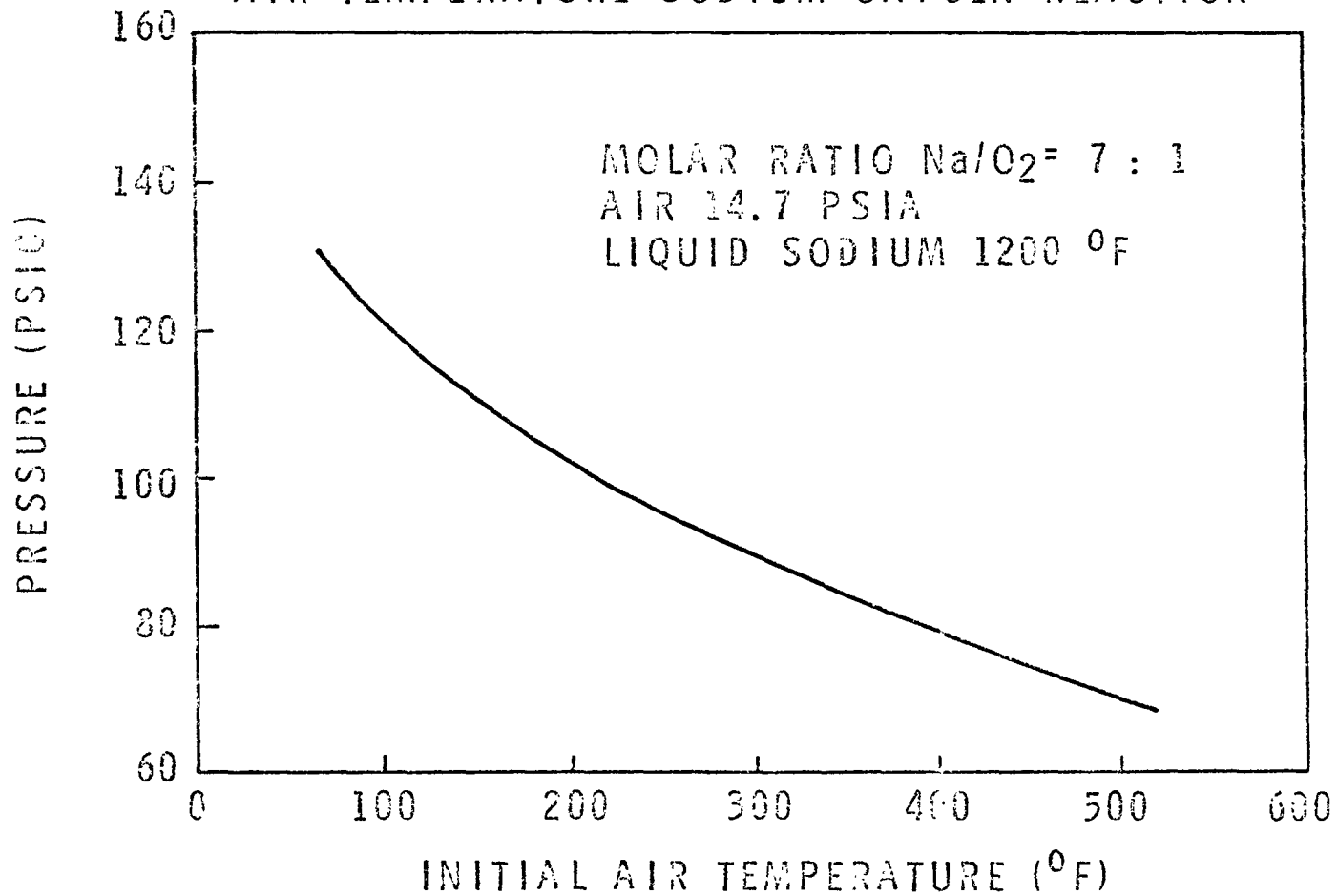


Fig. XIX.6

PEAK ADIABATIC PRESSURE VERSUS
INITIAL AIR PRESSURE SODIUM-OXYGEN REACTION

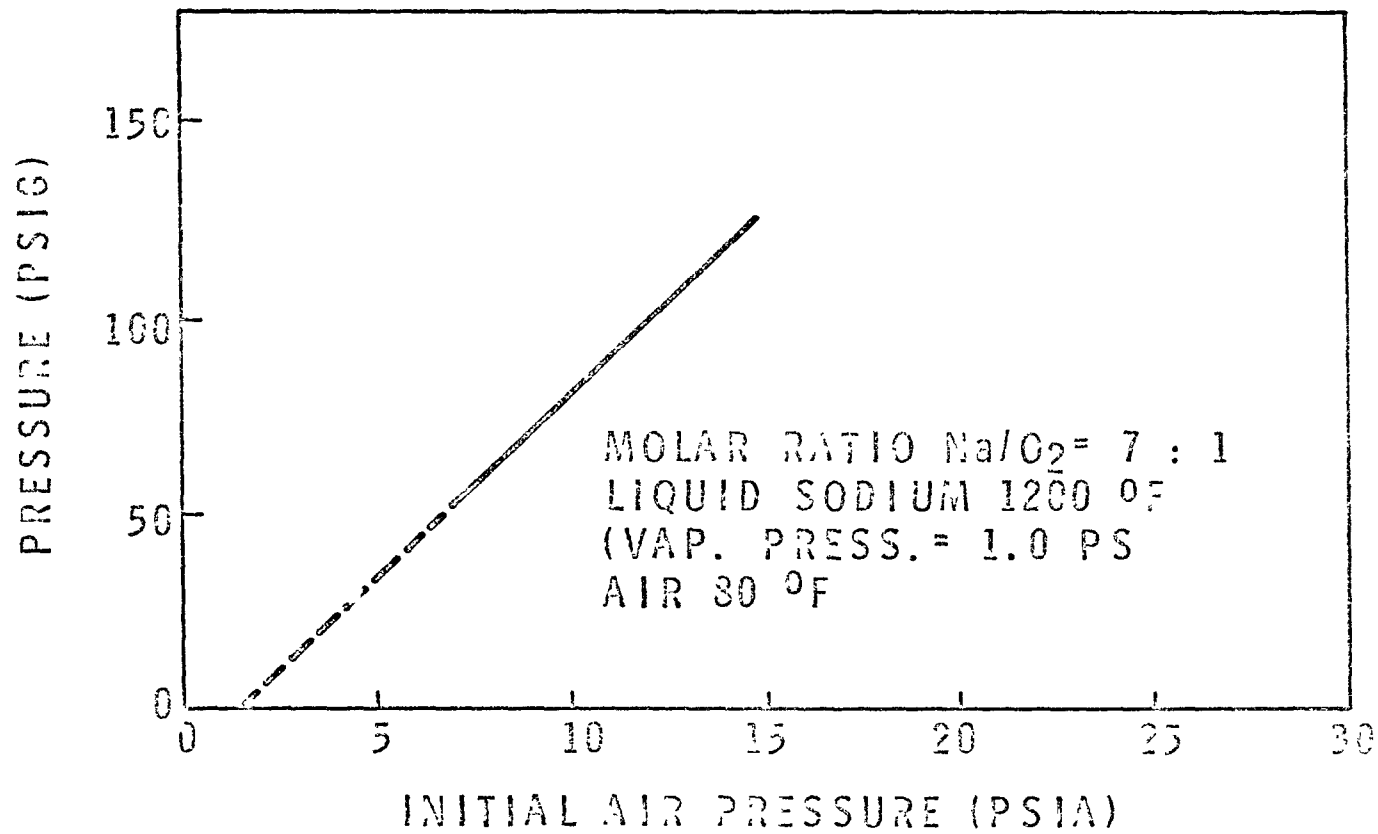


Fig. XIX.7

PEAK ADIABATIC PRESSURE VERSUS INITIAL
OXYGEN CONCENTRATION SODIUM-OXYGEN REACTION

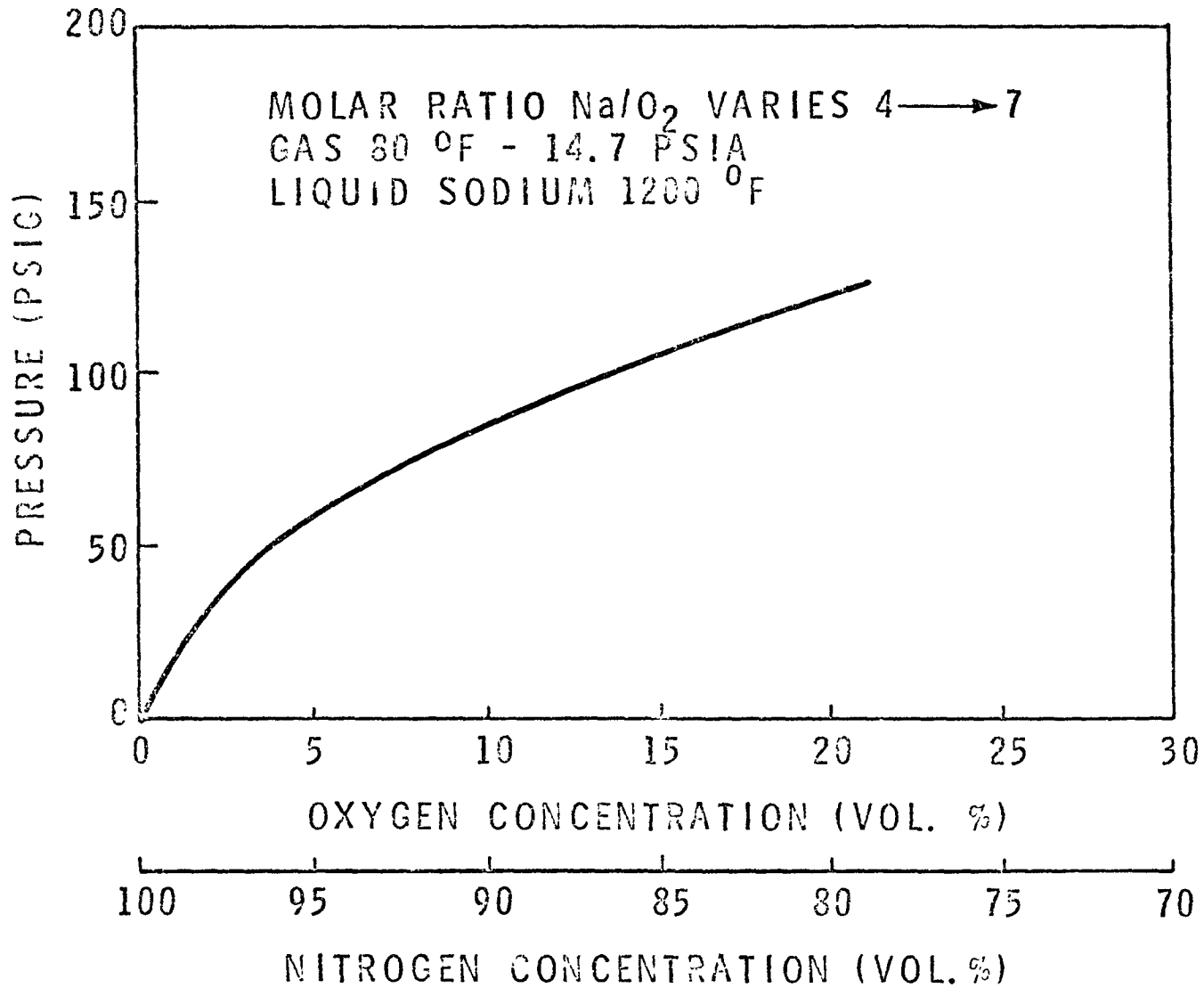


Fig. XIX.8

ADIABATIC PRESSURE VERSUS MOLAR RATIO FOR SODIUM-OXYGEN REACTION

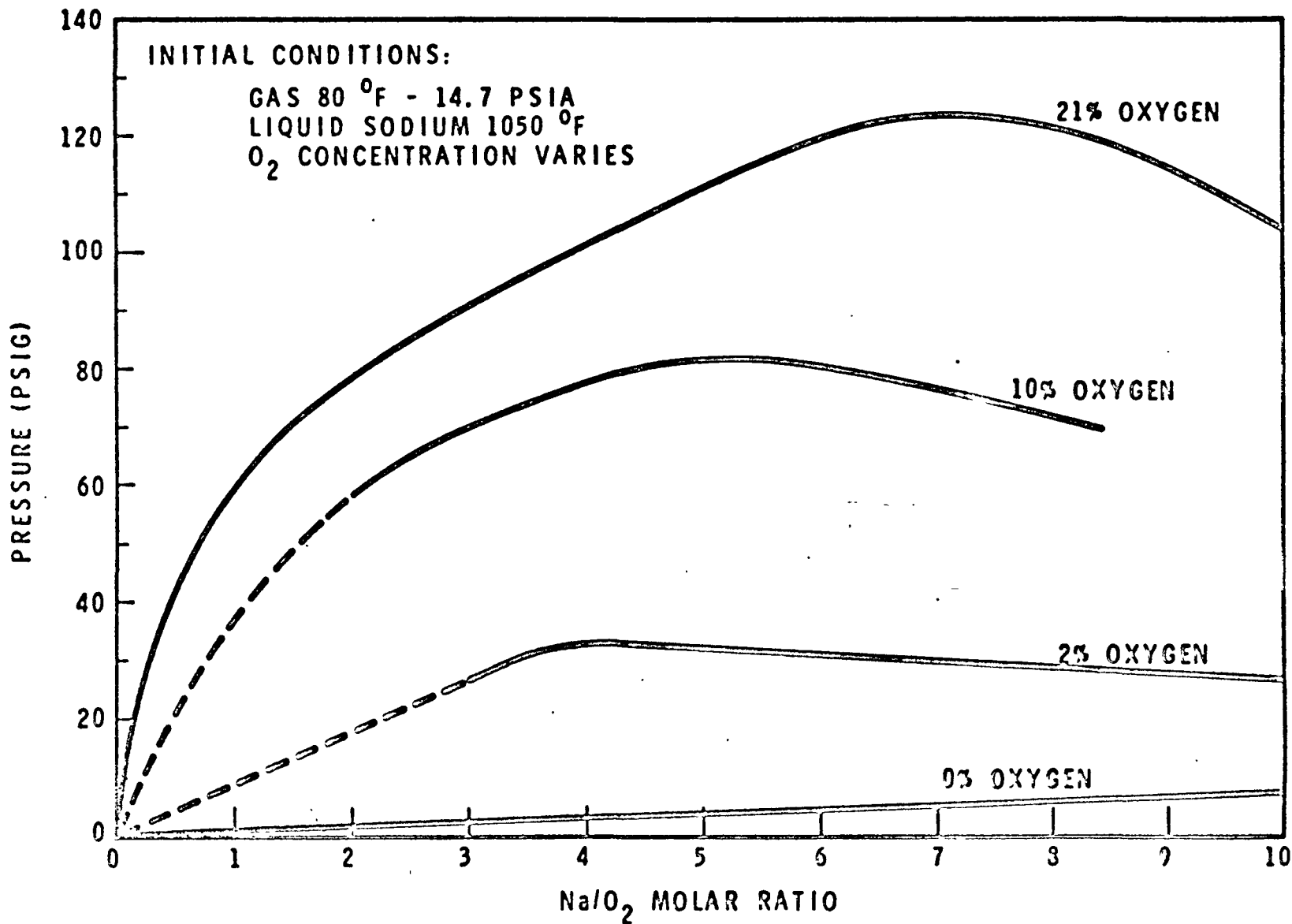


Fig. XIX.9

ADIABATIC PRESSURES AND TEMPERATURES FOR SODIUM-AIR REACTION-FREE ENERGY M.I.T. CODE

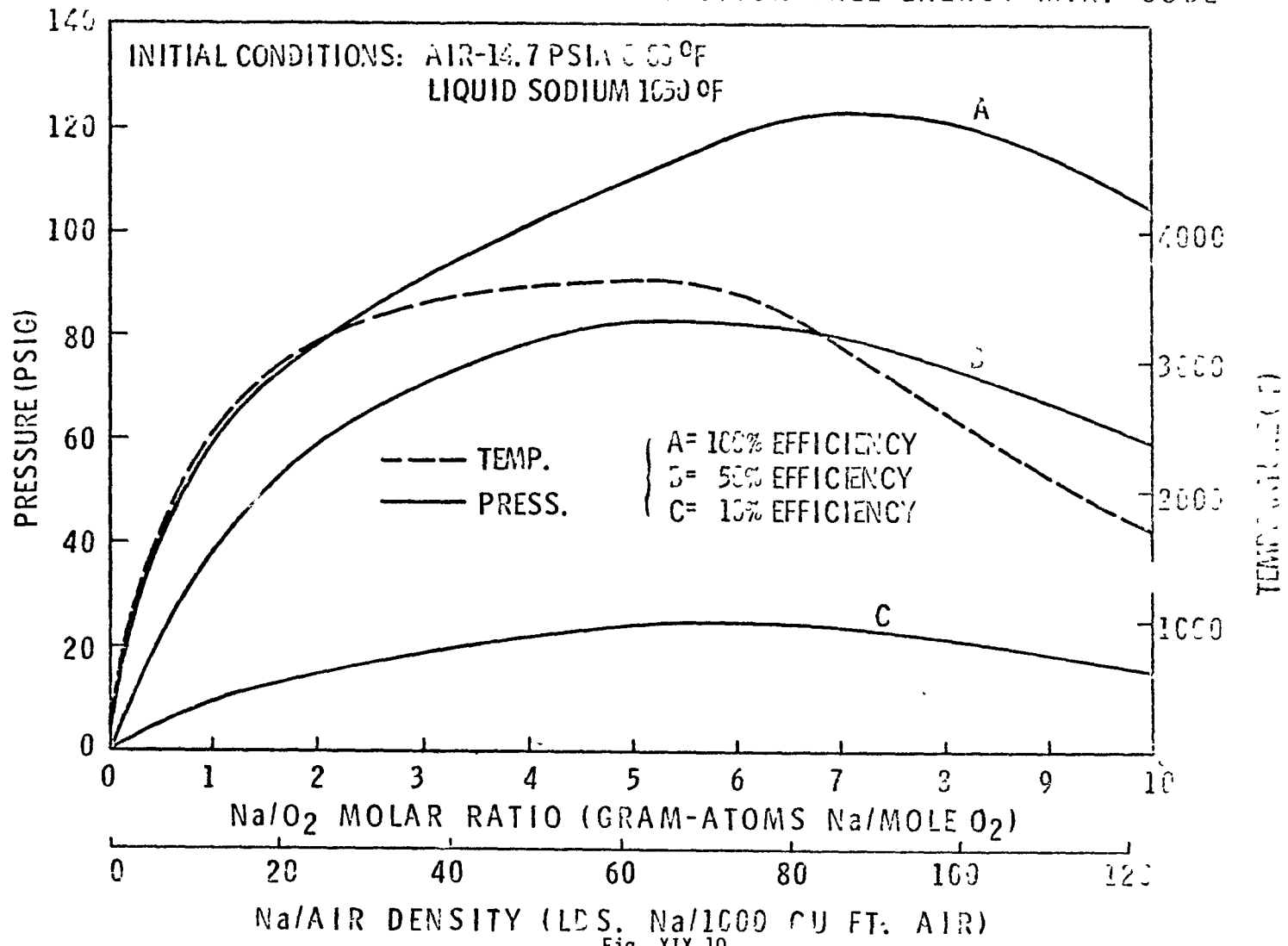
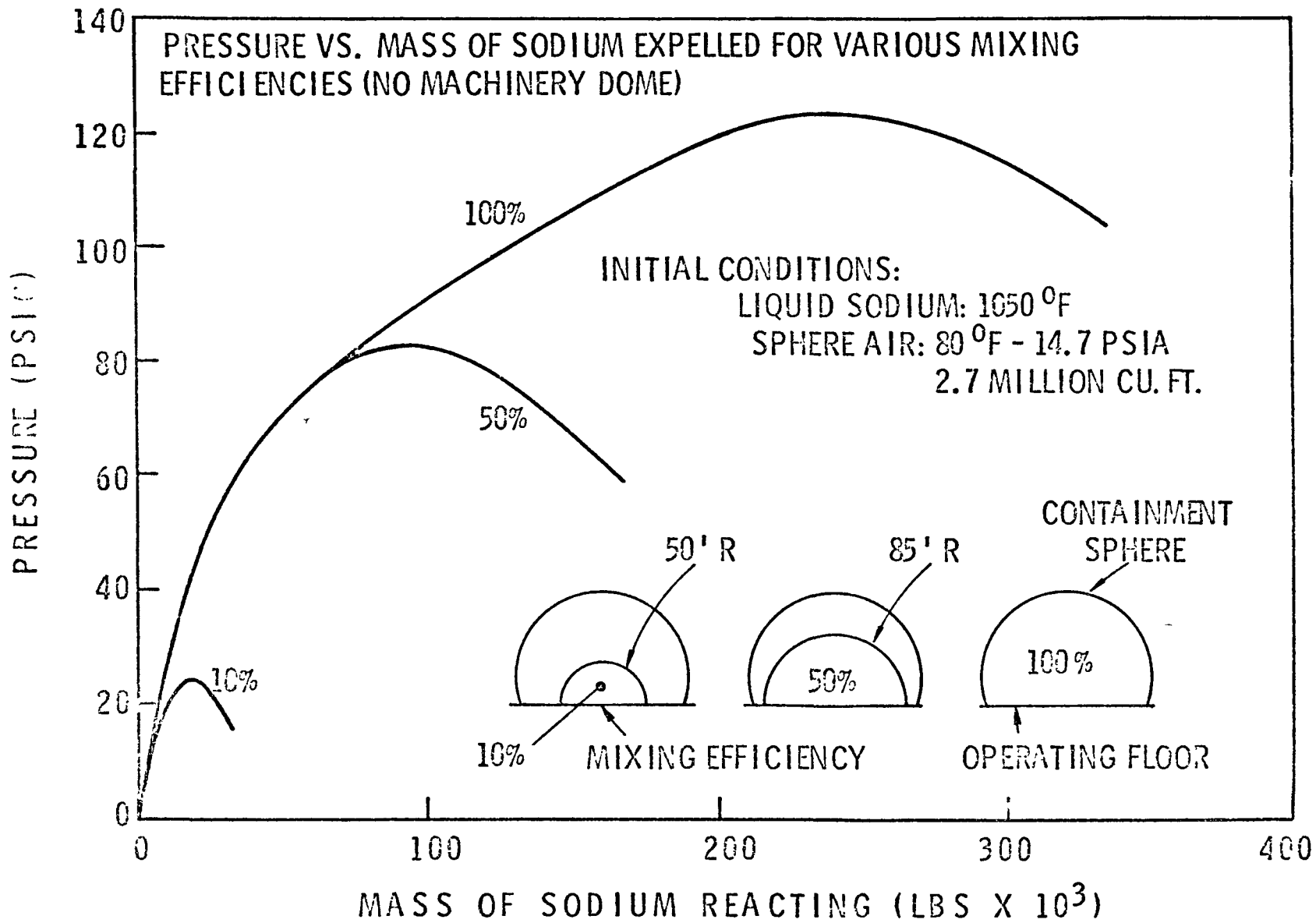


Fig. XIX.10

PRESSURE IN CONTAINMENT
 SPHERE FOR SODIUM SPRAY EXPULSION



XIX.40

Fig. XIX.11

PARTIAL PRESSURE OF
GASEOUS PRODUCTS OF SODIUM-AIR REACTION

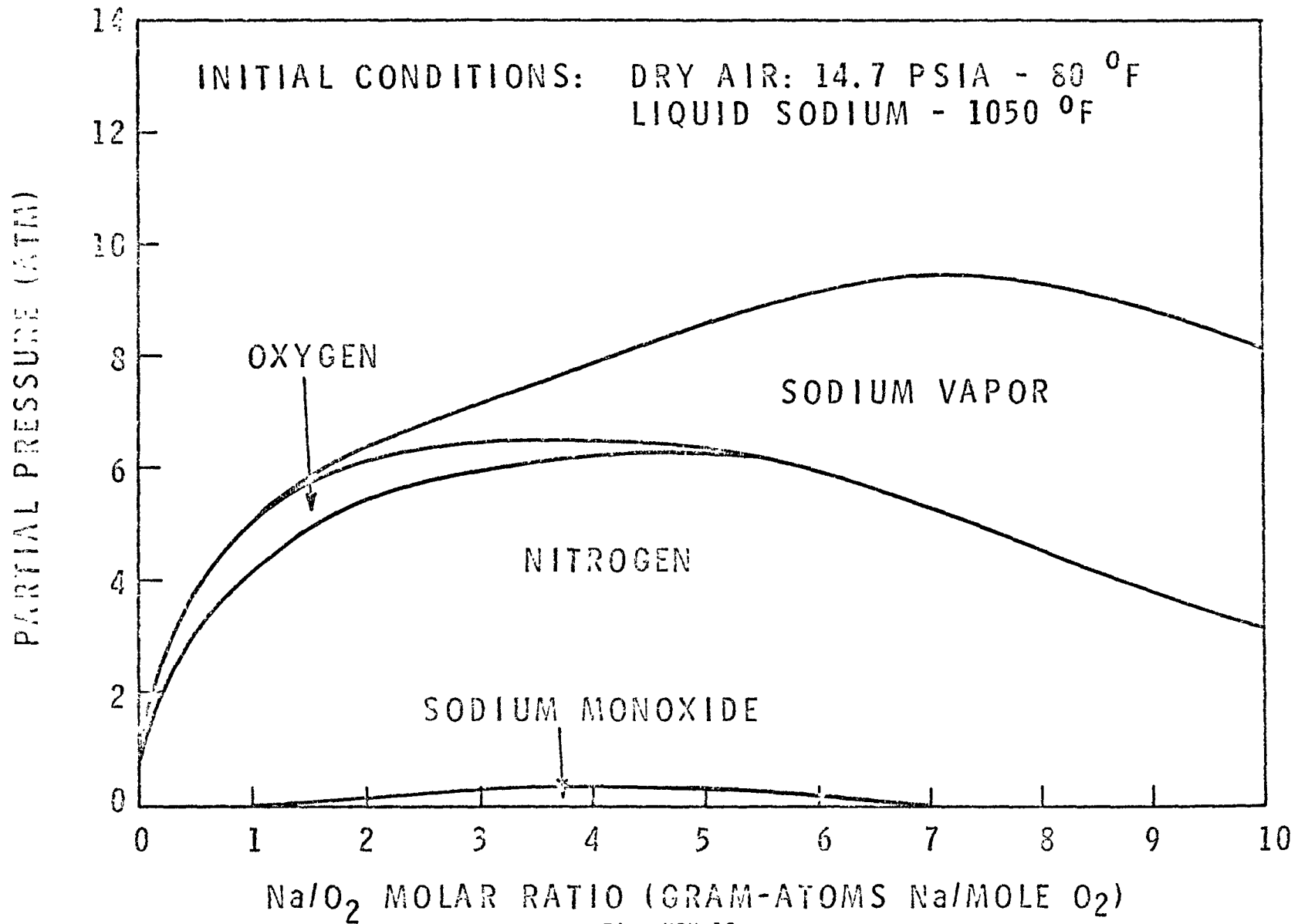


Fig. XIX.12

SODIUM POOL FIRE IN CONTAINMENT SPHERE - SOFIRE CODE

Initial Conditions:

Sphere 14.7 Psia - 80°F - Air
 Cells 14.7 Psia - 100°F - 2% O₂
 Sodium 1050°F - 270 Tons
 100% Decay Heat

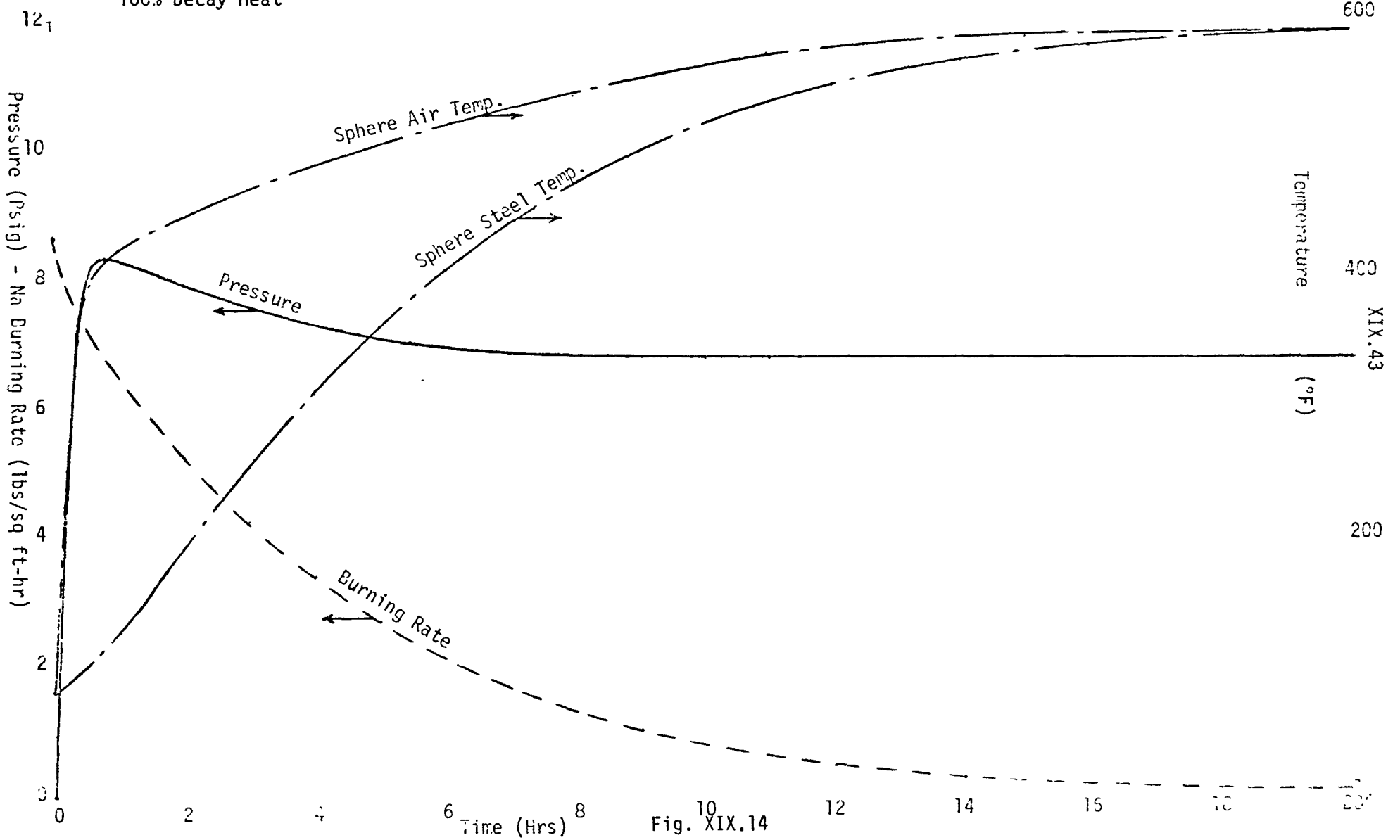


Fig. XIX.14

XX. SURVEY OF FAST REACTOR SAFETY R&D PROGRAMS

J. W. Hagan

A. Introduction

A number of the preceding lectures have touched upon various aspects of ongoing safety development programs. Of particular relevance are those lectures which described various analyses concerned with fuel failure thresholds, modes of failure, materials interactions, and other phenomena associated with disassembly-type accident analyses.

Certainly the present analyses have attempted to take full advantage of whatever experimental data are now available. Updating and even extensive revisions of the analyses have been typical throughout the past two years as new data have become available. However, major uncertainties on various aspects of the programs still are evident and have required what are considered to be quite conservative assumptions to assure a safe containment system design. In these cases, the experimental programs should narrow the uncertainties and, in some cases, even show some of the parallel paths now investigated for conservatism to be nonexistent.

The purpose of this lecture is to identify those development programs under way which are related to fast reactor safety and in turn indicate how these programs are related to the FFTF safety development and analysis.

Safety technology applicable to design and evaluation of the FFTF is available from three different sources -- at least if those sources are identified by program direction and control.

1. FFTF Development Programs

These programs are funded through FFTF Project 189s and performance of these programs is under direction and control of the Project. Typical programs within the category include: BNW thermal hydraulics and fuels development programs.

2. Offsite LMFBR Development Programs

These programs are funded directly to the performer by the AEC but the FFTF Project is requested to provide program guidance. Typical programs include: Pump and control rod drive development at LMEC.

3. LMFBR Development Programs

These programs are funded directly to the performer by the AEC and are independent of the FFTF Project, although we do have access to the information and have been encouraged to communicate our specific needs as related to each program.

B. Role of the LMFBR Program Office

To provide overall program guidance and coordination of those LMFBR development programs, the AEC/RDT directed the establishment of a program office located at Argonne National Laboratory. The LMFBR Program Office functions in a coordinating and advisory capacity to RDT and the functional responsibilities are well defined by the following general objectives of the LMFBR program.

- (1) Determine required technology to meet overall goals.
- (2) Evaluate present state-of-art.
- (3) Describe tasks to fulfill technological goals.
- (4) Establish priorities.
- (5) Assure development of broad industrial capability.
- (6) Provide basis for coordinating private and AEC R&D work.

To implement these objectives, the Program Office categorized the technological requirements into nine major elements as shown in the table below, and developed detailed program plans for each category.

Table XX.1 - *LMFBR Program Plans*

<u>Volume No.</u>	<u>Element</u>
1	<i>Overall Plan</i>
2	Plant Design
3	Components
4	Instrumentation and Control
5	Sodium Technology
6	Core Design
7	Fuels and Materials
8	Fuel Recycle
9	Physics
10	Safety

The program plans pertinent to safety are described in element No. 10 - Safety.

In defining the overall goals of the LMFBR development programs, the Program Office lists safety at the top of the list. In summary, the specific goals identified in the program plan and related to safety are:

- (1) Supply information and techniques for selection of appropriate DBA.
- (2) Demonstrate adequacy of containment design and site selection for protection of the public health and safety.
- (3) Demonstrate that probability of a major accident is very small.
- (4) Demonstrate that minor accidents cannot propagate to major occurrences.

The first two items demonstrate goals concerned with public safety and the latter two express goals related to protection from excessive economic losses for various faulted conditions. To implement these goals, the following program objectives have been established for the Safety Element.

- (1) Practical codes for analysis of accidents and evaluation of safety margins.
- (2) Establishment of a sound basis for development of safety criteria.
- (3) Fully developed protective and consequence-limiting safety systems.
- (4) Development of facilities required for implementation of these objectives.

The Safety Element program plan has defined five major task areas as shown in the outlined plan of action, Table XX.2. The guidance studies include development of safety analysis reports -- one source of data here is of course the FFTF preliminary safety analysis report. The second task area, accident analysis, deals with the development of each phenomenological area to allow realistic evaluation of accident consequences and overall safety margins. The third area, safety systems and instrumentation, is concerned with development of reliable plant protective systems and related consequence-limiting devices. Special studies, area 4, is rather self-explanatory. A probabilistic approach to accident analysis and risk is given emphasis in the United Kingdom and may someday be given emphasis in this country. The last area, safety facilities, is concerned with the availability of present facilities and development of new facilities to meet the experimental needs of the total program. These facility studies are now in process.

Figure XX.1 attempts to show the significant interfaces between the Program Office, AEC/RDT, and the development program performers. This is of course rather simplified but indicates the flow of information.

SAFETY ELEMENT PLAN OF ACTION

- 10-1 GUIDANCE STUDIES
 - 10-1.1 PLANT SAFETY ANALYSIS STUDIES
- 10-2 ACCIDENT ANALYSIS
 - 10-2.1 CODES FOR ANALYSIS OF INITIATING EVENTS
 - 10-2.2 CODES FOR ANALYSIS OF HYPOTHETICAL ACCIDENTS
 - 10-2.3 SODIUM BOILING
 - 10-2.4 FUEL FAILURE AND MELTING
 - 10-2.5 POST-BURST PHENOMENA
 - 10-2.6 SODIUM FIRES
 - 10-2.7 FISSION PRODUCT AND PLUTONIUM RELEASE
 - 10-2.8 MATERIALS INTERACTION PHENOMENA FOR ACCIDENT ANALYSIS
 - 10-2.9 PHYSICAL AND MECHANICAL PROPERTIES FOR ACCIDENT ANALYSIS
- 10-3 SAFETY SYSTEMS AND INSTRUMENTATION
 - 10-3.1 CORE PROTECTIVE SYSTEMS AND DEVICES
 - 10-3.2 CONTAINMENT AND CONSEQUENCE-LIMITING SAFETY SYSTEMS
 - 10-3.3 SAFETY INSTRUMENTATION
- 10-4 SPECIAL STUDIES
 - 10-4.1 CRITERIA, CODES, AND STANDARDS
 - 10-4.2 PROBABILISTIC EVALUATION
 - 10-4.3 DISSEMINATION OF INFORMATION
- 10-5 SAFETY FACILITIES
 - 10-5.1 ANALYSIS OF FACILITY REQUIREMENTS
 - 10-5.2 STEADY-STATE REACTOR FACILITIES
 - 10-5.3 TRANSIENT REACTOR FACILITIES
 - 10-5.4 STF (SAFETY TEST FACILITY)
 - 10-5.5 ETF (EXCURSION TEST FACILITY)

Table XX.2

C. Development Program Details

With that as background, the remainder of the lecture will be concerned with what specific programs are in progress throughout the U.S. with relevance to the FFTF safety performance, a brief description of these programs, and specifically how each of these programs is related to the FFTF.

For convenience, the programs are categorized under the major areas of safety development for the FFTF as shown in Table XX.3.

Table XX.3 - *Major Areas of Safety Development for the FFTF*

1. LOCAL FAULT PROPAGATION

(a) Fuel Element Failure Propagation

- (1) ANL Fuel Element Failure Propagation Program
- (2) ORNL Fuel Failure Mockup Program
- (3) BNW Fast Reactor Thermal Hydraulics

(b) Fuel Failure Propagation

- (1) ANL Coolant Dynamics Program
- (2) ANL Violent Boiling Program
- (3) AI Boiling Studies for Reactor Safety
- (4) ANL Fuel Meltdown Studies in TREAT
- (5) ANL Accident Analysis Model
- (6) GE PA-10 Task B - Defected Fuel Behavior
- (7) GE PA-10 Task C - Safety Experimentation
- (8) GE PA-10 Task G - Core Neutronics, Thermal Hydraulics, and Safety Analysis
- (9) BNW LMFBR Fuel Performance Testing and Analysis
- (10) BNW Core Development and Analysis
- (11) BNW LMFBR Materials Technology
- (12) Fuel and Assembly Structural Response

Table XX.3 - *Major Areas of Safety Development for the FFTF*
(cont'd)

2. TOTAL CORE DISTURBANCES

(a) Coolant Flow Disturbance

- (1) BNW Fast Reactor Thermal Hydraulics
- (2) Post-Accident Cooling - Intact Core

(b) Core Reactivity Disturbance

- (1) GE PA-10 Task C - Safety Experimentation
- (2) ANL Fuel Meltdown Studies in TREAT
- (3) BNW LMFBR Fuel Performance Testing and Analysis
- (4) Fuel Motion Within Pin

3. HYPOTHETICAL ACCIDENT STUDIES

(a) Core Response to Postulated Conditions

- (1) ANL Accident Analysis Model
- (2) BNW Core Development and Analysis
- (3) GE PA-10 Task G - Core Neutronics, Thermal Hydraulics, and Safety Analysis

(b) Core Disassembly Analysis

- (1) ANL Accident Analysis Model
- (2) BNW Core Development and Analysis
- (3) ANL Materials Behavior Equation of State and Energy Transfer

(c) Energy Evaluation and Partition

- (1) GE PA-10 Task G - Core Neutronics, Thermal Hydraulics, and Safety Analysis
- (2) BNW Core Development and Analysis

(d) Post-Disassembly Analyses

- (1) ANL Safety Features Technology -- Containment
- (2) BNW Safety Analysis
- (3) BNW Fast Reactor Safety Development

Table XX.3 - *Major Areas of Safety Development for the FFTF*
(cont'd)

(d) Post-Disassembly Analyses (cont'd)

- (4) ANL Post-Accident Heat Removal
- (5) AI Characterization of Sodium Fires
and Fission Products
- (6) BNL Chemical Reaction-Fission Product Release in Sodium
- (7) ORNL High Temperature Behavior of Gas-Borne
Fission Products

4. PROTECTIVE SYSTEM - DETECTION AND RESPONSES

(a) Onset of Boiling

- (1) ANL Coolant Dynamics
- (2) Wave Guide Development

(b) Fuel Failure Detection

- (1) BNW FEDAL Development

(c) Entrained Gas in Coolant

- (1) ANL Coolant Dynamics

1.(a)(1) ANL FUEL ELEMENT FAILURE PROPAGATION PROGRAM

OBJECTIVE

The major objectives of this program are as follows:

- Obtain test data on element-to-element propagation under normal or near-normal operation - determine thresholds
- Develop analytical descriptions for various phenomena
- Develop capability for performing in-reactor tests related to FEFP.

DESCRIPTION

This program is divided into four major task details:

- Program planning and test facility feasibility studies
- Out-of-reactor studies
- In-reactor studies
- Analytical studies.

The sequence of failure events relative to propagation as developed by ANL is described in Figure XX.2. This program assumes the initiating event under normal or near-normal operating conditions and is primarily concerned with evaluation of the modes of failure transport. The out-of-reactor experiments consist of various single and multiple pin tests, heated and unheated, in flowing water and sodium loops to evaluate the thermal and mechanical transport phenomena. The in-reactor experiments will investigate the characteristics of planned fuel failures within a package loop in ETR. The general arrangement is shown in Figure XX.3.

STATUS

Out-of-reactor experiments are in process. These tests are characterizing the modes of failure transport assuming three categories of fission gas release: (a) Rapid release (single slug ejection), (b) Gas jet impingement, (c) Low release (two-phase flow effects).

The in-reactor experiments are not expected to begin until late FY-1972.

FFTF SUPPORT

Data on effects of fission gas release are directly applicable to FFTF.

In addition to characterization of fuel failure modes and transport, the in-reactor tests should also give data relevant to fission product release and deposition throughout the loop.

1.(a)(2) ORNL FUEL FAILURE MOCKUP PROGRAMOBJECTIVE

Development of a flowing sodium loop for thermal-hydraulic testing of multiple-pin assemblies under normal and abnormal conditions.

DESCRIPTION

Loop description (see Figures XX.4 and XX.5).

Power to test section:	475 kW
Sodium outlet temperature:	1200 °F
Pump flow capacity:	500 gpm
Number of pins:	19-217 internally resistance heated.

The loop is intended to investigate fuel element failure propagation scaling factors (large bundle) and various initiating occurrences, e.g., various planned flow blockages (bowing, swelling, foreign material).

STATUS

Under construction. Calibration tests fourth quarter FY-1970.

FFTF SUPPORT

Phase I testing program will be 19 and 217-pin bundles with FFTF geometry to investigate subchannel blockages with foreign material and broken wires.

1.(a)(3) BNW FAST REACTOR THERMAL HYDRAULICS

OBJECTIVE

The objective of this program is to evaluate the thermal-hydraulic characteristics of FFTF fuel pin assemblies under normal and distorted geometries. In addition, the thermal consequences of various assumed accident conditions will also be investigated.

DESCRIPTION

Thermal-hydraulic investigations will be performed in two flowing sodium loops with internally heated pin bundles:

- Small heat transfer loop (lower floor 324 Bldg.)
(50 gpm, 7 pins, 300 kW)
- Fast Reactor Thermal Engineering Facility
(175 gpm, 7-39 pins, 1500 kW)

The SHTL will be used to study edge effects under normal geometry. The effects of distorted geometries (loose wire, bowed pins, spirally deformed pins) will also be investigated. A seven-pin bundle for SHTL is shown in Figure XX.6 with bowed pin geometry. The FRTEF will investigate voiding initiation from blockage or loss-of-flow conditions, accidents (e.g., high void effects, emergency cooling characteristics), and operational limit tests. The 39-pin bundle geometry is shown in Figure XX.7.

STATUS

SHTF began operational testing fourth quarter FY-1969.

FRTEF scheduled for third quarter FY-1971.

FFTF SUPPORT

All tests are direct support of FFTF.

1.(b)(1) ANL COOLANT DYNAMICS PROGRAMOBJECTIVE

Perform experiments and develop analytical models characterizing sodium superheat, sodium expulsion and voiding, liquid-coolant dynamics (critical flow measurements), and coolant reentry.

DESCRIPTION

This work is divided into five major task details.

- Sodium superheat - Static and dynamic (Transient Test Loop) incipient boiling experiments to evaluate effects of pressure, temperature, surface conditions, entrained gases on superheat.
- Sodium expulsion - Evaluation of transient convective flow and heat transfer and sodium expulsion under static and forced convection conditions on vapor growth rates, expulsion, and reentry. Figure XX.8 shows the results of one static test.
- Liquid-vapor dynamics - Evaluation of two-dimensional void-time measurements in nonmetallics for better understanding of bubble growth, collapse, critical flow.
- Sodium simulations - Application of Freon-11 static tests to evaluate phenomena of expulsion, flake-off, and reentry. Figure XX.9 shows expulsion progressing from nucleation site.
- Mathematical models of voiding and reentry.

STATUS

The Transient Test Loop is under construction. Boiling from surface cavities in TREAT test FY-1971. Freon-11 tests now going to single and multiple pin geometry.

FFTF SUPPORT

This work is all directly applicable to voiding models and reentry effects now assumed in the hypothetical accident studies.

1.(b)(2) ANL VIOLENT BOILING PROGRAMOBJECTIVE

Perform experiments and develop analytical models describing interactions of materials under violent mixing conditions.

DESCRIPTION

This work is divided into four major task details:

- Particle heat transfer - This task is to study heat transfer rates between fragmented (or molten) fuel and coolant. Experiments include transient heat transfer (swinging pendulum in sodium) and transient boiling studies (dropping hot spheres into sodium).
- Violent boiling with molten fuel and sodium - Evaluation of explosive pressure pulses from contact of molten fuel and sodium. Task consists of (a) fragmentation and mixing studies and (b) violent boiling and pressure generation upon contact of molten material, e.g., a water drop experiment in TREAT (see Figure XX.10) where plunger will allow water column to fall onto molten UO_2 .
- Simulations of fuel dispersal - In-reactor experiments with fuel heated beyond melting point in static sodium environment (piston autoclave experiments). Experiments are for evaluation of interactions and effects during nuclear transients. Figure XX.11 shows the fuel pin configuration (5 fueled, 4 dummies) and Figure XX.12 shows the autoclave testing assembly.
- Mathematical models of fuel-coolant dynamics.

STATUS

Swinging pendulum experiments into sodium to begin third quarter FY-1970.

Dropping multiple spheres into sodium ~third quarter FY-1971.

Autoclave experiments S2, S3, S4 run. Next run with evacuated pins planned for 1/70.

FFTF SUPPORT

Data are directly applicable in substantiating or changing present assumed models being applied in the FFTF hypothetical accident studies.

1.(b)(3) AI BOILING STUDIES FOR REACTOR SAFETY

OBJECTIVE

Perform experiments and develop models for sodium superheat and voiding simulations.

DESCRIPTION

- Boiling studies - Evaluation of superheat variables under flowing conditions
- Voiding simulation - Development of TRANS FUGUE I and II (no slip).

1.(b)(4) ANL FUEL MELTDOWN STUDIES IN TREAT

OBJECTIVE

Performance of fuel meltdown tests in TREAT to evaluate fuel failure thresholds and modes of failure with defected (sodium logged) fuel.

DESCRIPTION

- Checkout runs - Development and checkout of the Mark II test assembly (flowing sodium capsule for TREAT transient testing) Figure XX.13 shows this assembly.
- Sodium logged fuel tests - Transient tests in transparent capsules and sodium assembly to evaluate effects of logging on transient performance.

STATUS

Two checkout tests are now completed.

Sodium logged experiments with unirradiated fuel are planned.

Transparent tests should begin soon.

FFTF SUPPORT

Characterization of the performance of sodium logged fuel in FFTF is dependent upon these tests.

1.(b)(5) ANL ACCIDENT ANALYSIS MODELOBJECTIVE

Development of a complete accident analysis system for describing the transient progression of an accident given some initiating mechanism.

DESCRIPTION

The mathematical models developed under each related program, i.e., coolant dynamics, violent boiling, FEFP, meltdown studies, are to be integrated into an overall accident analysis system.

STATUS

Various modules of the SAS system are operational, e.g., fuel failure models, core neutronics, etc., and are applicable to present accident analysis studies. A coolant voiding model is scheduled to be incorporated about October, 1969.

FFTF SUPPORT

This program has already been used in various accident analyses for the FFTF.

1.(b)(6) GE PA-10 TASK B - DEFECTED FUEL BEHAVIOR

OBJECTIVE

Determine the consequences of fuel defects on performance and propagation, including evaluation of interactions and radioactivity release.

DESCRIPTION

Forced convection capsule development and tests in GETR. Looking at long-term effects of sodium-bonded fuel. Developing means of actuating a defecting device during in-reactor operation to evaluate consequences.

1.(b)(7) GE PA-10 TASK C - SAFETY EXPERIMENTATION

OBJECTIVE

Characterize the behavior of fuel under accident conditions.

DESCRIPTION

- Series 6 - Defected or sodium-bonded fuel experiments - Evaluate comparative transient characteristics of normal fuel, sodium-bonded pellet fuel pin, and sodium-bonded powder fuel pin.
- Series 10 - Loss-of-flow tests - Evaluation of the effects of loss of flow to an in-reactor test element in a forced convection capsule (FCC) in GETR. Parameters include rate of flow decay, scram delay, and fuel characteristics. Test may investigate coolant expulsion and reentry.
- C10X Capsule - Evaluation of the effects of contact of hot fuel/cladding with sodium. Plan to initiate action by a piston-driven punch.

STATUS

Series (10) and C10X capsule test are being planned.

FFTF SUPPORT

FFTF Project may specify flow decay rate and scram time after initial checkout of the loss-of-flow test and thus simulate flow coastdown and possibly pipe rupture accident conditions.

1.(b)(8) GE PA-10 TASK G - CORE NEUTRONICS, THERMAL-HYDRAULICS,
AND SAFETY ANALYSIS

OBJECTIVE

Provide analytical support and guidance for the experimental programs and to develop analytical models for the responses under accident conditions.

DESCRIPTION

The subtask related to fuel failure propagation is related to the molten fuel-sodium duct interaction study performed under contract for the FFTF Project. This task is investigating the energy (acoustic and inertial) available to do work on the surrounding structure and the energy containing capability of the duct wall. Figures XX.14 and XX.15 show results from the FFTF study which will now be continued under Task G.

STATUS

Initial work for FFTF Project is completed (assumes instantaneous loss-of-flow to a single fuel assembly). Work under Task G just beginning.

FFTF SUPPORT

This effort is directly applicable to FFTF evaluation of fuel sodium interactions and energy evaluations.

1.(b)(9) BNW LMFBR FUEL PERFORMANCE TESTING AND ANALYSIS

(Reference: Lecture No. X)

OBJECTIVE

Verification of the safety margins provided in the FFTF fuel design.

DESCRIPTION

Irradiated fuel pins (GETR and EBR-II) will be transient tested in TREAT to evaluate overpower transient performance up to 20% and 50% areal melting and cladding temperatures to 1300 °F and 1600 °F. In addition, fuel pins will be recycled to evaluate overpower effects on subsequent performance and runs to failure will be made to evaluate lifetimes and modes of failure.

STATUS

Transient checkout runs initiated.

FFTF SUPPORT

Direct for FFTF.

1.(b)(10) BNW CORE DEVELOPMENT AND ANALYSIS

(Reference: Lectures Nos. IX, XVII)

OBJECTIVE

Develop analytical models for coolant dynamics and fuel-sodium interactions under postulated accident conditions.

DESCRIPTION

The details of these development efforts applicable to characterization of assembly response and propagation under various postulated accident conditions are described in the referenced lectures.

1.(b)(11) BNW LMFBR MATERIALS TECHNOLOGY

OBJECTIVE

Evaluate materials properties data applicable under simulated accident conditions.

DESCRIPTION

One aspect of this program includes evaluation of the properties of stainless steel under high strain rate uniaxial loading conditions. These data are required to evaluate the capability of the duct wall to effectively isolate internal accident conditions from surrounding assemblies.

STATUS

Data are being generated for strain rates from 0.1-10 in./in./sec and temperatures to 1600 °F on unirradiated material. Depending on funding, tests will be run to 100 in./in./sec and irradiated material included.

FFTF SUPPORT

This effort is being performed for FFTF.

1.(b)(12) FUEL ASSEMBLY STRUCTURAL RESPONSE

OBJECTIVE

Evaluate thresholds for initiating failures in adjacent assemblies by mechanical effects generated within the affected assembly.

DESCRIPTION

- Pin deflection tests - Evaluate the effect of wire wrap on threshold of cladding failures initiated by pin bundle deflection tests.
- Duct deflection - Evaluate resistance of ducts to flexure.
- Duct explosive test - Evaluate resistance of the duct wall to acoustic and pressure loadings in terms of both strain and rupture.

STATUS

Nonexistent.

FFTF SUPPORT

These data are needed to evaluate resistance against propagation in FFTF fuel assemblies.

2.(a)(1) BNW FAST REACTOR THERMAL HYDRAULICS
(See item 1.(a)(3))

OBJECTIVE

Evaluate core response to total core flow disturbances including accident and emergency cooling conditions.

DESCRIPTION

The Fast Reactor Thermal Engineering Facility (FRTEF) will be used to evaluate thermal consequences of high void conditions and phenomena under natural convective cooling conditions. In addition, the inlet/outlet feature models will be used to evaluate characteristics of large gaseous bubbles within the primary system. Figure XX.16 shows pictorially gaseous bubble tests run in the inlet feature model where gas has been introduced by filling the downcomer with air (point #1) and also by direct introduction of air within the basket (point #2).

STATUS

Feature model tests are in process.

FFTF SUPPORT

Direct for FFTF.

2.(a)(2) POST-ACCIDENT COOLING - INTACT CORE

OBJECTIVE

Evaluate post-accident conditions of the core assuming that it essentially remains intact and determine cooling characteristics to prevent further damage.

DESCRIPTION

Evaluate cooling requirements and potential performance under post-accident conditions -- even though many of the normal flow channels are disturbed.

STATUS

Nonexistent.

FFTF SUPPORT

Direct support of FFTF safety studies.

2.(b)(1) GE PA-10 TASK C - SAFETY EXPERIMENTATION

(See Item 1.(b)(7))

OBJECTIVE

Characterize the behavior of fuel under accident conditions.

DESCRIPTION

- Series 4 - Axially restrained fuel - Evaluating transient overpower performance of fuel as a function of smeared density, burnup, areal melting. Also, planning to evaluate effect of sodium voiding and propagation to simulated adjacent pins in TREAT.
- Series 5 - Axial fuel relocation - Evaluating effects of holes penetrating blanket regions on transient performance of irradiated fuel pins.

STATUS

Tests without holes in blanket failed whereas pins tested under identical conditions but with central holes survived.

FFTF SUPPORT

Successful completion of those programs could potentially indicate a method of incorporating an inherent shutdown feature by assuring that fuel squirts out if melting occurs.

2.(b)(2) ANL FUEL MELTDOWN STUDIES IN TREAT

(See item 1.(b)(4))

OBJECTIVE

Performance of fuel meltdown tests in TREAT to evaluate fuel failure thresholds and modes of failure with prototypic fast reactor fuel pins -- zero burnup and irradiated -- under overpower and loss-of-flow conditions.

DESCRIPTION

- UO₂ experiments (General LMFBR) -- described under item 1.(b)(4)
- Mixed oxide tests -- transient tests on DFR (U.K.) pins
- Variables are smeared density (70-80%), cold-worked or annealed cladding, irradiation (7 pins @ 4-7.3 at.-% burnup and 66 unirradiated pins)
- Transient coolant behavior

Tests will be run in the Mark II assembly described in item 1.(b)(4).

STATUS

Tests are scheduled to begin FY-70 and be completed FY-72.

FFTF SUPPORT

The DFR irradiated pins represent the entire program for testing long pins irradiated in a fast flux environment.

2.(b)(3) BNW LMFBR FUEL PERFORMANCE TESTING AND ANALYSIS

(See item 1.(b)(9))

OBJECTIVE

Verification of the safety margins provided in the FFTF fuel design.

DESCRIPTION

Irradiated fuel pins (GETR and EBR-II) will be transient tested in TREAT to evaluate overpower transient performance up to 20% and 50% areal melting and cladding temperatures to 1300 °F and 1600 °F. In addition, fuel pins will be recycled to evaluate overpower effects on subsequent performance and runs to failure will be made to evaluate lifetimes and modes of failure.

Additional tests will evaluate restrictor characteristics, but otherwise same as described previously.

2.(b)(4) FUEL MOTION WITHIN PIN

OBJECTIVE

Evaluate motion of molten or partially molten fuel with the cladding just prior to and following failure of the cladding.

DESCRIPTION

In-reactor experiments to evaluate the effects of fission gas release and plenum pressures on motion of fuel during overpower transient conditions.

STATUS

No programs are set up to evaluate this effect. Post-transient evaluation of the debris distribution indicates where materials located finally but does not indicate the transient consequences.

FFTF SUPPORT

Direct application in hypothetical accident analyses for the FFTF.

3.(a)(1) ANL ACCIDENT ANALYSIS MODEL

(See item 1.(b)(5))

OBJECTIVE

Develop core response model for overpower and loss-of-flow transients of magnitude leading to core disassembly conditions.

DESCRIPTION

Development of SAS-1A program which looks at a single pin and characterizes total core response under extreme accident conditions. Program includes three fuel failure models: (a) fuel-cladding interference, (b) fuel hydrodynamic model (considers plasticity of fuel during transient), (c) fission gas release model. In each case failure depends on cladding strain.

STATUS

Operational and applied in FFTF DBA studies.

FFTF SUPPORT

SAS has been applied in parallel analyses for the FFTF hypothetical accident analyses.

3.(a)(2) BNW CORE DEVELOPMENT AND ANALYSIS

(Reference: Lecture No. XV)

OBJECTIVE

Develop core response model with provision for noncoherence in both radial and axial dimensions for overpower and loss-of-flow transients of magnitude leading to core disassembly conditions.

DESCRIPTION

This program has been described in detail in lecture No. XV. The code, MELT-II, has been developed which characterizes the fuel conditions in each of up to 10 radial rings by a detailed model of a typical pin in that ring. Both MELT-II and SAS-1A divide the axial dimension into many nodes to simulate axial power distribution and fuel movement in detail. MELT-II, with 10 radial nodes simulates radial power distributional effect in more detail than does SAS, but does not contain as extensive detail within the fuel pin, e.g., MELT-II does not contain the several fuel failure sub-routines in SAS-1A. Therefore, these two programs are complementary to some extent.

STATUS

MELT-II has been used extensively in the FFTF hypothetical accident analyses.

FFTF SUPPORT

Direct support of the FFTF studies.

3.(a)(3) GE PA-10 TASK G - CORE NEUTRONICS, THERMAL HYDRAULICS AND SAFETY ANALYSIS

(See item 1.(b)(8))

OBJECTIVE

Similar to the related programs at ANL and BNW (3.(a)(1) and 3.(a)(2)).

DESCRIPTION

GE is developing a code similar to MELT-II and SAS-1A and called FREADM (Fast Reactor Excursion and Accident Dynamics Model). Some of the features included in FREADM are transient power, heat transfer, sodium voiding, coolant flow, fuel redistribution, and failure propagation.

STATUS

Under development.

FFTF SUPPORT

None to date.

3.(b)(1) ANL ACCIDENT ANALYSIS MODEL

OBJECTIVE

Development of a model incorporating core hydrodynamics for analysis of the core disassembly phase under hypothetical accident conditions.

DESCRIPTION

ANL has been developing a disassembly code called VENUS with cylindrical geometry and Lagrangian coordinate system (moveable nodal system). Implosion effects can be evaluated with this flexible system since material can move in any direction dependent upon the pressure gradients.

STATUS

The SAS-1A system at the present time incorporates the APDA MARS code for disassembly calculations.

Some runs have been made directly on VENUS by Westinghouse in the FFTF studies.

FFTF SUPPORT

VENUS has been adapted to perform the FFTF disassembly calculations and is being used in the present studies.

3.(b)(2) BNW CORE DEVELOPMENT AND ANALYSIS

(Reference: Lecture No. XVI)

OBJECTIVE

Development of a model incorporating core hydrodynamics for analysis of the core disassembly phase under hypothetical accident conditions.

DESCRIPTION

The MAX disassembly code was developed at BNW for the initial FFTF hypothetical accident studies. MAX incorporated a Lagrangian coordinate system to allow movable mesh points and also was instrumental in evaluation of the consequences of sodium in the core region at the instant of disassembly along with those calculations which assume sodium-out. However, the difficulty of transfer from MELT-II to MAX due to the different assumed geometries (cylindrical MELT-II and spherical MAX) led to adaptation of VENUS for later calculations.

STATUS

VENUS is now fully adapted for the FFTF disassembly calculations.

FFTF SUPPORT

This work is all directly applicable to the FFTF.

3.(b)(3) ANL MATERIALS BEHAVIOR EQUATION OF STATE AND ENERGY TRANSFER

OBJECTIVE

Evaluation of the materials properties and equation of state for fuel, cladding, and coolant materials under conditions applicable to maximum hypothetical-type accidents.

DESCRIPTION

This work is concerned with the establishment of EOS and high temperature properties of the core materials for application in these studies. Both analytical and experimental studies are included with this task area.

STATUS

These are continuing research programs.

FFTF SUPPORT

At the present time, the materials properties have had to be estimated in the disassembly studies for conditions near or above the critical points. As empirical data become available these predicted data will be adjusted.

3.(c)(1) GE PA-10 TASK G - CORE NEUTRONICS, THERMAL-HYDRAULICS, AND SAFETY ANALYSIS

(See item 1.(b)(8))

OBJECTIVE

Provide analytical support and guidance for the experimental programs and to develop analytical models for the responses under accident conditions.

DESCRIPTION

One subtask under Task III of contract BDR-341 was concerned with evaluation of the fuel sodium interaction and partitioning of the work energy resulting from the interaction. While these studies were specifically oriented toward the single assembly accident and propagation, the analytical techniques developed for the fuel-sodium interaction are applicable to post-disassembly studies.

STATUS

Now being initiated under Task G of PA-10.

FFTF SUPPORT

This work is directly applicable as a parallel program to the BNW studies.

3.(c)(2) BNW CORE DEVELOPMENT AND ANALYSIS

(Reference: Lecture No. XVII)

OBJECTIVE

Develop methods of analysis for evaluation of the energy available to do work and partitioning of that energy, between acoustic and inertial, given the core material conditions at the instant of core disassembly.

DESCRIPTION

The BNW studies have been looking primarily at sodium as the working fluid since it theoretically is capable of doing more work on the surrounding structures than the fuel. However, realistic evaluation requires calculation of the transient aspects of heat transfer from the fuel to the coolant throughout the expansion process since the available work is limited by this heat transfer process.

STATUS

The present analyses have assumed various thermodynamic paths for the expansion process. Calculations are now including heat transfer effects to define the most efficient path available for a given size fuel particle. These studies are continuing.

FFTF SUPPORT

These studies are all in direct support of the FFTF.

3.(d)(1) ANL SAFETY FEATURES TECHNOLOGY - CONTAINMENT

OBJECTIVE

Develop techniques for evaluation of the hydrodynamic structural response to a high-energy core disassembly transient.

DESCRIPTION

This work has centered around development of a two-dimensional computer code for evaluation of the primary containment response to some high energy release in the core region. The core conditions at the instant of disassembly are the input conditions for the code which features: (a) EOSs for the various materials, (b) energy partitioning, (c) material motion (Lagrangian coordinates), (d) vessel break or not, and (d) plug loading evaluation. The program gives pressures, energies, and strains as the pressure wave propagates from the core. Output of one run is shown in Figure XXI.17 which shows the structural deformations during the first 811μ sec. (This run took ~68 minutes of computer time.)

STATUS

FFTF SUPPORT

This work is being adapted for FFTF studies and may be particularly relevant in evaluation of loads at the instant of sodium slug impact on the cover.

3.(d)(2) BNW SAFETY ANALYSIS

(Reference: Lectures Nos. XVIII and XIX)

OBJECTIVE

Evaluate the consequences of disassembly-type accidents upon the primary heat transport and inner containment systems. This task looks at both the immediate dynamic effects, work energy on the various structures and sodium fires, and the longer-term consequences of ultimate fuel heat removal and containment.

DESCRIPTION

This work was described in lectures XVIII and XIX. Lecture XVIII described the development of ASPRIN for evaluation of coolant slug effects and lecture XIX covered sodium fires and post-accident heat removal.

STATUS

See referenced lecture

FFTF SUPPORT

This work is all in direct support of the FFTF studies.

3.(d)(3) BNW FAST REACTOR SAFETY DEVELOPMENT

OBJECTIVE

Perform experiments to evaluate the sodium slug impact phenomena when the slug strikes the top cover.

DESCRIPTION

This proposed task will consist of a series of explosive model tests to evaluate sodium impact effects on the top cover. These data will be used to: (a) verify the ASPRIN model, (b) verify the structural integrity of the FFTF top cover under these load conditions, (c) determine stress distributions as a function of slug velocities, and (d) evaluate quantity of coolant ejected from the primary vessel under these conditions.

STATUS

This work has not yet been approved by RDT.

FFTF SUPPORT

Direct support of the FFTF hypothetical accident studies.

3.(d)(4) ANL POST-ACCIDENT HEAT REMOVAL

OBJECTIVE

Perform analyses and experiments to evaluate geometry changes due to fuel meltdown (development of slumping models and evaluation of heat sources), study various devices for effective heat removal from the generating materials, evaluate pertinent material interactions, and perform in-core and out-of-core slumping tests.

DESCRIPTION

Not yet firm.

STATUS

This program is proposed to begin FY-1971.

FFTF SUPPORT

It is expected that this work would mesh directly with the post-accident studies for the FFTF as described in item 3.(d)(3).

- 3.(d)(5) AI CHARACTERIZATION OF SODIUM FIRES AND FISSION PRODUCTS
- 3.(d)(6) BNL CHEMICAL REACTION - FISSION PRODUCT RELEASE IN SODIUM
- 3.(d)(7) ORNL HIGH TEMPERATURE BEHAVIOR OF GAS-BORNE FISSION PRODUCTS

OBJECTIVE

All three of these tasks are concerned with characterization of the released fuel material and fission products during post-accident conditions.

DESCRIPTION

The AI studies involve the evaluation of aerosol behavior within a volume of ~ 100 meter³ and use sodium-UO₂ in the experiments.

The BNL studies involve PuO₂ aerosols, but are limited to glovebox-size due to the biological hazards of the material.

STATUS

FFTF SUPPORT

See lecture No. VI.

4.(a)(1) ANL COOLANT DYNAMICS PROGRAM

(See item 1.(b)(1))

OBJECTIVE

Perform experiments and develop analytical models characterizing sodium superheat, sodium expulsion and voiding, liquid-coolant dynamics (critical flow measurements), and coolant reentry.

DESCRIPTION

A spin-off of this program is development of acoustic detection devices. While these devices are important for data evaluation of the experiments, they also have potential as boiling detectors and/or detectors for entrained gases.

STATUS

FFTF SUPPORT

If fully developed, this instrument may have direct application as a detection device in the FFTF for boiling and entrained gas detection.

4.(b)(1) BNW FEDAL DEVELOPMENT

OBJECTIVE

Development of a means of detection and location of defected fuel in the FFTF prior to potential propagation of the defect.

DESCRIPTION

Development of a FEDAL (failed element detection and location) system has been underway for the FFTF. This involves evaluation of sensitivities by activity in the reactor vessel cover gas and by disengagement of released fission product gases at the outlet of each fuel assembly.

STATUS

Continuation of this program is questionable at the present time.

FFTF SUPPORT

Direct support of the FFTF program for detection and location of defected fuel.

4.(c)(1) ANL COOLANT DYNAMICS PROGRAM

OBJECTIVE

The primary objectives of this program have been described in the referenced sections. Experimental evaluation of coolant transient response requires detection of voiding initiation. Therefore, development of sensitive detection devices for onset of boiling is of necessity, a secondary objective of this program.

DESCRIPTION

ANL is developing an acoustic device for detection of extremely small void fractions in sodium. These devices measure the acoustic velocity in the fluid and it has been found that this velocity is quite sensitive to the level of entrained gases.

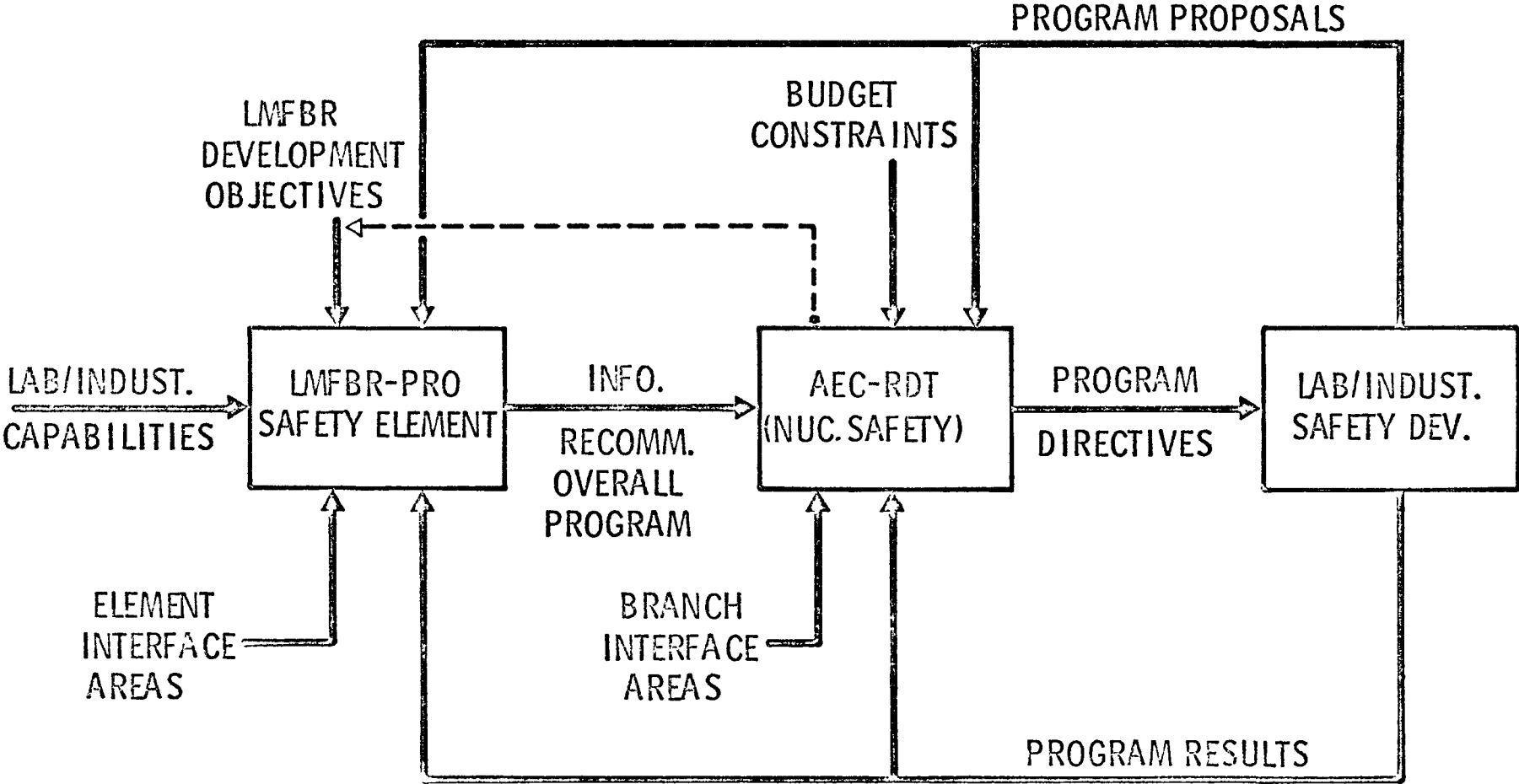
STATUS

This technique is still under development and only a laboratory device at present.

FFTF SUPPORT

This device does have a potential for detecting entrained gases which may be in transit and carried toward the core. One means of protection against the possibility of a coherent bubble pass-through is early detection and shutdown before the bubbles can affect reactivity.

LMFBR-PRO/RDT INTERACTIONS

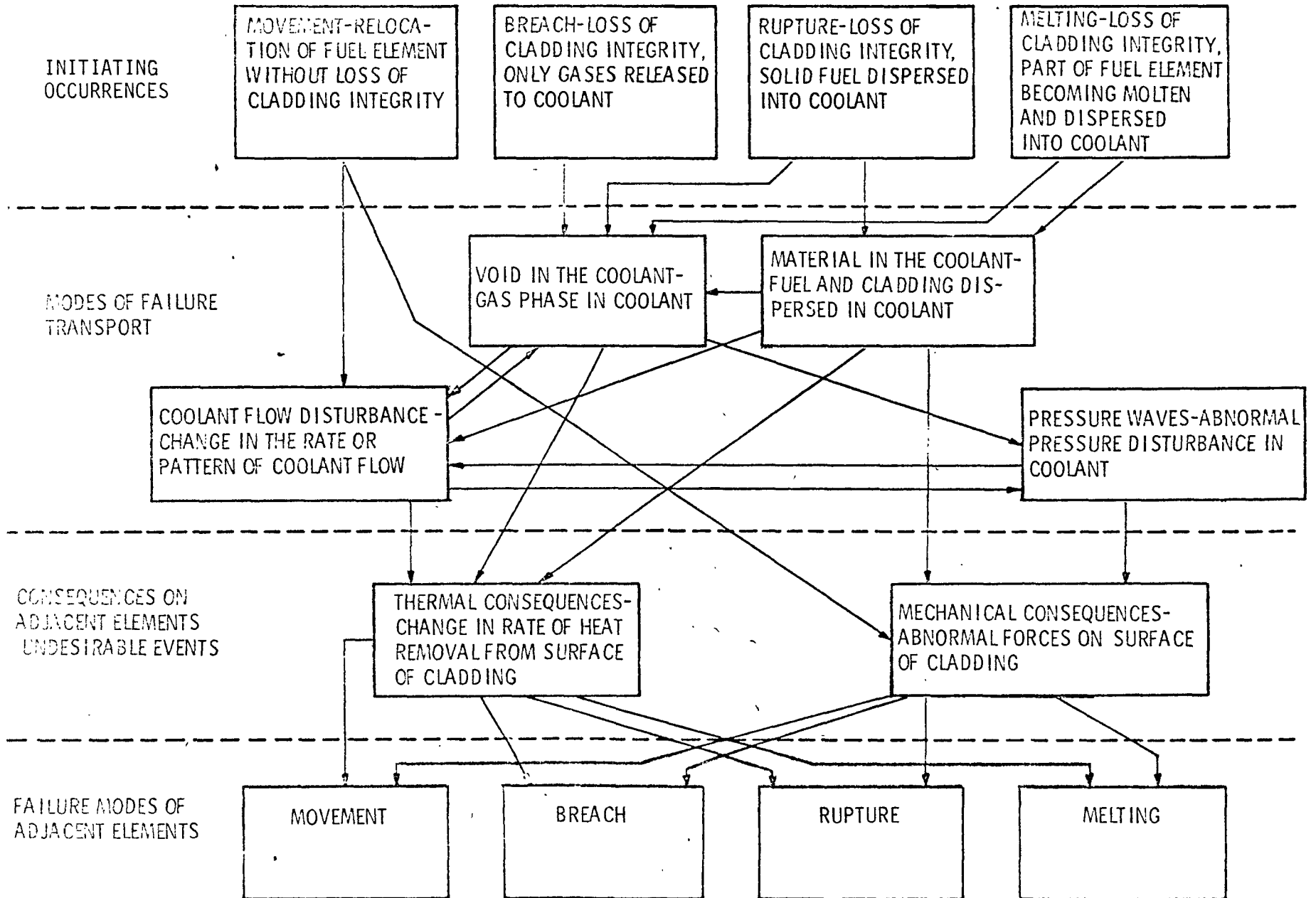


XX.48

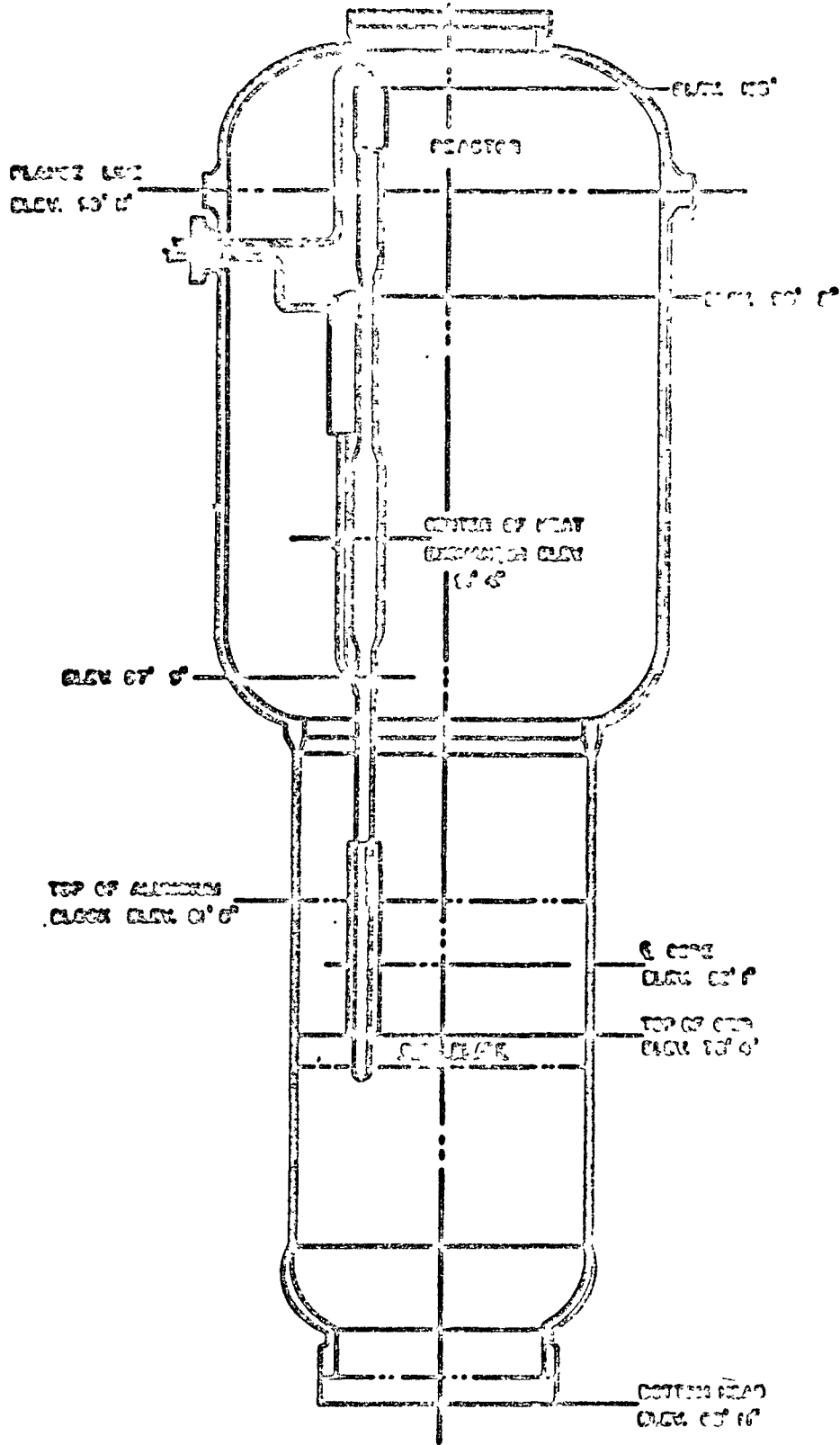
Fig. XX.1

Fig. XX.2

SEQUENCE OF EVENTS IN THE FAILURE PROPAGATION CHAIN



XX.50



LIFOR FUEL FAILURE PROPAGATION EXPERIMENT

GENERAL ARRANGEMENT

Fig. XX.3

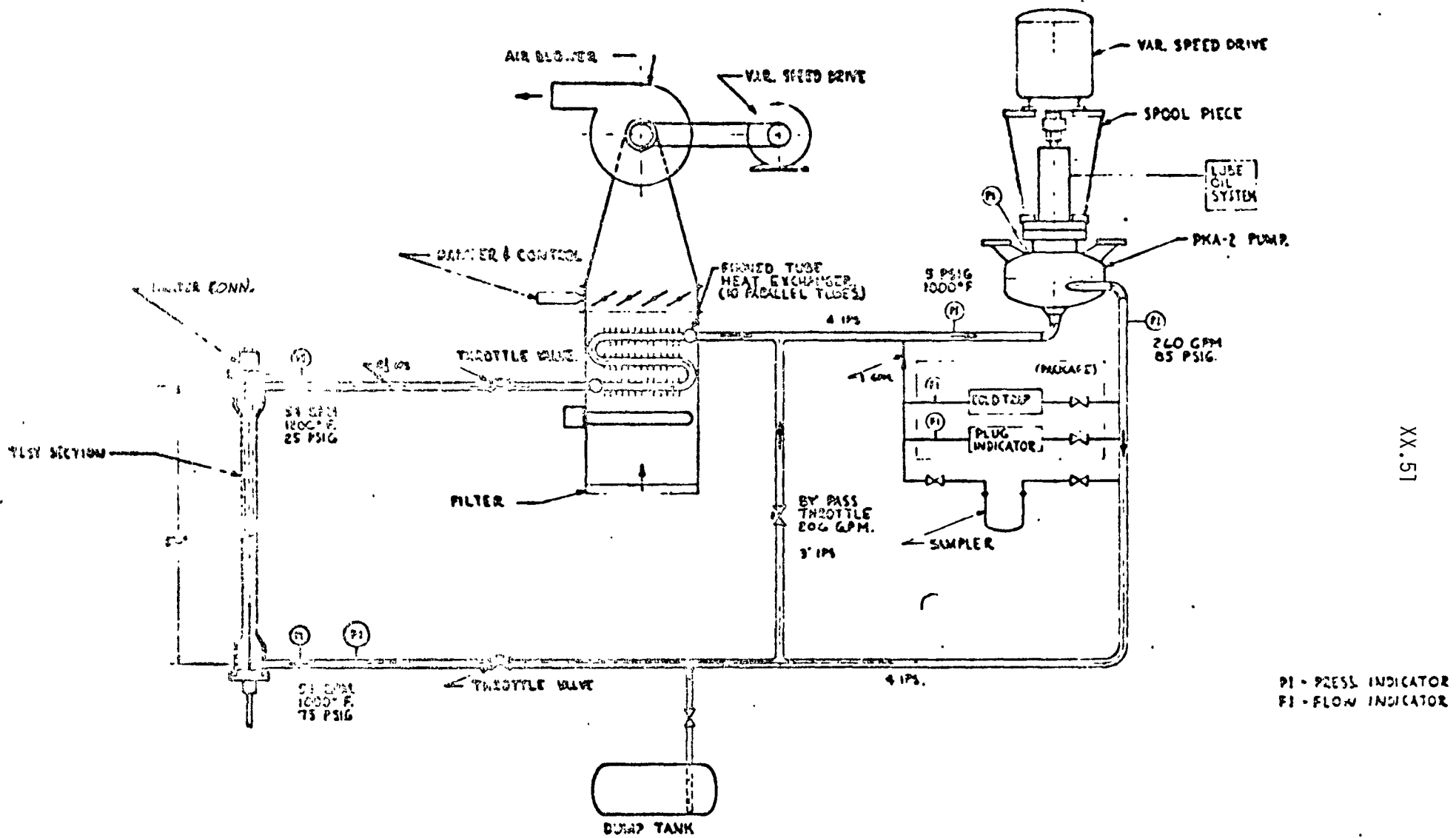
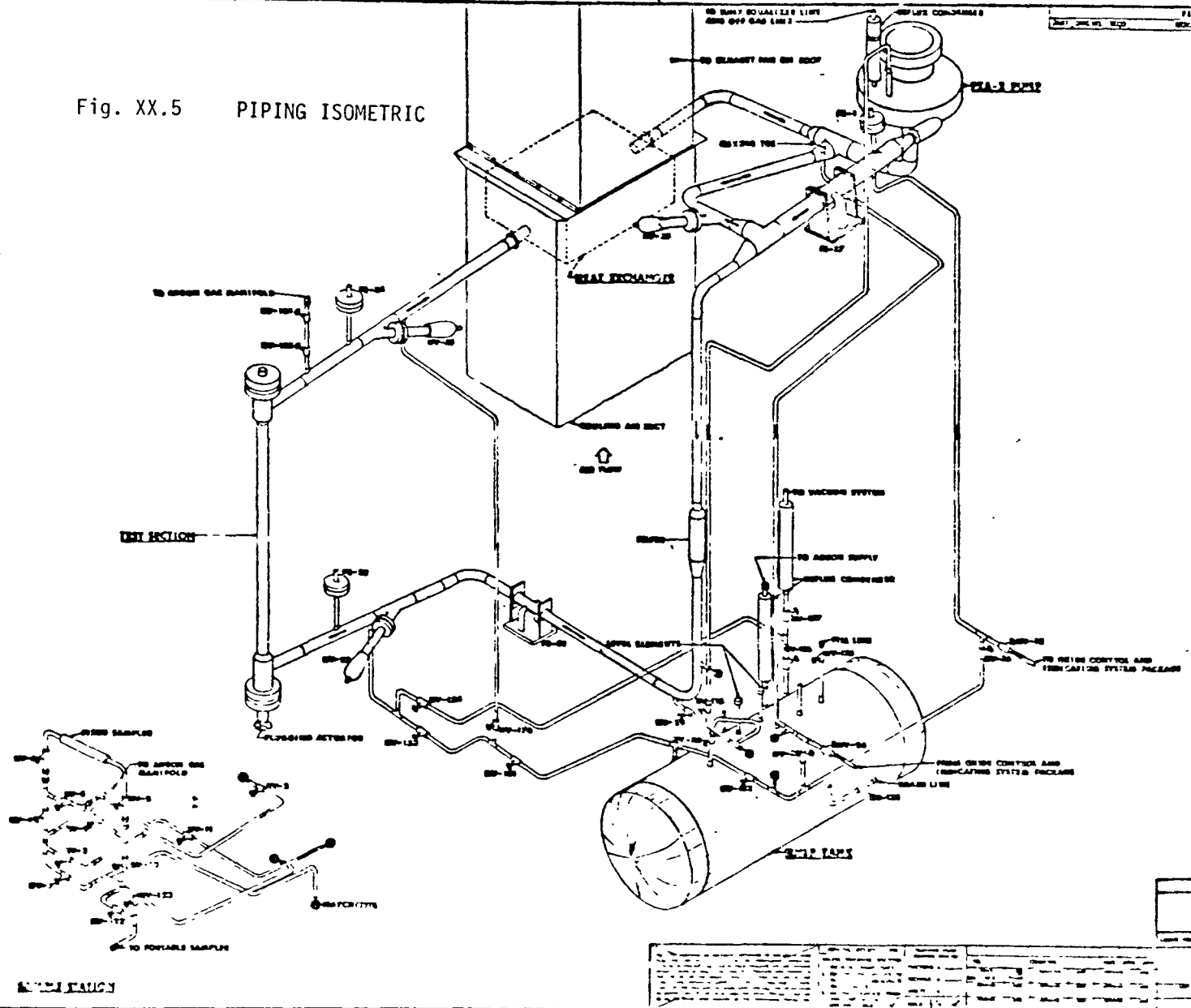


Fig. XX.4 Flow Diagram of FFM Facility.

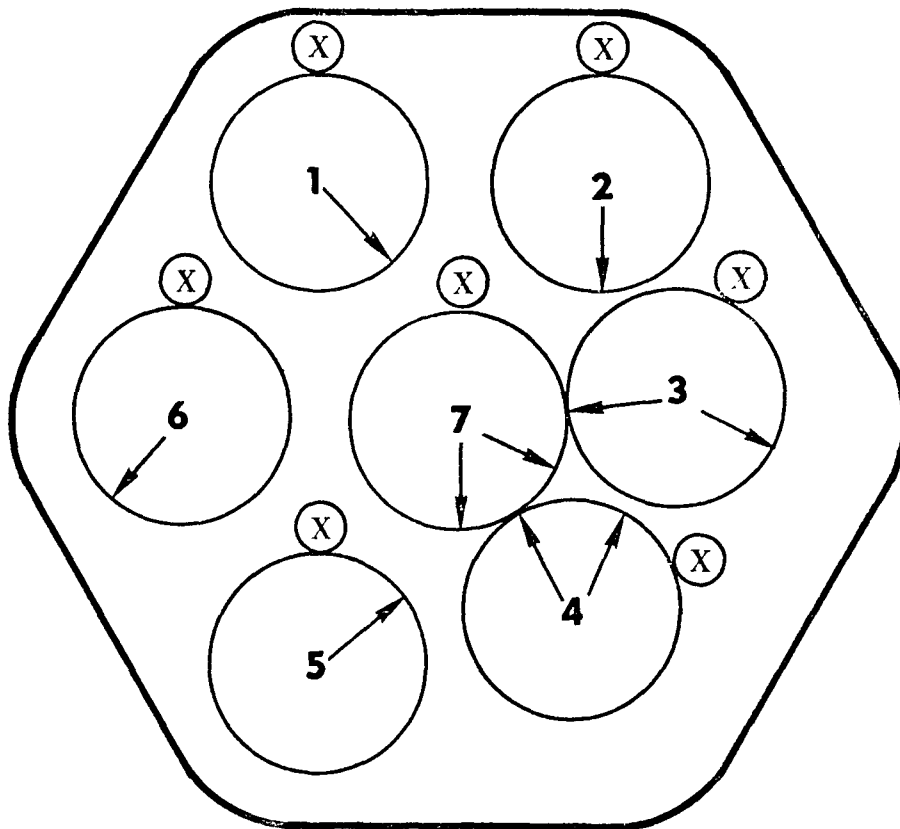
Fig. XX.5 PIPING ISOMETRIC



XX.52

REVISIONS	
NO.	DESCRIPTION
1	ISSUED FOR CONSTRUCTION
2	AS SHOWN
3	AS SHOWN
4	AS SHOWN
5	AS SHOWN
6	AS SHOWN
7	AS SHOWN
8	AS SHOWN
9	AS SHOWN
10	AS SHOWN
11	AS SHOWN
12	AS SHOWN
13	AS SHOWN
14	AS SHOWN
15	AS SHOWN
16	AS SHOWN
17	AS SHOWN
18	AS SHOWN
19	AS SHOWN
20	AS SHOWN
21	AS SHOWN
22	AS SHOWN
23	AS SHOWN
24	AS SHOWN
25	AS SHOWN
26	AS SHOWN
27	AS SHOWN
28	AS SHOWN
29	AS SHOWN
30	AS SHOWN
31	AS SHOWN
32	AS SHOWN
33	AS SHOWN
34	AS SHOWN
35	AS SHOWN
36	AS SHOWN
37	AS SHOWN
38	AS SHOWN
39	AS SHOWN
40	AS SHOWN
41	AS SHOWN
42	AS SHOWN
43	AS SHOWN
44	AS SHOWN
45	AS SHOWN
46	AS SHOWN
47	AS SHOWN
48	AS SHOWN
49	AS SHOWN
50	AS SHOWN
51	AS SHOWN
52	AS SHOWN
53	AS SHOWN
54	AS SHOWN
55	AS SHOWN
56	AS SHOWN
57	AS SHOWN
58	AS SHOWN
59	AS SHOWN
60	AS SHOWN
61	AS SHOWN
62	AS SHOWN
63	AS SHOWN
64	AS SHOWN
65	AS SHOWN
66	AS SHOWN
67	AS SHOWN
68	AS SHOWN
69	AS SHOWN
70	AS SHOWN
71	AS SHOWN
72	AS SHOWN
73	AS SHOWN
74	AS SHOWN
75	AS SHOWN
76	AS SHOWN
77	AS SHOWN
78	AS SHOWN
79	AS SHOWN
80	AS SHOWN
81	AS SHOWN
82	AS SHOWN
83	AS SHOWN
84	AS SHOWN
85	AS SHOWN
86	AS SHOWN
87	AS SHOWN
88	AS SHOWN
89	AS SHOWN
90	AS SHOWN
91	AS SHOWN
92	AS SHOWN
93	AS SHOWN
94	AS SHOWN
95	AS SHOWN
96	AS SHOWN
97	AS SHOWN
98	AS SHOWN
99	AS SHOWN
100	AS SHOWN

TEST ASSEMBLY INSTRUMENTATION FOR BOWED PIN TESTS

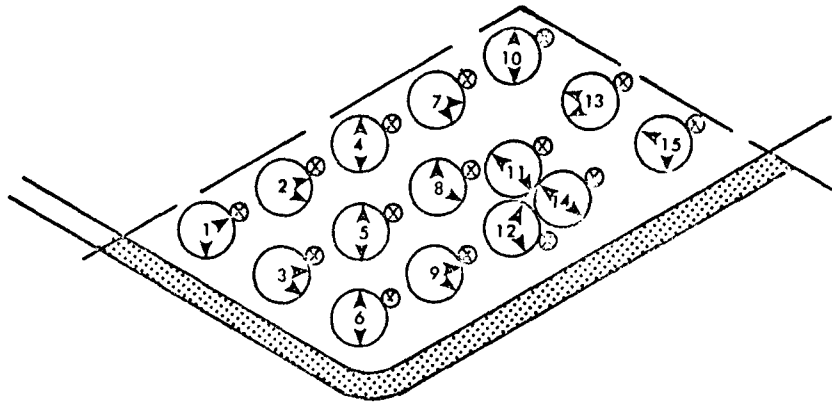


- NOTE:
- . ARROWS (\rightarrow) REPRESENT CLAD TEMPERATURE THERMOCOUPLES
 - . CROSSES (x) REPRESENT LOCAL COOLANT TEMPERATURE THERMOCOUPLES INSERTED IN WIRE WRAP SPACERS

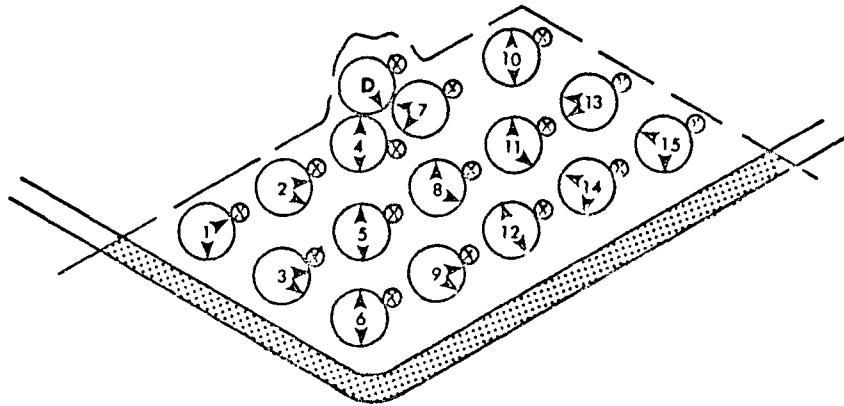
Fig. XX.6

TEST ASSEMBLY INSTRUMENTATION FOR FINAL PIN BOWING TESTS (39 PIN BUNDLE)

A. EDGE ROW BOWING (DETAIL)



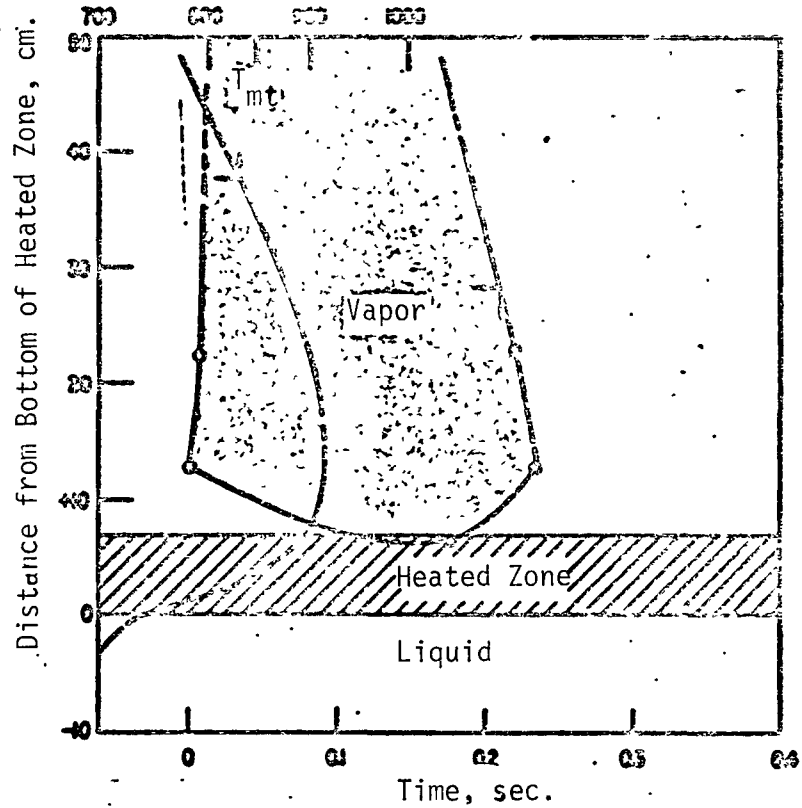
B. INTERNAL BOWING (DETAIL)



- NOTE:
- . ARROWS (\blacktriangledown) REPRESENT CLAD TEMPERATURE THERMOCOUPLE
 - . CROSSES (x) REPRESENT LOCAL COOLANT TEMPERATURE THERMOCOUPLES

Fig. XX.7

LIQUID TEMPERATURE AT INCIPIENT BOILING, °C

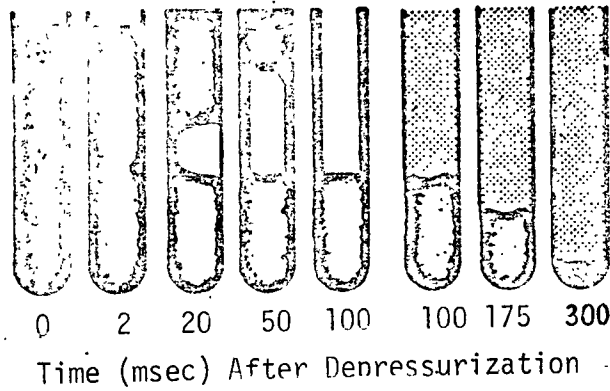


ONE-DIMENSIONAL TRANSIENT MAP OF LIQUID-VAPOR INTERFACE DURING SODIUM EXPULSION TEST IN WHICH LIQUID SUPERHEAT ΔT_s WAS 57 °C, SATURATION TEMPERATURE T_s WAS 850 °C, WALL HEAT FLUX q_w WAS 66.0 W/cm², HEIGHT OF LIQUID COLUMN ABOVE HEATER L_0 WAS 94 CM, AND HEIGHT OF HEATED ZONE L_h WAS 7.0 CM

Fig. XX.8

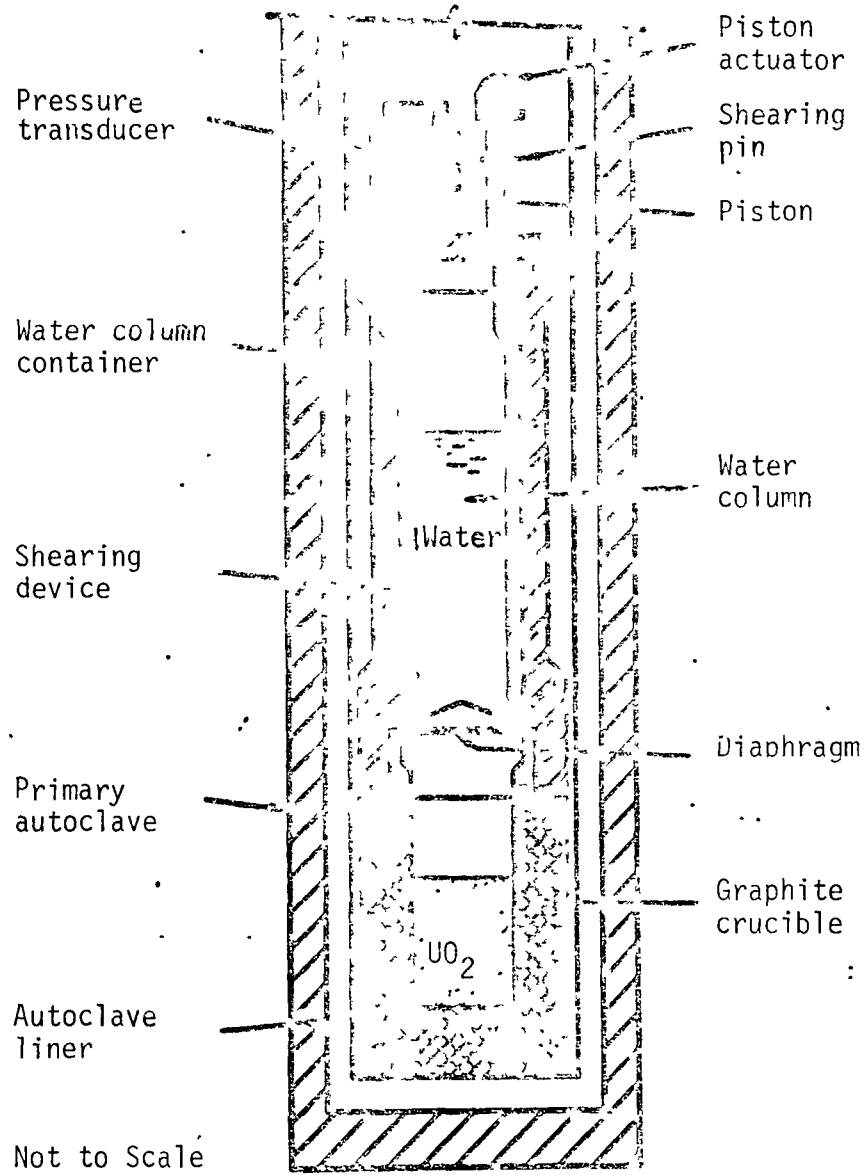
BOILING OF SUPERHEATED LIQUID
 BEGINS AT NUCLEATION SITES. BOILING IN-
 TENSIFIES LIQUID IN CHANNEL. AFTER
 NUCLEATION BEGINS, IT
 EXPELS LIQUID FROM TOP OF
 CHANNEL.

LIQUID SLUG DEPARTING FROM
 CHANNEL DEPRESSURIZES RE-
 MAINING LIQUID, CAUSING IT
 TO BOIL PROGRESSIVELY FROM
 SURFACE



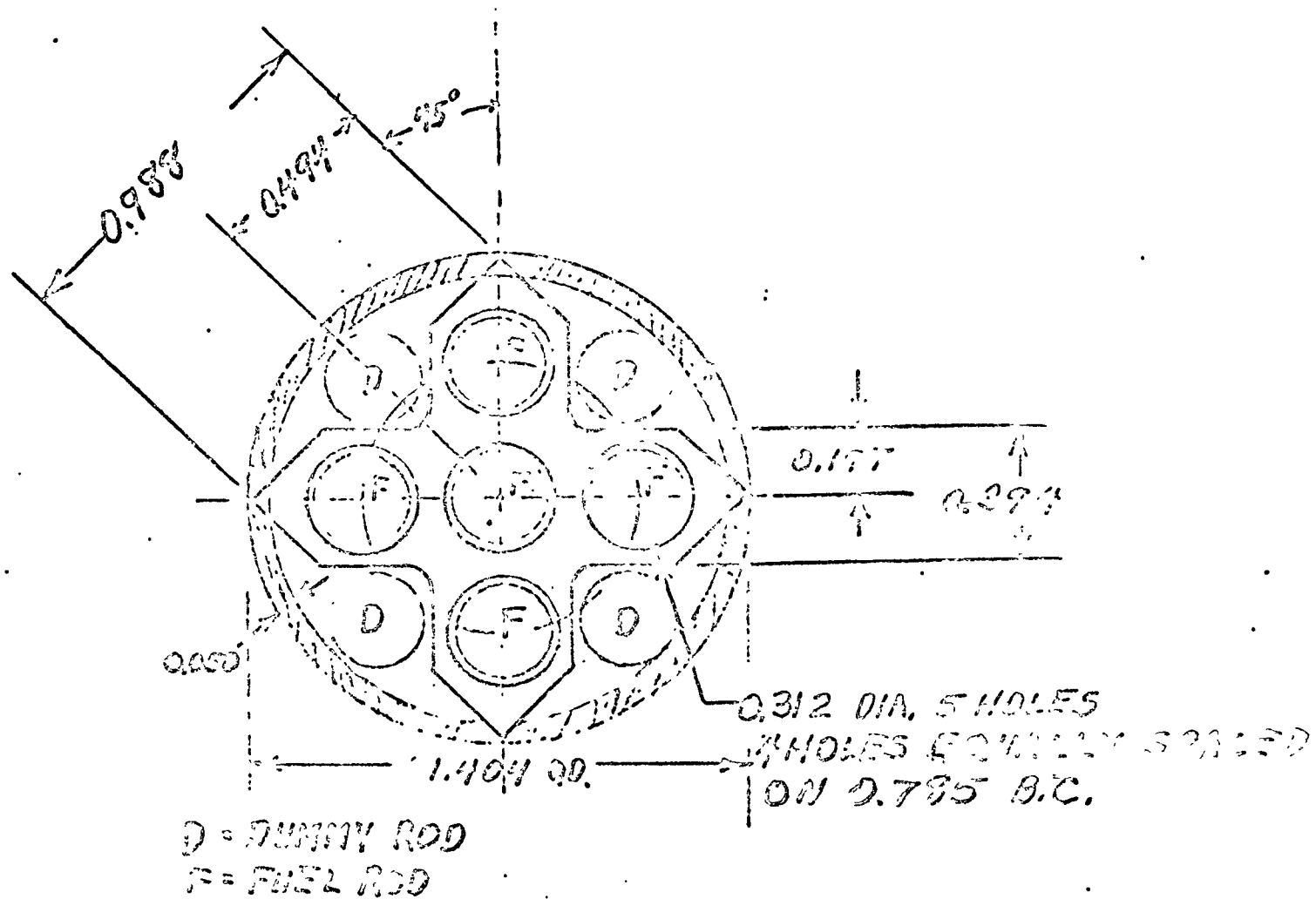
BOILING AND EXPULSION PATTERNS OBSERVED AFTER
 ATMOSPHERE ABOVE CHANNEL CONTAINING FREON-11
 IS SUDDENLY DEPRESSURIZED, CAUSING FREON TO
 BE SUPERHEATED INSTANTANEOUSLY

Fig. XX.9



APPARATUS FOR TREAT FACILITY WILL
EVALUATE CONSEQUENCES OF WATER
OCCURRING IN CONTACT WITH MELTED UO₂

Fig. XX.10



Stainless Steel Fuel Specimens Positioned
in Zircaloy Spacer

Fig. XX.11

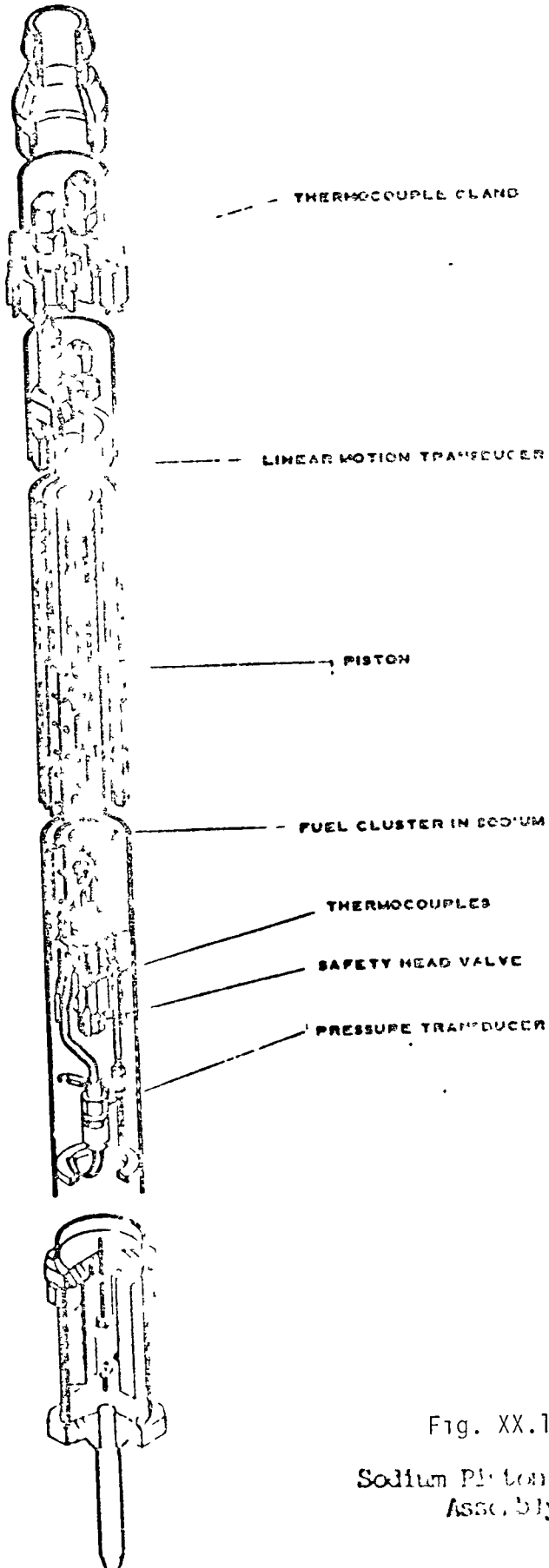


Fig. XX.12

Sodium Piston Autoclave
Assy. 51y

XX.60

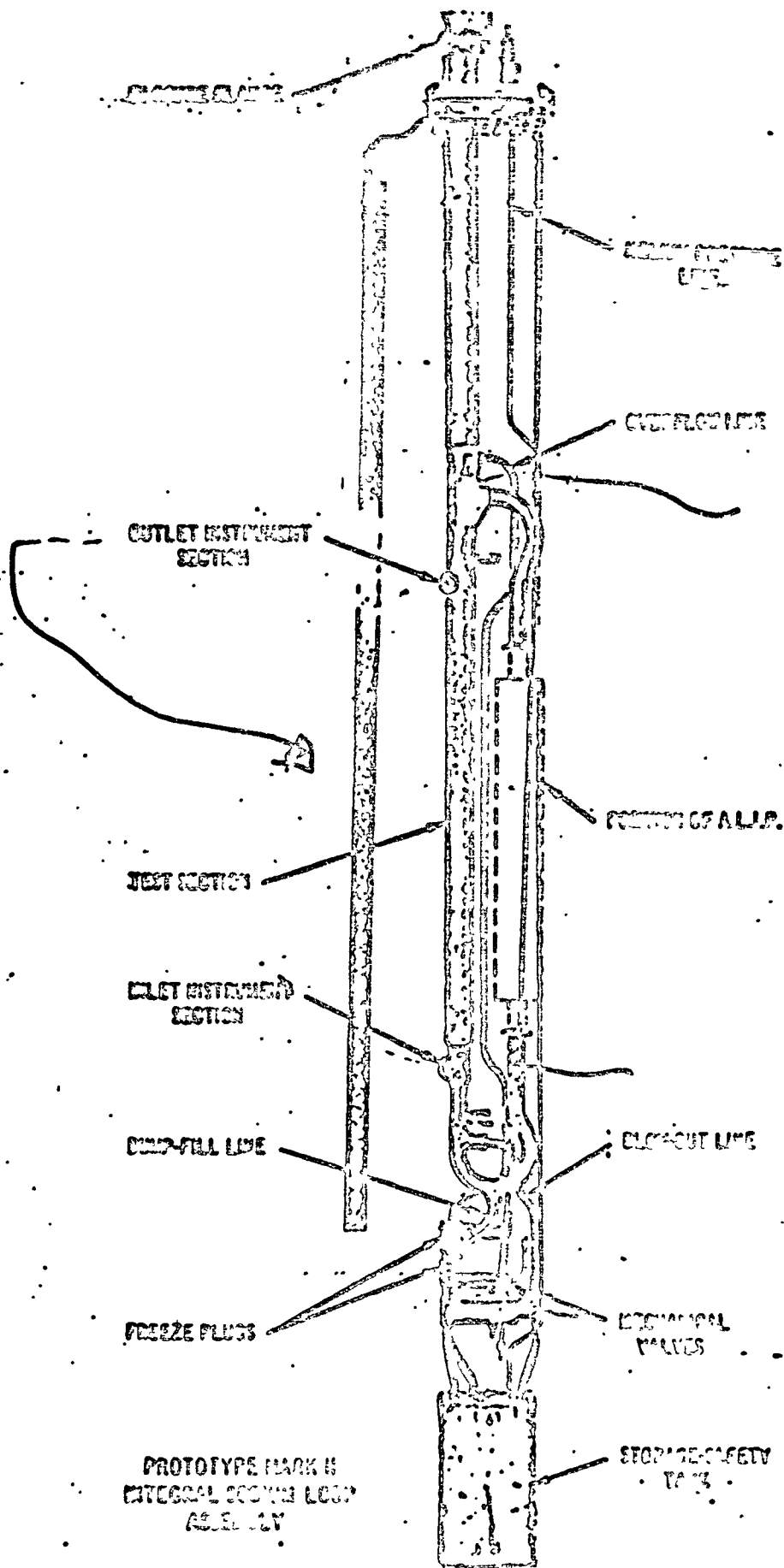


Fig. XX.13

Prototey Mark II Integral Sodium Loop Body

SODIUM VOIDING AND REENTRY FOR INSTANTANEOUS COMPLETE SUBASSEMBLY BLOCKAGE

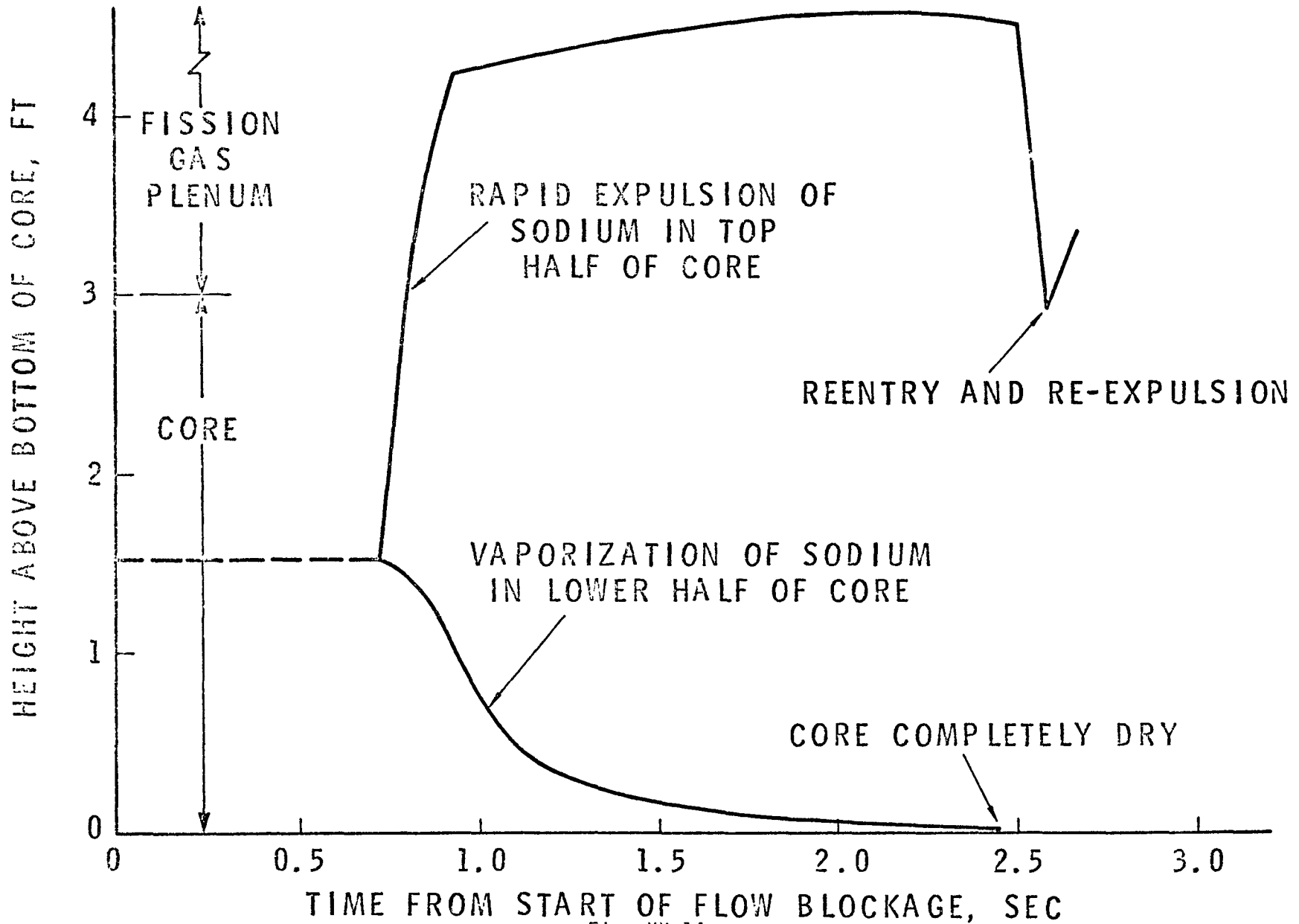


Fig. XX.14

ENERGY ABSORPTION CAPABILITY OF DUCT WALL

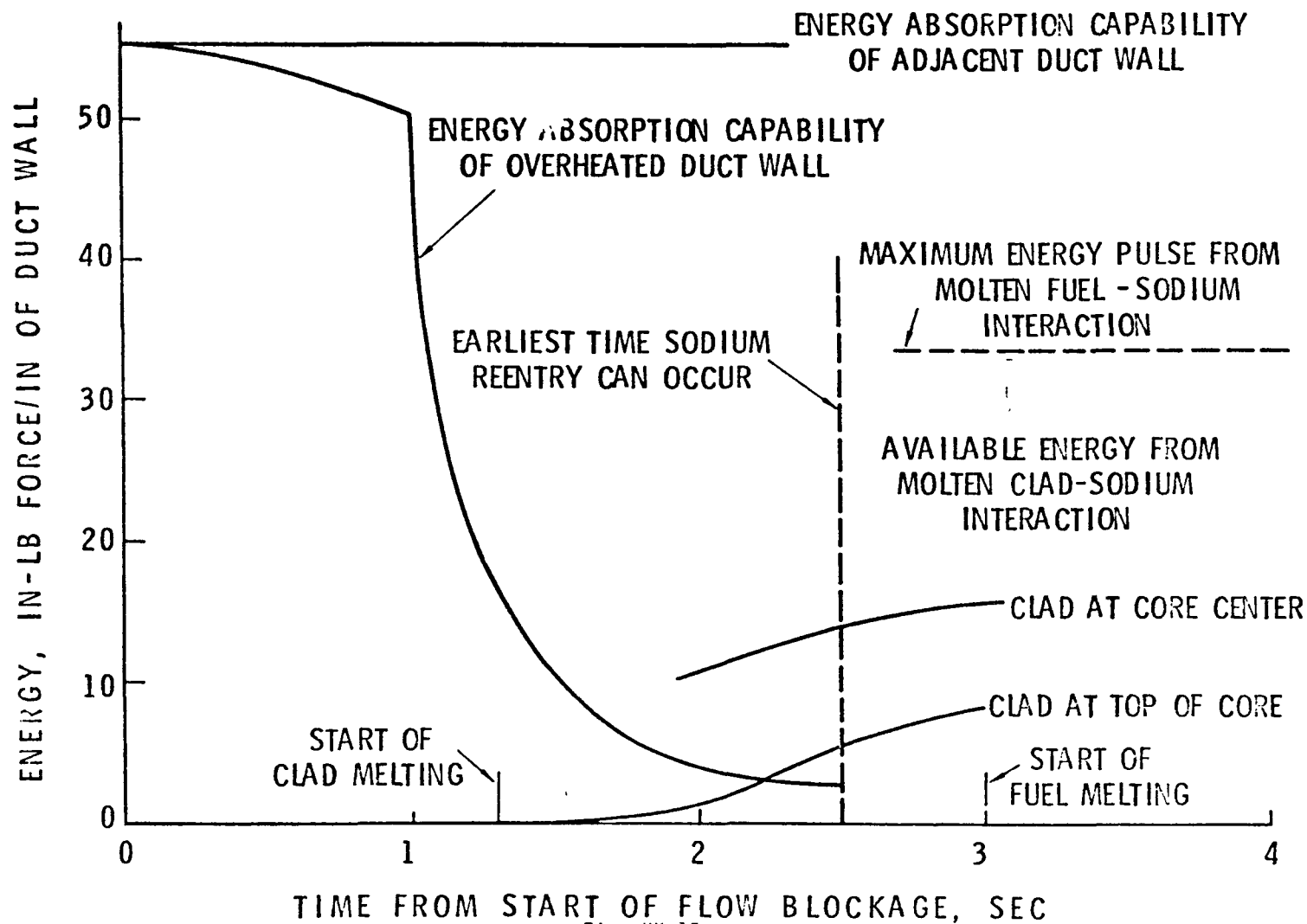


Fig. XX.15

XX.62

HYDRAULIC MODEL INLET PLENUM SECTION

AIR INJECTION POINTS

1. INTO 1 OF 8 DOWNCOMER PIPES
2. DIRECTLY INTO BASKET REGION

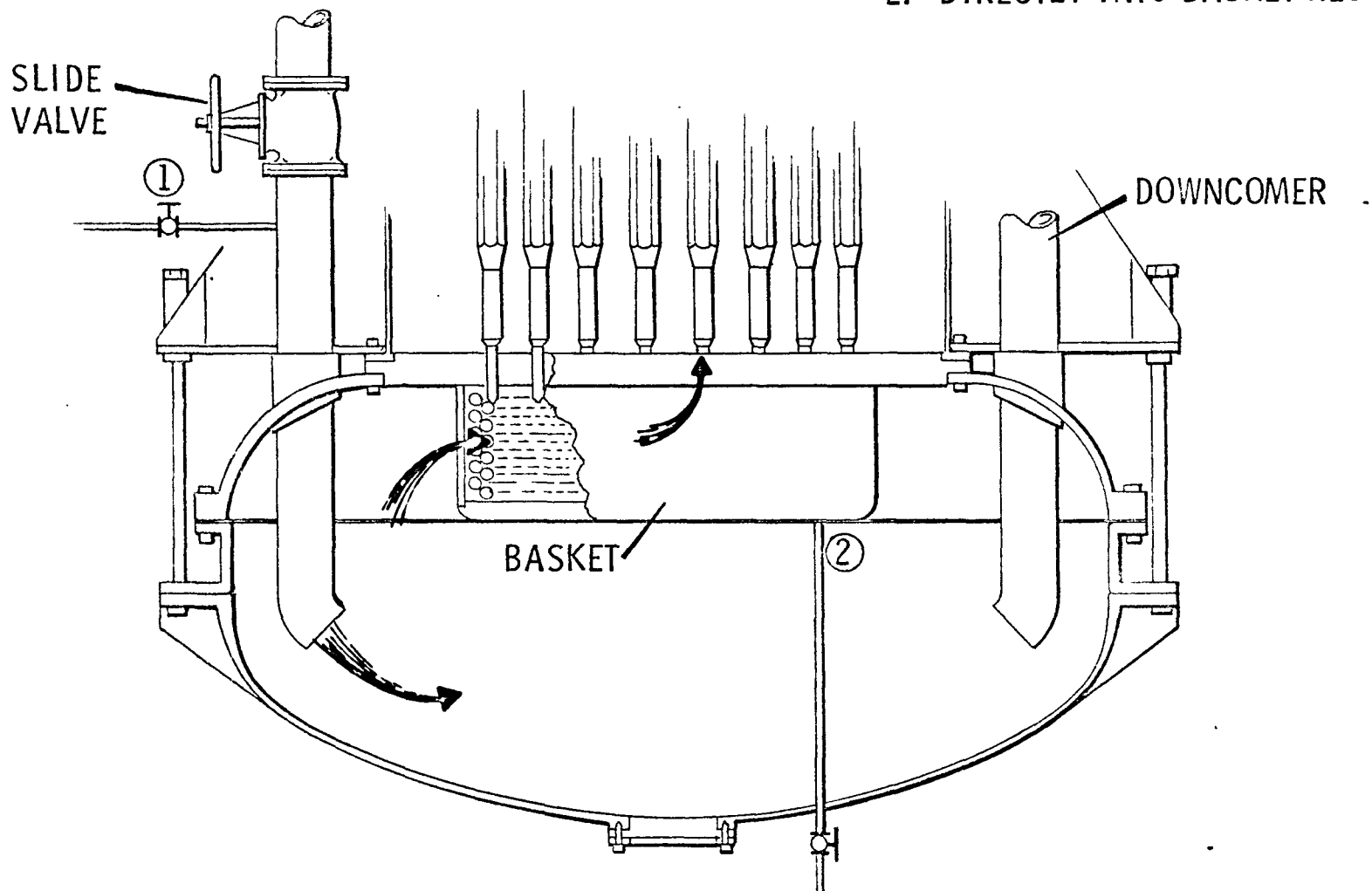
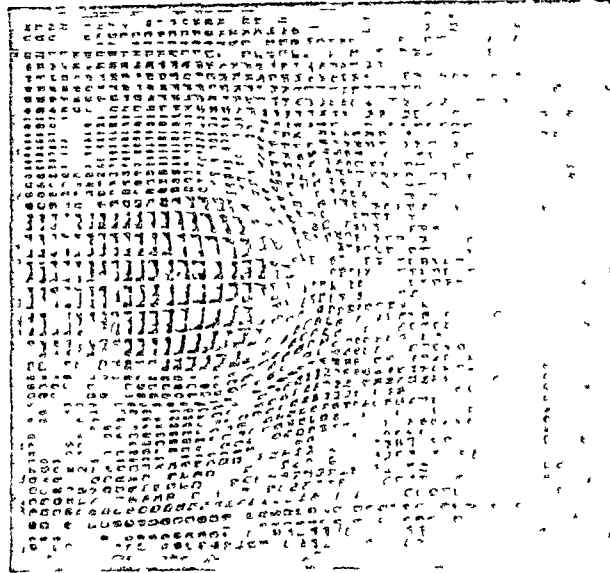


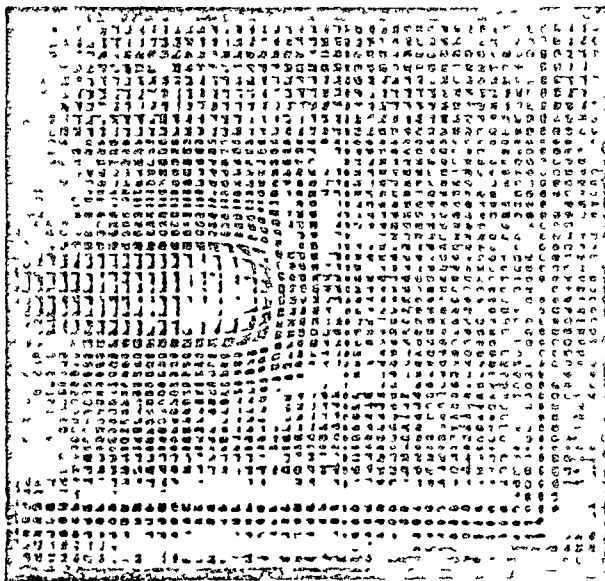
Fig. XX.16



$t = 0 \text{ sec}$



$t = 62.2 \mu\text{sec}$



$t = 322 \mu\text{sec}$



$t = 10.75 \text{ msec}$

Fig. XX.17

DEFORMATIONS OF LAGRANGIAN GRIDS AT VARIOUS TIMES
AFTER START OF A POWER EXCURSION IN A "PANCAKE"
CORE CONFIGURATION

REFERENCES

- Tables XX.1
and XX.2 LMFBR Liquid Metal Fast Breeder Reactor Program Plan, "Safety," Vol. 10, WASH-1170, August 1968
- Figure XX.2 J. F. Schuman, et al. "Fuel Element Failure Propagation Program Plan," ANL/MET-01, Argonne National Laboratory, Argonne, Illinois, August 1969.
- Figure XX.3 Letter, J. F. Schuman to J. W. Hagan (Transmittal of copies of slides used at the Fuel Failure Propagation Meeting, AEC Headquarters, September 30 and October 1, 1969), October 10, 1969.
- Figure XX.4 R. E. MacPherson, M. H. Fontana. "Fuel Failure Mockup Program Plan," ORNL-TM-2529, Oak Ridge National Laboratory, Oak Ridge, Tenn.
- Figure XX.5 Letter, M. H. Fontana to J. W. Hagan (Transmittal of copies of slides used at the Fuel Failure Propagation Meeting, AEC Headquarters, September 30 and October 1, 1969), October 8, 1969.
- Figures XX.6
and XX.7 J. M. Yatabe, et al. "Fast Reactor Fuel Assembly Thermal Hydraulic Development Program - Sodium Heat Transfer," BNWL-1136, Battelle-Northwest, Richland, Washington, February 1970.
- Figure XX.8 Reactor Development Program Progress Report - August 1969, ANL-7606, Argonne National Laboratory, Argonne, Ill.
- Figure XX.9 Reactor Development Program Progress Report - March 1969, ANL-7561, Argonne National Laboratory, Argonne, Ill.
- Figure XX.10 Reactor Development Program Progress Report - July 1969, ANL-7595, Argonne National Laboratory, Argonne, Ill.
- Figure XX.11 Letter, C. E. Dickerman to J. W. Hagan (Transmittal of information on the TREAT Autoclave Experiments), August 21, 1969.
- Figure XX.12 Reactor Development Program Progress Report - May 1968, ANL-7457, Argonne National Laboratory, Argonne, Ill.

REFERENCES (contd)

- Figure XX.13 C. E. Dickerman. "ANL TREAT Program of Fast Reactor Experiments, - Fuel Meltdown Studies in TREAT," Argonne National Laboratory, Argonne, Ill., October 7, 1969.
- Figures XX.14 and XX.15 L. M. McWetny. An Analytical Evaluation of the Consequences of a Hypothetical Instantaneous Loss of Coolant Flow to a Fast Flux Test Facility Driver Fuel Assembly, GEAP-10059, General Electric Co., Breeder Reactor Development Operation, Sunnyvale, California.
- Figure XX.17 Reactor Development Program Progress Report - February 1969, ANL-7553, Argonne National Laboratory, Argonne, Ill.